THE NEOGENE DEVELOPMENT OF THE EASTERN MEDITERRANEAN SEA AS MANIFESTED IN AND NEAR THE RHODES BASIN: AN INSIGHT INTO ARC-ARC JUNCTIONS

JONATHAN DION WINSOR

THE NEOGENE DEVELOPMENT OF THE EASTERN MEDITERRANEAN SEA AS MANIFESTED IN AND NEAR THE RHODES BASIN: AN INSIGHT INTO ARC-ARC JUNCTIONS

by

© Jonathan Dion Winsor

A thesis submitted to the

School of Graduate Studies

in partial fulfilment of the

requirements for the degree of

Master of Science

Earth Science/Memorial University of Newfoundland/Science

Memorial University of Newfoundland

September, 2004

St. John's Newfoundland

Abstract

New multi-channel seismic data were acquired by Memorial University of Newfoundland (MUN) over the Rhodes Basin, eastern Mediterranean Sea, during the summer of 2001. Imaging challenges imposed by the deep water depth, short receiver array and channel and frequency specific noise were overcome by careful data processing. The final processed data generally yields good image quality for the first 1.5 seconds below the seabed with significant improvements in areas where the geology is simple and the Pliocene-Quaternary basin fill is thick .

The Rhodes Basin is a deep (~4400 m) bathymetric trough located near the junction between the Hellenic and Cyprus Arcs. On the basis of this study, two major seismic-stratigraphic units are identified and described in detail: a pre-late Miocene unit (Eocene-Miocene) and a Pliocene-Quaternary unit separated by a laterally extensive unconformity, interpreted in this work as the M reflector. Hence, unlike most of the eastern Mediterranean, the Rhodes Basin has not preserved its Messinian stratigraphy (e.g., Messinian evaporites). This suggests that, since the late Miocene, it developed somewhat independently from the remainder of the eastern Mediterranean since the late Miocene.

Analysis of structural and stratigraphic architectures reveals that the Rhodes Basin can be divided into three structural domains: a) Domain 1- the heavily sheared plateau, b) Domain 2- the folded and faulted deep Rhodes Basin and c) Domain 3- the Turkish continental slope. Structural and stratigraphic relationships within and between these structural Domains suggest that the Rhodes Basin has been subjected to two major episodes of deformation during the Neogene. The first deformation episode, P_1, is characterized by southeast-verging Miocene thrusting and uplift consistent with the emplacement of the Lycian Nappes to the northeast and fold/thrust complexes on the Island of Rhodes to the west. Following an early Pliocene period of regional subsidence associated with the opening of the Aegean Graben System, a middle Pliocene-Quaternary phase of northeast-southwest sinistral transpression (P_2) developed in response to an actively curving Hellenic Arc and the increasing obliquity of its eastern limb (Pliny-Strabo trench system) to the African Plate convergence vector. The middle Pliocene introduction of this strike slip deformation into the proto-Rhodes Basin re-activated the P_1 structural fabric as transpressional faults and facilitated rapid subsidence (~555-740 m/Ma) along its margins in a strike-slip pull-apart regime. The identification of a structural trend reminiscent of the Cyprus Arc and Hoyran-Beysehir Nappes along the eastern margin of the Rhodes Basin suggest that the Rhodes Basin marks the apex of the structurally complex Hellenic Arc/Cyprus Arc junction.

Acknowledgements

I extend appreciation to my parents for their ever-present support and interest in my university education. I would also like to thank my friends and fellow graduate students in the Department of Earth Sciences (MUN) for providing moments of escape from my studies and for the countless memories that I now cherish.

I thank my supervisors, Dr. Jeremy Hall and Dr. Ali Aksu for their guidance during the synthesis of this thesis, Dr. Sharon Deemer for her assistance with the data processing and Anthony Kocurko for his technical support.

Financial support from NSERC to the author in the form of a PGS A grant enabled this project to be completed without interruption. Additional NSERC research funds to Dr. Jeremy Hall and Dr. Ali Aksu permitted the purchase of ship time and equipment used during the seismic acquisition cruise of 2001. I would like to recognize the efforts of the officer and crew of the research vessel *K. Piri Reis* during the 2001 cruise. This thesis also benefited from seismic processing software donated by Landmark Graphics Corporation.

Order of Contents

List of Tables

List of Figures

List of Abbreviations and Symbols

α: Ridge.
AB: Antalya Basin.
AF: Amanos Fault.
AGC: Automatic Gain Control.
AGS: Aegean Graben System.
AM: Anaximander Mountains.
AVA: Aegean Volcanic Arc.
β: Basin.
BFZ: Burdur Fault Zone.
BOS: Base of slope.
BZ: Bitlis Suture.
CA: Cyprean Arc.
CB: Cilicia Basin.
CFZ: Cephalonia Faullt.
DST: Dead Sea Transform Fault.
ε: Bathymetric escarpment.
EAT: East Anatolian Transform Fault.
ES: Eratosthenes Seamount.
FB: Finike Basin.
FR: Florence Rise.
GMT: Generic Mapping Tools (contouring software).
HA: Hellenic Arc.
HB: Herodotus Basin.
HBN: Hoyran-Beyşehir Nappes.
IA: Isparta Angle.
IB: Ionian Basin.
IBCM: International Bathymetric Charts of the Mediterranean.
IT: Ionian Trench.
KR: Kyrenia Rise.
LB: Latakia Basin.
LN: Lycian Nappes.
LvB: Levant Basin.
MR: Mediterranean Ridge.
MTL: Median Tectonic Line.
NAT: North Anatolian Transform Fault
PT: Pliny Trench.
PtT: Ptolemy Trench.
PST: Pliny-Strabo trench system.
RB: Rhodes Basin.
SAS: Southern Aegean Sea.
SF: Sungurlu Fault.
ST: Strabo Trench.
T: Thrust Fault.

List of Appendices

Chapter 1: Introduction

1.1: Scope of the Project

Tectonic plates change size and shape due to modifications that occur primarily at their edges- such as subduction at ocean trenches, generation of new oceanic lithosphere at mid-ocean ridges and accretion due to collision. These processes are slow (e.g. 1-10 cm/yr), but the surface of the Earth undergoes significant change on time scales of millions of years. Figure 1.1.1 illustrates the correlation between major plate boundaries and large morphological features such as ocean basins and mountain ranges along the Alpine-Himalayan belt.

Arcs are curved plate boundaries associated with subduction. Assuming unidirectional plate convergence, the angle between an arc and the plate convergence vector vary along the arc. There may be a section along an arc where it is near perpendicular to the vector while at some distance away the arc may be near parallel to the vector. In the former case, thrust/fold tectonics may characterize the plate edge deformation, whereas in the latter, horizontal strike slip shearing may predominate. Where arcs join at right angles, the junctions may mark a transition from thrusting along one arc to strike-slip along the other. Our understanding of arcs is still so incomplete that we still find ourselves asking fundamental questions regarding their character such as: What initiates plate subduction? Why are plate boundaries associated with subduction

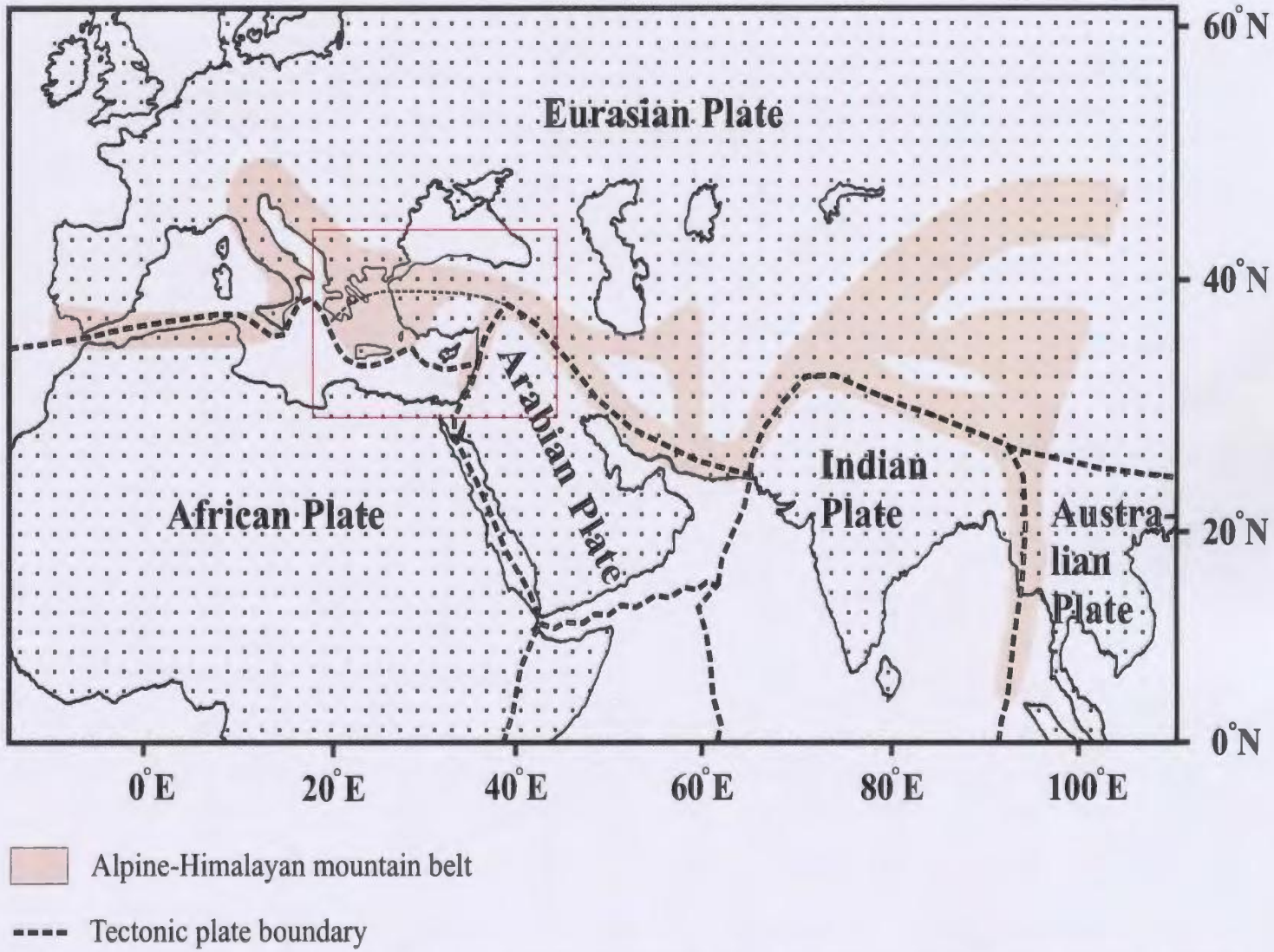

Figure 1.1.1: A schematic map of the major tectonic plates in the vicinity of the Alpine-Himalayan mountain belt. The red square outlines the region of convergence between the Eurasian, African and Arabian Plates considered in this study (enlarged in Fig. 1.1.2). Modified from Papazachos, Karakaisis, Papadimitriou and Papaioannou (1997).

commonly arcuate? How do arcs evolve and what is their final stage of development?

The two arcs of concern in this thesis are the Hellenic and Cyprus arcs, eastern Mediterranean (Fig. 1.1.2). They mark a convergent deformation zone between the Eurasian Plate to the north and the African and Arabian Plates to the south (Fig. 1.1.2). The nearly orthogonal intersection of these two arcs somewhere near southwestern Turkey (point A in Figure 1.1.2) is likely a focus for stress concentration leading to high strain. The Anatolian/Aegean Microplate is trapped in this nearly north-south convergence in the Alpine-Himalayan deformation zone. This thesis represents an increment in the understanding of this region, as the arcs change from subduction to collision, and contributes to the global understanding of arc junctions. This chapter examines the expected characteristics of arc-arc junctions and sets the Hellenic-Cyprus Arc junction within its regional tectonic framework.

One of the most throughly studied regions of active plate interactions around arc junctions is the Japanese Islands; a narrow region where the Eurasian, Pacific and Philippine Sea Plates join at a trench-trench-trench junction. In an effort to document what types of features may be present in zones of complex plate convergence, a brief investigation of this region is provided before exploring the junction between the Hellenic and Cyprus Arcs.

1.2: The Japanese Subduction Zone - a source of insight

The Japan triple junction represents the intersection of three major trench systems

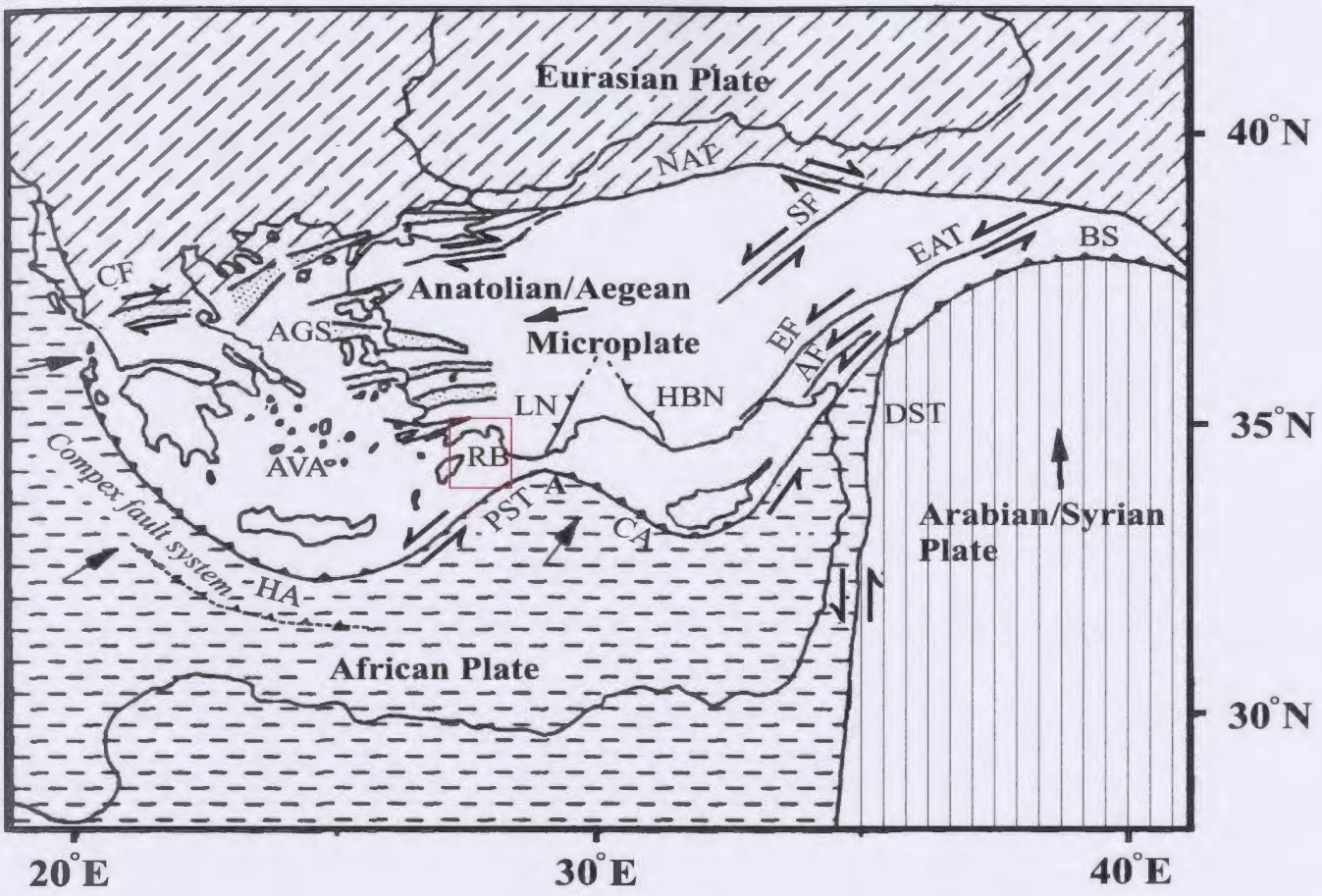

Figure 1.1.2: Simplified tectonic map of the eastern Mediterranean Sea and surrounding regions. The study area of this thesis is outlined in red. CF=Cephalonia Fault, HA= Hellenic Arc, AVA=Aegean Volcanic Arc, AGS=Aegean Graben System, RB=Rhodes Basin, PST=Pliny-Strabo Trench system, LN=Lycian Nappes and HBN=Hoyran-Beysehir Nappes (together outlining the Isparta Angle), CA= Cyprus Arc, NAT=North Anatolian Transform fault, EF=Ecemiş Fault, AF=Amanos Fault, SF=Sungurlu Fault, DST=Dead Sea Transform fault, EAT=East Anatolian Transform fault, BS= Bitlis Suture. Full-headed arrows indicate the direction of plate motion relative to a fixed Eurasian Plate. Half-headed arrows indicate relative motion across a fault plane. Northward subduction is occurring along the Hellenic Arc but not along the Cyprus Arc. Both arcs, especially the Hellenic Arc are a consequence of complex faulting (Huguen et al. 2001). Point A, where the Hellenic and Cyprus arcs intersect near the Rhodes Basin, may be a location of stress concentration. The location of this figure is outlined in Figure 1.1.1. Modified from Aksu et al. (1992).

that are each comprised of differently oriented smaller trench segments. These trench systems collectively delineate the convergence zone between the Pacific, Eurasian and Philipine Sea Plates (Fig. 1.2.1). The different orientations of these plate boundaries relative to the plate convergence results in a variety of deformation styles.

Northeast of the Japan triple junction, the Pacific Plate subducts obliquely beneath the Eurasian Plate along the northeast-southwest-trending southwest Kuril Trench (Fig. 1.2.1). The resulting Tertiary to Quaternary volcanic islands (southwest Kuril Arc) are arranged in an *en-échelon* fashion with a dextral-sense movement between the frontal and volcanic arcs (Kamata and Kodama, 1994). This strike slip motion is terminated at the intersection of the southwest Kuril Arc with the northeast Japan Trench where the change in trench orientation favours orthogonal subduction (Fig. 1.2.1). At the gently curved junction between these trenches, approximately east-west compression is dominant and has resulted in the development of the north-south-trending Hidaka Mountains (Fig. 1.2.1; Kimura, 1986). The northeast portion of the southwest Kuril Arc displays a well developed graben-style basin oriented perpendicular to the arc; indicating a northeast-southwest tensional stress field complementary to the northwest-southeast-directed compressional regime (Kimura, 1986). This example of trench intersection illustrates how even modest changes in the subduction trench azimuth with unidirectional plate motions can encourage the development of compressional, extensional, and transverse structural expressions in a small geographic area.

Forearc sliver translation is also occurring along the southwest portion of the

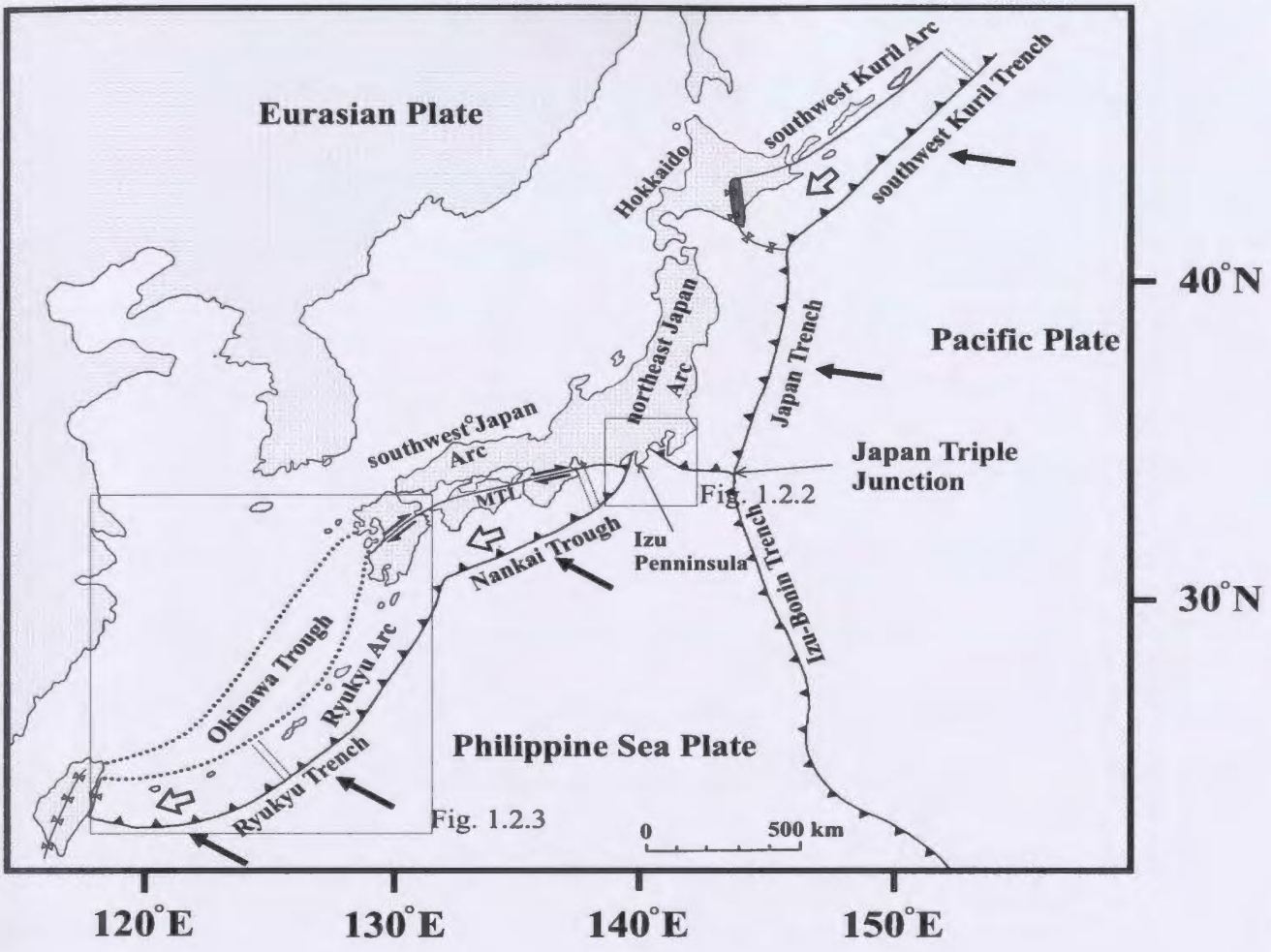

Hidaka mountains
Subduction direction
Convergence zone
Direction of plate motion
Extension zone
Direction of forearc sliver motion
MTL= Median Tectonic Line

Figure 1.2.1: Tectonic map of the Japan subduction zone modified from Kamata and Kodama (1994).

Japan Arc between the Nankai and Ryukyu troughs, where subduction is dominantly oblique, and the Median Tectonic Line (MTL)- a major, east-west-trending strike slip fault exposed for ~ 900 kilometres on land (Fig. 1.2.1) (Kamata and Kodama, 1994). Motion along the MTL was sinistral during the late Cretaceous but dextral since the late Miocene when the Philippine Sea Plate is known to have resumed northwestward subduction following a possible 5 million years cessation (Kamata and Kodama, 1994). This strike slip translation is terminated by the collision of the forearc sliver with Taiwan (Fig. 1.2.1) (Kamata and Kodama, 1994). In contrast to the dominantly strike slip character of the Nankai Trough convergence zone, the highly curved nature of the Ryukyu Arc encourages oblique trench retreat near its northern and southern ends (Kamata and Kodama, 1994). This trench retreat may be responsible for the clockwise rotation of the Okinawa trough and the forearc sliver near Taiwan (Fig. 1.2.2; Kamata and Kodama, 1994).

Since the middle Miocene, the acute convergence between the Suruga and Sagami troughs just inland of the Izu Peninsula has played a major role in determining the strain partitioning at the plate boundary between the Philippine Sea Plate and the Eurasian Plate (Fig. 1.2.3) (Mazzotti, Henry, Le Pichon and Sagina, 1999). The Izu Peninsula itself is divided into eastern and western sections by a north-northeast-south southwest-trending sinistral strike slip fault. The western zone shows conjugate sets of strike slip faults as well as east-west striking low angle reverse faults that imply a dominant northeast-southwest to north-south compression axis (Ida, 1991).

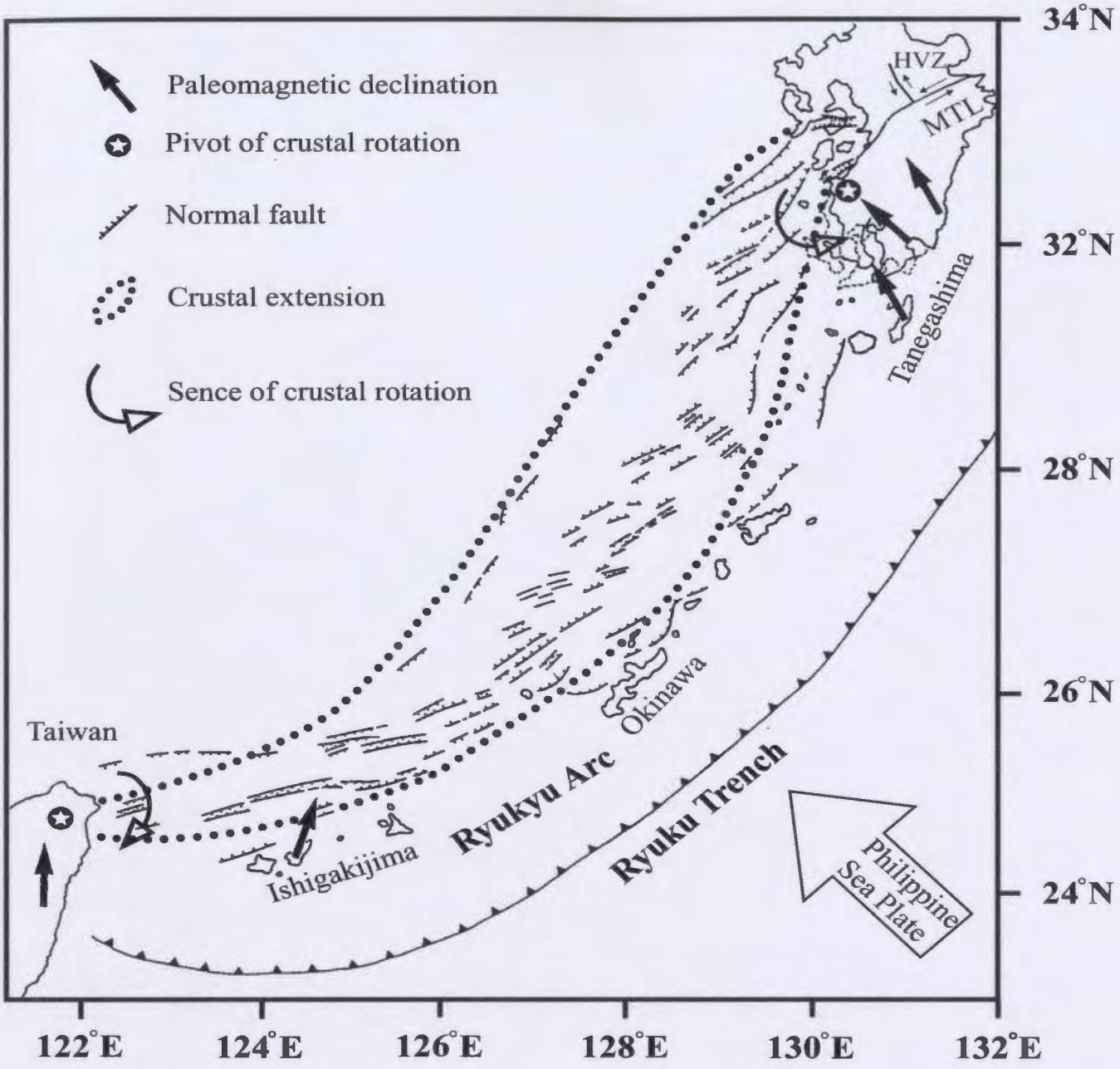

Figure 1.2.2: Crustal extension and rotation along the Ryukyu Arc. HVZ=Hohi Volcanic Zone, MTL=Median Tectonic Line. Modified from Kamata and Kodama (1994). The location of this figure is shown in Fig. 1.2.1.

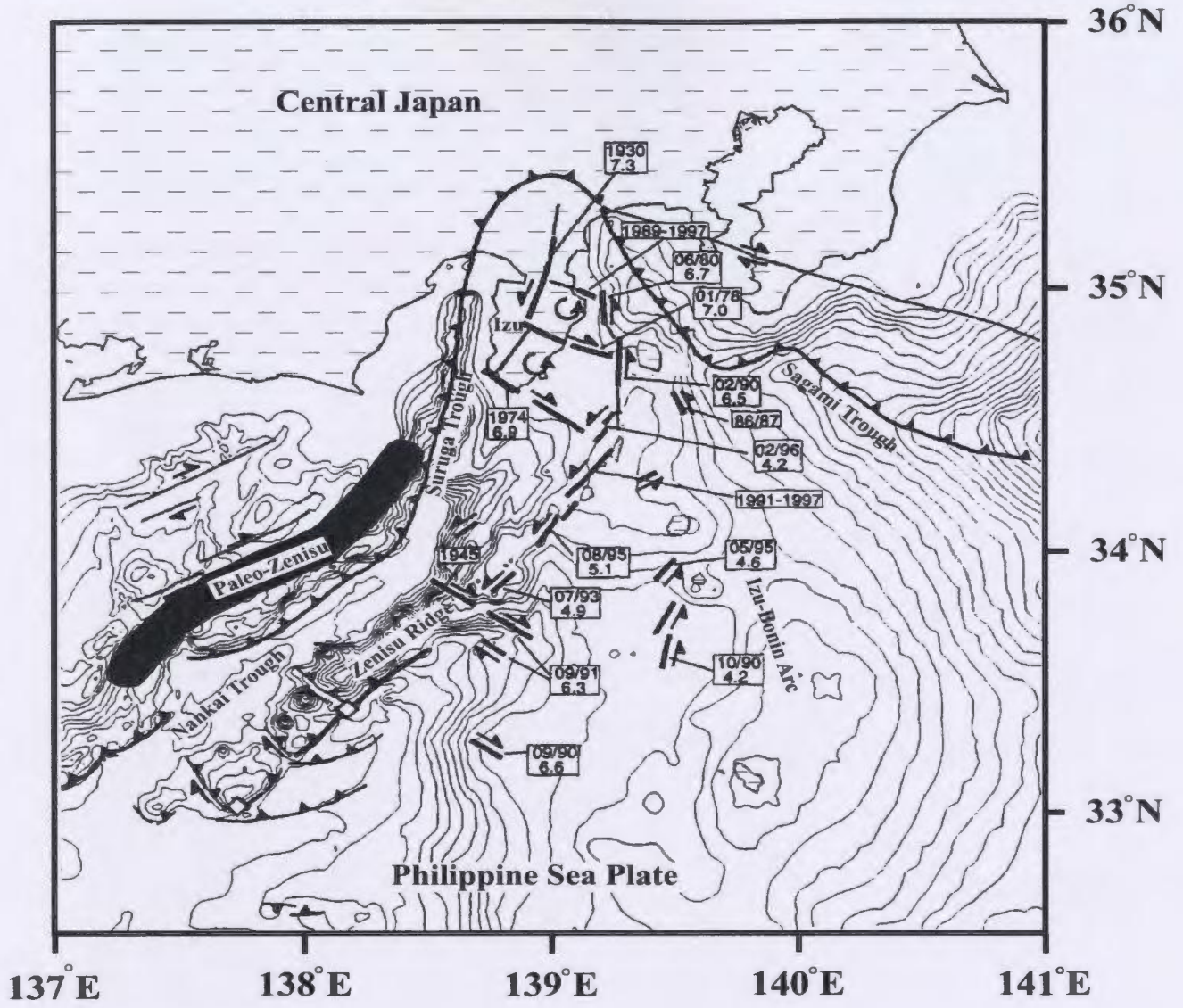

Figure 1.2.3: Deformation of nertheastern Philippine Sea Plate modified from Mazzotti et al. (1999). Dates and magnitudes of most important earthquakes are shown. The paleo-Zenisu body is interpreted from magnetic data. The location of this figure is shown in Fig. 1.2.1.

Paleomagnetic data suggests that the western Izu block has accommodated 10°-30° of clockwise rotation since its collision with the central portion of the Japan Arc in the late Pliocene (Mazzotti et al.,1999). The eastern block is dominated by a conjugate set of east-west to northwest-southeast dextral faults and north-south to northeast-southwest sinistral faulting (Fig. 1.2.3; Ida, 1991). In addition, 10°-30° of counterclockwise rotation has occurred in the eastern block since the late Pliocene (Mazzotti et al.,1999). The separate stress fields for the east and west blocks may be the result of the opposing slab pull forces of the Suruga and Sagami troughs (Fig. 1.2.3). It is conceivable that independent movement of eastern and western Izu may be permitted by thermal weakening of the crust due to the presence of the north-south trending Izu-Bonin Arc and mechanical separation of the blocks assisted by northeast-southwest trending sinistral strike slip shear zones (Mazzotti et al.,1999). Seismic activity from these sinistral faults along the Izu-Bonin Arc and fold structures within the Zenisu Ridge suggest that deformation may accommodate much of the oblique component of convergence and reduce the effective convergence rate of the Philippine Sea plate and Eurasian plate by nearly 30 percent (Mazzotti et al., 1999).

From the Japanese collision zone, it is clear that the kinematics of plate convergence will not be fully understood if we consider plates as internally rigid, homogeneous, indefinitely large blocks. Zones of structural weakness, created by either thermal weakening (e.g., Izu-Bonin Arc) or by the presence of pre-existing structures such as fold belts, fault systems or volcanic island arcs (e.g., Kuril and Ryukyu volcanic island

arcs), allow plates to interact plastically. Such predispositions are especially exploited along plate boundaries that demonstrate oblique plate convergence.

Like the Japanese collision zone, the African-Eurasian convergence zone contains ancient structural fabrics and volcanic island arcs that provide potential zones of weakness (discussed later). Unlike the Japanese example of arc convergence, the majority of the African-Eurasian plate boundary along the Hellenic and Cyprus arcs is normal to the plate convergence vector. Two regions of exception are the Pliny-Strabo trench system and the eastern limb of the Cyprus arc where the African-Eurasian plate boundary is near parallel to the plate convergence vector (Fig. 1.1.2). The intersection of the Hellenic and Cyprus arcs ('A' in Fig. 1.1.2), where the arc curvature is high, may encourage the development of multiple deformation modes (compressional, transpressional and extensional) in a relatively small geographic area.

1.3: Development of Southern Turkey and the Eastern Extent of the Hellenic Sedimentary Arc as Inferred from Land Geology

The present-day geology and structure of the eastern Mediterranean has developed in direct response to the opening and closing of two ancient seaways: the Paleotethys Sea, a Paleozoic to early Mesozoic seaway, and the Neotethys Sea, the seaway that joined the Atlantic and Pacific Oceans from the Mesozoic to early Tertiary (Bozkurt and Mittewede, 2001). Although nearly completely consumed, the Neotethys has not yet been entirely destroyed by subduction beneath the Eurasian Plate: the present day Mediterranean Sea

represents the last vestiges of this major seaway.

Turkey comprises much of the Anatolian portion of the Anatolian/Aegean Micro plate. The land geology of Turkey consists of a suite of dominantly east-west-trending micro-continental fragments and small ocean basins compressed together along five major sutures: the Izmir-Ankara-Erzincan, Intra-Pontide, Inner Tauride, Antalya, and Southeast Anatolian sutures (Bozkurt and Mittewede, 2001). Each suture retains complete or partial ophiolite complexes and ophiolitic mélanges (Fig. 1.3.1) (Robertson, 2000). The northernmost structural block, referred to as the Pontides, contains several largely dismembered meta-ophiolite assemblages interpreted to have been emplaced during the late Triassic during the closure of the Paleotethys (Bozkurt and Mittewede, 2001).

South of the Pontides, the uplifted Anatolide-Tauride Platform (Taurus Mountain Range) lies between the Southeast Anatolian and Izmir-Ankara-Erzincan sutures (Fig. 3.2.1). It documents the convergence between ocean terranes and the overriding Pointides from the north (Bozkurt and Mittewede, 2001) resulting in the early Tertiary destruction of the Neotethys Sea. The northern, Anatolide region of the Anatolide-Tauride Platform documents footwall metamorphism due to its proximity to this north-south compression and northward subduction. It consists of upper Triassic to Cretaceous limestone blocks within a highly tectonized matrix, metamorphosed clastics and deformed volcano-sedimentary rocks (Bozkurt and Mittewede, 2001). The southern, Tauride portion of the Anatolide-Tauride Platform occupies much of the land geology of southern Turkey. This

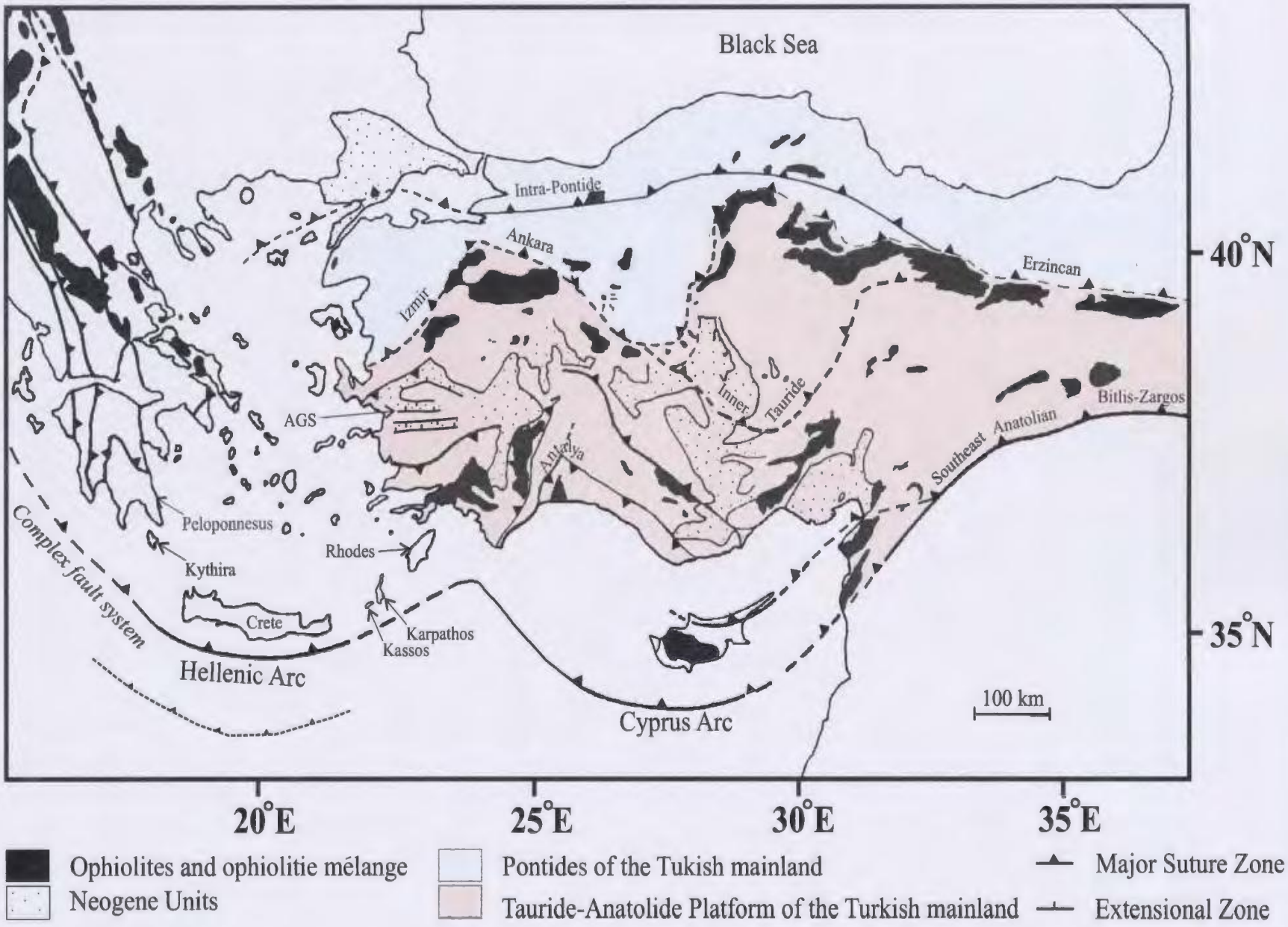

Figure 1.3.1: A simplified map of the Pontides and Anatolide-Tauride Platform (Taurus Mountains) of mainland Turkey showing the major suture zones and ophiolitic emplacements. AGS = Aegean Graben System. Modified from Robertson (2000).

mountain range is comprised of lower Paleozoic to lower Tertiary platform-type carbonates, turbidites, continental clastic rocks, and occasional ophiolites often tectonically emplaced along Tertiary nappes (e.g., Lycian Nappes; Bozkurt and Mittewede, 2001). Neogene-Quaternary basins filled with fluvial-lacustrine sediments unconformably overlie these deformed Paleozoic-lower Tertiary Neotethyan units. Based primarily on geography, the Taurides are divided into eastern, central and western segments (Fig. 1.3.2; Robertson, 2000).

The eastern segment of the Taurides is characterized by the Arabian-Eurasian convergence zone where Neotethyan-related units overthrust the Arabian continental margin along the Bitlis Suture (Figs. 1.3.1, 1.3.2). This suture marks the closure of the Bitlis ocean upon the north-south collision of Arabia with the eastern Anatolian segment of the Aegean/Anatolian Microplate during the middle Miocene (Fig. 1.1.2; Bozkurt and Mittewede, 2001). This terminal collision of the Arabian Plate with the Anatolian Segment of the Anatolian/Aegean Microplate is also accommodated along the sinistral/compressional East Anatolian Fault System and the sinistral/extensional Dead Sea Transform Fault (Fig. 1.3.2; Bozkurt and Mittewede, 2001).

The central Taurides consist of autochthonous Palaeozoic pre-rift platform units overlaid by Mesozoic carbonates that are, in turn, tectonically overthrusted by ophiolitic mélanges and dismembered ophiolites of Cretaceous age (Robertson, 2000). The northeast trending Misis-Andırın Complex is a major structure of the central Taurides (Fig. 1.3.2). In Turkey, the Misis Mountains are dominanted by volcanogenic turbidites

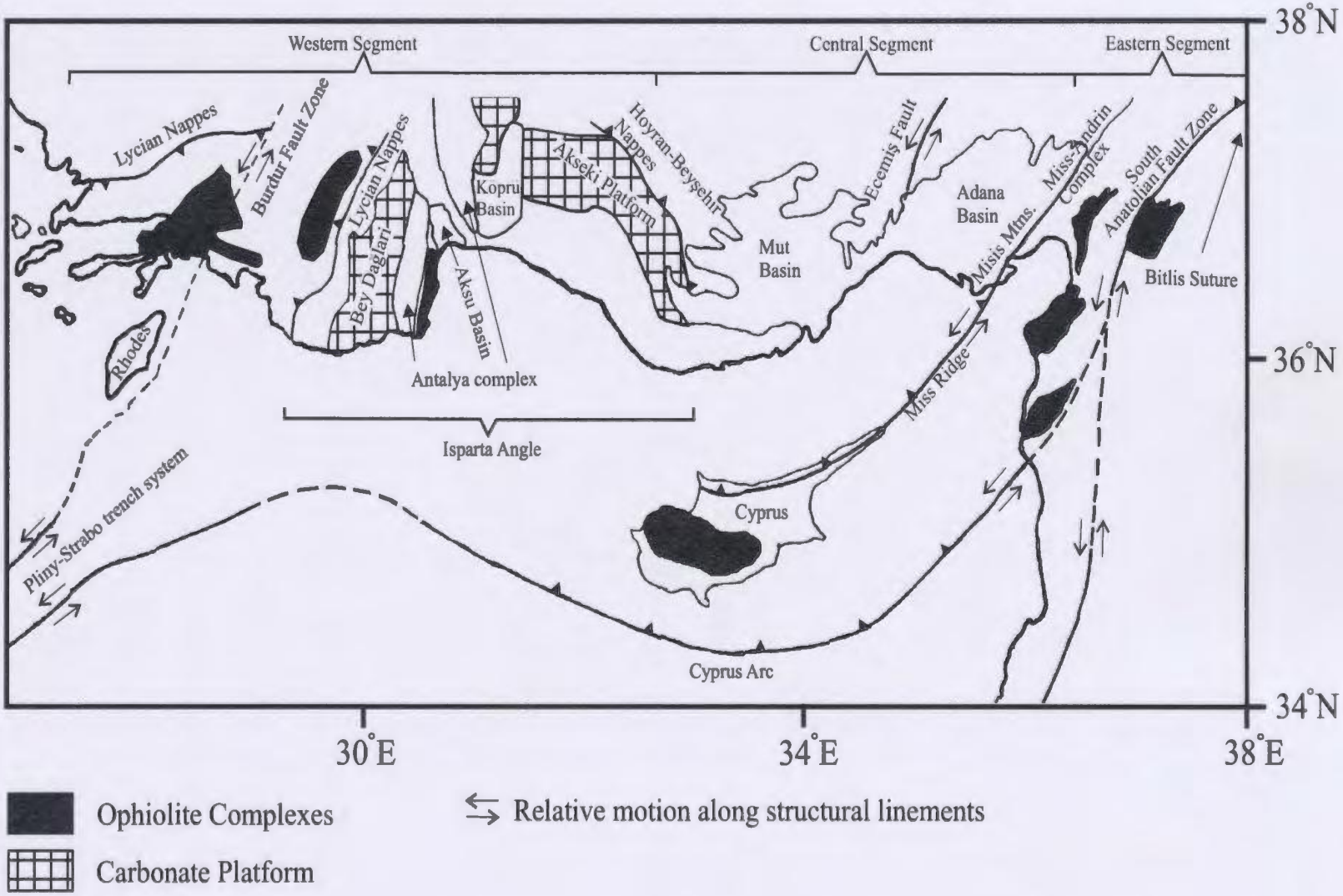

Figure 1.3.2: Simplified map of the Tauride Mountain Range showing its three segments with major geological units and structural lineaments. Modified from Robertson (2000).

(Karataş Formation) of early Miocene-late middle Miocene age overlain by a mélange of Mesozoic-Tertiary limestones, ophiolitic rocks and volcaniclastic blocks contained within late Oligocene-early Miocene calcareous claystone (Robertson, 2000). To the northeast, the Misis-Andırın Complex consists of Upper Cretaceous carbonates and Eocene mafic flows, volcaniclastics and bioclastic limestones and late Oligocene mass flows. Miocene basins such as the Adana and Mut Basins unconformably overlie these Neotethyan units (Fig.1.3.2; Robertson, 2000).

Within the western Taurides, the southwest-verging Hoyran-Beysehir Nappes overlie Mesozoic to Cambrian-Permian shallow platform lithologies (Fig. 1.3.2). The nappe package itself consists of late Paleozoic-Mesozoic platform carbonates, volcanic rocks, volcaniclastic sediments and ophiolites. The southeastward-thrusted Lycian Nappes overlie a Miocene, mainly terrigenous, turbiditic succession and underlying Bey Dağlari carbonate platform (Fig.1.3.2). These nappes are composed mostly of carbonate thrust sheets capped by late Paleozoic-Oligocene volcaniclastics and Eocene sedimentary rocks overthrusted by the Triassic-late Cretaceous Lycian Ophiolitic Mélange: a mélange of ocean related sediments and volcanic-sedimentary units that are, in turn, overthrusted by the Lycian Peridotite Thrust Sheet (Collins and Robertson, 1998). This entire nappe package is then unconformably overlain by supra-allochthon Palaeogene limestones (Robertson, 2000). Both the Hoyran-Beysehir and Lycian nappes are thought to be rooted in the closure of a northerly Neotethyan ocean basin. However, the Hoyran-Beysehir Nappes were emplaced during the late Eocene, whereas the Lycian Nappes were emplaced

during the late Miocene (Robertson, 2000). Positioned between these two nappe packages, the Bey Dağlari carbonate platform is overthrusted from the northwest by Triassic-late Cretaceous thrust-imbricated, deep water, passive-margin sediments and ophiolitic rocks, Paleozoic sedimentary rocks, Mesozoic shallow water carbonates and upper Cretaceous (Neotethyan) ophiolites to form the Antalya Complex (Robertson, 2000). Unlike the surrounding nappes, the Antalya Complex is dominated by high angle (strike slip?) faults to its east and west and low angle structures near the Isparta Angle Apex to its north. The Antalya Complex may represent the termination of a southerly Neotethyan oceanic basin (Robertson, 2000). To the west, the Burdur Fault Zone marks a northeast-southwest-trending lineament between the Lycian Nappes to its southeast and the east-west-trending Aegean Graben System to the northwest (discussed later) (Fig. 1.3.2). This fault zone has been interpreted as a sinistral strike slip zone that represents the northeast continuation of the Pliny trench (Barka et al., 1995). However, Price and Scott (1994) provide evidence that suggest the Burdur Fault Zone accommodates dominantly dextral-extensional stress by the clockwise rotation of small fault blocks between the shear zone boundaries.

Hence, the Isparta Angle marks the three-phase destruction of a Mesozoic oceanic basin that separated several large carbonate platforms; with evidence of each destruction phase preserved in the Hoyran-Beysehir Nappes, Lycian Nappes, and Antalya Complex respectively. Each of these regional structures in the western Taurides is unconformably overlain by Miocene-Pliocene basins. One such basin, the east-west trending Köprü

Basin, is filled with course delta conglomerates, patch reefs and sandy turbidites (Robertson, 2000). Further west, the Aksu Basin is believed to have developed during the lower Miocene and is infilled with lower Miocene transgressive limestones as well as mudstones, turbidites, and conglomerates that are interpreted to have been derived from the Lycian Nappes (Figure 1.3.2; Robertson, 2000).

Along the western extremity of Turkey, basin infilling has occurred in the Aegean Graben System- a series of large (up to 125 km long, 12 km wide) east-west trending grabens (Figs. 1.1.2, 1.3.1; Bozkurt, 2000). Based on the chronostratigraphic correlation of a well-distributed red sediment layer at the base of the Büyük Menderes Graben with those found elsewhere in western Anatolia, it has been suggested that the Büyük Menderes Graben has been active since the early-middle Miocene (Seyitoğlu and Scott 1991,1992). However, Bozkurt (2000) notes that the age of the red sediment unit is ill-constrained and has been found to be of late Pliocene-early Pleistocene age at other localities outside the graben system. Bozkurt (2000) suggests that the red colour is simply due to the oxidation of whatever sediments happened to be present at the surface during the Miocene-early Pliocene, a time when western Anatolia is known to have had a sub-tropical, highly oxidizing climate (Steininger and Rögl, 1984). Hence, these red sediments cannot be used for chronostratigraphic correlation. In addition, earlier work has grouped this lower red bed layer and the overlying Pliocene-Pleistocene sediments into a single, conformable, sequence package. However, more detailed study shows that the boundary between the horizontally layered Pliocene-Pleistocene deposits and the red sediments

found in the graben system is an angular unconformity, generated by the northward dip of the underlying red beds. These observations are not confined to the Büyük Menderes Graben, but are valid for many of the major east-west trending grabens in western Turkey (e.g., Gediz, Gökova, and Simav graben), implying uplift of the red beds and therefore an early Pliocene age for many of the grabens of the Aegean Graben System (Bozkurt, 2000). Another way of estimating the age of the Büyük Menderes Graben is to divide its total extension (~5 km) by the extension rate (~1 mm/yr). This yields a 5 Ma history of extension. An earlier phase of extension in western and central Anatolia is suggested by the presence of steeply dipping normal faults of Oligocene-lower Miocene age (Bozkurt, 2000). Hence, the extensional system in western Anatolia may represent two eras of unrest: an early Miocene stage of extension possibly due to the orogenic collapse of the Taurides followed by Pliocene rifting possibly attributable to the collision of the Arabian Plate to the east and subsequent development of the east-west-trending North Anatolian Transform Fault in conjunction with trench retreat to the south along the Hellenic Arc (Bozkurt, 2000).

Offshore from mainland Turkey, the Hellenic Sedimentary Arc -a forearc- is primarily composed of southern Greece (Peloponnesus) and five major Greek islands - from west to east: Kythira, Crete, Kassos, Karpathos and Rhodes (Fig. 1.3.1). Each island has a similar geological succession, with Neogene sediments resting discontinuously above Mesozoic-Tertiary Alpine nappes (Mascle et al., 1986). Crete is the largest and southernmost island of the Hellenic Sedimentary Arc (Fig. 1.3.1). Its geology consists of

Pleistocene alluvial deposits overlying shallow marine and late Pliocene sediments. An interval of deep marine sediments (marls and clays) occurs between the shallow marine sediments and early Pliocene debris flows that overlie the Messinian evaporites. The evaporites overlie a Neogene transgressive succession which, in turn, lies above pre-Neogene nappes (Ten Veen and Postma, 1999). Today, central Crete contains two large graben (the northern Heraklion Basin and the southwestern Messara Graben) along which much of the shallow, Recent seismicity is concentrated. Despite proximity to the Hellenic Arc convergence zone, families of shallow (< 60 km) extensional faults generally trend east-west in western Crete, northeast-southwest in central Crete and north northwest-south southeast in eastern Crete (Delibasis, et al., 1999). Ten Veen and Meijer (1998) recognize six major fault groups present in the central and eastern portions of Crete with average azimuths of 130, 100, 020, 075, 050, and 160. These trends have been interpreted as a record of the five-stage structural development of the Island of Crete since before the late Miocene (Fig. 1.3.3).

The second largest island, the island of Rhodes, represents the easternmost portion of the uplifted segment of the Hellenic Sedimentary Arc (Figs. 1.3.1 and 1.3.4). Its geology is dominated by the syn-tectonic deposition of late Miocene to middle Pliocene lacustrine sediments and a transgressive marine package of late Pliocene-early Pleistocene age (Ten Veen and Kleinspehn, 2002). These units lie unconformably on Alpine overthrusts and Oligocene molasse (Laj et al., 1982). Before the late Pliocene, the northeast coast of Rhodes consisted of elevated, metamorphosed, Mesozoic age

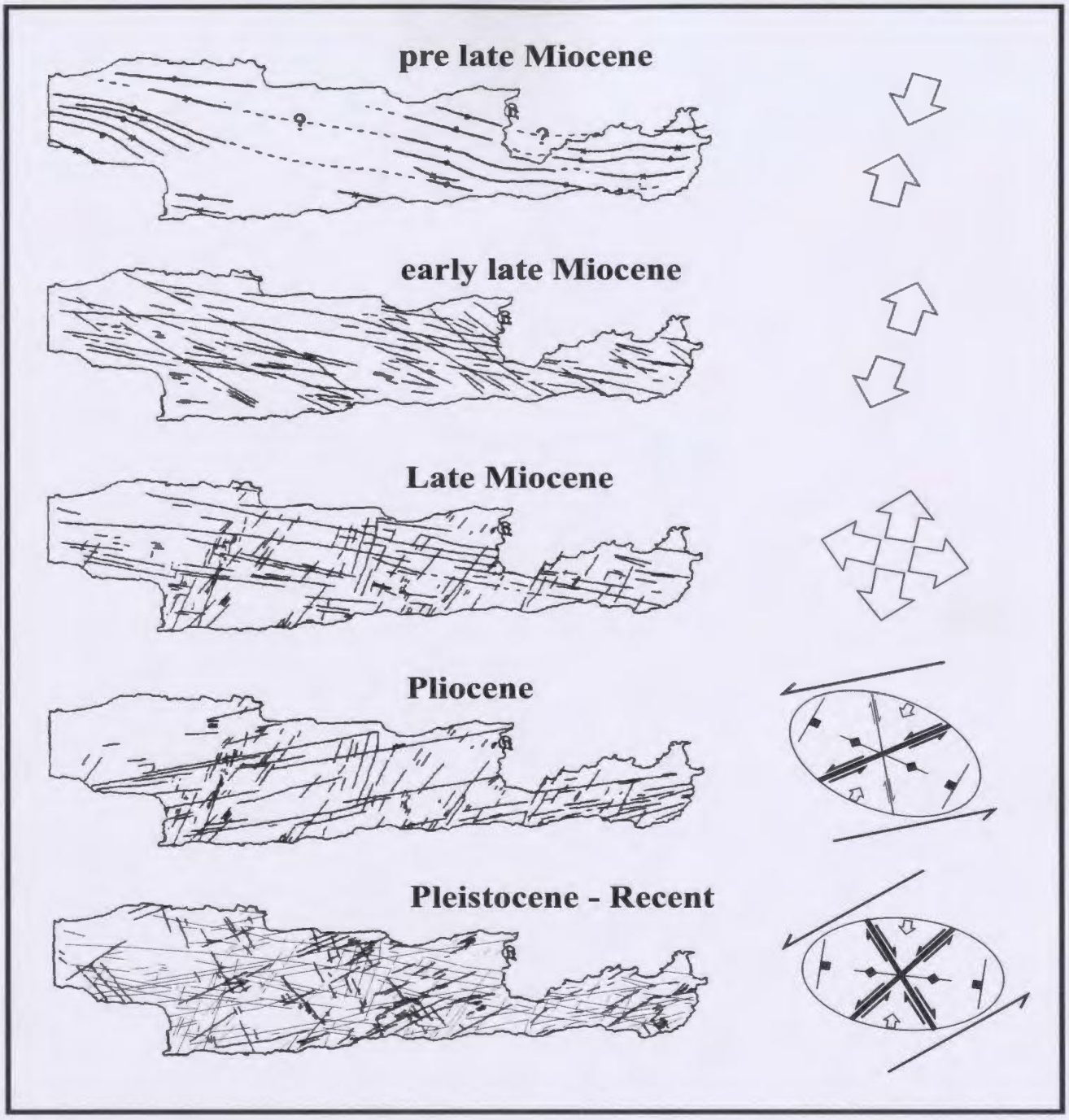

Figure 1.3.3: The five-stage development of Crete as suggested by Ten Veen and Meijer (1998). Light lines indicate reactivated faults. Bold lines represent newly formed faults. Arrows indicate the stress field orientation. Modified from Ten Veen and Meijer (1998).

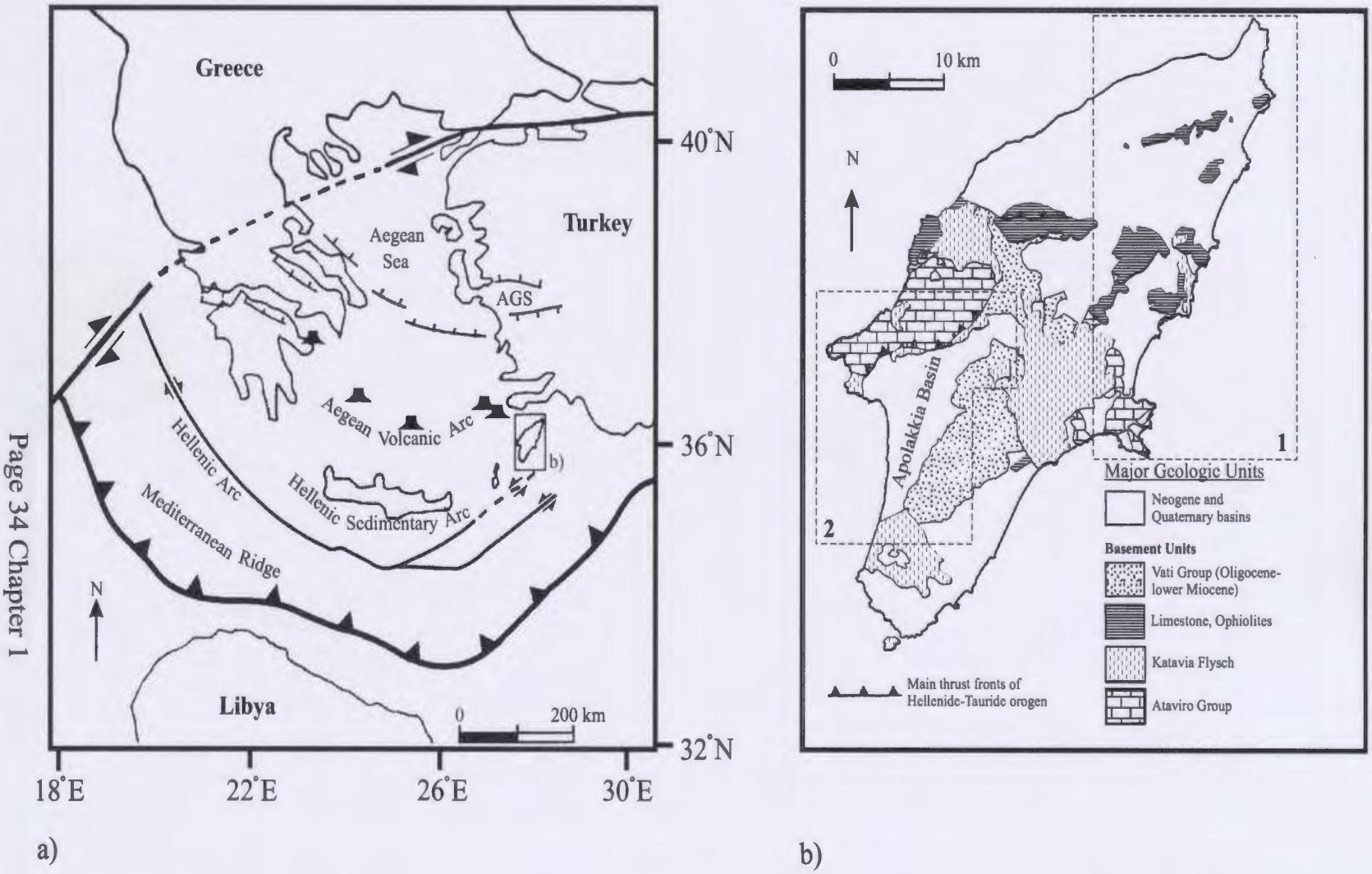

Figure 1.3.4: a) A simplified map of the southern Aegean region showing the Aegean Sea, Aegean Graben System (AGS), Aegean Volcanic Arc, Hellenic Sedimentary Arc, Hellenic Arc and Mediterranean Ridge with southern thrust front. b) Enlargement of the island of Rhodes showing a simplified representation of its major geological units. 1. Study area of Hanken et al. (1996), 2. Study area of Ten Veen and Kleinspehn (2002). Modified from Ten Veen and Kleinspehn (2002).

limestones (Hanken et al., 1996; Fig. 1.3.4;). Late Pliocene-Pleistocene transgressions and subsidence due to regional extension led to the development two major trends of normal faults: a north northeast-south southwest trend transected by a northwest-southeast trend (Hanken, et al., 1996). Together, these faults formed a horst-graben geometry in which late Pliocene and Pleistocene carbonate-rich sediments accumulated (Hanken, et al., 1996). Holocene uplift that increased in magnitude from south to north is also observed along the northeast coast of Rhodes (Hanken, et al., 1996). In the southwestern region of Rhodes, the large Apolakkia basin is interpreted to be a late Miocene wedge basin that formed in response to syn-depositional northeast-southwest extension (Fig. 1.3.4) (Ten Veen and Kleinspehn, 2002). The geometry of the numerous late Miocene-Recent fault trends within and around the Apolakkia basin can be understood by invoking changes in the regional stress field from the ~northwest-southeast compression of the Alpine orogeny to northeast-southwest extension (deformation phase D1 of Ten Veen and Kleinspehn, 2002; Fig. 1.3.5) some time around the late Miocene and again to northwest-southeast transtension some time in the early Pliocene (~4.5-5.0 Ma; Fig. 1.3.5, deformation phase D2 of Ten Veen and Kleinspehn, 2002; Fig. 1.3.5).

1.4: The eastern Mediterranean: A Dynamic Environment

The post Miocene structural evolution of the eastern Mediterranean has been influenced greatly by the interaction of the north northeast-south southwest convergence of the African and Eurasian plates and the more recent (~ late Miocene-early Pliocene)

Deformation Phase **D1**

Late Miocene

Northeast-Southwest Extensioin (~216-trending)

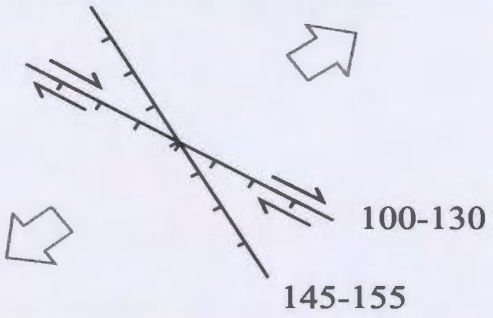

100-130 trending faults: Sub vertical, south-dipping, dextral-normal and normal-dextral sense of movement.

145-155-trending faults: Steeply dipping normal slip faults.

Deformation Phase **D2**

Middle Pliocene to Late Pliocene

~East northeast-west southwest transtension (~025-trending)

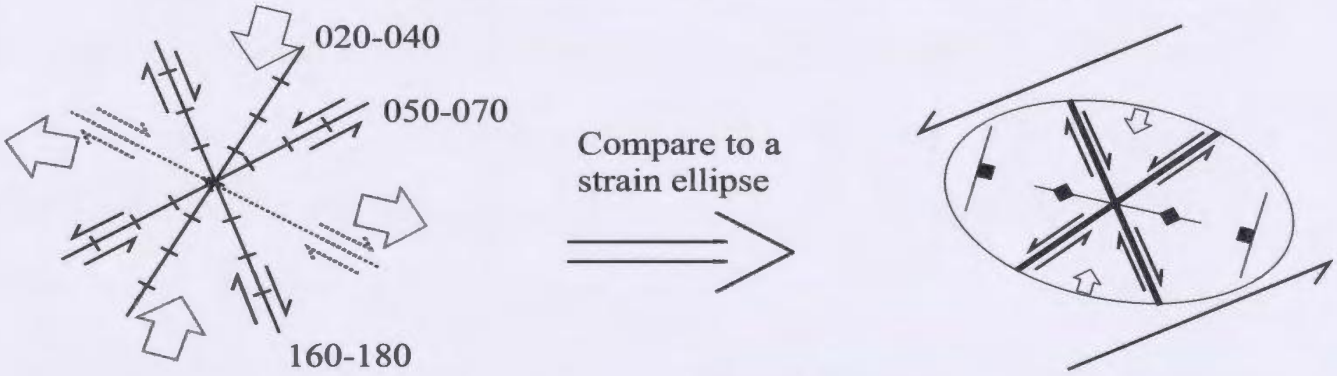

020-040-trending faults: Nearly all pure normal faults.
Offset the 100-130-trending faults.
Middle to Late Pliocene.

Reactivation of 100-130-trending faults in Middle to Late Pliocene. (Dotted lines)

050-070-trending faults: Vary from dominantly normal slip to sinistral-normal slip.
Offset 020-040-trending faults.
Late Pliocene to Pleistocene.
??Primary synthetic faults??

160-180-trending faults: Mostly normal-dextralor dextral-normal.
??Antithetic faults??
Pleistocene.

Figure 1.3.5: Major fault trends observed by Ten Veen and Kleinspehn (2002) within and near the Apolakkia Basin, Rhodes. They propose that two very different stress fields are necessary to generate the present-day fault orientations.

northward intrusion of the Arabian/Syrian Plate (relative to a fixed Eurasian Plate). The Aegean/Anatolian microplate helps distribute stress between the gigantic colliding plates by rigid body translation and rotation and internal deformation. Major contributions to understanding the most recent (Miocene-Recent) plate motions have been made through the use of satellite Global Positioning System (GPS) measurements, fault plane solutions to earthquake seismicity, paleomagnetic reconstructions and bathymetric and source seismic interpretations.

1.4.1: Global Positioning System (GPS) Data

Satellite GPS measurements of plate motion serve as a very useful tool for determining present-day plate motion. However, due to the complexity of the Aegean/Anatolian region, there is not always complete agreement on the details of plate motion among the published literature. Mantovani et al. (2001) present GPS data that suggests uniform velocities of 24 +/- 2 mm/yr toward the west for the Anatolian segment of the Anatolian/Aegean Microplate and 30 +/- 2 mm/yr southwest for the Aegean segment, relative to a fixed Eurasian Plate (Fig. 1.4.1). Kahle et al. (1999) similarly suggest that the Anatolian segment of the Anatolian/Aegean Microplate (east of ~30° E) is moving westward at a rate between 20 and 24 mm/yr. However the findings of Kahle et al. (1999) imply that the Aegean portion of the Anatolian/Aegean Microplate (west of 30° E) moves west southwest to southwest at velocities that increase from nearly 0 mm/yr along its northern boundary with the Eurasian Plate in the northern Aegean Sea to 28-33

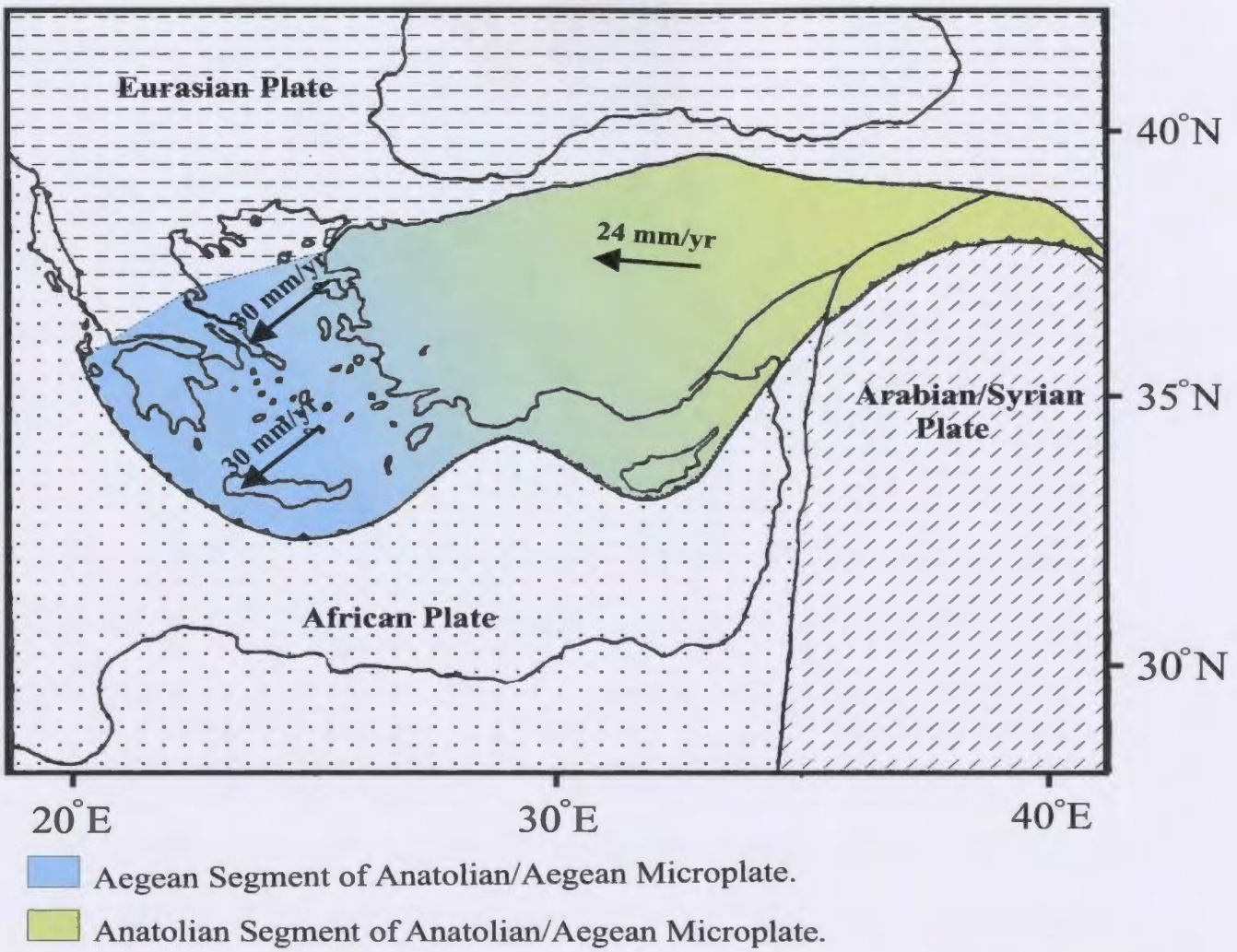

Figure 1.4.1: Average Plate motions relative to a fixed Eurasian Plate as suggested by Mantovani et al. (2001). The Anatolian segment of the Anatolian/Aegean Microplate is moving west northwest at a constant velocity of 24 mm/yr and the Aegean segment of the Microplate is moving southwestward at 30 mm/yr. The basemap is modified from Aksu et al. (1992).

mm/yr at its southern extent near the Hellenic Arc (Fig. 1.4.2). The average plate velocities suggested by Papazachos (1999) agree with those presented by Mantovani et al. (2001). However, Papazochos (1999) concludes that the Anatolian segment of the Anatolian/Aegean Microplate is moving westward at a velocity of 24 mm/yr near its boundary with the Eurasian Plate but only 18 mm/yr toward the west further to the south, implying a pole of counterclockwise rotation located in northern Africa; whereas the Aegean segment of the Anatolian/Aegean Microplate travels in a south southwest direction with velocities that increase toward the southwest from 25 mm/yr in western Turkey to 30 mm/yr in the central Aegean Sea, to 35 mm/yr in the southern Aegean Sea near the Hellenic Arc (Fig. 1.4.3). From these studies, the concensus is that the Anatolian segment of the Anatolian/Aegean Microplate is translating toward the west at a relatively constant velocity (~22 mm/yr) relative to the Eurasian Plate whereas the Aegean segment is experiencing nearly westward translation in the north along the North Anatolian Transform Fault that becomes increasingly southward-verging and of increased magnitude (~30 mm/yr) toward the south.

1.4.2: Seismicity and Fault Plane Solutions

Relative motion of tectonic plates along active fault planes can be determined from analysis of earthquake focal mechanisms. These fault plane solutions provide information concerning the relative kinematics of the tectonic plates and hence clues concerning the orientation of the regional stress field. Dziewonski et al. (1981) and

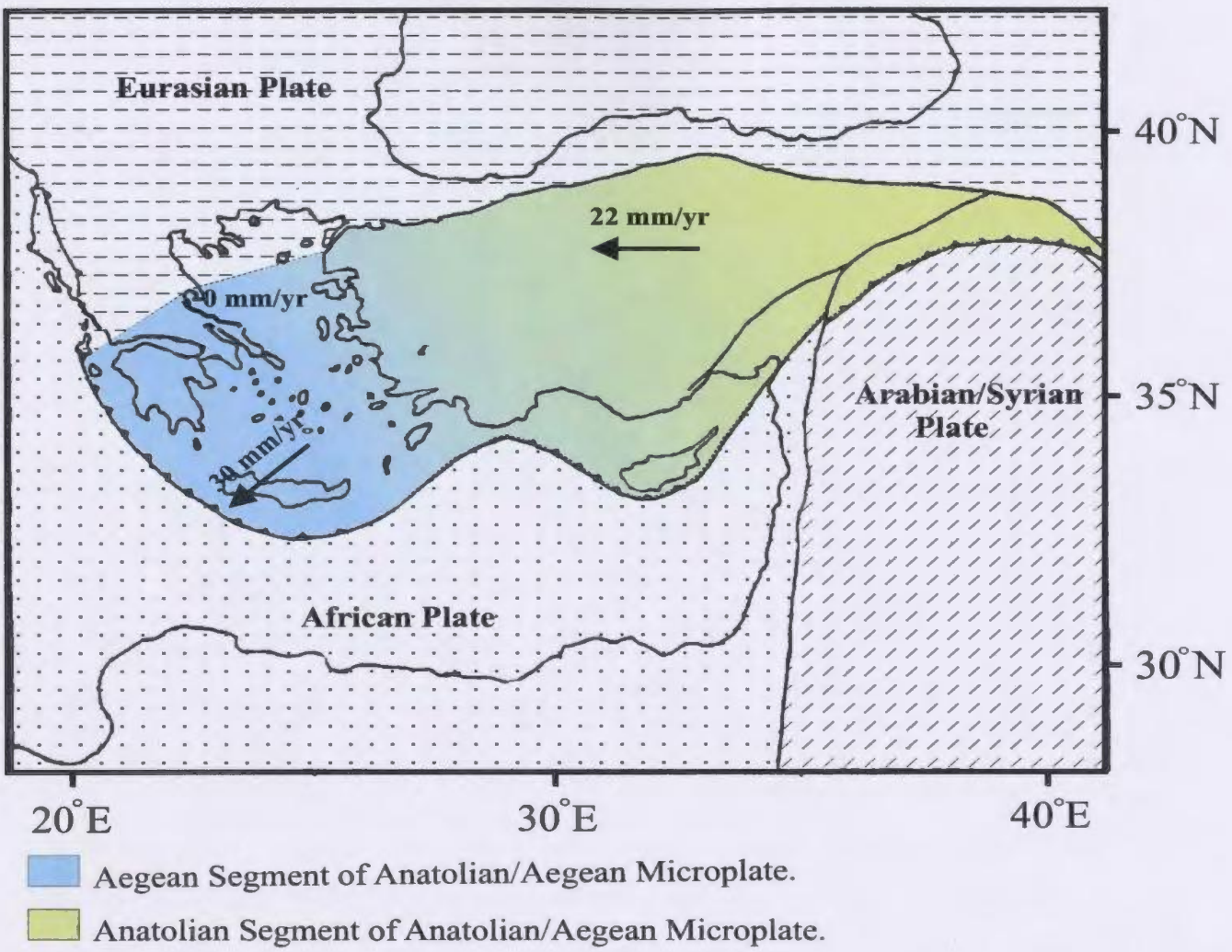

Figure 1.4.2: Average Plate motions relative to a fixed Eurasian Plate as suggested by Kahle et al. (1999). The Anatolian segment of the Anatolian/Aegean Microplate is moving westward at a constant velocity whereas the Aegean segment moves southwestward at velocities that increase from zero in the north to 30 mm/yr near its southern boundary. The basemap is modified from Aksu et al. (1992).

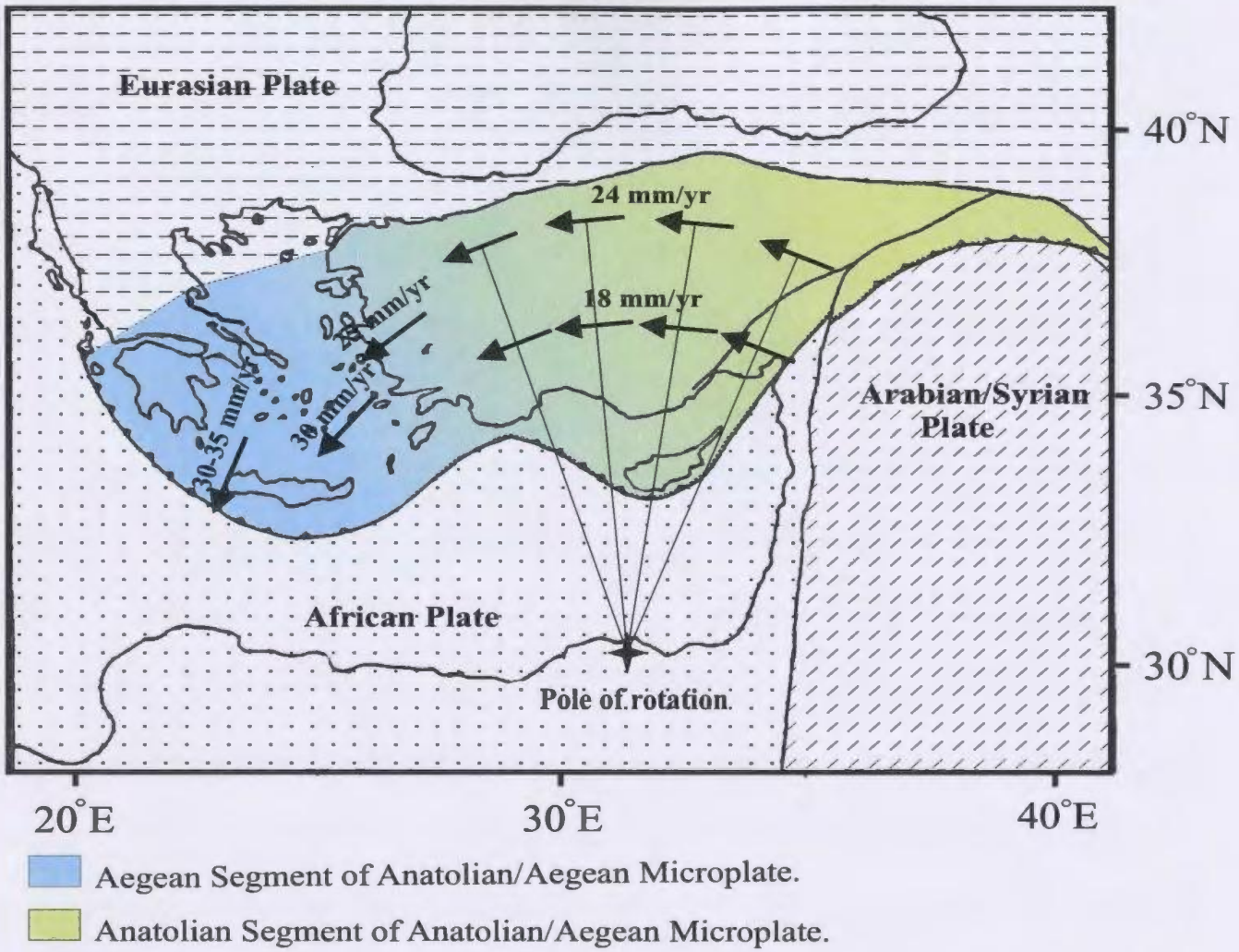

Figure 1.4.3: Average Plate motions relative to a fixed Eurasian Plate as suggested by Papazachos (1999). Note that neither the Anatolian or Aegean segments of the Anatolian/ Aegean Microplate move uniformly or in a straight line. Rather, they rotate counterclockwise around a pole located to their south. The basemap is modified from Aksu et al. (1992).

Jackson and Mckenzie (1988), have presented focal mechanism solutions for major earthquakes near the African/Eurasian convergence zone (Fig. 1.4.4). The concentration of seismic activity along the North Anatolian Transform Fault (NAT), East Anatolian Transform Fault (EAT), Hellenic Arc (HA), Cyprean Arc (CA) and the Dead Sea Transform Fault (DST) clearly define the boundaries of the Eurasian, African, Arabian/Syrian Plates and the Aegean/Anatolian Microplate. The interior of the Anatolian segment of the Anatolian/Aegean Microplate is essentially inactive relative to the Aegean segment and the diffuse boundary between them, where a northwest-southeast-trending zone of seismic activity can be traced across western Turkey and the Aegean Sea.

Although the areal density of major earthquake epicentres provides valuable information concerning the seismic activity of the region, fault plane solutions to these motions are also of great importance for determining the type of faulting deformation (e.g., normal, reverse, or strike slip) and hence, the causative stress fields. Strong correlations exist between the earthquake focal mechanisms and the dextral and sinistral strike-slip movement along the North Anatolian and East Anatolian Faults respectively and reverse faulting along the Bitlis (BS) suture and Cyprus Arc (Fig. 1.4.4). It is interesting to note that the fault plane solutions scattered around the perimeter of the Aegean segment of the Microplate have considerable variation. For example, although northwest-southeast-trending reverse faults are dominant along the southern convergence zone between the Aegean segment of the Microplate and the Hellenic Arc, a large

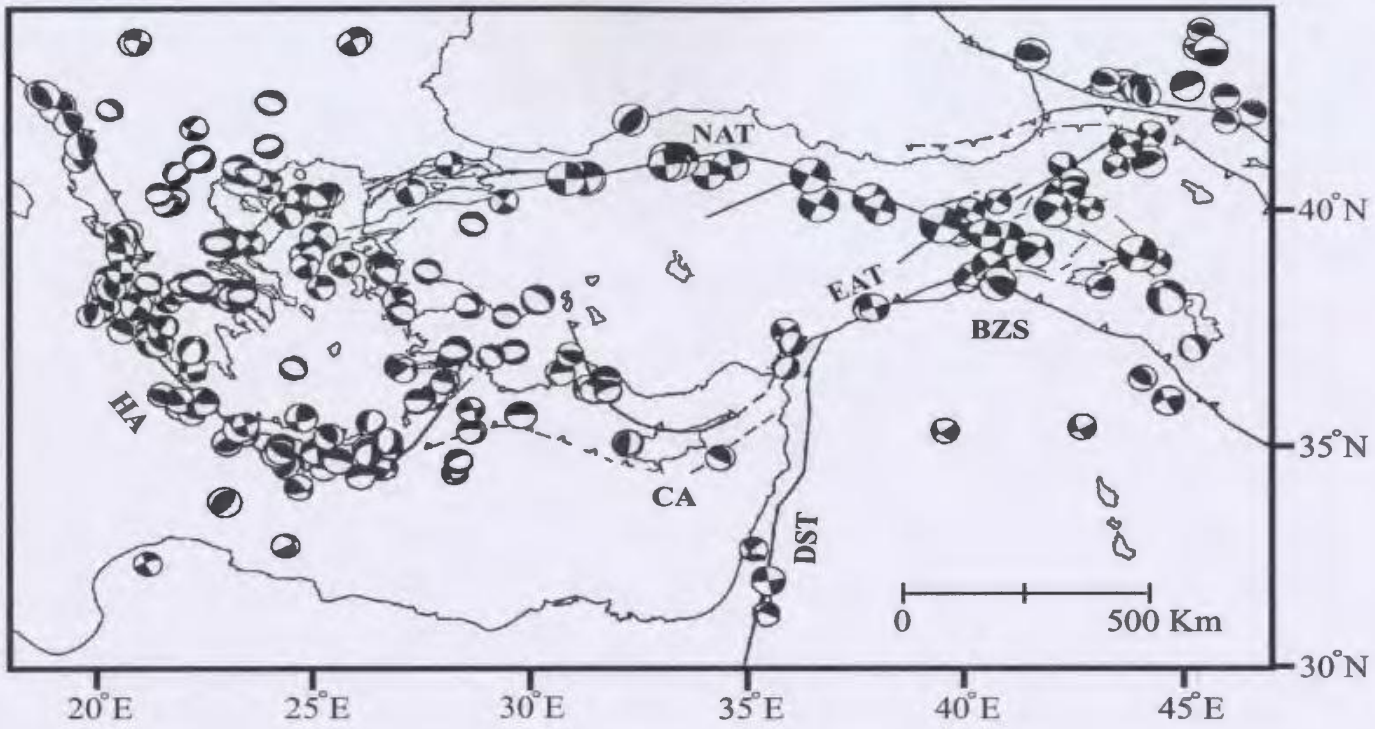

a)

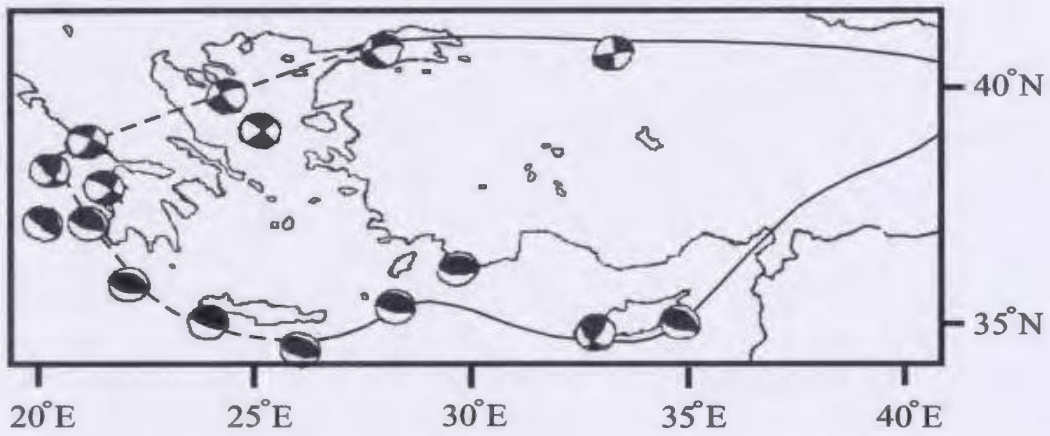

b)

Figure 1.4.4: a) Lower hemisphere projections of focal mechanisms for major earthquakes in the eastern Mediterranean region (modified from Reilinger and McClusky, 1997). b) Averaged focal mechanisms along major plate boundaries (modified from Papazachos, 1999). Black indicates compression, white indicates extension.

population of high angle extensional faults with some expression of strike slip faulting are also present. To the northwest, southern Greece is cut by east-west-trending normal faults. Further northwest, where the Aegean segment of the Anatolian/Aegean Microplate shares a boundary with the Adriatic Plate, reverse and dextral strike slip faulting occur. The northwest-trending array of east-west to northwest-southeast-striking extensional seismic activity mark the Aegean Graben System (Fig. 1.4.4).

1.4.3: Comparison of GPS Data and Seismicity

The relative movement between Aegean and Anatolian segments of the Anatolian/Aegean Microplate suggest that they are kinematically to some degree independent. This portioning likely occurs across the diffuse Aegean Graben System and/or Isparta Angle. The orientation and magnitude of the GPS motion vectors in Aegean region are in general agreement with the dominant extensional axes implied by the fault plane analyses of graben structures in central Greece, the northern Aegean microplate, and the Aegean Graben System as well as the compressional axes along the Hellenic Arc (Kahle et al., 1999). The presence of such wide-spread extensional faulting in the central Aegean Sea and western Anatolia also helps explain the motion of the Aegean segment of the microplate recorded by Papazachos (1999) who implied that the Aegean region was moving at a rate significantly faster than what would be expected from a rigid Anatolia/Aegean Microplate that is rotating counterclockwise about an Euler pole located to the south. The higher than expected velocities measured in the Aegean region can be

explained by allowing internal, north-south to southwest-northeast extension of the Aegean segment of the microplate to compound its rigid body rotation and translation. The internal deformation of the Aegean segment makes it difficult to determine if it rotates about a Euler pole that is significantly different from that of the Anatolian segment or if they share a common pole of rotation.

1.4.4: Block Rotation and Paleomagnetics

Paleomagnetic studies can provide valuable information concerning the rotational motion of 'rigid' blocks. Laj et al. (1982) measured the magnetization directions of samples from sedimentary formations of southern Greece, Crete, and Rhodes. Most of the samples were marine in origin and could be stratigraphically dated using planktonic foraminifera and nanofossils. The samples ranged from the Serravallian-Tortonian boundary (~11.5 Ma) to the early Quaternary (~1.8 Ma). However, those from Rhodes were limited to upper Miocene and Pliocene. Laj et al. (1982) concluded that the paleomagnetic azimuths of samples from Rhodes and Crete are essentially aligned north-south, implying that neither Rhodes nor Crete have rotated significantly since the Miocene. Furthermore, the paleomagnetic pole for Crete lay within the 95% confidence circle of the paleomagnetic poles of both the Eurasian and African Plates, indicating that there has not been any appreciable relative rotation between them. In contrast, a recent study by Duermeijer et al. (1998) proposes that Crete has rotated counterclockwise since the early Messinian. They site three populations of rotation values found on Crete,

suggesting that the rotation has been partitioned into three independently moving structural blocks. According to Duermeijer et al. (1998), the largest of these blocks, composing the central portion of Crete, has rotated counterclockwise by 27°-40°. The smaller, western and eastern blocks have rotated in a similar sense by 14°-19° and ~12° respectively. A later study by Duermeijer, et al. (2000) sampled the easternmost islands of Kassos, Karpathos and Rhodes to determine their paleomagnetic declinations. Although a wide array of declinations were determined for the island of Rhodes (18° +/- 12°), there was a consistent counterclockwise sense of rotation (Fig. 1.4.5). Paleomagnetic measurements from the islands of Kassos and Karpathos are as ill-constrained as those from Rhodes, but they too consistently support a counterclockwise sense of rotation (Duermeijer et al., 2000). More precise dating by Duermeijer et al. (2000) than those presented in earlier studies (e.g.: Laj et al., 1982; Kissel and Laj, 1988) constrain these rotations to have been active during the Pleistocene (since ~1.8 Ma).

Kissel and Laj (1988) documented that upper Eocene carbonates in western Turkey (along the western limb of the Isparta Angle) demonstrate 30° of counterclockwise rotation relative to the Eurasian Plate (Fig. 1.4.5). Because no significant rotation is observed in Turkey west of the Isparta Angle, between the Paleocene and late Oligocene, rotation of this region can be broadly constrained to have occurred between the early and middle Miocene; possibly coinciding with the last phase of the 'Alpine' tectonic activity in the area resulted in the emplacement of the Lycian nappes onto the Bey Dağları at approximately 15 Ma (Kissel and Laj, 1988). To the east,

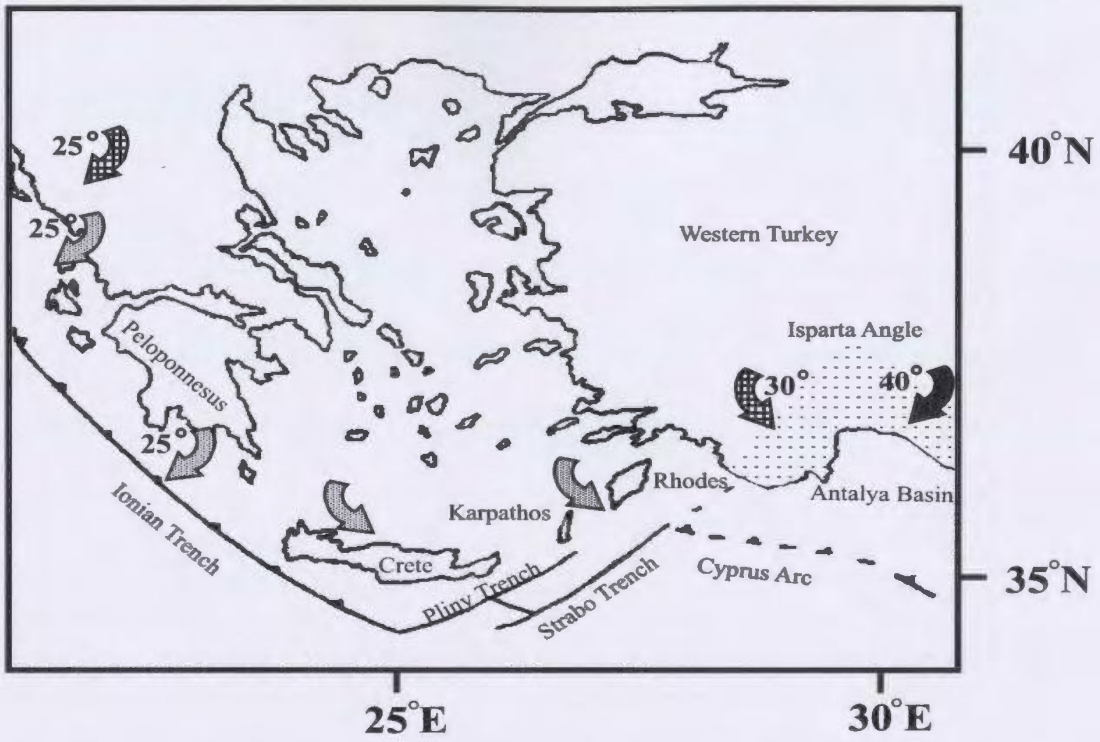

Figure 1.4.5: A map of the southern Aegean region showing the middle Eocene-Oligocene (solid arrow), Miocene (hatched arrow) and Pliocene-Quaternary (shaded arrow) rotations of Greece and southwestern Turkey relative to a fixed Eurasian Plate. Note how the ends of the arc are rotated with an opposite sense. Kissel and Laj (1988) suggest that only the western extent of the arc is affected by the Plio-Quaternary phase of rotation and that the central portions (Crete and Rhodes) demonstrate no appreciable rotation. More recent investigations by Duermeijer et al. (1998), Duermeijer et al. (1999) and Duermeijer et al. (2000) generally agree with those done in earlier studies with the most distinct difference being their claim of considerable counterclockwise rotations of Crete and Rhodes. Because the magnitude of these Crete Rhodes rotations are highly variable (see text), they are not given magnitudes in this figure but are displayed to show a sense of motion. Figure modified from Kissel and Laj (1988).

the lack of rotation observed in the lower Miocene deposits of the Antalya Basin by Kissel et al. (1993) helped limit the age of an ~ 40° clockwise rotation of the eastern limb of the Isparta Angle to pre-early Miocene (Eocene-Oligocene) times (Fig. 1.4.5).

Paleomagnetic results from southern Greece (Ionian Islands and Peloponessos) showed that the western portion of the Hellenic Sedimentary Arc has undergone ~ 26° of clockwise rotation since ~ 5 Ma (Laj et al., 1982) (Fig. 1.4.5). Kissel and Laj (1988) suggest that this rotation may have occurred during an early Pliocene compressive phase when an abrupt change in the Miocene arc position from the Ionian-Lycian Arc to the present Hellenic Arc is thought to have occurred (Kissel and Laj, 1988). More recent studies of this area agree that an ~25° clockwise rotation of southern Greece has occurred. However, they constrain the timing of this ~25° clockwise rotation to have occurred since ~ 0.8 Ma in some portions of southern Greece but as late as ~ 1.8 Ma in others (Duermeijer et al., 1999; Duermeijer, et al., 2000). These very recent times for the initiation of clockwise rotation imply a rate of rotation 2.8-6.25 times faster than the ~ 5°/Ma rotations proposed by Laj and Jamet (1982).

Samples studied by Kissel and Laj (1988) from northwestern Greece display ~50° of clockwise rotation. This total 50° rotation is thought to have been achieved as two separate, 25° rotations; the first of which occurred during the Miocene around the same time as that of the rotation of the western limb of the Isparta Angle (Kissel and Laj, 1988). The second phase of rotation imposed an additional 25° of clockwise rotation upon northwestern Greece and may corresponds with the timing of the afore mentioned 25°

clockwise rotation phase of southern Greece (Kissel and Laj, 1988; Fig. 1.4.5).

The orientation of the maximum axis of anisotropy for the magnetic susceptibility in a sediment can be used to infer the orientation of the stress field in which the sediments developed. In a weakly deformed sediment, magnetic susceptibility tends to align either perpendicular to the maximum compression stress axis or parallel to the maximum extension stress axis. Measurements of from the Miocene to Pleistocene sediments from the Hellenic Sedimentary Arc show that the maximum axis of anisotropy of the magnetic susceptibility is aligned northwest-southeast in southern Greece and Crete whereas Plio-Pleistocene samples from the eastern portion of the Hellenic Sedimentary Arc (Rhodes and Karpathos) demonstrate a general northeast-southwest alignment of magnetic susceptibility (Duermeijer, 2000). These alignments indicate that the western portion of the arc has been subjected to either northwest-southeast extension or northeast-southwest compression whereas the eastern portion has undergone either northeast-southwest extension or northwest-southwest compression.

These rotations, in conjunction with the GPS derived velocity vector field and seismicity, testify to the complex history of deformation within the Aegean segment of the Aegean/Anatolian Microplate and especially near the junction between the Hellenic and Cyprus arcs during the past 15 Ma. For further information on the structural evolution of the Aegean region incorporating both paleomagnetic and fault slip analysis, see Doutsos and Kokkalas (2001a, 2001b) and Walcott and White (1998).

1.4.5: Source Seismic and Bathymetric Features

Bathymetric data can provide a great deal of structural information (Fig. 1.4.6). The Hellenic Arc runs approximately 1000 km along the southern margin of the Aegean segment of the Aegean/Anatolian Microplate where its arcuate shape is well defined by the 2000 m isobath contour (Huchon et al., 1982). Its western, ~northwest-southeast-trending limb, the Ionian Trench, is characterized by several parallel, *en-échelon* depressions that reach depths as great as 5500 m and contain up to 1000 m of Quaternary sediments (Ryan et al., 1973, Huchon et al., 1982, Rotstein and Ben-Avraham, 1985). South of Crete, the trend of this trench system changes to a northeast-southwest orientation along three lineations: the Ptolemy, Pliny, and Strabo trenches. The Ptolemy Trench trends between Crete and the submarine Ptolemy Mountains where it reaches a maximum depth of 2200 m before terminating against the Cretan margin. The Pliny Trench follows a 065 azimuth along the southern edge of the Ptolemy Mountains. This deep (4000 m), narrow trench illustrates steeply dipping slopes (northern slope dip ~23°, southern slope dip ~13°). Between these slopes, three 040 oriented, *en-échelon* troughs (each trough ~10 km long and ~2 km wide) contain small amounts of (Pliocene-Quaternary) fill (Huchon et al., 1982, Peters and Huson, 1985). The Strabo Trench is a shallow (~ 3000 m depth), 055-trending depression (Huchon et al., 1982) separated from the Pliny Trench by the Strabo Mountains (Ariane Plateau; Huchon et al., 1982). Its northern and southern slopes dip gently at ~ 12° toward its centre where little sedimentary fill is observed (Peters and Huson, 1985). The Strabo Trench lies in bathymetric

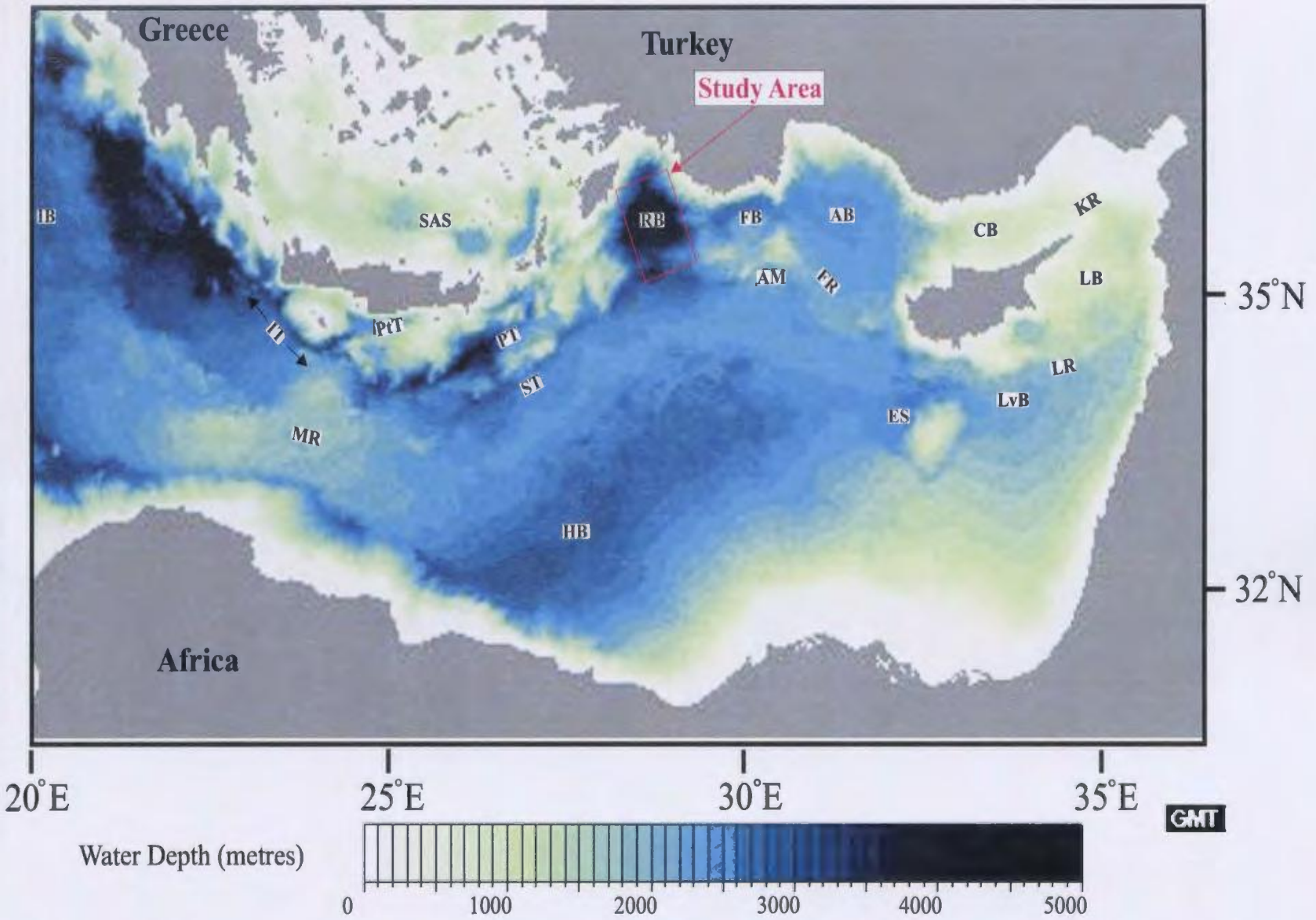

Figure 1.4.6: Bathymetric map of the eastern Mediterranean Sea. MR=Mediterranean Ridge, IB=Ionian Basin, IT=Ionian Trench, SAS=Southern Aegean Sea, PtT=Ptolemy Trench, PT=Pliny Trench, ST=Strabo Trench, LvB=Levant Basin, RB=Rhodes Basin, FB= Finike Basin, AM=Anaximander Mountains, AB=Antalya Basin, FR=Florence Rise, HB= Herodotus Basin, ES=Eratosthanes Seamount, CB=Cilicia Basin, KR=Kyrenia Rise, LB=Latakia Basin, LR=Latakia Rise. Data from the International Bathymetric Charts of the Mediterranean (IBCM).

continuity with the Rhodes Basin to the northeast (Fig. 1.4.6).

The Cyprean Arc is not as seismically active as the Hellenic Arc. Analysis of earthquake motions show that the north-south compression along central portion of the Cyprean Arc transforms to left-lateral motion along its easternmost, northeast-trending leg (Ben-Avraham et al., 1995). Because subduction does not appear to be the dominant process along the Cyprean Arc, it is best identified bathymetrically as an uplifted lineament (Ben-Avraham et al., 1995).

Several basins (e.g., the Ionian, Rhodes, Finike, Antalya, Cilicia, Levant and Latakia Basins) distributed throughout the eastern Mediterranean can be identified on the basis of their bathymetric character. The depths of the basins vary considerably from less than 1300 m in the east (e.g., the Cilicia and Latakia Basins) to greater than 4300 metres depth to the west (e.g., the Rhodes and Ionian Basins) (Fig. 1.4.6). Many explanations for the possible developmental histories for these basins have been presented in the literature (Rotstein and Ben-Abraham, 1985; Woodside et al., 2000).

Numerous bathymetric highs such as the Anaximander Mountatins and Eratosthenes Seamount, Missis-Kyrenia and Latakia Ridges, the Florence Rise and the Mediterranean Ridge, are also identified on the basis of bathymetry (Fig. 1.4.6). The Mediterranean Ridge lies south of the Hellenic Arc where it traces the southern edge of the Aegean segment of the Aegean/Anatolian Microplate. This gentle bulge reaches a length of ~ 1300 km and a width of 150-300 km and is thought to represent a 10-12 km-thick wedge of accreted sediments that stands ~750-1000 m above its immediate

surroundings (Huguen et al., 2001). Its eastern extremity, near the junction of the Hellenic and Cyprus Arcs, trends toward a connection with the Anaximander Mountains and Florence Rise. The Anaximander Mountains are dominated by localized reverse thrusting to their northwest, folding in the southeast and fault-related subsidence to the northeast (Robertson, 2000). Anastasakis and Kelling (1991) also note the presence of a positive Bouguer gravity anomaly over the mountains. Southeast of the Anaximander Mountains, the Florence Rise is a broad, gently elevated (relief of only 200-300 m) terrain that demonstrates transpressional deformation in the form of folded sediments, southward directed nappe packages and positive flower structures (Woodside et al., 2002). Unlike the Mediterranean Ridge, the Florence Rise displays a well imaged basement 'core' that shares the trend of the Rise's surface expression and appears to connect the Anaximander Mountains with the remainder of the Cypus Arc lineaments (e.g., the Latakia Ridge) to its southeast.

The Antalya Basin is a large, 2400-2600 m-deep basin constrained to the north by the Turkish mainland, to the south by the Florence Rise, to the east by the Island of Cyprus and the Cilicia Basin and to the west by the Anaximander Mountains (Taviani and Rossi, 1989). It represents a northwest-southeast-trending asymmetrical graben (Glover and Robertson, 1998) whose western margin is marked by steep down-to-the-east normal faulting and northeast margin is defined by a horst-graben structure. Normal faults within the basin trend dominantly northwest-southeast and north-south. A thick cover of Pliocene-Quaternary fill (up to ~1 km-thick) lies on top a thick evaporitic sequence that

demonstrates active diapiric activity (Taviani and Rossi, 1989). The Antalya Basin is thought to be an extensional basin formed behind the Hellenic-Cyprean subduction zone (Glover and Robertson, 1998) although this has assertion has been challenged (Işler et al.; in press).

Located near the junction of the Hellenic and Cyprus arcs, the deep (nearly 4500 m-deep) Rhodes Basin is bound to the north and northeast by the Turkish mainland, to the south by the Mediterranean Ridge, to the west by the Hellenic Island Arc and to the east by the Anaximander Mountains (Fig. 1.4.6). The shallow, southern portion of the basin lies in bathymetric continuity with the Strabo Trench and is bounded to the south by northward directed nappes related to the Mediterranean Ridge (Woodside et al., 2000). The Rhodes Basin and Anaximander Mountains to its east are distinct from the vast majority of the eastern Mediterranean in that they appear to lack Messinian evaporites and thick, Pliocene-Quaternary sedimentary sequences. As such, Woodside et al. (2000) suggest that the Rhodes Basin, Anaximander Mountains, and Strabo Mountains share a common stratigraphy of generally well bedded, thin, Pliocene-Quaternary sediments unconformably overlying a variably deformed and indurated Cretaceous to Miocene rock sequence similar to that exposed in Crete, Rhodes, and southern Turkey. Based on these observations, Woodside et al. (2000) interprets the Rhodes Basin to be a post-Messinian tectonic trough formed by transtensional regional tectonics. This interpretation is supported by Rotstein and Ben-Avraham's (1985) observation of a positive Bouguer anomaly over the Rhodes Basin. Anastasakis and Kelling (1991) note the presence of a

strong gravity gradient just north of the Finike Basin. They interpret the Rhodes and Finike Basins to be remnants of older (pre-middle Miocene) Mediterranean ocean crust trapped north of a newly developed convergence zone to the south. Mascle et al. (1986) suggest that the Rhodes trough represents a former (upper Miocene) subduction trench, abandoned upon a southward shift of the subduction zone. In this case, the positive Bouguer anomaly may be responding to a remnant piece of partially subducted oceanic crust.

1.4.6: The Hellenic and Cyprean Arcs: Major Stress Partitioning Structures

The consistent east-west trend of Paleogene accreted terranes in southern Anatolia suggests that the imposing compressive stress axis during that time was oriented north-south. Presently, the Hellenic and Cyprean Arcs display a southward convex shape with a nearly orthogonal, sinistral strike slip, link between them via the Pliny-Strabo trench system. Rotstein and Ben-Avraham (1985) propose that this complicated arrangement can be explained by the accretion of various sized, oceanic terranes during subduction. The northward collision of a terrain large enough to penetrate the continental crust of Anatolia before its final accretion may have pushed the subduction zone to the north near the present-day Pliny-Strabo trench system. Such a northward migration would create a northward convex curve in the central portion of the trench system. Once this bend was established, the resolution of plate motion vectors suggests that strike slip motion would be dominant along the present-day Pliny-Strabo portion of the trench system. Unlike large

terranes, smaller terranes (such as the Eratosthenes Seamount) are not large enough to penetrate the continental crust. However, the northward accretion of several smaller terranes eventually leads to a shift of the trench axis to the south; behind the pile of accreted terranes. This continuous collision of small terrains provides a possible mechanism for the inferred southward migration of the eastern Cyprean Trench as implied by the southward progression of ridge systems from the Misis-Kyrenia Ridge to the town of Larnaca in eastern Cyprus and finally, the Latakia Ridge (Ben-Avraham et al, 1995).

The commencement of subduction along the eastern Cyprus Arc is ill-defined. Northward-tilted middle Miocene reflectors in the Cyprus Basin suggests that subduction started by the Middle Miocene (Anastasakis and Kelling, 1991). However, Robertson and Woodcock (1986) propose an Oligocene onset to subduction. In either case, the post - Miocene collision of the Eratothenes Seamount (believed to be a continental fragment based on refraction data; Anastasakis and Kelling, 1991) may be playing a key role in reducing the amount of subduction occurring along the Cyprus Trench and encouraging the development of lateral (strike slip) displacement along its curved, eastern limb (Woodside et al., 2002). Hence, the Cyprus Arc seems to be now more collisional/transpressional than subductive.

The Hellenic Arc is connected to the Cyprus Arc via the sinistral Pliny-Strabo trench system. The Pliny Trench has been correlated with the Burdur Fault Zone in western Turkey which trends on land nearly parallel to the western boundary of the Isparta Angle. The central and western Hellenic Arc shows shallow, intermediate and deep

seismicity earthquakes that imply orthogonal subduction of Mediterranean lithosphere beneath the Aegean section of the microplate; especially along the Ionian Trench (Papazachos et al., 2000). However, note that several shallow, extensional faults are observed along the northern side of the trench. The far western extremity of the Hellenic Trench, near western Greece, curves sharply northward where it accommodates dominantly dextral strike slip motion imparted to it by its merger with the northeast trending Cephallonia fault.

1.4.7: Inferred Dynamics of Plate Motions

With the kinematics established, questions concerning the dynamics of the system must be explored. For example: If the Aegean/Anatolian Microplate is situated in the middle of a compressional domain, why do the Aegean and western Anatolian regions undergo extension? Why is the Aegean segment of the Aegean/Anatolian Miroplate moving faster and in a different direction than the Anatolian segment? Why is subduction not active along the Cyprus Arc? The westward escape of the Anatolian/Aegean Microplate was likely initiated by the late Miocene terminal collision of the Arabian Plate with the African Plate to the east. The westward extrusion of the Anatolian segment forces the Aegean segment to collide with the Adriatic Plate to its west where the lack of buoyancy contrast between the continental crusts of the Aegean segment of the Anatolian/Aegean Micorplate and the Adriatic Plate results in a resistance to subduction. Similarly, the Aegean segment of the Microplate is bounded to the north by the

continental Eurasian Plate. Therefore, the Aegean portion of the Microplate migrates southward along its boundary with the Adriatic Plate until it eventually finds easy escape by overriding the thin oceanic crust of the Mediterranean along the western segment of the Ionian Trench. This southward deflection may be the primary contributor to the measured counterclockwise rotation of the Aegean region. The faster motion of the Aegean segment of the Microplate relative to the Anatolian segment may then be explained as a consequence of the slab pull force generated by the subducting Mediterranean lithosphere below the Aegean segment of the Microplate (McClusky and Balassanian, 2000). Martinod et al. (2000) explored the potential role of gravity spreading of the Aegean lithosphere over the Mediterranean lithosphere in their layered sand/silicone model of the Anatolian/Aegean convergence zone. Their findings implied that both Arabian intrusion and lateral density contrasts at the boundary between the northern fringe of the African Plate and the Anatolian/Aegean Microplate across the Hellenic Arc are requirements for the westerly escape of the Aegean/Anatolian Microplate. Mantovani et al. (2001) offer an alternative explanation for the velocity difference between Anatolian and Aegean segments of the Microplate whereby the accelerated motion of the Aegean region may be due to sequential, relatively short-term decoupling along the North Anatolian Transform Fault. They note that strain from the initial 1939 earthquake that occurred near the Erzincan Basin along the North Anatolian Transform Fault has been migrating westward ever since; generating ruptures along its western portion (e.g., the 1999 Izmit earthquake; Cakir et al., 2003). This migrating

'stress pulse' model predicts that the Aegean region should now be moving ~8 mm/yr faster than the eastern Anatolian region where the rupture originated. This value is in good agreement with those determined by GPS data, and raises the issue of the potential relevance of time scaling when considering focal mechanism solutions and GPS measurements. We must be cautious not to blindly project present day, instantaneous, movements onto geological timescales.

1.5: Research Objectives

My research project will use seismic reflection methods to image and interpret the active convergence zone between the African and the Eurasian Plates as manifested locally in the Rhodes Basin. The proximity of this area to the peculiar intersection of the Hellenic and Cyprus Trenches should serve as an ideal location for studying the evolution and mechanics of the plate convergence at the intersection of arcs. By interpreting the geomorphology of the Rhodes Basin and incorporating work done by others in this area, I hope to gain further insight into how this stressed region has evolved since the Miocene, thereby contributing to our understanding of arc convergence and the role it plays in strain partitioning.

Chapter 2: Methods

2.1: Seismic Data Acquisition

Multichannel, seismic reflection data from the Rhodes Basin, eastern Mediterranean Sea were acquired during the summer of 2001 by Memorial University of Newfoundland (MUN) in conjunction with the Institute of Marine Science and Technology, Dokuz Eylül University, Izmir, Turkey aboard the research vessel *K. Piri Reis*. The seismic source array was a 200 cubic inch air gun array consisting of four 40 in^3, two 10 in^3, and one 20 in^3 sleeve guns in a configuration with two of the 40 in^3 guns closely spaced to simulate a single 80 in^3 gun and the rest hung separately. Each gun was towed at a depth of 3 m and fired on time at approximately 25 m intervals. The source array volume was reduced several times during the survey due to gun failure or other complications but generally provides signal bandwidth in the range of 50-200 Hz. Reflections were detected on a 287.5 m-long, 48 channel, Western Geophysical hydrophone streamer with a 12.5 metre group interval and a source offset of 80-95 (or less) m (Fig. 2.1.1). Depth compensators were positioned along the streamer to maintain a streamer depth of 3 m. This acquisition geometry constitutes a maximum 12 fold coverage. Each 3072 millisecond (ms) trace was recorded through a OYO DAS-1 digital seismograph onto DAT magnetic tapes with a 1 millisecond sampling interval (500 Hz Nyquist frequency). Instances of less than maximum fold coverage are usually due to one

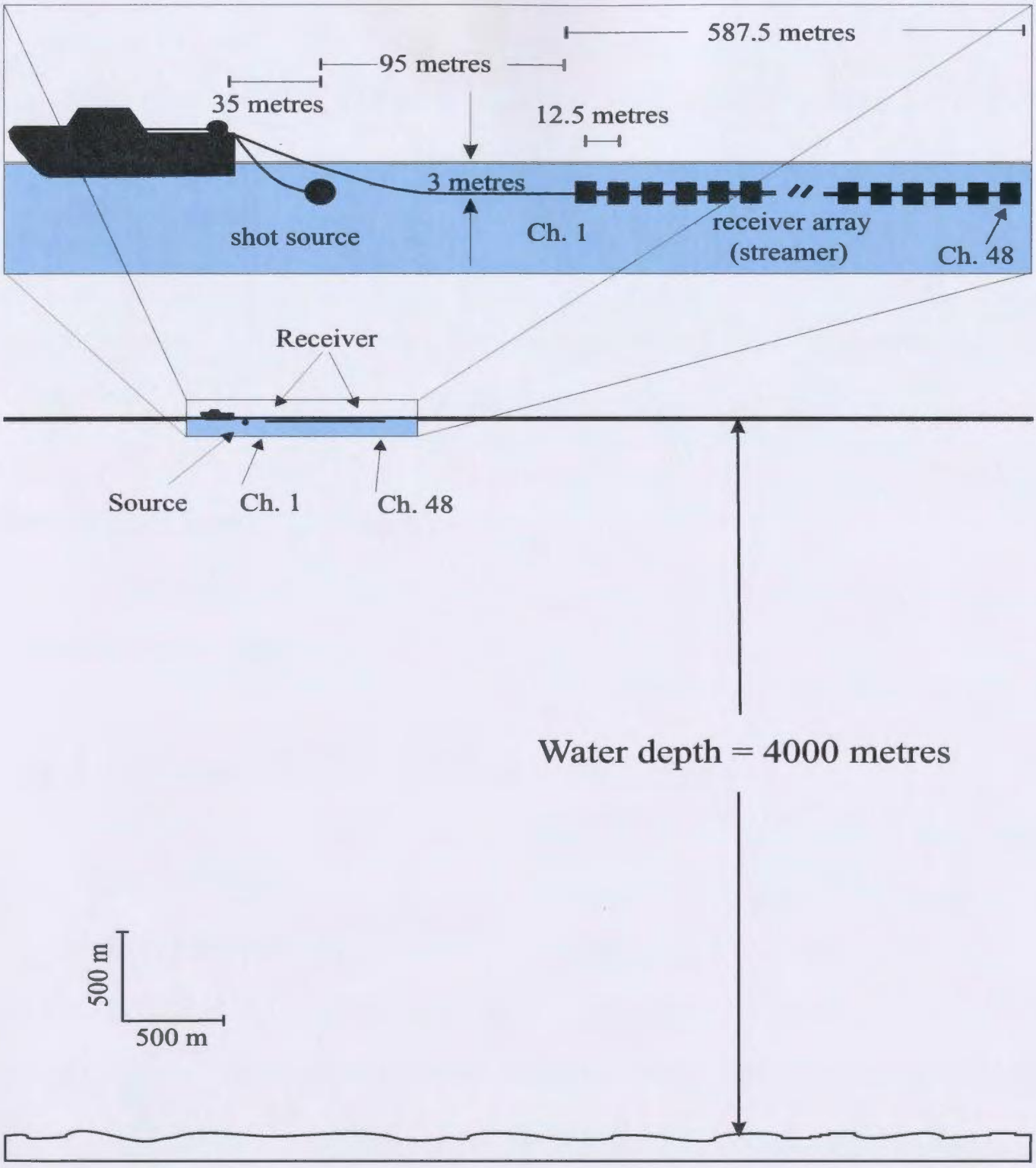

Figure 2.1.1: The geometry of the multi-channel seismic data acquisition array for the 2001 Rhodes Basin survey.

of two events: (1) Tape drive errors resulted in not recording some shots, (2) One of the OYOs had a bad 12-channel A/D board so the seismograph only recorded the nearest 36 channels. Because of the excessive water depths, (up to nearly 4500 m; ~6 second (sec.) two-way travel time), recording delays were introduced to the data at integral multiples of 500 ms in an effort to reduce the amount of 'dead' recording time. These data were collected in a grid pattern consisting of ~950 km of seismic data and a line spacing of ~20 km between both east-west and northwest-southeast-oriented survey lines (Fig. 2.1.2).

2.2: Seismic Data Processing

Seismic processing was carried out using Landmark Graphics ProMax software, running on a SUN SunFire server.

2.2.1: Impact of Water Depth on Data Quality and Processing

Water depth in the study area is consistently greater than 2.5 km and is often greater than 4 km. Together, the water depth and relatively short receiver array result in a very small amount of normal move-out on the shot gathers (e.g., ~23 ms on a common depth point (cdp) gather) resulting in poorly-constrained velocity functions. Consequently, the data were easily stacked, but migration velocities had to be chosen by a process of trial and error rather than from well-contrained velocity picks from velocity analysis (Figs. 2.1.1 and 2.2.1).

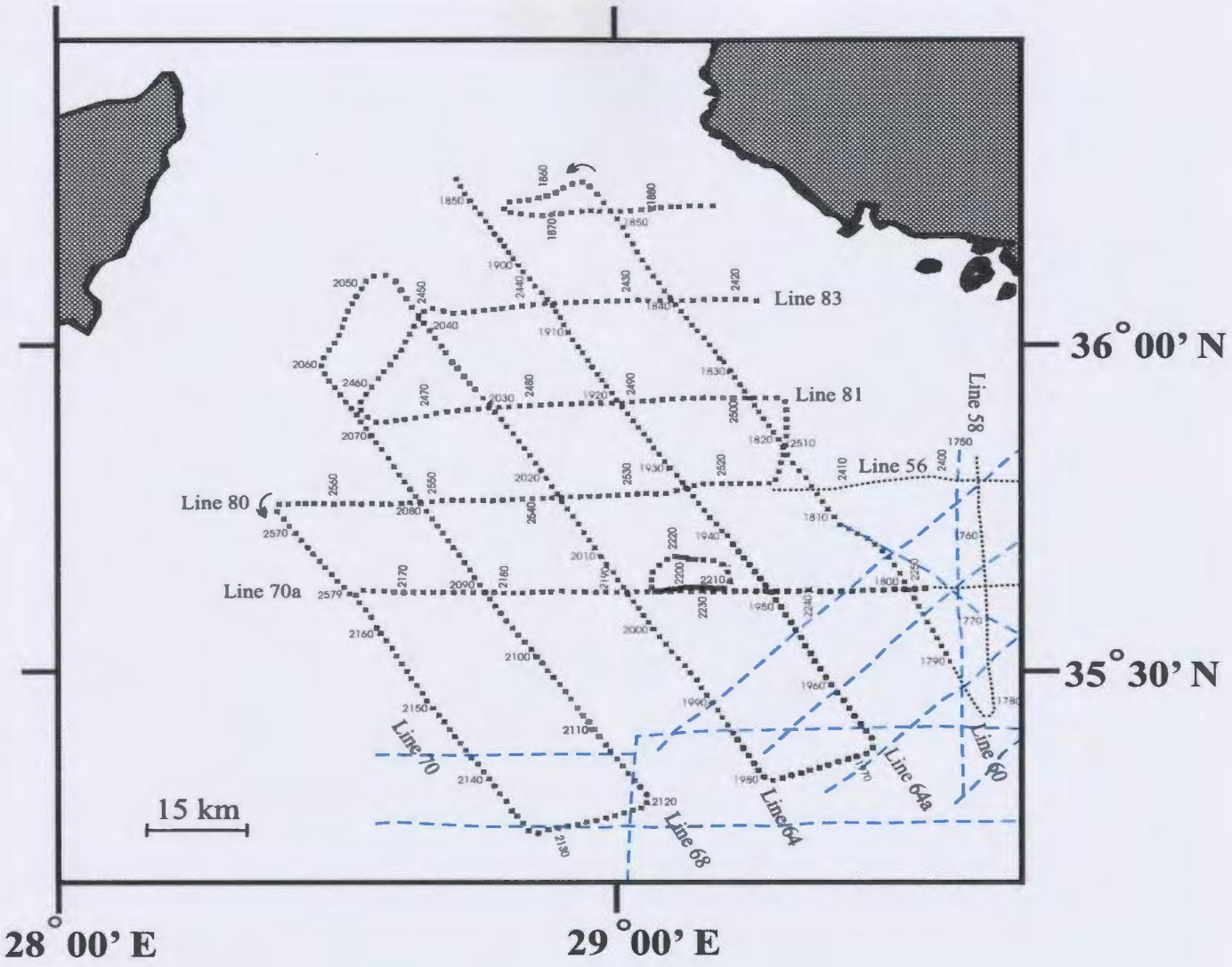

..... 2001 survey lines not processed by the author.

– – – – – Survey lines from the research vessel *Gelendzhik*.

..... 2001 survey lines processed by the author.

Figure 2.1.2: A Map of the survey area showing the seismic lines used for the correlation of structures. Line numbers and location (fix) numbers are shown for the 2001 survey grid.

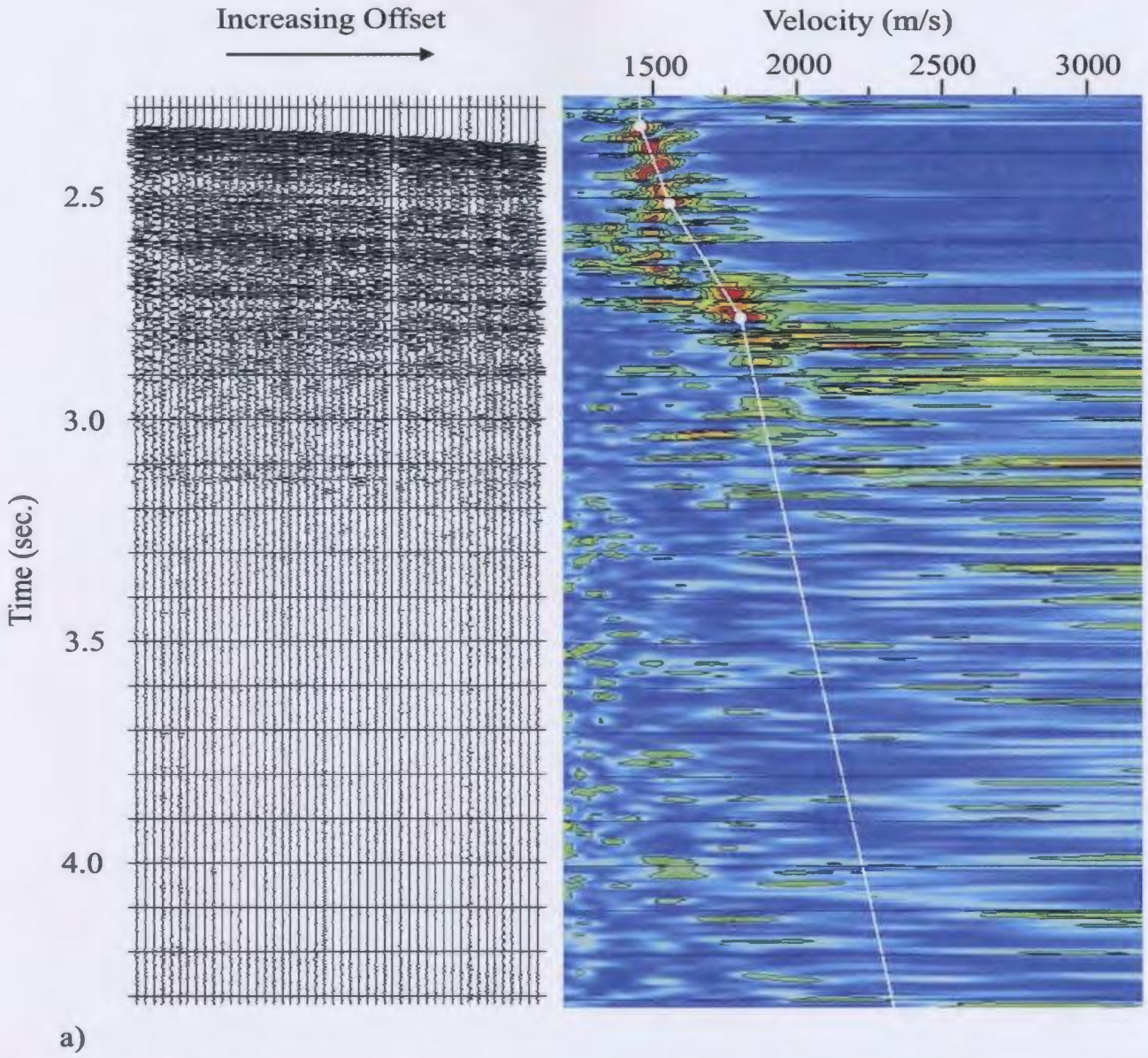

Figure 2.2.1: 5-cdp supergather ensemble (5x12=60 traces) and associated semblance plots from lines 81 and 81 to demonstrate the role of water depth and active recording channels on velocity resolution. a) Centred on cdp 800 where the water depth is relatively shallow. b) Centred on cdp 11244 where the water depth is deep. c) Centred on cdp 5800 where the water depth is deep and channels 37-48 are not recording.

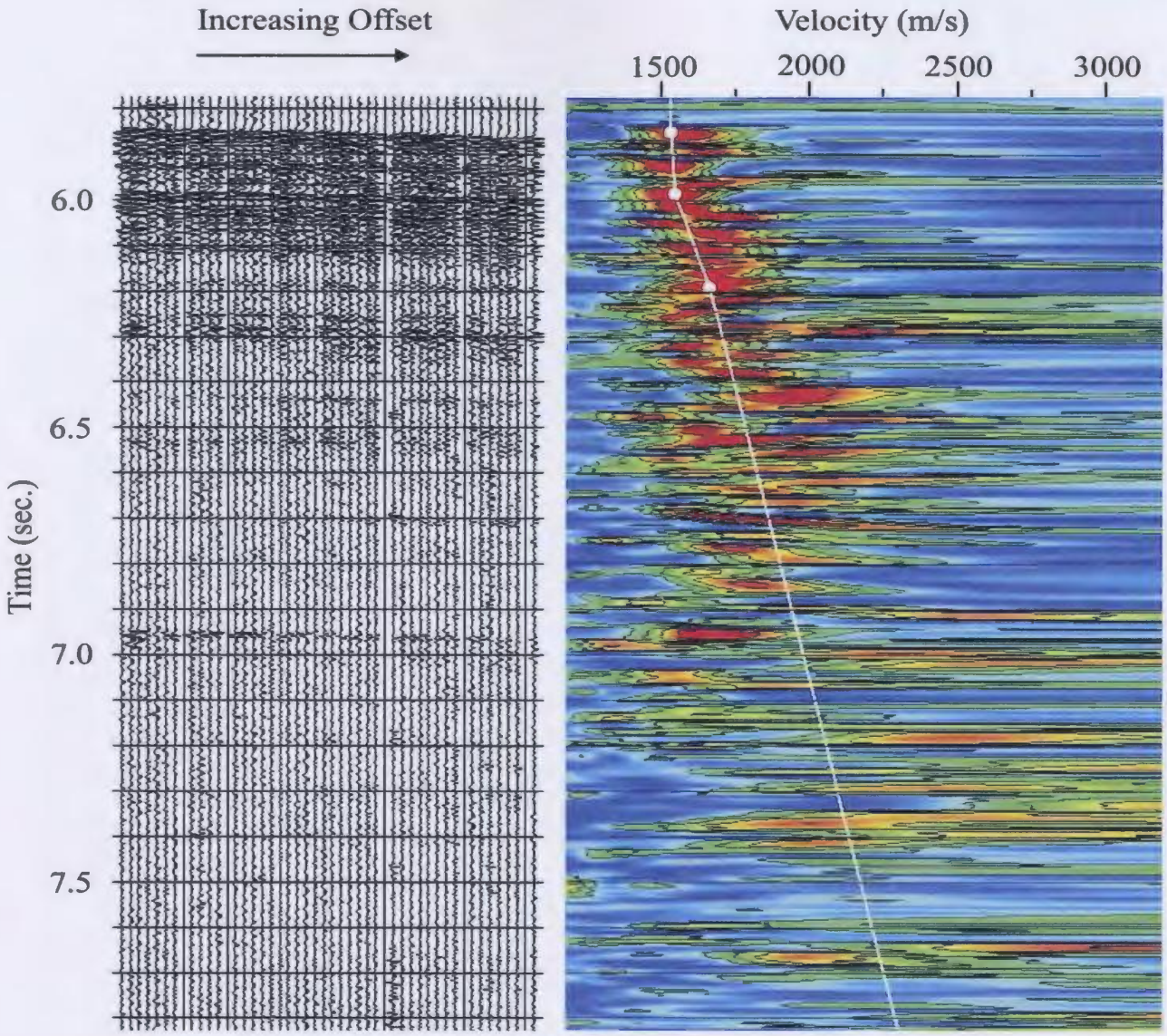
Increasing Offset
Velocity (m/s)
1500
2000
2500
3000
6.0
6.5
7.0
7.5
Time (sec.)

Figure 2.2.1 b)

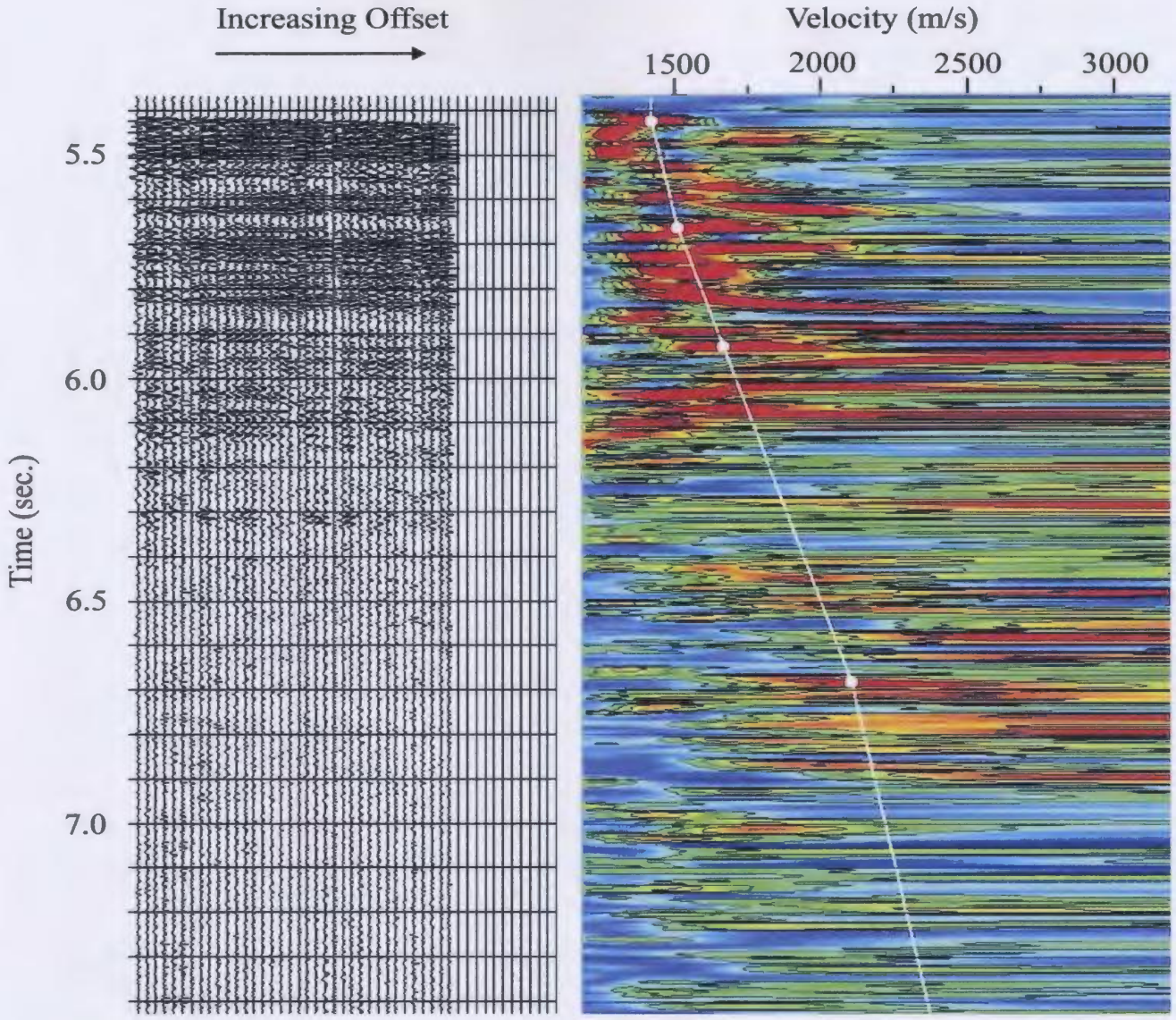
Increasing Offset
Velocity (m/s)
1500
2000
2500
3000
5.5
6.0
6.5
7.0
Time (sec.)

Figure 2.2.1c)

The complex bathymetry and subsurface structure of the Rhodes Basin degrade seismic imaging by introducing irregularity to the wave field and ray paths. Regions of steep seabed slopes and out-of-plane reflections from adjacent bathymetric and subsurface structures often require special attention during the migration process. In many instances, it is unclear which of the superimposed reflections originate from reflectors in the vertical plane of the profile (if any) and which reflections originate from reflectors out of the profile plane. In addition, a high amplitude reflector located at only a modest depth below the seabed over a large portion of the Rhodes Basin commonly results in early attenuation of the source signal.

2.2.2: Trace Editing and Frequency Filtering

Throughout the cruise, several recording channels operated poorly. In some instances a particular channel (or group of channels) was consistently noisy, while in other instances the noisy channels change along a line in an unpredictable manner. For this reason, a significant portion of the time invested in processing the lines was devoted to trace editing and frequency filtering. Most of the data has a 20-40-180-250 Hz Ormsby bandpass frequency filter initially applied to it. In addition, notch filters were often used to attenuate noise associated with frequencies in the vicinity of 52 Hz, 56.8 Hz and 169 Hz (Figs. 2.2.2, 2.2.3). Originally, it was thought that applying the minimum phase frequency notch filters to all the traces would be the best course of action since targeting the noisy traces was not always simple as they sometimes changed from shot to shot.

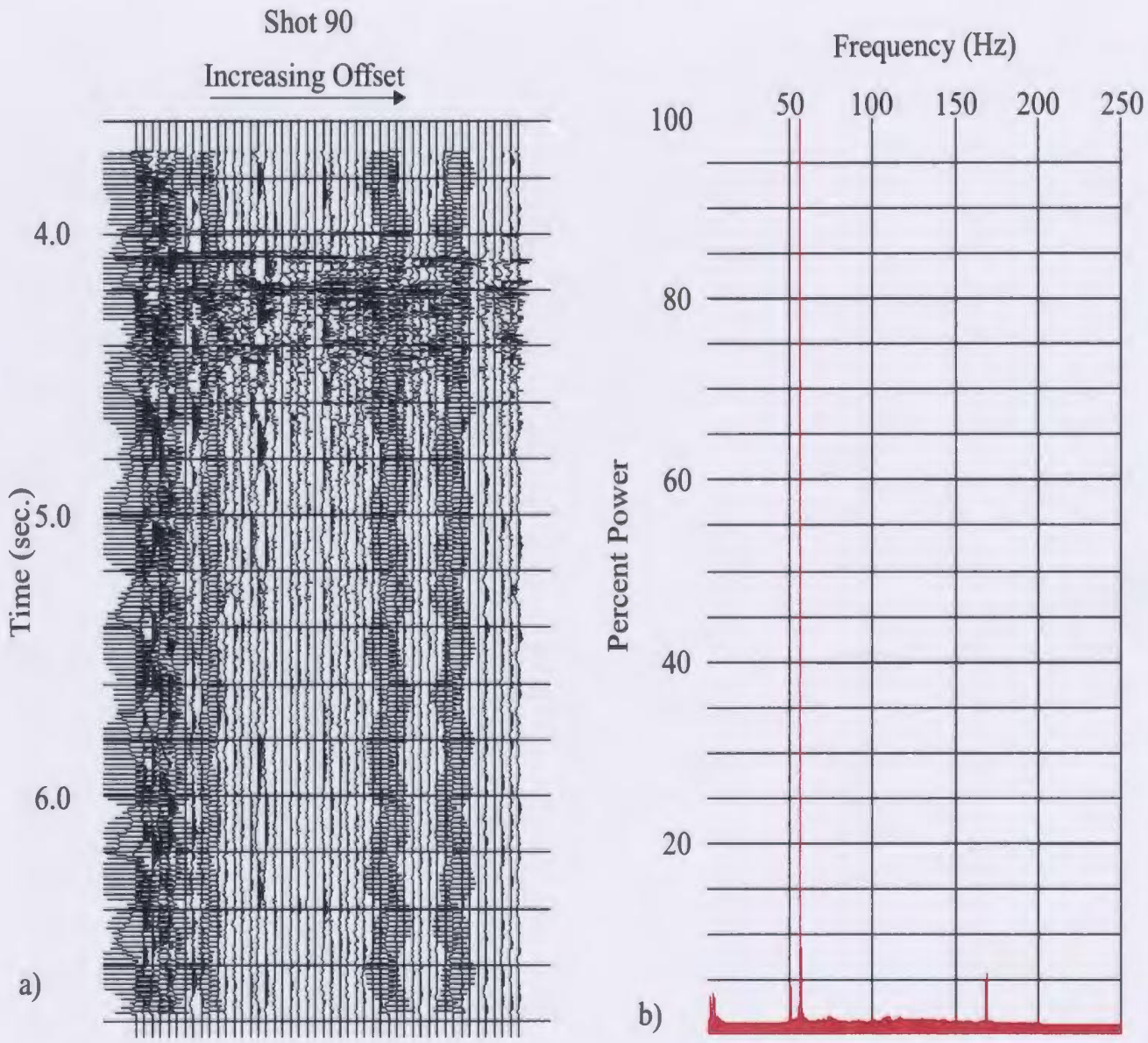

Figure 2.2.2: a) A shot gather showing shot # 90 of line 64 before frequency filtering. b) Note the dominance of 52, 57 and 169 Hz noise. As can be seen directly from the shot gather, these dominant frequencies are confined to particular recording channels.

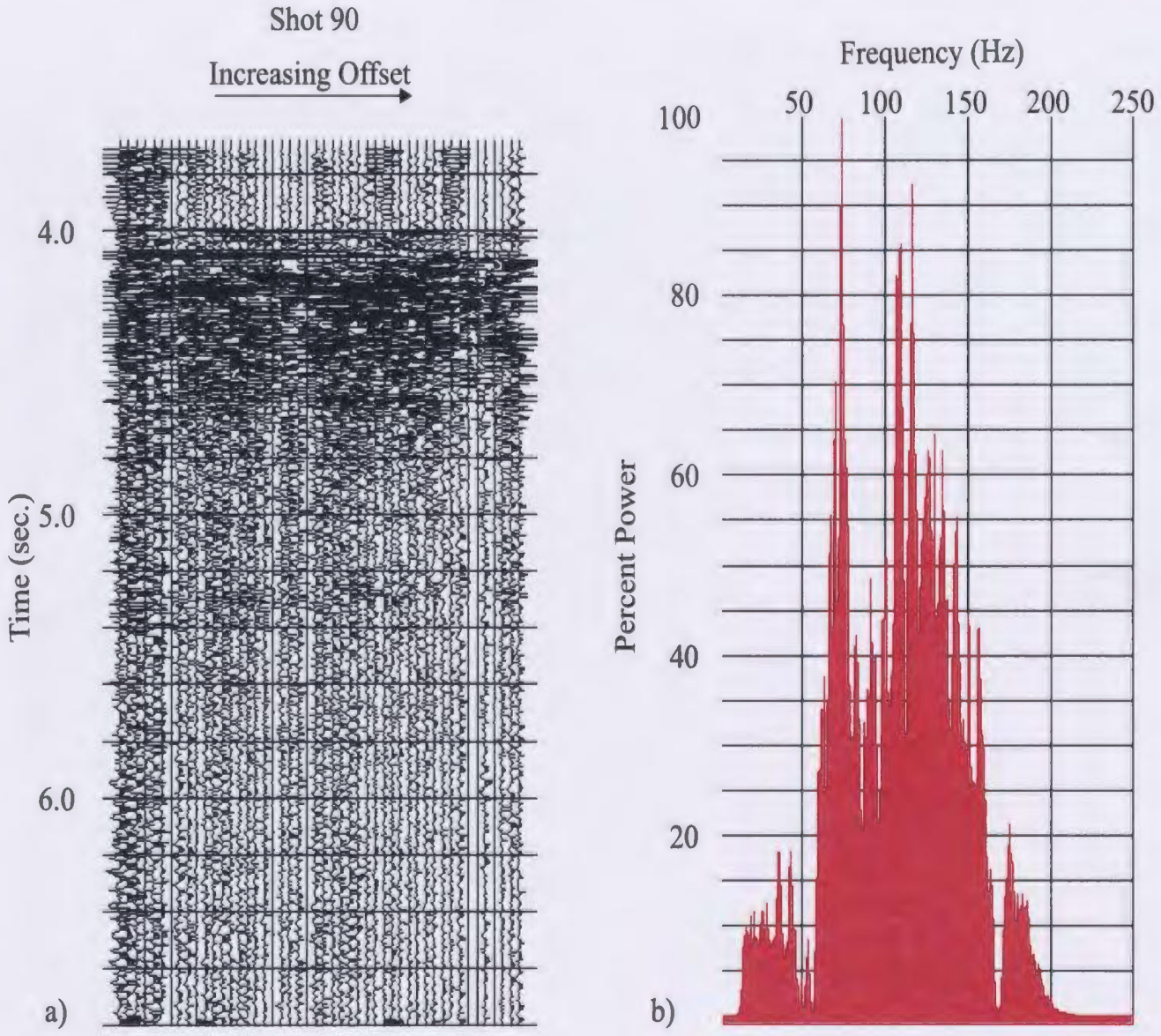

Figure 2.2.3: a) A shot gather showing shot # 90 of line 64 after Ormsby bandpass and notch frequency filtering. b) Note the removal of 52, 57 and 169 Hz noise and the relative boost of signal after re-equalization.

There seemed to be no problem with this approach initially, however, later deconvolution attempts revealed that such wide application of the notch filters has devastating effects on the seismic response due to its over amplification of those frequencies that were removed from the spectrum during the notch filtering process. For this reason, the data were reprocessed with notch filters applied only to those shots/channels that would benefit most from their application before deconvolution was attempted. A detailed documentation of the process that led to this approach is provided in the upcoming deconvolution discussion. If the noise present on a shot gather was extreme and did not appear to be limited to any specific frequencies, the problematic channels were zeroed and omitted from any of the following processes. Shots #2001-2005 of line 64 illustrate a series of noisy shot gathers following a 'good' shot (shot #2000). These noisy shots were removed from the processing stream due to a lack of signal, possibly as a result of the guns failing to fire (Fig. 2.2.4).

Once the initial trace editing and initial frequency filtering was completed, the geometry was assigned for each line. Examination of specific trace gathers allowed for further checks for noisy/missing shots and correct locations of changes in recording delays. These delays were removed from the data by applying appropriate bulk static shifts to the recorded data. Care had to be taken here because delays recorded in the observers logs were not always accurately recorded or applied correctly. In some cases, analysis of the near trace gathers showed saw-tooth changes in recording delay with a

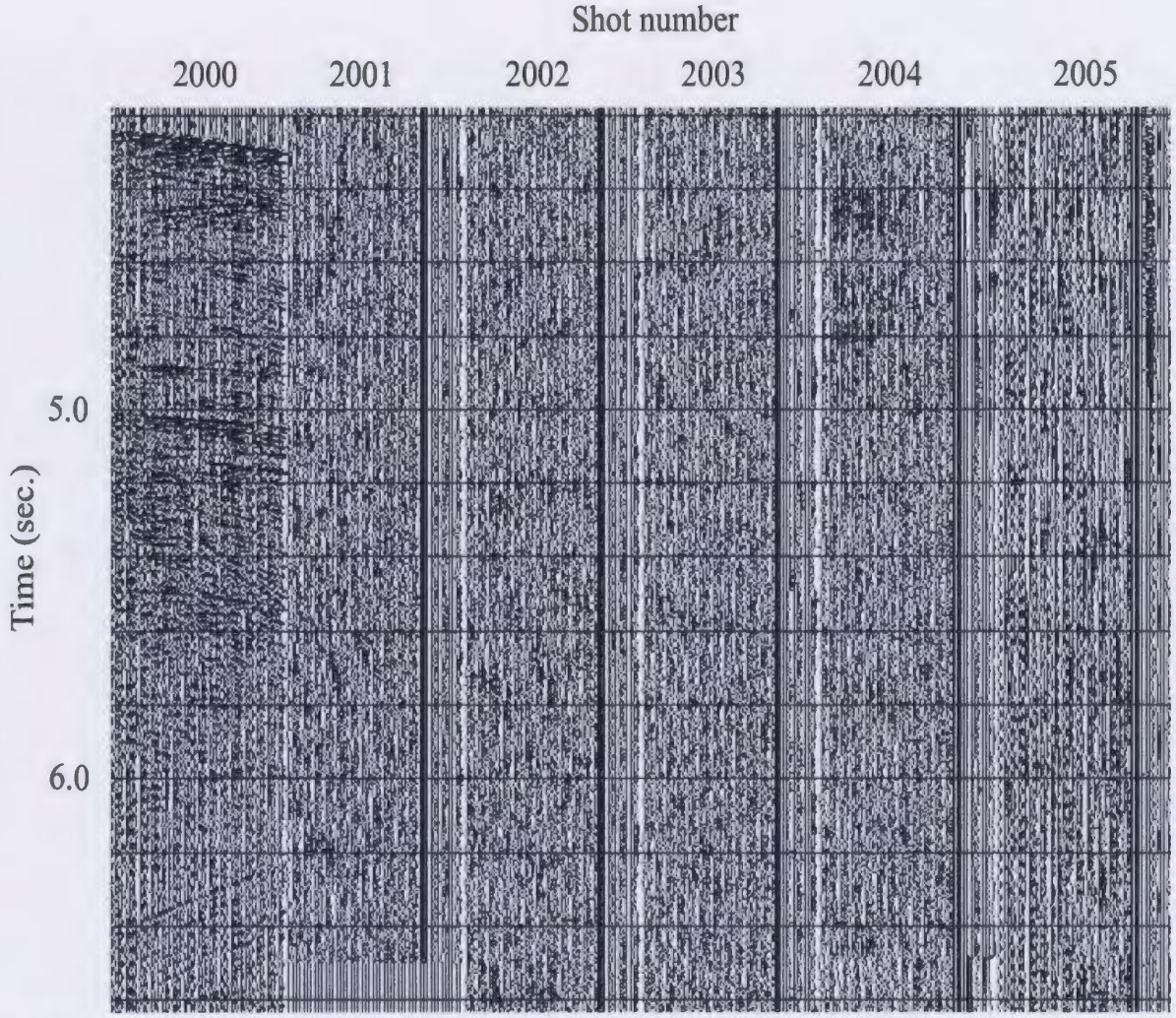

Figure 2.2.4: Shots 2001-2005 carry very poor signal relative to shot 2000. data from shots 2000-2005 were removed from further processing.

period of 22-24 shots. Over each affected zone, static shifts with a linear interpolation from 0 ms to 21 ms were applied to realign the reflections (Fig. 2.2.5).

2.2.3: Velocity Analysis

Velocity analysis was performed every 200 cdp's (1250 m) on ensembles of 5 cdp gathers ('super-gathers') per analysis location (60 traces). These super-gathers were used to enhance the signal to noise ratio of each gather in an effort to improve the velocity semblance. This procedure worked best in areas where dips were low. Stacking velocity picks were determined using semblance plots and constant velocity stacks. Velocity constraint is considerably better in regions with a shallow water depth due to the correspondingly greater normal move-out on the reflection hyperbolae. In addition, zones where all 48 channels are recording allow better velocity determinations because of the favourable effect that an increased number of far-offset traces has on the semblance calculation (Fig. 2.2.1).

2.2.4: Stacking and Migration

Due to the deep water and short streamer, effective stacking could be accomplished with a wide range of velocities for normal move-out correction. Following normal move-out corrections, the traces in each cdp gather were summed at constant time and the resultant amplitude divided by the number of live traces in the gather at each time to produce the stacked cdp trace in the seismic section.

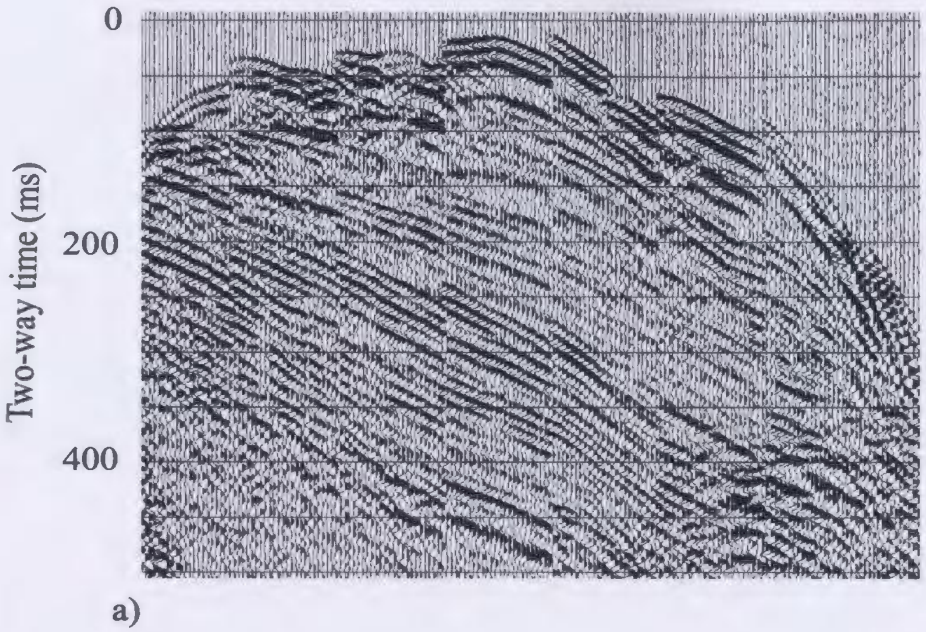

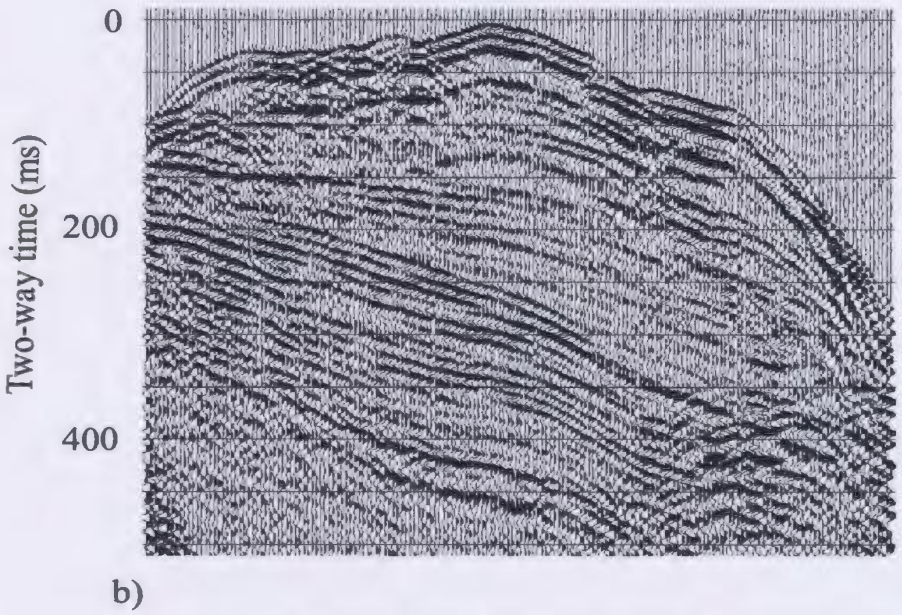

Figure 2.2.5: A near trace gather of 180 shots a) without and b) with the 21 ms interpolation delay shifts. Note the saw-tooth pattern in the timing errors of the uncorrected data.

Migration of the data presented a considerable challenge. Due to the presence of out of plane reflections and rough seabed surface, rather unusual velocities and lateral changes of velocity were sometimes required to better focus the images. The Kirchhoff time migration algorithm used allowed for suitable lateral and vertical velocity variations and executed reasonably quickly. Figures 2.2.6 and 2.2.7 illustrate the effect that changing the migration velocity has on the focussing of reflections. The seabed reflection at the base of the slope in Figure 2.2.6 (migrated at 1500 m/s) extends beyond the base of the slope to the right. In Figure 2.2.6 (migrated at 1600 m/s), this event is collapsed nicely, but the underlying basement reflectors are clearly overmigrated. Optimum imaging of both events requires a velocity inversion in the migration velocity function below the seabed. Such severe velocity inversions are likely the result of oblique nature of the seabed structure and not the actual velocity profile. Because the Kirchhoff time migration algorithm requires an input average velocity rather than interval velocities at any given point, it has potential to give a smoother response to extreme interval velocity inversions than algorithms that utilise interval velocities. Figures 2.2.6 and 2.2.7 also emphasize the important role of interpretative processing during the migration stage. The stacked section in Figure 2.2.7a displays many diffraction hyperbolae or "bowties". Some of these events appear asymmetrical with respect to both the slopes of the tails along a single event and the energy distribution along one tail relative to the other (Fig. 2.2.7a); indicating that this is a zone of complex structure that may involve out-of-plane and/or dipping reflectors. Figures 2.2.7b and c show constant velocity migrations of this panel of cdp's at velocities

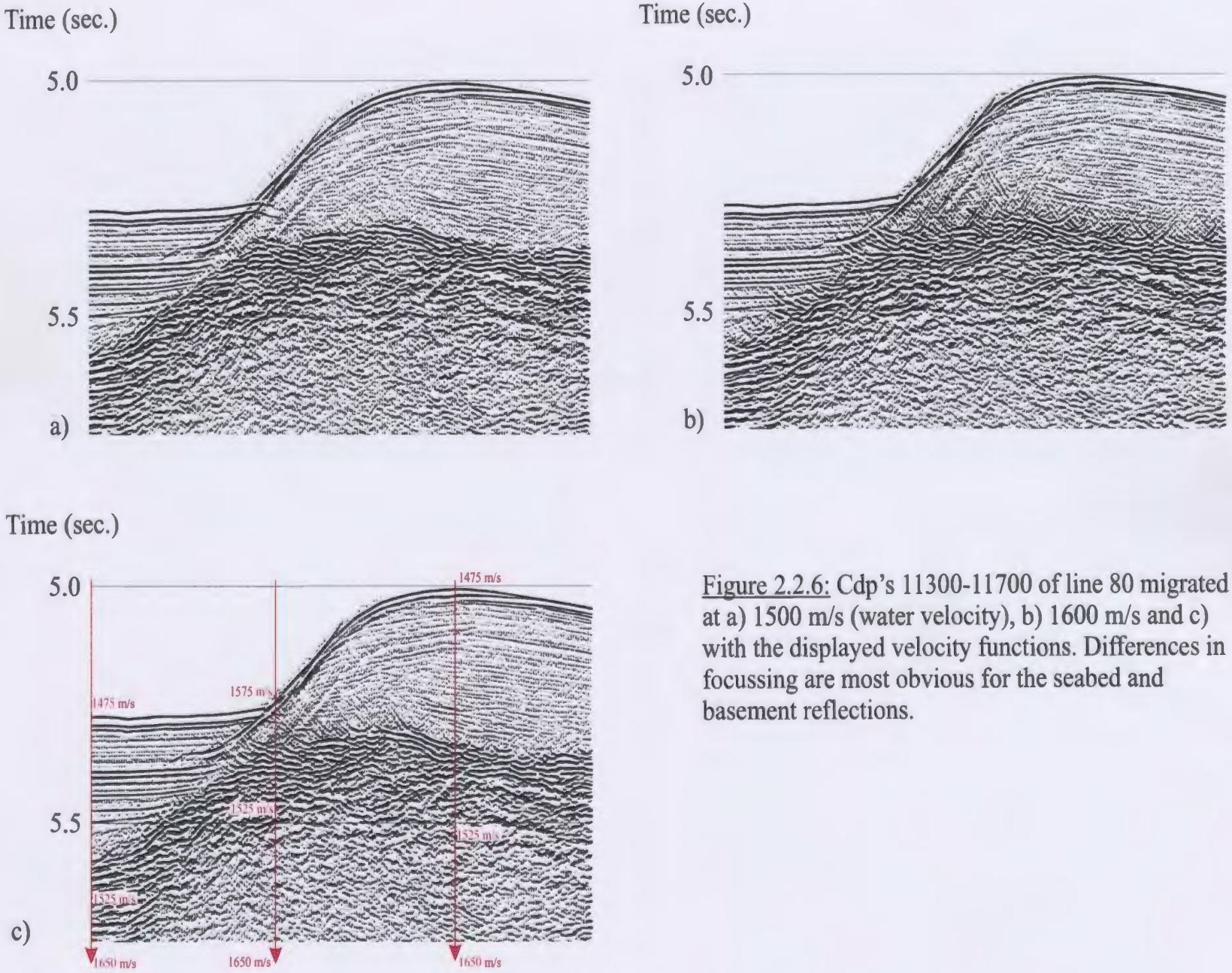

Figure 2.2.6: Cdp's 11300-11700 of line 80 migrated at a) 1500 m/s (water velocity), b) 1600 m/s and c) with the displayed velocity functions. Differences in focussing are most obvious for the seabed and basement reflections.

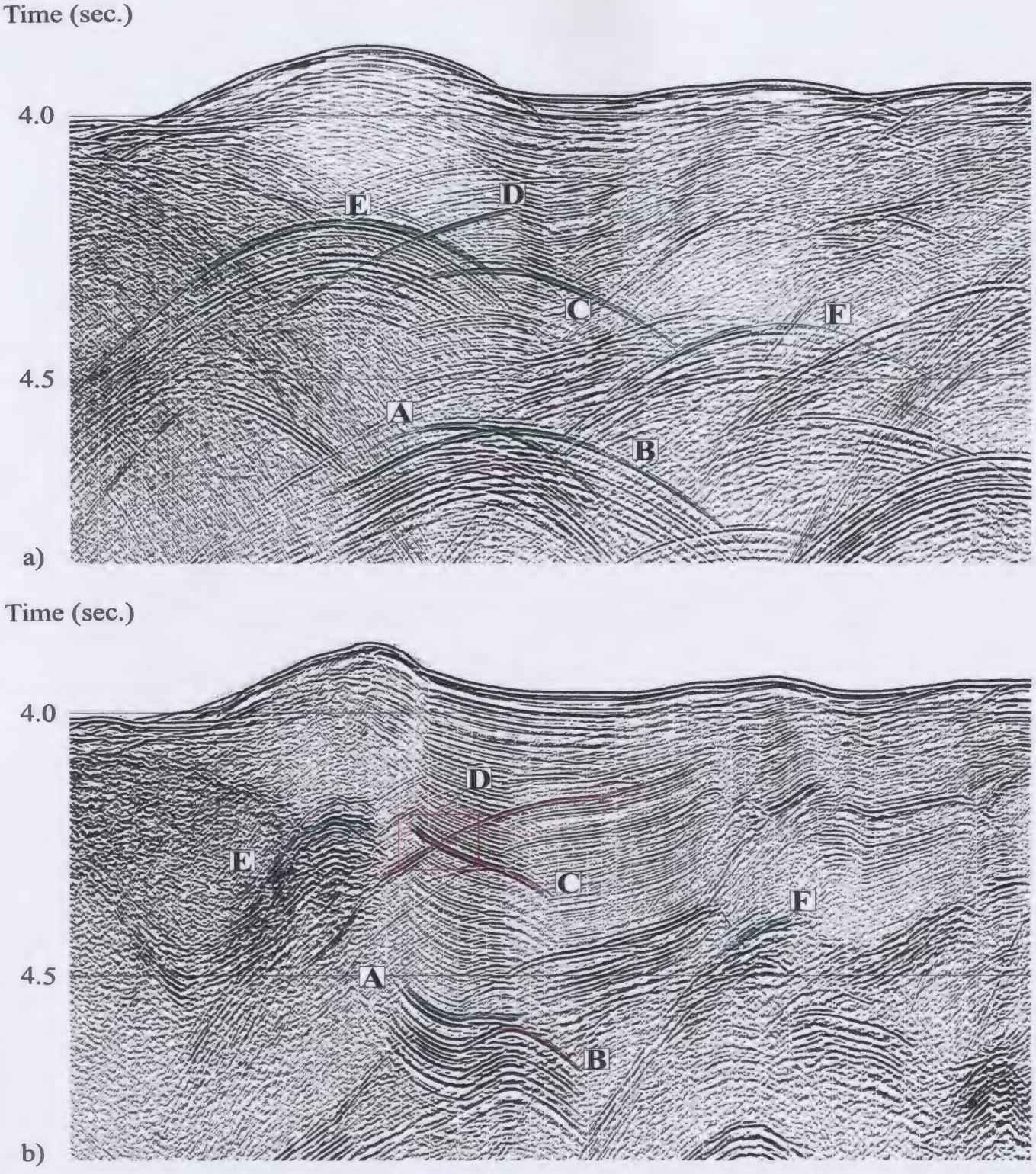

Figure 2.2.7: Cdp's 3500-4300 of line 64; a) stacked section, migrated at b) 1500 m/s (water velocity), c) 1700 m/s and d) the displayed velocity function. Red indicates poor imaging whereas bl indicates more acceptable results.

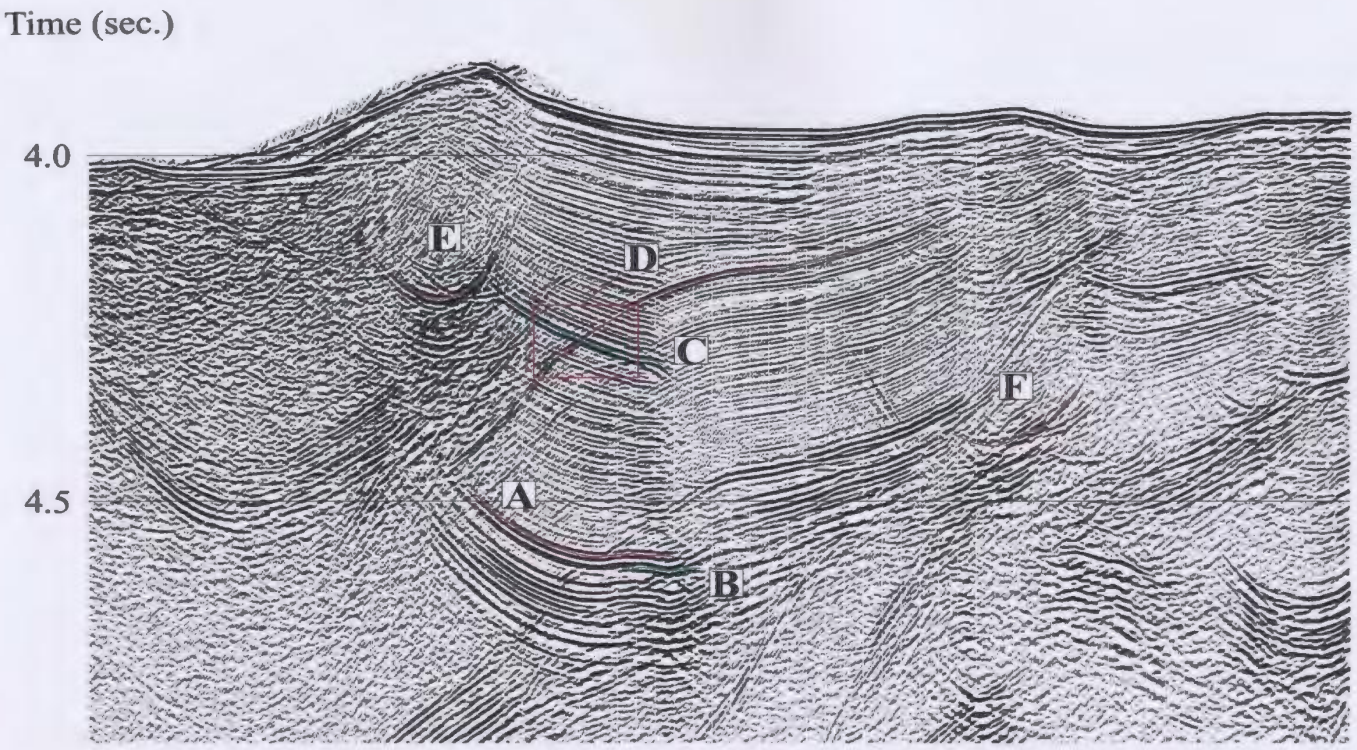

Figire 2.2.7c)

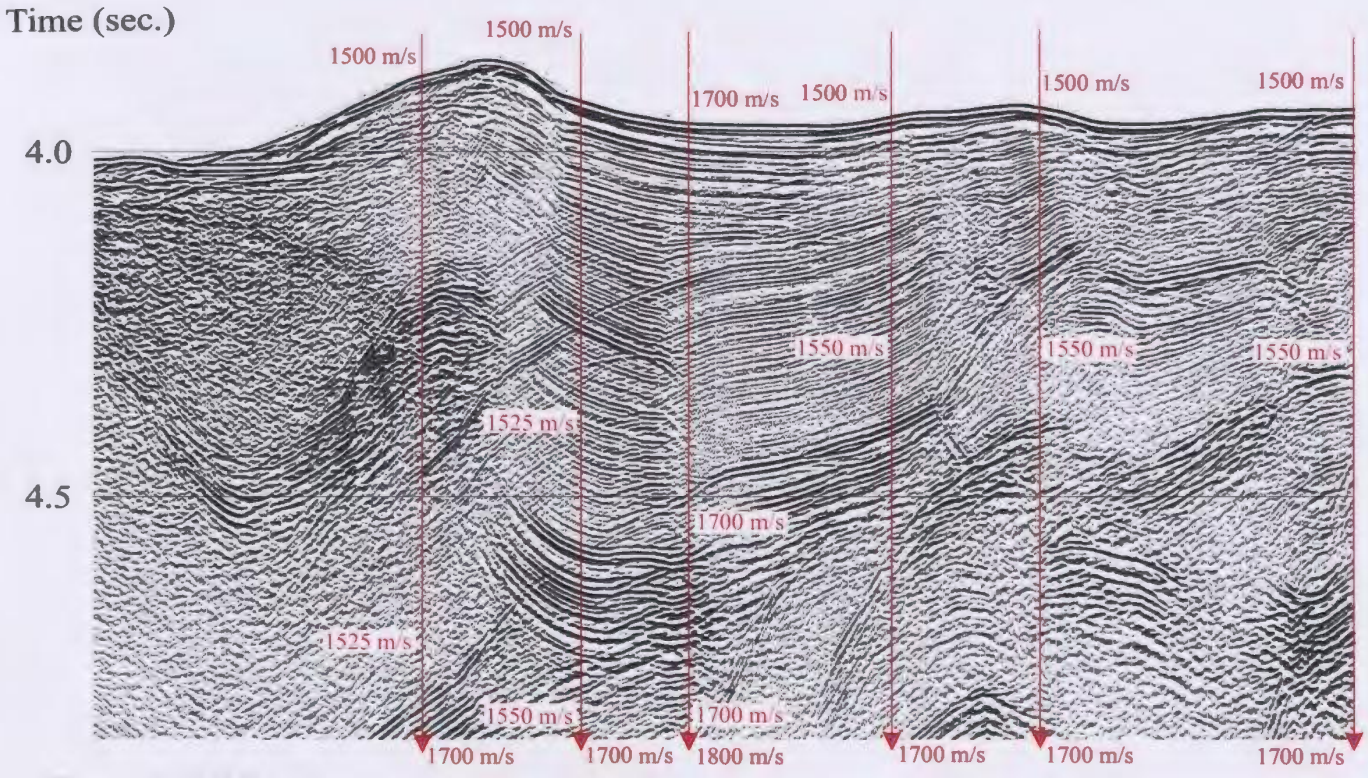

Figure 2.2.7d)

1500 m/s and 1700 m/s, respectively. While the1500 m/s migration does a reasonable job of migrating the shallow reflections, many of the apparent out-of-plane reflections (as determined by the crossing of reflectors; e.g., events C and D) are better focussed by the 1700 m/s migration. Event A could be migrated at a very low velocity (~1200 m/s) to make it appear flat-lying. However, a velocity of 1500 m/s allows it to conform to the perfectly reasonable synformal-like geometry of the overlying package. This interpretation is supported by the fact that while dipping and oblique events are known to migrate at velocities greater than those of their flat-lying, in-plane equivalents, there is no simple geometry that allows for events to migrate at an anomalously low velocity. The residual diffraction tails of events B, C and D suggests that they do not focus well with a migration velocity of 1500 m/s whereas events E and F both appear to focus nicely. Increasing the migration velocity to 1700 m/s over migrates events A, E and F but focuses event B to a clear, flat reflector (Fig. 2.2.7c). Event C is also focussed better at this higher velocity as its energy is less distributed in Figure 2.2.7c than in Figure 2.2.7b; especially on the right-hand side of the reflector. However, events D and C still cross-over one another and do not separate even at anomalously high migration velocities (> 2000 m/s). The velocity profile used in the final migration of this section and the resulting data are illustrated in Figure 2.2.7d. The strong reflectivity, thickness and proximity of event B to event A suggests that event B could be interpreted as an out-of-plane stratigraphic equivalent of A and therefore requires a higher migration velocity to image properly. These events confirm the large role of out-of-plane reflections and the short comings of 2-D data

coverage and migration in an area that clearly requires 3-D considerations.

2.2.5: Deconvolution

The following discussion addresses the issue of increasing the temporal resolution of the data by compressing the wavelet to a spike via spiking deconvolution. Figure 2.2.8 shows the first several hundred milliseconds of cdp's 3868-4357 from line 64 and its corresponding autocorrelogram and power spectrum. These data are representative of the output of the original frequency filtering where the notch filters were applied to all shots and channels (frequency filtering discussed earlier). The seismic data for Figure 2.2.8, and the following figures of similar format, are displayed as variable area only with a bias of -10%, a gain scalar of unity and a clip limit of two trace spacings. Beginning at the seabed reflection, a 600 ms trace length was input into the autocorrelation function. The autocorrelograms display only one autocorrelation trace for every fourth trace displayed in the seismic data. These traces are displayed as variable area only with a bias of zero, a gain scalar of 0.5 and a clip limit of one trace spacing to allow easy observation of amplitude variations. The power spectrum for each window of data is displayed as 'percent power' where the maximum power (the reference value) achieved at a particular frequency is given a value of 100%. The percent power contribution of each of the other frequencies present is then calculated relative to the reference valued and displayed as a percentage of the reference maximum power.

The seabed reflection suggests that the wavelet consists of multiple lobes and a

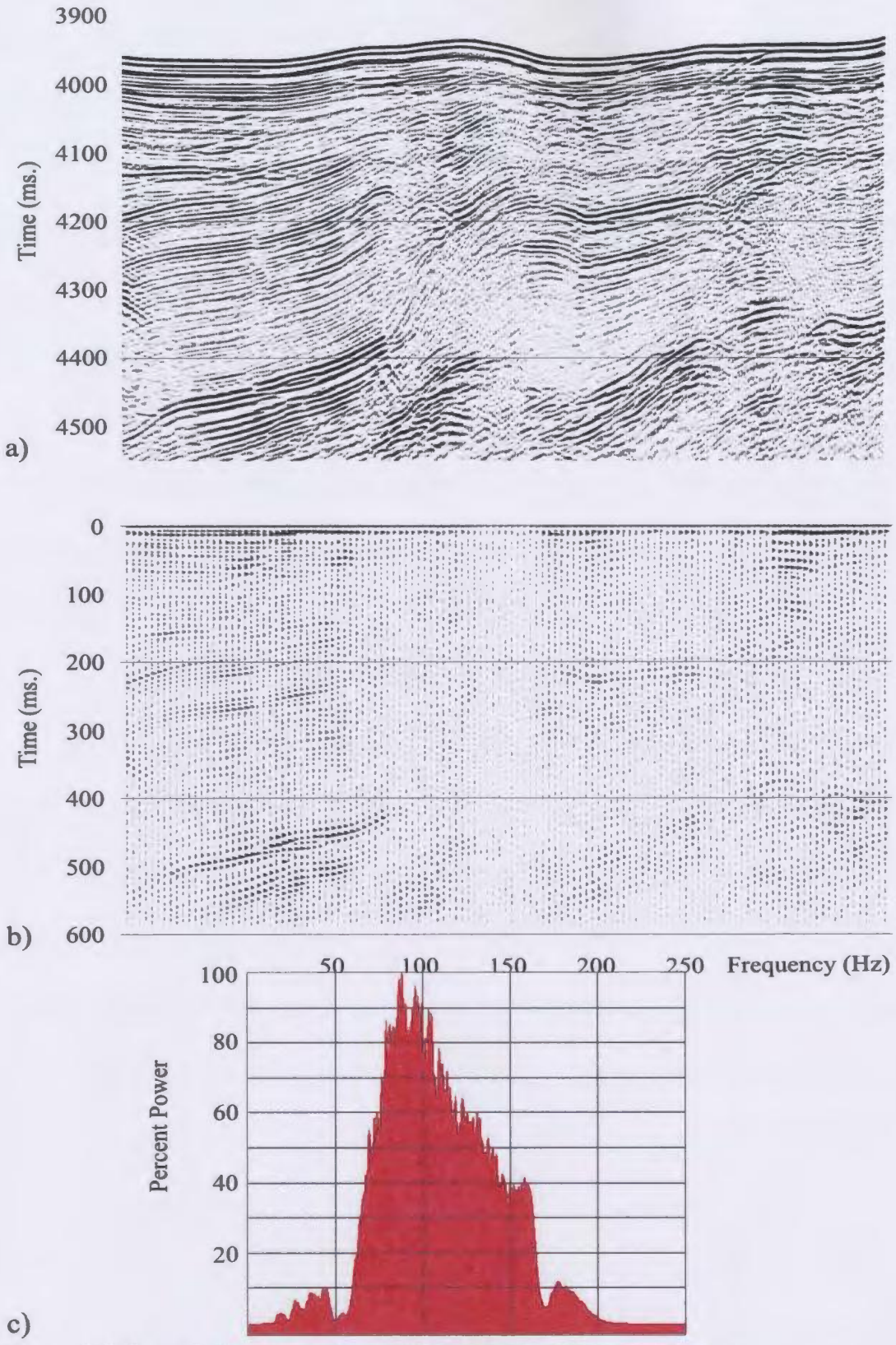

Figure 2.2.8: a) Migrated cdp's 3868-4357 of line 64. b) Autocorrelogram of every fourth trace in (a). c) Power spectrum of the data shown in (a).

faint, ~ 200 ms long, reverberatory tail (Fig. 2.2.8a). These reverberations inhibit our ability to locate reflections temporally and may mask underlying reflections of lower amplitude; especially those near the seabed. From the autocorrelogrm, most of the energy is contained within the first ~ 35 ms. The low frequency tail is not visible on the autocorrelogram, perhaps due to its low amplitude relative to the seabed reflection on a true amplitude section. Stacking the autocorrelogam traces together did not provide an increased ability to identify this weak, ~80 ms periodicity. Figure 2.2.8c illustrates the power spectrum for the data shown in part a). Note the low power levels from 50-60 Hz and the notch in the power spectrum at 169 Hz.

Based on the low frequency reverberations seen in Figure 2.2.8a, an attempt is made at spiking deconvolution using a Wiener-Levinson, least-squares, minimum-phase filter. This first attempt utilizing a 200 ms operator length and 0.5% pre-whitening gives rise to the data shown in Figure 2.2.9. Although the power spectrum indicates that the spectrum is flattened nicely by this process, low frequencies dominate the seismic section. A 30-80-180-250 Hz minimum phase Ormsby bandpass filter is applied to this deconvolved data in an effort to reduce the amplitude of these low frequencies (Fig. 2.2.10). The result is a section with an attenuated low frequency tail but enhanced higher frequency (170-200 Hz) reverberations than that of the original data set.

A second minimum phase spiking deconvolution is attempted by choosing a 35 ms operator length. In this case, the goal is to compress only the higher amplitude lobes

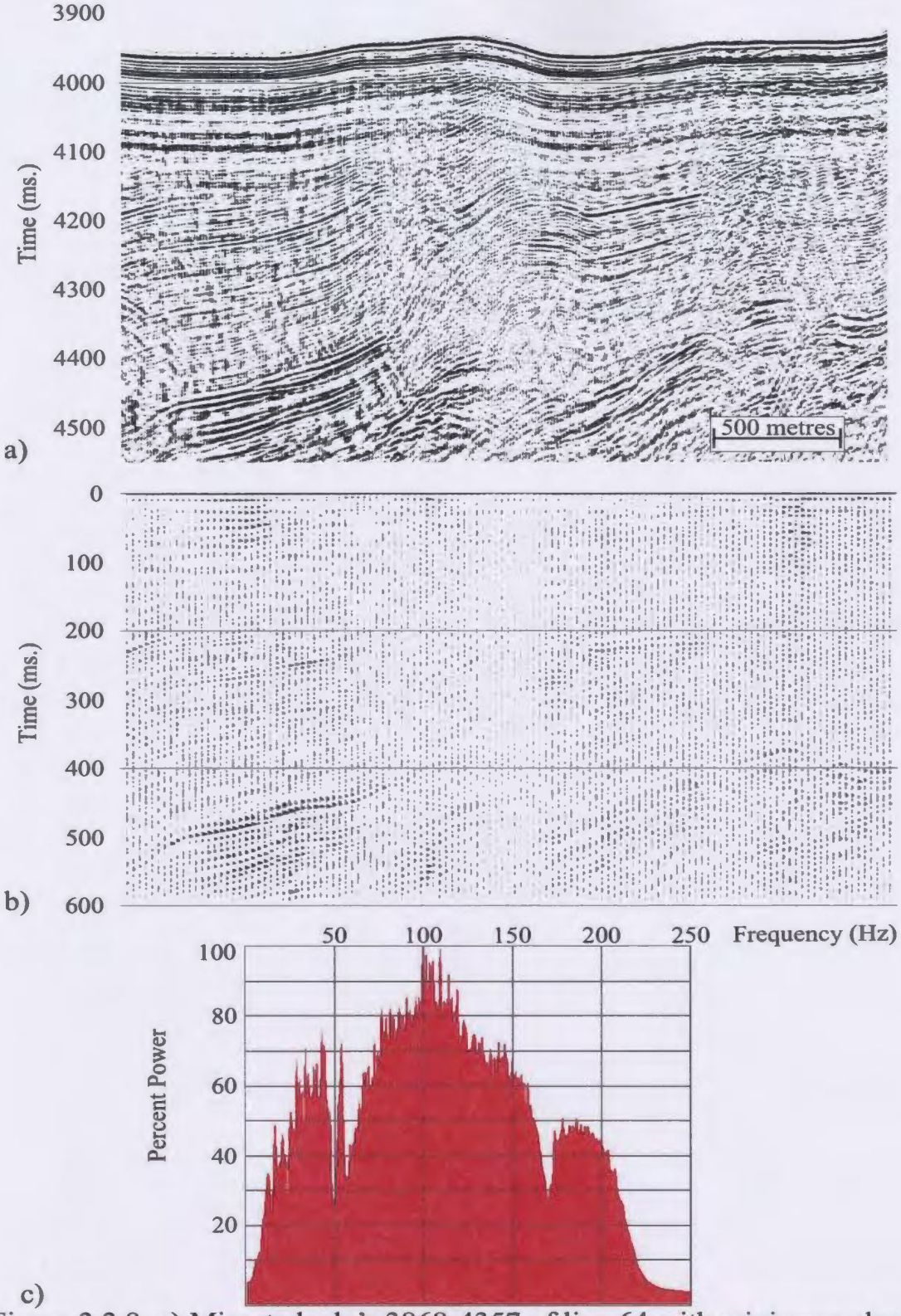

Figure 2.2.9: a) Migrated cdp's 3868-4357 of line 64 with minimum phase spiking deconvolution applied (200 ms operator length). b) Autocorrelogram of every fourth trace in (a). c) Power spectrum of the data shown in (a).

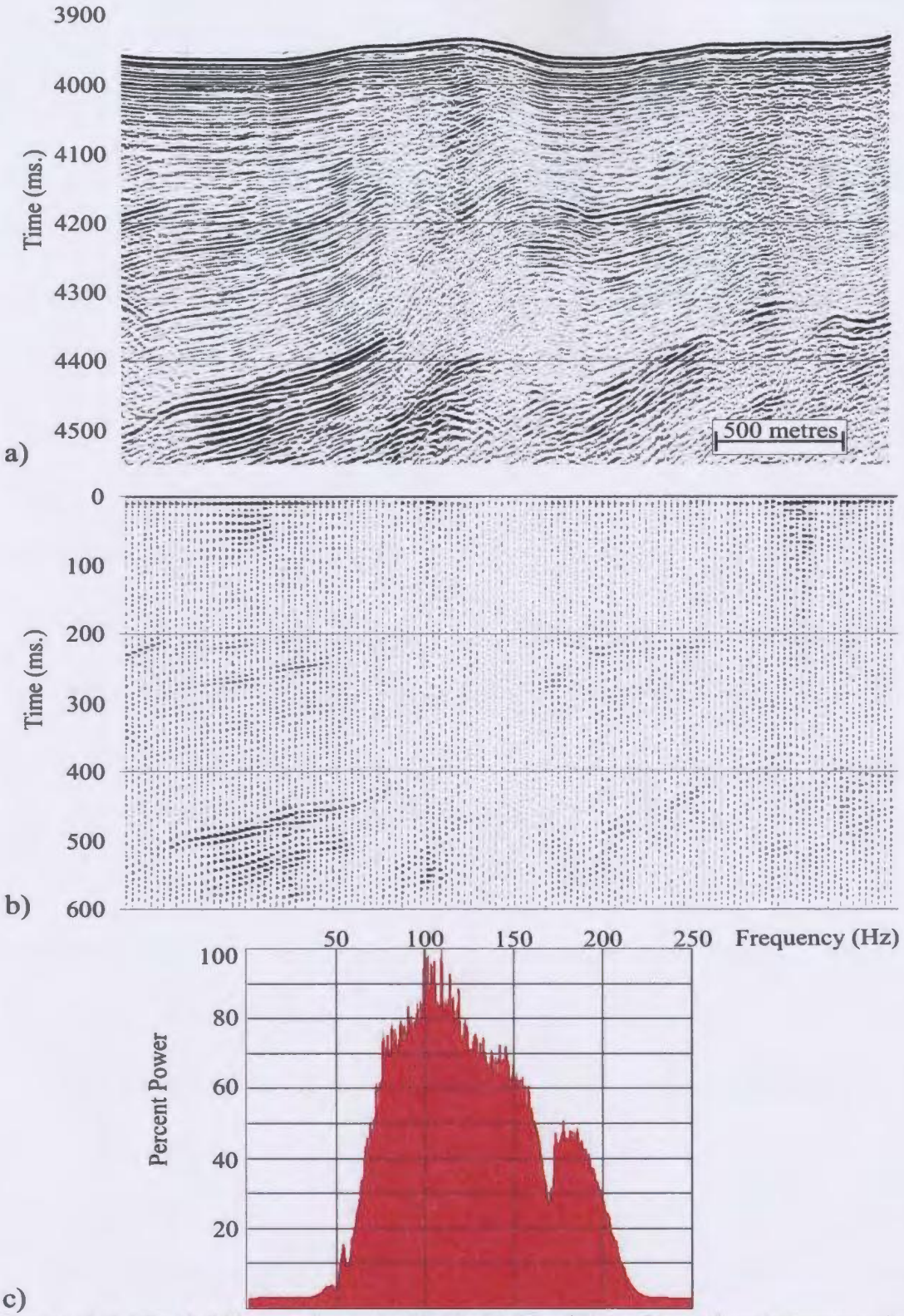

Figure 2.2.10: a) Migrated cdp's 3868-4357 of line 64 with minimum phase spiking deconvolution (200 ms operator length) and 30-80-180-250 Hz Ormsby minimum phase bandpass filter applied. b) Autocorrelogram of every fourth trace in (a). c) Power spectrum of the data shown in (a).

located toward the onset of the wavelet. Not surprisingly, amplification of the low and high-end frequencies is more pronounced in this deconvolution (Fig. 2.2.11) than for the 200 ms operator length deconvolution. Application of a 30-80-180-250 Hz minimum phase Ormsby bandpass filter removes the anomalously powerful frequencies generated by the deconvolution but still shows high-frequency reverberations in the data (Fig. 2.2.12). Experimentation with larger pre-whitening levels during deconvolution yields less amplification of the lower frequencies, but serves only to degrade the data by reducing the signal-to-noise ratio and producing a result much like the earlier deconvolved, bandpass-filtered data.

Although the frequency-filtered minimum phase spiking deconvolution attempts are somewhat effective at broadening and equalizing the frequency spectrum, they do not produce superior results to the input data. Several other minimum phase deconvolution operators of differing lengths were tested. None of these attempts yielded results that improved upon the original data. Zero phase spiking deconvolution was also attempted but produced results similar to those of the minimum phase spiking deconvolutions (Figs. 2.2.13, 2.2.14).

The failure of both the minimum and zero phased spiking decovolutions suggests that the data does not closely approximate either minimum or zero phase data; and therefore must be of mixed phase. This prompted an investigation into the potential of a deterministic approach to spiking deconvolution rather than the previously attempted statistical approach. However, because no direct measure of the source wavelet is

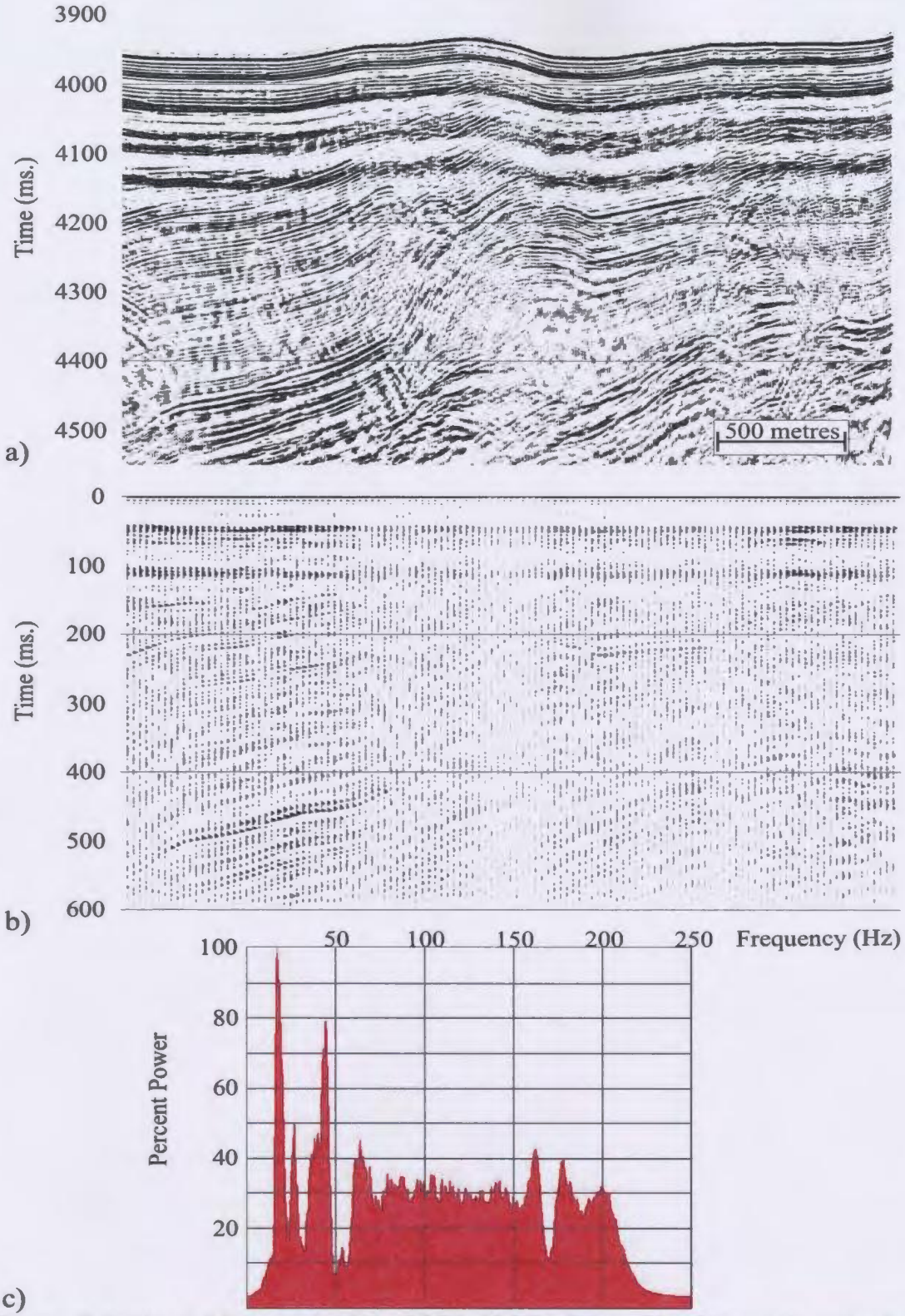

Figure 2.2.11: a) Migrated cdp's 3868-4357 of line 64 with minimum phase spiking deconvolution applied (35 ms operator length). b) Autocorrellogram of every fourth trace in (a). c) Power spectrum of the data shown in (a).

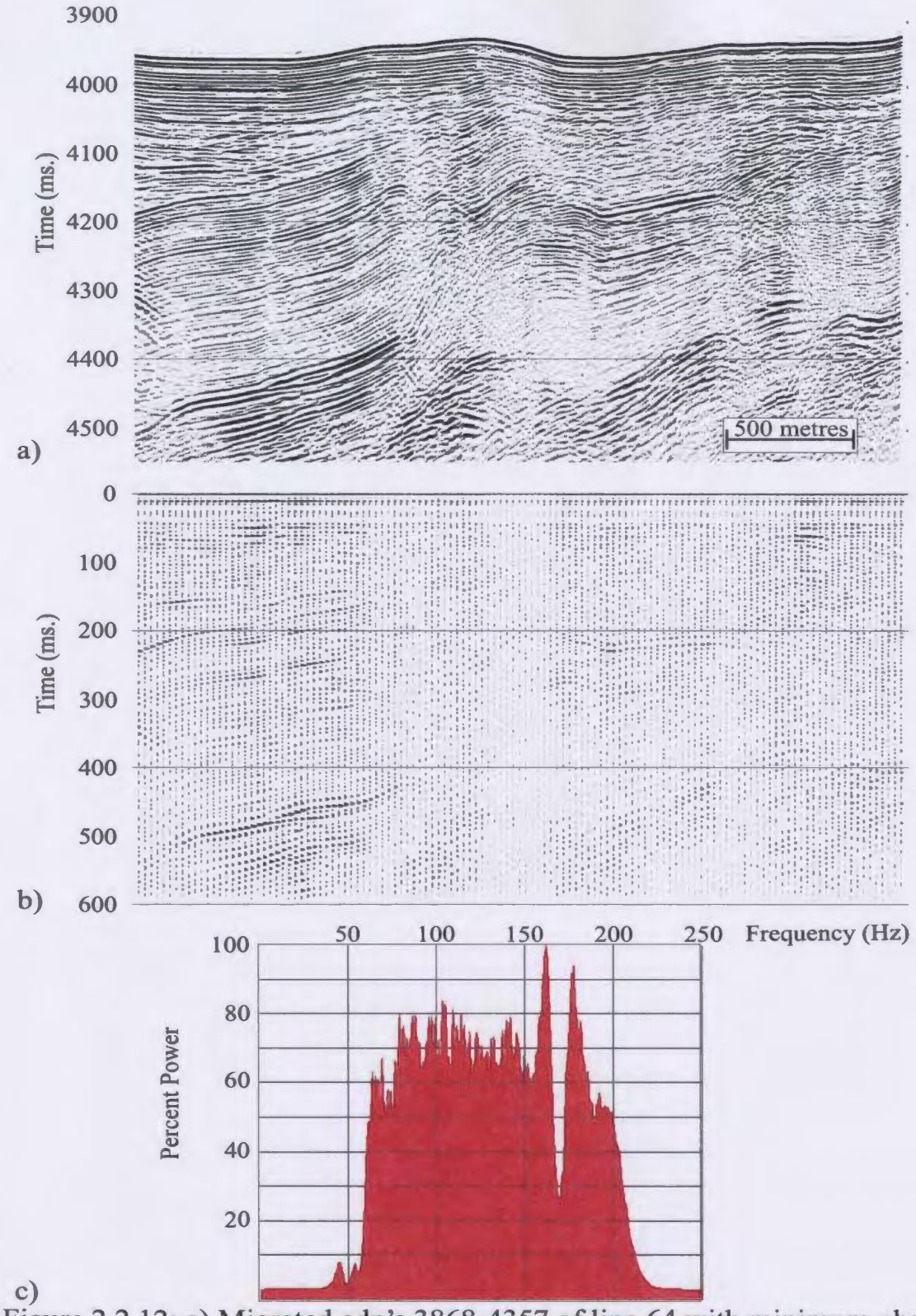

Figure 2.2.12: a) Migrated cdp's 3868-4357 of line 64 with minimum phase spiking deconvolution (35 ms operator length) and a 30-80-180-250 Hz Ormsby bandpass filter applied. b) Autocorrellogram of every fourth trace in (a). Correlation window length = 600 ms, gain = 0.5, bias = 0. c) Power spectrum of the data shown in (a).

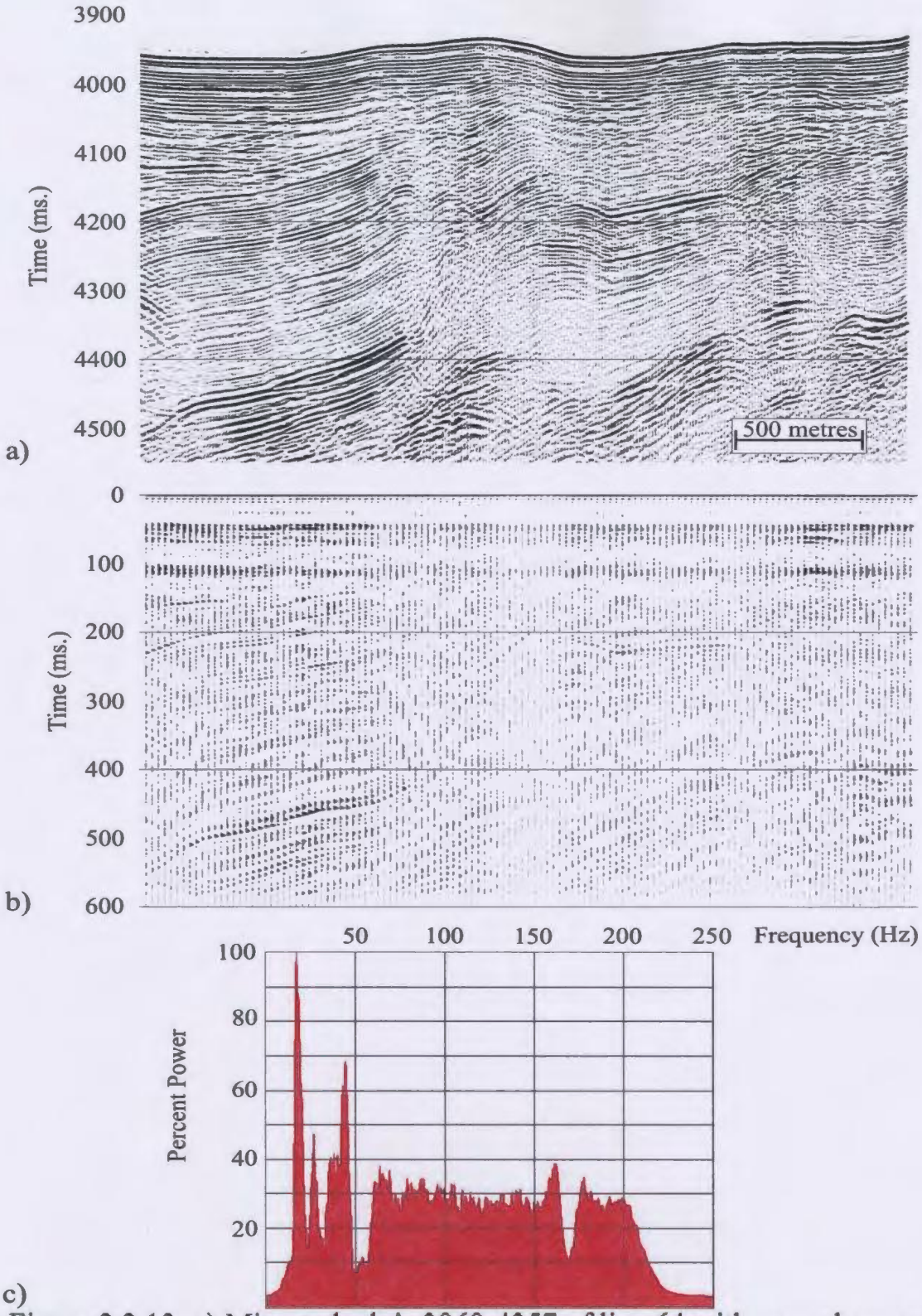

Figure 2.2.13: a) Migrated cdp's 3868-4357 of line 64 with zero phase spiking deconvolution applied (35 ms operator length). b) Autocorrellogram of every fourth trace in (a). c) Power spectrum of the data shown in (a).

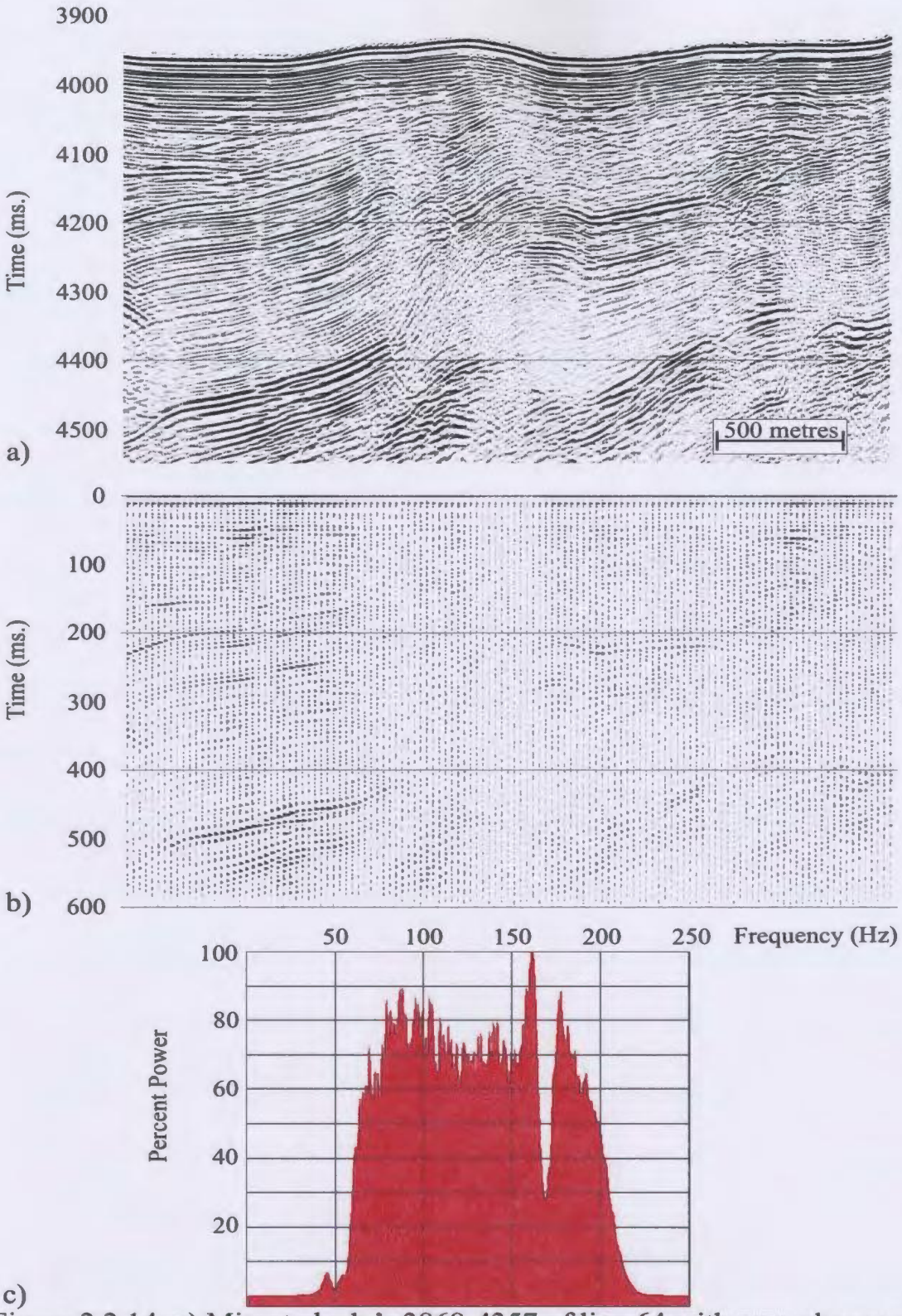

Figure 2.2.14: a) Migrated cdp's 3868-4357 of line 64 with zero phase spiking deconvolution (35 ms operator length) and 30-80-180-250 Hz zero phase Ormsby bandpass filter applied. b) Autocorrellogram of every fourth trace in (a). c) Power spectrum of the data shown in (a).

available, the deterministic deconvolution process must be preceded by a form of wavelet estimation.

The method of wavelet estimation chosen for this study is one that allows the extraction of a mixed-phase wavelet from stacked seismic traces by using fourth-order cumulants - high-order covariance functions in the time domain that, unlike lower order cumulants such as autocorrelations (second-order) and skewness (third-order), retain phase information (Lazear, 1993). A parametric model of the wavelet that specifies the wavelet length and its time of maximum amplitude is provided to reduce computation time. Solving for the wavelet then proceeds along an iterative process through which the difference between the fourth-order cumulant of the seismic data and the fourth-order moment function of the wavelet is minimized in a mean-square error sense. The resulting wavelet will correspond with the seismic wavelet if the reflection series is a non-Gaussian, stationary, statistically random process and if the noise is random (these conditions force the noise and reflectivity cumulants to be uncorrelated up to the fourth-order). However, numerical simulations and seismic data examples have shown that results from this process are good even for data sets with high levels of signal-to-noise (white noise) and reflectivity probability distribution functions that approach a Gaussian distribution as long as the data set used for the cumulant estimation is large ($>10^3$ samples) and stationary (Lazear, 1993).

Four issues are of immediate concern: (1) How long is the wavelet? (2) At what time is its maximum amplitude? (3) Does the wavelet change significantly from trace to

trace? And (4) How stationary is the wavelet in time? The length of the wavelet trace is not of great concern. If a length too long is chosen, then the latter terms are very small. If too short a length is chosen, then the wavelet is truncated. Several trace lengths were extracted with minimal difference in their deconvolution results. Because this experimentation is chiefly concerned with the initial three lobes of the wavelet, a wavelet length of 35 ms is selected for presentation here. Wavelets are extracted from four zones (zones 1-4) that each contain 300-490 cdp traces and time windows that range from 200 ms to 1600 ms in length (Fig. 2.2.15). These variations allow exploration of questions regarding the variation of the wavelet over large distances as well as its stationarity in time along a single trace.

Zone 1 is chosen as the starting point for the wavelet estimation. Through trial and error it was determined that a window length of 1000 ms provides consistent wavelet estimates for a wide assortment of wavelet parameters. For this reason, a 1000 ms window length is used to test the impact of changing the 'time of maximum amplitude' of the wavelet to be extracted at this location. Twenty iterations is considered to be appropriate as any further iterations increase the processing time considerably and produce a negligible reduction in the mean-square error. With these parameters held constant, the time of maximum amplitude is allowed to vary so that the best parametric model for the wavelet extraction can be identified. Because the wavelet extraction algorithm can estimate the wavelet to within a polarity reversal, it is only necessary to test the time of maximum amplitude between T/4 to T/2; where T = wavelet length.

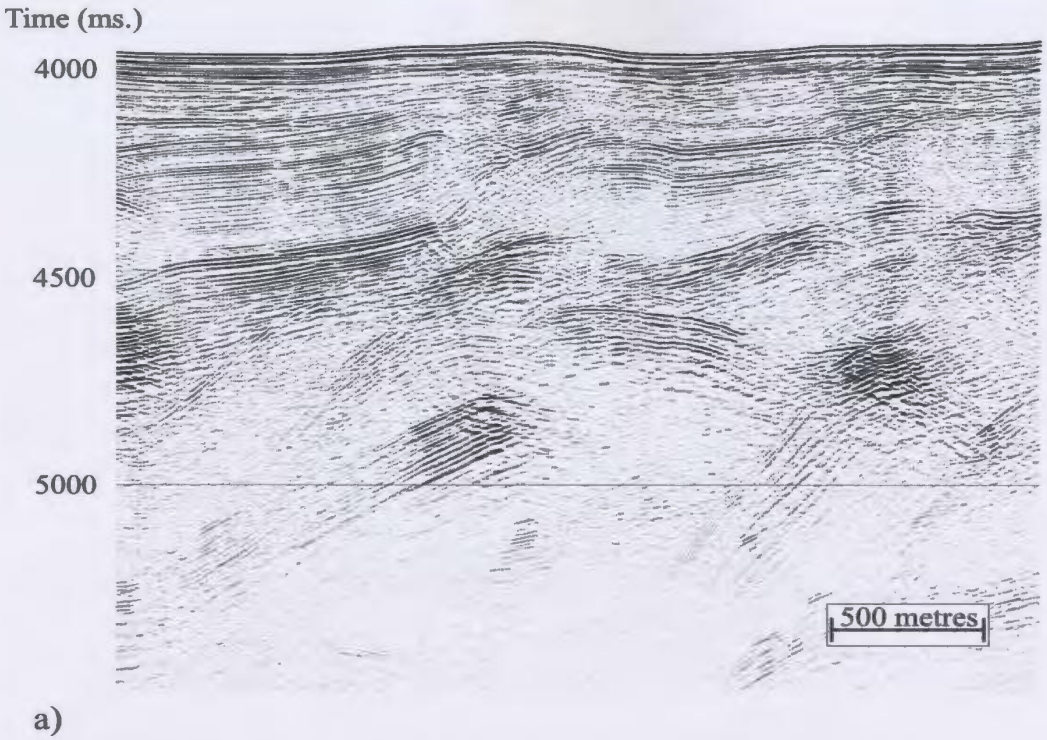

a)

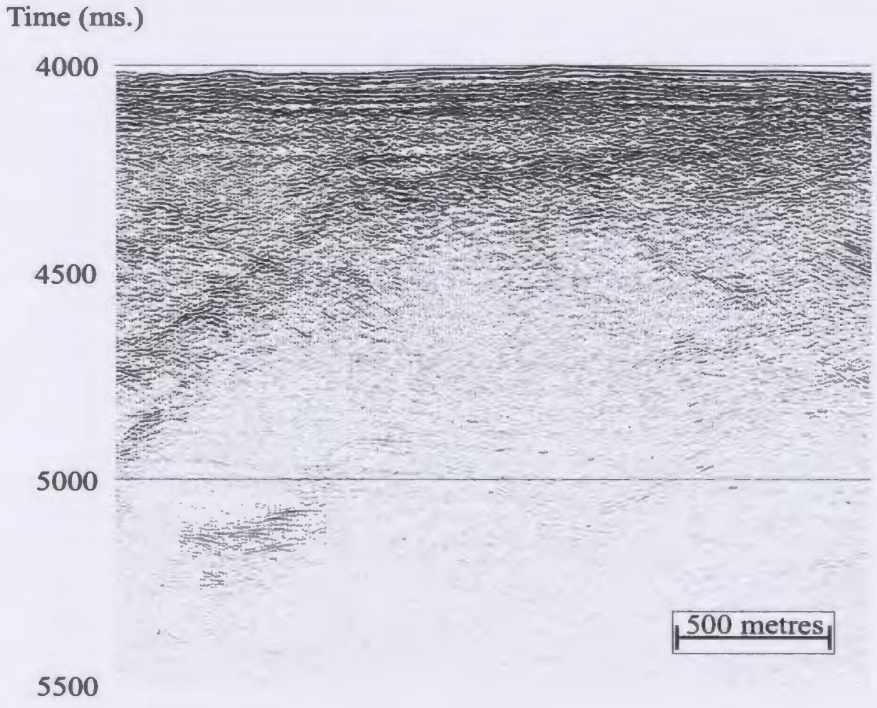

b)

Figure 2.2.15: Wavelet extractions were performed on four zones of line 64. a) cdp's 3868-4357: zone 1- parallel, disorganized reflectors, b) cdp's 3000-3400: zone 2- scattering, segmented reflectors, c) cdp's 14400-14700: zone 3- thick, clean, parallel, continuous reflectors and d) cdp's 19100-19400: zone 4- thin package of parallel continuous reflectors overlying a strongly reflective lower package.

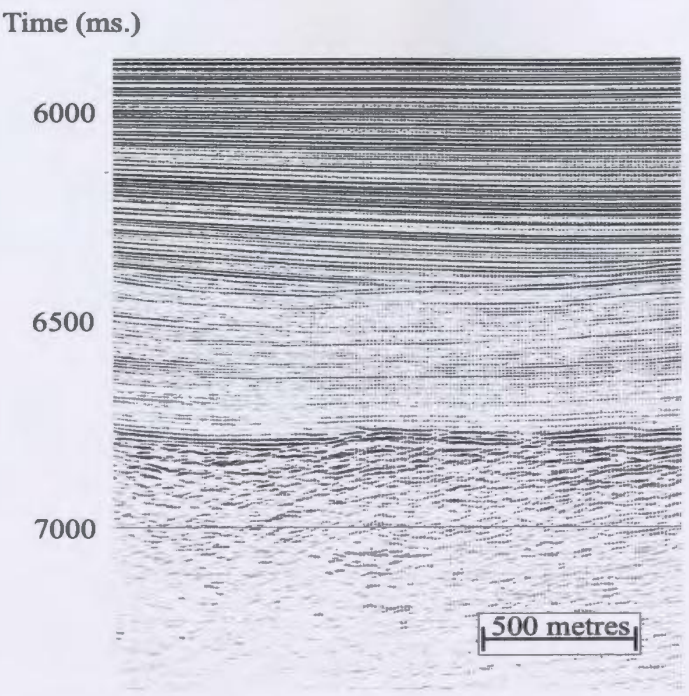

Figure 2.2.15c)

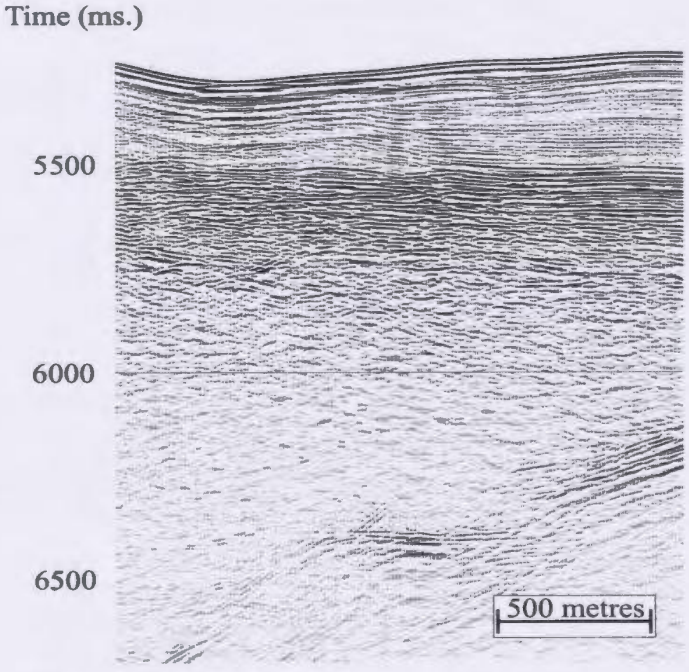

Figure 2.2.15d)

Table 2.2.1 illustrates the results of varying the peak time from 7 ms to 17 ms. Best results are considered to be those that have a low 'final error (δ)' and a fast convergence to a stable solution as represented by a large improvement of the final error from over the initial error ($\Delta\delta$) over the twenty iterations. The best result within the T/4 to T/2 range is reached for a time of maximum amplitude equal to 9 ms.

Wavelets were extracted from all four zones for extraction time windows that ranged from 200 ms to 1600 ms, using t = 9 ms as the time of maximum amplitude and 35 ms as the wavelet length. The results of these extractions are shown in Tables 2.2.2-2.2.5. In each case the optimum result occurs at an intermediate window length. Therefore, it seems that window lengths shorter than this value may not have an adequate number of samples with which to reliably extract a wavelet and larger window lengths may suffer from statistical degradation due the non-stationarity of the wavelet. Comparison of the results in Tables 2.2.1-2.2.5 with Figure 2.2.15 allows a correlation between the extraction results and the parent seismic data to be made. For example, the shortest optimum extraction window (400 ms) of the four zones corresponds with Zone 2, a section of data that demonstrates strong, incoherent reflectivity for only the first ~ 300-400 ms below the seabed. Below 400 ms, the section is generally unreflective. In addition, a very large decrease in the error for Zone 3 from 0.788062 to 0.444462 occurs when the extraction window length is increased from 800 ms to1000 ms. This increase in the window length corresponds perfectly with a jump across the bright reflector located at ~6780 ms. At longer extraction window lengths, the final error is fairly stable but

Extracted Wavelet	Time of Max. Ampl. (ms)	Final Error (δ_f)	Convergence ($\Delta\delta = \delta_i - \delta_f$)	Window Length (ms)	# of Iterations
35_z1_7	7	0.156949	0.153934	1000	20
35_z1_8	8	0.168422	0.138026	1000	20
35_z1_9 *	9	0.161731	0.120132	1000	20
35_z1_10	10	0.156986	0.091169	1000	20
35_z1_11	11	0.156930	0.088946	1000	20
35_z1_12	12	0.156930	0.088946	1000	20
35_z1_13	13	0.156939	0.090164	1000	20
35_z1_14	14	0.156963	0.057462	1000	20
35_z1_15	15	0.156924	0.079580	1000	20
35_z1_16	16	0.156923	0.075774	1000	20
35_z1_17	17	0.156926	0.054395	1000	20

Table 2.2.1: Changing the 'time of maximum amplitude' of the extracted 35 ms wavelet from a 1000 ms window in Zone 1 has a significant impact on the quality of the result. The best solution between times T/4 and T/2 is marked with an *.

Extracted Wavelet	Time of Max. Ampl. (ms)	Final Error (δ_f)	Convergence ($\Delta\delta = \delta_i - \delta_f$)	Window Length (ms)	# of Iterations
35_z1_200	9	1.00003	0.00963	200	20
35_z1_400	9	1.00004	0.00992	400	20
35_z1_600	9	0.999884	0.013626	600	20
35_z1_800 *	9	0.139012	0.146667	800	20
35_z1_1000	9	0.161731	0.120132	1000	20
35_z1_1200	9	0.168977	0.113405	1200	20
35_z1_1400	9	0.174607	0.108904	1400	20
35_z1_1600	9	0.178910	0.105899	1600	20

Table 2.2.2: Using a value of 9 ms for the time of maximum amplitude, different time windows were experimented with to determine the optimum window for wavelet extraction in zone 1. The best solution is marked with an *.

Extracted Wavelet	Time of Max. Ampl. (ms)	Final Error (δ_f)	Convergence ($\Delta\delta = \delta_i - \delta_f$)	Window Length (ms)	# of Iterations
35_z2_200	9	0.896064	0.064708	200	20
35_z2_400 *	9	0.138391	0.119001	400	20
35_z2_600	9	0.206627	0.068000	600	20
35_z2_800	9	0.239031	0.053563	800	20
35_z2_1000	9	0.256352	0.048226	1000	20
35_z2_1200	9	0.266758	0.045993	1200	20
35_z2_1400	9	0.273649	0.045060	1400	20
35_z2_1600	9	0.278542	0.044728	1600	20

Table 2.2.3: Using a value of 9 ms for the time of maximum amplitude, different time windows were experimented with to determine the optimum window for wavelet extraction in zone 2. The best solution is marked with an *.

Extracted Wavelet	Time of Max. Ampl. (ms)	Final Error (δ_f)	Convergence ($\Delta\delta = \delta_i - \delta_f$)	Window Length (ms)	# of Iterations
35_z3_200	9	1.00003	0.01576	200	20
35_z3_40	9	1.0003	0.02397	400	20
35_z3_600	9	0.998726	0.023634	600	20
35_z3_800	9	0.788062	0.047257	800	20
35_z3_1000 *	9	0.444462	0.19531	1000	20
35_z3_1200 *	9	0.370600	0.175197	1200	20
35_z3_1400 *	9	0.364268	0.144402	1400	20
35_z3_1600	9	0.376029	0.116206	1600	20

Table 2.2.4: Using a value of 9 ms for the time of maximum amplitude, different time windows were experimented with to determine the optimum window for wavelet extraction in zone 3. The best solutions are marked with an *.

Extracted Wavelet	Time of Max. Ampl. (ms)	Final Error (δ_f)	Convergence ($\Delta\delta = \delta_i - \delta_f$)	Window Length (ms)	# of Iterations
35_z4_200	9	1.00005	0.008980	200	20
35_z4_400	9	0.782467	0.030883	400	20
35_z4_600	9	0.214683	0.073933	600	20
35_z4_800 *	9	0.145097	0.070177	800	20
35_z4_1000	9	0.167725	0.052453	1000	20
35_z4_1200	9	0.187838	0.043227	1200	20
35_z4_1400	9	0.202751	0.039280	1400	20
35_z4_1600	9	0.213534	0.037003	1600	20

Table 2.2.5: Using a value of 9 ms for the time of maximum amplitude, different time windows were experimented with to determine the optimum window for wavelet extraction in zone 4. The best solution is marked with an *.

converges to a solution more slowly than it does for the 1000 ms extraction window. A similar effect may present in Zone 4 when the window length jumps from 200 ms to 400 ms, but it is indistinguishable from the improved extraction result expected from increasing the window length from one the 200 ms window that is almost certainly inadequate. The best wavelet result from each zone is illustrated in Figure 2.2.16. While wavelets from Zones 1 and 2 are very similar, they appear to be 180° out of phase with the wavelet extracted from Zone 4. The wavelet extracted from Zone 3 looks nothing like the other wavelets and carries the largest error and convergence values.

With a mixed phase wavelet trace for each zone now extracted, each one can be used to design its own custom filter trace that can be convolved with itself to produce a minimum phase wavelet with the same amplitude spectrum as the mixed phase wavelet. The output of this convolution is then used to design a custom minimum phase spiking deconvolution filter trace that can be convolved with the phase-converted wavelet trace to produce a spiked output. Likewise, the same filter traces used to transform the wavelet trace to minimum phase and perform spiking deconvolution can be convolved with the seismic data from which the wavelet was extracted to produce a phase-converted, spiked output. Considering that the solution to a successful spiking deconvolution confined to a single zone at relatively shallow times (to avoid non-stationarily issues) offers a more solvable problem, efforts are focussed on Zone 1 in hopes that the key to a more widely applicable operator might be found. The results of this deterministic process on both the wavelet extracted from Zone 1 and on Zone 1 itself are shown in Figures 2.2.17-2.2.21.

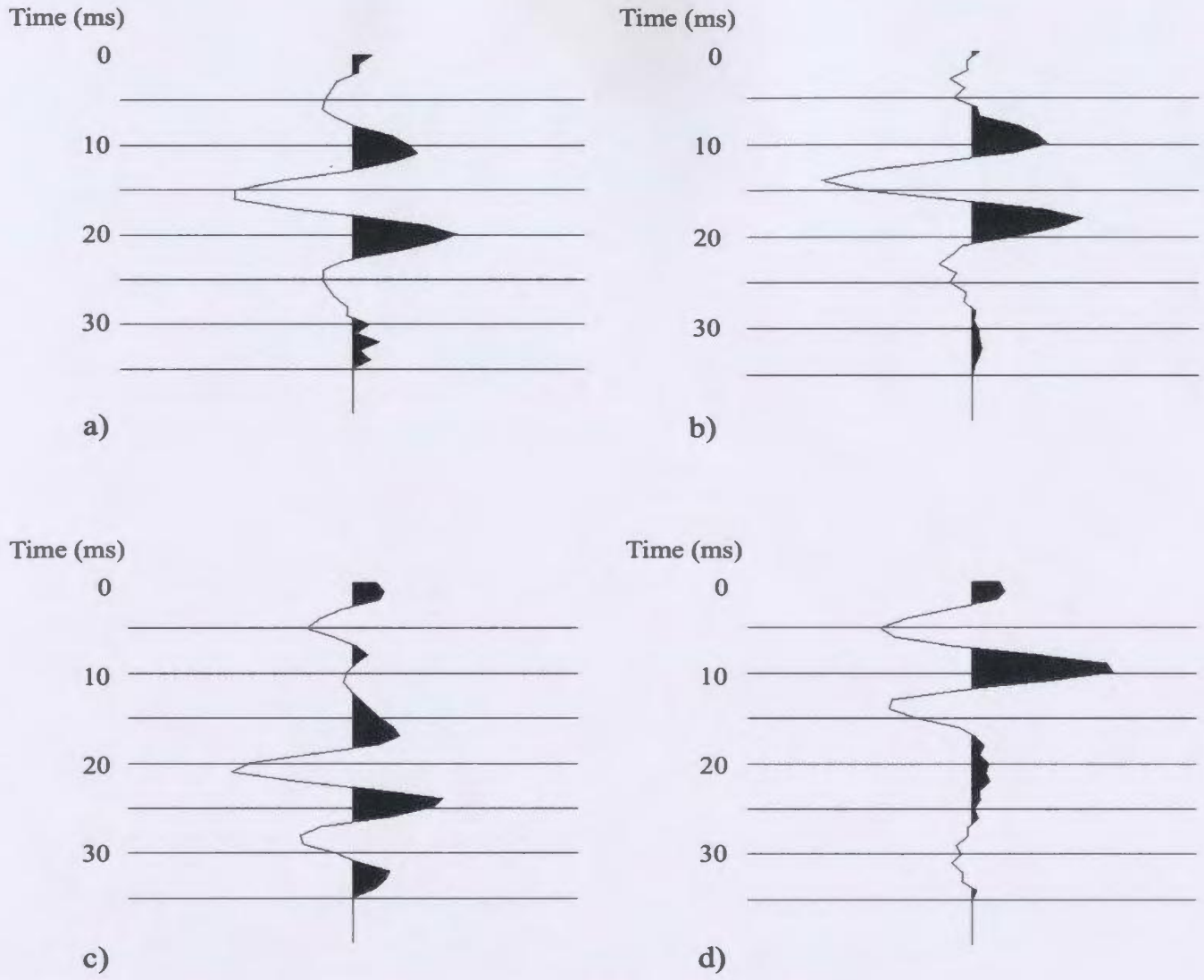

Figure 2.2.16: 35 ms wavelets extracted from the migrated data (line 64) at four different locations. a) The best wavelet extracted from zone 1 was extracted from the first 1000 ms below the seabed and was specified as having a maximum amplitude at 9 ms. Using this time of maximum amplitude for extractions from the other zones over window lengths varying from 200 ms to 1600 ms below the seabed, best results yielded b) a wavelet from zone 2 extracted from a window length of 400 ms, c) a wavelet from zone 3 extracted from a window length of 1200 ms, and d) a wavelet from zone 4 extracted from a window length of 800 ms.

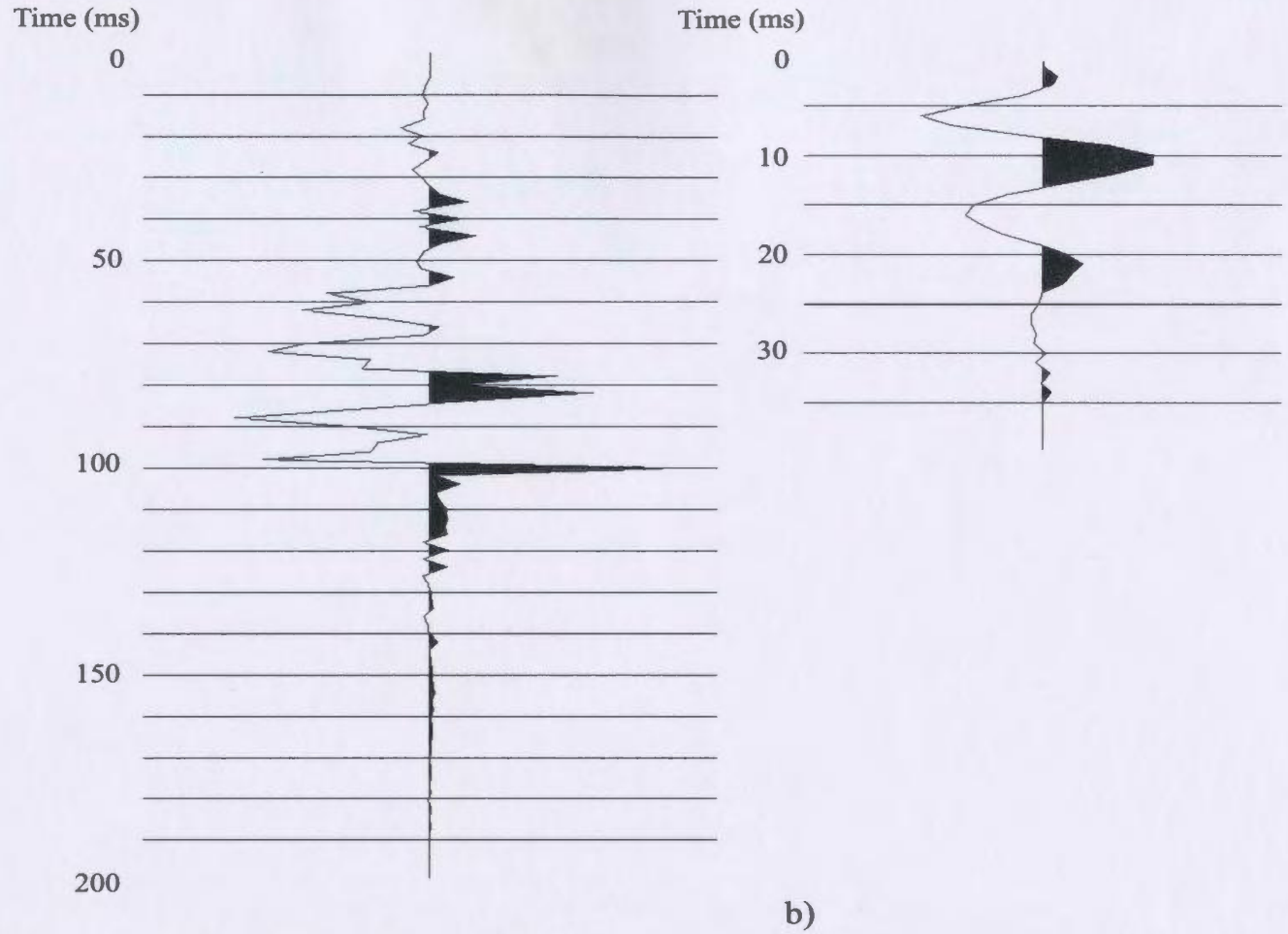

Figure 2.2.17: a) The minimum phase filter used to attempt to transform the original wavelet (Fig.2.2.16a) from mixed phase to minimum phase. b) The wavelet resulting from the convolution of the filter in a) with the original wavelet in Figure 2.2.16a.

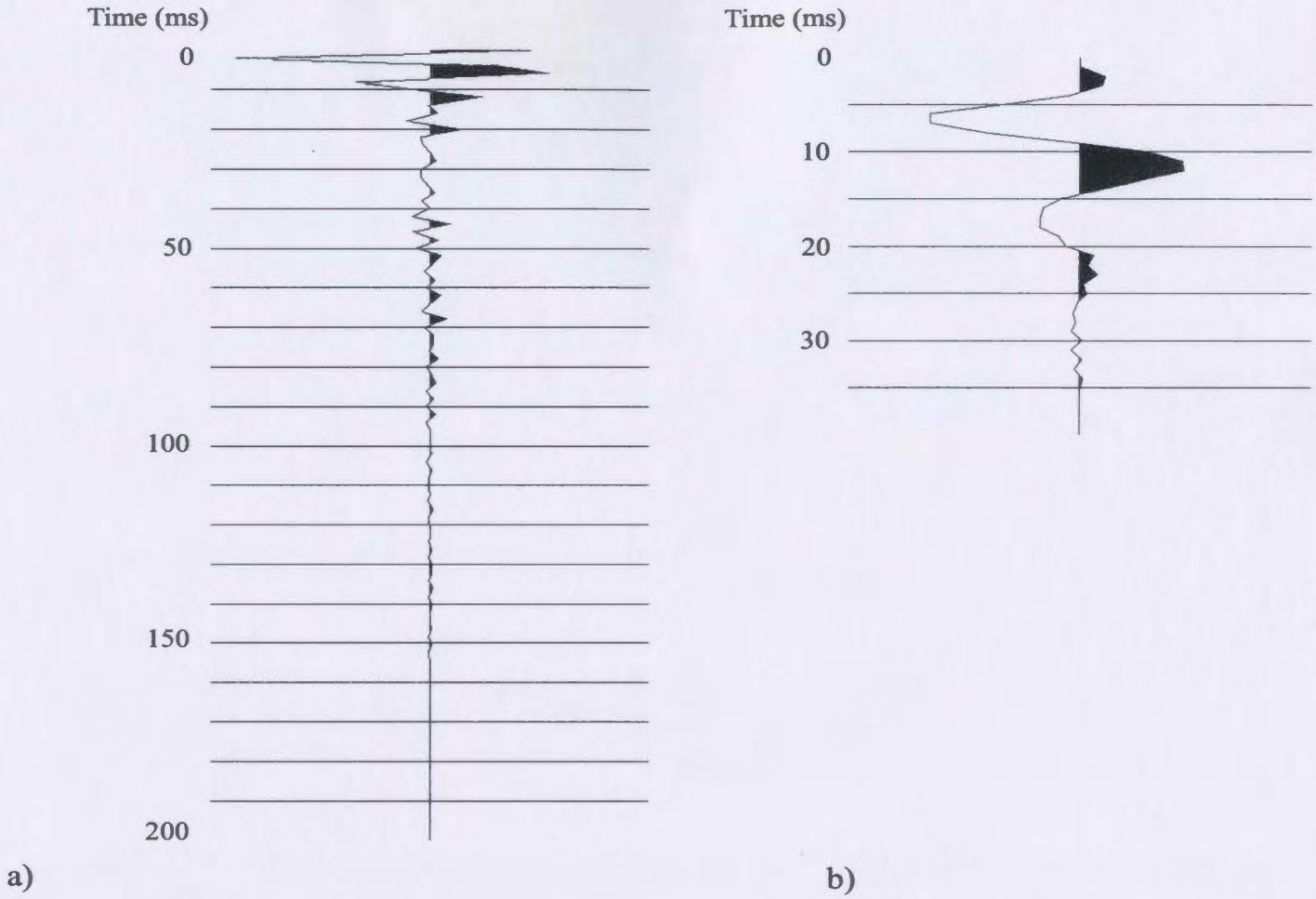

Figure 2.2.18: c) A minimum phase spiking deconvolution filter trace generated from the wavelet in Figure 2.2.17b. b) The result of the convolution of the spiking deconvolution filter trace in a) with the wavelet in Figure 2.2.17b.

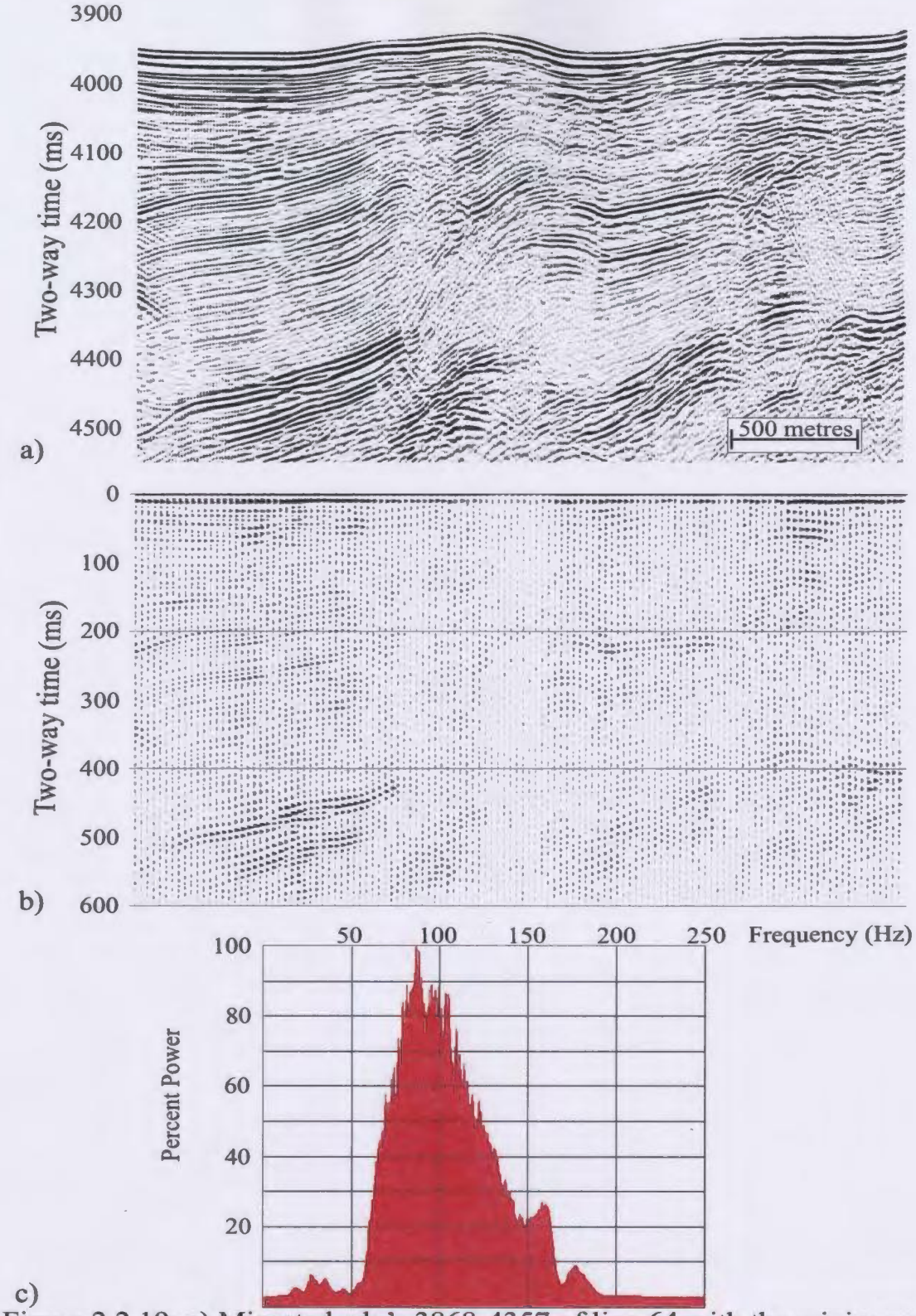

Figure 2.2.19: a) Migrated cdp's 3868-4357 of line 64 with the minimum phase filter from Fig. 2.2.17a applied . b) Autocorrellogram of every fourth trace in (a). c) Power spectrum of the data shown in (a).

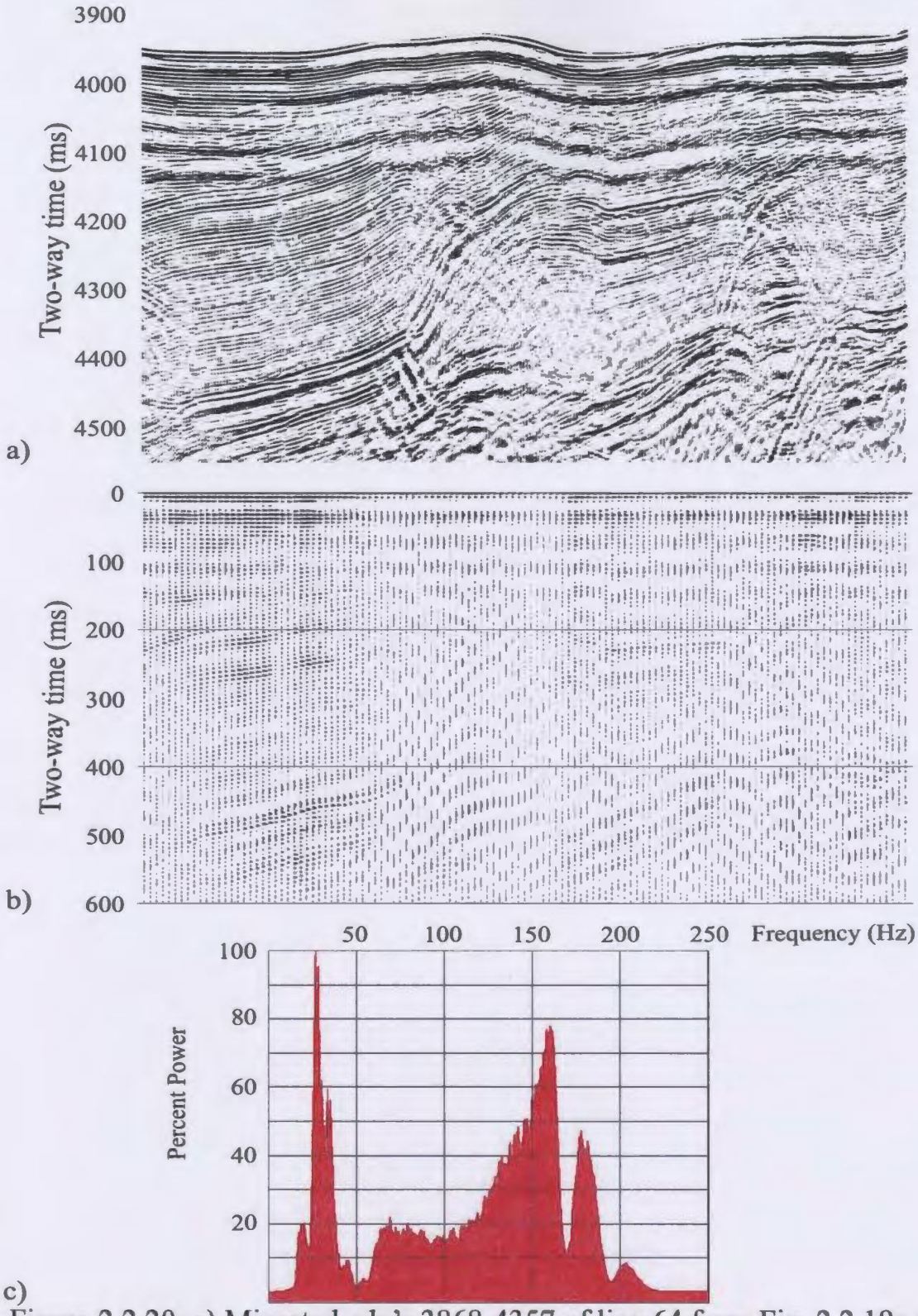

Figure 2.2.20: a) Migrated cdp's 3868-4357 of line 64 from Fig. 2.2.19a with the minimum phase spiking deconvolution filter from Fig. 2.2.18c applied. b) Autocorrellogram of every fourth trace in (a). c) Power spectrum of the data shown in (a).

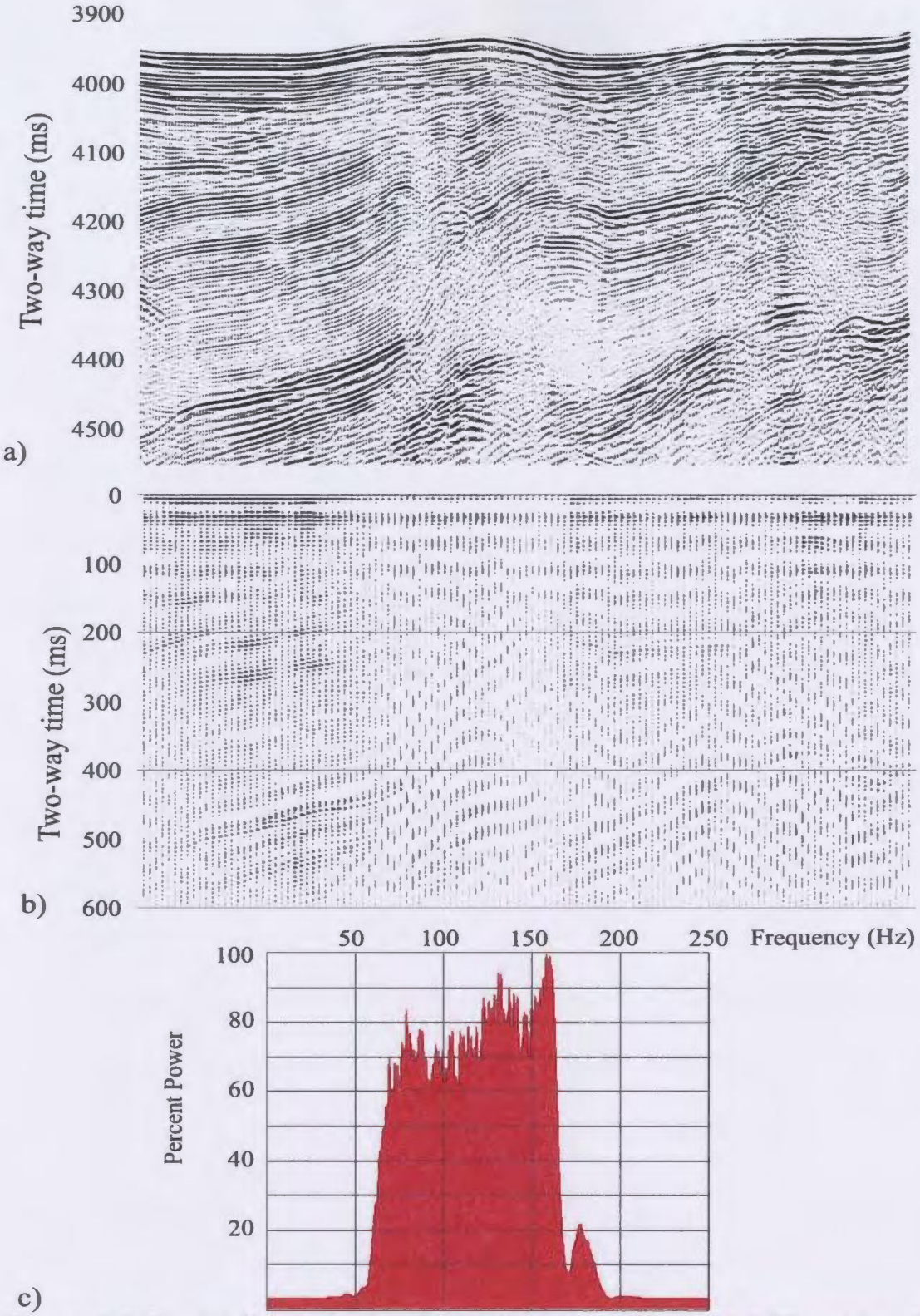

Figure 2.2.21: a) Migrated cdp's 3868-4357 from Figure 2.2.20a with a 30-80-100-225 Hz minimum phase Ormsby bandpass filter applied. b) Autocorrellogram of every fourth trace in (a). c) Power spectrum of the data shown in (a).

The application of the minimum phase filter to the wavelet does change the phase of the wavelet (Fig. 2.2.17). A spiking deconvolution of this wavelet does offer a modest improvement by reducing the amplitude of the wavelets' third lobe, but it also enhances the amplitude of the dominant, early trough while leaving the main positive energy peak essentially unchanged (2.2.18). The application of this process to the dataset is equally as unproductive (Figs. 2.2.19-2.2.21).

To be certain that the trouble associated with spiking deconvolution was not simply an artifact of the algorithms used by ProMax™ , Seismic Unix™ was used to perform Wiener-Levinson, least square, minimum phase spiking and predictive deconvolution on the data. Because the algorithm is very similar to that used by ProMax™, the results were very similar. A wavelet shaping process in Seismic Unix™ capable of designing a filter trace that could then be convolved with the input wavelet to produce a user-specified wavelet shape allowed an attempt at deterministic deconvolution. The output wavelet is defined as a series of 35 values that specify the amplitude of the desired output wavelet at each time sample allowing more flexibility in the design of the output wavelet than ProMax™ offered. Hence, the results of wavelet shaping in Seismic Unix™ differed from those of ProMax™. However, they suffered from similar frequency amplifications when applied to the seismic data set and gave no better solutions than those provided in ProMax™.

Because predictive deconvolution does not attempt to whiten the spectrum as much as spiking deconvolution does, it offers a less extreme approach to suppressing the

low frequency tail. The best predictive deconvolution results were obtained by using a 100 ms operator length with gaps of 20-35 ms. The result of a 35 ms gap predictive deonvolution applied to Zone 1 is shown if Figure 2.2.22. Note how the reflectors below the sea bed are more easily visible than those in the original data set (Fig. 2.2.16a) due to the removal of the low frequency reverbatory tail. Unlike the results from the spiking deconvolution attempts, the minor frequency amplification resulting from the predictive deconvolution does not require the deconvolved data to be frequency filtered. Predictive deconvolutions with gap lengths shorter than ~5 ms; however, show frequency amplification results approaching those produced by spiking deconvolution. Figure 2.2.23a illustrates a section of line 64 that has a pronounced contrast between an upper, highly reflective and well bedded succession and a lower, weakly reflective succession. Note the effect of decreasing the prediction gap (Fig. 2.2.23c-e) and using time variant deconvolution operators (Fig. 2.2.23b versus Fig. 2.2.23c). The time variant 35 ms predictive deconvolution appears to focus the energy trailing behind the contact between the two layers better than the single operator. Observation of the strong reflection from the layer interface in Figure 2.2.23d-e suggests that shortening the prediction gap of the time variant deconvolution to 20 ms and 10 ms attenuates the third lobe of the wavelet. In addition, these shorter prediction gap lengths remove the low frequency tail following layer interface but replace it with higher frequency reverberations. These high frequency reverberations also mask the definition of the scattering package within the upper succession. Hence, time variant predictive deconvolution with a prediction gap between

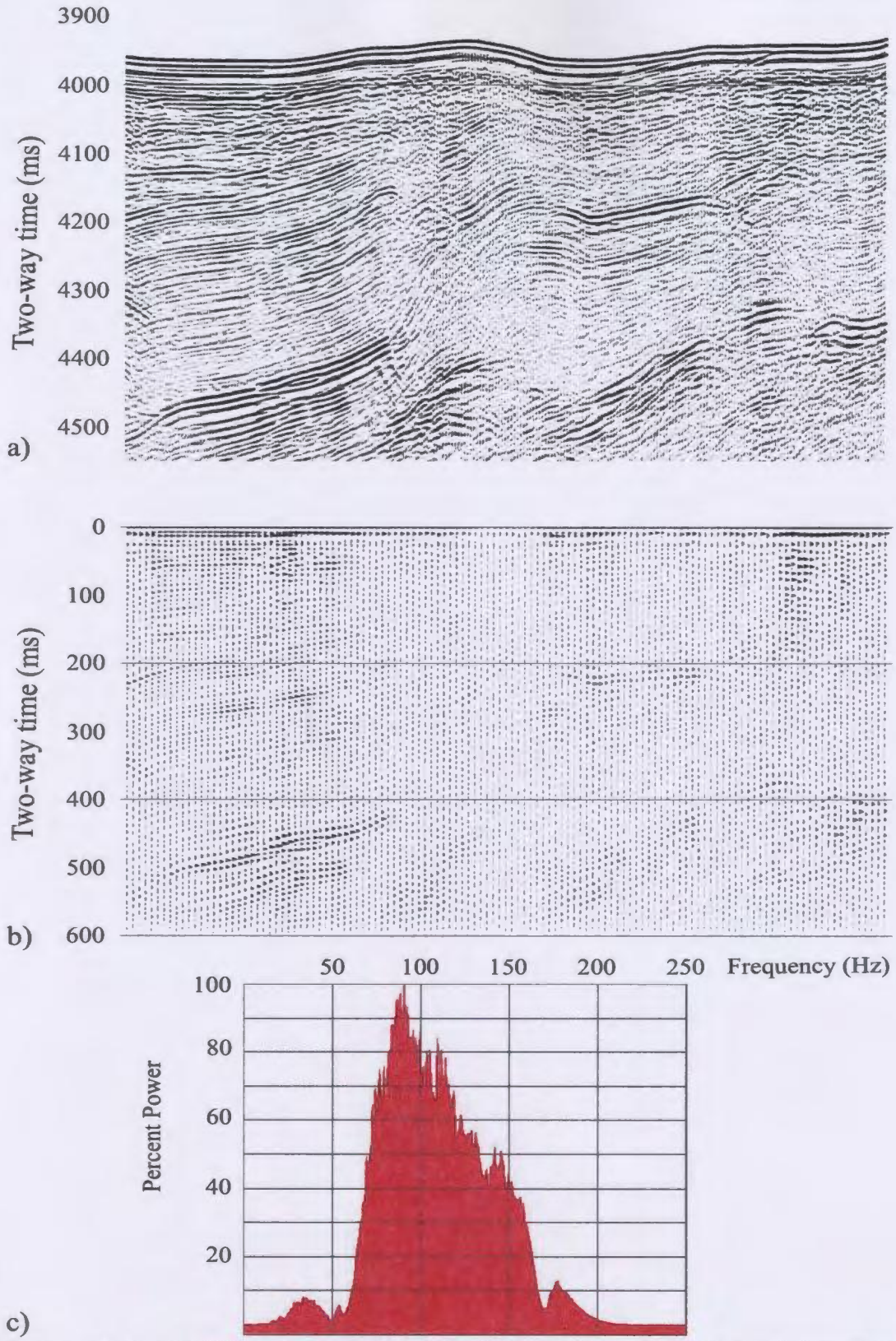

Figure 2.2.22: a) Migrated cdp's 3868-4357 of line 64 with a minimum phase predictive deconvolution applied (35 ms gap, 100 ms operator length). b) Autocorrellogram of every fourth trace in (a). c) Power spectrum of the data shown in (a).

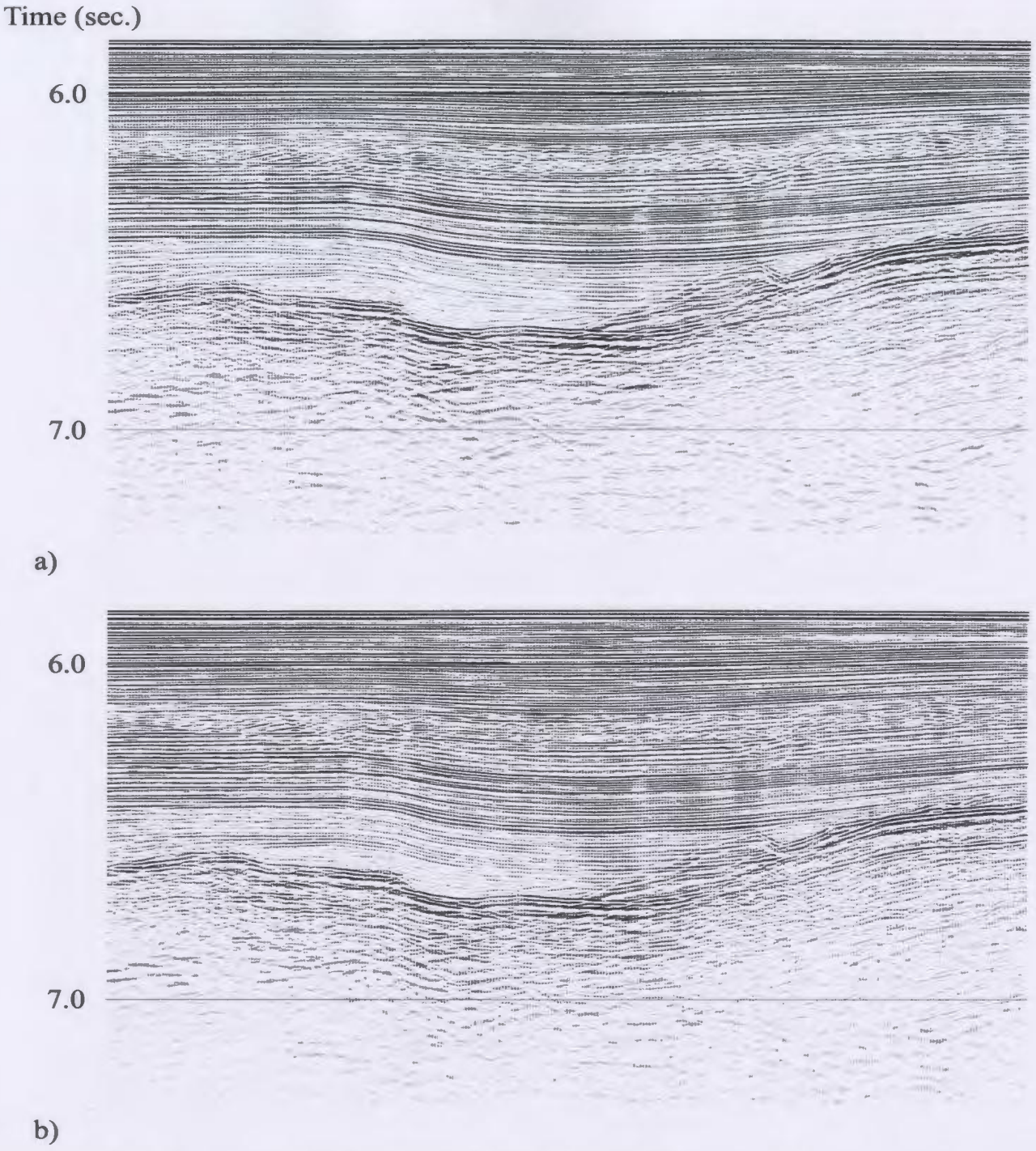

Figure 2.2.23: a) Cdp's 21700-22300 of line 64. b) Data in a) with a predictive deconvolution operator (prediction gap = 35 ms, operator length = 100 ms) derived from and applied to the whole data set. c)-e) Time variant predictive deconvolutions of the data in a). Two design/application windows are indicated by the colour-coded time gates. Deconvolution parameters for illustrations c)-e) are prediction gaps = 35, 20 and 10 ms respectively with operator lengths of 100 ms.

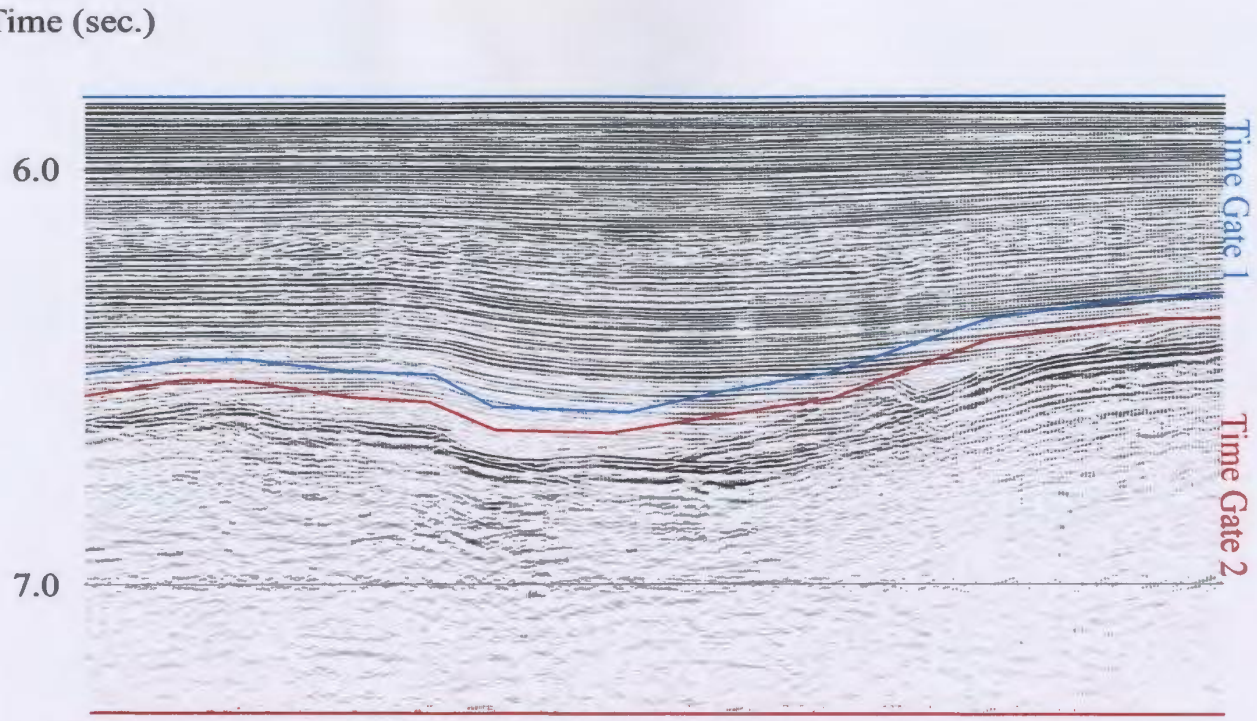

Figure 2.2.23c)

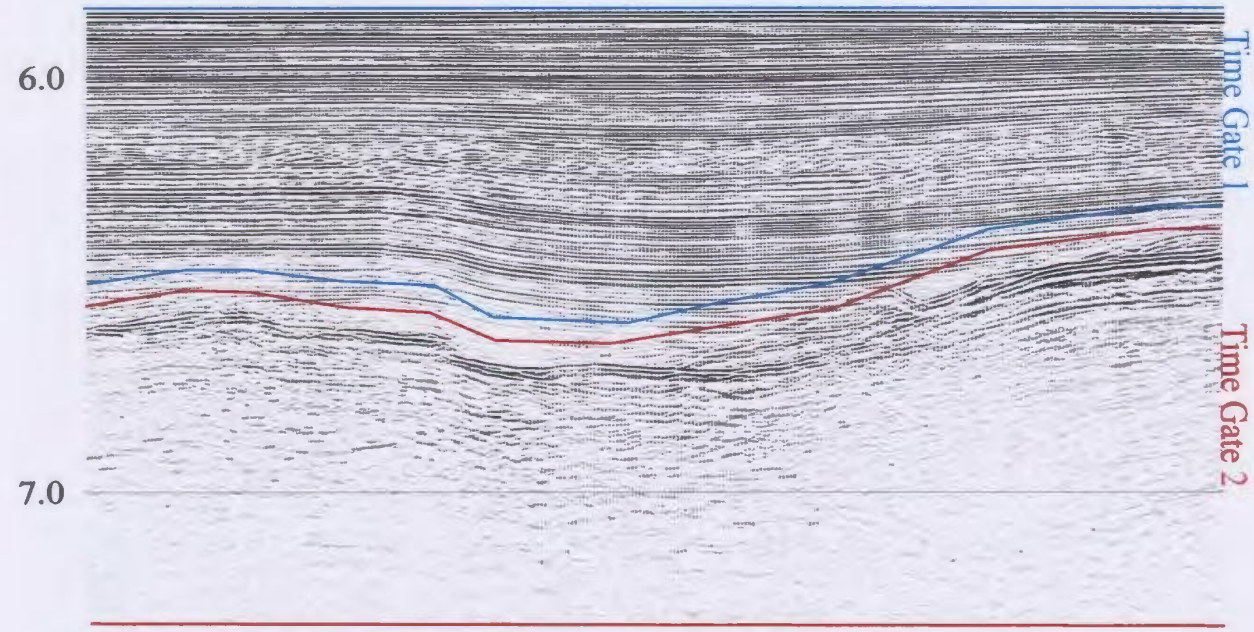

Figure 2.2.23d)

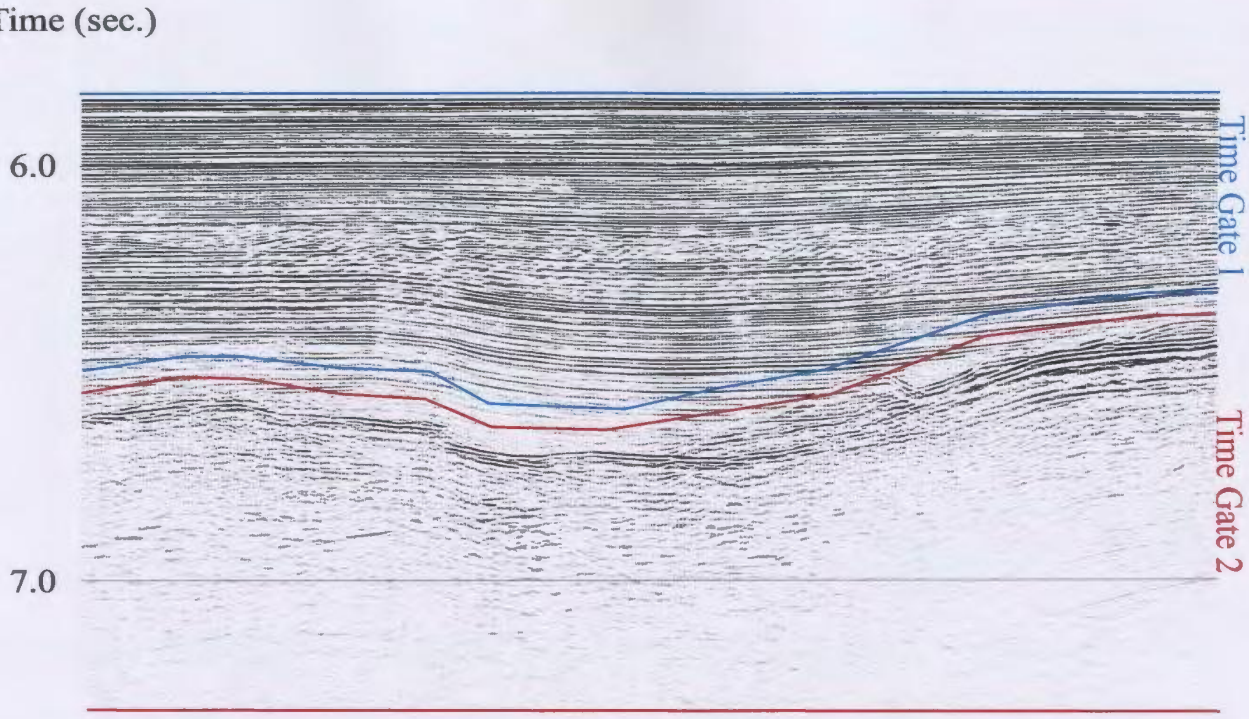

Figure 4.2.23e)

of 35 ms and 20 ms and an operator length of 100 ms does offer some improvement on the original data.

An outstanding question remains: "why is the wavelet mixed in phase in the first place?" Indeed, inspection of the unprocessed shot gathers does suggest that the original data did more closely approximate a minimum phase wavelet; although it still had a significant, preceding trough and a trailing trough of comparable amplitude to the main, positive energy burst (Fig. 2.2.24a). Application of a minimum phase Ormsby bandpass filter does not appear to have an effect on the seabed reflection response (Fig. 2.2.24b). However, the application of notches in the frequency filtering at 50, 56, and 169 Hz introduces extra lobes to the wavelet (Fig. 2.2.24c). It seems therefore, that the steep notch-filter cut-offs that have a width of only 4 Hz may be responsible for generating the three lobed wavelet. Unfortunately, enlarging the notch filter width results in increased loss of signal amplitude at frequencies close to the notch frequencies and provides no improvement over the 4 Hz notch width. The notch filtering is necessary in order to reduce the number of traces removed from this already low fold data set. The solution is to notch filter only those shots and channels that carry the anomalously large proportions of frequency specific noise. When these notch-filtered traces are summed with several other traces that are not filtered, the net result is a cdp trace that contains a more continuous spectrum and minimum phase character than that of a cdp trace resulting from the summation of only notch-filtered traces. Figure 2.2.25 illustrates the results of applying the notch filter to only the necessary channels and then stacking and migrating

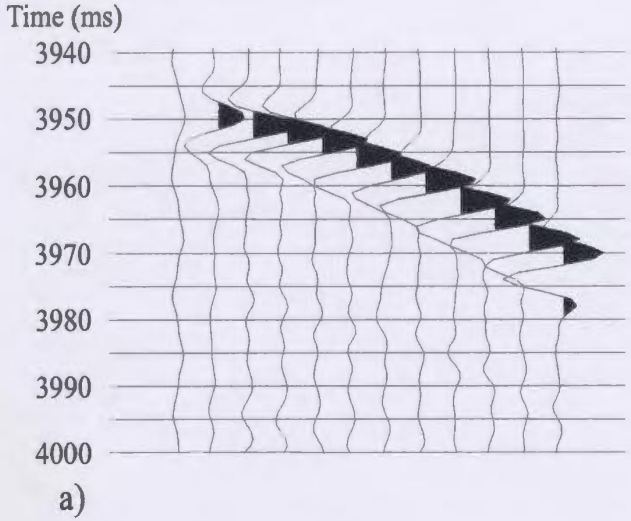

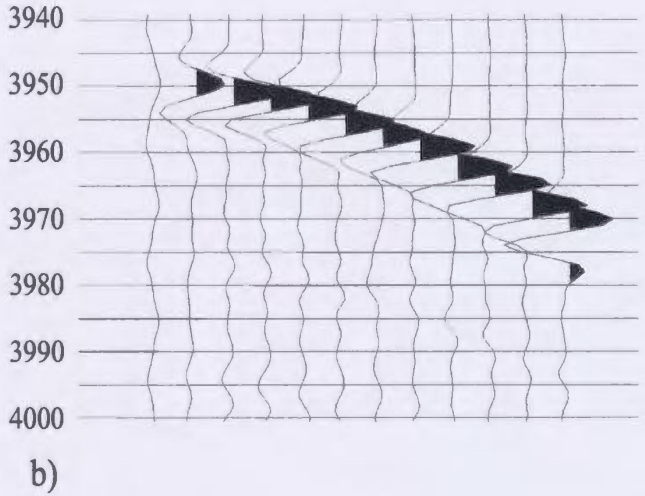

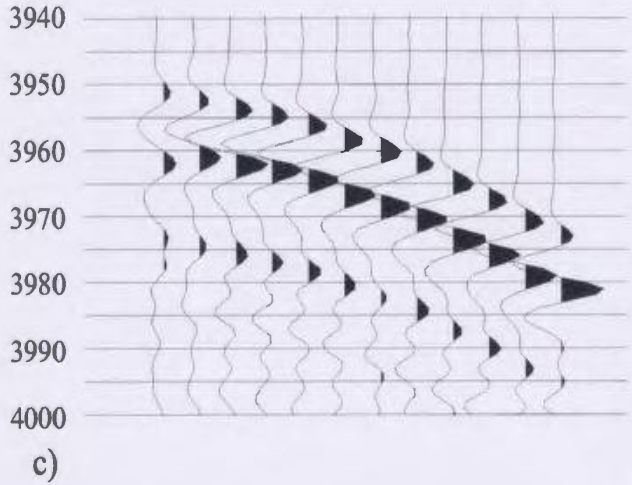

Figure 2.2.24: Cdp gather (cdp 4000 of line 64) showing the seabed reflection with a) no processing applied. Notice that the wavelet is not truly minimum phased as evidenced by the large troughs on each end of the large, positive peak. b) Data from a) with a 8-16-180-250 Hz minimum phase Ormsby bandpass filter and trace re-equalization applied. c) Data from a) with a 8-16-180-250 Hz minimum phase Ormsby bandpass filter applied and notches at 50, 56, and 169 Hz followed by trace re-equalization.The result is a wavelet triplet. Since each display re-equalizes the traces, the signal level on the first channel of c) is increased relative to that of a) and b) due to the removal of the frequency specific noise that previously dominated the trace energy. Each figure has a -10% bias applied to highlight the higher amplitude seabed response from that of the underlying reflectors.

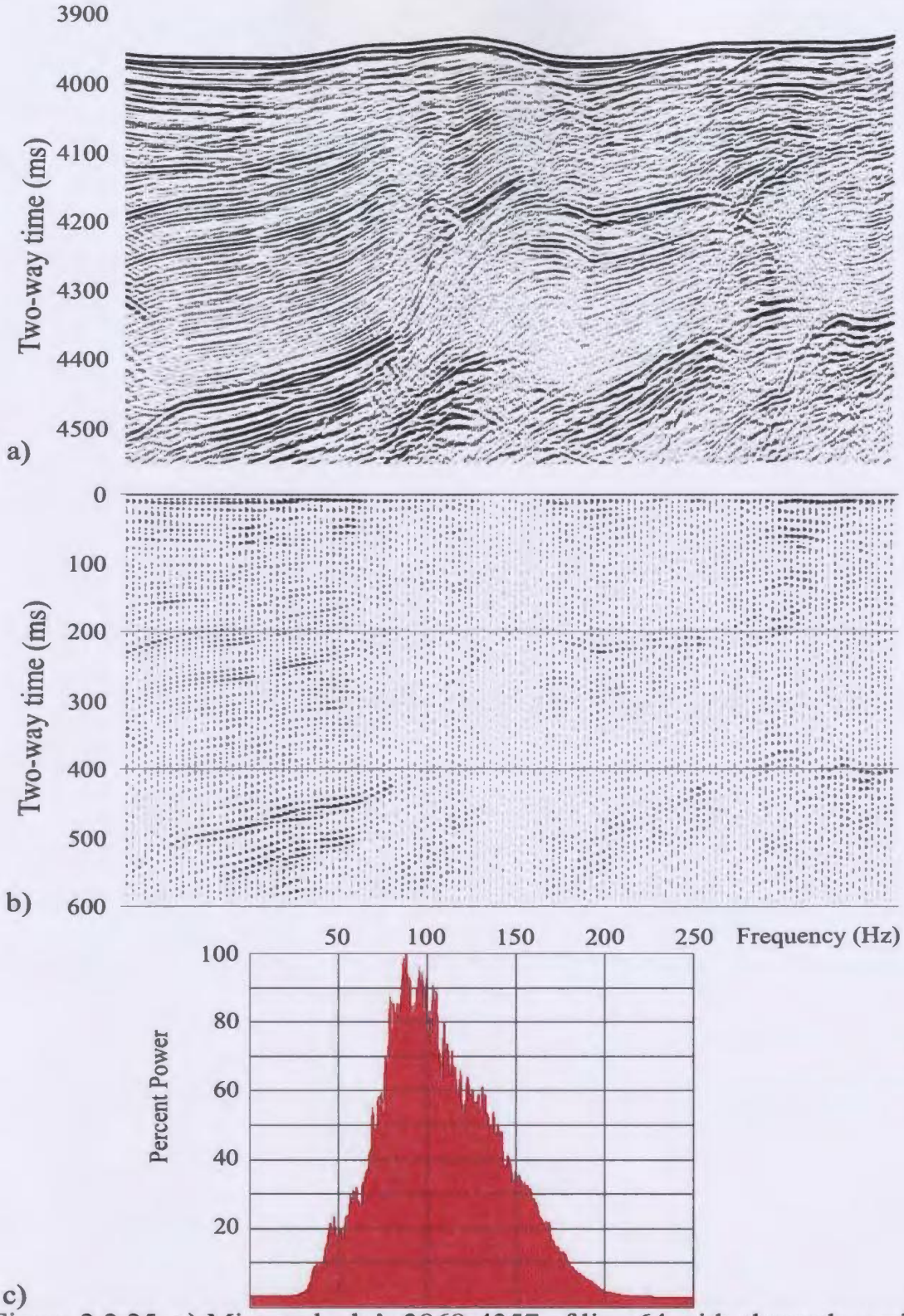

Figure 2.2.25: a) Migrated cdp's 3868-4357 of line 64 with channel specific frequency filtering applied in addition to a 30-80-180-250 Hz minimum phased Ormsby bandpass filter. b) Autocorrellogram of every fourth trace in (a). c) Powerspectrum of the data shown in (a).

as before. This figure can be compared directly with Figure 2.2.8 to note the difference that channel specific notch filtering can make to the data and power spectrum. Figure 2.2.26 illustrates the data from Figure 2.2.25 with a 35 ms operator length spiking deconvolution applied. A comparison of this spiking deconvolution with that of Figure 2.2.10 demonstrates the impact of maintaining a more continuous frequency content has on the amplification of low and high frequency noise. However, the data set in Figure 2.2.26 would still benefit from post-deconvolution bandpass filtering as is illustrated in Figure 2.2.27.

Much of the difficulty associated with applying a successful deconvolution to this dataset was largly created by an oversight during an earlier processing stage. It was, however, a beneficial exercise to perform. Two valuable lessons were learned from this experience: firstly, from a technical perspective, deconvolving mixed phase data, for which there is no independent record of the source wavelet, can prove to be very difficult. Secondly, and perhaps often overlooked by most processors, is that a simple procedure such as notch filtering can have extremely important effects on the amplitude, phase and spectral content of the data and therefore on the success of any following processing algorithms that make assumptions concerning the phase of the input data.

2.2.6: F - K Filtering

A short streamer, great water depth and rugged bathymetry contribute to the likelihood of receiving reflections that have a negative move-out on a shot gather record.

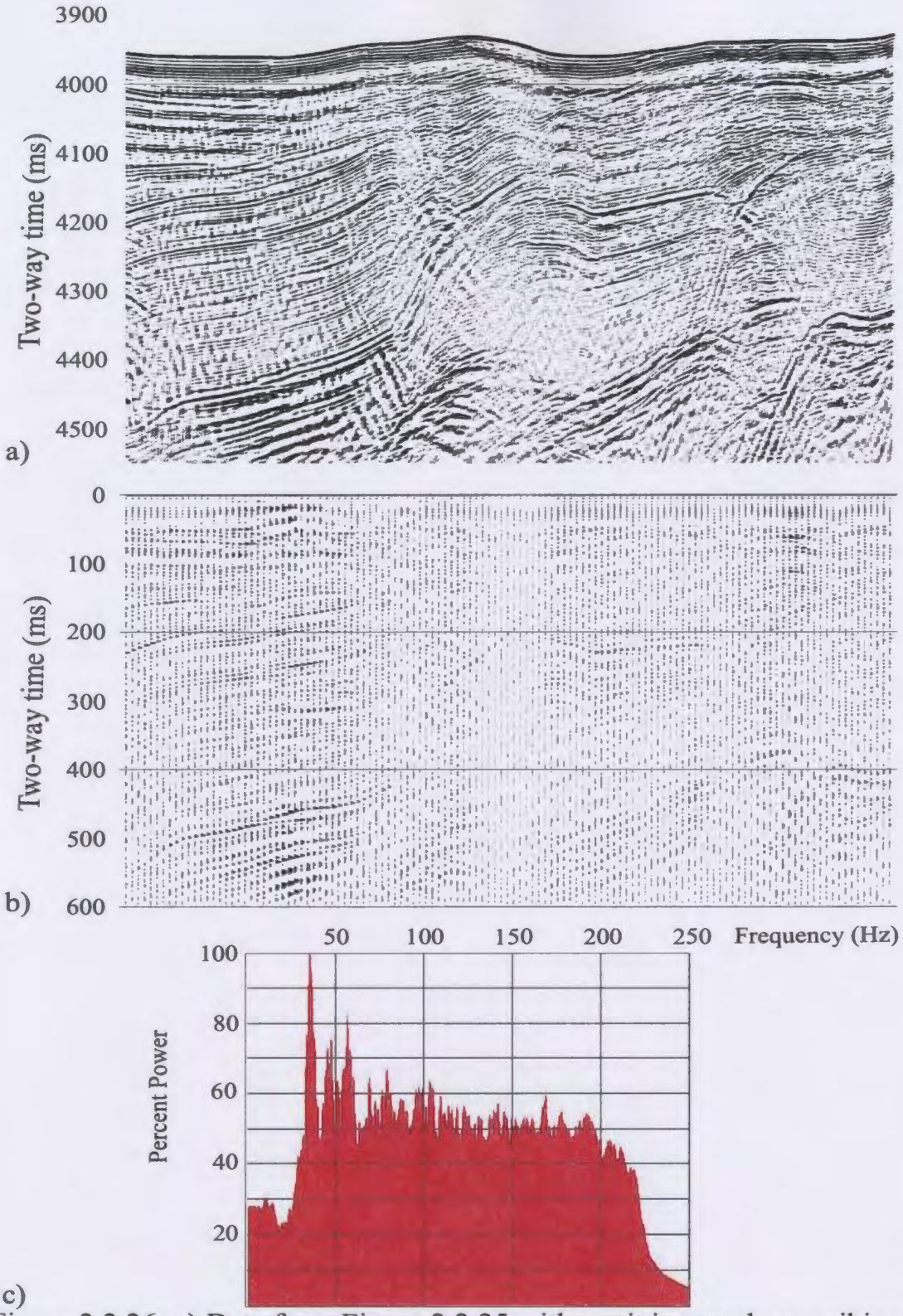

Figure 2.2.26: a) Data from Figure 2.2.25 with a minimum phase spiking deconvolution filter applied (35 ms operator length). b) Autocorrellogram of every fourth trace in (a). c) Power spectrum of the data shown in (a).

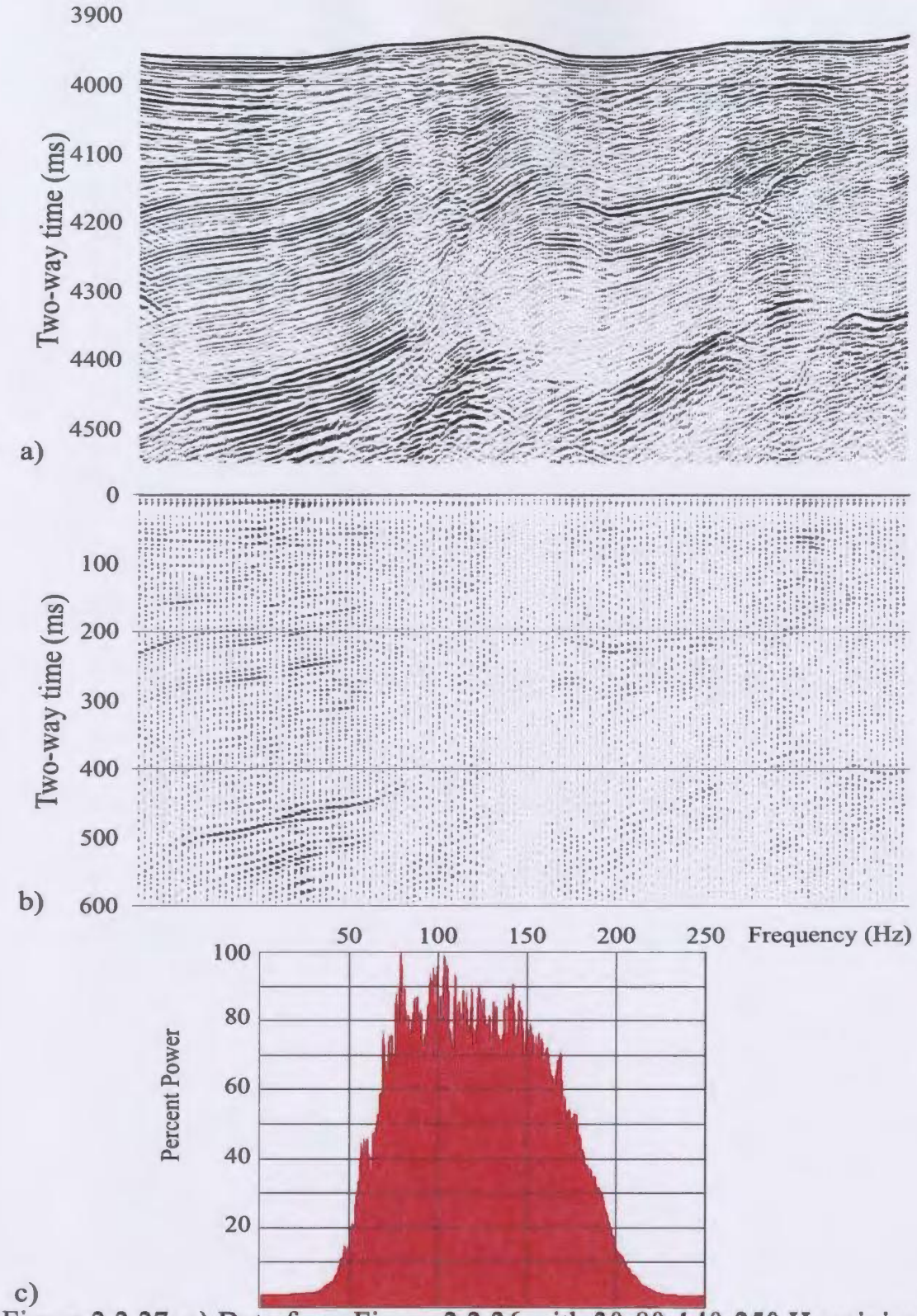

Figure 2.2.27: a) Data from Figure 2.2.26 with 30-80-140-250 Hz minimum phase Ormsby bandpass filter applied. b) Autocorrellogram of every fourth trace in (a). c) Power spectrum of the data shown in (a).

These events often represent 'unwanted' diffraction-like events that occur in zones complex geology and bathymetry. F-K filtering offers a tool that can remove these events before stacking, thereby diminishing their contribution to degrading the imaging of 'wanted' reflections. Figure 2.2.28 shows a shot record with both positive and negative move-out arrivals. The F-K spectrum of this shot record effectively separates the positive and negative move-out energy by plotting them in the positive and negative K domains respectively. A 'reject' polygon is picked that surrounds the unwanted data in the negative K domain (Fig. 2.2.28b) and a F-K filter is applied using this 'rejection window' (Fig. 2.2.28c,d). The pre-stack, F-K-filtered data is then stacked and migrated. A comparison of the stacked, migrated F-K-filtered data with the original data shows that the removal of events with negative move-out attenuates steeply dipping 'wanted' events that dip in the direction of ship's travel along with any 'unwanted' events that may be present (X in Fig. 2.2.29). Unfortunately, the factors that make this data set prone to this sort of dipping noise also limit our ability to resolve and therefore separate 'wanted' energy from 'unwanted' energy in the F-K domain. Such F-K filtering is not advisable for this data set.

2.2.7: Multiples

Due to the extreme water depth and short record length of the data, energy from water layer reverberations are seldomly recorded. However, multiple energy from previous shots is found in some zones. In such cases, predictive deconvolution is

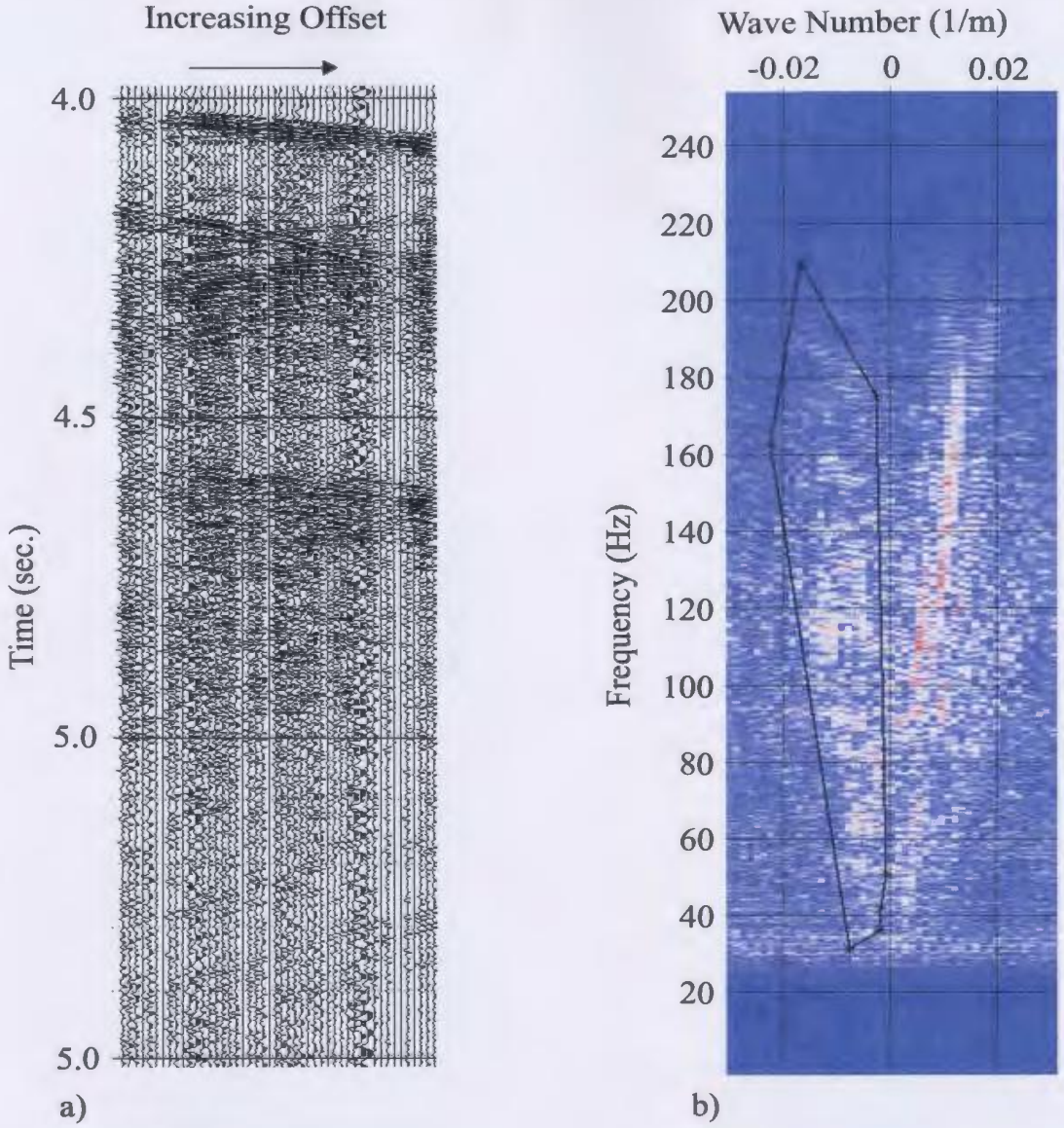

Figure 2.2.28: a) Shot 1 of line 64 displays events that have both positive and negative move-out. b) To remove the events with negative move-out, a polygon defining the 'rejection window' of a F-K filter chosen. c) The shot gather and d) F-K spectrum of the data with the F-K filter applied. Not the reduction in events showing negative move-out on the shot gather.

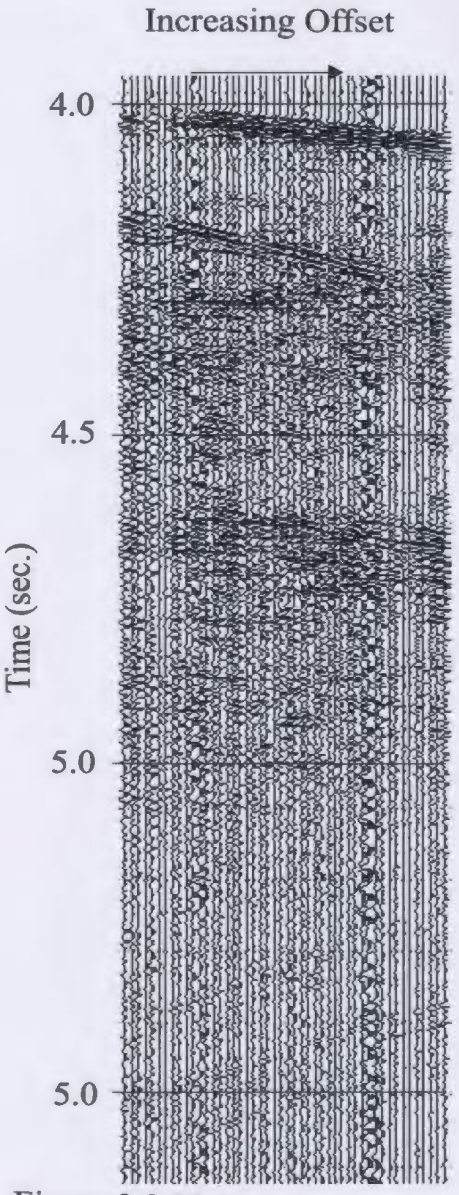

Figure 2.2.28c)

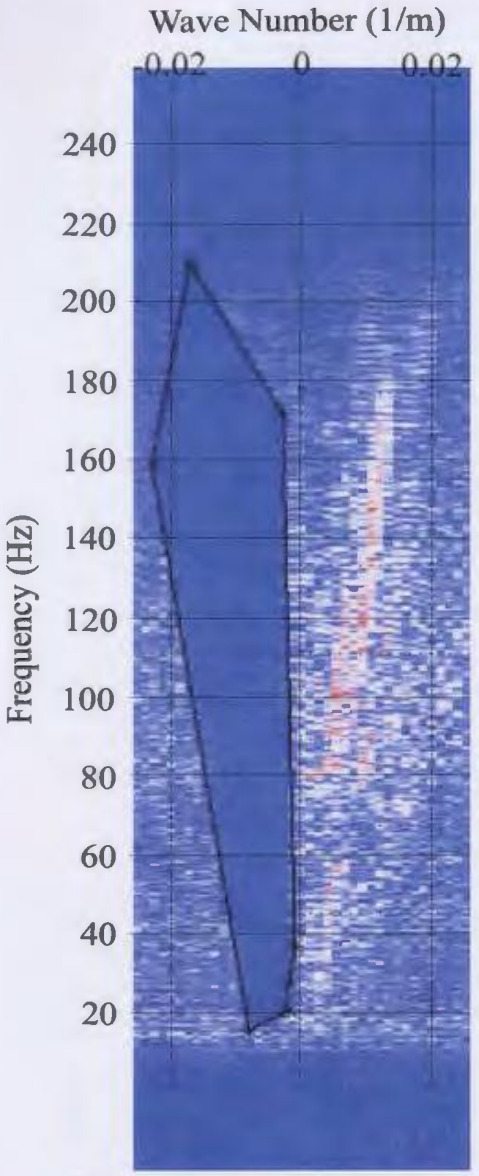

Figure 2.2.28d)

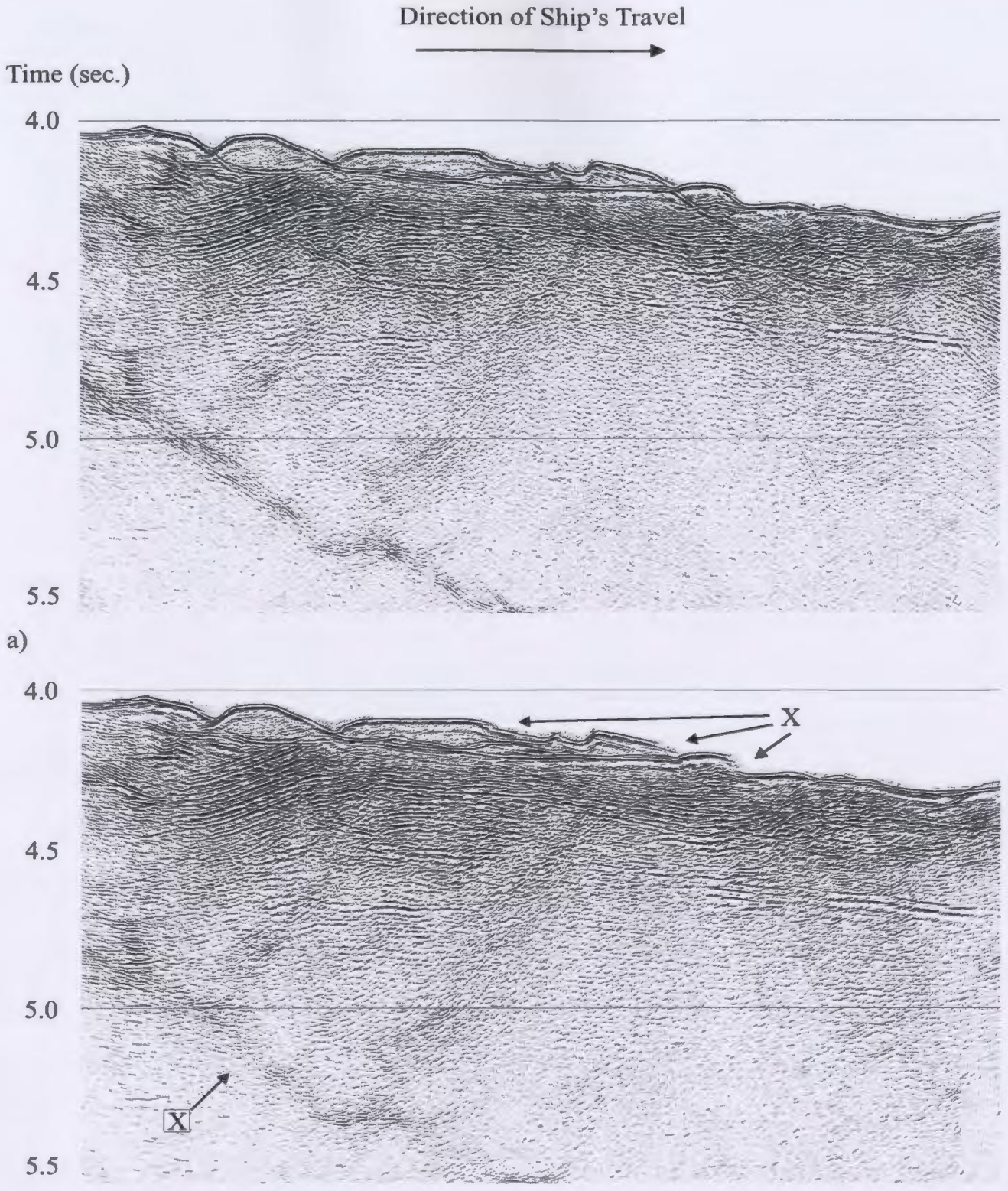

Figure 2.2.29: a) Cdp's 1-1000 of line 64 without and b) with the F-K filter illustrated in Figure 2.2.28. Note the attenuation of those events dipping in the direction of ship travel (X).

ineffective at removing the multiple energy because the time periodicity of the multiple arrival is not preserved. Figure 2.2.30a shows a stacked profile of a seabed multiple that occurs along line 64. The multiple is generated by a shot ('shot 1' in Fig. 2.2.30b) but is recorded on the record of the following shot ('shot 2'). When the data is stacked, the multiple is then seen on each Cdp trace. At T_1 = 0 ms shot 1 is fired. The section in 2.2.30a shows that the primary seabed reflection occurs at t=5840 ms. This is all the information we need to predict the arrival of the first multiple at 2 x 5840 ms = 11680 ms and the second multiple at 3 x 5840 ms = 17520 ms. Clearly these are not the multiples observed on the record of the first shot since they both arrive well past the recording time interval of shot 1. The observers' logs record that the ships speed at this location is ~ 5.0 knots (~ 2.55 m/s). A shot spacing of 25 metres suggests that the time between shot 1 and shot 2 is T_1 ~9.80 sec.. This can also be referred to as T_2 = 0 ms. The second multiple of shot 1 is then predicted to be recorded as T_2 = (17520 - 9800) ms = 7720 ms. An illustration of these time relationships is provided in Figure 2.2.30b. From the seismic section, the recorded multiple actually occurs at 7620 ms. A reasonable explanation that accounts for this discrepancy is the uncertainty in the ship speed. The observers logs show that it varies by +/- 0.4 knots within 2 fix locations of this area. Indeed, changing the approximated ship speed to 4.95 knots allows this slight discrepancy to be accounted for.

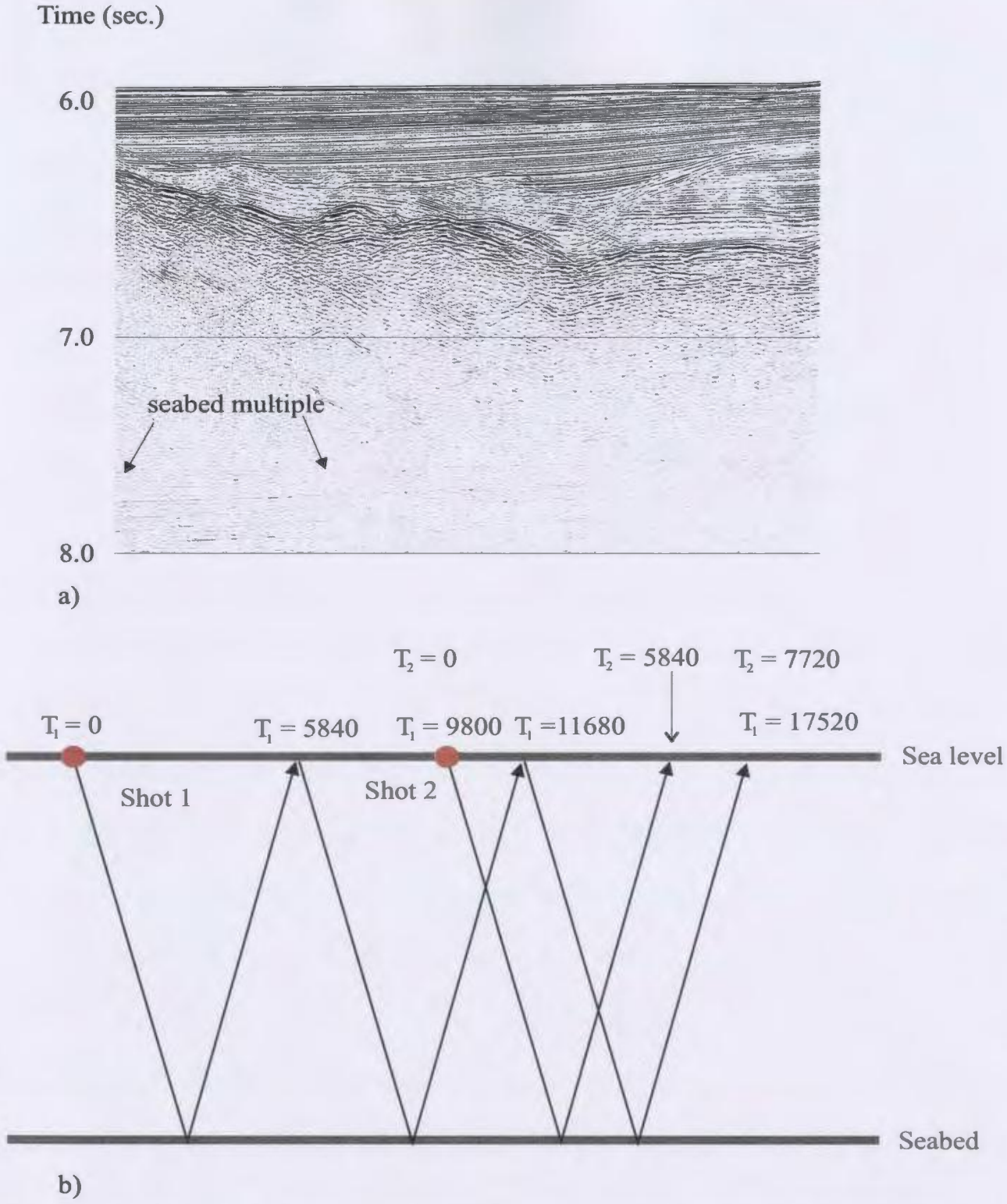

Figure 2.2.30: a) Cdp's 14000-15000 (stacked and migrated) from line 81 showing a seabed multiple. b) A ray diagram illustrating arrival time of this multiple relative to both the recording time of its initiating shot and that of the following shot.

2.2.8: Other Processing

Figure 2.2.31 shows how trace mixing was applied along particularly noisy sections in an effort to enhance flat lying and shallowly dipping reflections and remove migration smiles that originated from noise spikes or abrupt amplitude changes. The best compromise between filtering out the noise and maintaining coherency of dipping reflectors was reached by using a mix of five traces with weights of 0.25, 0.5 ,1, 0.5 and 0.25 respectively. The resultants of these multiplications were then averaged and assigned to the centre cdp location.

Zones of especially high levels of noise due to either a reduced source array or poor recording required special attention. Figure 2.2.32 shows a stacked section with an 8-16-180-250 Hz Ormsby bandpass filter and trace zeroing applied to zero the noisiest traces. Part b) of the figure shows the corresponding migration. Upon migration, the remaining anomalous amplitudes distort of the data. Figure 2.2.33 illustrates the results of a second application of trace zeroing to remove the large amplitudes missed by the first phase of trace zeroing and the migration of these data. Finally, a 30-40-180-250 Hz Ormsby bandpass filter was applied to the central zone of these data and a 3072 ms automatic gain control (AGC) operator applied to all traces in the line to equalize the trace to trace amplitudes (Fig. 2.2.34a). As can be seen from Figure 2.2.34b, migration of these data shows significant improvement over the previous migrations (Figs. 2.2.31 and 2.2.32).

Figure 2.2.35 provides a generalized flow diagram of the processing path taken

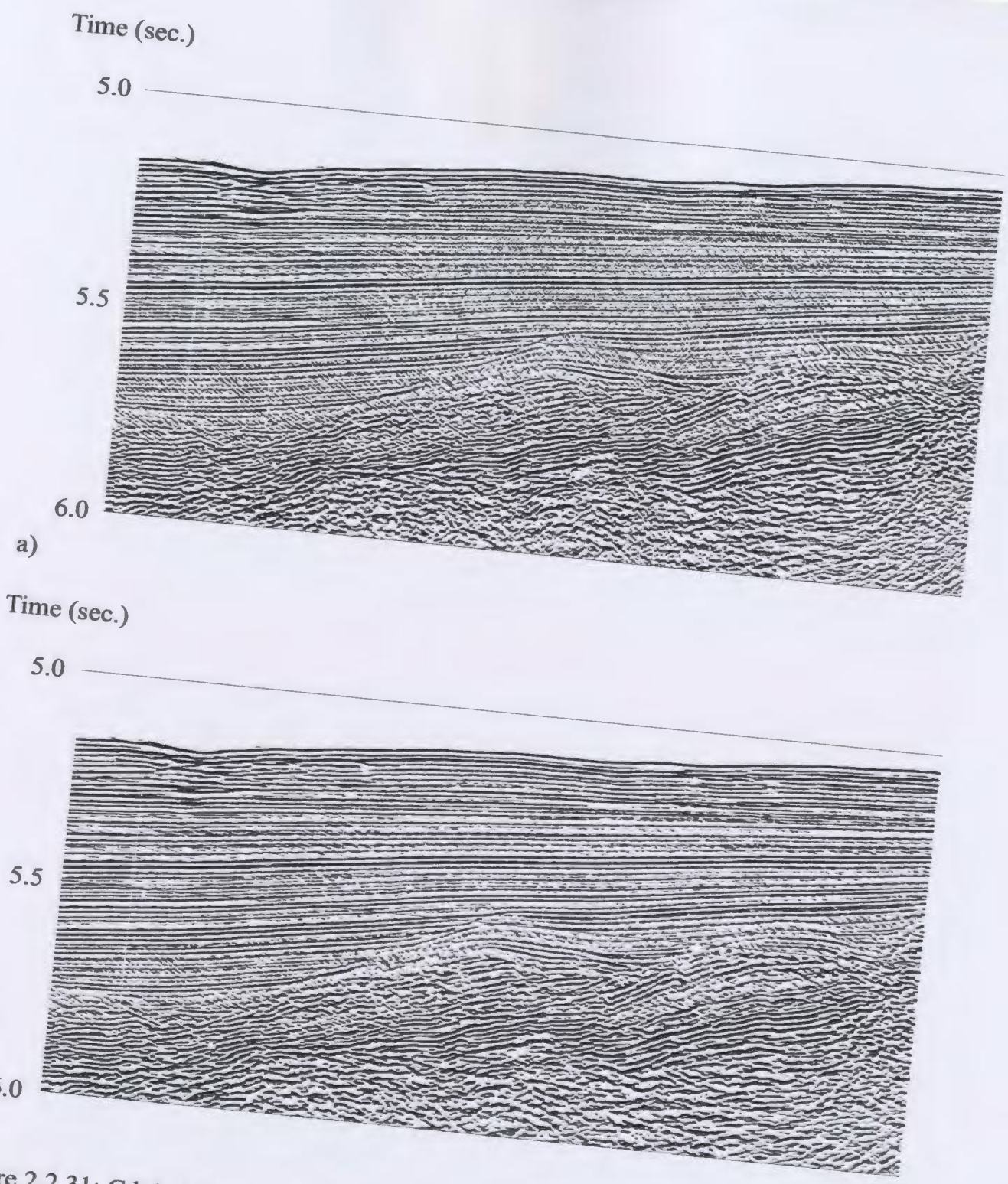

Figure 2.2.31: Cdp's 18000-18750 of line 80 a) without and b) with weighted mix of 5 traces. Note how the coherency of the reflections is increased and how the migration smiles from the basement reflection are reduced.

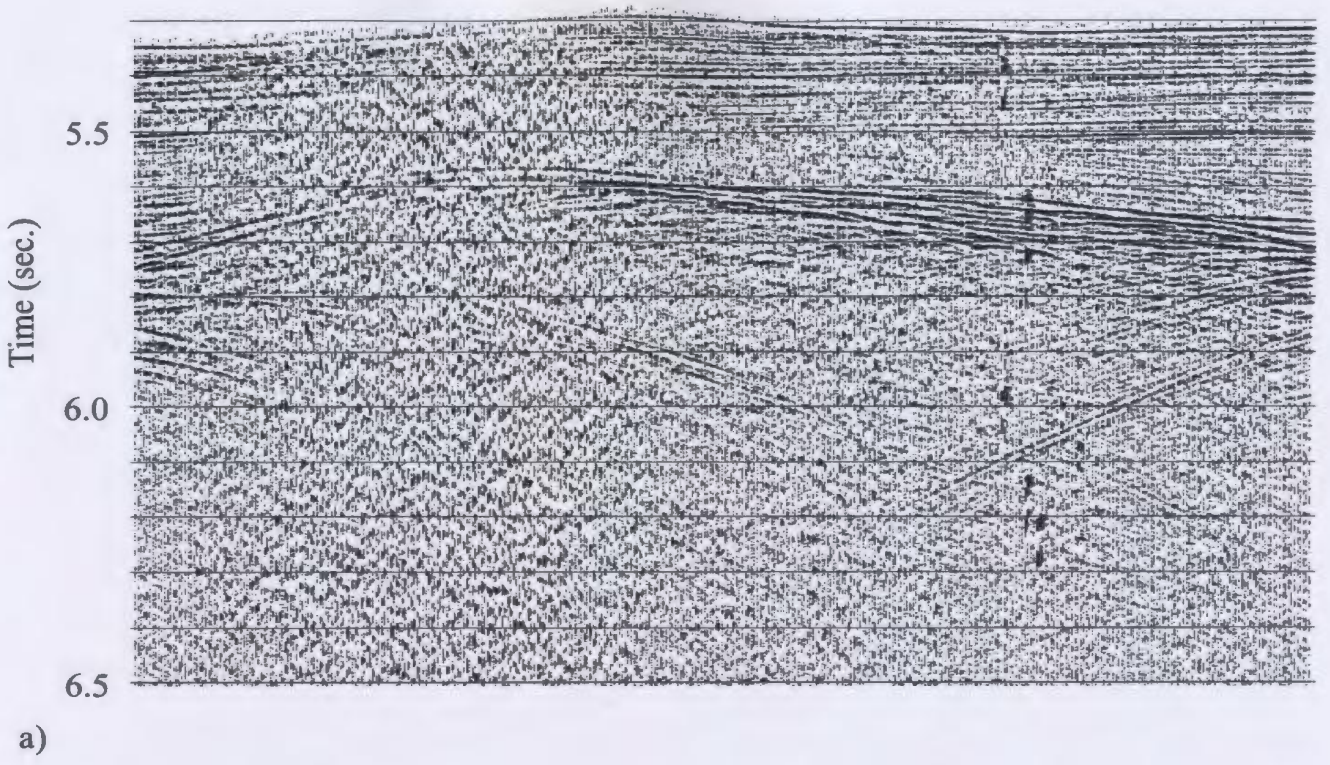

a)

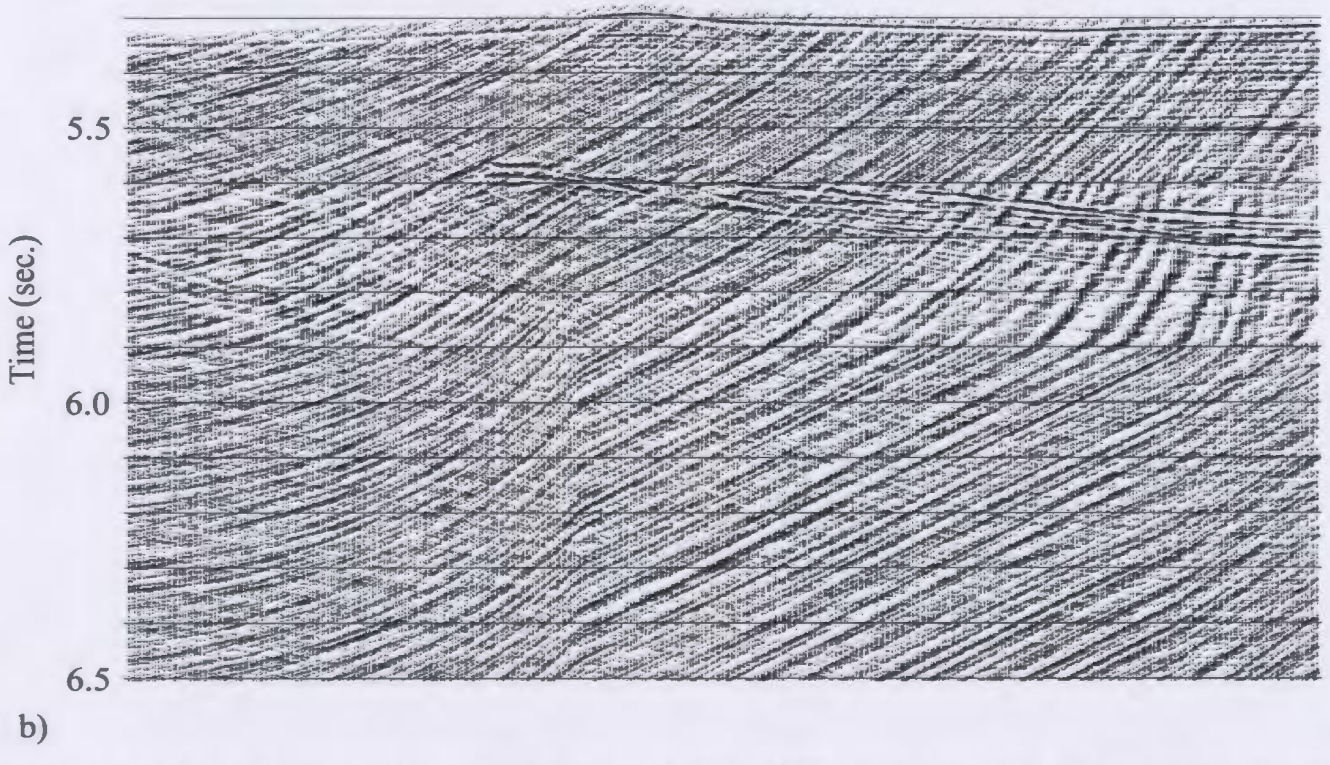

b)

Figure 2.2.32: a) A stacked section of cdp's 16500-16900 from line 80 with an 8-16-180-250 Hz minimum phase Ormsby bandpass filter and 'bad trace zeroing' applied. The data quality improves toward the end of the data set. b) The associated migrated section.

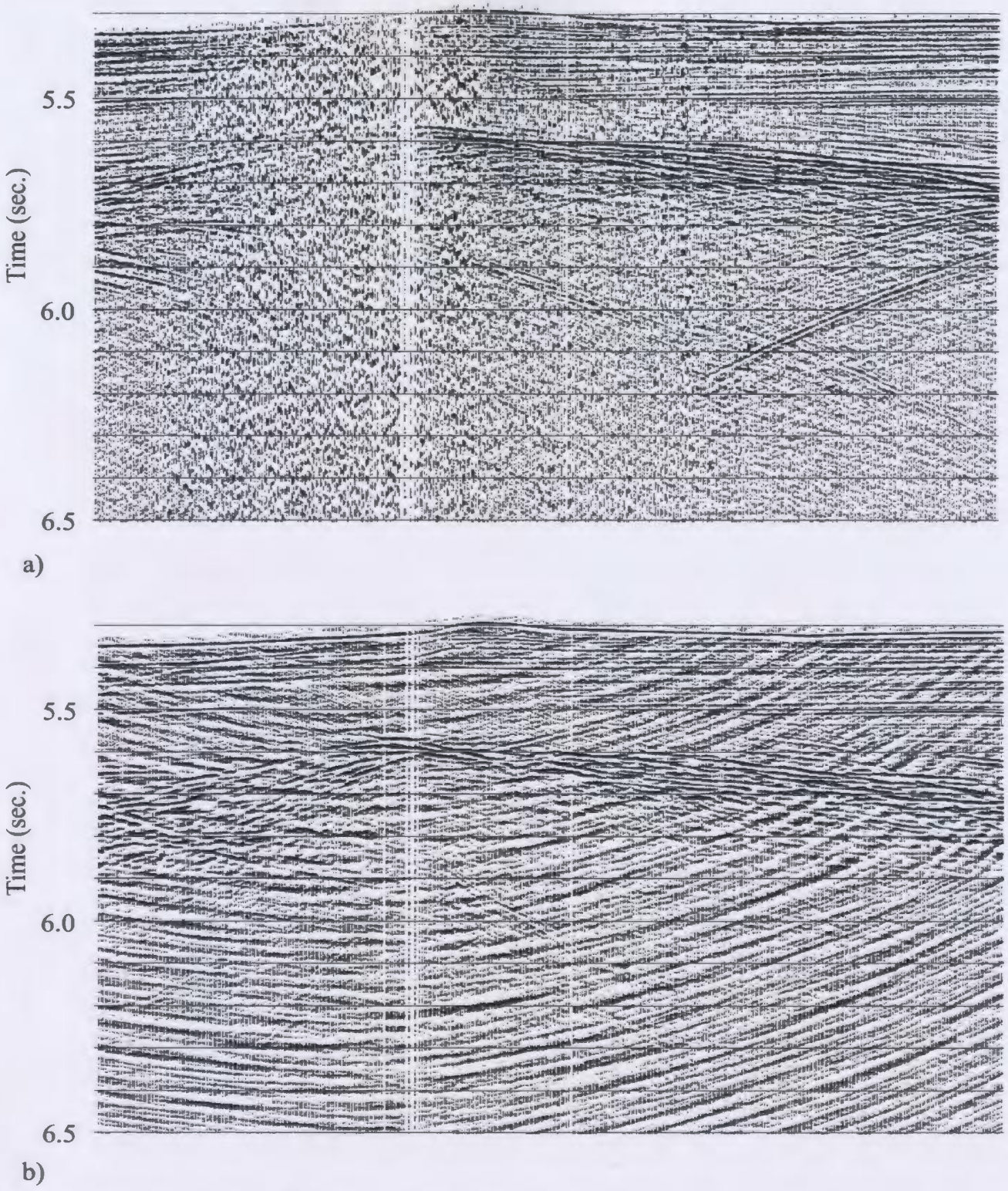

Figure 2.2.33: a) Data from Figure 2.2.32a with 'bad trace zeroing' applied. Many anomalous amplitudes are still present but are localized to a narrower zone of cdp's. b) The associated migrated section.

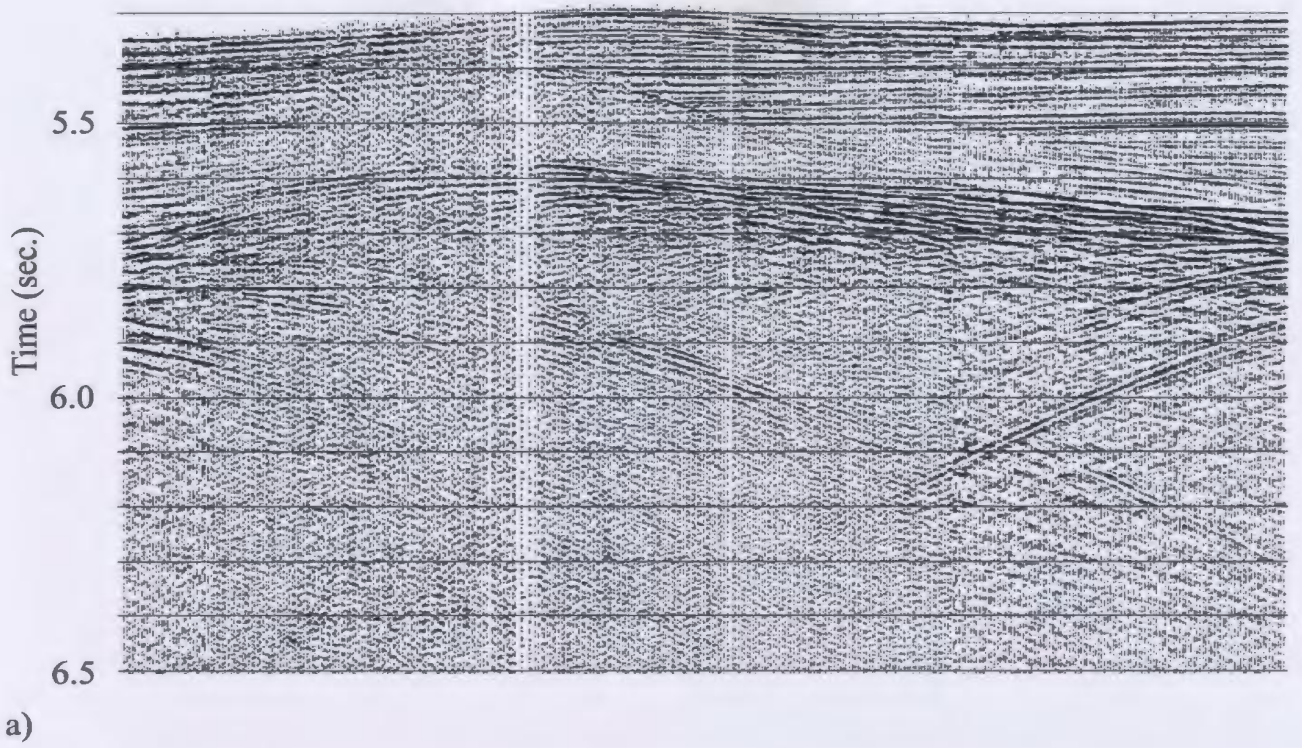

a)

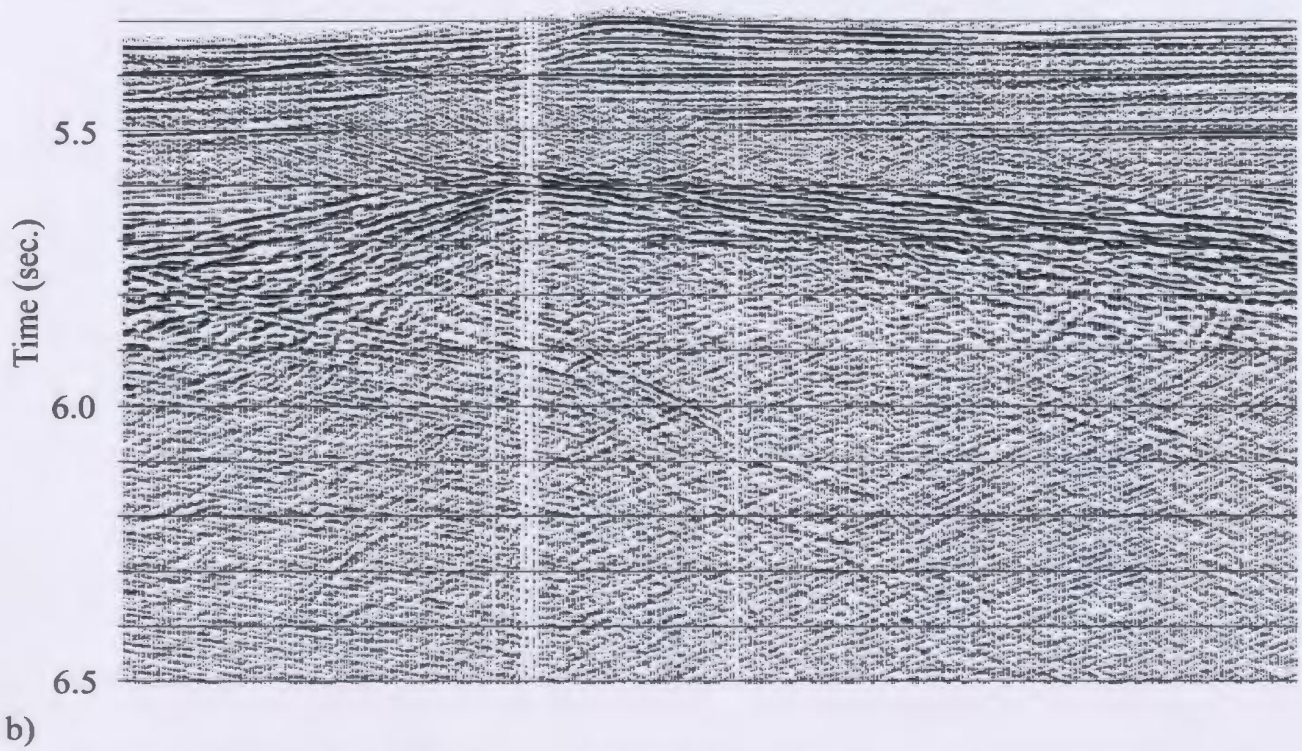

b)

Figure 2.2.34: a) Data from Figure 2.2.33a with the application a 30-80-180-250 Hz minimum phase Ormsby bandpass filter and a 3072 ms AGC operator applied. b) Associated migrated section.

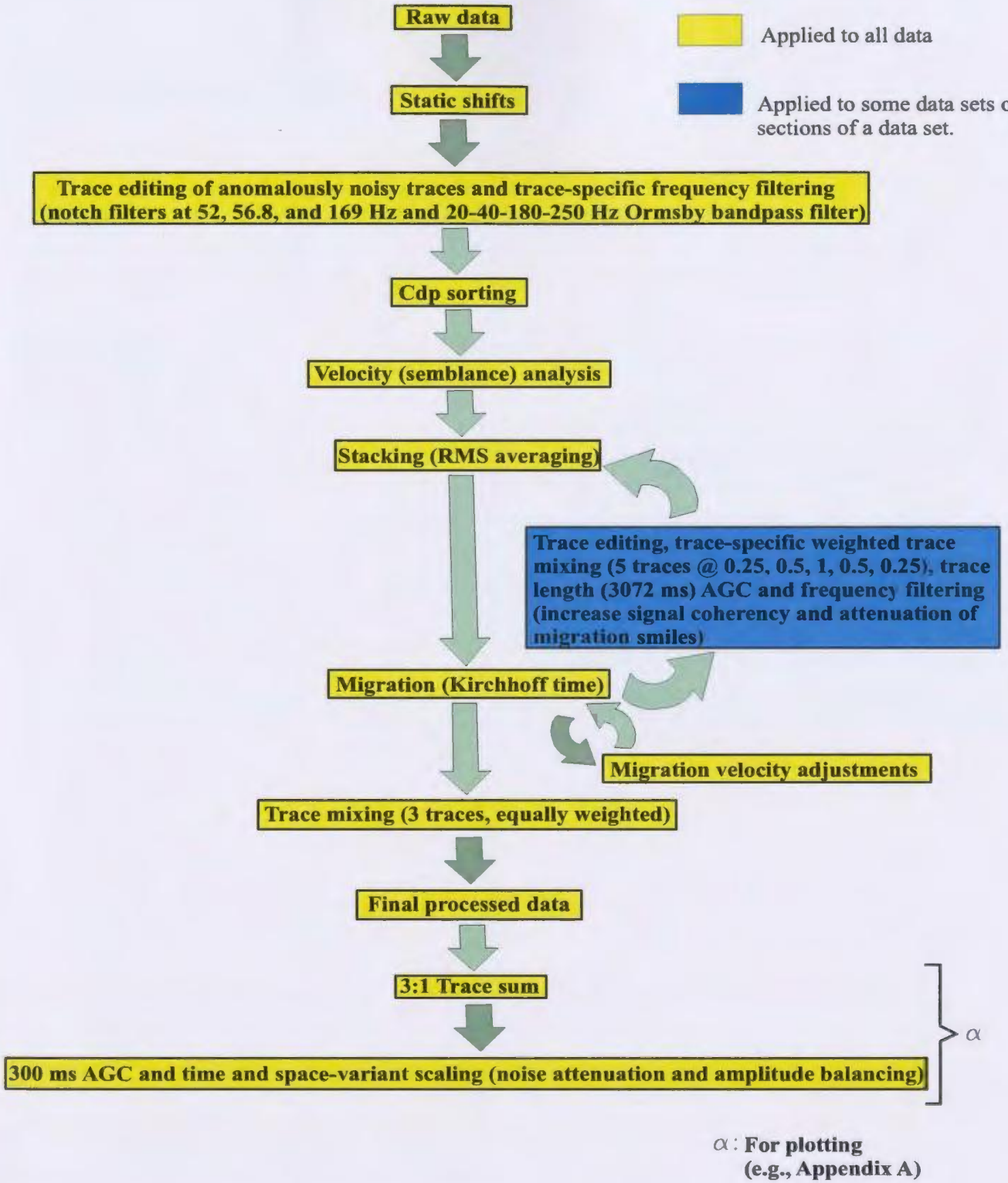

Figure 2.2.35: Generalized processing stream.

with this data set. Uninterpreted copies of each of the seismic lines processed (e.g., Fig. 2.1.2) are provided in Appendix A.

2.3: Interpretation

Seismic data collected by the 2001 cruise are complemented with data from the research vessel *Gelendzhik* to improve spatial sampling in the eastern portion of the Rhodes Basin (Fig. 2.1.2). Using this array of seismic survey lines, major morphological structures and stratigraphic (seismic) units are identified and their architectures documented. Structures are mapped across the survey area beginning with those regions nearest to survey cross-over points where spatial sampling is best, revealing dominant structural trends. Using these data, kinematic style and timing of activation are inferred and incorporated into the regional geo-tectonic framework of the eastern Mediterranean.

Chapter 3: Geological Descriptions

3.1: Establishment of Stratigraphic and Structural Framework

The following is a description of the major structural and stratigraphic features of the Rhodes Basin. Basins, ridges and bathymetric escarpments (steep slopes) are represented by the Greek letters β, α and ϵ, respectively. Subscripts are used to distinguish one basin/ridge/escarpment from another. The thickness of stratigraphic units and relative reliefs are measured in two-way reflection time (milliseconds; ms). The orientation of dipping planes is given as dip magnitude (derived from the travel time and using a depth conversion velocity of 1500 m/s) followed by the apparent dip direction as observed on the seismic profile (ex: 10°SW=dipping 10 degrees toward the southwest). The term "onlap" refers to a contact between an overlying, shallowly inclined horizon and a more steeply inclined, underlying horizon. Conversely, "downlap" describes the contact between an overlying, steeply inclined horizon and an underlying, shallowly inclined horizon. It should be emphasized that this determination is made at the point of contact of the horizons and need not be related to the more general dipping relationship of the two surfaces.

3.1.1: Major Stratigraphic (Seismic) Units

On the basis of their acoustic character, two stratigraphic units: Units 1 and 2 are identified within the Rhodes Basin survey area. Each of these units is widely distributed

but, shows considerable internal variation over the study area. Despite the wide lateral extent of each unit, the correlation of internal reflectors becomes increasingly difficult with increased distance from survey line cross-over points and with the introduction of structural complexities.

Unit 1: Pre-Messinian

Unit 1 constitutes the deepest of the recognisable stratigraphic successions. Its base is not detected. It generally has a weak internal reflectivity with little lateral continuity of its internal reflectors (Fig. 3.1.1a). However, there are locations where it clearly shows parallel reflectors and moderate reflectivity (Fig. 3.1.1b and c). The top of Unit 1 is identified over the entire survey area as a strong, often segmented but, laterally widespread event that frequently shows discontinuous offsets and an irregular, erosive-like relief that forms an angular unconformity with the underlying Unit 1 reflectors (Fig. 3.1.1b and c). Others have established that a layer of Messinian salt is virtually ubiquitous throughout the eastern Mediterranean. The top of this salt layer has been denoted as the M reflector and assigned a late Messinian age by Ryan (1969). Similarly, the base of the salt has been identified as the N reflector. Because of the erosive nature of the top of Unit 1 in the Rhodes Basin study area and the lack of salt, its laterally extensive surface is herein identified as the M reflector. Admittedly, the M reflector in the Rhodes Basin may more accurately represent a cumulative unconformity that envelopes both the M and N

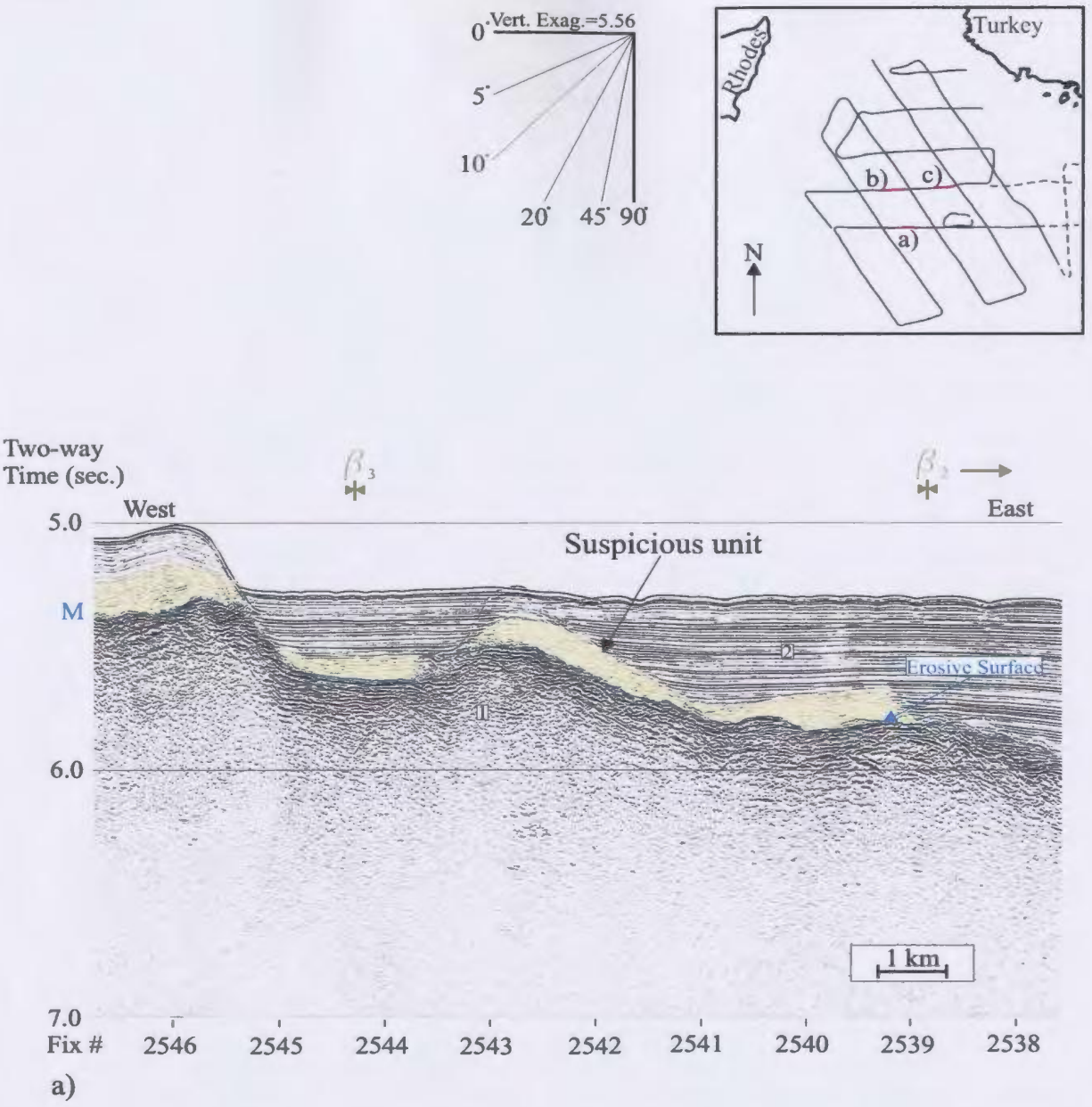

Figure 3.1.1: a) Line70a shows an example of the well bedded (and in this case, folded nature) of Unit 1 and its angular truncation at the M reflector. b) A portion of line 8 showing the erosive and discontinuous nature of the M reflector as well as the rather discontinuous nature of Unit 1. The rather transparent, suspicious unit is highlighted in yellow (discussed later). c) A second example of the peculiar geometry of the transparent unit from line 80. The locations of these profiles are marked by the red line on the survey grid above. Line locations are illustrated in Fig. 2.1.2.

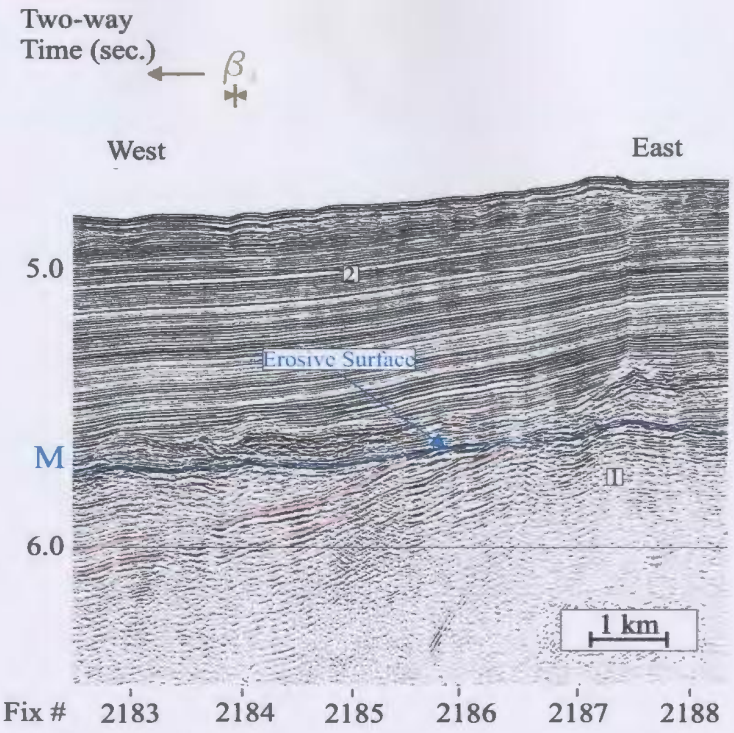

Figure 3.1.1b)

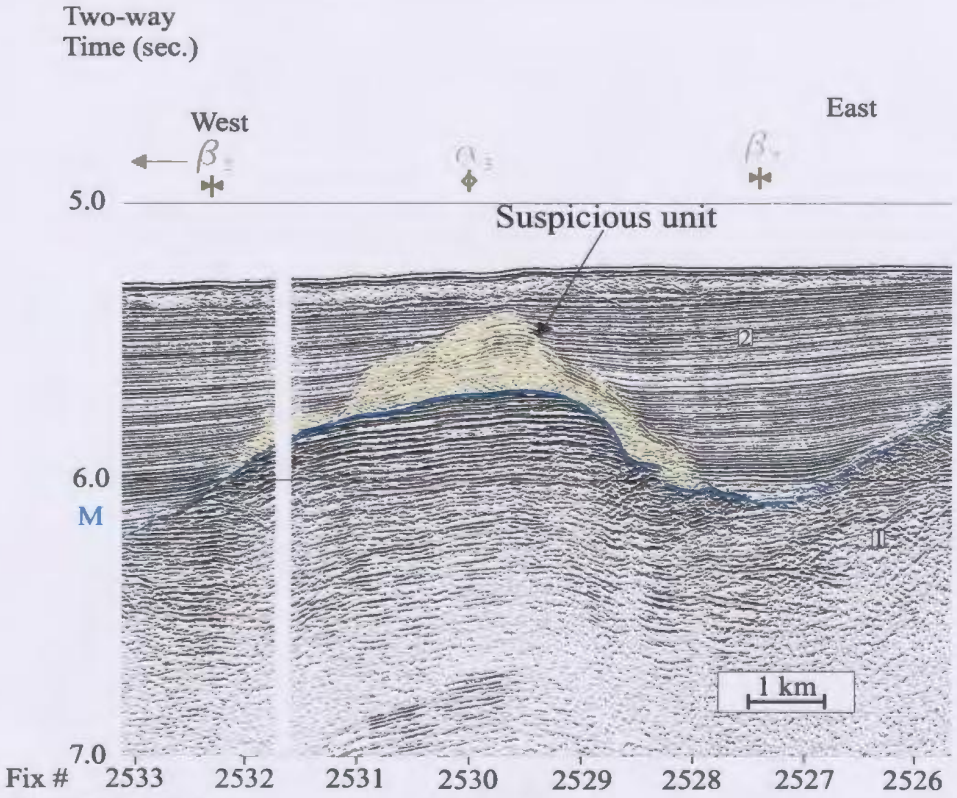

Figure 3.1.1c)

reflectors (M+N). Because the M reflector is often clearly imaged as an unconformity, it cannot be used as an absolute time line. However, in agreement with its uses elsewhere in the Mediterranean, all stratigraphic levels below the M reflector are interpreted to be of pre-Pliocene age (>5 Ma).

Unit 2: Pliocene-Quaternary

Unit 2 lies stratigraphically above the M reflector and is therefore interpreted to represent a Pliocene-Quaternary succession (Fig.3.1.1). Unit 2 is also found throughout the study area and can be broadly described as a sometimes thick, northwest-dipping, highly reflective and continuous package that shows both northwest directed downlap and distal onlap onto the M reflector especially in the deep central portion of the Rhodes Basin. Several subunits with differing seismic expression and stratigraphic architecture occur within Unit 2.

At the base of Unit 2, a weakly reflective and relatively thin (usually <150 ms) seismic unit lies directly on top of the M reflector and is only detected in the central, deep portion of the Rhodes Basin (Fig 3.1.1a and c). Its peculiar tendency to be preserved, and even thicken, over present-day high-standing features make this seismic unit somewhat suspicious. The surrounding, highly reflective Unit 2 reflectors occasionally pass through this weakly reflective unit while other times they appear to be abruptly terminated at their contact with it. Therefore, even though this thin, transparent package is rather wide spread, it is not interpreted as a stratigraphic unit and is interpreted to represent either

side-scattering energy off the highly reflective M reflector, or possibly even a seismic response due to fluid escape. This transparent unit is not considered further.

Subunit 2a is stratigraphically above Unit 1 and is present throughout much of the survey area. It demonstrates a relatively uniform thickness of 100-350 ms even where it drapes over the Turkish slope (Fig. 3.1.2). Its seismic character is typically reverberatory and of higher amplitude and lower frequency than that of the other Unit 2 reflectors. Its internal reflectors are most often parallel and slightly undulated. Its often conformable relationship with Unit 1 make it difficult to identify the M reflector at its base.

Subunit 2b comprises the vast majority of the basin fill, ranging in thickness from ~ 0-1400 ms. It is characterized by high amplitude, high frequency, reflectivity and continuous reflectors that demonstrate a variety of well-imaged internal architectures and structures such as onlap/downlap surfaces, scattering lenses, stratal wedging and faults (Fig. 3.1.3). Subunit 2b is subdivided into Subunits $2b_1$-$2b_3$, each of which are correlated across the survey in an effort to provide an indication of how basin development has changed over time (from the early-middle Pliocene to the late Pliocene-Quaternary).

Table 3.1.1 summarizes the inferred ages of each of the pre-Pliocene and Pliocene-Quaternary seismic units. The age of the Pliocene-Quaternary units (and subunits) are derived by averaging of the results of a linear interpolation along a line orthogonal to the reflectors within several basins that contained the complete succession (e.g., Fig. 3.1.3). It is assumed that the base of Subunit 2a represents ~5 Ma and the top of

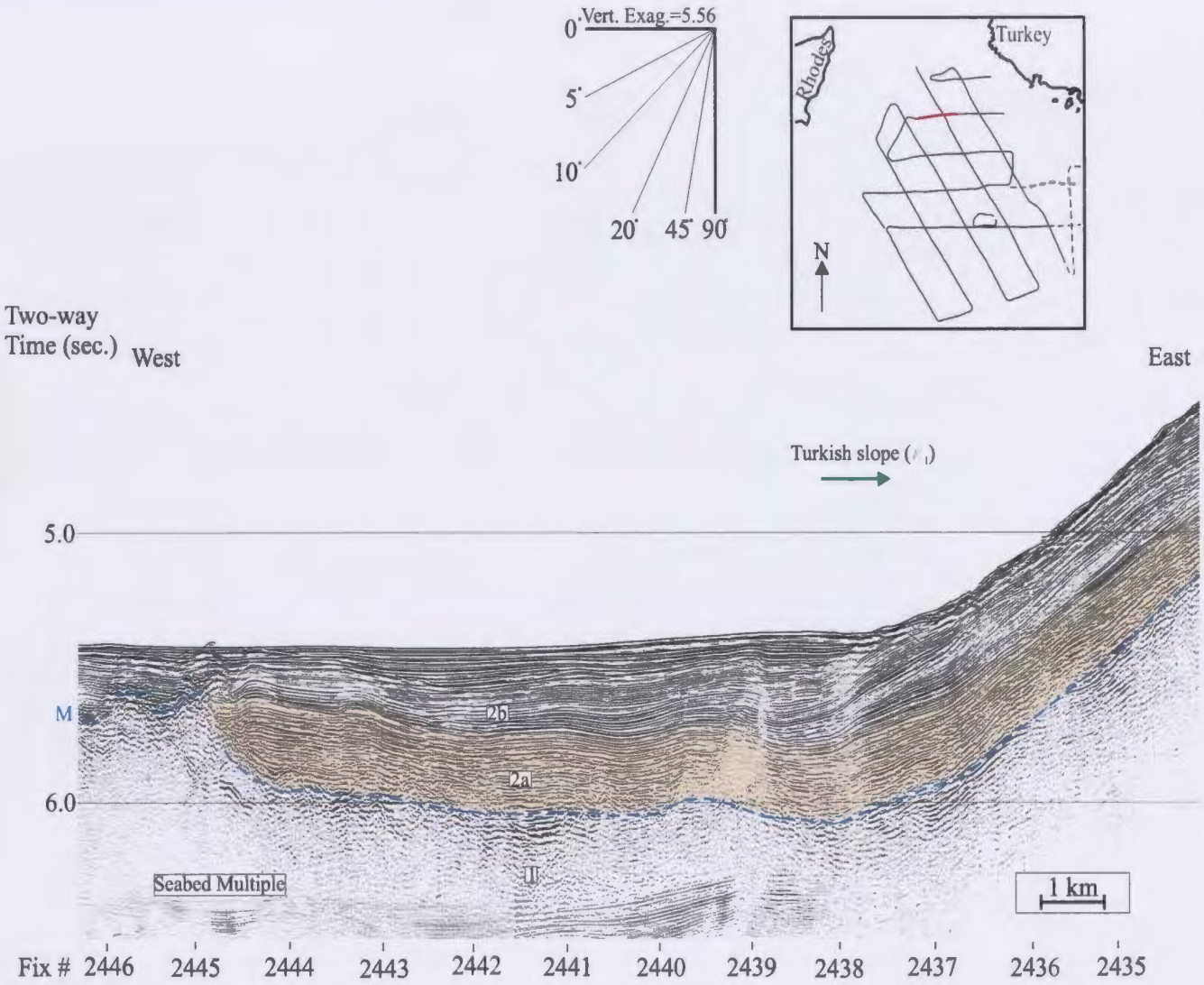

Figure 3.1.2: Unit 2a generally gives a high amplitude response as it drapes over Unit 1 and the eastern slope of the Rhodes Basin. Its contact with Unit 1 is ill defined and is taken to exist along the diffuse transition from the strong, continuous reflectivity of Unit 2b to the weakly reflective Unit 1.

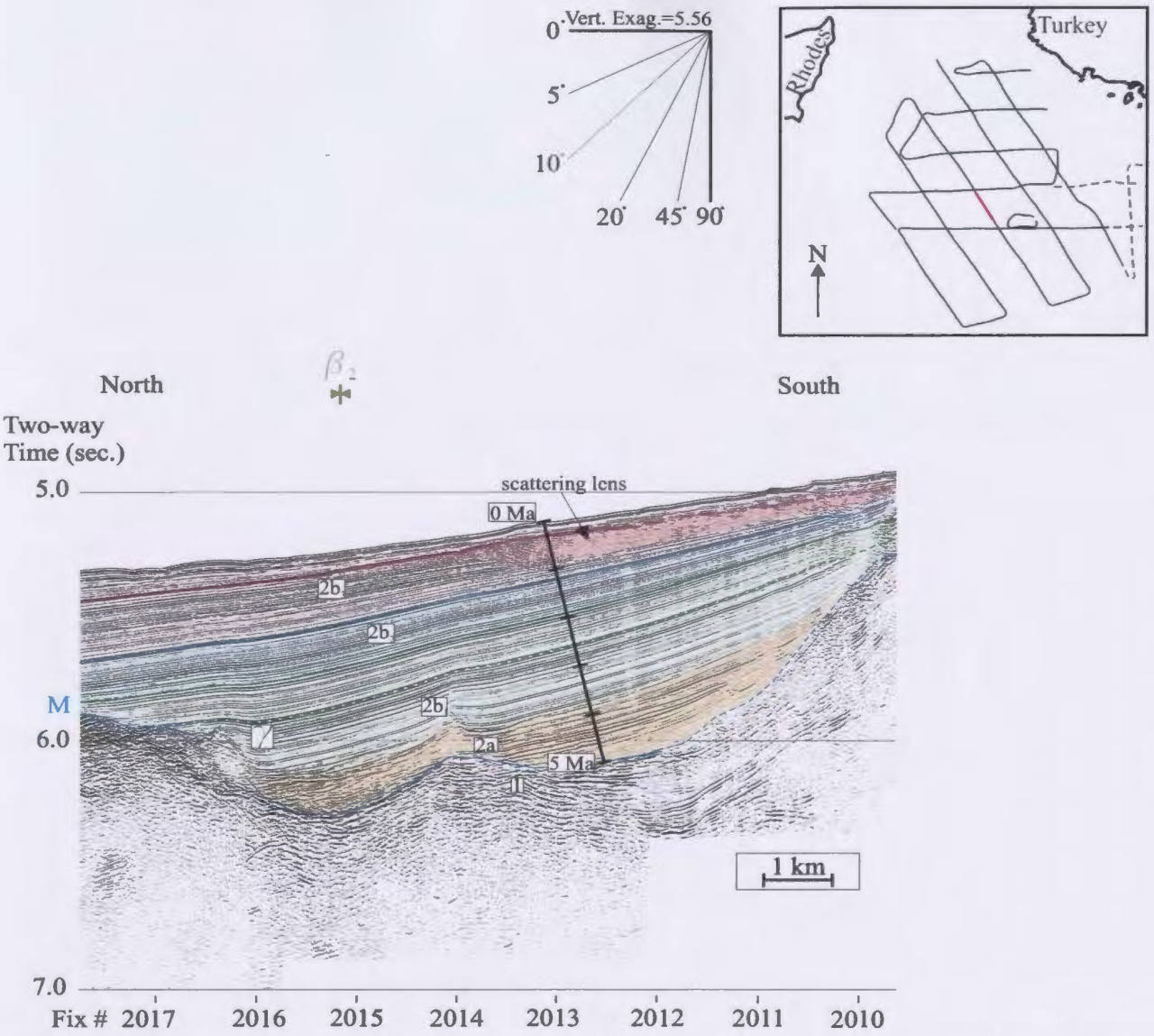

Figure 3.1.3: A portion of line 64 showing all of the subunits of Unit 2 and their northward dipping and thickening nature; especially Subunit 2b.

Stratigraphic (Seismic) Unit	**Inferred Age (Ma)**
Subunit $2b_3$ (late Pliocene-Recent)	~1.0-0
Subunit $2b_2$ (~late middle-late Pliocene)	~2.0-1.0
Subunit $2b_1$ (~early middle- middle Pliocene)	~4.0-2.0
Subunit 2a (early Pliocene)	~4.5-4.0
Unit 1	> 5.0

Table 3.1.1: The seismic units identified in the Rhodes Basin survey area and their inferred ages based on a simple linear interpolation of vertical stratigraphic thickness.

Subunit $2b_3$ marks 0 Ma. An isochron map of the study area derived from Unit 2 thicknesses measured vertically at each fix number location is displayed in Figure 3.1.4. This map was hand-contoured and digitized for presentation.

3.1.2: Prominent Bathymetric Escarpments and Bathymetric Domains

The portion of the Rhodes Basin imaged by the 2001 seismic grid consists of three bathymetric domains: a deep central zone (up to 5800 ms or 4350 m water depth) bound between an elevated, rough-surfaced platform to the south (~4000 ms or 3000 m water depth) and the Turkish slope to its east. Laterally extensive bathymetric escarpments (ϵ_1-ϵ_2) mark pronounced gradients in the seabed slope and define the boundaries between each of the domains (3.1.5). Similar to stratigraphic correlations, these structural correlations are valid in regions where seismic profiles are near to one another or crossover, but become tentative away from crossovers.

Escarpment ϵ_1

Escarpment ϵ_1 trends northeastward at its westernmost location, but abruptly turns to run east-west for a short distance before altering its trend again toward a more northerly azimuth along the edge of the Turkish slope (3.1.5). At its southern end, escarpment ϵ_1 provides 600-880 ms of bathymetric relief along an ~12°NW slope where it separates the relatively uplifted, rough-surfaced domain from the deep, central portion of the Rhodes Basin (Fig. 3.1.6a-c). Here, escarpment ϵ_1 is also associated with apparent

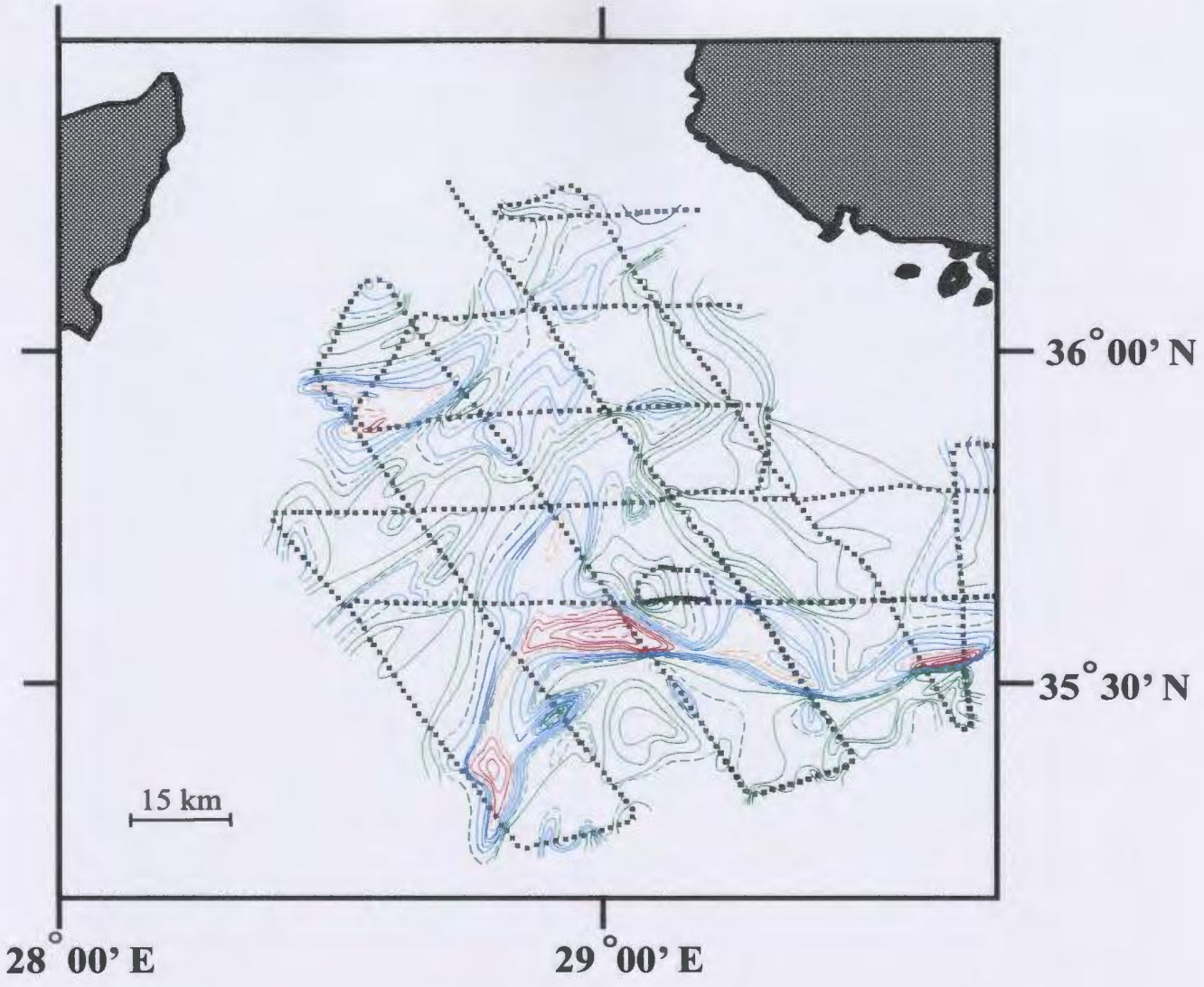

Figure 3.1.4: An isochron contour map of Unit 2 (Pliocene-Quaternary succession) within the study area. Vertical thickness (in time (ms))were recorded at each fix location. Contouring was done manually.

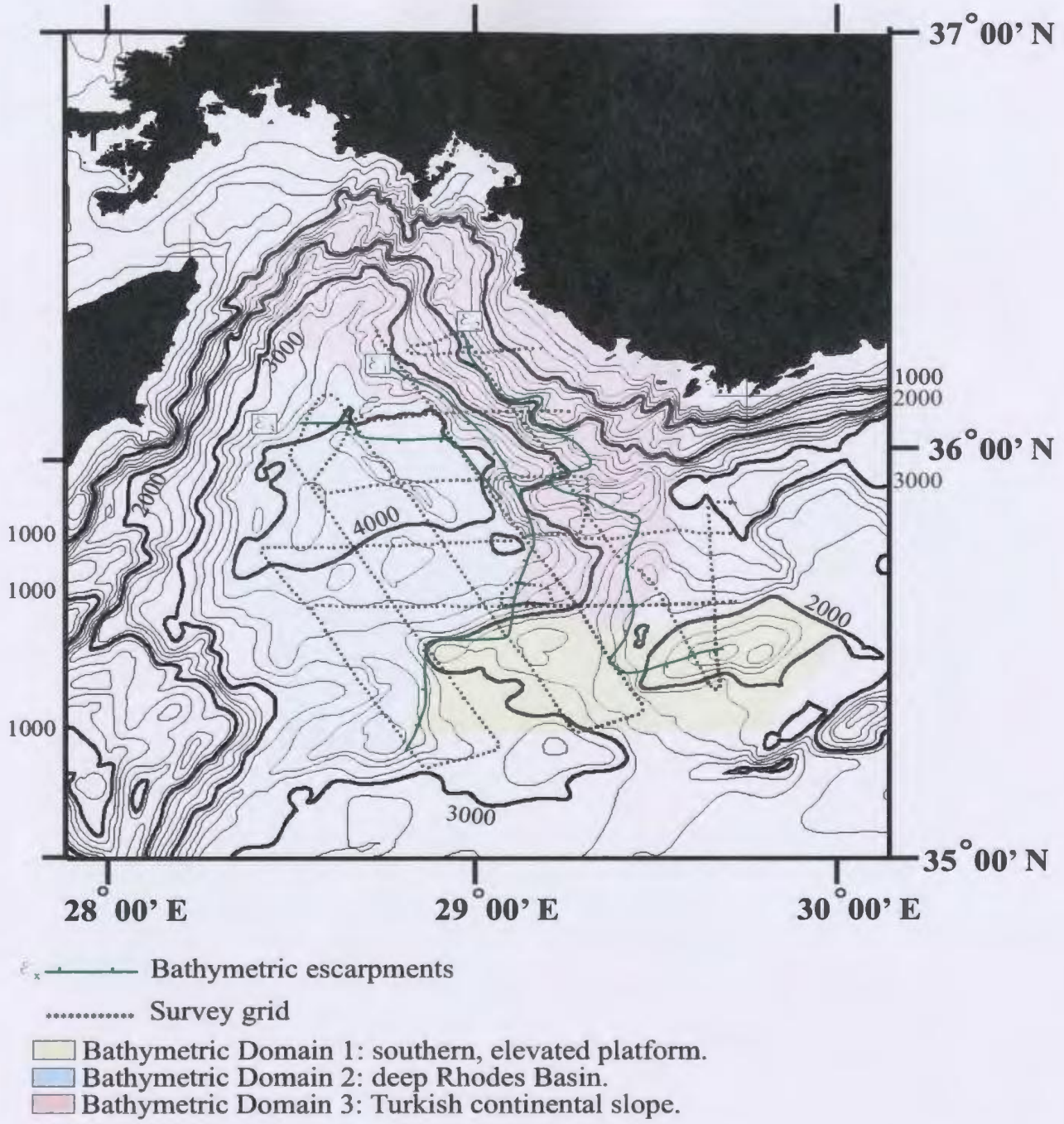

Figure 3.1.5: Bathymetry of the Rhodes Basin showing the 3 bathymetric zones. Contour interval = 200 metres, every 1000 metres labelled and highlighted with bold font.

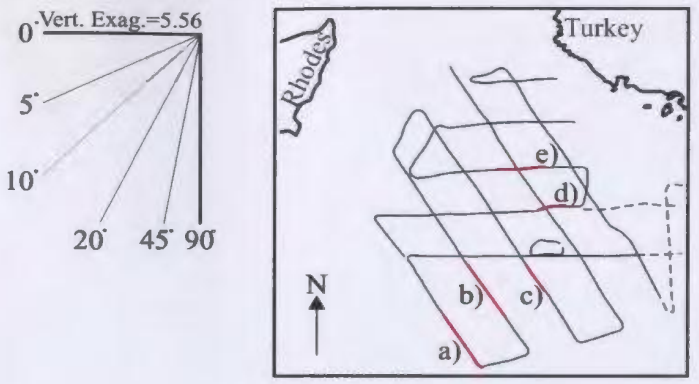

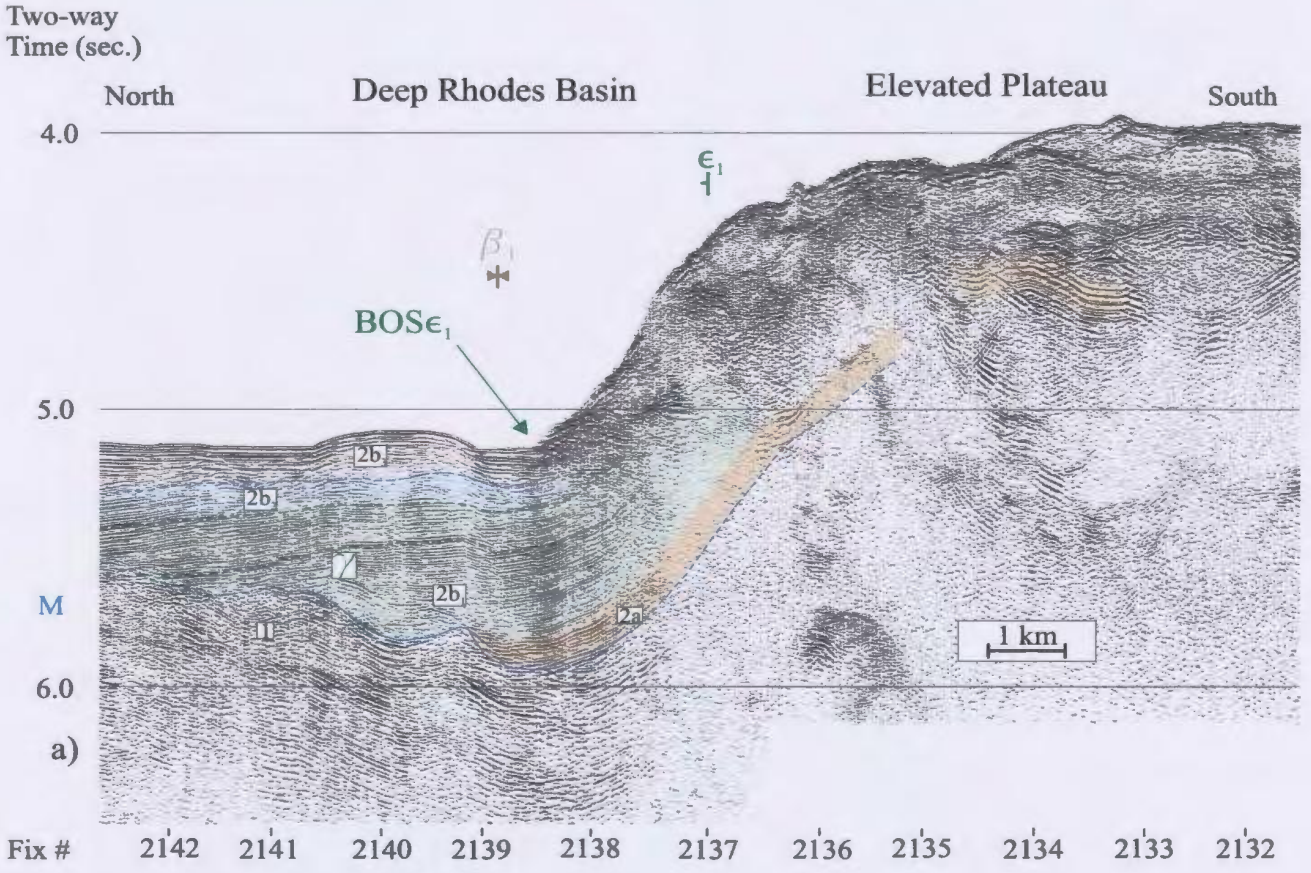

Figure 3.1.6: Escarpment ε_1 can be traced along the southern and eastern margins of the Rhodes Basin. Here, the intersections of the escarpment with lines a) 70, b) 68, c) 64, d) 80 and e)81are shown.

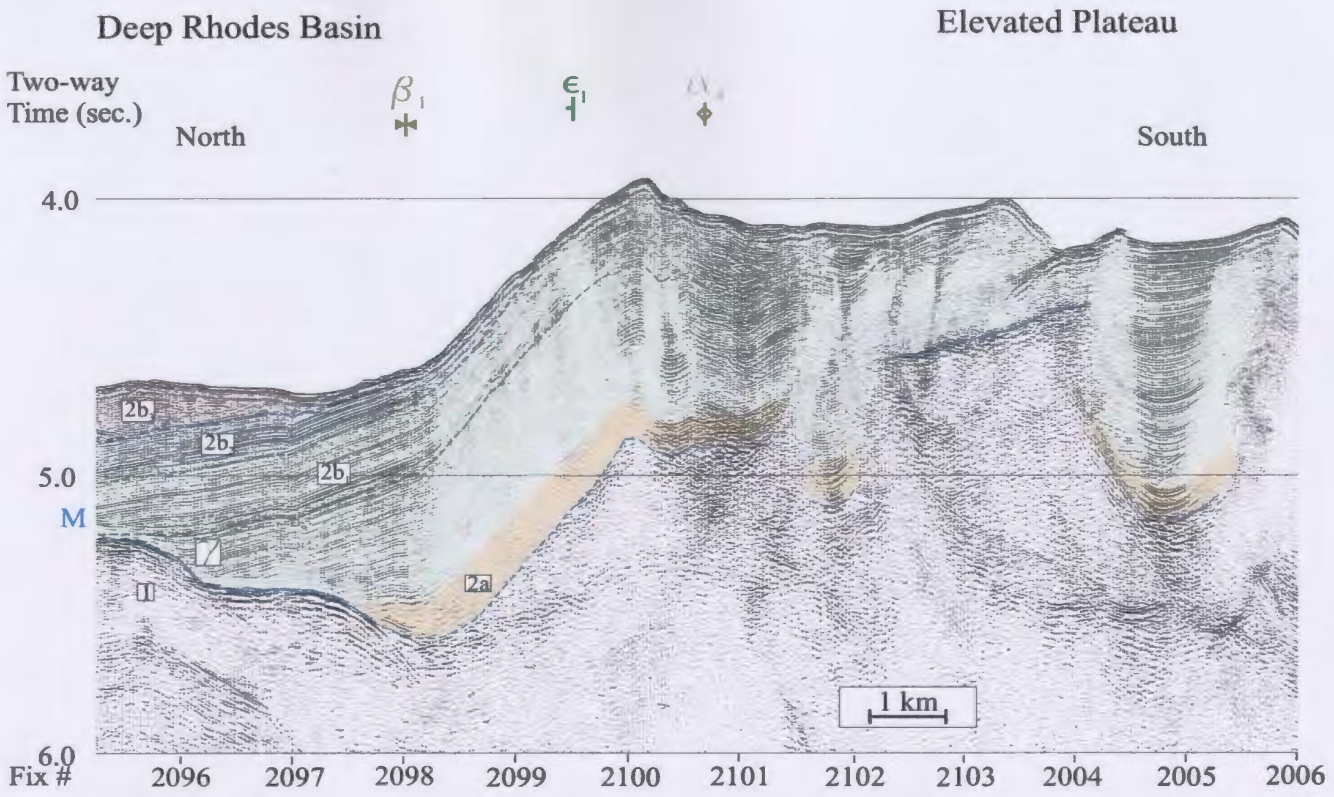

Figure 3.1.6b)

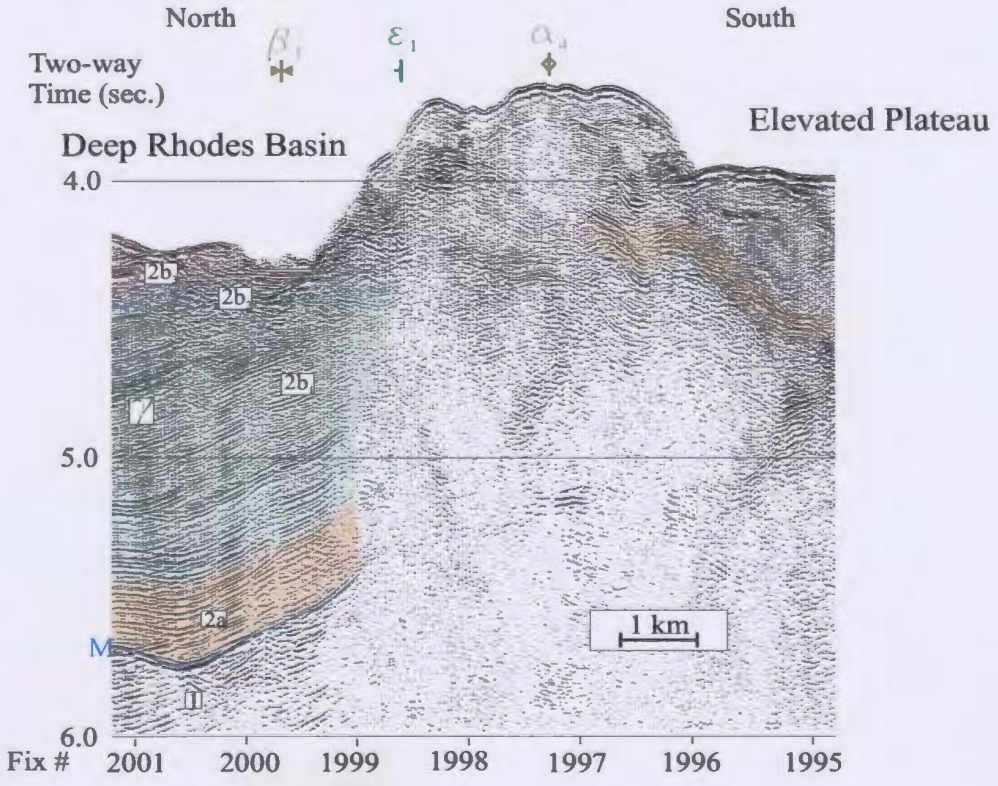

Figure 3.1.6c)

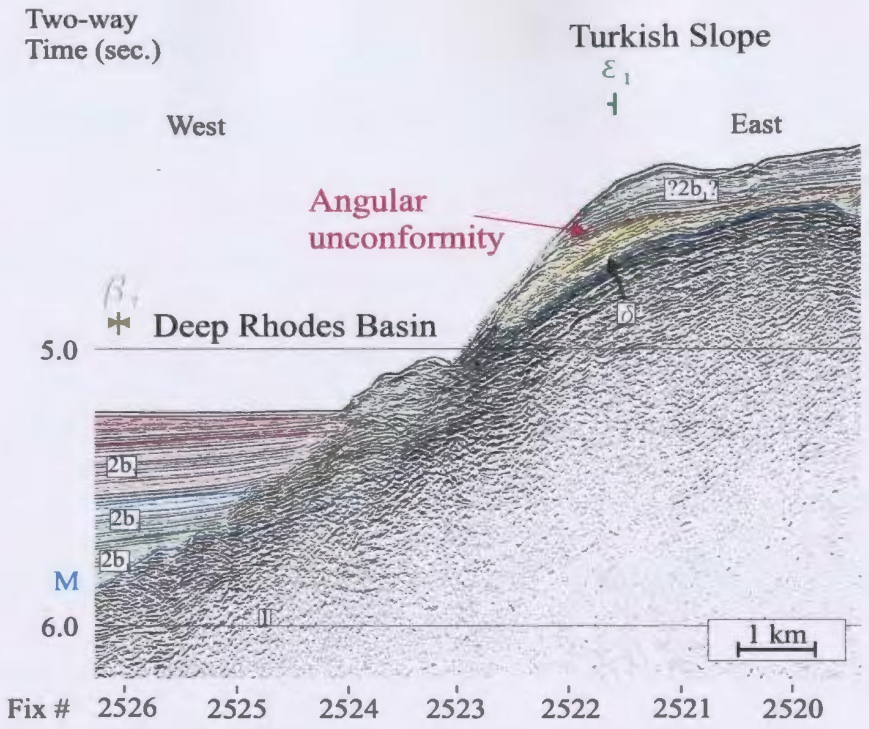

Figure 3.1.6d)

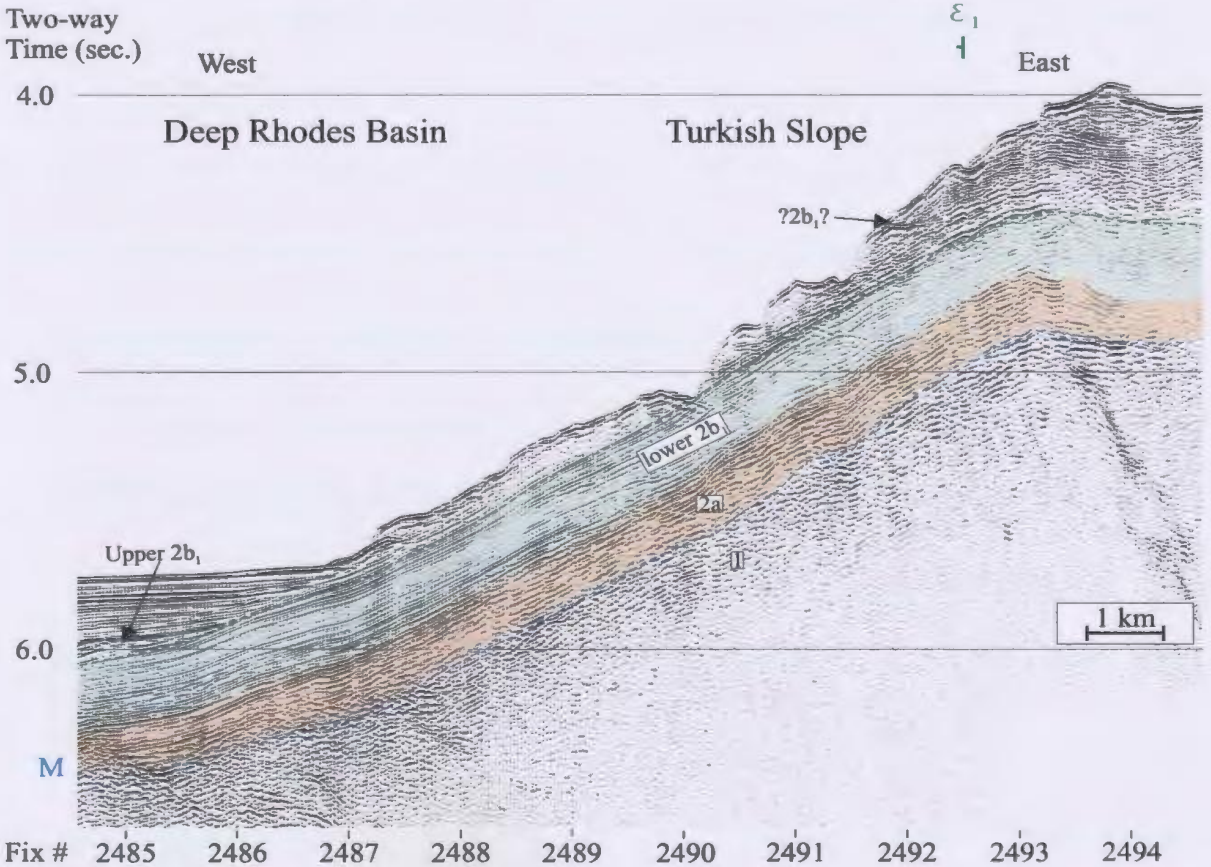

Figure 3.1.6e)

down-to-the-north offsets of the M reflector by more than 1000ms. The rough-surfaced plateau is relatively flat, lying at a water of ~4000 ms (~3000 m) +/- 200 ms (Figs. 3.1.5, 3.1.6a-c).

The deep Rhodes Basin occupies that portion of the survey area basinward of the base of escarpment ϵ_1 (Fig. 3.1.5). Its southern portion dips at ~1.5°NW from its shallowest point at the base of escarpment ϵ_1 in the south where it lies at a water depth of ~4800 ms (~3600 m). Toward the north, the gentle northwest slope flattens to form a deep plateau that defines the deepest portion of the Rhodes Basin (water depth ~ 5800 ms, or ~4350 m) (Fig. 3.1.5).

Along the eastern, Turkish slope, escarpment ϵ_1 is most clearly identified to the south where it illustrates ~700-900 ms of bathymetric relief along a 10-15°NW slope (Fig. 3.1.6d). Here, escarpment ϵ_1 marks the boundary between the Turkish slope and the deep Rhodes Basin. Using bathymetry contours as a guide, escarpment ϵ_1 is correlated northward where it dips ~5-10°W-SW (Figs. 3.1.5 and 3.1.6e). The seabed at these northern escarpment ϵ_1 localities is usually less scarped than those to the south. The Turkish slope, ranges in water depth from 1000 ms (~750 m) at the extreme northeast corner of the survey area to 5200 ms (~3900 m) at the base of escarpment ϵ_1. Generally, the descent of the slope increases from an average of ~4°SW in the north to ~8°SW in its southern region (Fig. 3.1.5).

Escarpment ϵ_2:

Escarpment ϵ_2 trends north northeast, east of escarpment ϵ_1 (Fig. 3.1.5). Due to its meandering trend, the dip direction of this 6-20°-dipping escarpment varies from south to west to north and provides bathymetric reliefs of 300-1200 ms (Figs. 3.1.5, 3.1.7). Generally, escarpment ϵ_2 generates ~720 ms of bathymetric relief along an ~7°W slope at its southern end but is more gently-dipping (~4°SW) in the north. Although, some of the ϵ_2 correlations may appear somewhat ill-constrained, they are supported by the general trend of the bathymetry contours (Fig. 3.1.5) as well as the consistent depth of the base of the slope for escarpment ϵ_2 (3500-4000 ms) among each of its locations; a depth much shallower than the bases of escarpments ϵ_1 and ϵ_3 (discussed later) (Fig. 3.1.7). The M reflector is also occasionally offset across escarpment ϵ_2 by as much as 1000 ms. Despite ample accommodation and channels provided by escarpment ϵ_2, the Turkish slope is generally sediment starved; the only exception being a single basin located in the south of the Turkish slope, near the junction of the three bathymetric domains (discussed later).

Escarpment ϵ_3:

Escarpment ϵ_3 is the only escarpment located inside the deep Rhodes Basin (Fig. 3.1.5). It is best observed in the northwestern portion of the survey area where it illustrates a steep (10-20 SE), southward slope that accommodates ~600 ms of bathymetric relief. Escarpment ϵ_3 trends eastward along a sigmoidal path (Figs. 3.1.5 and

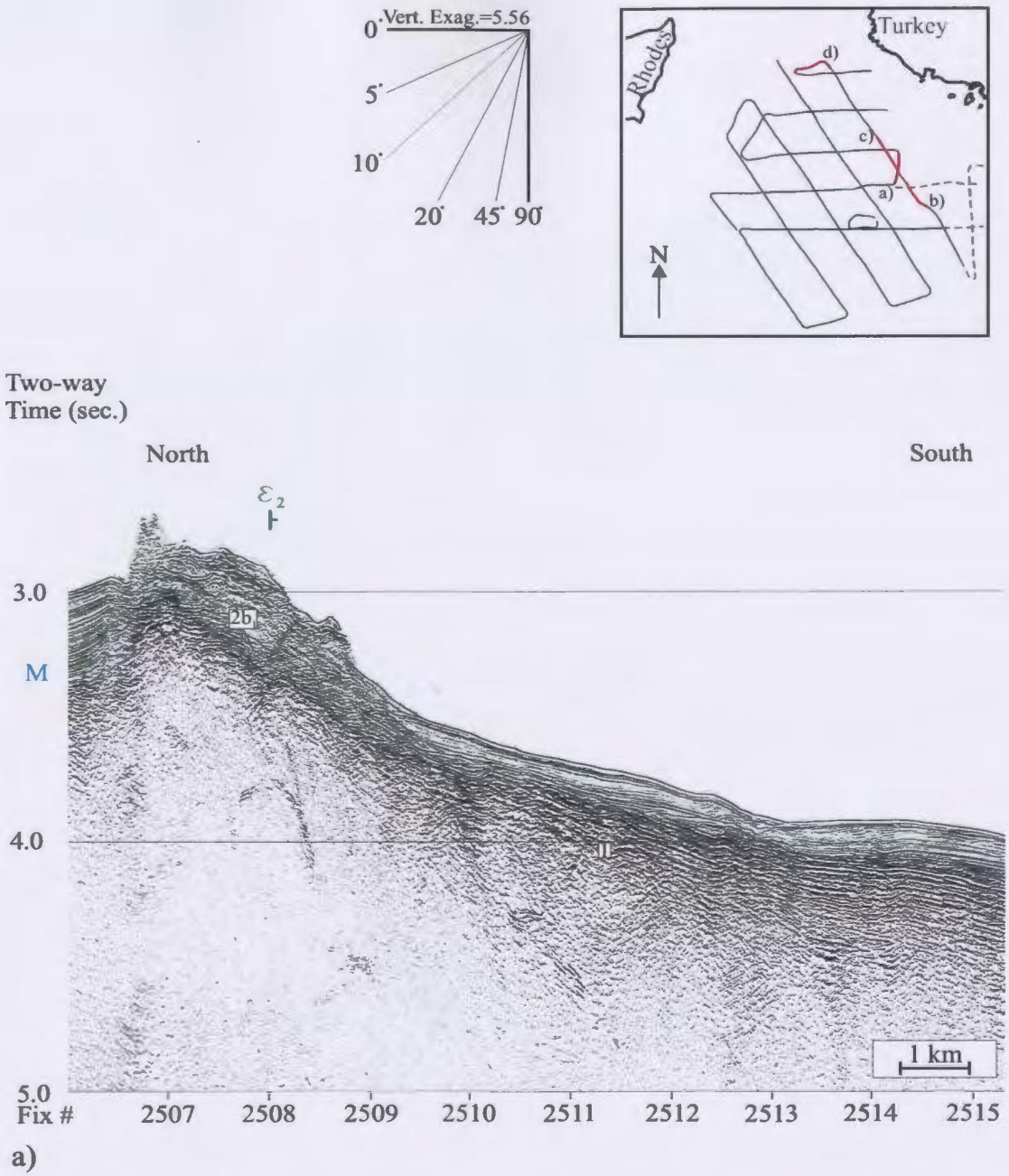

Figure 3.1.7: Escarpment ε_2 winds northward, crossing line 60 at several locations. At some localities, it shows an erosive, channel-like nature while at other locations, especially toward the north, it appears more smoothly dipping. Intersections of ε_2 with a) line 80 and c)-d) line 60 are illustrated.

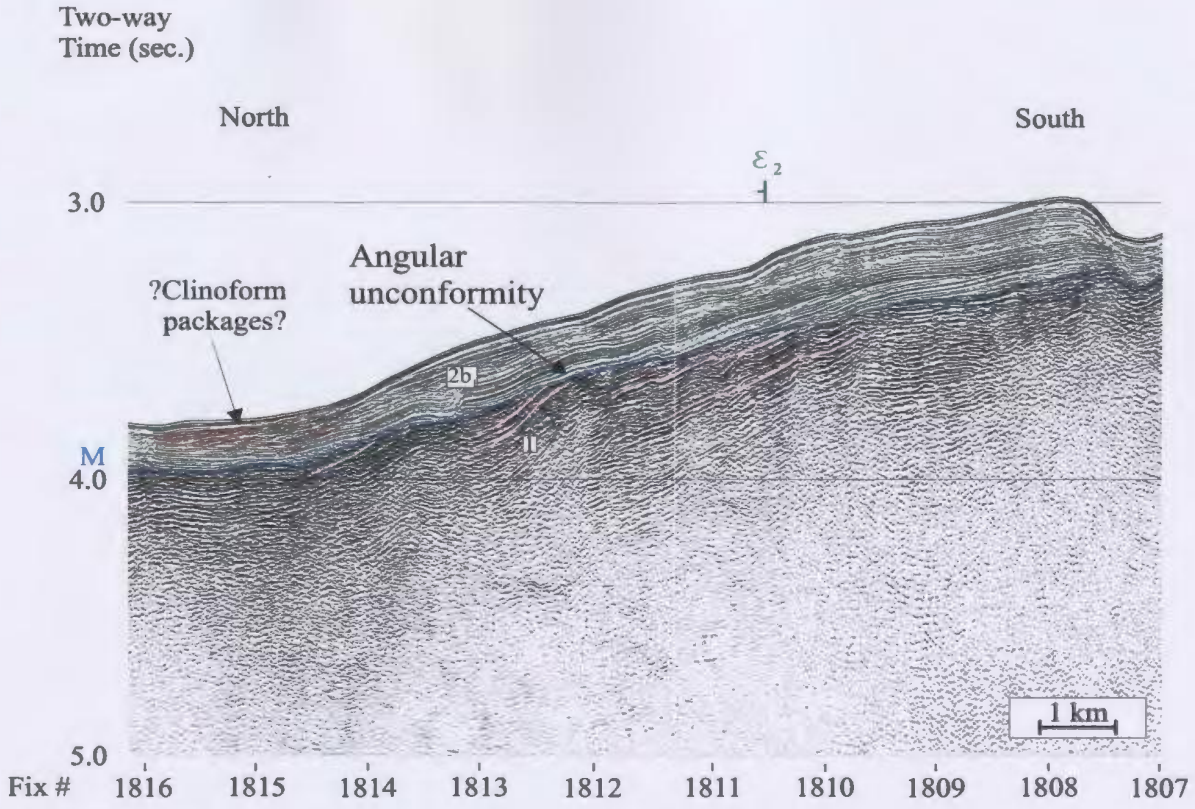

Figure 3.1.7b)

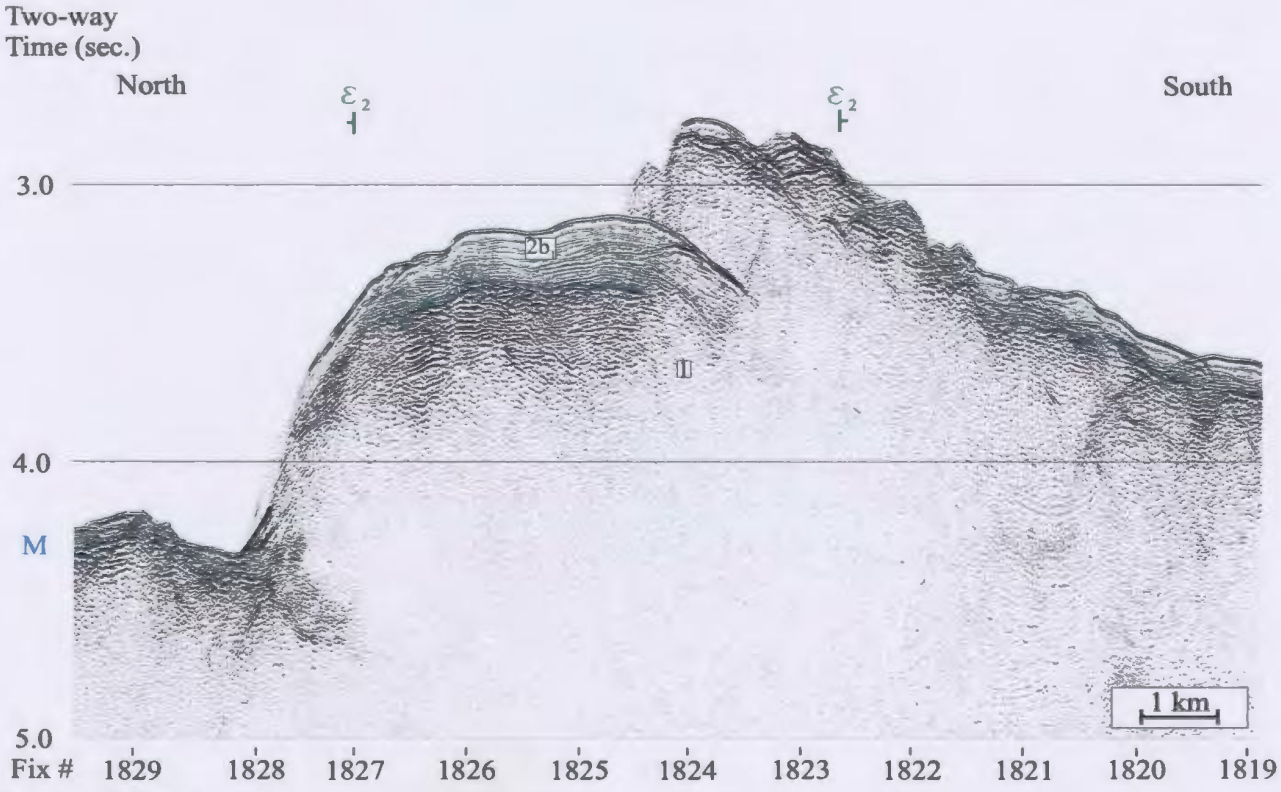

Figure 3.1.7c)

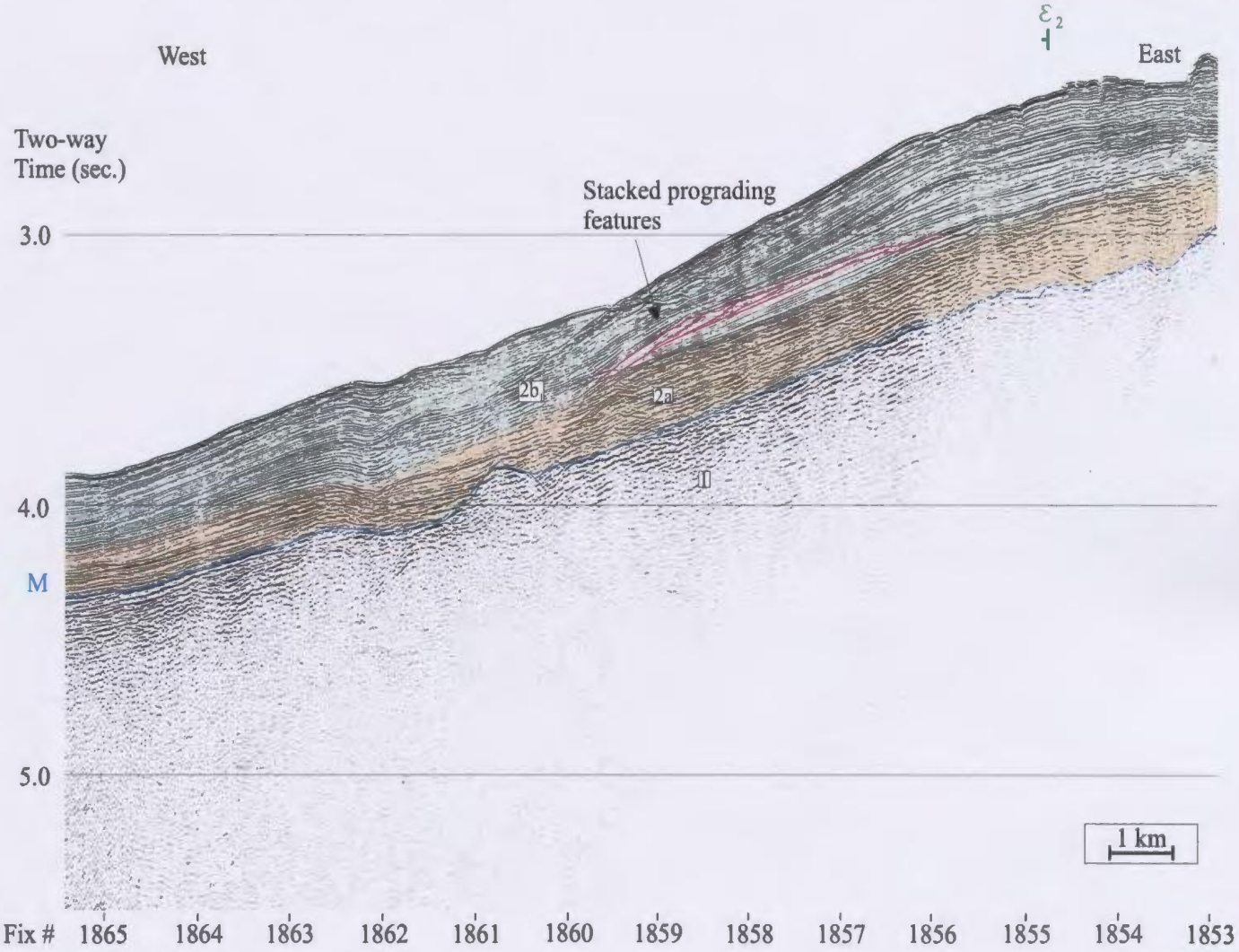
West
East
ε_2
Two-way
Time (sec.)
Stacked prograding
features
3.0
2b
2a
1
4.0
M
5.0
1 km
Fix #
1865
1864
1863
1862
1861
1860
1859
1858
1857
1856
1855
1854
1853

Figure 3.1.7d)

3.1.8. The base of slope ϵ_3 (*BOS*ϵ_3) rests at 5820-5860 ms (nearly 4400 m) water depth.

3.2: Basin and Ridge Descriptions

The M reflector represents the most prominent and widely correlatable reflector found in the study area. Using the M reflector as a structural datum, several prominent basins and ridges are identified within the survey area. Adjacent seismic profiles show similar occurrences and associations of basins and ridges, allowing them to be correlated and mapped (Fig. 3.2.1). Although a few of the structural correlations are made across considerable distances, these correlation 'leaps' are supported by those areas where a determination of the structural trend is permitted by adequate sampling near cross-over points.

Because ridges and basins are generally adjacent to one another along the M reflector, the margins of these structures (used to determine ridge width) are mapped half way along their flanks. Unless clearly specified otherwise, the relief of a ridge refers to the distance (in time measured in milliseconds (ms)) between the M reflector at the highest point on the ridge and its margin with its adjacent basins. A description of the defined basins and ridges is presented below. Where possible, holistic descriptions in both space and time are provided. However, the changing morphology and style of many of the basins and ridges across the survey area often requires description to be done on a more localized basis.

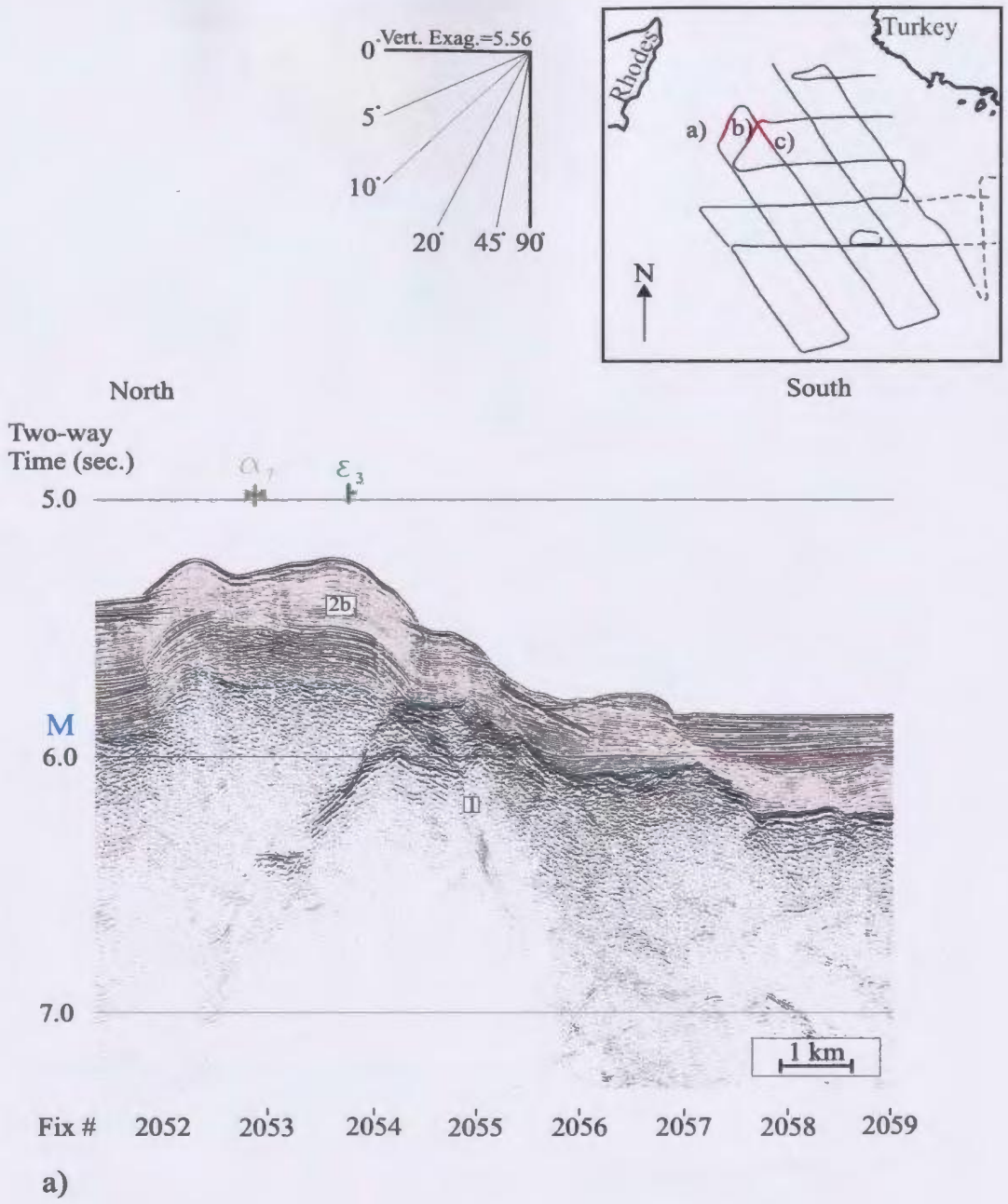

Figure 3.1.8: Escarpment ε_3 and ridge α_7 cross a) line 64, b) line 83 and c) line 64 a second time.

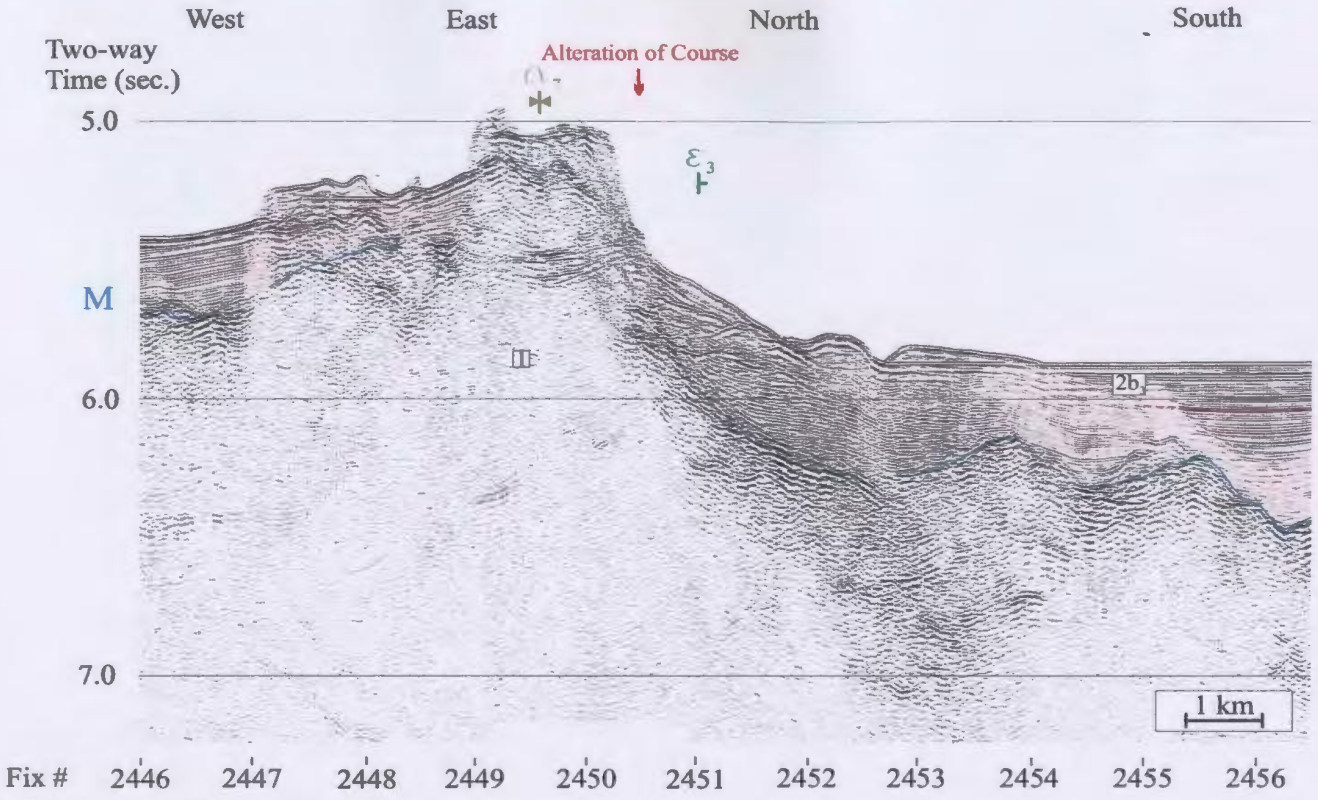

Figure 3.1.8b)

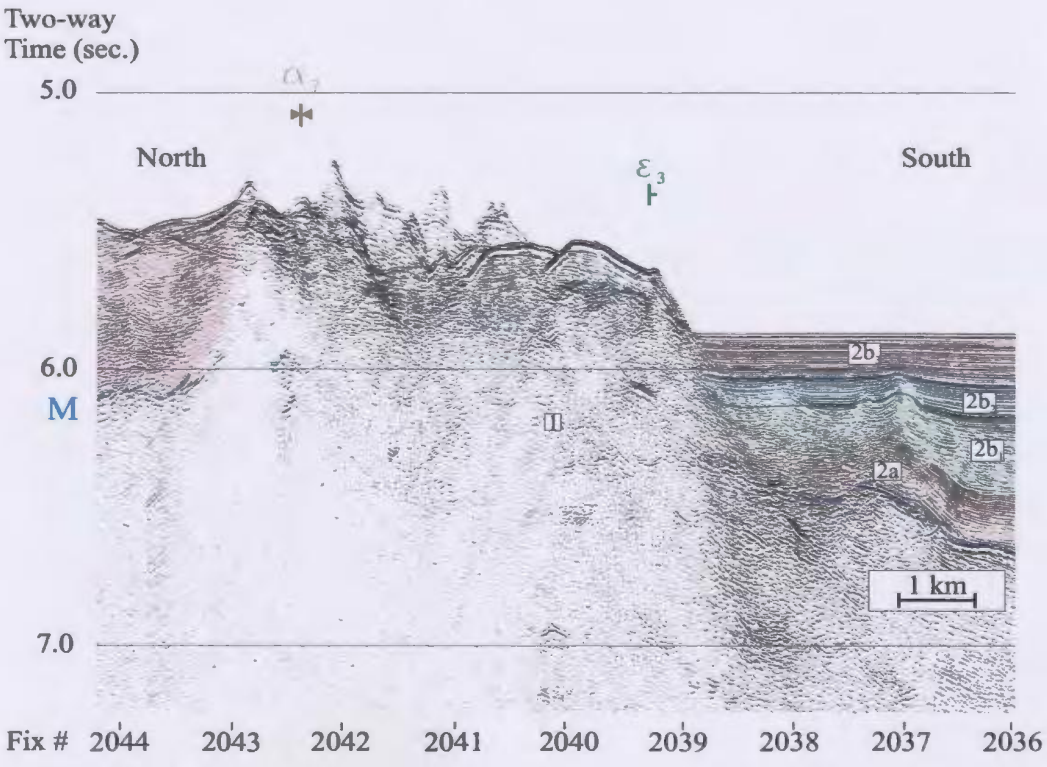

Figure 3.1.8c)

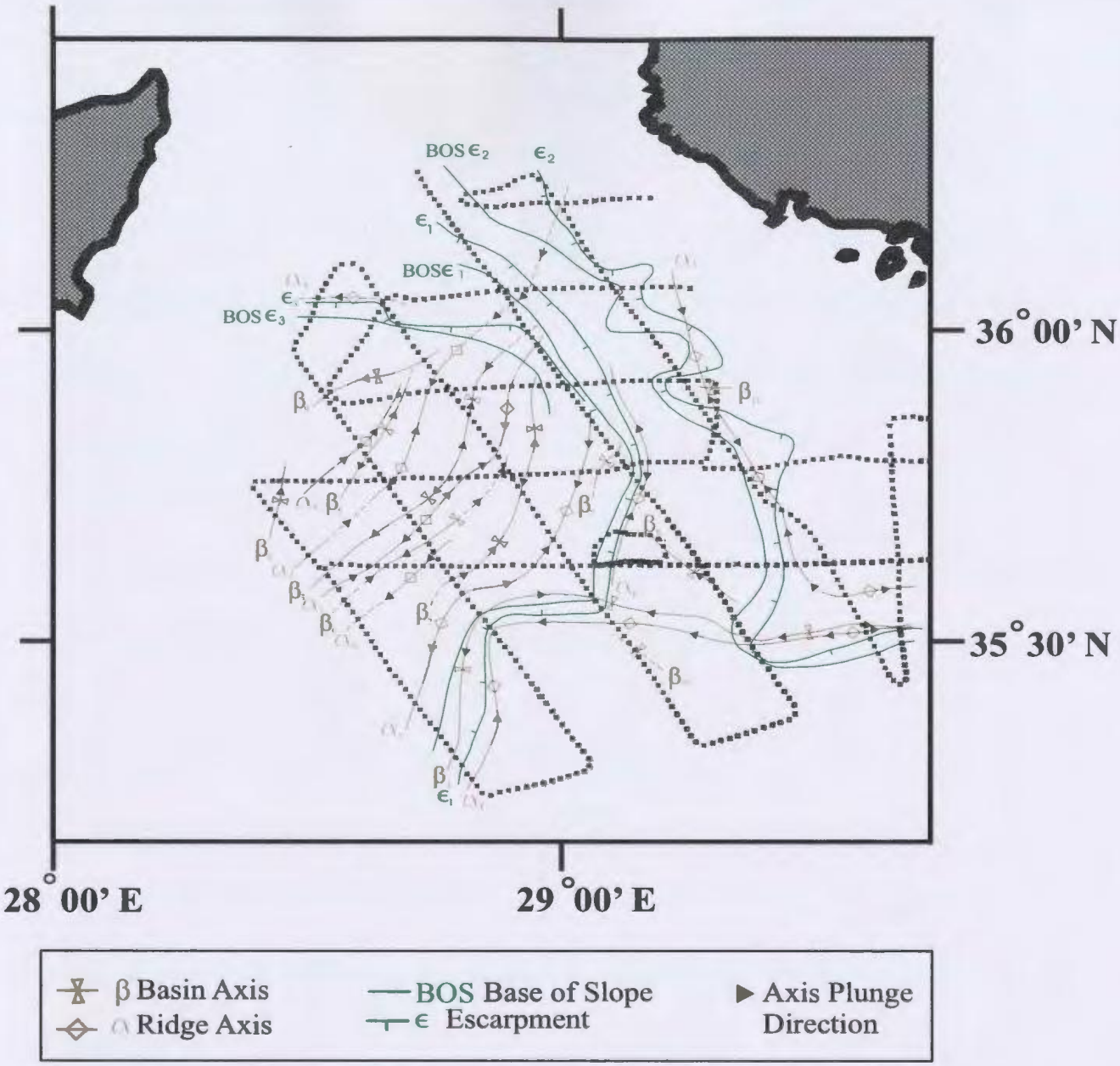

Figure 3.2.1: Map of the survey area showing the correlation of major structural features.

3.2.1: Basins

The basins identified in the study area can be grouped into three Families based on their axial trends. Basin Family 1 comprises the vast majority of the basins and is characterized by a dominant northeast-southwest trend through the centre of the survey area that is commonly diverted along a S-shaped trajectory (Fig. 3.2.1). Basin Family 1 consists of the short, western leg of basin β_1 and basins β_2, β_3, β_4, β_5, β_6, β_7 and β_9. The long, eastern leg of basin β_1 represents an east-west basin trend that comprises Basin Family 2. A third, northwest-southeast basin trend includes basins β_8 and β_{10} (Basin Family 3). Because basin β_{11} is only cut once by the survey grid, its trend orientation (and hence family designation) cannot be confidently determined.

Basin β_1:

Basin β_1 is a prominent depocentre located at the base of escarpment ϵ_1 in the southern portion of the study area. It reaches up to 16 km wide and contains as much as ~1500 ms of Pliocene-Quaternary succession that dips ~3°NW and generally consists of subunits 2a through to $2b_3$. Its long east-west-trending eastern segment and a shorter north-south-trending western segment meet at a near orthogonal junction in the western portion of the study area (Fig. 3.2.1).

In the southwestern extremity of the study area, basin β_1 is ~16 km wide and contains a maximum thickness of ~780 ms of Unit 2 succession that dips ~0.5°NW (Fig. 3.2.2a). Below the basin axis, Unit 1 illustrates a folded fabric that is truncated at the M

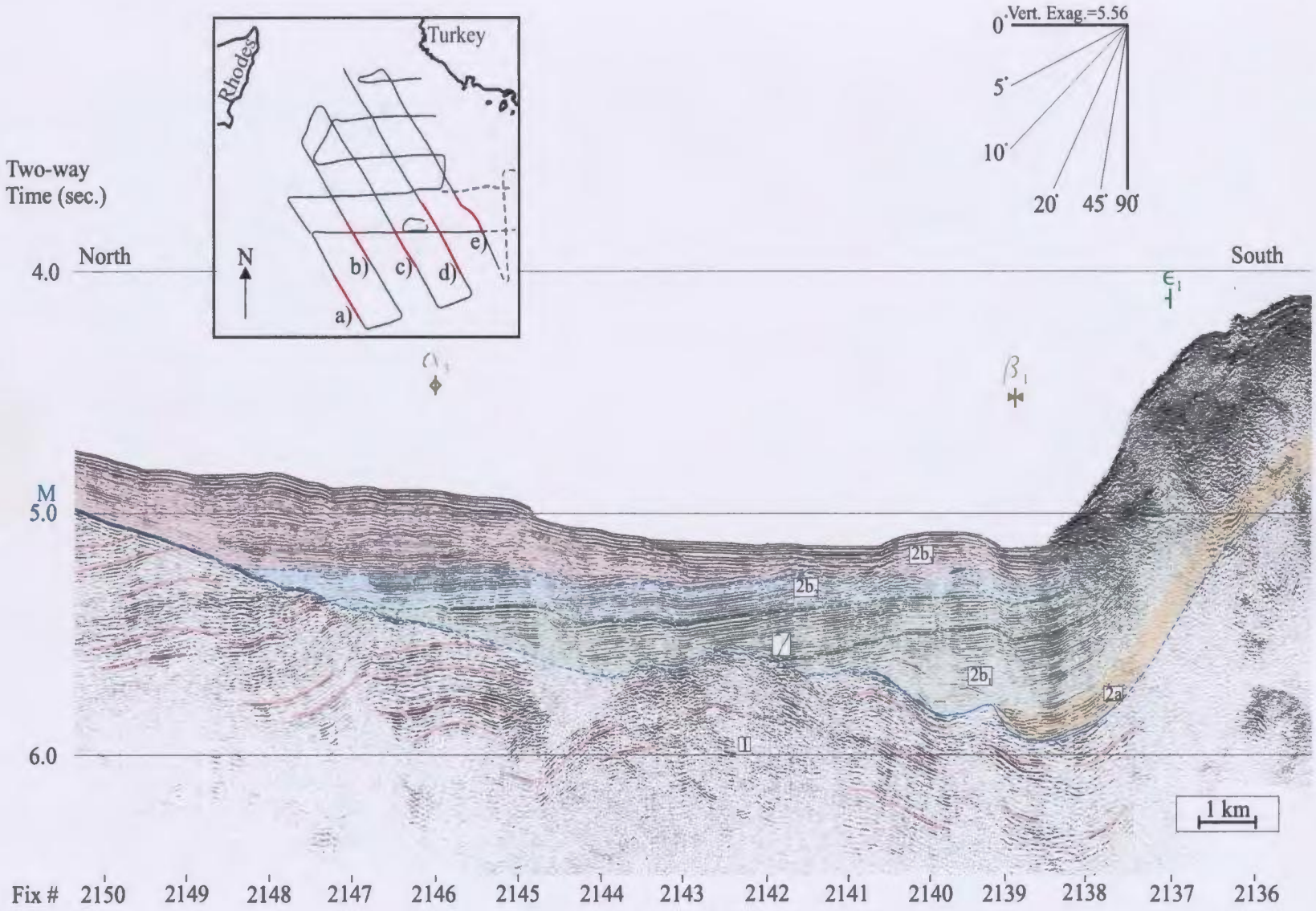

a)

Figure 3.2.2: The correlation of ϵ_1 and β_1 across a) Line 70, b) Line 68, c) Line 64 and d) Line 64a can be made with a high degree of confidence.Pink highlights basement fabrics.

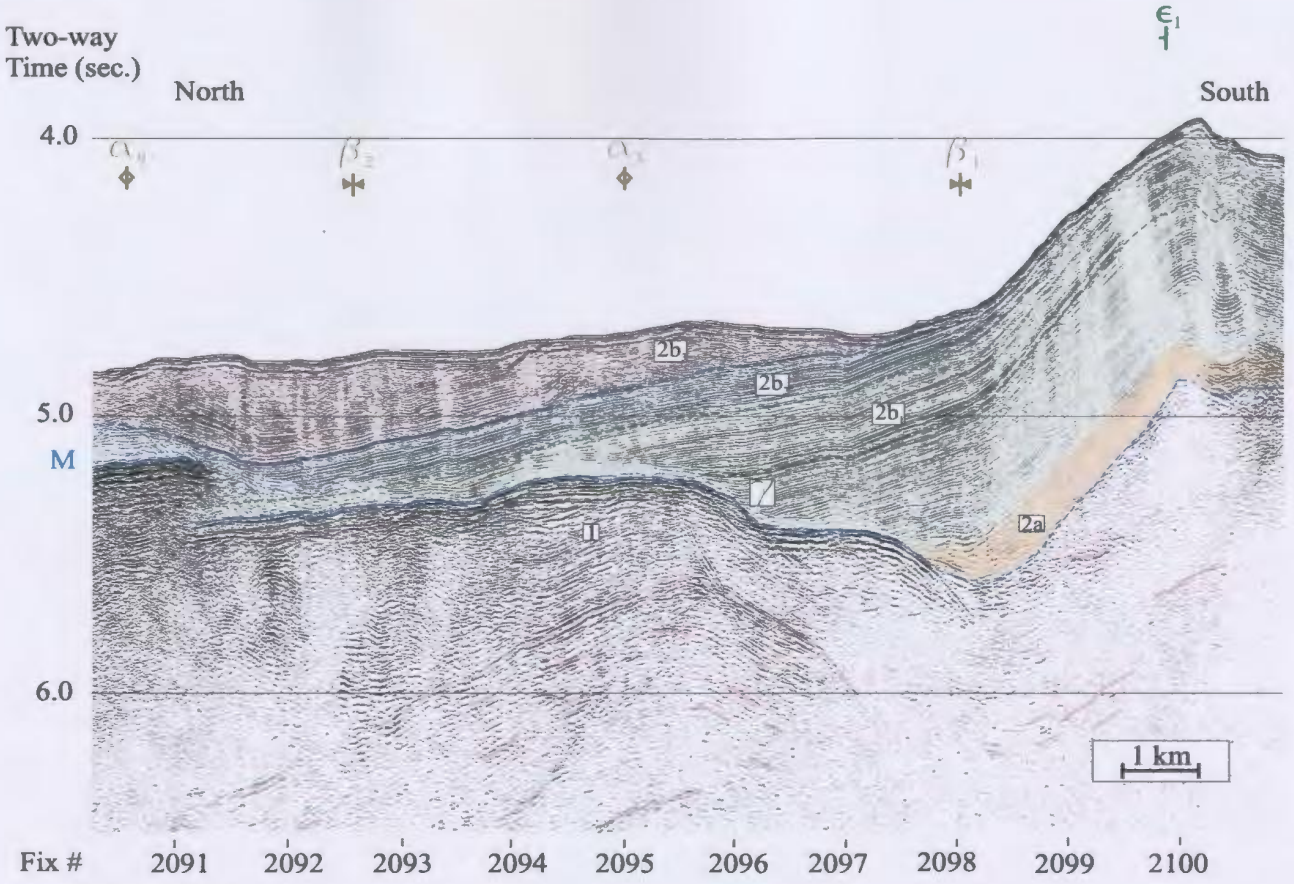

Figure 3.2.2b)

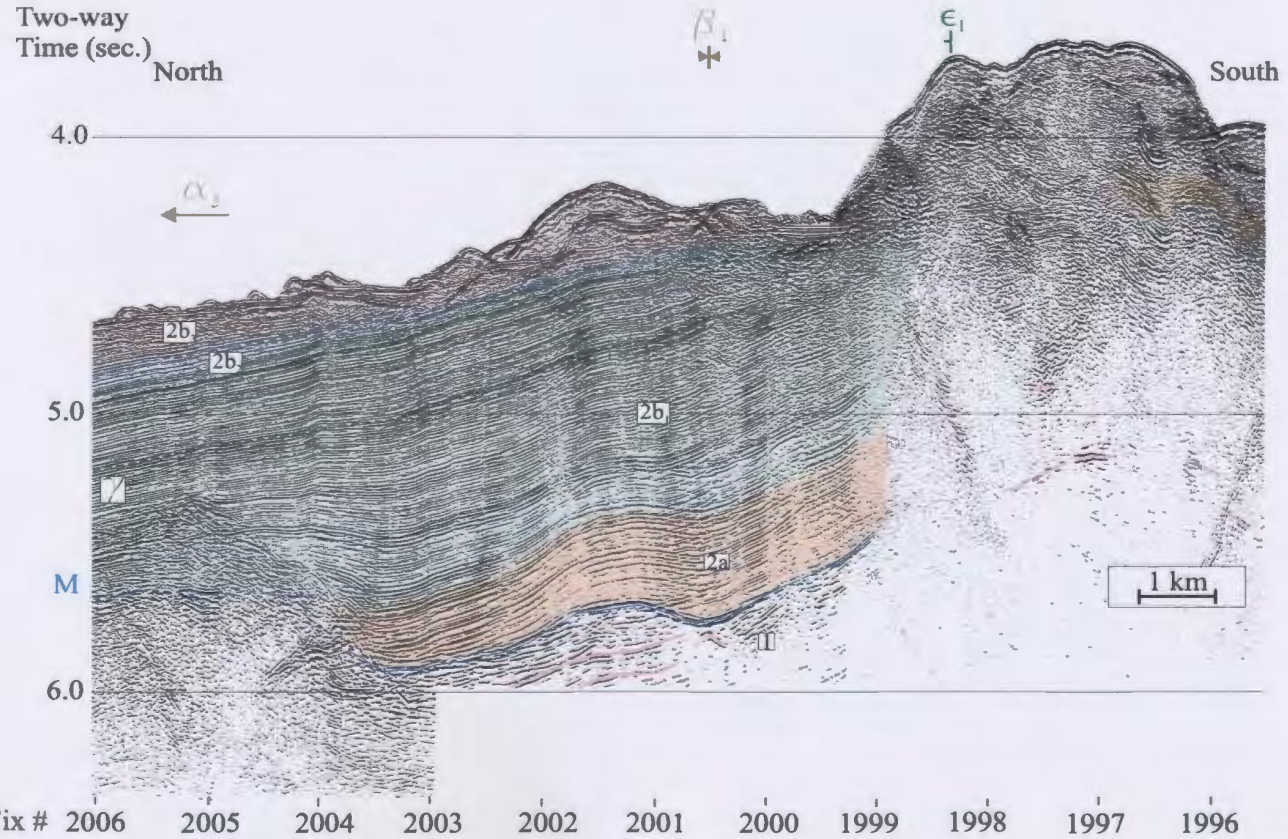

Figure 3.2.2c)

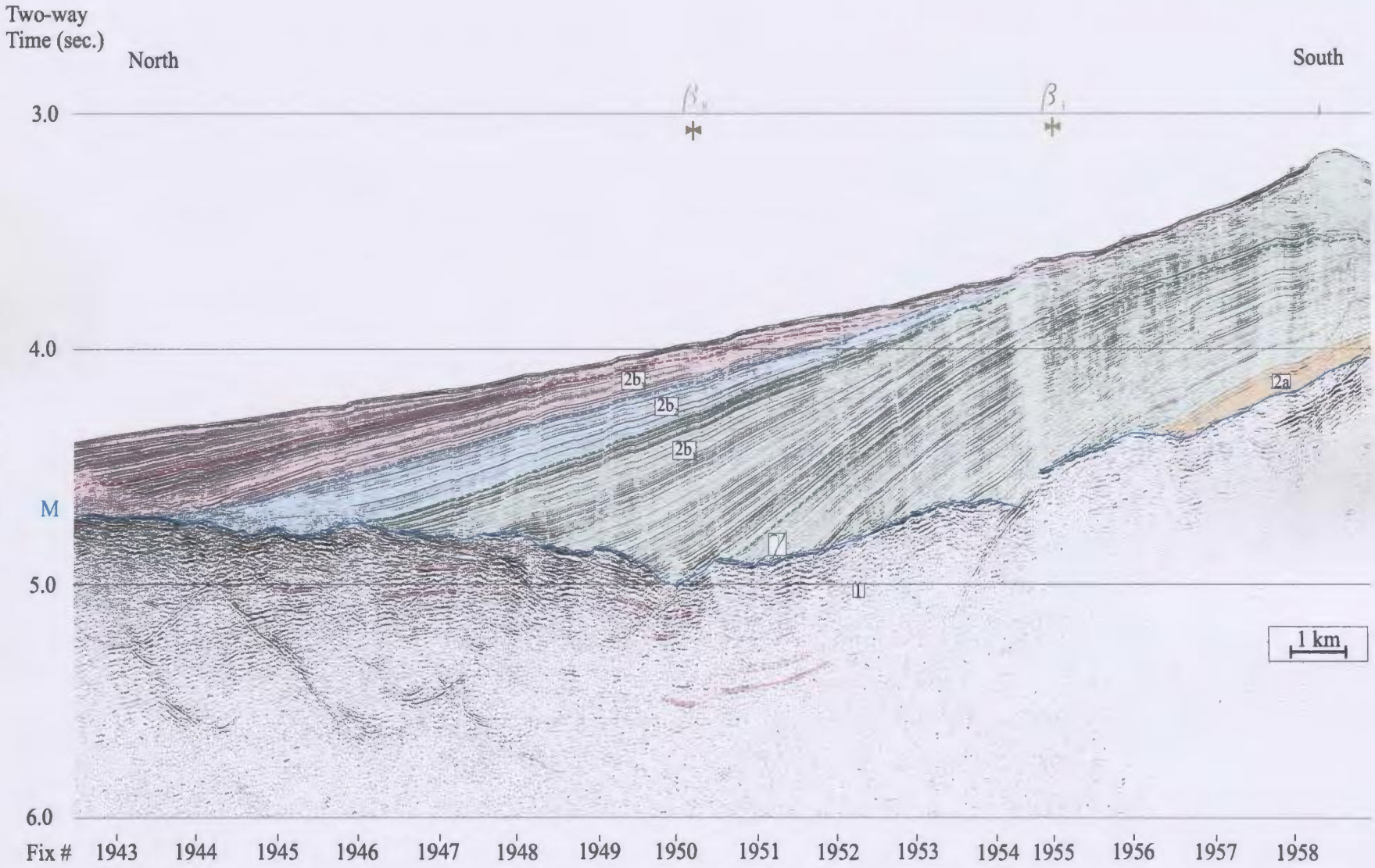
Two-way
Time (sec.)
North
South
3.0
4.0
5.0
6.0
M
2b
2b
2b
2a
1 km
Fix #
1943
1944
1945
1946
1947
1948
1949
1950
1951
1952
1953
1954
1955
1956
1957
1958

Figure 3.2.2d)

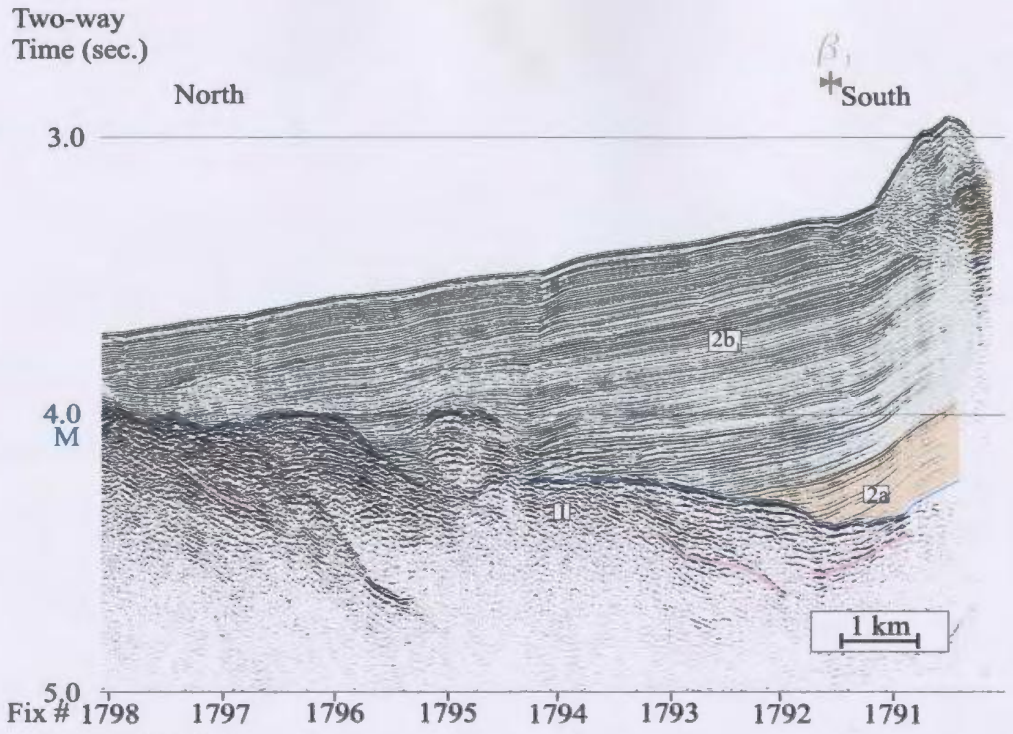
Two-way
Time (sec.)
North
South
3.0
4.0
M
5.0
2b
2a
1
1 km
Fix # 1798
1797
1796
1795
1794
1793
1792
1791

Figure 3.2.2e)

reflector, forming an angular unconformity. Although not imaged well underneath the escarpment, the M reflector shows an ~1420 ms vertical separation from its location at the top of the slope to the base of basin β_1. The steep, southern basin slope is covered by a discontinuous and poorly imaged Pliocene-Quaternary package. At the base of the southern slope these strata curve upward to the south, parallel with the M reflector. This package, including its disturbed section overlying the southern margin, is interpreted to contain mostly subunits 2a and $2b_1$. Progression northward through the basin yields more familiar characteristics of Subunit 2b such as parallel, continuous and well bedded reflectors. Subunits 2a-$2b_3$ onlap against the M reflector along the basins northern, gently southward dipping margin. Steeply inclined minor discontinuities populate the Pliocene-Quaternary sediments, especially those of Subunit $2b_3$ along the basin's northern margin (Fig. 3.2.2a).

To the northeast, basin β_1 is ~10 km wide and contains up to 1200 ms of ~2°NW-dipping Pliocene-Quaternary succession (Fig. 3.2.2b). Although generally poorly reflective, a synformal architecture within Unit 1 is centred below the basin axis and a corresponding antiformal structure is located beneath the northern margin of the basin with ridge α_9 and ridge α_3 (Fig. 3.2.2a,b). A 200 ms-thick drape of Subunit 2a conformably covers the M reflector as it descends by ~700 ms over the southern basin margin (escarpment ε_1), but it shows apparent onlap onto the M reflector immediately north of the basin axis (Fig. 3.2.2b). A thick package of Subunit $2b_1$ strata drapes over escarpment ε_1. A transition from this draping architecture to northward-directed

thickening and southward onlap is defined by a reflector identified as the γ reflector (Fig. 3.2.2b). The overlying Subunits $2b_2$-$2b_3$ demonstrate clear northward thickening via the divergence of their reflectors and internal onlap toward the south. These Subunit $2b_2$-$2b_3$ reflectors onlap onto Subunit $2b_1$ to the south and Unit 1 toward the north. However, due to the irregular morphology of the M reflector irregular, intervals of downlapping successions exist where the slope of the M reflector is near horizontal. Subunit $2b_3$ displays the most dramatic thickening (~0 ms to 440 ms-thick) and becomes increasingly segmented and discontinuous as it approaches ridge α_9 to the northwest.

Further to the east, basin β_1 is ~10.5 km wide and contains ~1500 ms of Unit 2 (Fig. 3.2.2c). Although poorly imaged itself, the M reflector is clearly delineated by the truncation of ~3°NW-dipping Unit 1 reflectors. Along the central portion of the basin, the M reflector and the overlying subunits 2a and 2b are gently folded and truncated to the south below the escarpment ϵ_1 where the M reflector is offset by ~1500 ms. These undulations are gradually reduced up section from Subunit 2a through Subunits $2b_1$-$2b_3$. Subunit 2a forms an ~280 ms-thick package that generally dips ~3°NW and onlaps onto the M reflector near the northern margin of the basin. The thick (~1000 ms), overlying Subunit 2b succession extends across the northern margin of basin β_1 where it onlaps onto the flank of ridge α_3. These Subunit 2b sediments are affected by several minor, steeply dipping (>60°) discontinuities. The majority of the Subunit 2b thickness is contributed by a relatively isopachous Subunit $2b_1$. The remaining portion is contributed by Subunits $2b_2$ and $2b_3$ as they thicken toward the north dominantly by the divergence of

their reflectors.

The size and east-west trend of basin β_1 suggests that it would continue into the southeastern portion of the Rhodes Basin. However, basin β_1 is not clearly observed as a discrete basin separate from β_8 at this locality (Fig. 3.2.2d). However, the isochron map (Fig. 3.1.4) suggests that basin β_1 may comprise the southern extremity of basin β_8 where it is characterized by an ~150 ms-thick Subunit 2a package and the dominance of the sub-γ reflector, relatively isopachous Subunit $2b_1$ reflectors (~ 450-620 ms thick) that strongly downlap onto the M reflector marks the transition from parallel stratigraphy to southward onlap of Subunits $2b_2$ and $2b_3$ (Fig. 3.2.2d).

At its easternmost point, basin β_1 is only ~ 4.5 km wide. Here, the M reflector is a clearly imaged, high amplitude reflection that separates the unreflective Unit 1 from the overlying ~2.5°NW-dipping Unit 2 reflectors that fill the basin. These Unit 2 reflectors are vertically truncated to the south against Unit 1 along the flank of ridge α_3 (Fig. 3.2.2e). At the base of this Unit 2 package, an ~220ms-thick package of Subunit 2a dips steeply at ~7° NW. These Subunit 2a reflectors genearlly downlap onto the M reflector along the flank of ridge α_5. A transition from downlap to onlap is made approximately midway through Unit 2a and defines a northward transition to a more shallowly dipping (~3°NW) ~970 ms-thick package of Subunit $2b_1$.

Basin β_2:

Basin β_2 is a major depocentre (7-11 km wide, >880 ms of Unit 2 succession)

located between ridge α_3 to its southeast and ridge α_2 to its northwest. Its basin axis trends northeast-southwest and plunges toward the northeast (Figs. 3.2.1, 3.2.3). The underlying Unit 1 reflectors often show a folded fabric that forms an angular unconformity with the M reflector. Comparison of east-west versus northwest-south east oriented survey lines suggests that the basin fill thickens toward the northwest and dips at ~2-3°NW.

In the central portion of the survey area, basin β_2 is ~8 km wide and contains a maximum thickness of 880 ms of Unit 2 (Fig. 3.2.3a). The M reflector has an irregular topography that truncates the relatively flat-lying reflectors of Unit 1. Subunits $2b_1$-$2b_3$ lie sub-horizontally and onlap the M reflector toward both the east and west, eventually overstepping it to the east to become continuous with basin β_7, but terminating to the west by onlapping against the flank of ridge α_2. The eastern edge of basin β_2 contains the western extremity of a 13.5 km-wide lens-shaped package that reaches a maximum of 70 ms thick. The scattering internal character of this lens and its shallow depth suggest that it is correlatable with the scattering lens found to the southwest (Figs. 3.2.3a,b).

Immediately to the southwest, β_2 widens to ~11 km and contains a maximum of 1020 ms of Unit 2 (Fig. 3.2.3b). Unit 1 reflectors have a synformal architecture in the southern and northern portions of the basin with an antiformal architecture near the basin centre. Here also, this Unit 1 fabric is truncated by the M reflector to form an angular unconformity. Subunit 2a dips ~3-4°NW and onlaps onto the M reflector toward both the north and south. It maintains a nearly constant thickness of ~200 ms along the base of the

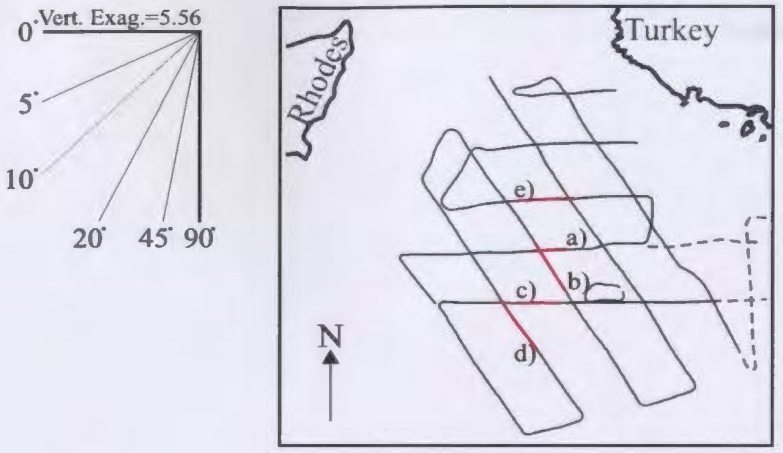

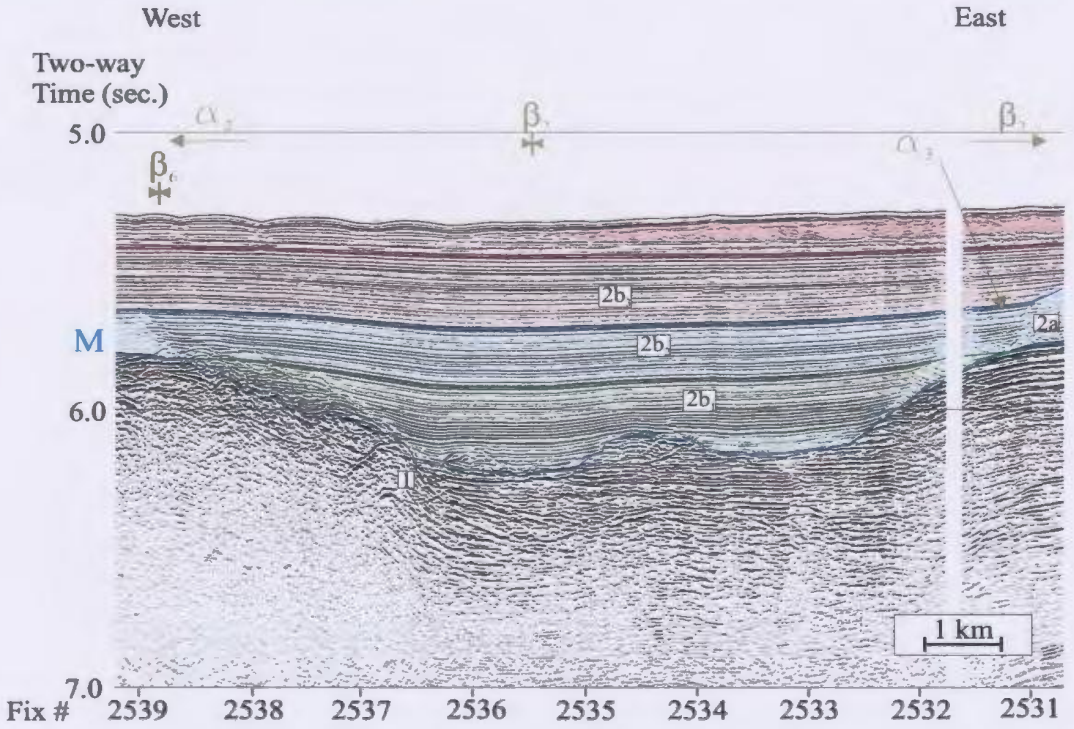

a)

Figure 3.2.3: Basin β_2 is seen to cross a) line 80, b) line 64, c) line 70a, d) line 68 and e) line 81 along its northeast-southwest trend.

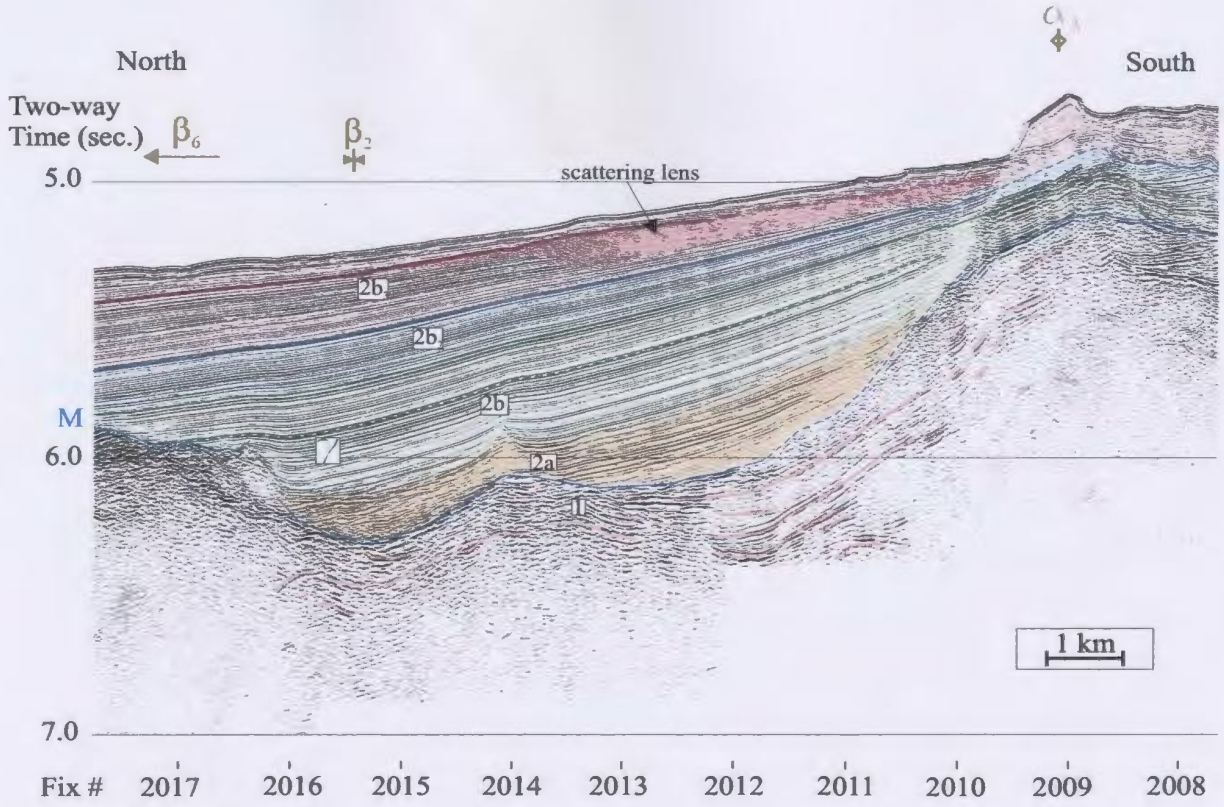

Figure 3.2.3b)

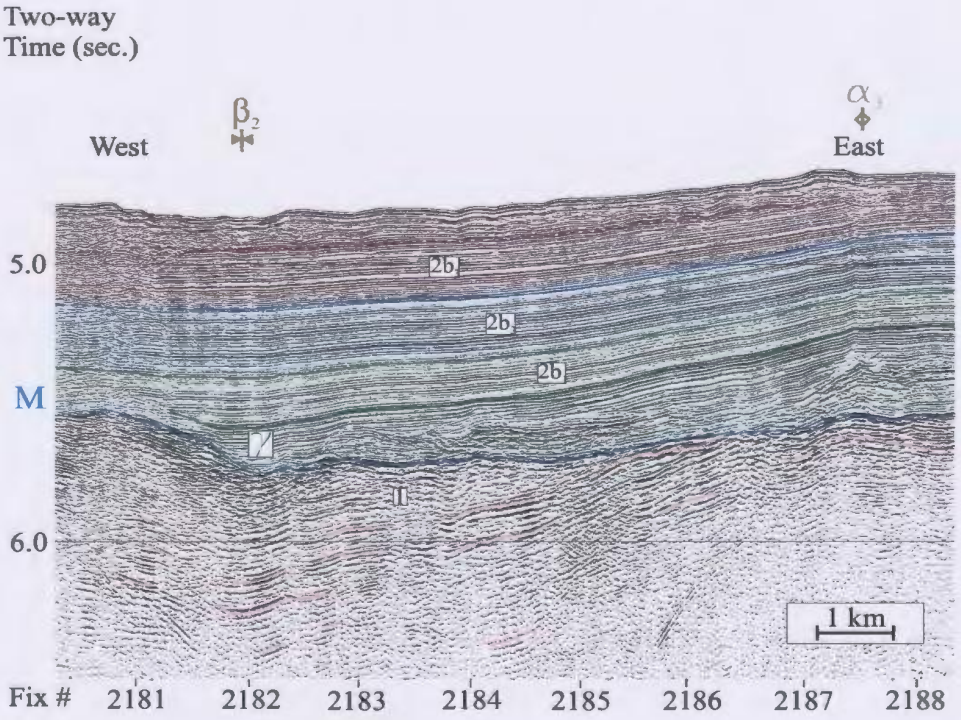

Figure 3.2.3c)

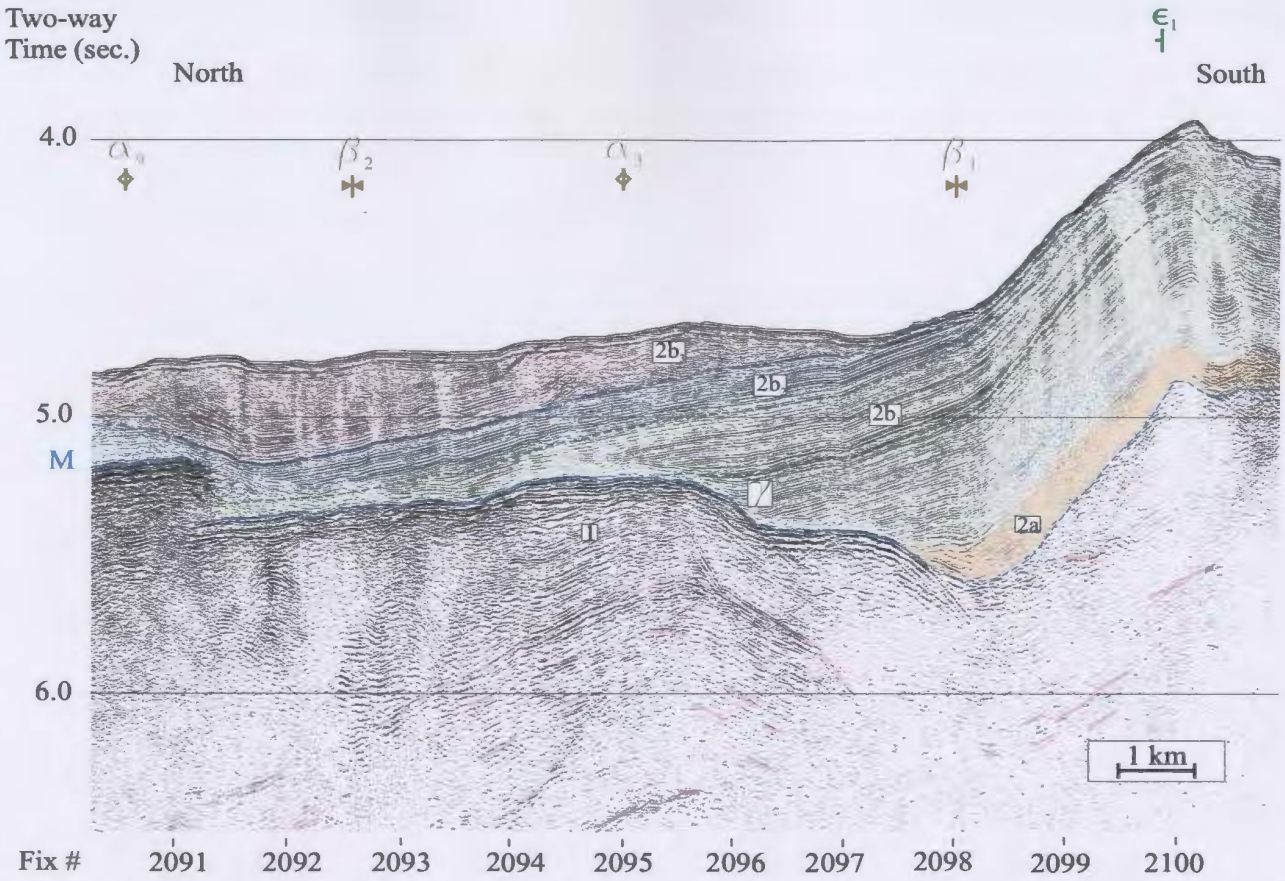

Figure 3.2.3d)

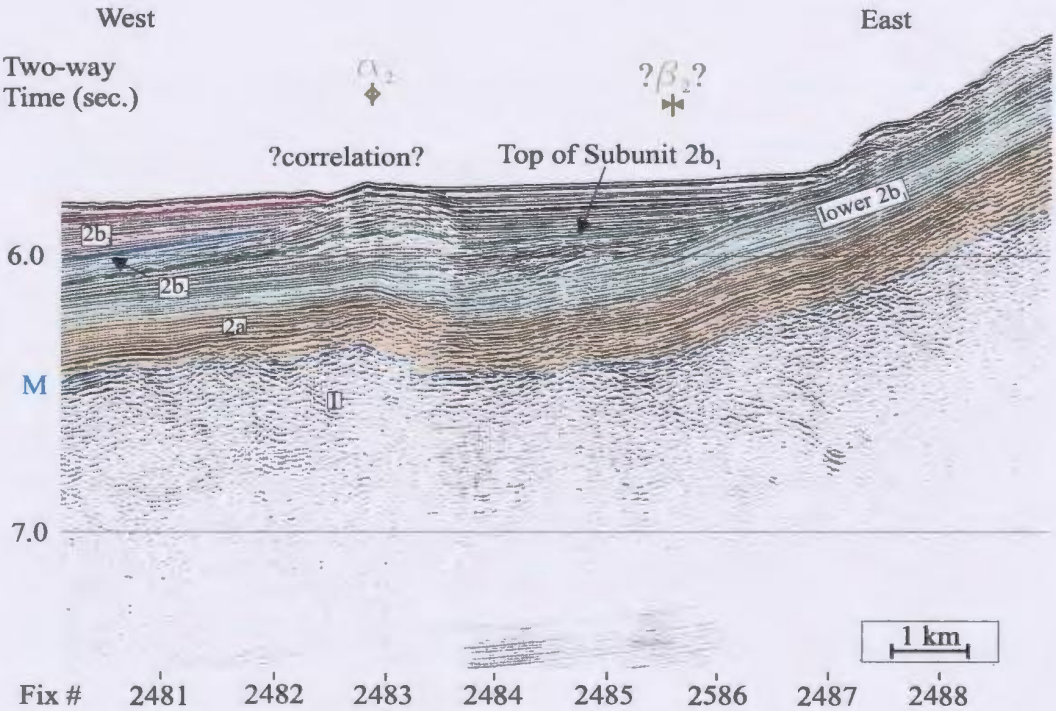

Figure 3.2.3e)

basin, except where it thins over the central, small antiformal feature (Fig. 3.2.3b). Although generally coherent in character, the northern portion of Subunit 2a shows minor internal discontinuity (Fig. 3.2.3b). Subunit 2b lies in apparent conformity with Subunit 2a. The dip magnitude of the Subunit $2b_1$-$2b_3$ succession decreases up section from ~4°NW to ~1.5°NW as a result of its northward-thickening by the northward divergence of its reflectors and weak internal onlap toward the south. Subunit $2b_1$ thickens from ~130 ms-thick in the south where it covers the crest of ridge α_3 to 360 ms-thick in the northwest where the it onlaps onto the M reflector (Fig. 3.2.3b). Subunits $2b_2$ and $2b_3$ also thicken toward the north from 70 ms to 190 ms and 80 ms to 310 ms, respectively. Both of these subunits also continue over the crest of ridge α_3 to the south and continue northward to onlap onto the flank of ridge α_2. Subunit $2b_3$ contains an asymmetric, northward thickening lens of scattering reflectors that forms a finger-like feature pointing down dip from its starting point at the southern extremity of the basin. This lens reaches a maximum thickness of ~100 ms and measures 7 km in length. Its base clearly cuts downward into the underlying Subunit $2b_3$ reflectors.

At its southernmost limit, basin β_2 measures ~6 km across and contains ~900 ms of well-bedded, parallel and continuous Subunit $2b_1$-$2b_3$ reflectors that onlap onto the M reflector toward both the west an east (Fig. 3.2.3c). Reflectors within Unit 1 clearly have an synformal fabric with 6°E-dipping and 5°W-dipping limbs (Fig. 3.2.3c). These westward-dipping Unit 1 reflectors are truncated to the east by the M reflector where they culminate to form the core of ridge α_3. Each of the Subunits $2b_1$-$2b_3$ (certainly Subunits

$2b_2$ and $2b_3$) demonstrate modest westward thickening by the divergence of their 0.5-1°W-dipping reflectors. Subunit $2b_1$ oversteps and buries the subdued relief of ridge α_3 to the east. The upper 140 ms of Subunit $2b_3$ is cut by closely spaced (~500 m), near vertical discontinuities that bound convex upward curved strata (Fig. 3.2.3c). A similar behaviour of the upper Subunit 2b reflectors is noticed a short distance to the southwest (Fig. 3.2.3d) where the Subunit $2b_2$ and especially Subunit $2b_3$ clearly illustrate northward thickening of its ~2.5°NW-dipping reflectors.

Extrapolation of basin β_2 northeast toward the base of the Turkish shelf is difficult. If present at this northern location, it is diminished in character and runs between the base of the Turkish shelf and is adjacent to ridge α_2 (Fig. 3.2.3e).

Basin β_3:

Basin β_3 is a large depocentre trending northeast-southwest through the centre of the Rhodes Basin between ridge α_2 to its southeast and ridge α_1 to its northwest (Figs. 3.2.1 and 3.2.4). It attains a maximum width of ~11 km and contains up to 850 ms of Unit 2. This Pliocene-Quaternary fill dips considerably steeper on the north northwest-south southeast oriented lines (~2-3°NW) relative to the east-west lines (~0.5-1°W), indicating that they dip in a dominantly northward direction with a minor western component (Fig. 3.2.4). Basin β_3 plunges both to the northeast and southwest from its most elevated and narrowest point in the central region of the survey area.

Near the northern limit of basin β_3, a deformed, discontinuous, weakly reflective

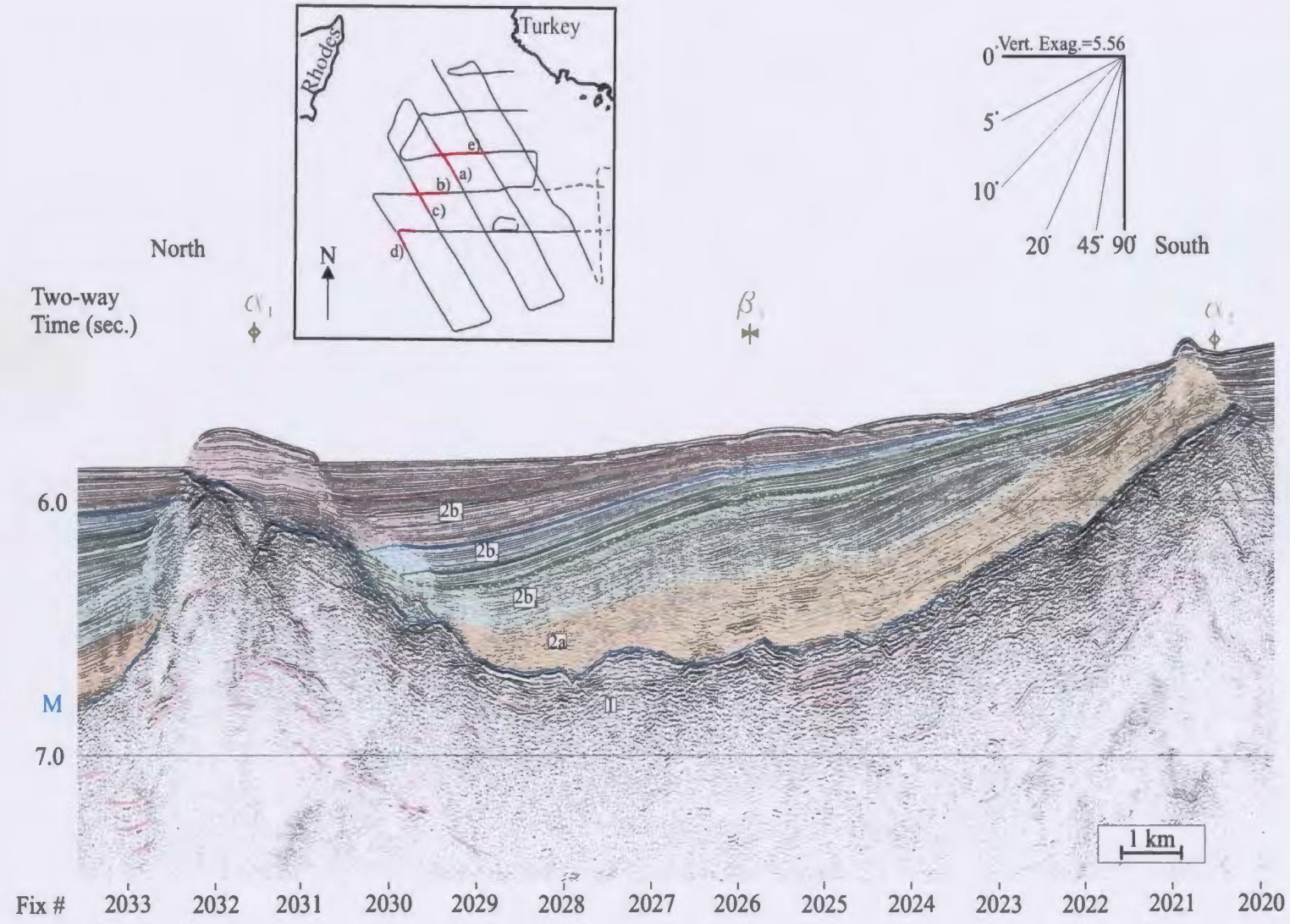

a)

Figure 3.2.4: Basin β_3 trends northeast-southwest across a) line 64, b) line 80, c) line 68, d) lines 70 and 70a and e) line 81.

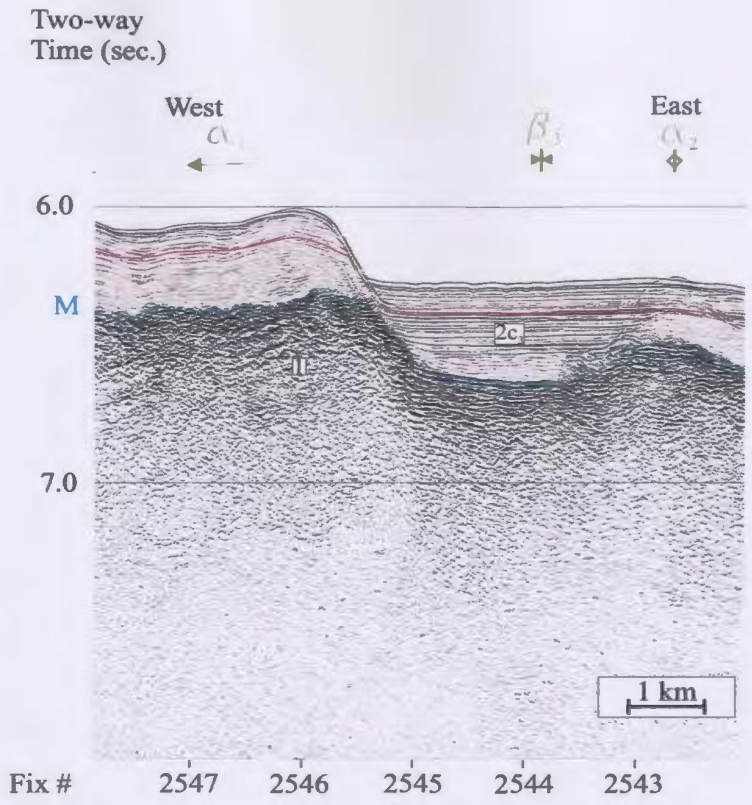

Figure 3.2.4b)

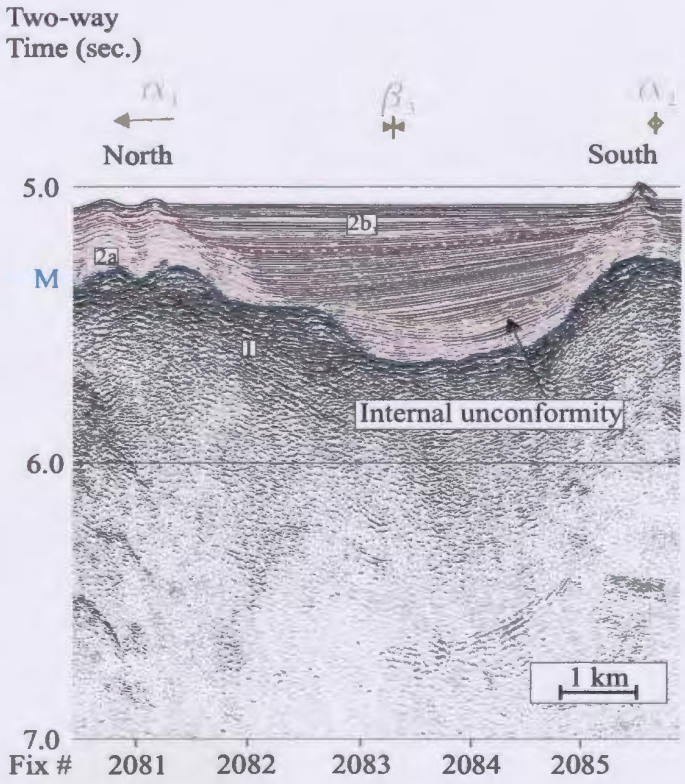

Figure 3.2.4c)

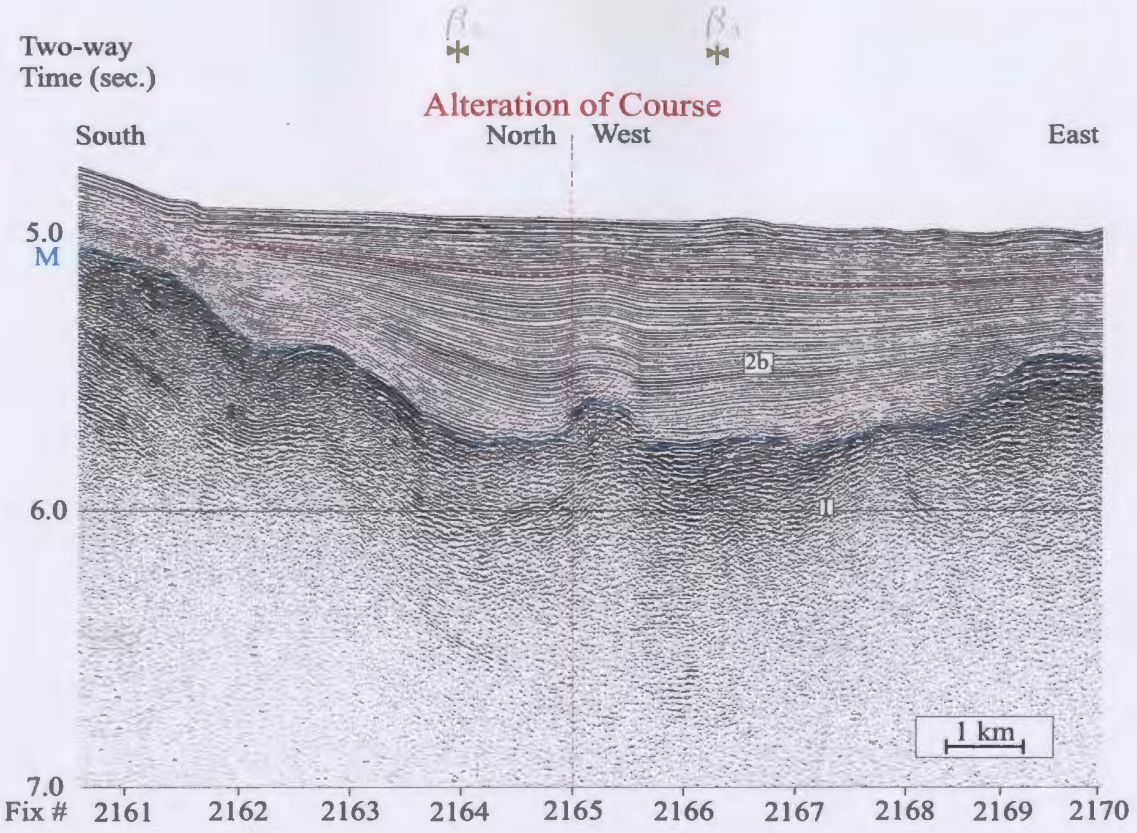
Two-way
Time (sec.)
Alteration of Course
South
North
West
East
5.0
M
6.0
7.0
2b
II
1 km
Fix #
2161
2162
2163
2164
2165
2166
2167
2168
2169
2170

Figure 3.2.4d)

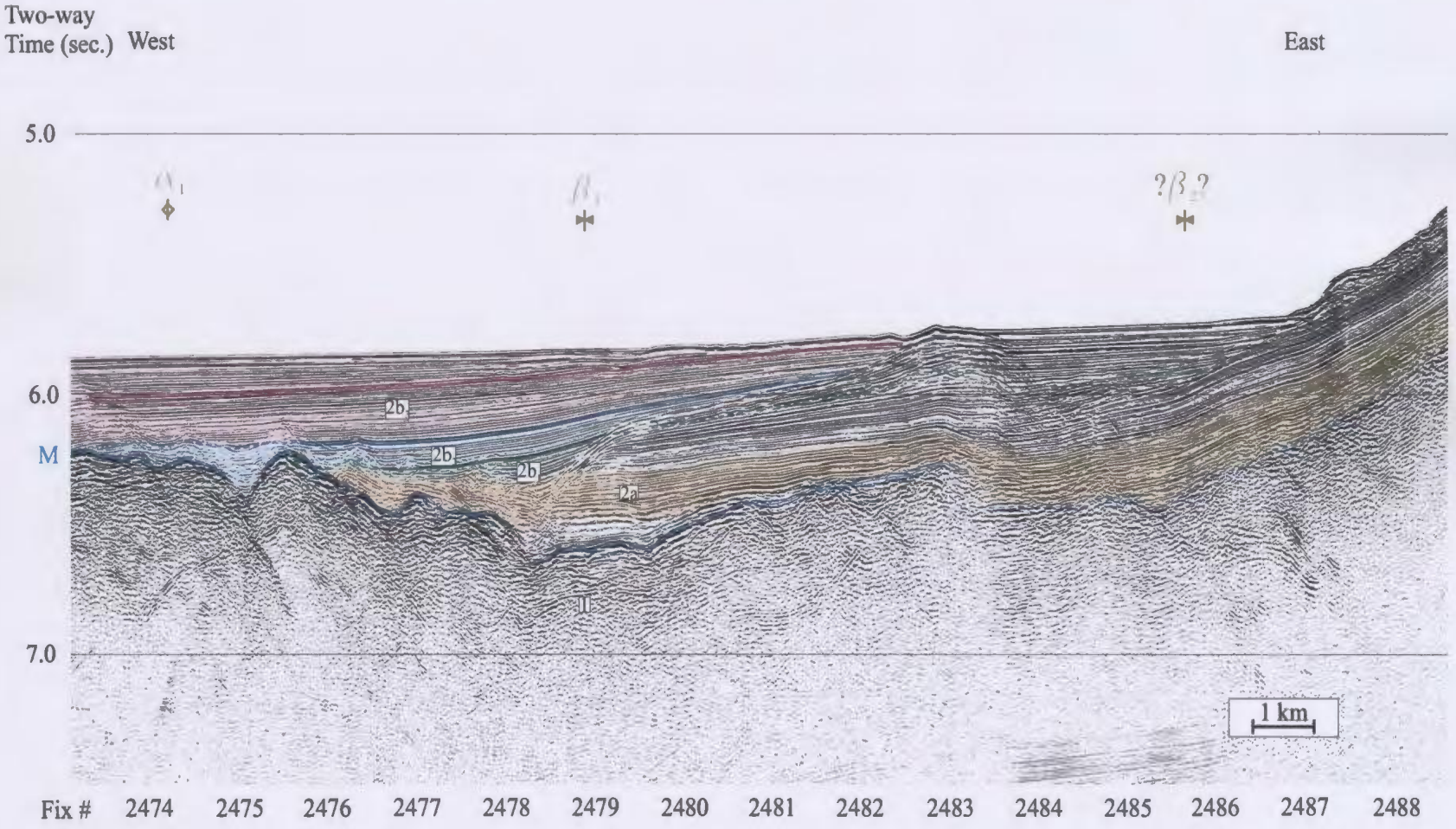
Two-way
Time (sec.)
West
East
5.0
6.0
7.0
M
2b
2b
2b
2a
1
1 km
Fix #
2474
2475
2476
2477
2478
2479
2480
2481
2482
2483
2484
2485
2486
2487
2488

Figure 3.2.4e)

Subunit 2a package forms a 250 ms-thick drape over the ~5° NW-dipping M reflector that defines the margin of basin β_3 with ridge α_2 (Fig. 3.2.4a) but pinches out against the ~8°SE dipping margin of basin β_3 with ridge α_1 to the north. Subunit $2b_1$ onlaps onto Subunit 2a toward the south. Its lower portion demonstrates agressive thickening toward the basin centre from the south via the divergence of its reflectors and the insertion of internal onlapping packages and scattering lenses. The largest of the lenses included in this package measures ~10 km long and attains a maximum thickness of 70 ms before pinching out toward both the north and south. Above this large lens, the upper portion of Subunit $2b_1$ is internally conformable but thickens gently toward the north via the divergence of its reflectors (Fig. 3.2.4a). Although reflectors in these Subunits near the central portion of basin β_3 are discontinuous and poorly imaged, the more steeply dipping lower Subunit $2b_1$ reflectors appear to downlap onto the surface of Subunit 2a. Subunits $2b_2$ and $2b_3$ also onlap against the underlying Subunit 2a along the basin margins and dip ~2.5-4°NW. Each of Subunits $2b_2$ and $2b_3$ thicken considerably toward the northwest due to the divergence of their reflectors and minor onlap in the southern portion of the basin; reaching maximum thicknesses of 100 ms and 360 ms respectively. The successive increase in the amount of north-directed stratal wedging from the upper portion of Subunit $2b_1$ through to Subunit $2b_3$ results in the successive decrease of the dip magnitudes up the section (Fig. 3.2.4a).

Only ~11 km to the southwest, basin β_3 is a small, 2.5 km-wide depocentre with ~340 ms of Subunit $2b_3$. Its western margin is marked by an abrupt termination against its

discontinuous margin with ridge α_1 (Fig. 3.2.4b). Although the east-west-oriented section (Fig. 3.2.4b) suggests that the Pliocene-Quaternary package is internally conformable, a nearby northeast-southwest-trending line illustrates definite northward-directed growth and internal onlapping unconformities toward its southern end (Fig. 3.2.4c).

At its southwestern extremity, basin β_3 contains ~800 ms of $2b_3$ (Fig. 3.2.4d). Because of its proximity to a turning point of the survey line, the western margin of basin β_3 is not observed and therefore the width of the basin at this location is unknown. A discrepancy between the apparent dips and degree of thickening of Subunit $2b_3$ on the east-west portion of the line (dip ~1°W, modest westward thickening) and the northwest-southeast-oriented portion of the line (dip ~3°NW, considerable northwestward thickening) reinforces that there is a dominant northward dip and thickening directionality to the Pliocene-Quaternary succession. In each case, the dip of the reflectors decreases to near horizontal up section due to the northward thickening of the package via the divergence of its reflectors. A convex upward curvature of Subunit $2b_3$ reflectors is present over a minor basement high near the centre of the basin. The amplitude of this undulation decreases up section and correlates with an uplifted portion of Unit 1.

The trend and large size of basin β_3 in the centre of the study area suggests that it is likely to continue northeast toward the Turkish slope (Figs. 3.2.1, 3.2.4e). Following its established trend, basin β_3 is correlated with a 4 km-wide basin to the northeast. Toward the east end of basin β_3 at this locality, stratigraphic correlations become speculative. However, it is established that basin β_3 contains Subunits 2a-$2b_3$ and that the Subunit 2b

succession dips and thickens toward the west.

Basin β_4:

Basin β_4 is a northeast-southwest trending depocentre that is ~8 km wide and contains ~680 ms of Subunit $2b_3$. Along its southern margin (flank of ridge α_1), reflectors of Unit 1 show varying dip magnitudes from 0°-4°NW and are cut by ~60°NW dipping discontinuities that vertically offset the M reflector by ~120 ms (Figs. 3.2.1 and 3.2.5). These dipping Unit 1 reflectors form an angular unconformity with the overlying M reflector. Elsewhere, Unit 1 shows little internal character. Subunit $2b_3$ onlaps onto the M reflector toward both the northwest and southeast but is internally conformable as it dips ~2° NW and thickens from ~200ms to ~620ms by the northward divergence of reflectors (Fig. 3.2.5). Here also, the amount of thickening increases with progression up the succession and the east-west profile shows a far gentler dip (~0.5°W) than the northwest-southeast-oriented line and very little thickening, implying that the dip and thickening direction has a strong northward component.

Basin β_5:

Basin β_5 is a narrow northeast-southwest-trending depocentre situated in the western portion of the study area, nestled between ridges α_1 and α_8 (Fig. 3.2.1, 3.2.6). Its basin axis plunges steeply both to the northeast and southwest from its central location.

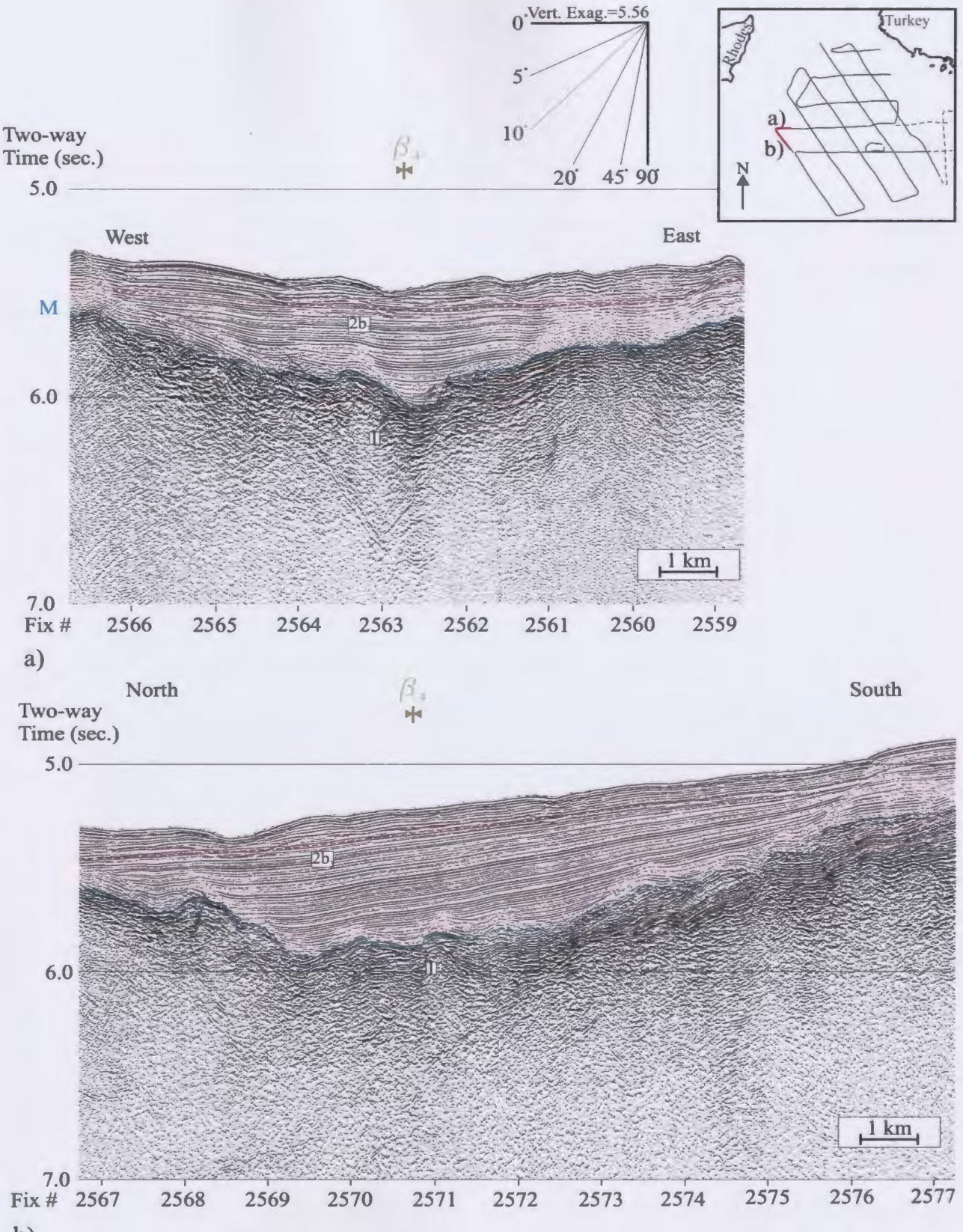

Figure 3.2.5: Basin β_4 crosses line 80 at two locations along its northeast-southwest trend.

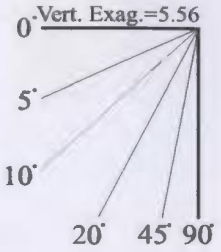

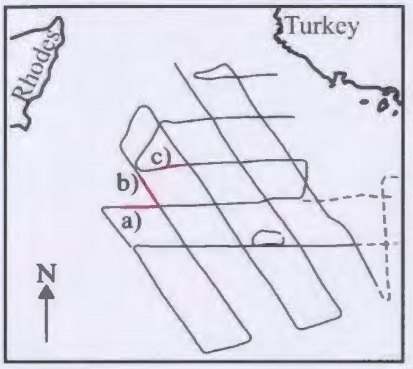

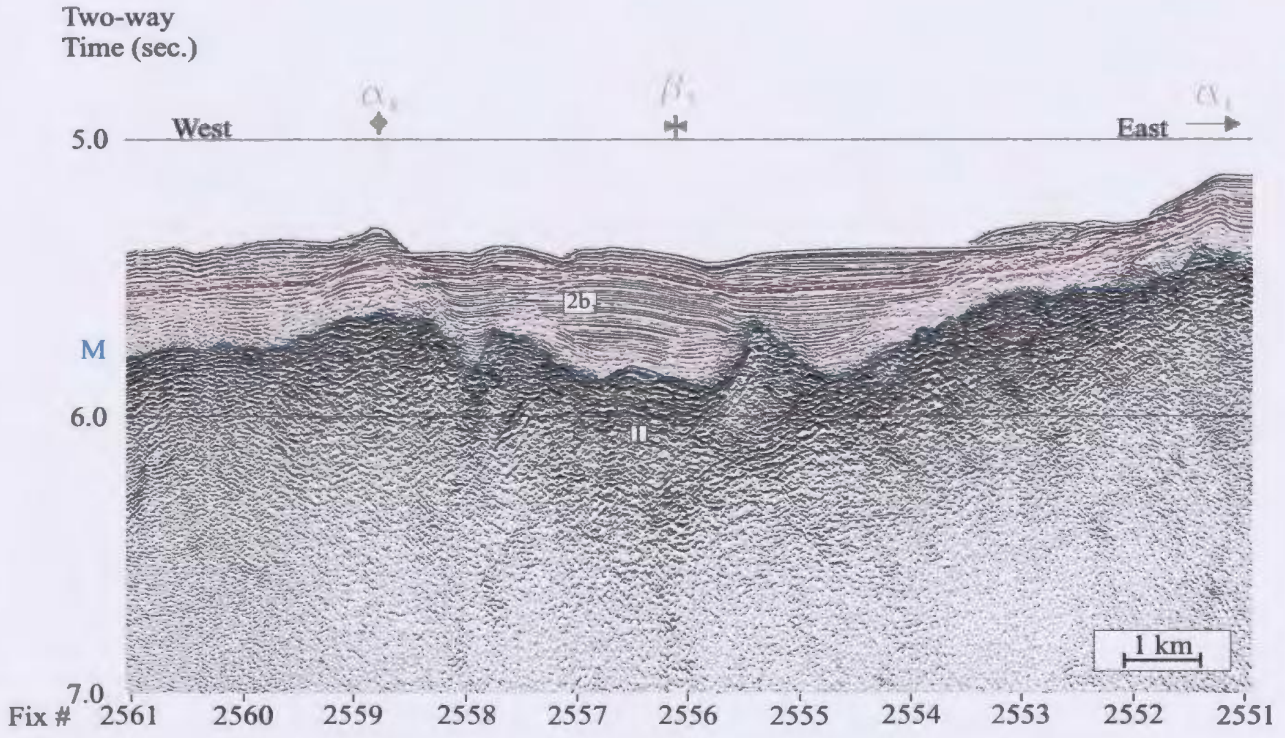

a)

Figure 3.2.6: Basin β_5 and ridge α_8 trend northeast-southwest across lines a) 80, b) 68 and c) 81.

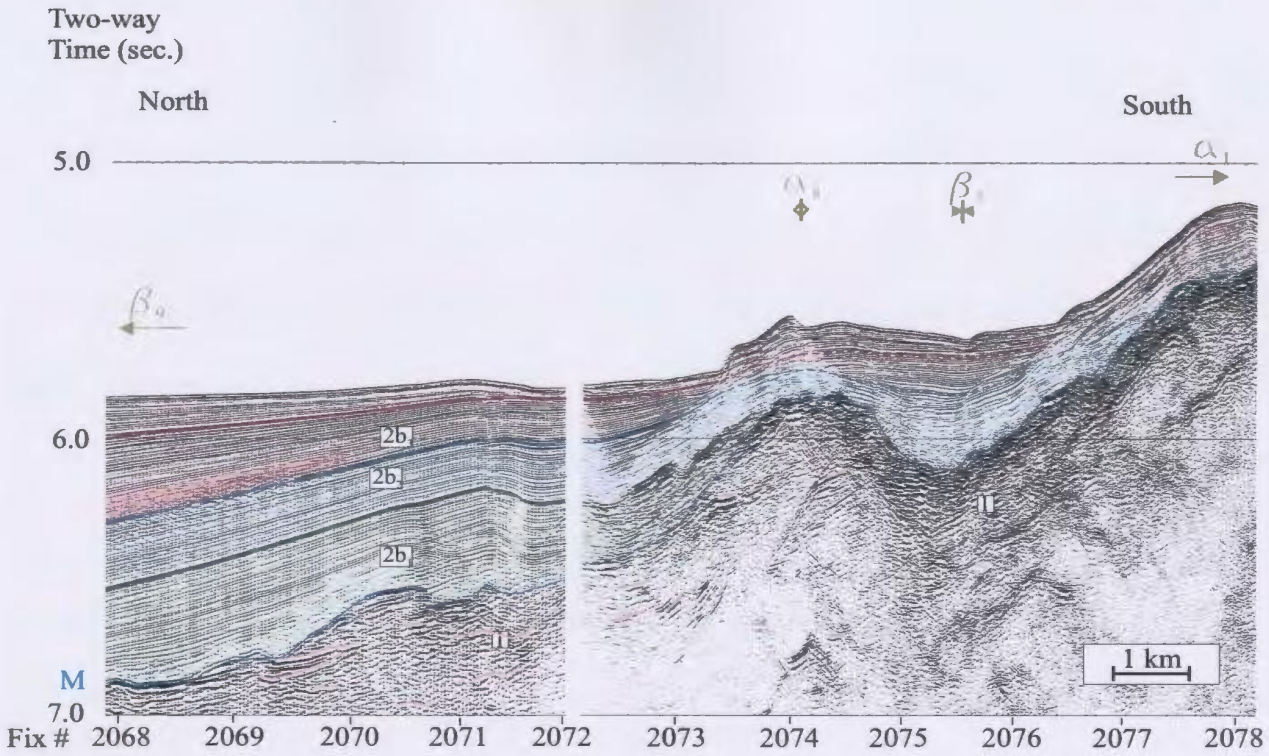

Figure 3.2.6b)

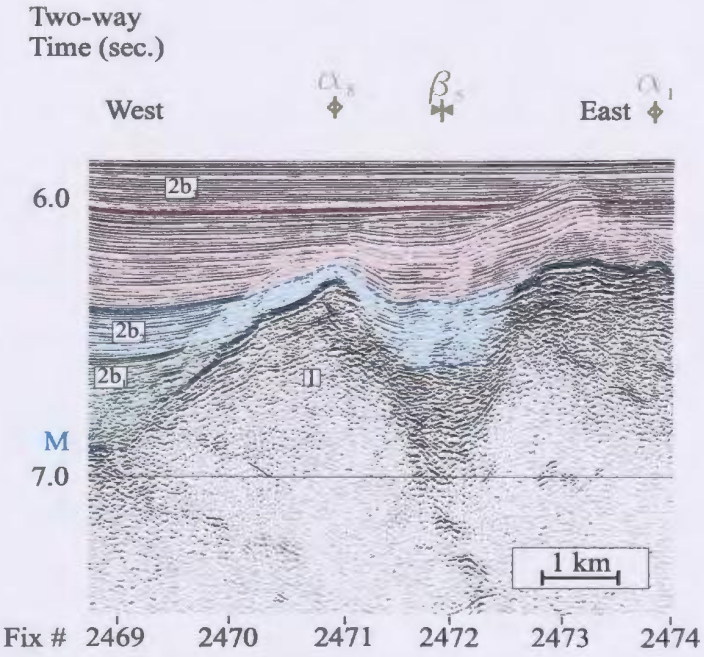

Figure 3.2.6c)

The poorly imaged contact relationship between the Subunit $2b_3$ basin-fill and the irregular morphology of the M reflector near the basin margins suggest that the lower portion of Subunit $2b_3$ onlaps onto the M reflector while the upper portion oversteps the basin flanks. This package thickens toward the basin centre from both margins where it achieves a maximum thickness of ~450 ms (Fig. 3.2.6). Toward the northeast, β_5 narrows successively from its 5 km width at its southwestern end to 3 km and 1.5 km wide toward the northeast. Its Pliocene-Quaternary fill correspondingly thickens to 480 ms and 750 ms respectively. The northwesternmost locality of basin β_5 demonstrates steeper, discontinuous basin margins that offset of the M reflector (Fig. 3.2.6c). A reasonably confident stratigraphic correlation of this site with that of the adjacent basin β_9 (discussed later) suggests that Subunit $2b_2$ lies at the base of the basin fill at these northernmost localities where it thickens symmetrically toward the basin centre (Fig. 3.2.6b,c). Further north, basin β_5 may merge with basin β_9 (Fig. 3.2.1).

Basin β_6:

Basin β_6 is an ~3.5 km-wide depocentre that trends northeast-southwest between ridges α_2 and α_9 in the western portion of the survey area. It contains up to 600 ms of Pliocene-Quaternary succession that dips 2-3°NW and thickens toward the northwest. Basin β_6 becomes continuous with basin β_2 at its northeastern extent where ridge α_9 no longer partitions the two as it does to the southwest.

Near its southwestern extremity (Fig. 3.3.7a), basin β_6 contains a 100ms-thick

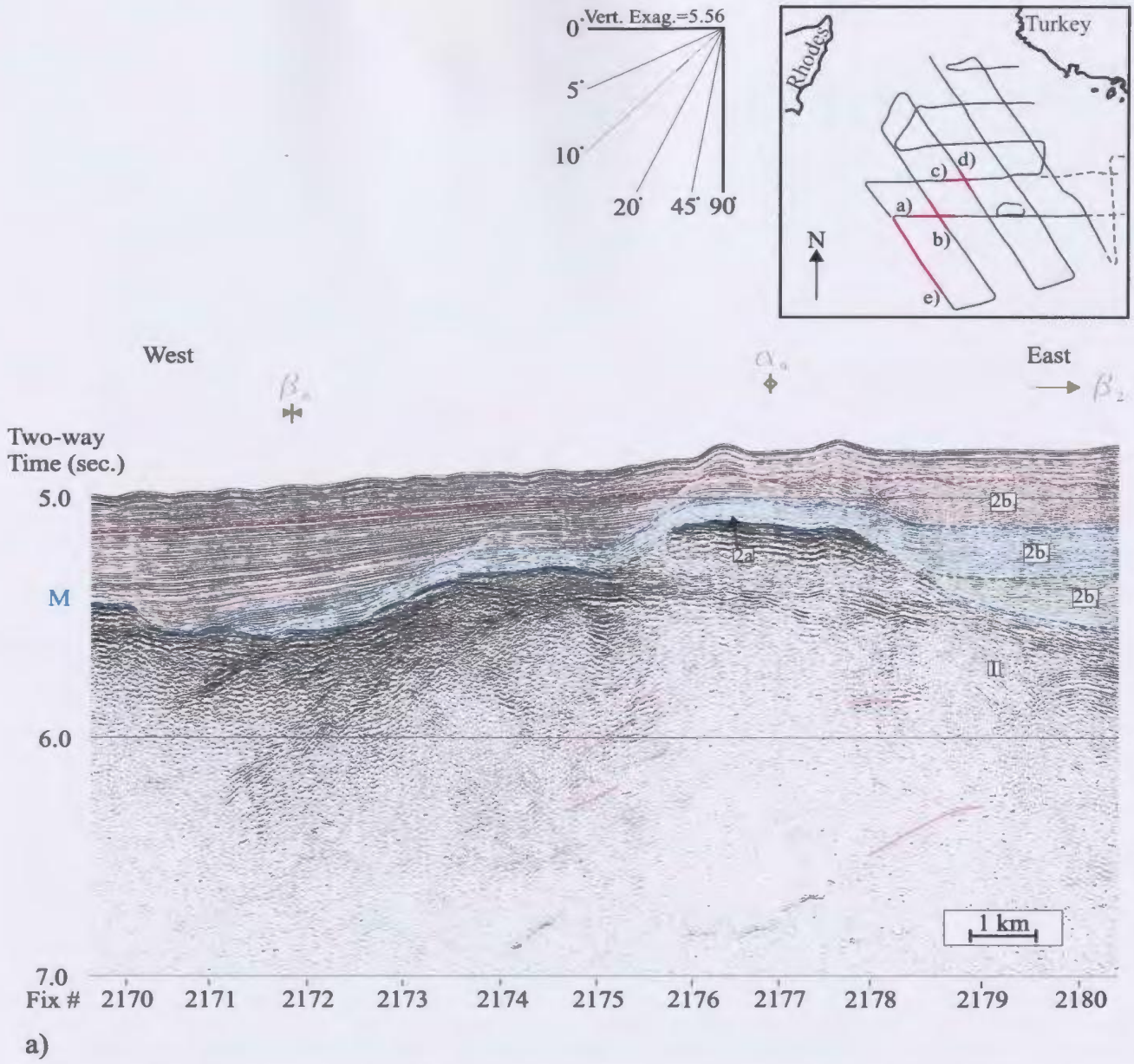

Figure 3.2.7: Basin β_6 and ridge α_9 run northeast-southwest across Zone 3. While both structures are well developed at their intersections with a) line 70a and b) line 68, only basin β_6 is correlated further northeast where it intersects with c) line 80 and d) line 64. Toward the southwest (d) line 70), basin β_6 is attenuated but interpreted to be perched on the northern limb of the very broad ridge α_9.

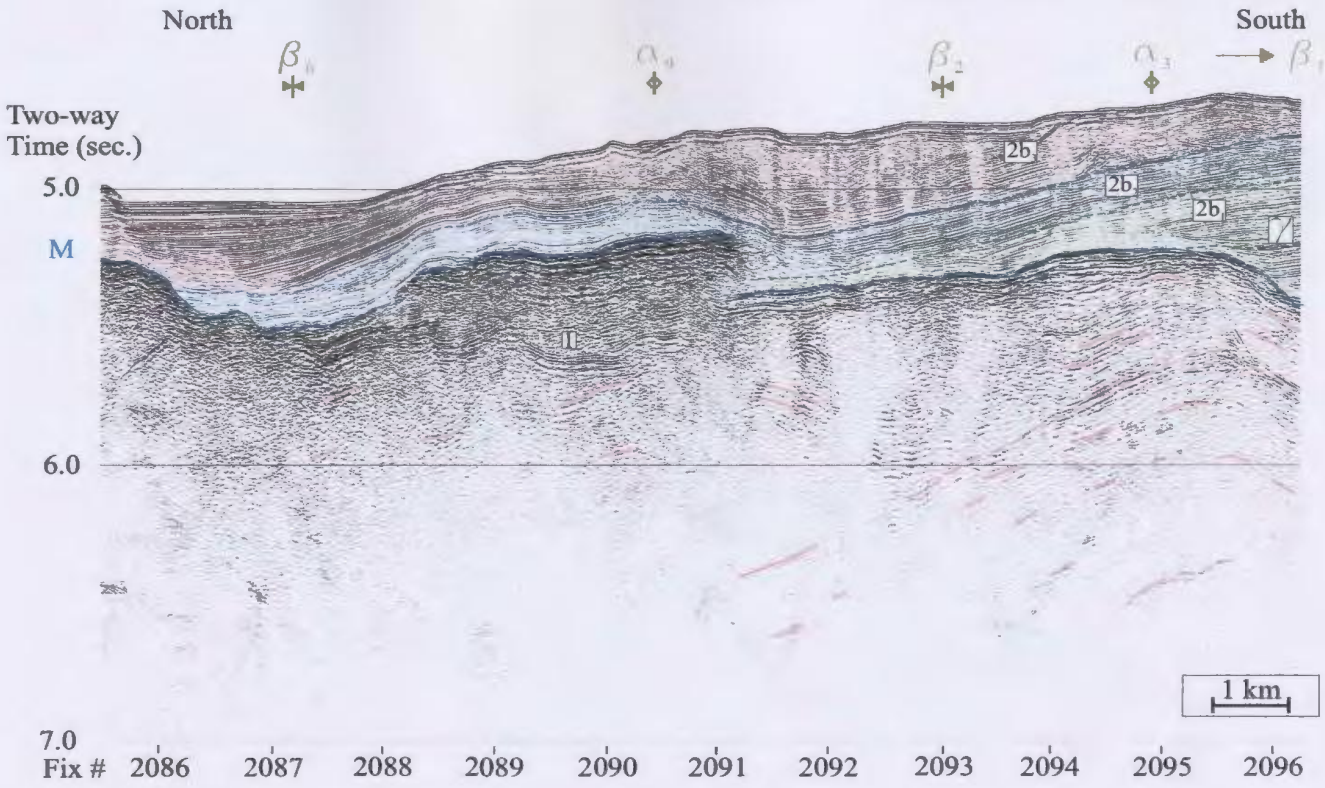

Figure 3.2.7b)

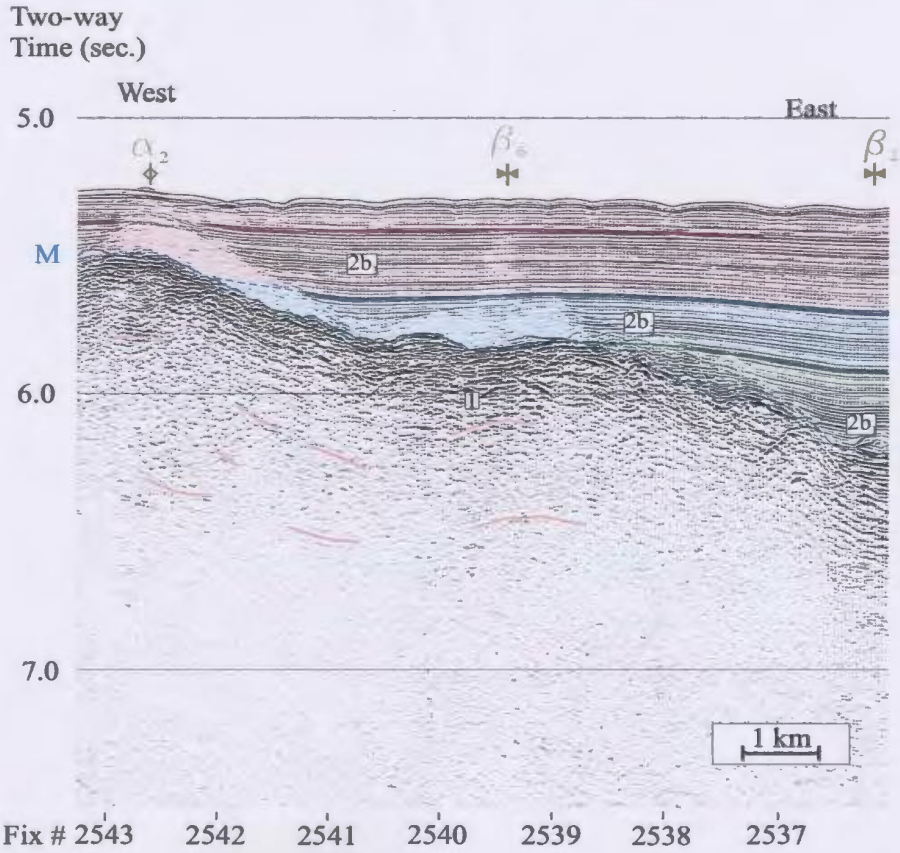

Figure 3.2.7c)

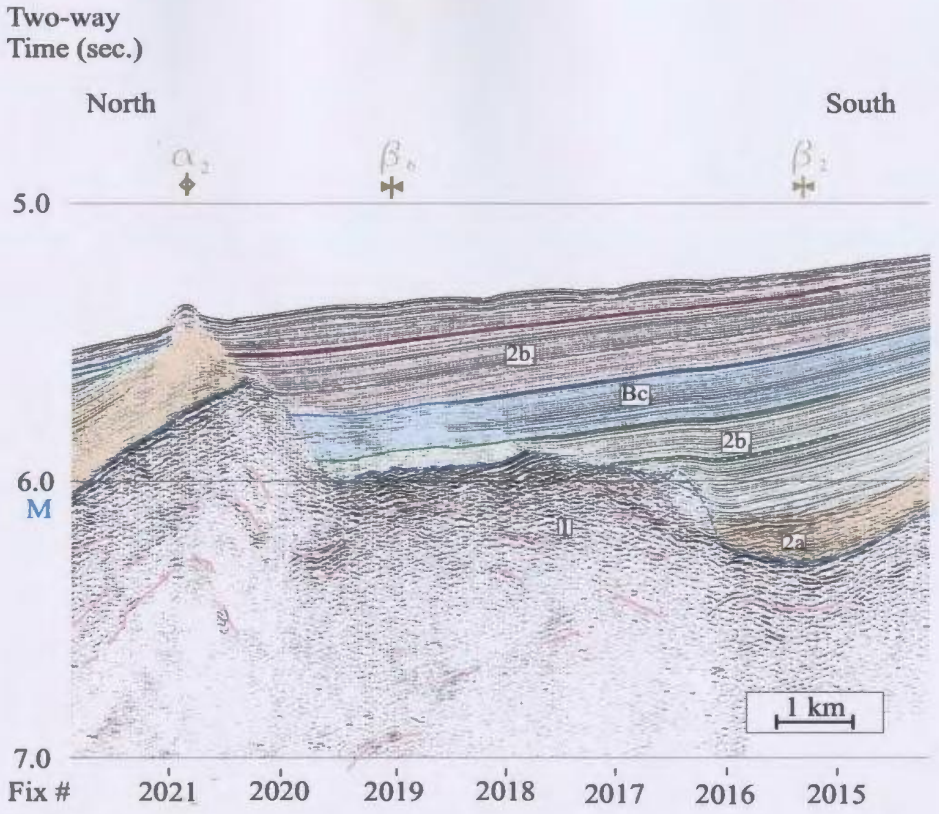
Two-way
Time (sec.)
North
South
5.0
6.0
M
7.0
2b
Bc
2b
II
2a
1 km
Fix #
2021
2020
2019
2018
2017
2016
2015

Figure 3.2.7d)

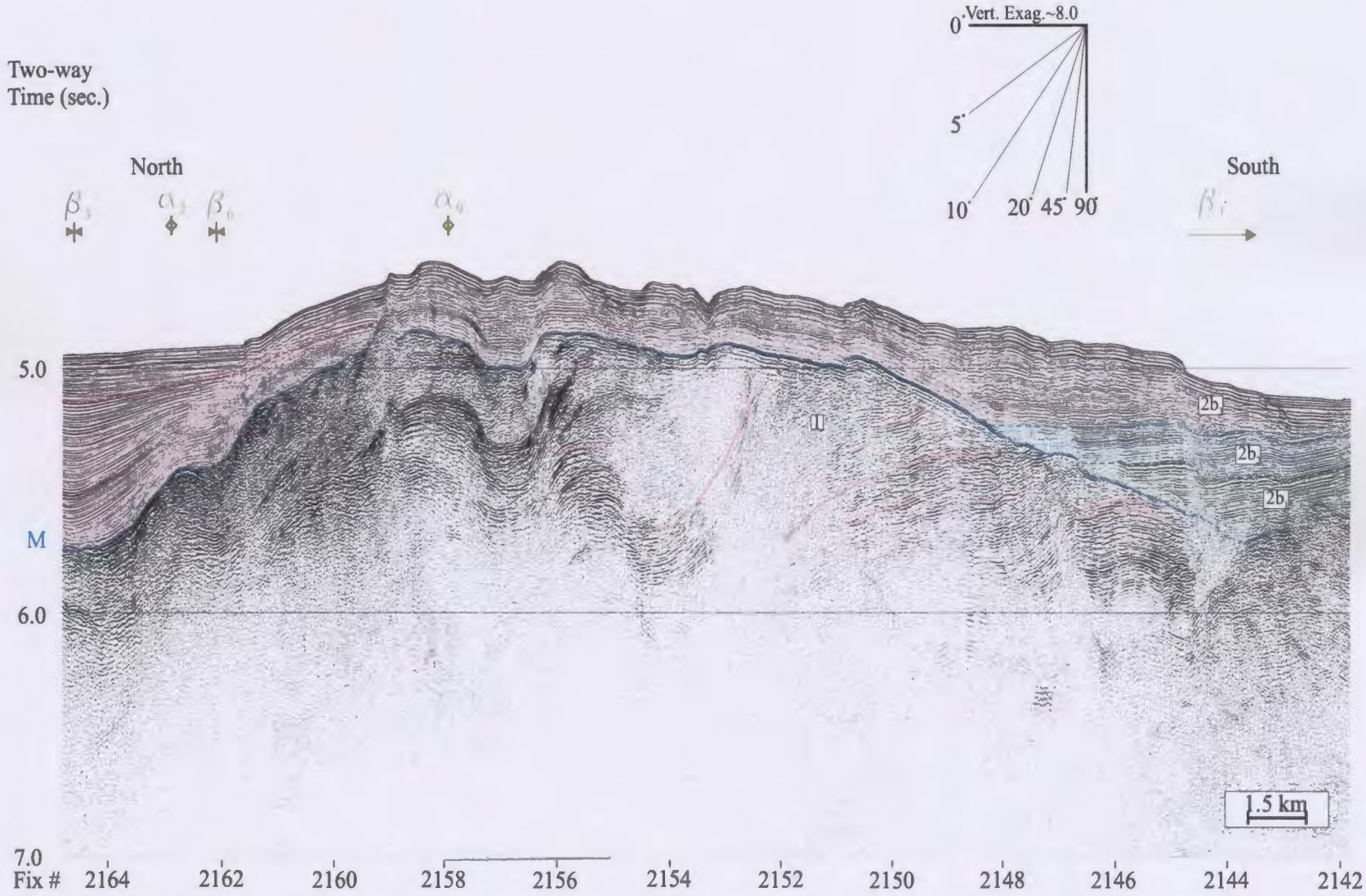
Two-way
Time (sec.)
North
South
0
Vert. Exag.~8.0
5
10
20
45
90
5.0
M
6.0
7.0
II
2b
2b
2b
1.5 km
Fix #
2164
2162
2160
2158
2156
2154
2152
2150
2148
2146
2144
2142

Figure 3.2.7e)

cover of Subunit $2b_2$ that drapes into the basin from the east where it covers ridge α_2. This thin veneer of Subunit $2b_2$ thickens slightly toward the west immediately before it downlaps onto the M reflector in the centre of the basin. Subunit $2b_3$ overlies Subunit $2b_2$ and dips ~1°W as it thickens down-dip by the divergence of its reflectors. Subunit $2b_3$ reaches a maximum thickness of 600 at the basin centre immediately before onlapping onto the M reflector. The lower portion of Subunit $2b_3$ onlaps onto Subunit $2b_2$ toward the east. Immediately to the northeast, basin β_6 appears very much like it does to the southwest, with the exception that this northwest-southeast-oriented section images the internal architecture of the Subunit $2b_3$ thickening and reveals progressive onlap surfaces (3.2.7b).

To the northeast, basin β_6 represents a small (~5 km-wide) elevated, northwestern extension of basin β_2 underlaid by an antiformal fabric of Unit 1 reflectors (Fig. 3.2.7c, d). The lack of dip and thickening of Subunits $2b_2$ and $2b_3$ on the east-west-trending profile (Fig. 3.2.7c) as compared to that of Subunits $2b_2$-$2b_3$ on the northwest-southeast-trending profile (Fig. 3.2.7d) indicate that the dip (~1.5°NW) and thickening direction of these subunits must be dominantly toward the north. These Subunits, and the occasional, uppermost portion of Subunit $2b_1$ comprise the ~600 ms fill near the centre of the basin (Fig. 3.2.7d).

If present in the southwestern portion of the survey area, basin β_6 is expressed as only a small depression south of ridge α_2 and on the northwest-dipping flank of ridge α_9 (Fig. 3.2.7e).

Basin β_7:

Basin β_7 is an ~5 km-wide, northeast-southwest-trending depocentre situated between escarpment ϵ_1 and ridge α_3. The M reflector forms an erosive unconformity that truncates the underlying, synformal Unit 1 reflectors. This basin is filled with a maximum thickness of ~840 ms of Subunits $2b_{1\text{-}3}$. These reflectors dip ~1°NW and thicken toward the northwest until they reach horizontal at the seabed (Fig. 3.2.8) Although most of Subunit $2b_1$ onlaps onto the M reflector, Subunits $2b_1$-$2b_1$ onlap onto an internally discontinuous δ package of Subunit $2b_1$ at the base of escarpment ϵ_1 (Fig. 3.2.8). Toward the west, Subunit $2b_3$ illustrates the most pronounced westward-thickening via the divergence of its reflectors and oversteps ridge α_3 to become continuous with basin β_2 with which it shares a large scattering lens that occurs just below the water bottom (Fig. 3.2.8).

Basin β_8:

Basin β_8 is a prominent northwest-southeast-trending depocentre that has a maximum width of ~17.5 km. It contains an ~750-1000 ms-thick, northwestwardly dipping Subunits $2b_1$-$2b_3$ that rotates from downlap onto the M reflector to in its southern portion to onlap toward the north (Figs. 3.2.1 and 3.2.9).

Near the axis of basin β_8, Unit 1 reflectors illustrate a gentle synformal architecture that is clearly truncated by the M reflector (Fig. 3.2.9). At the southern end of basin β_8, the lower portion of Subunit $2b_1$ forms a 740 ms-thick (maximum thickness)

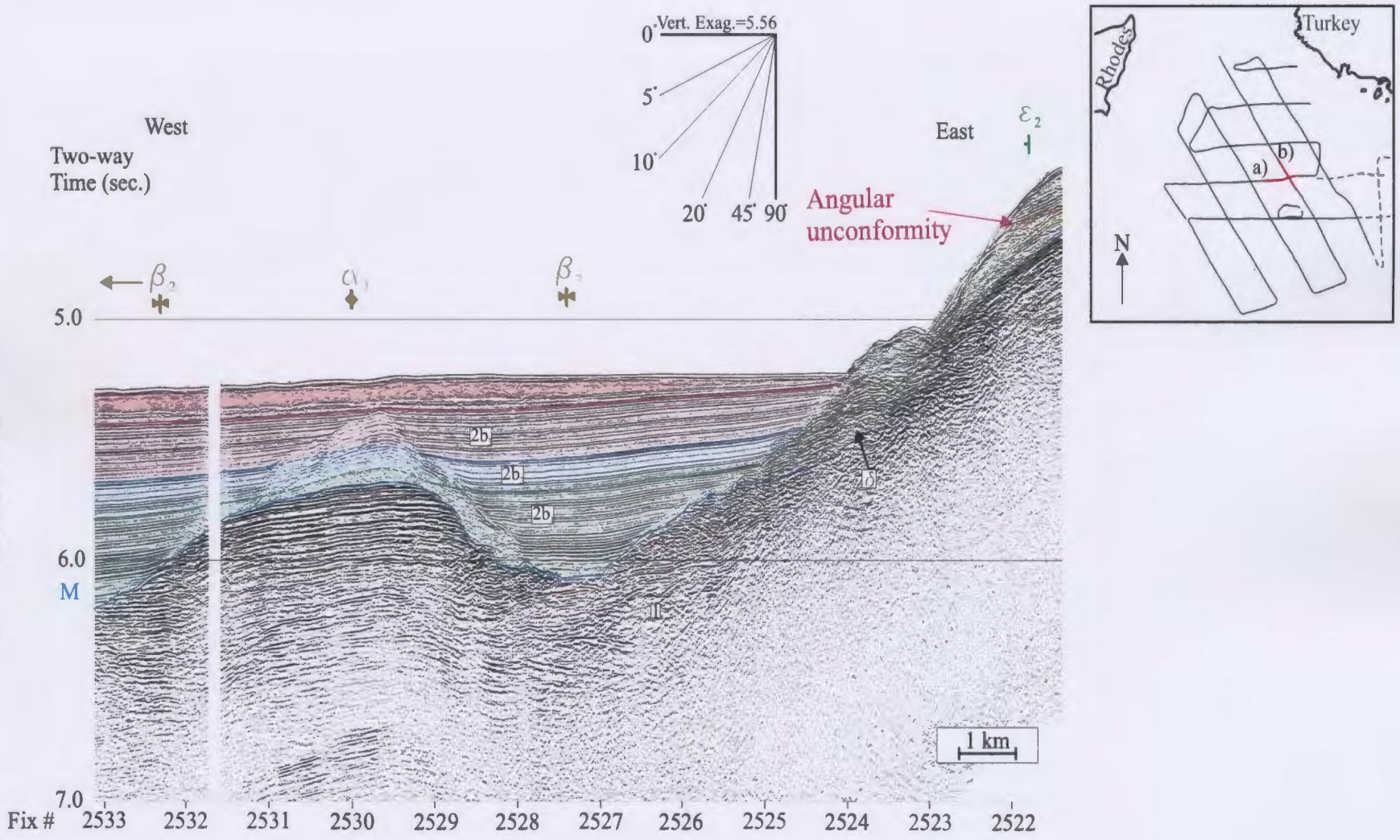

a)

Figure 3.2.8: Basin β_7 trends northeast - southwest between α_3 and the base of the Turkish shelf through a) line 80 and b) line 64a.

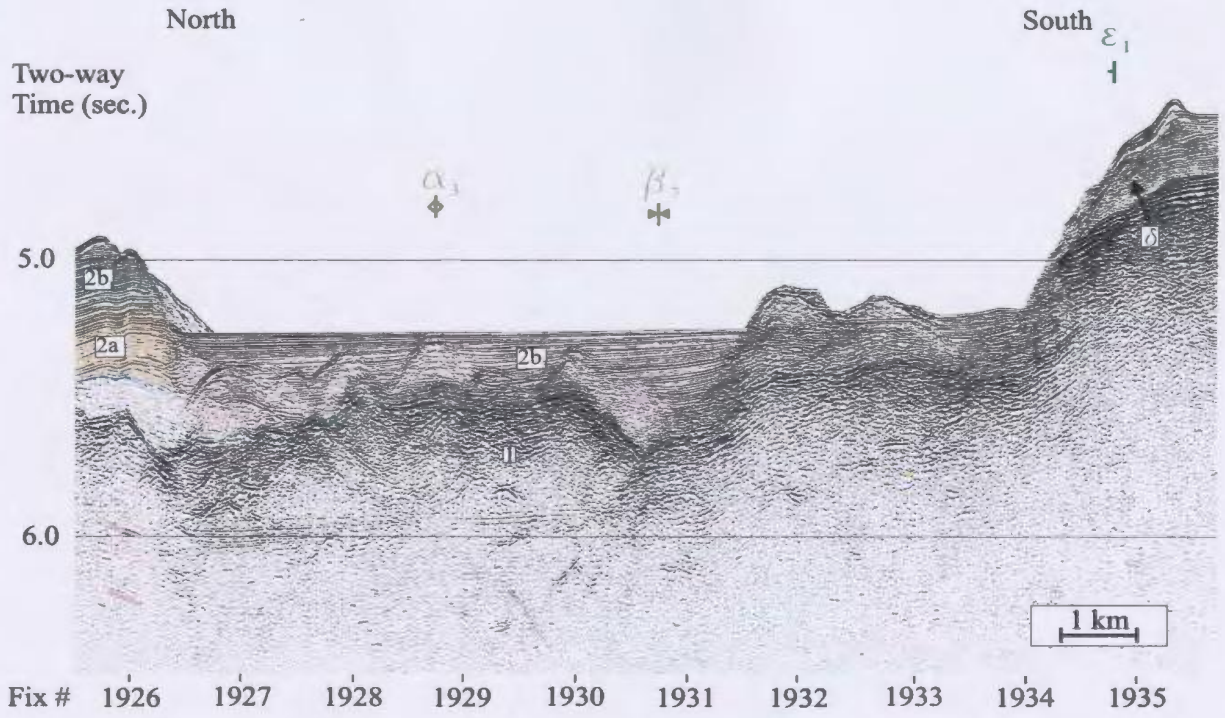
North
South
Two-way
Time (sec.)
5.0
6.0
2b
2a
2b
II
1 km
Fix #
1926
1927
1928
1929
1930
1931
1932
1933
1934
1935

Figure 3.2.8b)

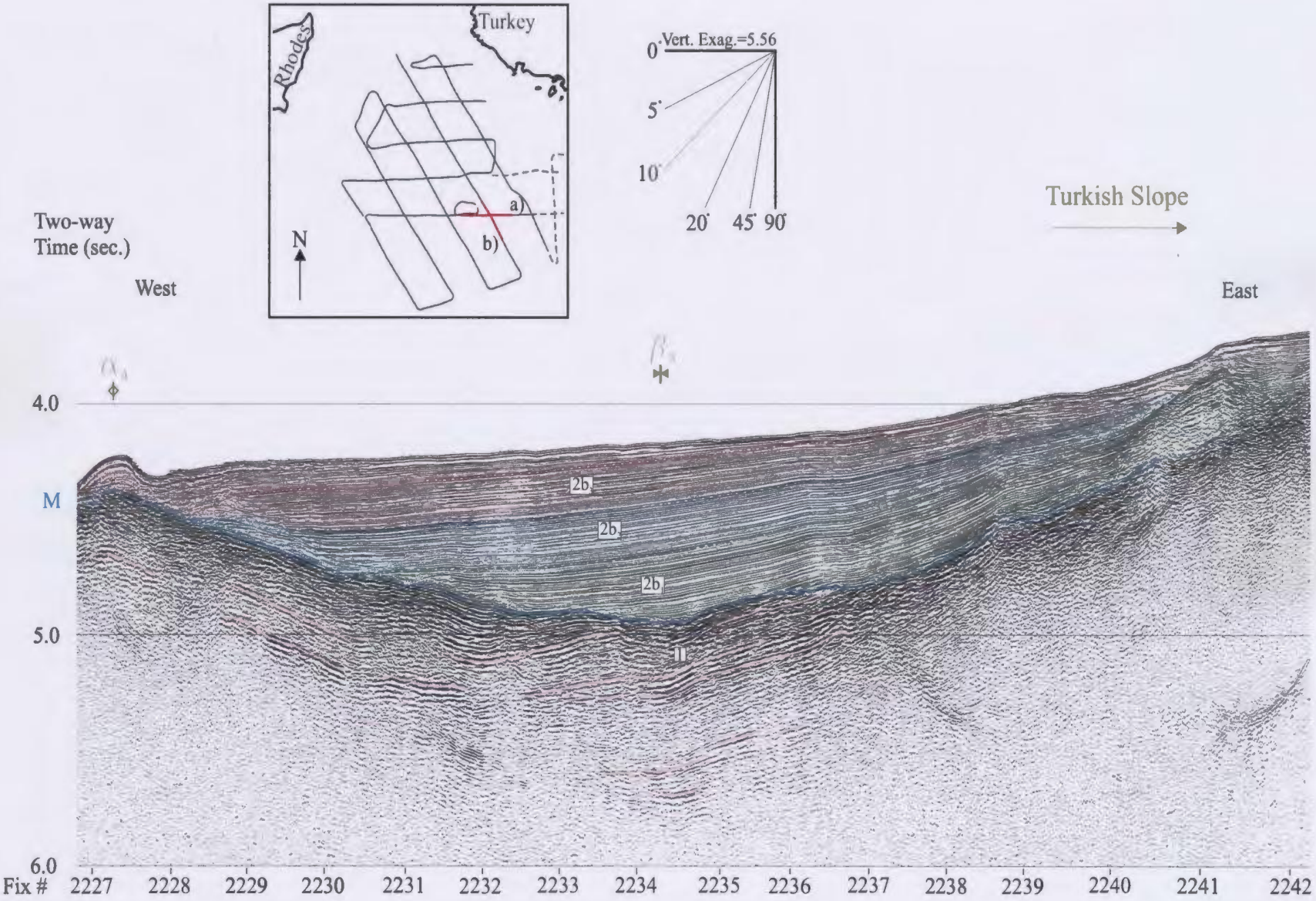

a)

Figure 3.2.9: Basin β_8 intersects a) Line 70a and b) Line 64a along its northwest-southeast trend.

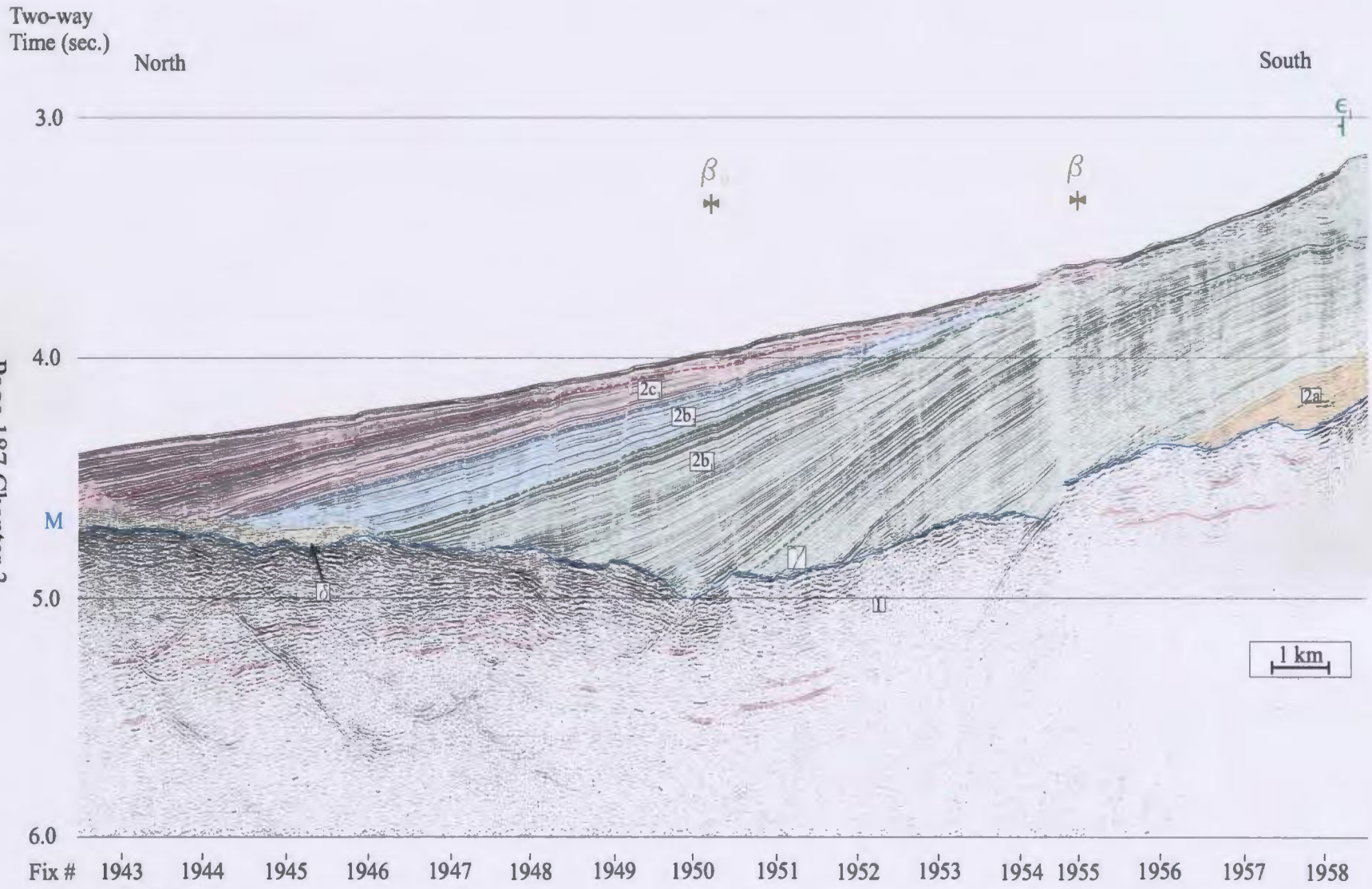
Two-way
Time (sec.)
North
South
3.0
4.0
5.0
6.0
M
β
β
2c
2b
2b
2a
1 km
Fix #
1943
1944
1945
1946
1947
1948
1949
1950
1951
1952
1953
1954
1955
1956
1957
1958

Figure 3.2.9b)

package that shows slight northward-directed internal thickening as its internal reflectors rotate from horizontal near the axis of basin β_1 to the south, to a dip angle of ~8°NW near the basin β_8 basin axis. This antiformal architecture results in a downlap relationship between the lower Subunit $2b_1$ and the gently, northward-dipping M reflector (Fig. 3.2.9b). The top of this culminated succession is marked by the γ reflector. Above the γ reflector Subunits $2b_1$-$2b_3$ cumulatively thicken from 220 ms in the southern end of basin β_8 to 940 ms near the basin centre dominantly by the strong northward divergence of their reflectors and progressive internal onlap surfaces toward the south. This northward thickening also has the effect of reducing the dip magnitude of these upper Subunit 2b reflectors up the section to as low as ~1.5°NW at the seabed and rotating the downlap relationship between Subunit $2b_1$ and the M reflector to one of onlap. Both the lower, sub-γ and supra-γ Unit 2 reflectors show several steep, minor discontinuities that display both small down-to-the-south and down-to-the-north vertical separations. The narrow zone of especially disturbed Subunit 2b reflectors coincides with a discrete down-to-the-north offset of the M reflector below (Fig. 3.2.9).

The significant difference between apparent dips measured for Subunit 2b on the northwest-southeast line versus the east-west line in Figure 3.2.9 implies that the supra-γ reflector portion of the Subunit 2b dips and thickens strongly to the north, with a small westward component. In addition, the lack of Pliocene-Quaternary discontinuities seen on the east-west line as compared to the northwest-southeast line implies that the strike of these features is likely ~east-west (Fig. 3.2.9).

Basin β_9:

Basin β_9 is a large northeast-southwest-trending depocentre located in the northwestern portion of the Rhodes Basin (Figs. 3.2.1 and 3.2.10). It narrows from ~20 km wide at its westernmost location between ridges α_7 and α_8 to ~10.5 km wide to the northeast where it is nestled between ridges α_1 and α_7. Its ~1100 ms-thick Pliocene-Quaternary fill dips of ~2°NW at its westernmost extremity and generally thickens toward the northwest. These reflectors onlap onto a poorly reflective Unit 1. There are large vertical offsets of the M reflector across steep discontinuites.

At its westernmost location basin β_9 contains a maximum up to 1070 ms of fill comprising of Subunits $2b_1$-$2b_3$ (Fig. 3.2.10). The basin is divided into two, approximately equal-sized parts by a pronounced Unit 1 high-standing block that is bounded by 70-80°-dipping discontinuities that cut from Unit 1 through to the upper portion of Subunit $2b_3$ (Fig. 3.2.10). This high-standing block is not identified as a linear ridge because it cannot be correlated with any other location and therefore its trend cannot be unambiguously determined. The M reflector is a very bright event that clearly shows up to 420 ms of vertical separation across the southern boundary of this uplifted block. Subunits $2b_2$-$2b_3$ are also vertically offset, however the magnitude of their offset decreased successively up section and the seabed shows no influence of these underlying vertical offsets. Weak reflectivity within Unit 1 outlines a relatively flat-lying fabric with minor undulations, except within the central, high-standing block which exhibits a faint antiformal architecture.

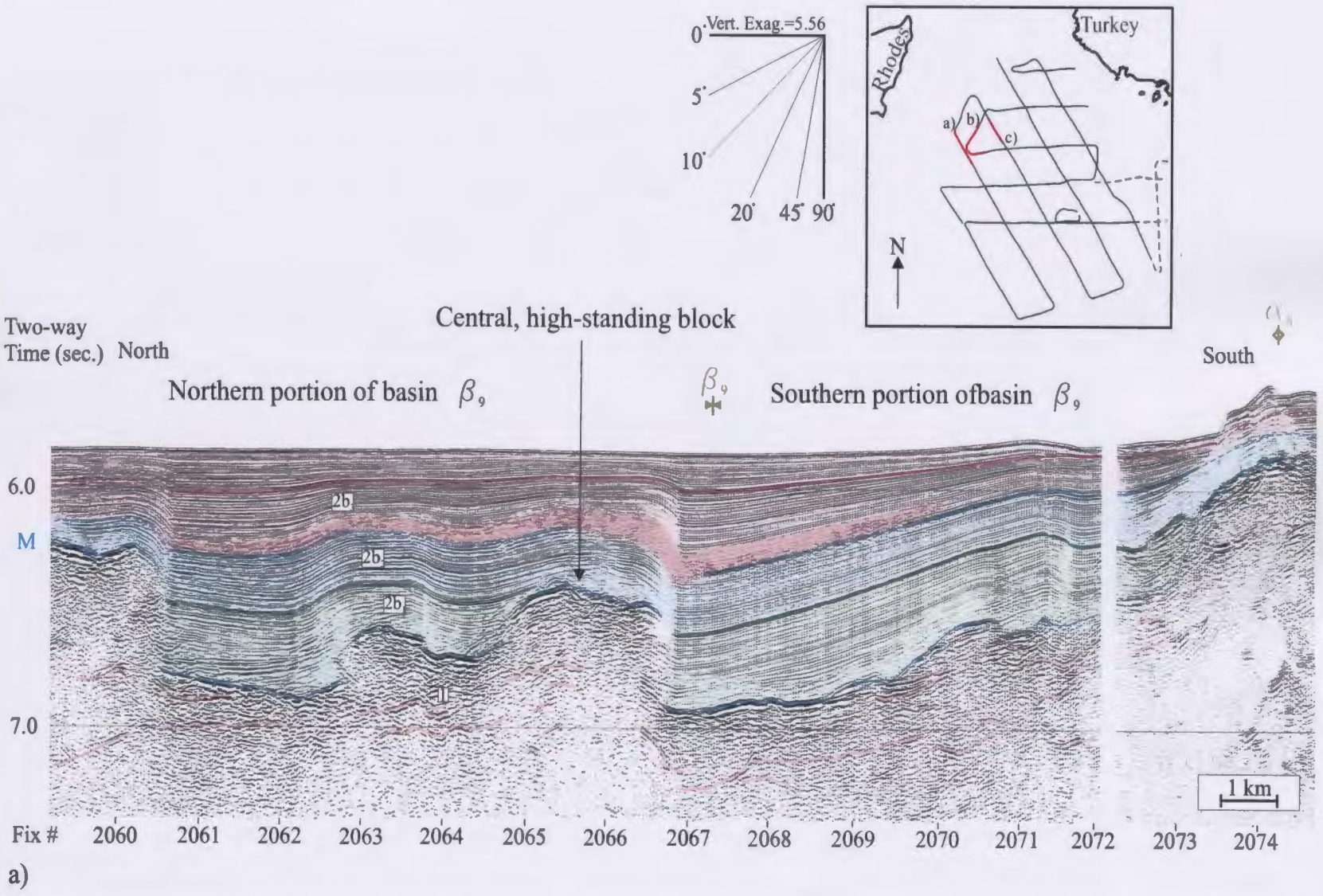

Figure 3.2.10: Basin β_9 is a broad basin that trends northeast-southwest in the northwestern portion of the survey area. It is seen to cross lines a) 64, b) 83 and 81 and c) 64. The base of the basin is affected by numerous discontinuities that generate considerable vertical offsets of the M reflector.

Alteration of Course

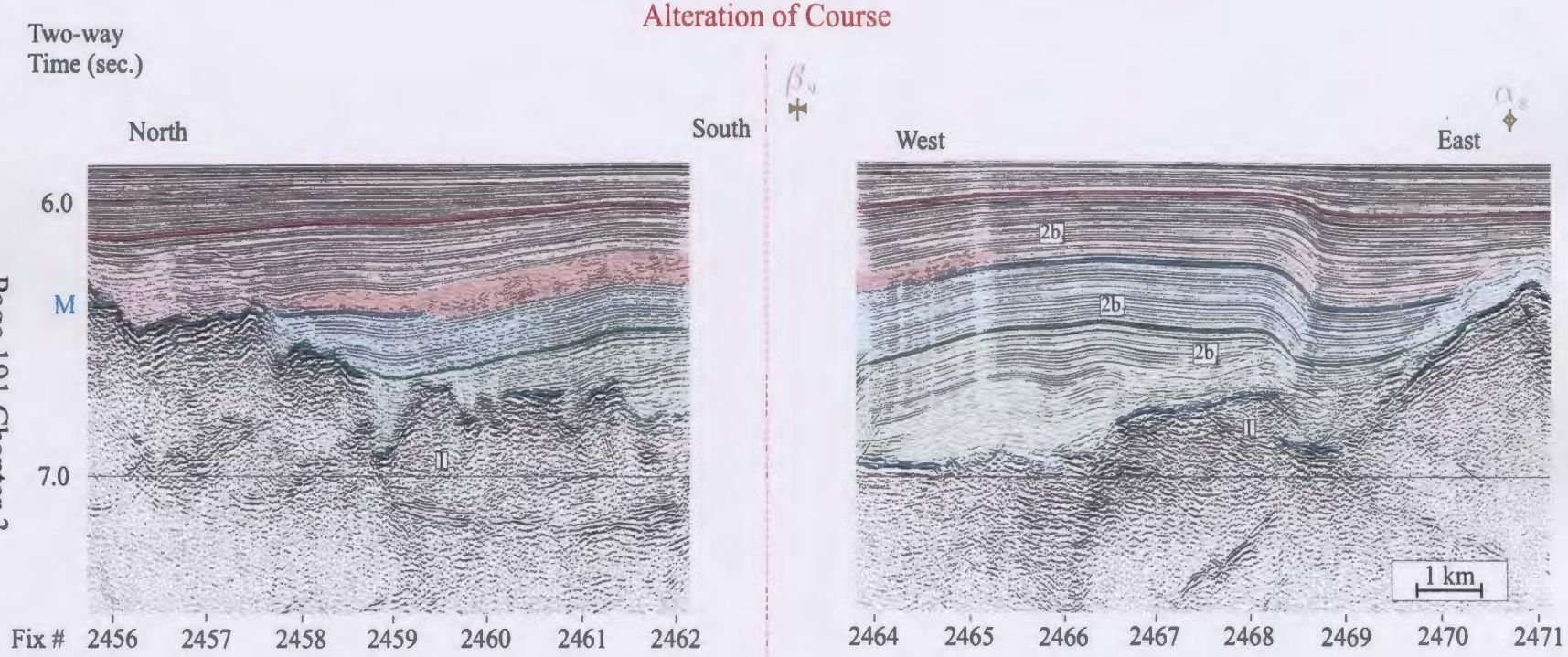

Figure 3.2.10b)

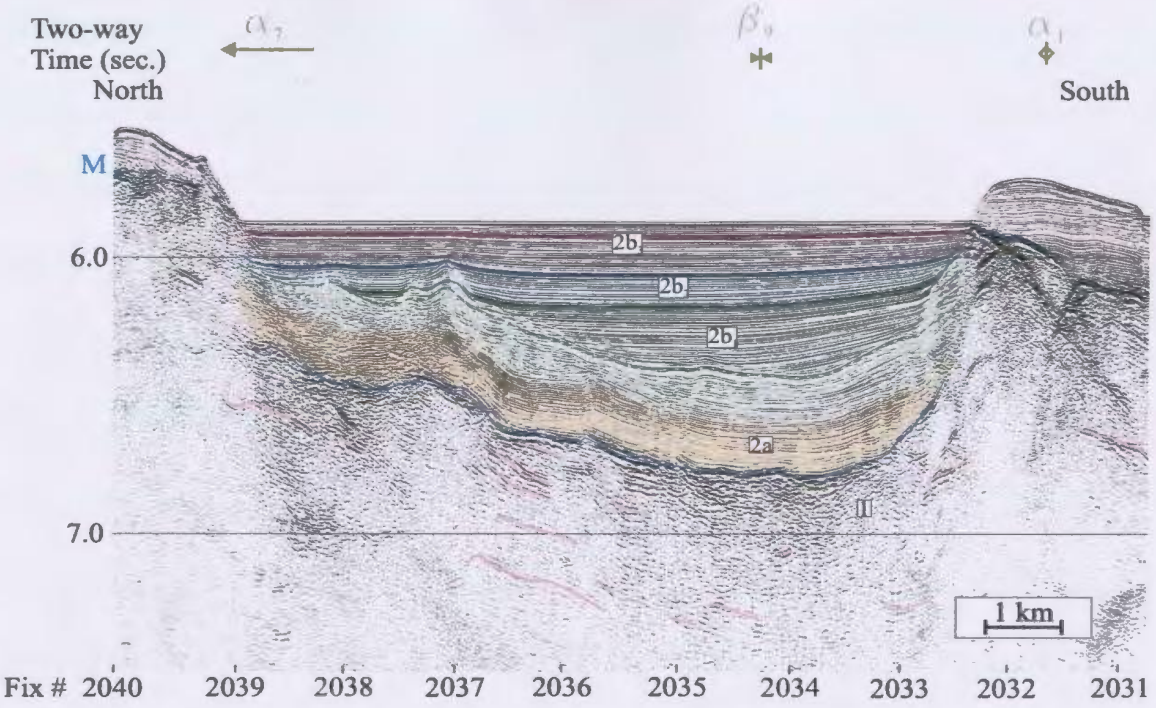

Figure 3.2.10c)

In the southern end of the basin, Subunit $2b_1$ demonstrates the least amount of northward thickening, maintaining a relatively constant thickness of ~300 ms across the centre of the basin until it onlaps against a steeply-inclined contact with Unit 1 to the north (Fig. 3.2.10). Subunit $2b_2$ conformably overlies Subunit $2b_1$, but thickens toward the north to 260 ms-thick via divergence of its reflectors. Unlike Subunit $2b_1$, most of Subunit $2b_2$ can be traced across the central, high-standing block into northern portion of the basin. Subunit $2b_3$ thickens the to 410 ms-thick toward the north where it is confidently correlated across the central Unit 1 block, its shallowest strata being virtually unaffected by the underlying vertical offsets. At the base of Subunit $2b_3$, a lens-shaped body containing a maximum of ~100 ms of discontinuous reflectors that spans ~15 km across both the northern and southern portions of basin β_9. The southern end of this lens is vertically offset by ~120 ms across the central, high-standing block but is easily correlated across the discontinuity where it pinches out to the south. Continuing to the south, two steeply north-dipping discontinuities produce minor offsets of the M reflector and Subunit 2b (Fig. 3.2.10a and b).

The northern portion of basin β_9 contains up to 1040 ms of Subunits $2b_1$-$2b_3$ (Fig. 3.2.10a). It is bounded to its north by a near vertical (70-80° NW) discontinuity that offsets Unit 1 by ~520 ms. Subunit 2b has an undulatory appearance that mimics the abrupt vertical offsets of the M reflector by discontinuities that cut Unit 1 in the central portion of the basin (Fig. 3.2.10a). Subunit $2b_1$ shows modest thickening from ~220 ms in the southeast to ~300 ms thick at the basin's northern end where the reflectors terminate

abruptly against a subvertical contact with Unit 1. Subunit $2b_2$ conformably overlies Subunit $2b_1$ and maintains a constant thickness of ~210 ms. Unlike Subunit $2b_1$, Subunit $2b_2$ completely oversteps the central Unit 1 block rather than onlapping against it. Subunit $2b_3$ thickens northward form ~280 ms thick to ~380 ms thick via the northward divergence of its reflectors (Fig. 3.2.10a)

Northeast-southwest-trending isochron contours support a correlation of basin β_9 toward the northeast even though the stratigraphic correlation over this large distance is not very compelling (Figs. 3.1.4, 3.2.10a,b vs. c). At this northeastern location, basin β_9 is ~8.5 km wide and contains ~900 ms of Pliocene-Quaternary fill. Below the basin axis, Unit 1 illustrates 5°SE-dipping reflectors. The northwest and southeast margins of the basin are strongly defined by large discontinuities that display 500 and 900 ms vertical separations from the north and south along the flanks of ridges α_7 and α_1 respectively (Fig. 3.2.10c). Here, an ~200 ms-thick cover of Subunit 2a conformably overlies the M reflector and exhibits a moderate reflectivity that allows identification of minor discontinuities and internal deformation. Subunit $2b_1$ illustrates two internal packages, the lower of which demonstrates only modest reflectivity and little coherency through its undulating architecture (Fig. 3.2.10c). The upper portion of Subunit $2b_1$ illustrates a more typical Subunit 2b reflectivity and northward thickening nature as it onlaps onto its lower portion toward both the north and south. Subunits $2b_2$ and $2b_3$ each thicken toward the northwest and onlap against the exposed flanks of ridges α_7 and α_1 (Fig. 3.2.10c). Here, basin β_9 has more in common with the neighbouring basin β_3 to its south than it does to

the southwest (Figs. 3.2.4a and 3.2.10c).

Basin β_{10}:

Basin β_{10} is a northwest-southeast trending depocentre located south of the escarpment ϵ_1. It measures ~8.5 km wide and has an ~750 ms-thick Pliocene-Quaternary succession (Fig. 3.2.11). Its southern margin is situated at a diffuse boundary between the well layered Subunit $2b_1$ strata and the discontinuous, scattering reflectivity of the region to its south whereas its northern boundary is more clearly defined by ridge α_4 (Fig. 3.2.11). Numerous high angle discontinuities provide up to 150 ms of vertical separation on the M reflector and much of the overlying Pliocene-Quaternary succession. Subunit 2a forms an ~120 ms-thick package over the M reflector and is clearly offset by each of the discontinuities. Subunit $2b_1$ conformably overlies Subunit 2a and is also cut, at least part way up its succession, by multiple discontinuities. Folding and segmentation associated with the reflectors of Subunit $2b_1$ make it difficult to determine if they suffer the same discontinuous offsets as the underlying Subunit 2a and Unit 1.

Basin β_{11}:

Basin β_{11} is a small, ~2.5 km-wide basin located in the eastern extremity of the survey area, where it is perched east of ridge α_5 (Fig. 3.2.12). Its basin axis is tipped toward the north and its southern margin with ridge α_5 is defined by a Unit 1-cutting discontinuity that offsets the M reflector by ~320 ms. It contains a maximum thickness of

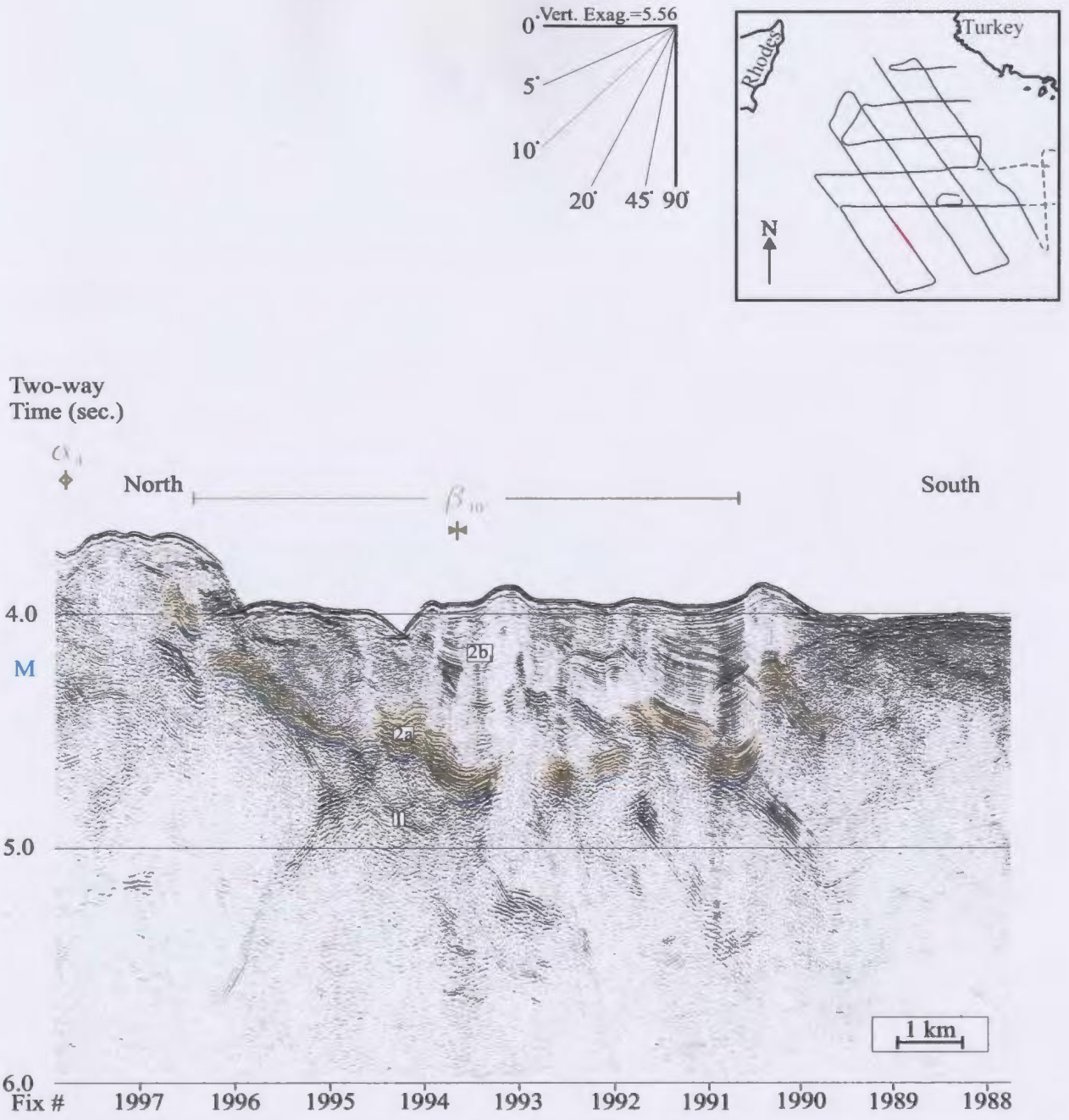

Figure 3.2.11: Basin β_{10} contains a thick succession of Unit 2 strata that is frequently offset and deformed.

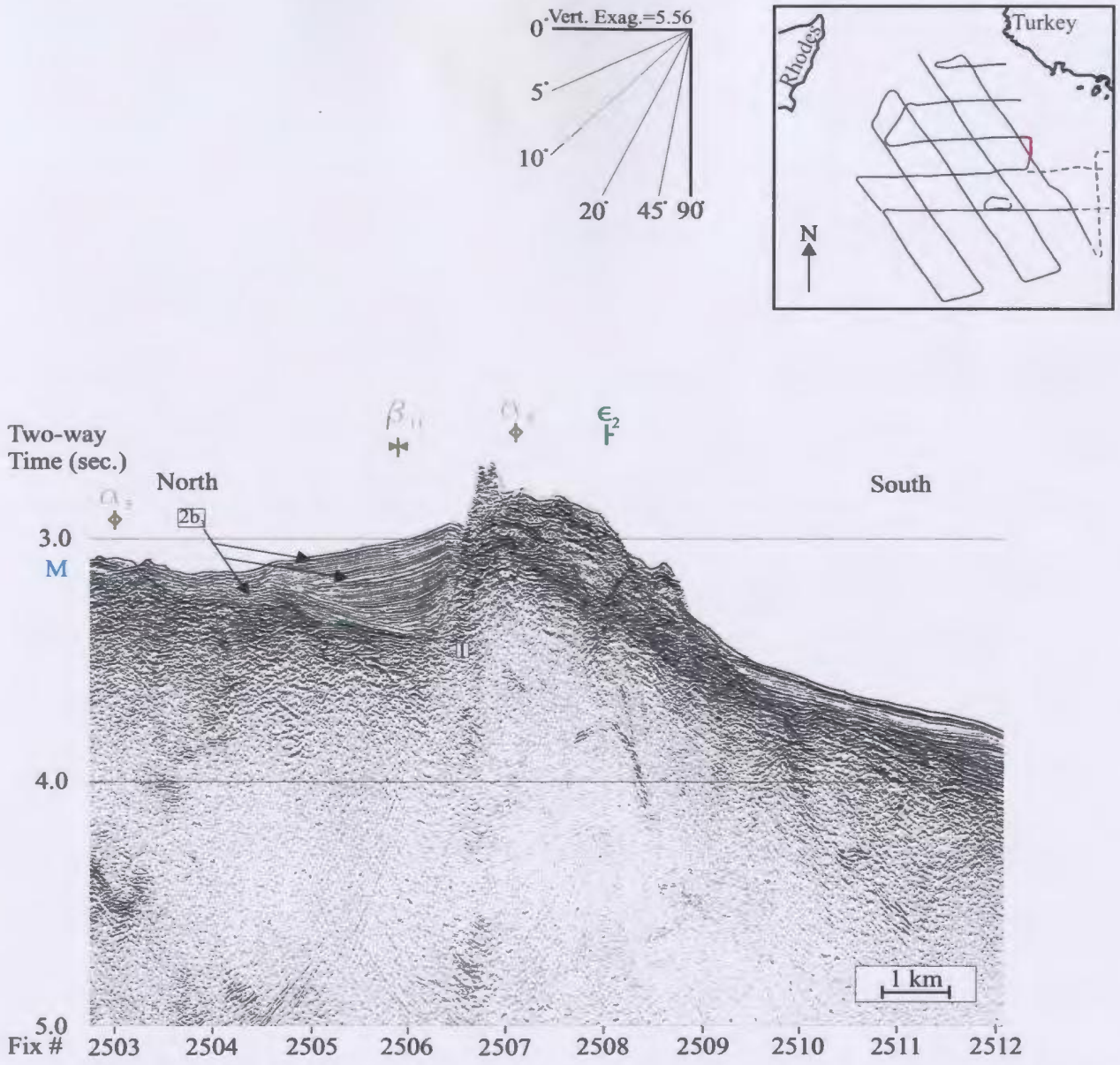

Figure 3.2.12: Basin β_{11} demonstrates both symmetrical and asymmetrically thickening packages of Subunit $2b_1$.

~180 ms of Subunit $2b_1$ that is tipped northward in accordance with the tilt of the basin axis. This Subunit $2b_1$ succession consists of 3 packages that display different thickening patterns. The lowermost package thickens toward the south, by the divergence of its reflectors, to a maximum of ~50 ms. These reflectors then curve sharply upward and onlap onto the southern basin margin, but drape over the northern margin of the basin. An ~80 ms-thick package onlaps onto this lower package toward the north and thickens symmetrically from both basin margins toward the basin centre by the divergence of its reflectors. This middle package curves upward and thins as it onlaps onto the southern margin of the basin. The upper ~50 ms package maintains a relatively uniform thickness across the basin (Fig. 3.2.12).

3.2.2: Ridges

Several ridges are identified within the study area. The morphology of these structural highs varies tremendously from both one ridge to another as well as along the trend of an individual ridge. These variations often make correlation of a single ridge across the study area difficult. The structural trend established by the basin correlations provides a helpful constraint on the anticipated trends of the ridges across the study area. Like the basins, ridges can be divided into three families: Ridge Family 1 ridges include ridges α_1, α_2, α_3, the western limb of ridge α_4 and ridges α_8 and α_9. These ridges trend northeast-southwest along a gentle, S-shaped trajectory. Ridge Family 2 includes the east-west-trending eastern limb of ridge α_4 and ridge α_7. Ridge Family 3 consists of ridges α_5

and α_6 as they trend ~north northwest- south southeast along the Turkish slope.

Ridge α_1:

Ridge α_1 is a northeast-southwest-trending structural high that separates basin β_3 to its southeast from basins β_5 and β_9 to its northwest (Figs. 3.2.1 and 3.2.13). It plunges from both the northeast and southwest toward the centre of the Rhodes Basin. Generally broad (~7.5-11.5 km wide) and providing a 125-450 ms relief above the adjacent basins, this ridge is cored by an antiformal architecture of Unit 1. An exception to this description exists along its northeastern segment where it narrows to ~3.5 km wide and stands 520 ms above its margin with the adjacent basin β_9 and 460 ms above its margin with basin β_3 (Fig. 3.2.13b, c). Further to the northeast, toward the Turkish slope, correlation of ridge α_1 becomes increasingly difficult.

At is southwestern extremity, ridge α_1 is cored by strongly reflective, generally 5°NW-dipping, gently undulated Unit 1 reflectors that form an angular unconformity with the overlying M reflector (Fig. 3.2.13a). The southern limb of the ridge is not imaged due to the termination of the survey line. Both the M reflector and the internal reflectivity of Unit 1 demonstrate vertical offsets along steeply dipping (~60°NW) discontinuities. The northern flank and crest of the ridge is onlapped from the northwest by ~2°NW-dipping and northward-thickening Subunit $2b_3$ refectors(Fig. 3.2.13a).

Further northeast, ridge α_1 broadens to ~11 km-wide and exhibits a flat-crested morphology (Fig. 3.2.13b, c). Here, Unit 1 is internally discontinuous but outlines a weak

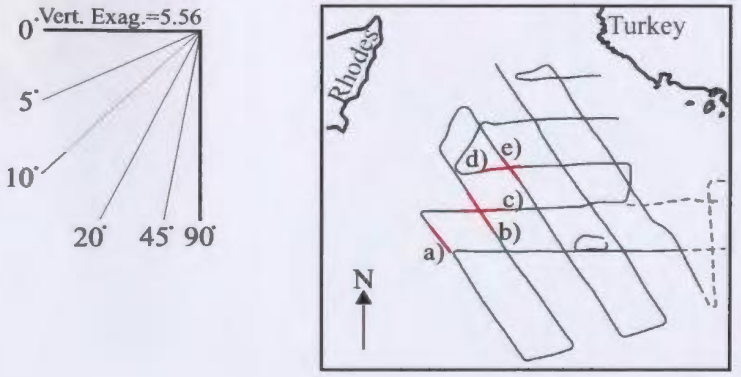

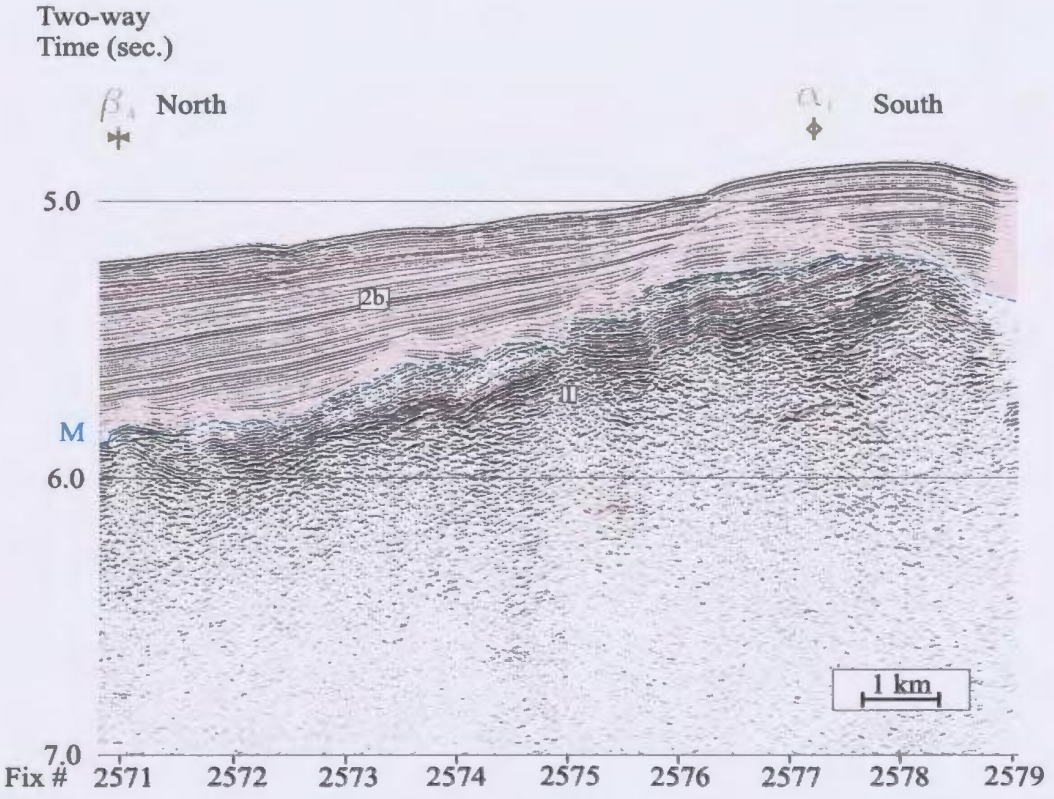

a)

Figure 3.2.13: Ridge α_1 trends northeast-southwest across lines a) 80, b) line 68, c) line 80 and d) line 81 and e) line 64.

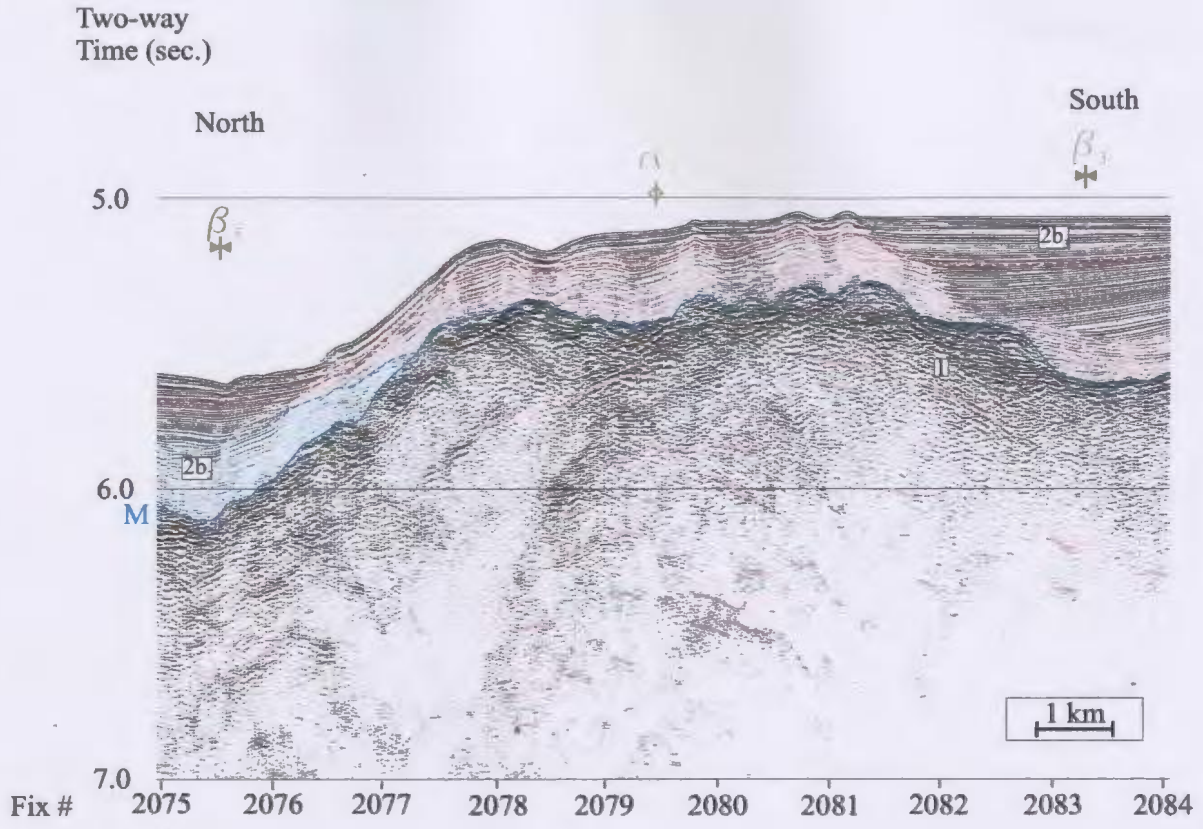

Figure 3.2.13b)

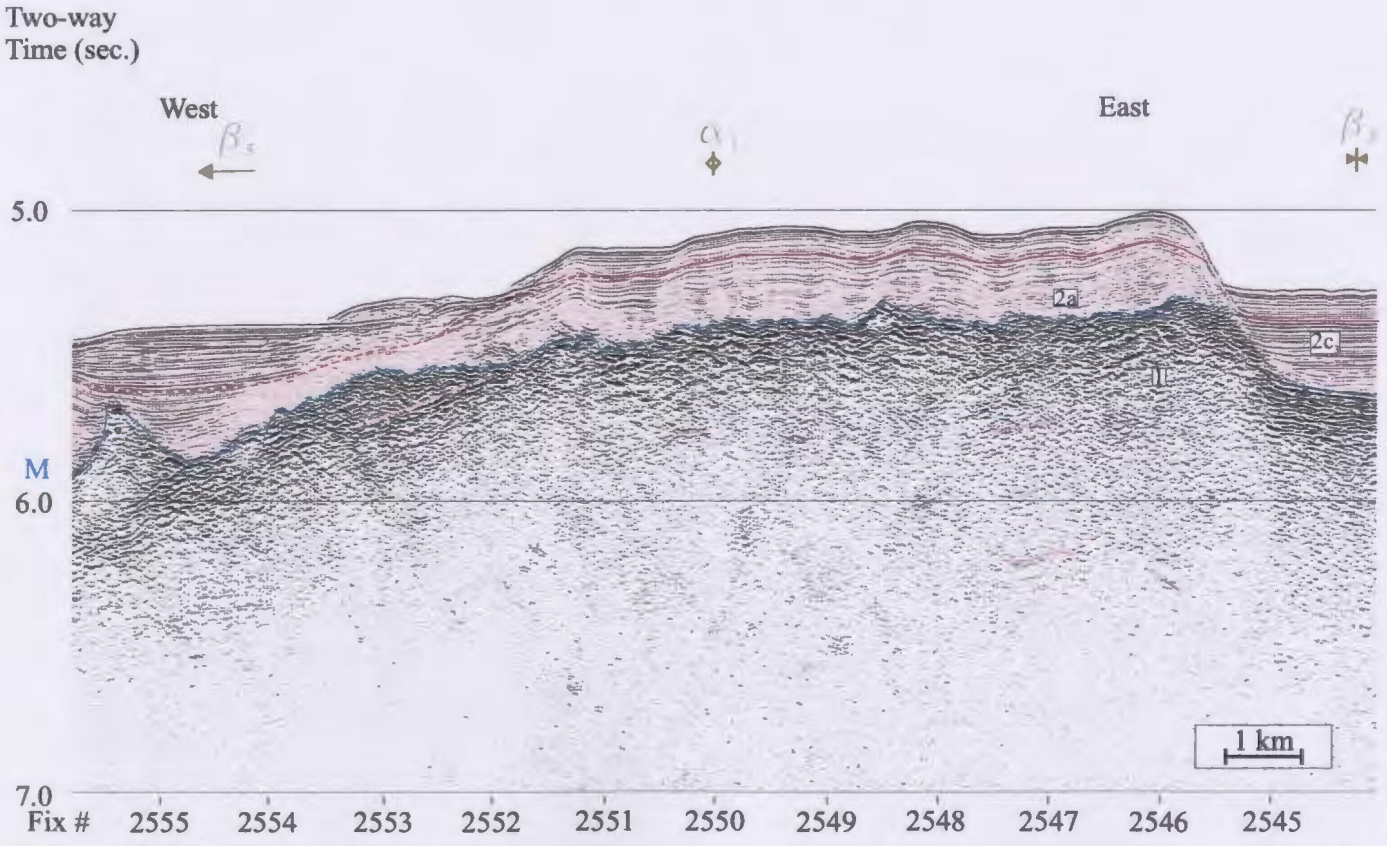

Figure 3.2.13c)

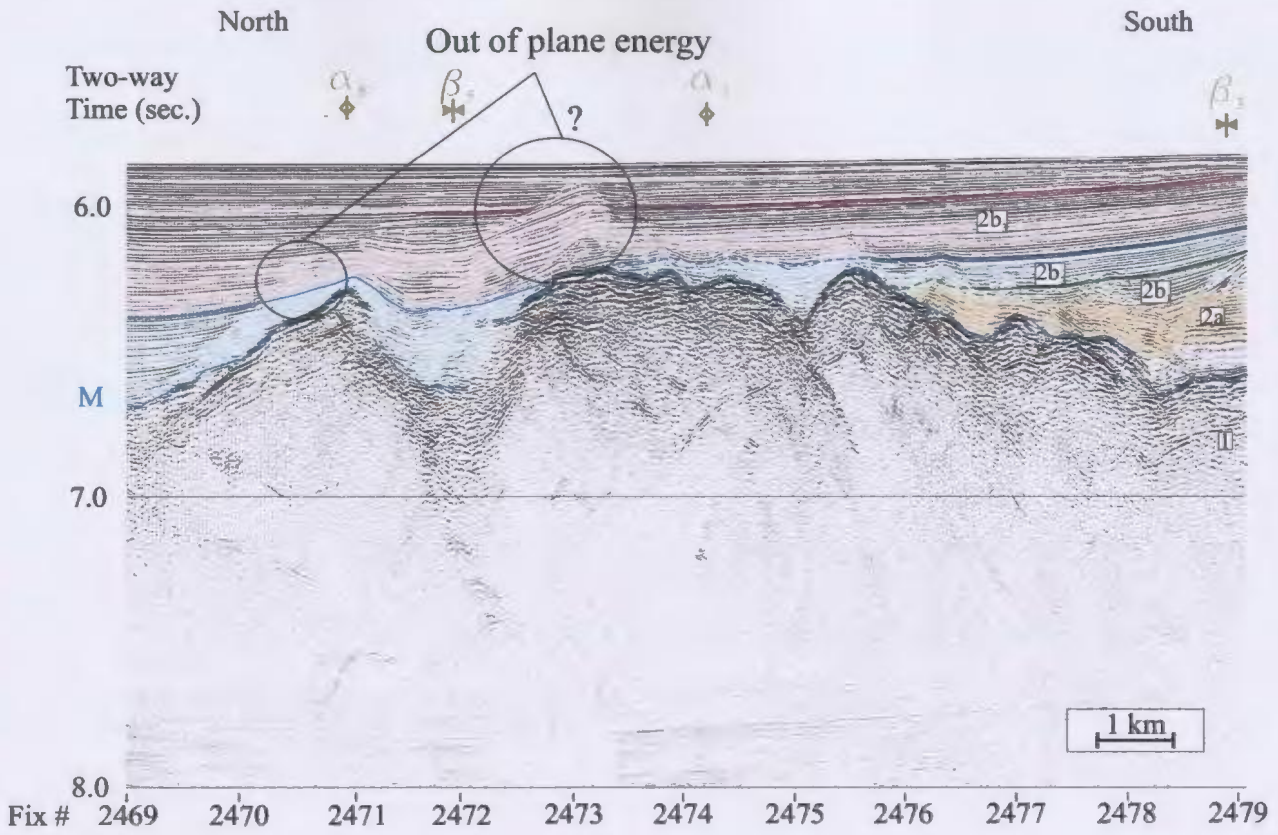

Figure 3.2.13d)

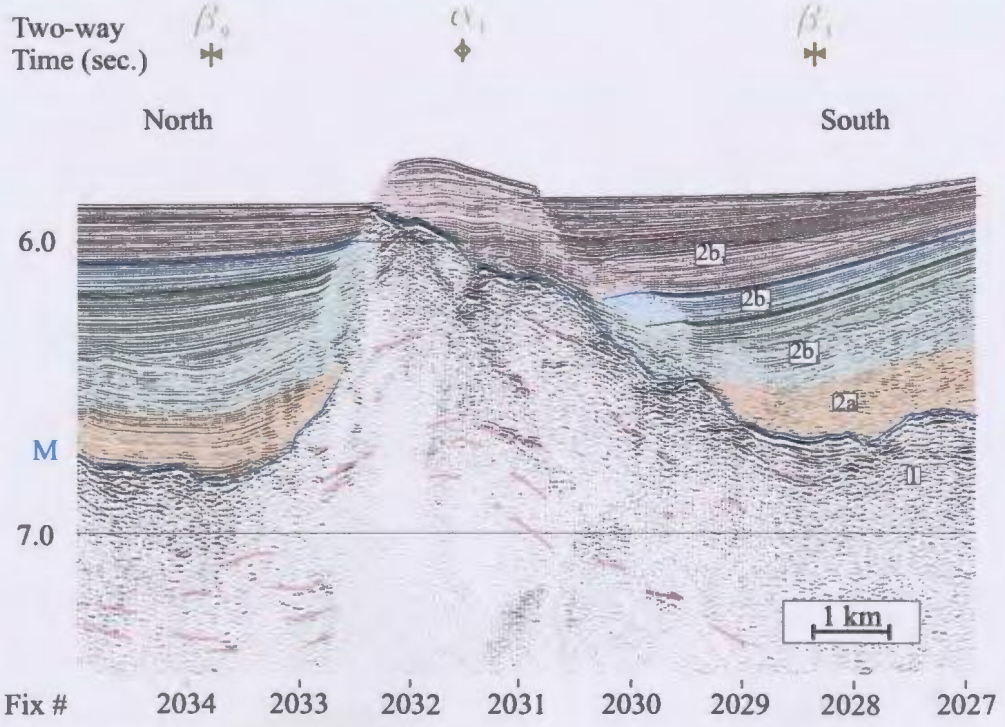

Figure 3.2.13e)

antiformal fabric, especially on the northwest-southeast-oriented survey line (Fig. 3.2.13b). The M reflector is also discontinuous but strongly reflective as it forms an irregularly-shaped surface whose undulating morphology is mimicked by the overlying ~250-300 ms-thick, isopachous Subunit $2b_3$ and the seabed. On the east-west-oriented section, its boundary with basin β_3 to the east is defined by a single discontinuity that vertically separates the M reflector and Subunit $2b_3$ in a down-to-the-southwest sense by ~220 ms (Fig. 3.2.13c). This relationship is not as clearly observed on the northwest-southeast-trending section despite their close proximity (Fig. 3.2.13b). Nevertheless, due to its crossing these two lines over a short distance, this discontinuity is determined to have a true orientation of ~23°ESE. Its northwestern margin with basin β_5 shows a greater relief than that with basin β_3 and is accomplished along a gentler, more continuous slope.

Approximately 11 km to the northeast, ridge α_1 retains a broad, unimposing morphology (Fig. 3.2.13d). Its irregular surface demonstrates minor, discontinuous offsets of the M reflector. This irregular morphology is onlapped from both the east and west by Subunits $2b_1$ and $2b_2$. Each of Subunits $2b_1$ and $2b_2$ have an apparent dip of ~0.5°W and thicken gently away from the ridge toward the west via the divergence of their reflectors. Subunit $2b_3$ also demonstrates an apparent dip and thickening polarity toward the west, but oversteps the crest to bury it beneath ~350 ms of sediment. The internal character of Subunit $2b_3$ is especially influenced by what is interpreted to be out-of-plane energy (Fig. 3.2.13d). Although ridge α_1 changed very little over the ~11 km between its occurrence at this locality from that to the southwest, only ~3 km to the northeast of this location the

ridge suddenly appears very different (compare Figs. 3.2.13d and e). At this northeastern end, the northwestern flank of ridge α_1 is represented by an ~45° NW-dipping discontinuity that offsets the M reflector by ~520 ms. Its southeastern flank dips at only ~5°SE and displays a far more continuous M reflector that may be offset by a few minor discontinuities (Fig. 3.2.13e). Unit 1 cores the ridge with a clear antiformal fabric that appears truncated below the ridge's northwestern edge. Both ridge flanks are onlapped by Subunits 2a and 2b. Although those Subunit 2b onlaps onto the northern flank of ridge α_1 and shows modest thickening away from the ridge flank, those Subunit 2b packages to its south (basin β_2) thicken toward its more gently-dipping, southern flank, especially Subunit $2b_3$ which is bulged upward over the ridge crest (Fig. 3.2.13e). Correlation of ridge α_1 further north onto the Turkish shelf is difficult and cannot be accomplished with confidence.

Ridge α_2:

Ridge α_2 is a major, northeast-southwest-trending antiformal structure that separates basin β_3 to its northwest from basins β_6 and β_2 to its southeast. Its width and relief vary along its trend from ~2-8 km and ~20-400 ms respectively. Although ridge α_2 is most pronounced in the central portion of the survey area, it generally plunges by ~ 1000 ms toward the northeast from its most elevated position in the southwest. The core of ridge α_2 is formed by reflectors of Unit 1 which often demonstrate an anticlinal fabric below the ridge crest (Figs. 3.2.1 and 3.2.14).

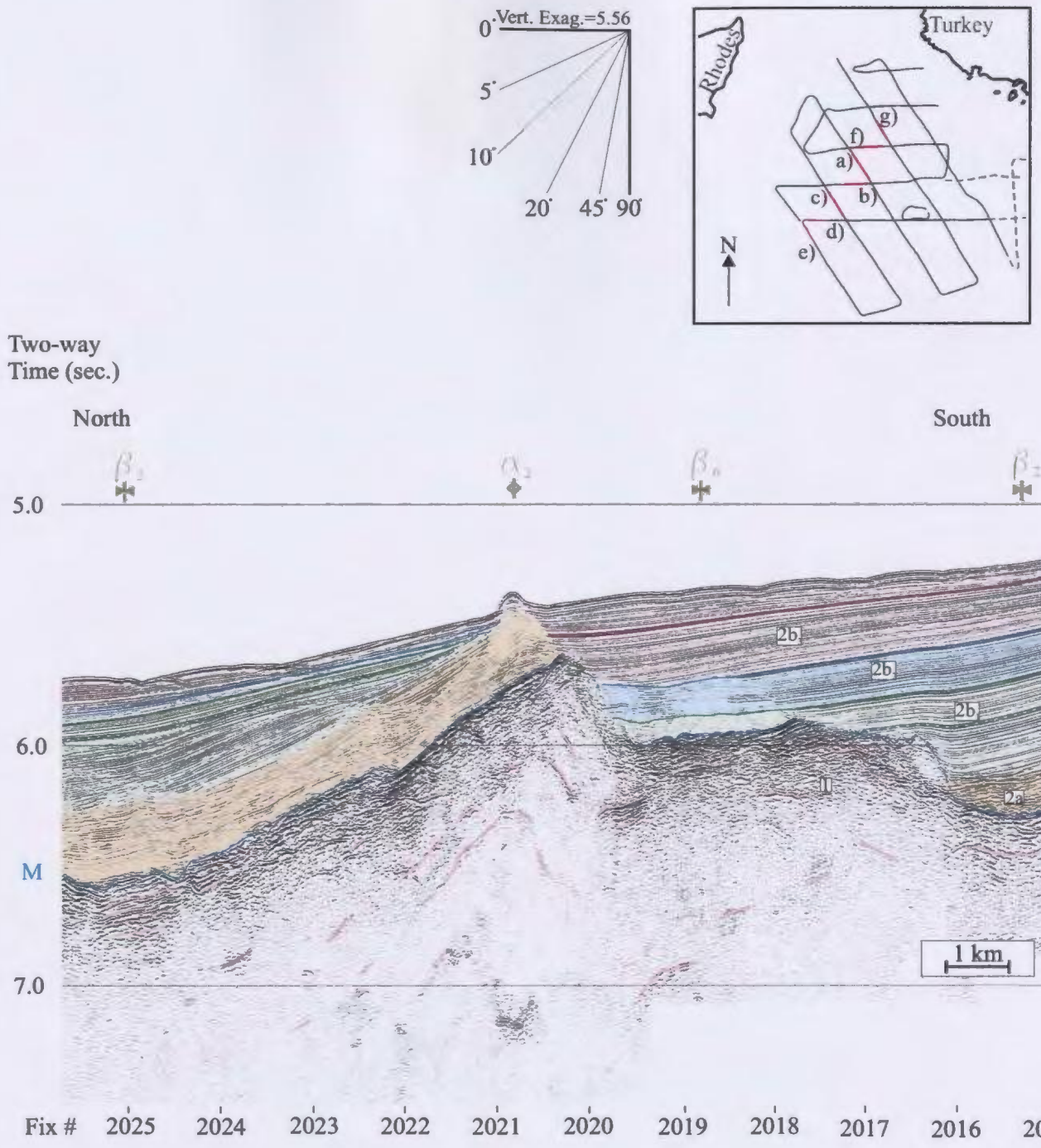

a)

Figure 3.2.14: Ridge α_2 trends northeast-southwest across lines a) 64, b) 80, c) 68 d) 70a, e) 70, f) 81 and g) 64a.

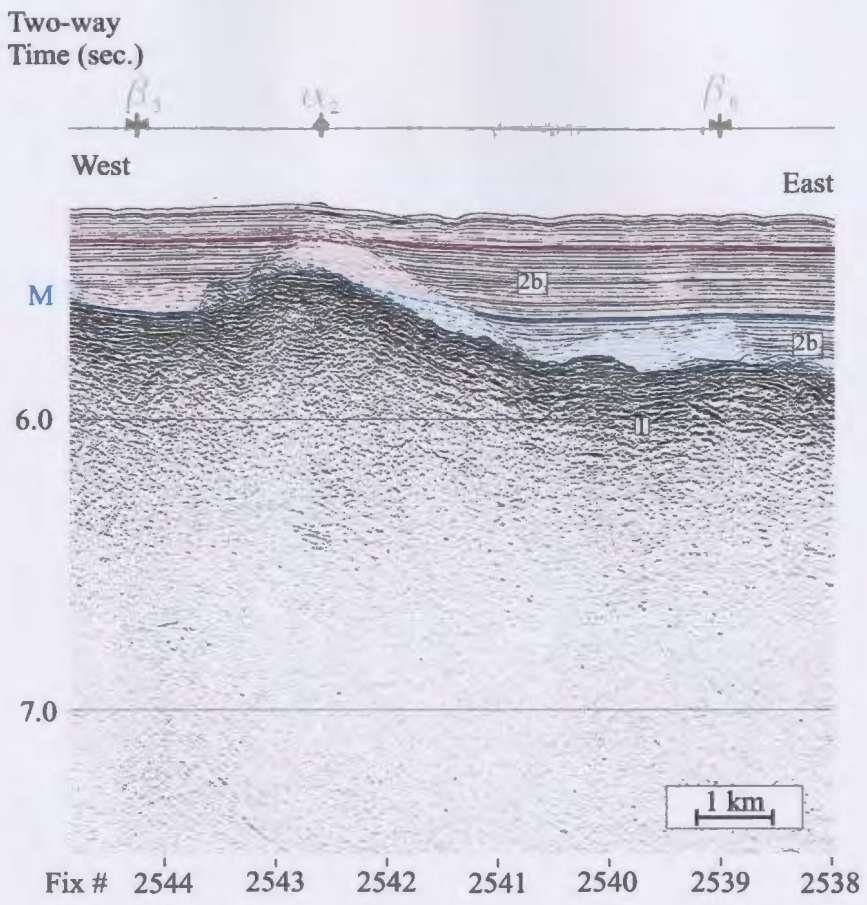

Figure 3.2.14b)

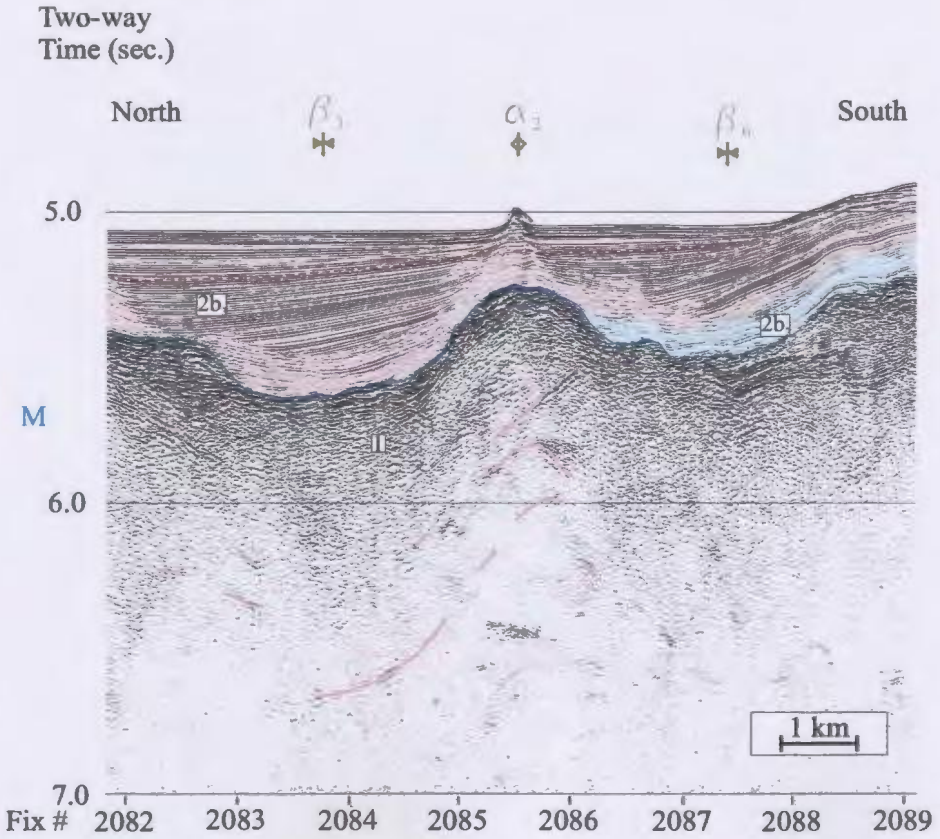

Figure 3.2.14c)

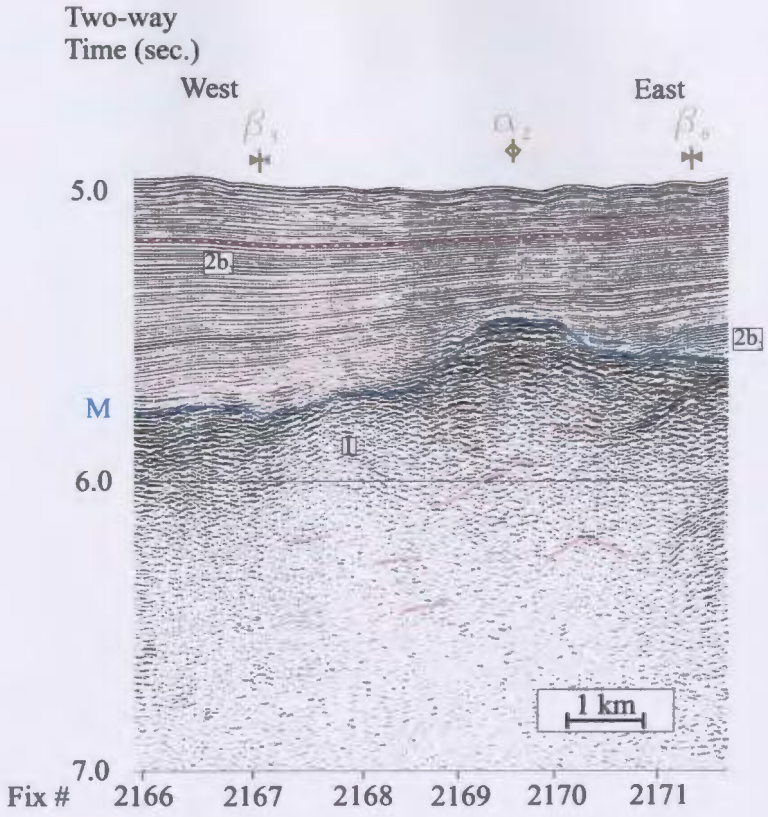

Figure 3.2.14d)

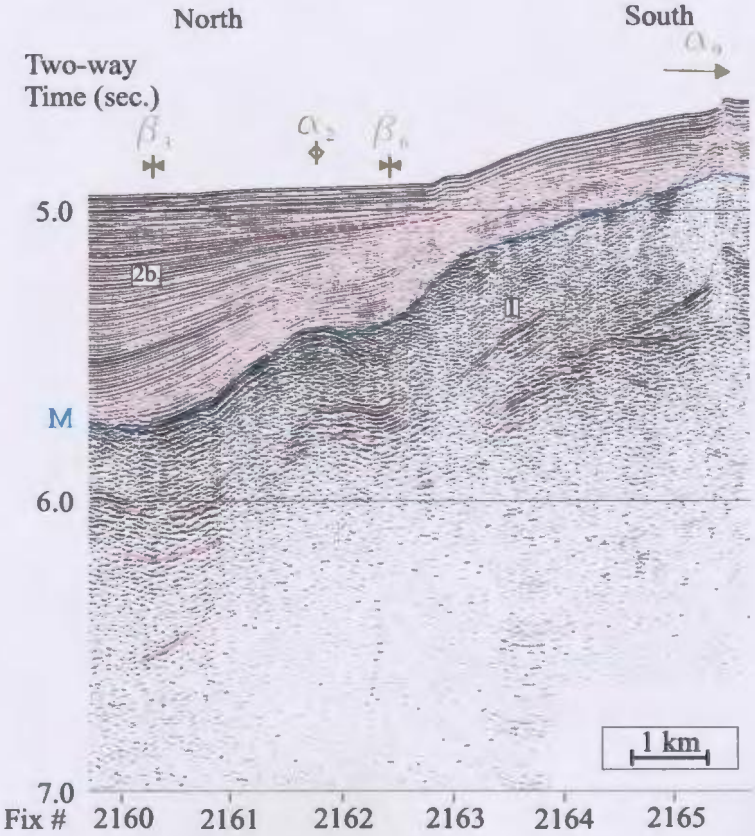

Figure 3.2.14e)

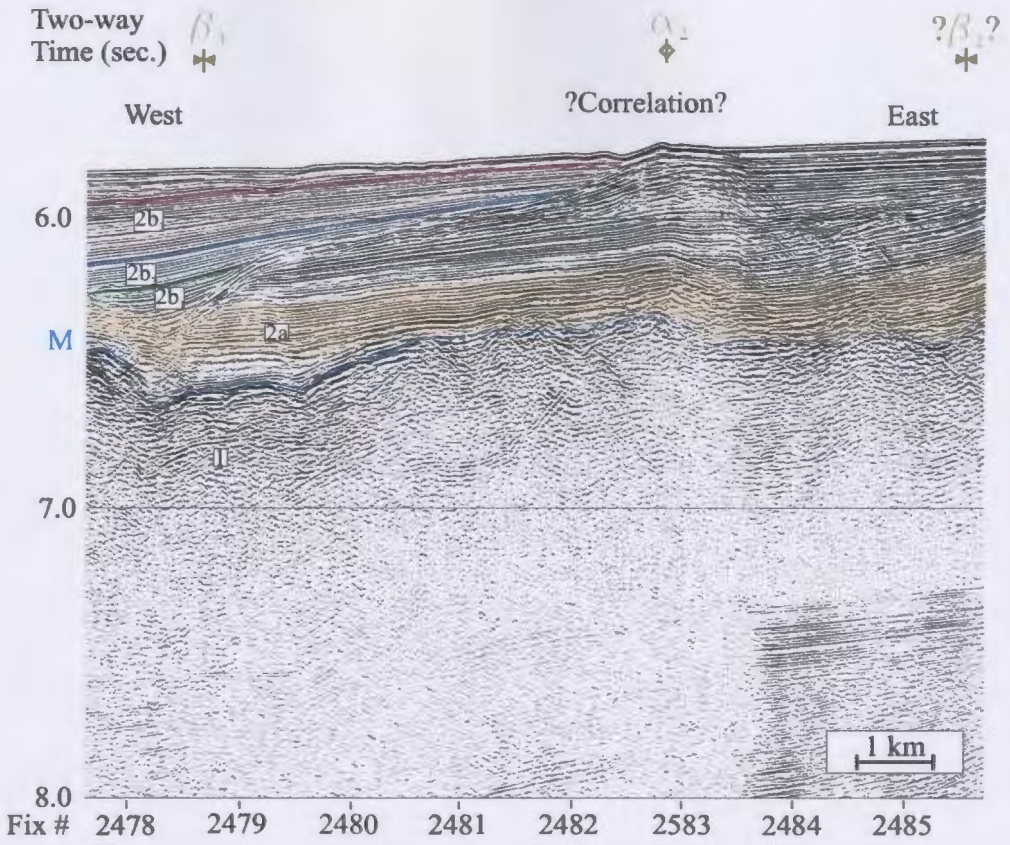

Figure 3.2.14f)

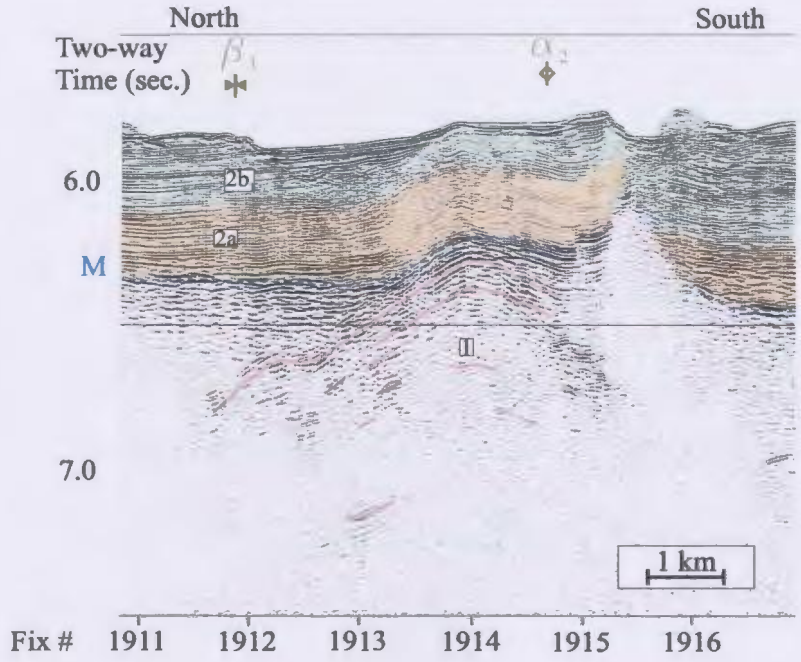

Figure 3.2.14g)

In the central portion of the study area, ridge α_2 is ~7 km wide and has a relief of ~400 ms above the adjacent basins (Fig. 3.2.14a). Unit 1 forms the core of the ridge and exhibits a weak antiformal fabric. Its northern flank is defined by a clearly imaged M reflector that dips ~7° NW. Subunit 2a covers this flank with a thick, lower portion that forms an ~200 ms-thick drape that generally lies parallel to the M reflector and demonstrates internal folding. A lower northward thickening portion of Subunit $2b_1$ onlaps onto Subunit 2a and clearly thickens toward the north via progressive internal onlap surfaces and the insertion of interbedded scattering lenses (Fig. 3.2.14a). Subunits the upper portion of $2b_1$ and Subunits $2b_2$ and $2b_3$ also thin up the northwestern flank of ridge α_2 as they onlap onto the surface of Subunit 2a. The southern flank of ridge α_2 is largely represented by an ~15° SE-dipping discontinuity across which the M reflector is vertically offset. Northward dipping and thickening Subunit 2b strata from basin β_2 and β_6 onlap against this discontinuous surface. A small bump on the seabed is observed just north of its shallowly-buried ridge peak (Fig. 3.2.14a).

Only ~7 km to the southwest where ridge α_2 intersects an east-west oriented survey line, it is considerably more subdued in appearance (Fig. 3.2.14b). The eastern flank of the ridge dips at ~5°E and is onlapped by sub-horizontal Subunit $2b_2$ and $2b_3$ reflectors that demonstrate slight upward bending toward the ridge (Fig. 3.2.14b). To the west of the crest, a small, down-to-the-west discontinuous offset affects Unit 1 of the ridge's western flank. Subunit $2b_3$ over steps the ridge crest and forms a 200 ms-thick

cover over the crest of the ridge.

Further southwest, ridge α_2 reaches a maximum width of only ~2 km wide and a relief of ~160 ms above basin β_3 to its north (Fig. 3.2.14c,d and e). Its northern slope dips ~15°NW whereas the southern flank has a more gentle ~10°SE slope. Both flanks are characterized by a discontinuous M reflector. Unit 1 forms the core of the ridge and, although it is generally unreflective, an anticlinal fabric is visible (Fig. 3.2.14c). Subunit $2b_2$ onlaps onto ridge α_2 from the southeast. On northeast-southwest oriented lines, Subunit $2b_3$ thickens toward the north, both away from the ridge crest (basin β_3) and toward the ridge crest from the south (basin β_6; Fig. 3.2.14c, e). The buried crest of ridge α_2 illustrates a slight, symmetric bulge of Subunit $2b_3$ directly over the ridge axis; generating a small rise on the seabed directly over the ridge (Fig. 3.2.14c). The far southwestern end of ridge α_2 attenuates rapidly and becomes little more than a bump on the northern limb of the much larger ridge α_9 (Fig. 3.2.14d, e).

At its northeastern extremity, ridge α_2 separates basin β_3 from basin β_2 (Fig. 3.2.14f, g). Here, the underlying discontinuous Unit 1 shows an antiformal internal fabric (Fig. 3.2.14f). The M reflector is also discontinuous, but outlines the asymmetric shape of the small ridge. Its shallowly-dipping, irregularly-shaped western flank is onlapped by Subunit 2b from the west. The thickness of this Subunit 2a succession stays between ~160 and 200 ms. The southeastern edge of ridge α_2 is marked by an ~200 ms vertical offset of the M reflector and the overlying Subunit 2b across a discontinuity. Subunit 2a maintains a constant thickness on both sides of the discontinuity. The overlying Subunit 2b

reflectors appear conformable with Subunit 2b. At this location, ridge α_2 is buried under ~550 ms of subunits 2b and 2c. As at its other localities, the seabed bulges slightly upwards directly above the crest of the ridge.

Ridge α_3:

Ridge α_3 is a northeast-southwest trending antiformal structure that lies just northwest of escarpment ϵ_1 (Fig. 3.2.1). It reaches a maximum width of ~6 km and achieves a maximum vertical relief of ~700 ms above the adjacent basins.

The most pronounced expression of ridge α_3 in the southeastern area illustrates ~13°NW-dipping Unit 1 reflectors that run nearly parallel to the M reflector along the ridge's northwestern flank and are continuous with a synformal Unit 1 architecture in the southern part of basin β_2 (Fig. 3.2.15a). Beneath the crest of the ridge, these fabrics turn over to form an antiform. The northwestern flank of ridge α_3 provides ~500 ms of relief over its ~15°NW-dipping margin with basin β_2. Its southeastern, more steeply dipping flank displays two discontinuous offsets that each provide ~ 450 ms and ~200 ms of vertical separation of the M reflector respectively. The southernmost of these two discontinuities also cuts the overlying, well-bedded, high amplitude reflectors of Subunit 2a. Subunits 2a and $2b_1$ onlap onto both flanks of the ridge. The upper portion of Subunit $2b_1$ and subunits $2b_2$-$2b_3$ bulge upwards over the ridge and cover its crest with an ~350 ms cover that becomes increasingly disturbed in appearance with progression toward the ridge apex. The seabed is also deformed upward directly over the ridge crest.

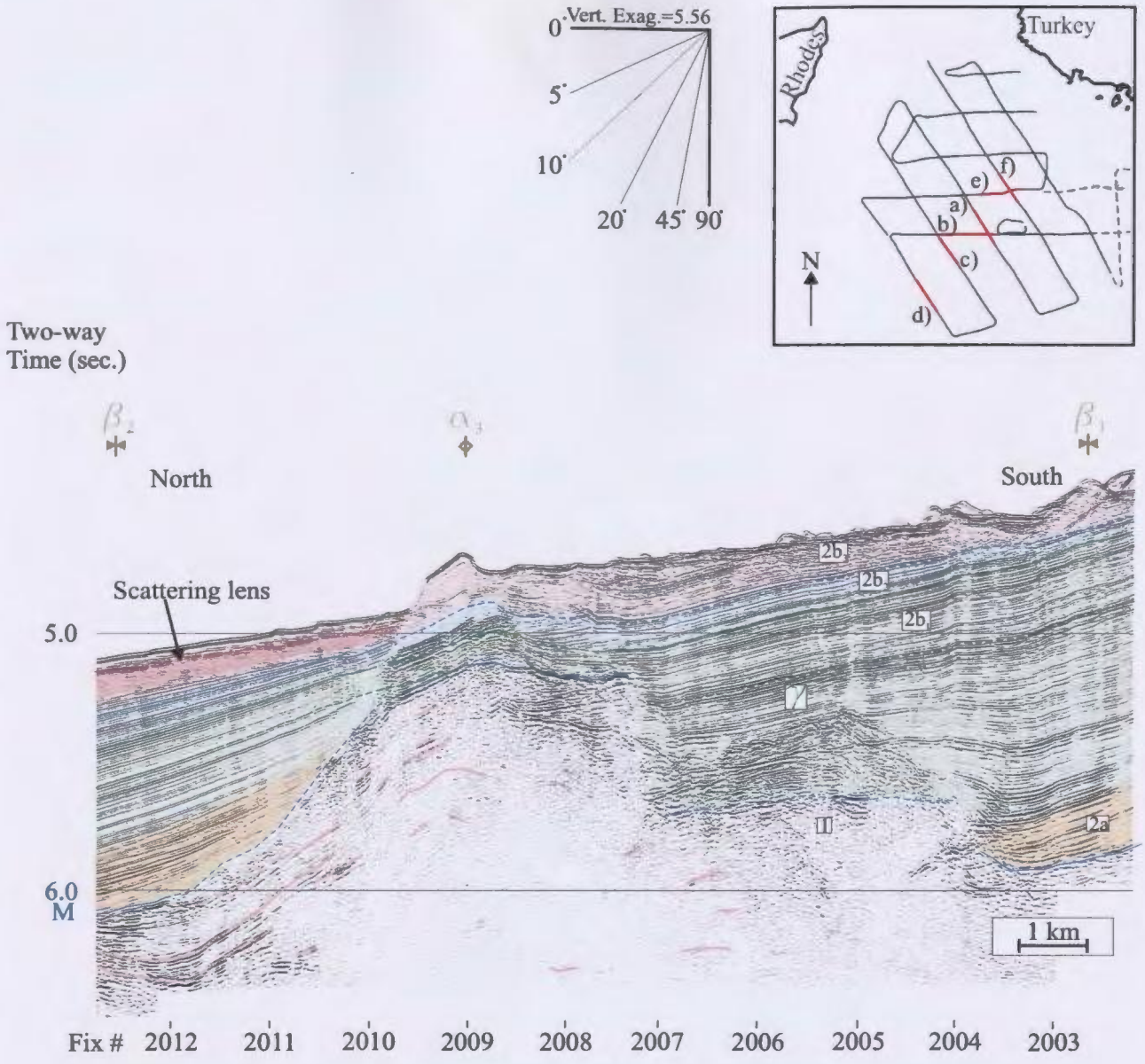

a)

Figure 3.2.15: Ridge α_3 trends northeast-southwest across the central portion of the survey area. It is most pronounced on a) line 64 but is also seen to cross lines b) 70a, c) 68, d) 70, e) 80 and f) 64a.

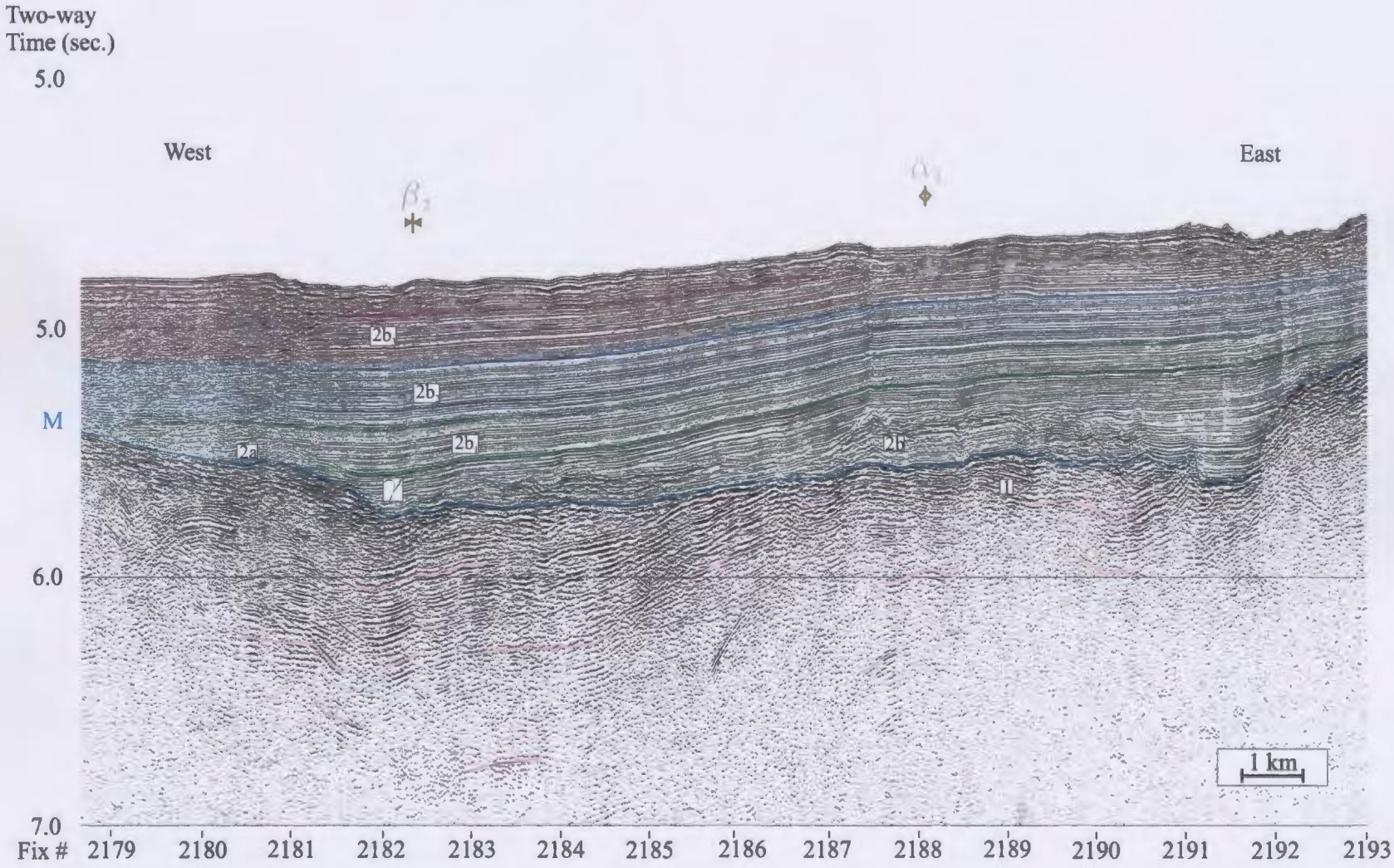

Figure 3.2.15b)

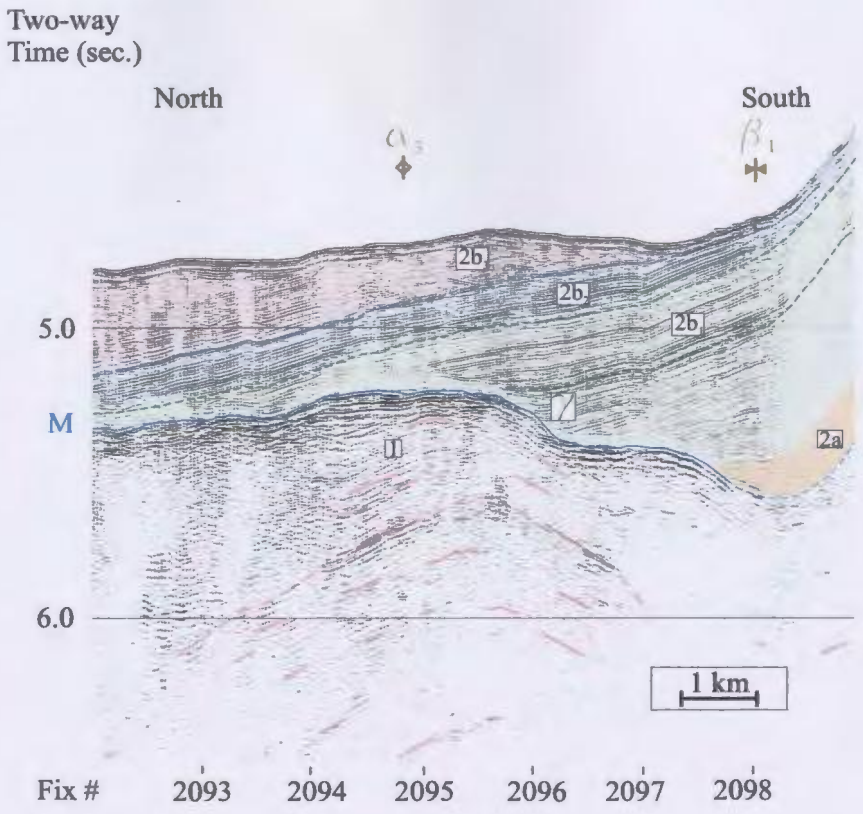

Figure 3.2.15c)

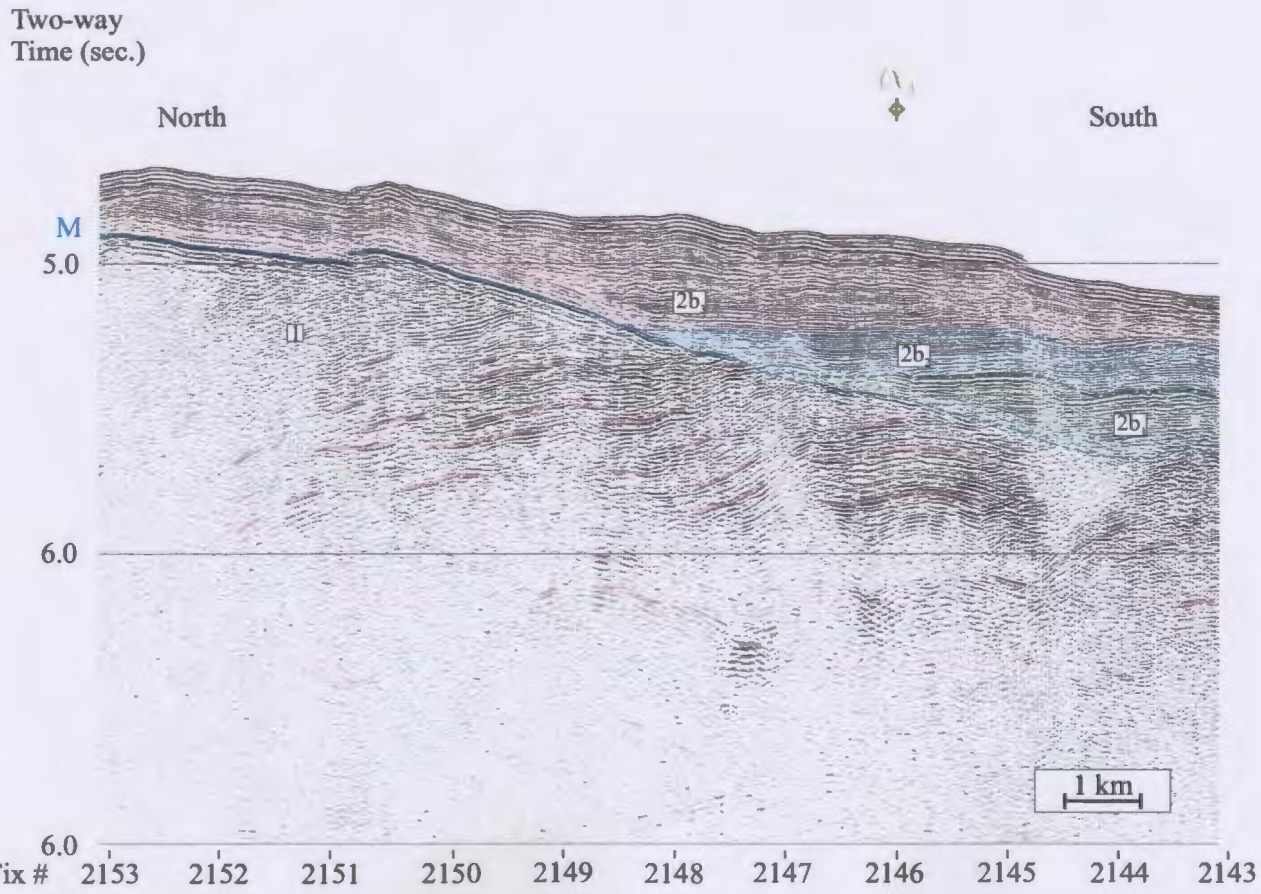

Figure 3.2.15d)

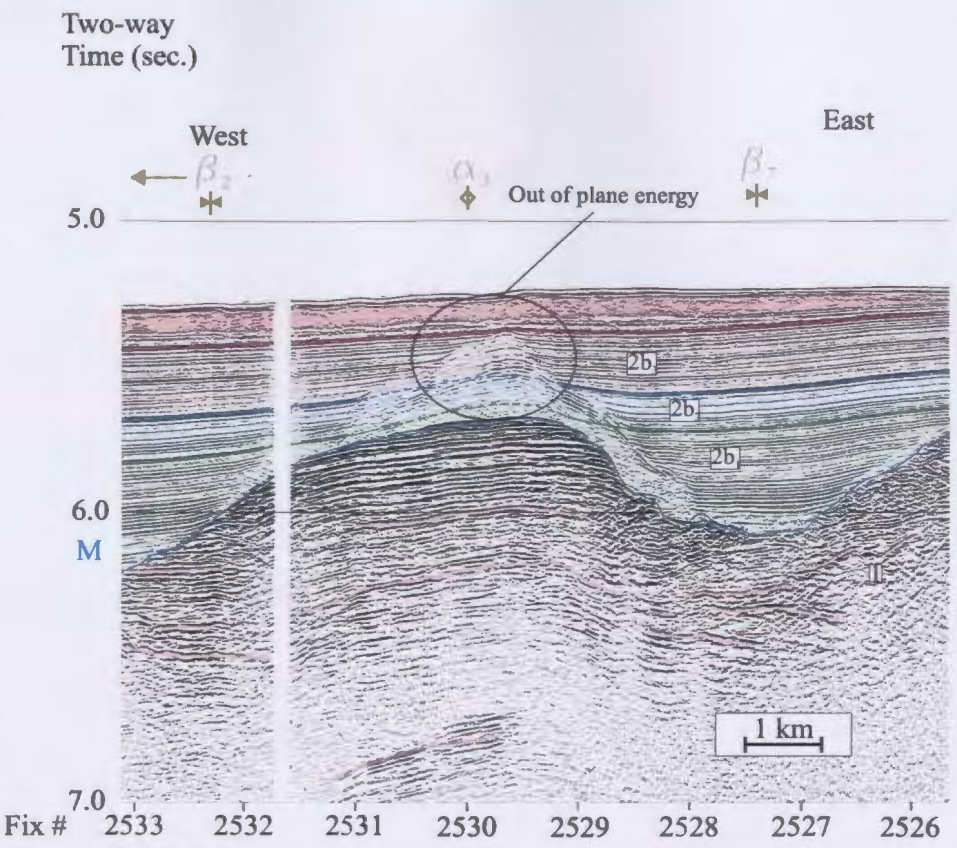

Figure 3.2.15e)

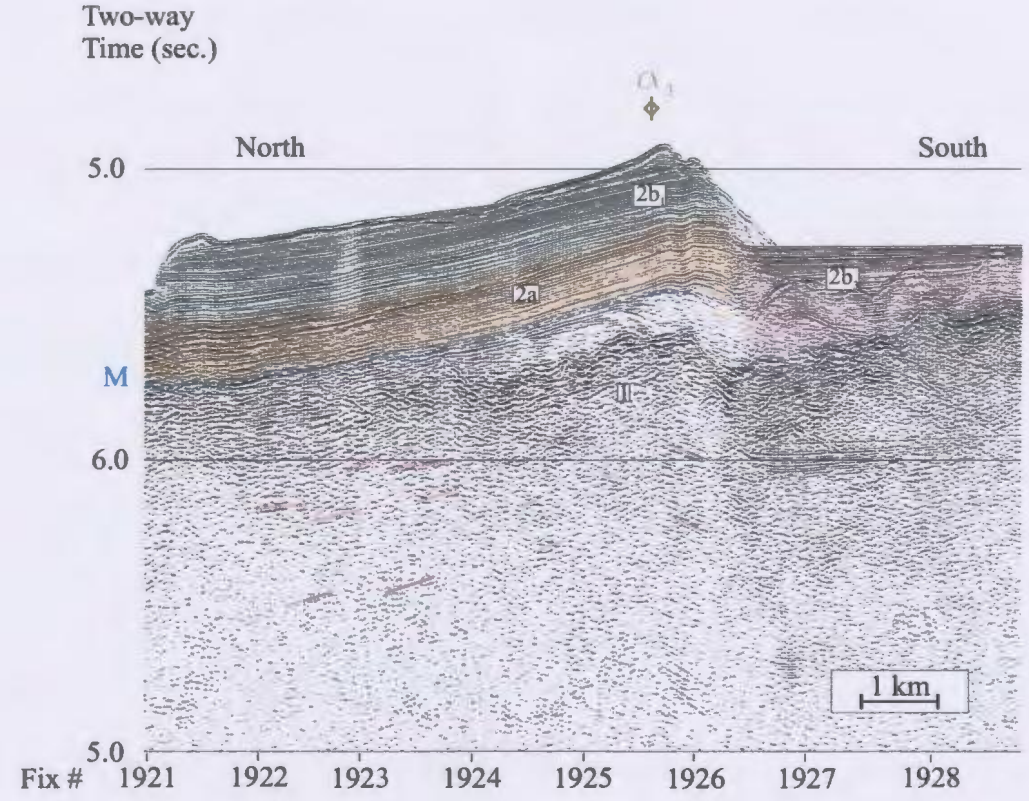

Figure 3.2.15f)

Only 4.5 km to the southwest, ridge α_3 lies east of basin β_2 and is ~7.5 km wide, but shows minimal relief along its sub-horizontal (>1°W and E-dipping) limbs (Fig. 3.2.15b). Unit 1 reflectors show an antiformal architecture with both ~3°W and ~1°E dipping reflectors that form an angular unconformity with the overlying M reflector. Gently westward-dipping Subunit $2b_1$, continuous with basin β_2, onlap onto the M reflector from both the east and west before quickly overstepping and burying the subdued ridge. Subunits $2b_2$ and $2b_3$ also gently dip and thicken toward the west. The combined thickness of Subunit 2b covers the crest of ridge α_3 below ~860 ms of sediment (Fig. 3.2.15b).

Further toward the southwest, ridge α_3 is ~6-7 km wide and contains a clear, antiformal Unit 1 fabric beneath the ridge crest (Fig. 3.2.15c). The erosive M reflector defining its morphology is onlapped by the northwest-dipping subunits 2a and $2b_1$ from basin β_1. Subunits $2b_2$ and $2b_3$ overstep the ridge crest and continue to thicken northward, burying the crest of the ridge under ~550 ms of basin fill (Fig. 3.2.15c). A short distance to the southeast a Unit 1 antiformal fabric marks the crest of ridge α_3 but is more heavily eroded that it is to the northeast (Fig. 3.2.15d). Here, the ridge is overstepped and buried by Subunits $2b_1$-$2b_3$.

To the northeast of its most pronounced location, ridge α_3 is a 4.25 km-wide high-stand located between basins β_2 and β_7 (Fig. 3.2.15e). The gently westward-dipping (~1°W), highly reflective Unit 1 reflectors illustrate a flat-crested antiformal architecture directly below the ridge crest with a steeper limb (~3°E) on the antiform's eastern flank.

Outside of each of the ridge margins, the Unit 1 fabric is nearly horizontal. The M reflector shows a relief of ~ 200 ms along its ~6°W-dipping western margin and ~50 ms of relief along its ~9°E-dipping eastern margin. Subunit 2b reflectors maintain a rather uniform thickness and lie sub-horizontal, except for a slight upward bulge over the ridge crest. Subunit $2b_1$ onlaps onto the flanks of the ridge and narrowly oversteps the ridge crest to thinly cover it (Fig. 3.2.15e). Subunits $2b_2$ and $2b_3$ completely cover the ridge crest and bury it under ~440 ms of sediment. The thickness of this $2b_2$ and $2b_3$ cover may decrease slightly over the ridge crest and thicken symmetrically toward the east and west. A symmetric scattering lens reaches its maximum thickness over the crest of ridge α_3 and is continuous with both β_2 and β_7 where it pinches out toward both the east and west.

If correlatable any further to the northeast, ridge α_3 may exist as a minor elevation of Unit 1 that borders the northern end of basin β_7 (Fig. 3.2.15f). The M reflector outlines an irregular basement surface that truncates poorly imaged, discontinuous Unit 1. This ridge is overlaid by an ~2°NW-dipping, ~500 ms-thick drape of Subunits 2a and $2b_1$ that are internally conformable and appear to be conformable with the M reflector. These are juxtaposed against the northwestward thickening and dipping reflectors of Subunit $2b_3$ from the neighbouring basin β_7 (Fig. 3.2.15f). Here, ridge α_3 measures ~4 km wide and provides ~100 ms of relief above the basin β_7 margin along a 10°SE down-to-the-southeast-dipping discontinuity (Fig. 3.2.15f).

Ridge α_4:

Ridge α_4 represents the northernmost portion of the elevated plateau. Like basin β_1, ridge α_4 is correlated across the southern portion of the study area with a short, north northeast-south southwest trend at long eastern leg that rotates sharply to a more east-west trend across the remainder of the study area (Figs. 3.1.6 and 3.2.16). Its core consists of a weakly reflective Unit 1 that occasionally demonstrates an antiformal fabric culminating directly below the ridge axis. The M reflector is elevated by as much as 1500 ms above the basin β_1 axis directly to its north (Figs. 3.2.16) The ~15° northward-dipping flank of the ridge accommodates this gradient in the elevation of the M reflector, and overlying Subunit 2a and $2b_1$, along both continuous (e.g., Fig. 3.2.16a and b) and discontinuous (e.g., Fig. 3.2.16c) margins with the neighbouring basin β_1. The overlying Subunit 2a and $2b_1$ reflectors often form a thick, cover over the crest of the ridge and occasionally illustrate gentle folding and/or discontinuous offsets. The younger, Subunit $2b_2$ and $2b_3$ reflectors appear more discontinuous and demonstrate increased northward thickening into basin β_1 from the edge of the ridge's northern flank.

Ridge α_5:

Ridge α_5 trends ~north northwest-south southeast along the Turkish slope immediately east of the westwardly-dipping escarpment ϵ_2. Its axis generally plunges gently toward the north (Fig. 3.2.1). It enters the southern extent of the survey area from the east where it is trending ~east-west. At its southernmost extent, ridge α_5 is a broad

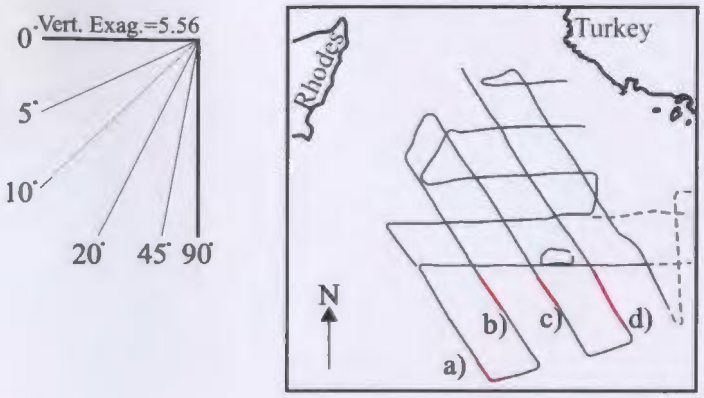

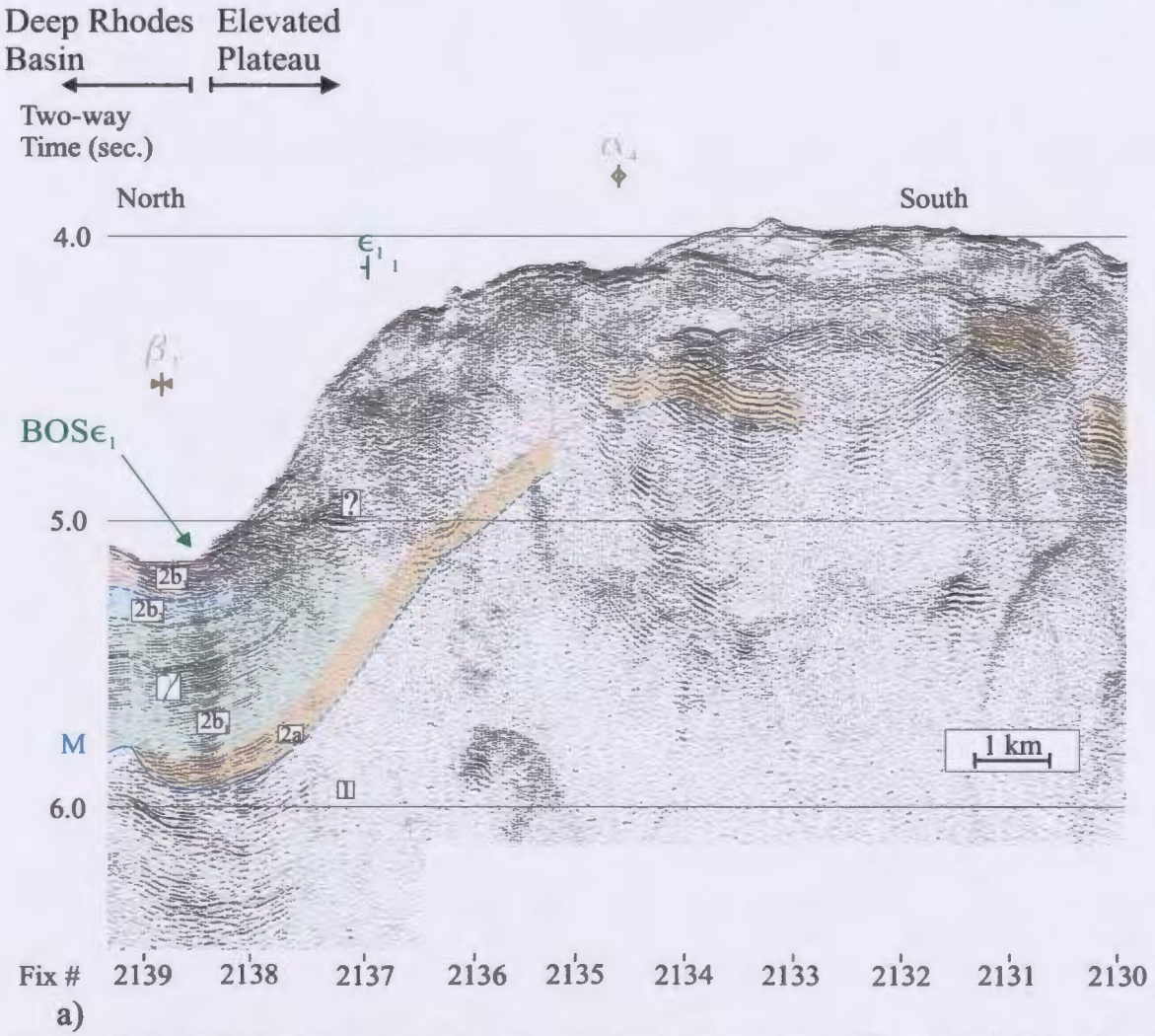

Figure 3.2.16: Ridge α_4 represents the northmost portion of Domain 1. It is shown here at its intersections with a) line 70, b) line 68, c) line 64 and d) line 64a.

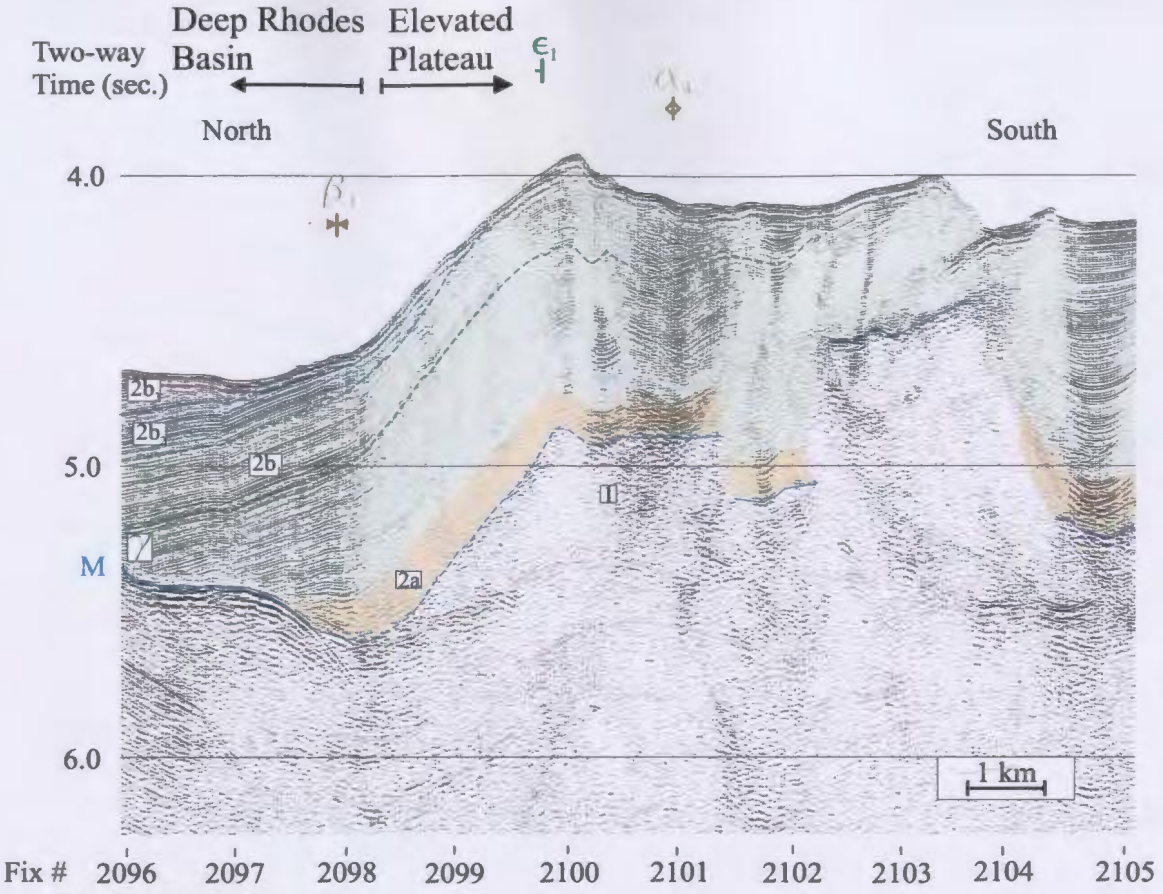

Figure 3.2.16b)

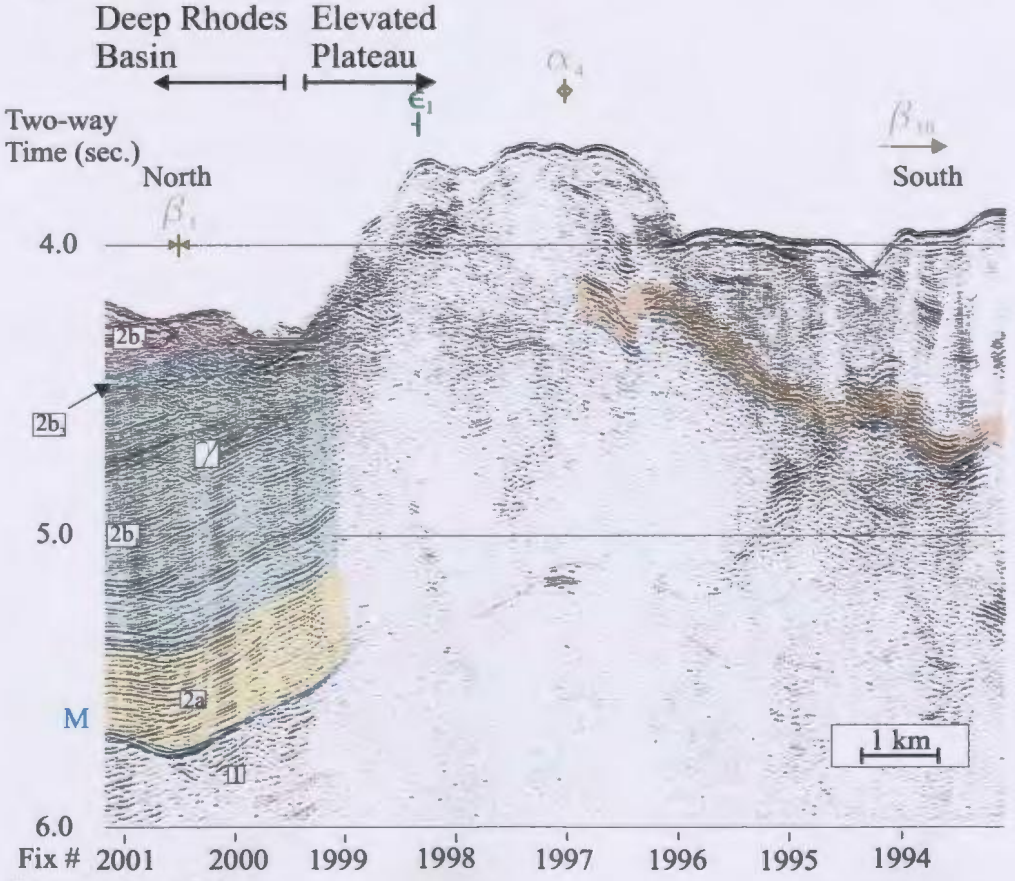

Figure 3.2.16c)

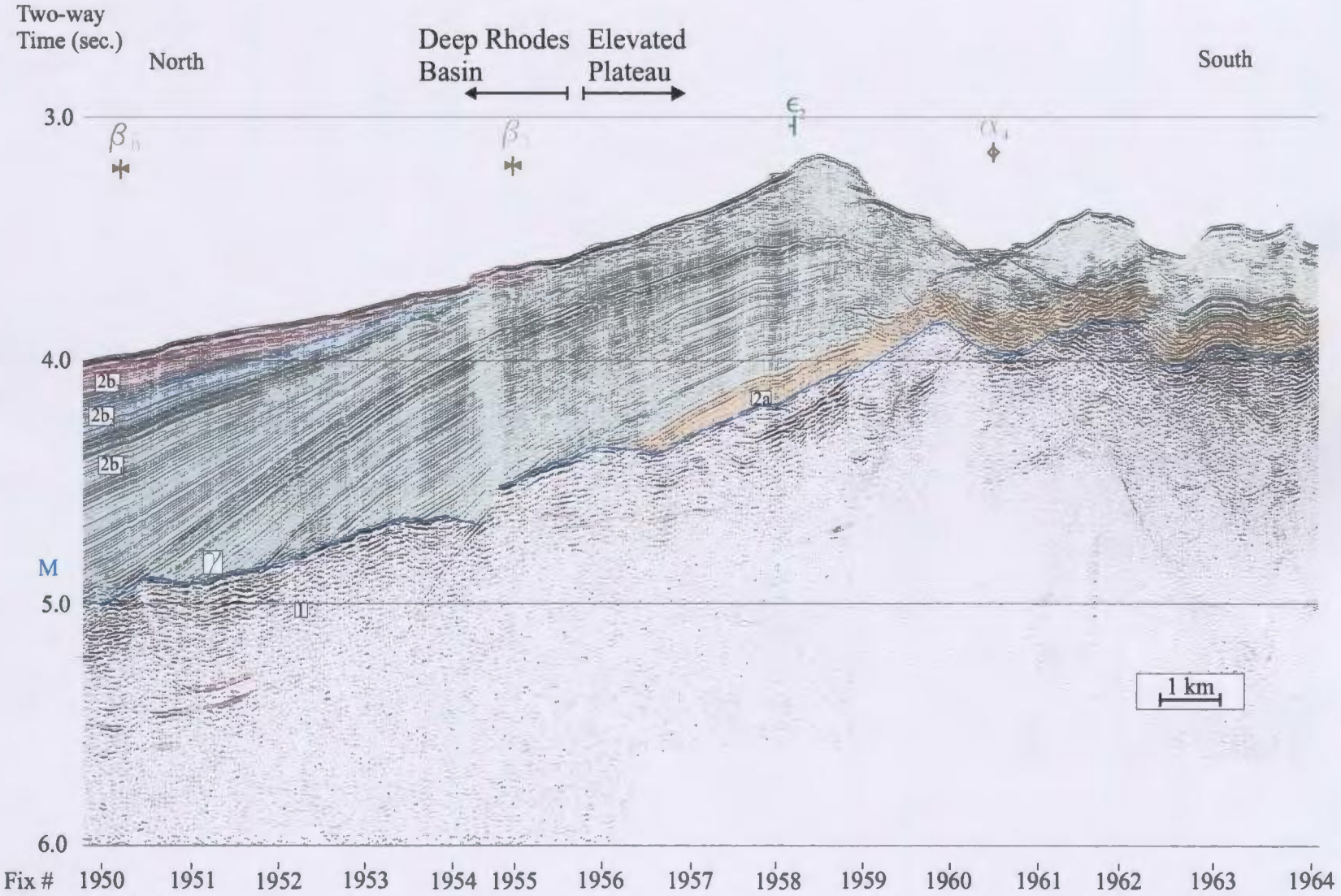

Figure 3.2.16d)

(~9 km wide), subdued Unit 1 high-stand buried underneath ~300 ms of gently northwestward-dipping Pliocene-Quaternary (Subunit $2b_1$) sediment (Fig. 3.2.17a). Immediately to the west of this location, ridge α_5 turns sharply toward the north where the M reflector is clearly erosive and forms an angular unconformity with the underlying, ~5°NW-dipping Unit 1 reflectors (Fig. 3.2.17d). The ridge crest has a large vertical relief of ~1900 ms above the axis of the adjacent basin, basin β_8 (Fig. 3.2.17d). The thickness of the Pliocene-Quaternary cover over the ridge generally decreases and becomes more intermittent toward the north, often onlapping onto the M reflector along the ridge flanks. Basin β_{11}, immediately adjacent the to ridge, illustrates clear internal growth and onlapping unconformities within its Subunit $2b_1$ fill (Fig. 3.2.17c).

Ridge α_6:

Ridge α_6 is a broad, northward-trending high that lies immediately east of escarpment ϵ_1 (Fig. 3.2.1). Its crest has a large vertical relief of ~ 340-850 ms above the adjacent basins β_2 and β_8 (Fig. 3.2.18).

At its southernmost end where it separates basin β_2 from basin β_8, ridge α_6 is cored by a weakly reflective Unit 1 whose reflectors delineate an antiformal architecture continuous with the synformal architecture below basin β_8. The M reflector is onalpped by Subunit 2b ($2b_1$-$2b_3$) of basins β_2 and β_8. Only Subunit $2b_3$ oversteps the ridge to thinly cover its crest. The seabed directly above the ridge apex is bulged upward.

Further north, ridge α_6 is bound to the west by the escarpment ϵ_1 (Fig. 3.2.18b and

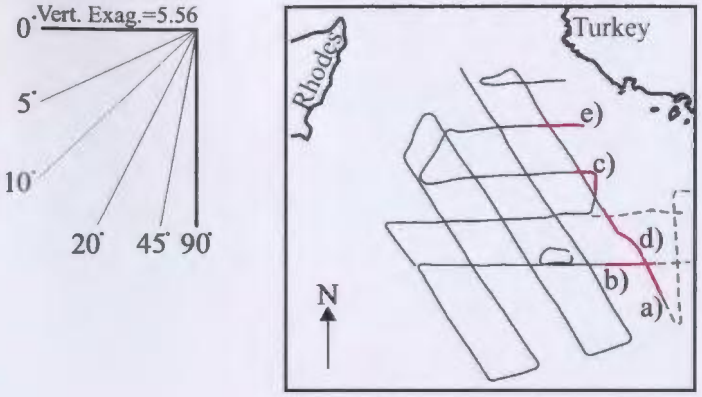

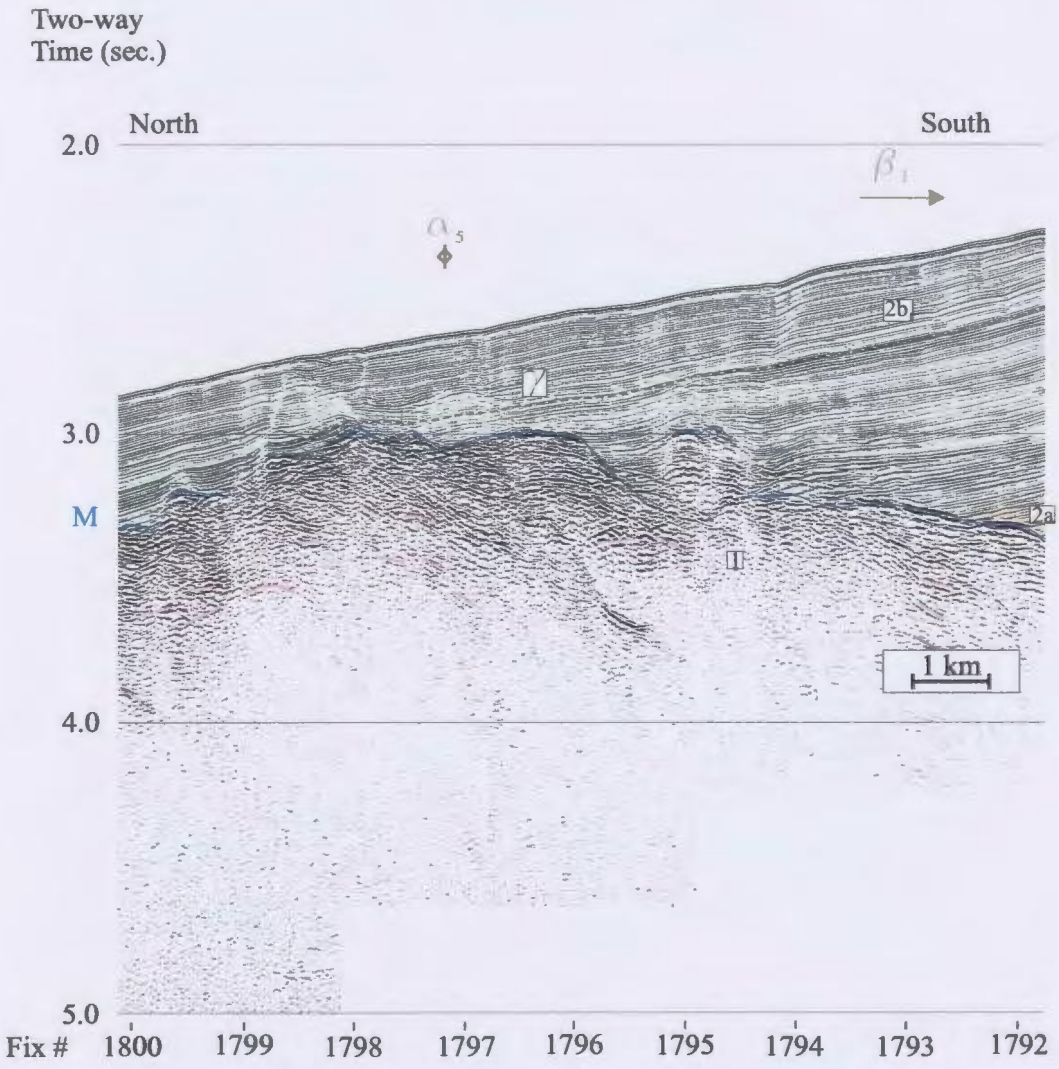

a)

Figure 3.2.17: Ridge α_5 parallels the edge of the Turkish slope along the eastern edge of the Rhodes Basin where it crosses a) line 60, b) line 70a, c) line 80, d) line 60 and e) line 83.

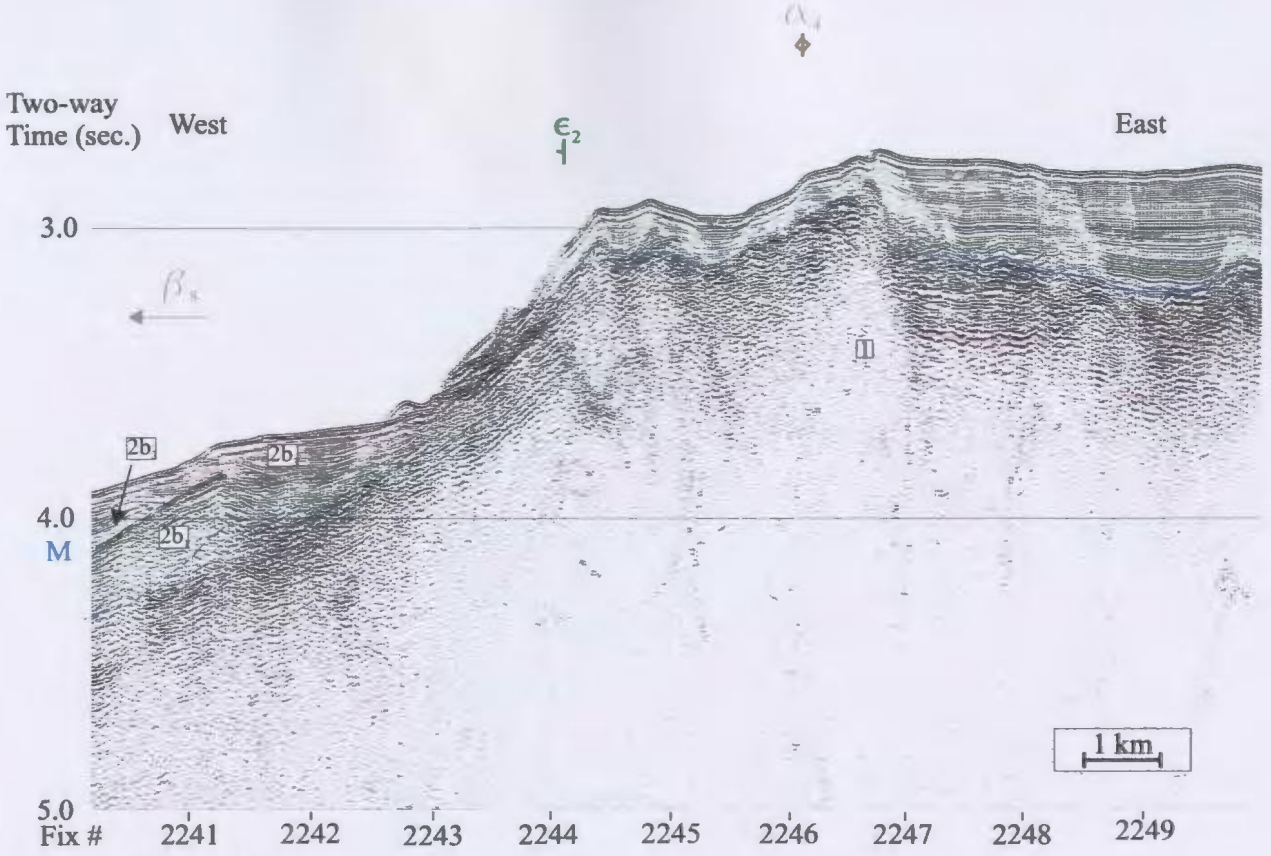

Figure 3.2.17b)

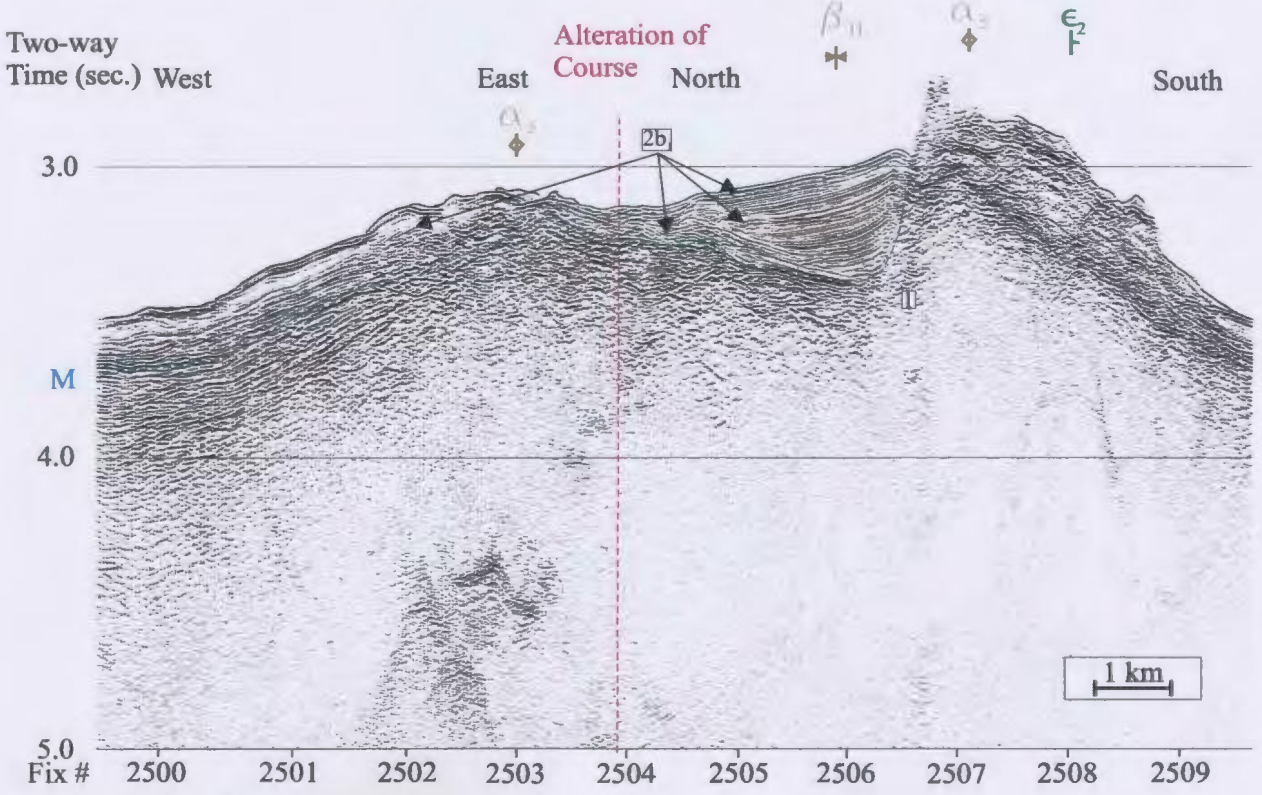

Figure 3.2.17c)

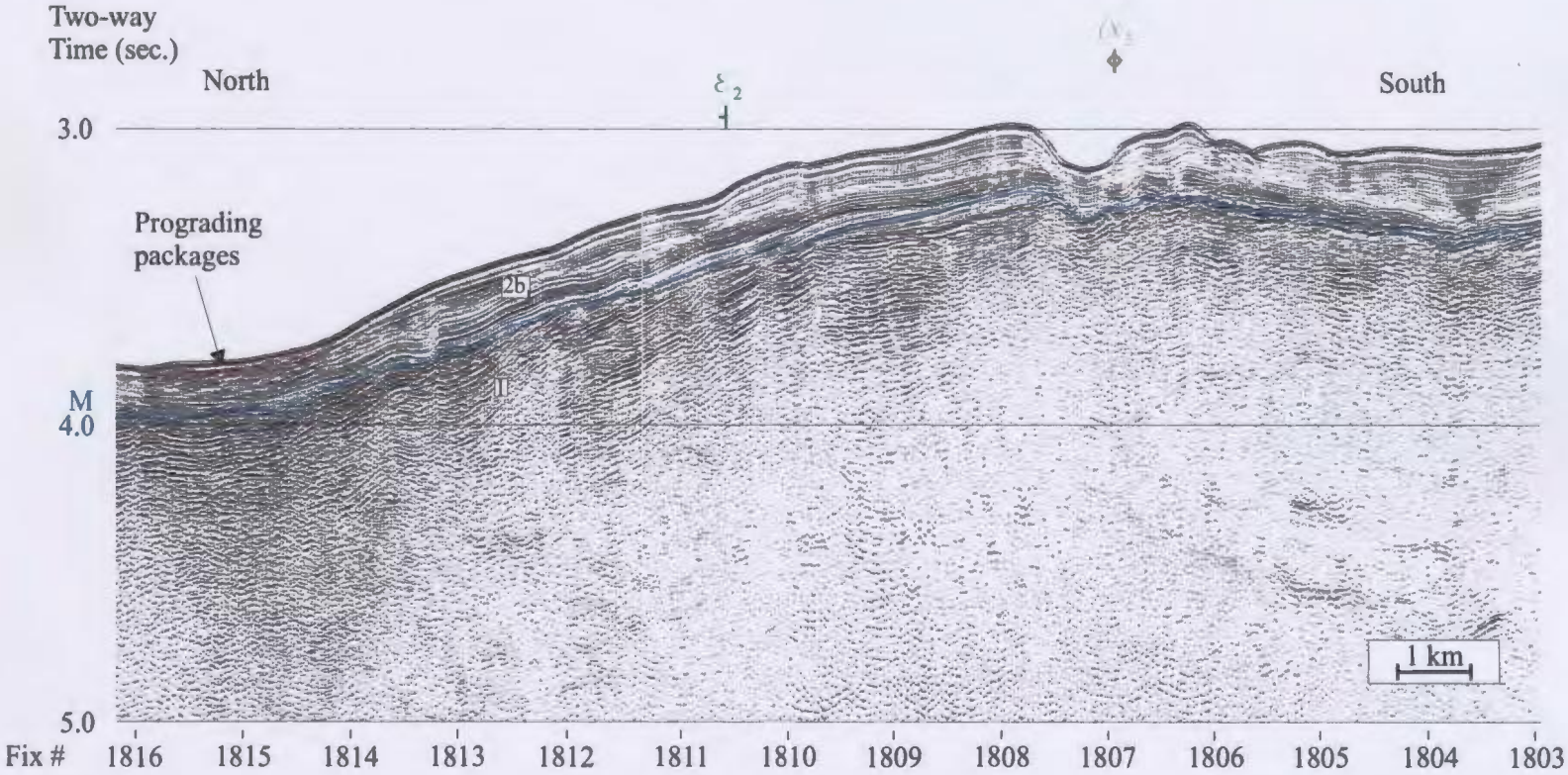

Figure 3.2.17d)

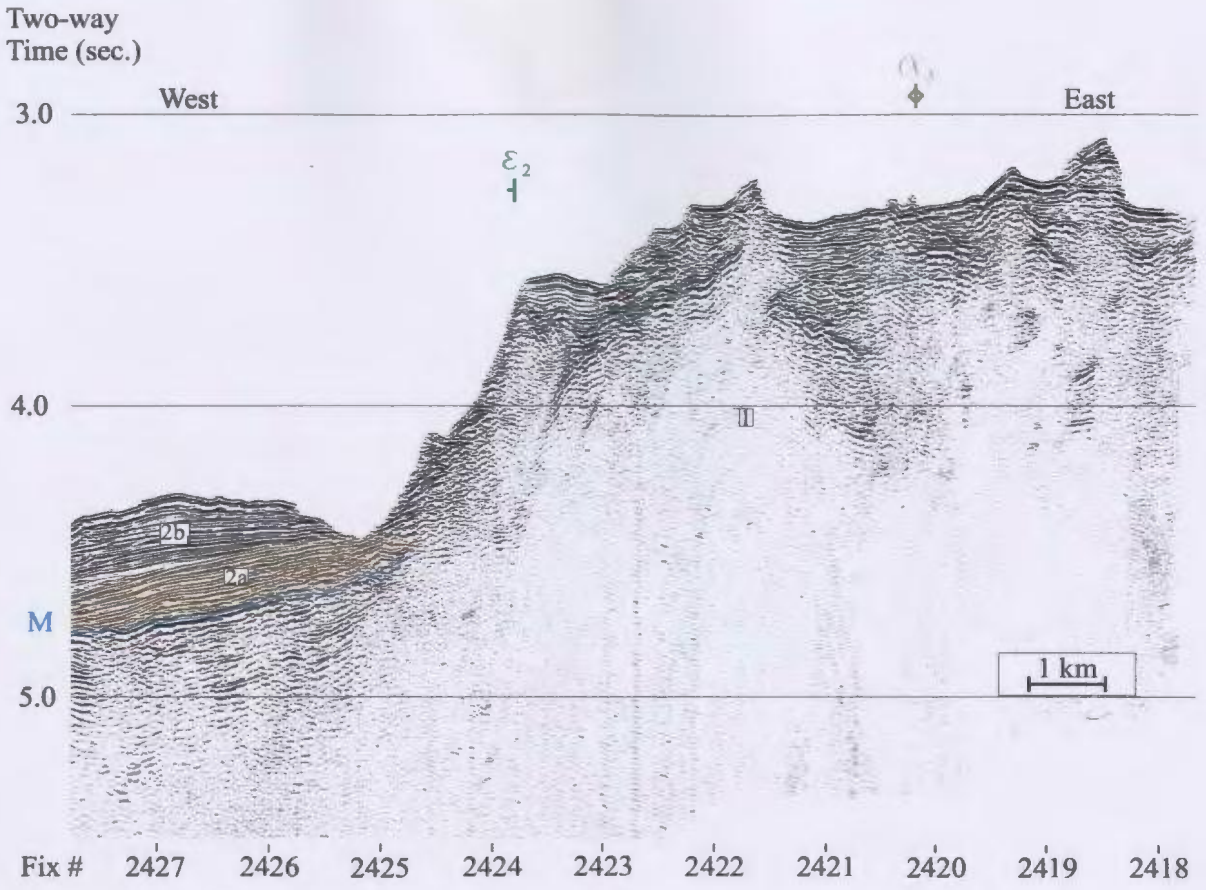

Figure 3.2.17e)

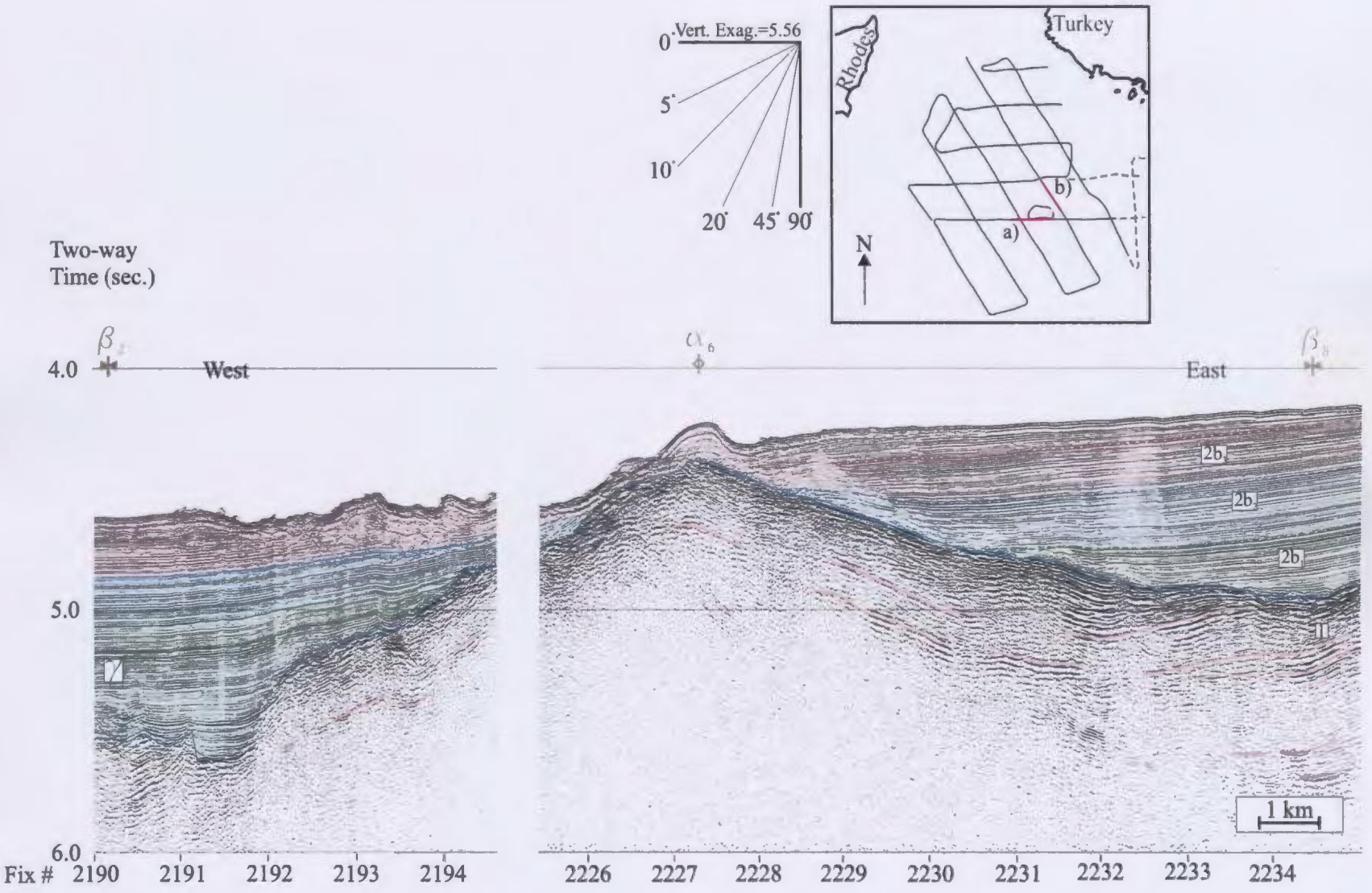

a)

Figure 3.2.18: Ridge α_6 trends north northwest-south southeast across the eastern portion of the survey area. a) line 70a, b) line 64a and c) line 80.

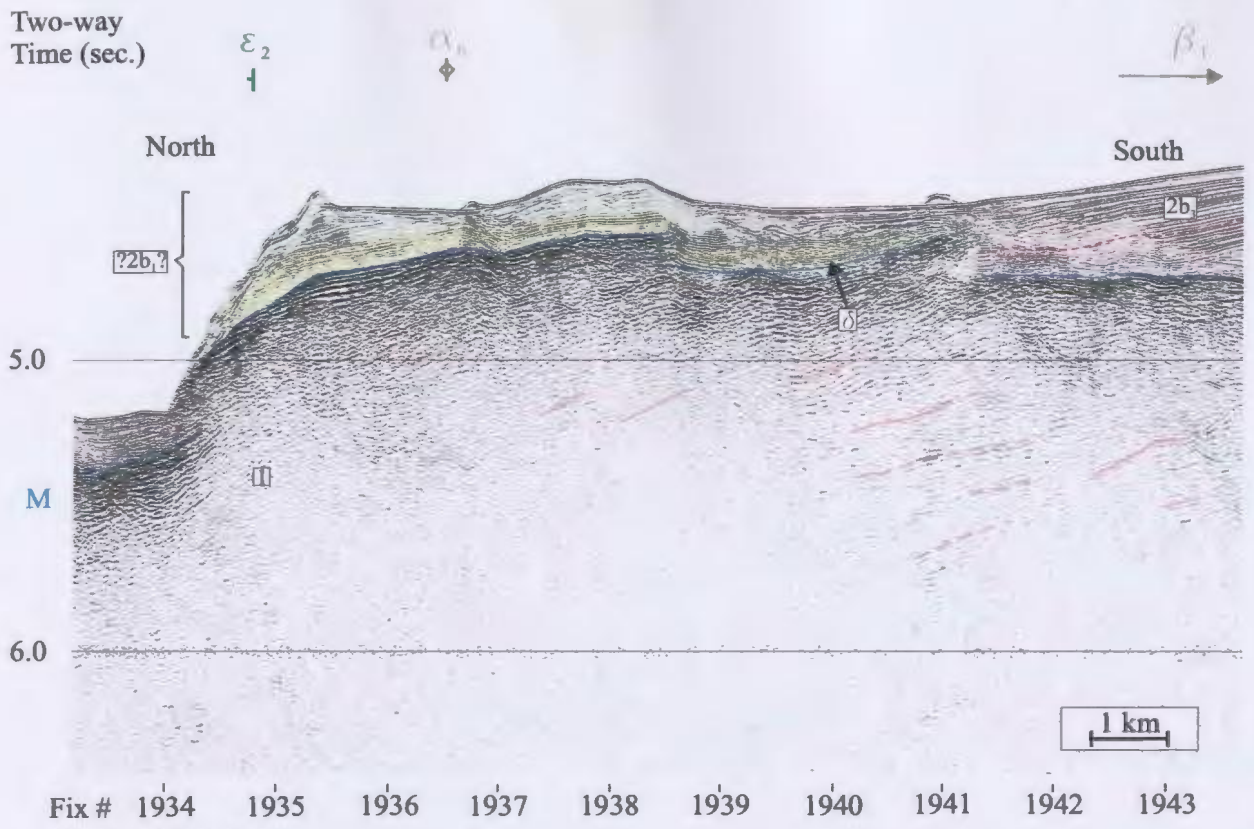

Figure 3.2.18b)

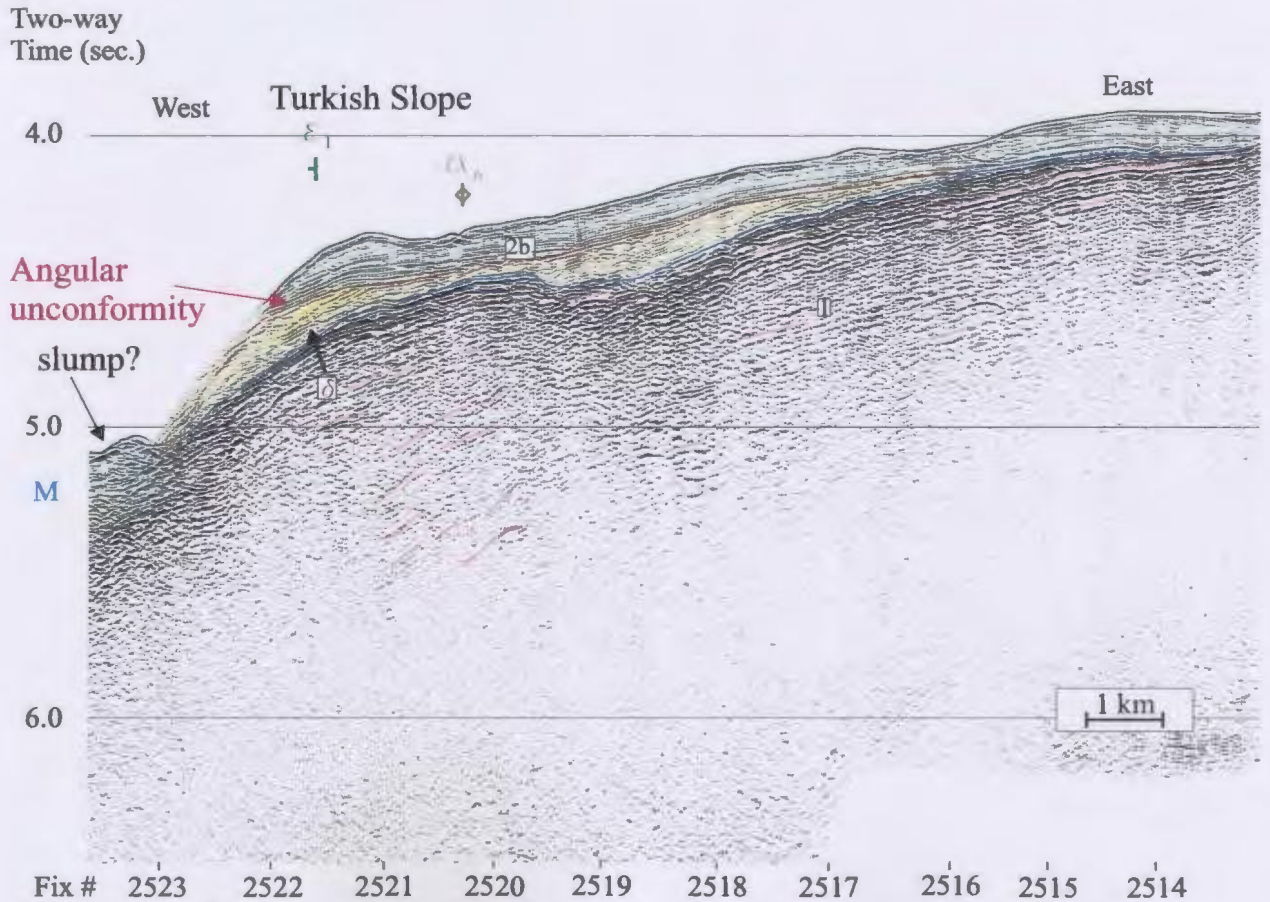

Figure 3.2.18c)

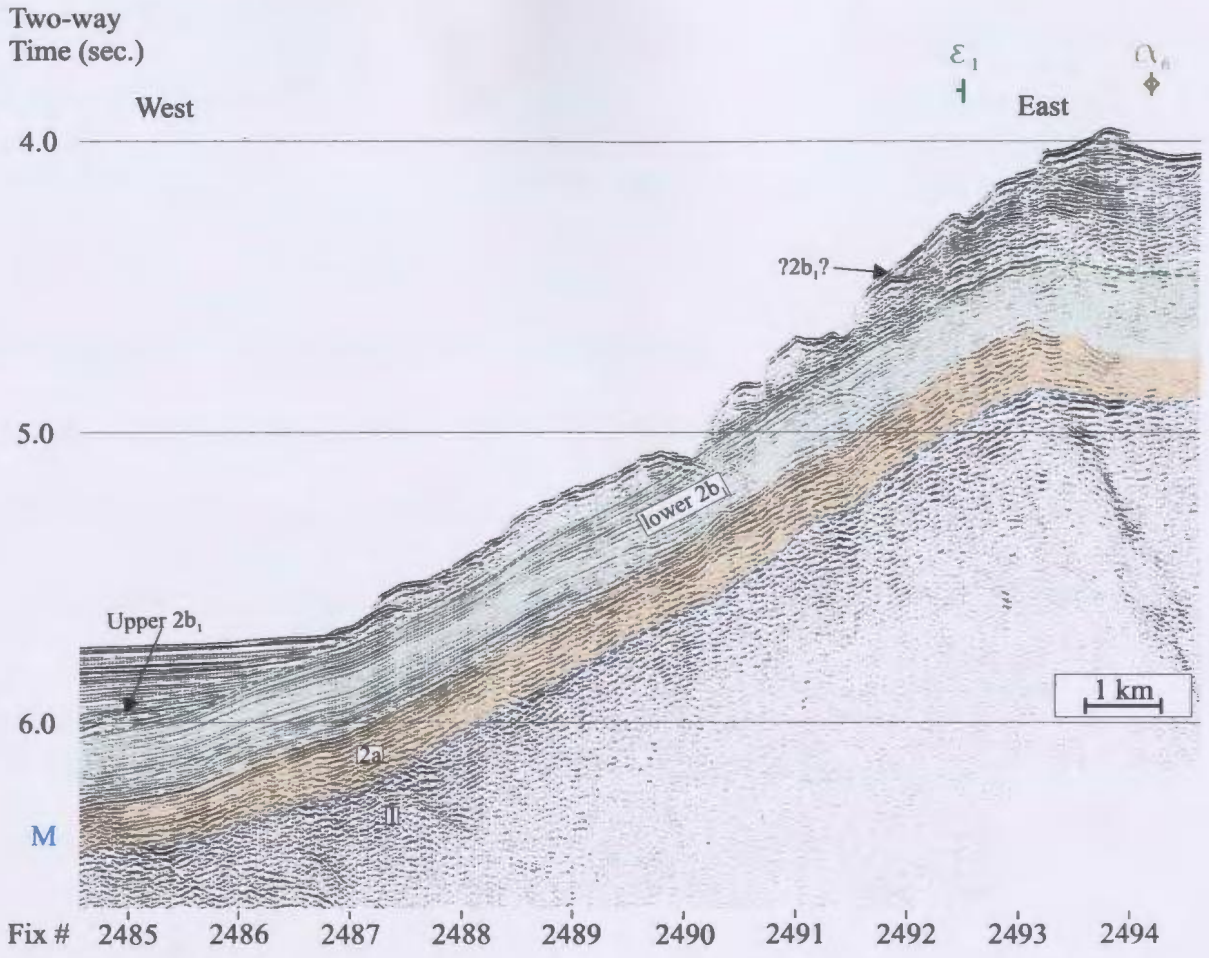

Figure 3.2.18d)

c). At its core, Unit 1 reflectors dip ~2-4°NW but appear to culminate further to the east near the margin with basin β_8. Toward the east these dipping reflectors are truncated at the M reflector to form an angular unconformity (Fig. 3.2.18c). Over the crest of ridge α_6, a thin cover of what has been identified as the δ package (older than Subunit $2b_1$) forms a westward-dipping supra-M reflector package bound on its top surface by an angular unconformity. Parallel-bedded Subunit $2b_1$ reflectors overlie this unconformity and appear onlapped by Subunit $2b_3$ from the southwest.

It is possible that ridge α_6 continues northward along the edge of the Turkish slope where its crest is covered by a thick (~900ms) layer of Subunit 2a and $2b_1$ that drape westward over the escarpment ϵ_1 (Fig. 3.2.18d). However, correlations along the Turkish slope, however, are uncertain due to rapidly changing morphology.

Ridge α_7:

Ridge α_7 is an east-west-trending, ~6 km-wide antiformal structure located in the northwestern corner of the survey area (Fig. 3.2.1). Its margins are defined by discontinuous vertical offsets of the M reflector.

At its westernmost locality, the transition of the M reflector from ridge α_7 to the deepest portion of the Rhodes Basin is accomplished along discontinuous, stepped, vertical offsets that lead toward basin β_9 (Fig. 3.1.8a). The crest of ridge α_7 is overlaid by a ~360 ms-thick drape of Subunit $2b_3$ which is discontinuously offset, along with the M reflector, across the margin of the ridge (Fig. 3.1.8a).

To the east, ridge α_7 is poorly imaged (Fig. 3.1.8b and c). The M reflector is inferred to exist between the weakly reflective basement and the overlying, ~100-340 ms-thick Pliocene-Quaternary package that shows a higher frequency content of discontinuous reflectors (Subunit $2b_3$?) and an irregular bathymetric expression (Fig. 3.2.8c). Here, ridge α_7 displays a ~500 ms of vertical offset of the M reflector across a 30-45° NW-dipping discontinuity along its northwestern margin and ~380 ms of vertical offset of the M reflector across a 45°SE-dipping discontinuity that marks its margin with basin β_9. Although the internal reflectors of the Pliocene-Quaternary basin fill appear poorly imaged upon approach to the ridge, both ridge discontinuous margins appear to be onlapped by the Pliocene-Quaternary basin fill (Fig. 3.2.8b and c).

Ridge α_8:

Ridge α_8 is a relatively narrow northeast-southwest-trending, antiformal structure located in the western portion of the survey area (Fig. 3.2.1). Its gently northeast-plunging crest is buried under 200-350 ms of Subunit $2b_2$ and $2b_3$.

At its southwesternmost extent, ridge α_8 is its broadest (~6.5 km) and separates basin β_4 from basin β_5. Unit 1 reveals no evidence of any particular fabric. The M reflector illustrates an irregular morphology and is frequently vertically offset across discontinuities (Fig. 3.2.6a). The overlying Subunit $2b_3$ is also affected by these discontinuous offsets.

Further northeast, ridge α_8 measures 4.25 km wide and has a relief of 680 ms

along its 6°NW-dipping, continuous margin with β_9 but only 80 ms of relief along its 10° SE slope that marks its northern boundary with basin β_5 (Fig. 3.2.6b). The M reflector is identified as a sharp, strong reflection between a strongly reflective but discontinuous Unit 1 succession and the overlying, well stratified, Subunit 2b reflectors. Subunit $2b_1$ onlaps onto the ridge's northwestern flank and thickens toward basin β_9. Subunits $2b_2$ and $2b_3$ form a 300 ms-thick drape over the crest of ridge α_8 and thicken both toward the northwest and southeast via the divergence of their reflectors (Fig. 3.2.6b). An asymmetric rise in the seabed above the ridge illustrates a small, northwest-dipping bathymetric escarpment. Toward the northeast, ridge α_8 is more deeply buried beneath the seabed (~400 ms-thick cover of Subunit $2b_3$ over its crest) but shows very similar geometry and stratigraphic relationships to those observed to the southwest (Fig. 3.2.6c). The distinction between the two is likely primarily due to the different orientations of the sections through the structures, the east-west oriented line providing less amplification of the structure (shallower dips).

Ridge α_9:

Ridge α_9 is a broad, southwest-plunging high-stand that separates basin β_6 from basin β_1 in the southwestern portion of the deep Rhodes Basin (Fig. 3.1.6 and 3.2.7). Unit 1 illustrates a clear antiformal fabric terminated at the M reflector to form an angular unconformity. The M reflector clearly truncates a Unit 1 antiformal fabric and is overlain by ~200-250ms of Subunit $2b_2$ and $2b_3$.

At its southwestern extremity, ridge α_9 is an ~18.5 km-wide antiformal structure that separates basin β_1 from basin β_3 (Fig. 3.2.7e). Its ~4°NW-dipping northern flank and ~1°SE-dipping southern flank each have a relief of ~380 ms above basins β_3 and β_1 respectively. Unit 1 synform/antiform pairs are clearly truncated at the M reflector which forms an angular unconformity. The more gently dipping southern flank of the ridge is onlapped by sub-horizontal subunits $2b_1$ to $2b_3$. Upper Subunit $2b_3$ reflectors remain parallel but curve upward along the ridges' southern slope where they continue northward over the ridge crest and maintain a relatively uniform layer thickness (~200 ms-thick) and mimic the irregular morphology of the M reflector (Fig. 3.2.7e). The seabed also tends to follow the morphological characteristics of the underlying M reflector. Along its more steeply dipping northwestern limb, Subunit $2b_3$ thickens rapidly northward into basin β_3 where it reaches 800 ms-thick. Midway down its northwestern flank, where the thickening initiates, the Subunit $2b_3$ are less continuous thereby obscuring the clear identification of the stratigraphic relationships in this vicinity (Fig. 3.2.7e).

Toward the northeast, ridge α_9 a ~6-9 km wide structural high whose relief above the adjacent basins varies from 200-360 ms (Fig. 3.2.7a and b). Its proximity to the antiform of Unit 1 below ridge α_3 suggest that the core of ridge α_9 may also have an antiformal nature, however such a fabric is not easily identified as to the southwest. There is a vertical repetition of the M reflector associated with a discontinuous vertical offset of ~230 ms near the southern extremity of the ridge (Fig. 3.2.7b). Subunit $2b_2$ conforms to the shape of the ridge as it drapes (100 ms-thick) over its crest and dips gently toward the

northwest. The discontinuous and strongly northwestward-thickening Subunit $2b_3$ thins over the southwest flank of ridge α_9 but maintains a constant thickness of ~200-250 ms, regains its coherent reflectivity and conforms to the gently undulating morphology of the M reflector over the ridge crest (Fig. 3.2.7b). The seabed above the ridge also displays a flavour of this uplifted, undulating morphology. The northwest dipping limb of the ridge shows considerable northwest thickening of Subunit $2b_3$ into basin β_9.

Chapter 4: Structural Interpretations

In geological mapping, whether on rock exposures or from seismic images, it is often necessary to infer major structures from the associated minor structures and stratigraphic relationships. For the interpretation of the seismic images presented later in this chapter, it essential to describe, firstly, how the major causative structures can be inferred from their associated structures and stratigraphy.

4.1: Recognition of Causative Structures

Faults are formed by the mechanical failure of rocks when placed under stress. There are three primary categories of faults: normal (extensional), reverse (compressional) and strike slip (lateral). Each of these correspond with one of three unique orientations of the principal compressive stresses σ_1-σ_3 ($\sigma_1>\sigma_2>\sigma_3$), where the shear stress at the Earth's horizontal surface is assumed to be zero (Park, 1997). The Mohr failure criterion for brittle failure of homogeneous substances correctly predicts that the dip angles for normal faults typically occur at angles greater than 45°, and reverse faults at less than 45°; strike slip faults dip sub-vertically (Fig. 4.1.1). All three types involve complementary pairs intersecting along σ_2 and forming an acute angle bisected by σ_1 (Park, 1997; Fig. 4.1.1). These relationships apply to a homogeneous, isotropic Earth.

However, in nature rocks are often heterogeneous and stress conditions change

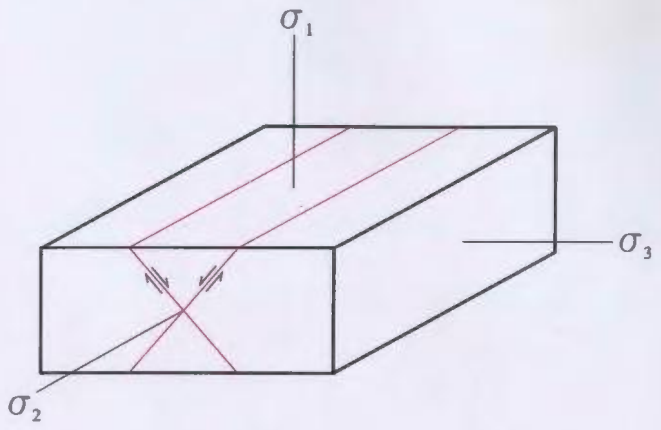

a)

- Hanging wall down relative to the footwall
-Horizontal separation of strata
- Dip of fault plane >45 degrees.
- Strike of fault plane at 90 degreee to σ_1 and σ_3.

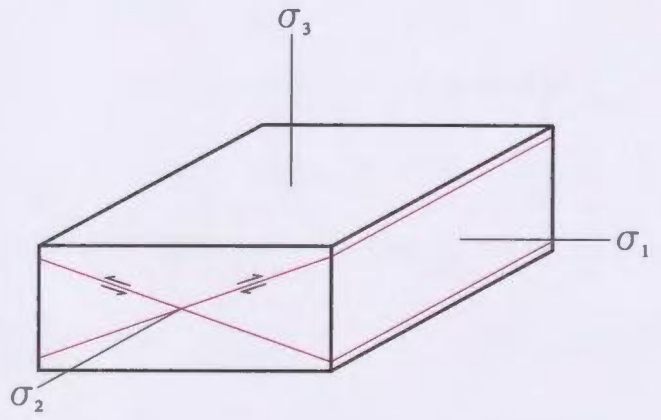

b)

- Hanging wall up relative to the footwall.
-Horizontal overlap of strata and vertical stratigraphic repetition.
- Dip of fault plane <45 degrees.
- Strike of fault plane at 90 degreee to σ_1 and σ_3.

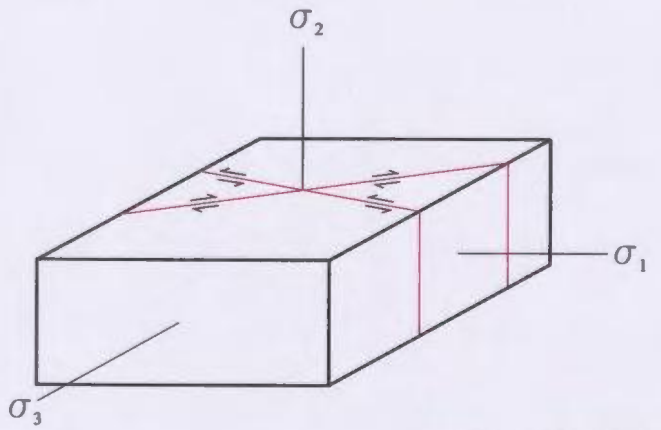

c)

- Lateral displacement of hanging wall and footwall.
- Dip of fault plane subvertical.
- Strike of fault plane at a low angle to both σ_1 and σ_3.

σ_x Principal compressive stress axis
$\sigma_1 > \sigma_2 > \sigma_3$.

Figure 4.1.1: Fault orientations relative to the three principal stress axes for a) normal, b) reverse and c) strike slip faulting.

with depth. Features such as rock layering and preexisting faults provide zones of weakness that allow very different fracture orientations to develop. In addition, rocks are capable of plastic deformation and absorb strain by folding. These conditions require that fault movements be considered as part of evolving, brittle/ductile processes rather than as an instantaneous fracture phenomenon.

Reverse Faults

Crustal shortening via reverse faulting typically occurs along low angle (<30° dip fault plane) thrust faults. One of the most widely applied models for thrust fault geometry is the planar, ramp-flat model (Fig. 4.1.2; Park, 1997). In this model, thrust flats develop along sub-horizontal planes of weakness (detachment surfaces) such as those along bedding planes between massive beds or along beds of low competence, whereas thrust ramps cut upward through competent strata. A geometric consequence of this ramp-flat architecture is an anticlinal fold (thrust anticline) near the thrust front (Fig. 4.1.2). Folding near thrust fronts has been documented in nature (e.g., Faill, 1973; Mitchell and Woodward, 1988; Suppe et al., 1992; Shaw and Suppe, 1994) and a variety of kinematic models has been developed using both planar (e.g., Suppe, 1983; Suppe and Medwedeff, 1984; Jamison, 1987) and non-planar (Fischer et al., 1992) causative thrust faults. A detailed review of each of these models is not presented here. However, an overview of these works reveals that thrust anticlines generally exhibit long, shallowly-dipping back

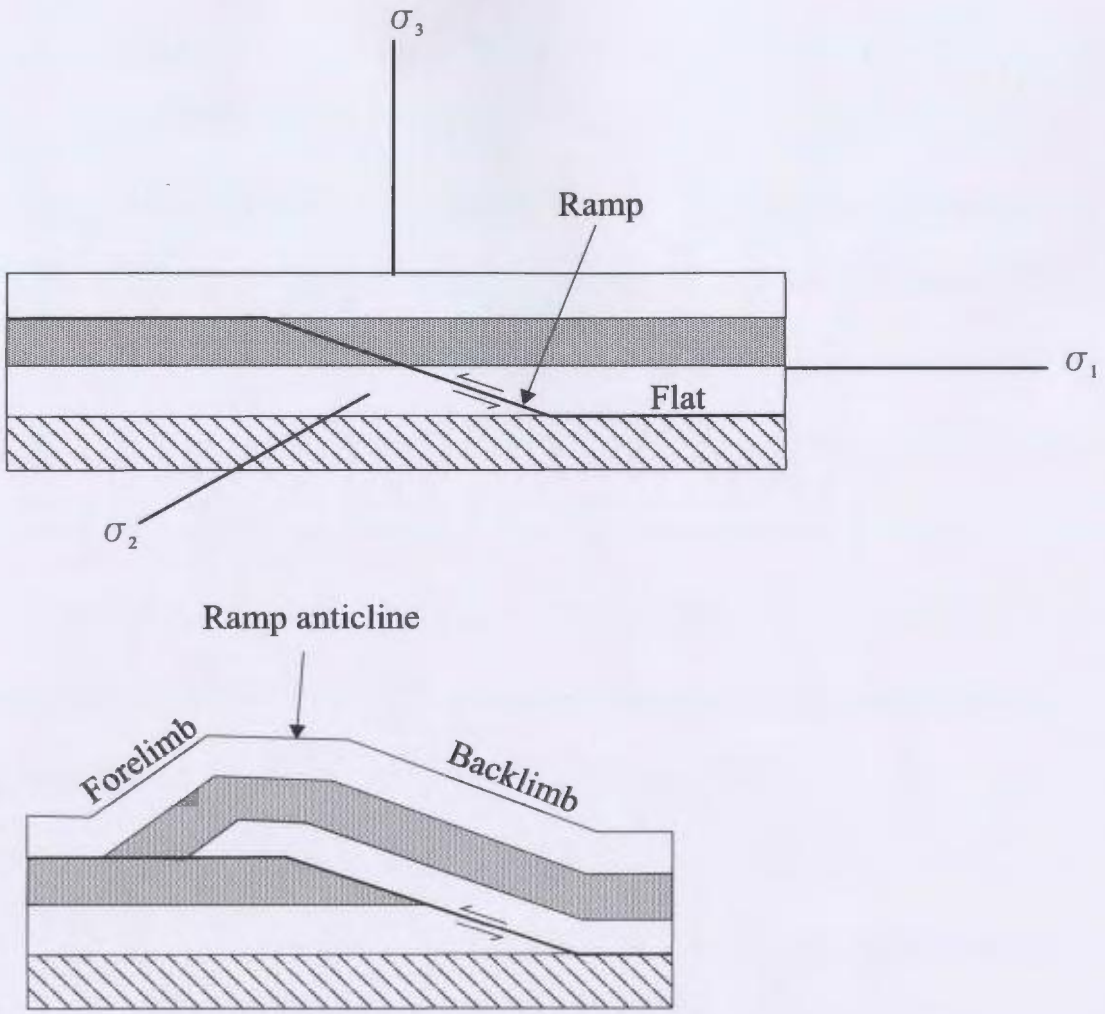

Figure 4.1.2: Reverse faults often form along a ramp-flat trajctory.

limbs and short, steeply-dipping (possibly even overturned or 'recumbent') forelimbs from which a sense of thrust vergence can be inferred (Fig. 4.1.3). In addition, the trajectory of the ramp portion of the thrust can be identified by the abrupt transition from the steeply inclined pre-tectonic growth strata in the forelimb and the flat-lying strata in front of the thrust front (Fig. 4.1.3). Each of the thrust-fold models produces unique syn-tectonic growth strata architectures (Sorti and Pablet, 1997; Suppe et al., 1992). Previous work by Sorti and Pablet (1997) and Suppe et al. (1992) indicates that the most important factors affecting the geometry of the syn-sedimentary growth strata deposited during the motion of a thrust fold anticline are: (1) syn-tectonic variations in limb lengths of the anticline, (2) syn-tectonic variations in limb dip (rotation) and (3) relative uplift - to - sedimentation rate around the thrust anticline. Figure 4.1.4 clearly shows that growth strata related to uplift of a fold anticline thicken, forming a wedge, away from the anticline crest on both the forelimb and backlimb, and curve upward toward the fault plane. The direction of onlap migration provides an indication of the rate of uplift relative to sedimentation.

A family of thrust faults may form in sequence. When younger thrust faults develop in the footwall of older faults, the fault system propagates forward and is referred to as a 'piggy back sequence'. Conversely, if younger thrust faults develop behind older faults, the system propagates backward and is termed as an 'overstep sequence' (Fig. 4.1.4b; Park, 1997). Sandbox modelling of thrust sheets performed by Bernard et al. (1995) show that the geometry of these thrust fault families is dependent on the

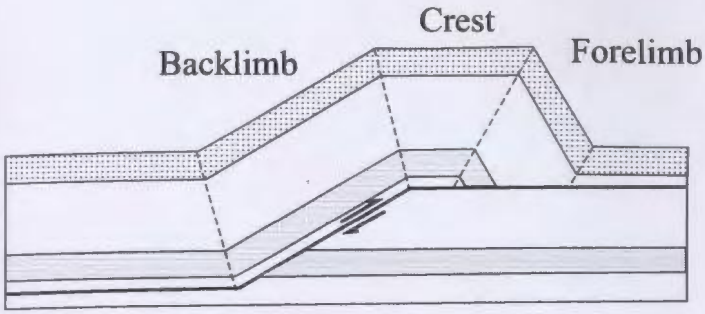

Fault-bend folding
- Instantaneous faulting followed by pushing of the thrust sheet over the thrust ramps and flats.

a)

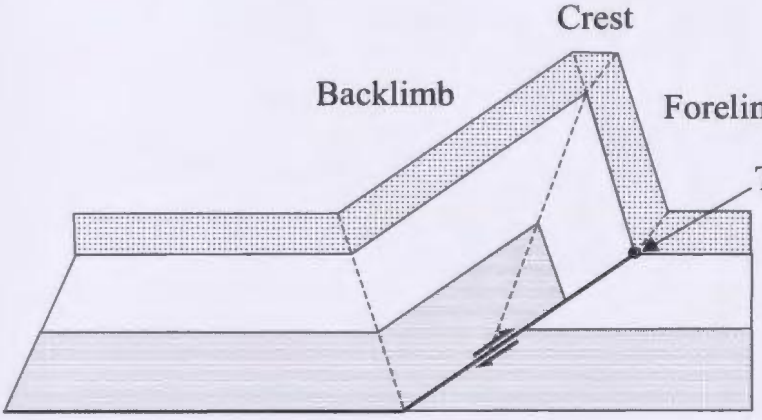

Fault propagation folding
- The thrust fold develops as the thrust tip point propagates.
- Strata folded in front of and eventually cut by the thrust fault.

b)

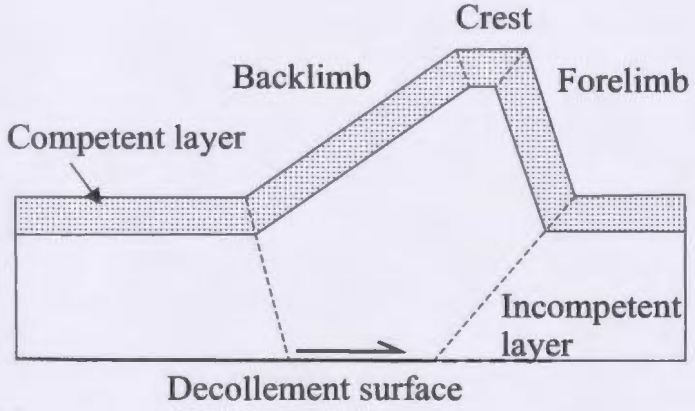

Decollement folding
- Differential shear of an underlying plastic unit causes synchronous kink fold development in the overlying, competent layer.

c)

Figure 4.1.3: Examples of planar thrust fold geometries. a) Fault-bend folding as proposed by Suppe (1983) (modified from Suppe (1983)) b) fault propagation fold (Storti, 1997) (modified from Storti, (1997)) and c) decollement fold (Storti, 1997) (modified from Storti (1997)).

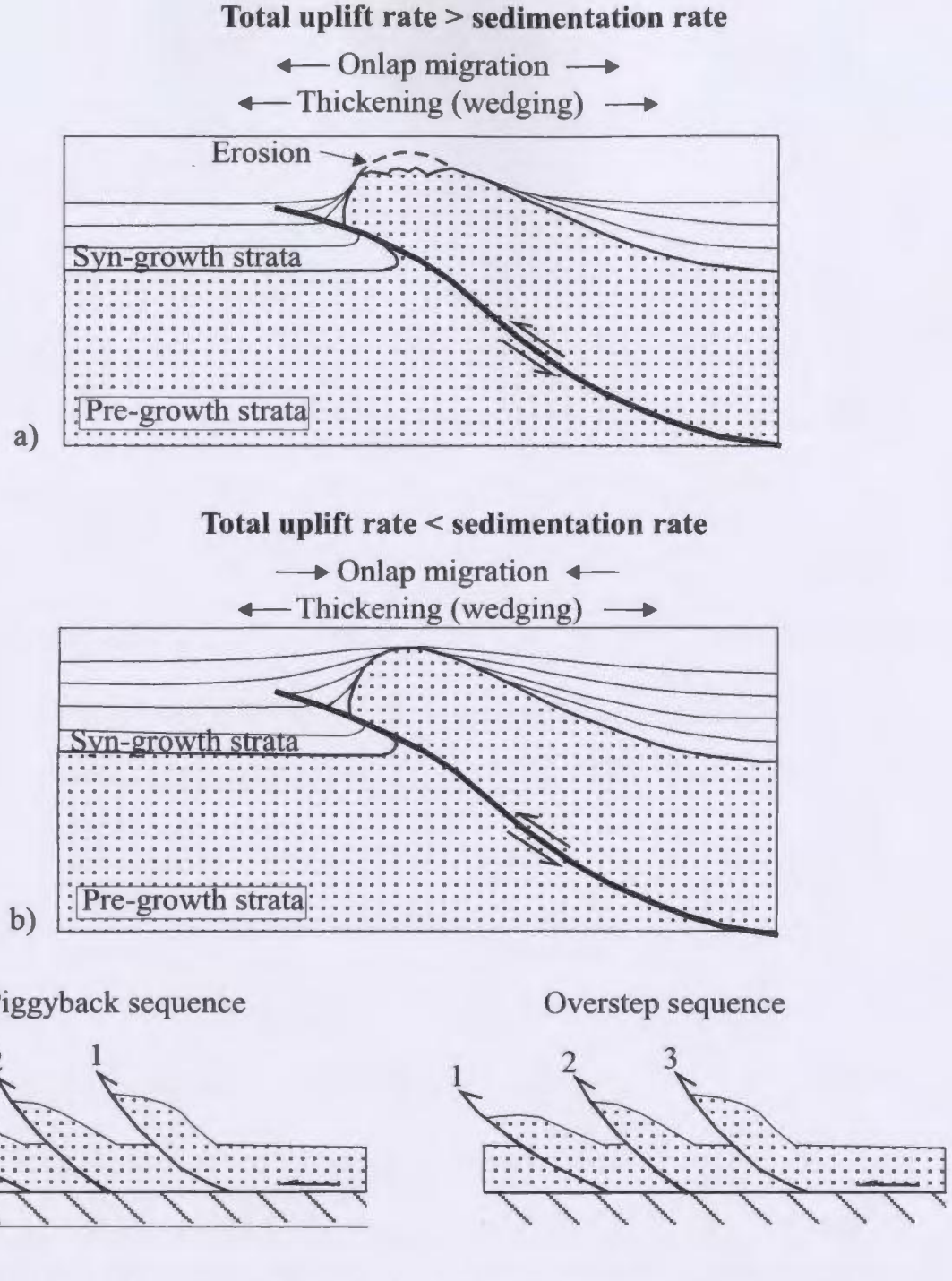

Figure 4.1.4: a) If the total rate of uplift (= fold uplift rate - subsidence rate) greater than the rate of sedimentation, growth strata onlaps migrate away from the fold crest. If the total uplift rate is positive, then fold crest erosion is probable. b) If the total rate of uplift is less than the rate of sedimentation, then growth strata onlaps migrate toward the fold crest. c) Fold-thrust belts often form as a piggy back sequence where older, relatively inactive faults are carried on the backs of younger faults. The opposite is also possible, where younger faults cut into the hangingwall of older fault blocks thereby generating an overstepping sequence. Figures a) and b) modified from Doglioni and Prosser (1997). Figure c) modified from Park (1997).

distribution and rheology of the deforming substance. For brittle deformation, the spacing of thrust sheets is primarily determined by the basal friction and depth to décollement (Bernard et al., 1995).

Normal Faults

The most commonly used kinematic model of faulting used to accommodate extensional stress is a listric fault trajectory (Fig. 4.1.5), widely documented in nature (e.g., Lopez, 1990; Beach and Trayner, 1991). For crustal scale extensional faults, the gradual reduction in dip magnitude of the plane with depth may be due to shearing detachment along a brittle-ductile transition, the depth of which may depend on temperature gradient and basement lithologies (Lister et al., 1991). Near mountain ranges, this brittle-ductile transition may coincide with shallowly dipping mylonite zones along which detachment is likely to occur (Crittenden et al., 1980). Faults contained within the upper crust may be similarly affected by horizontal detachment planes between beds, or along beds of low competence such as over pressured shales or salt layers (Shelton, 1984). Reduction of fault dip angle with depth (due to decreased internal friction) is also predicted by the Mohr envelope and may be an additional contributing factor to the listric shape of normal faults. The most striking consequence of a listric normal fault is the geometrically necessary 'roll-over anticline' that forms in the hanging wall (Fig. 4.1.5; Gibbs, 1984). This roll-over geometry provides accommodation space for syn-sedimentary growth stratal wedges to be deposited. Unlike those of reverse faults,

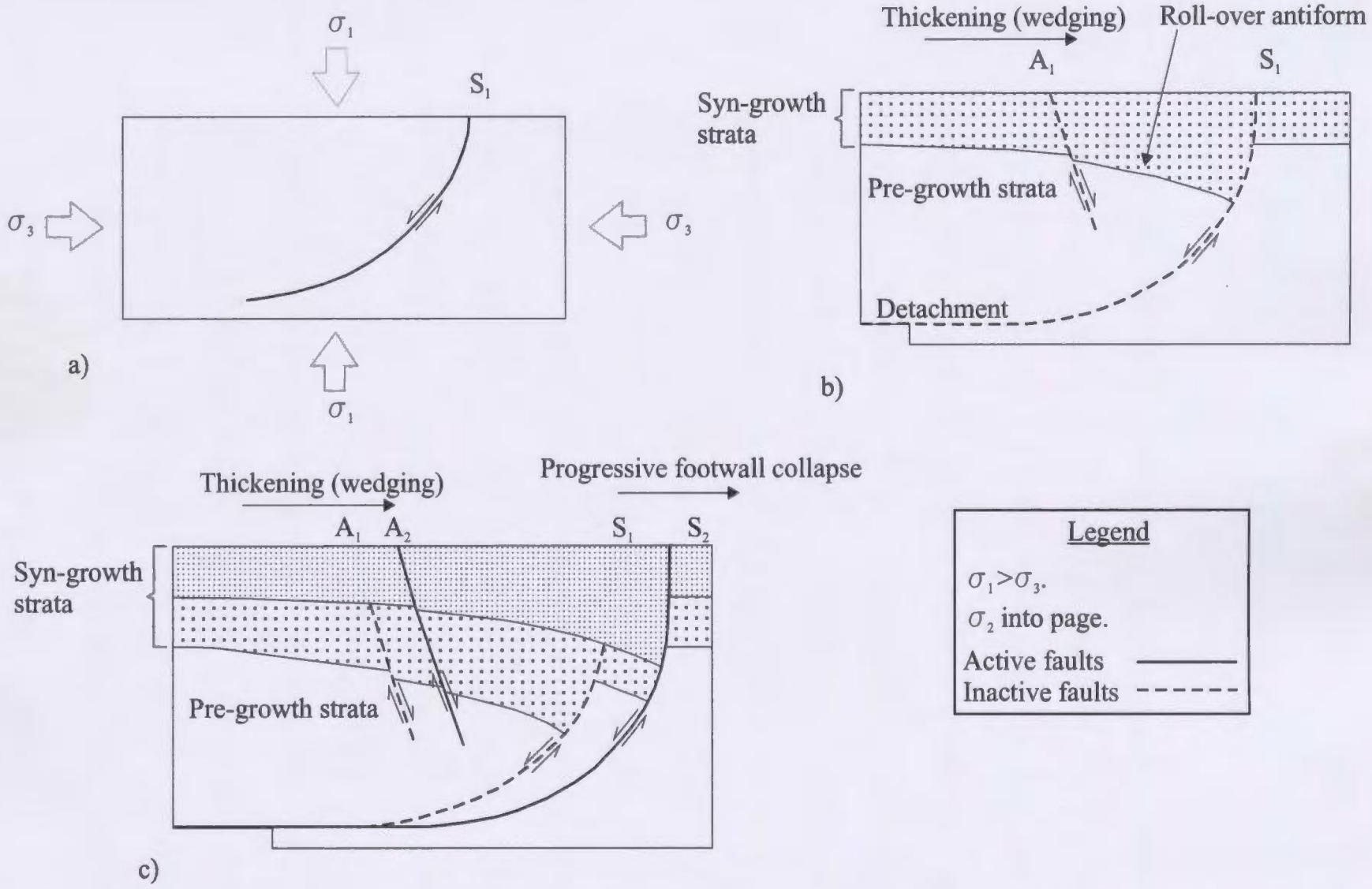

Figure 4.1.5: A model of listric normal faulting. a) The initial fault block at the onset of deformation, b) The first phase of synthetic (S_1) and antithetic (A_1) faults generate the listric fault trajectory and roll-over anticline. c) Continued extension. Note the thickening of syn-growth strata toward the footwall- assumming sufficient sediment supply and the migration of the deformation into the footwall of the structure (progressive footwall collapse). Figure modified from Imber et al. (2003).

stratal thickening for growth wedges covering the hanging wall of a normal increases toward the fault surface where strata are typically dipping downward toward their contact with the fault plane (Fig. 4.1.5; Imber et al., 2003). Provided that there is sufficient sediment supply, the initiation of fault activity can be inferred to have occurred at a time marked by the boundary between the isopachous pre-sedimentary growth strata and the overlying syn-sedimentary growth strata. Continued extension often leads to the migration of extensional failure toward the footwall (progressive footwall collapse), increased curvature of the roll-over anticline, increased syn-sedimentary growth and subsequent antithetic fault development (Fig. 4.1.5; Imber et al., 2003). Similar to fold-thrust belts, the stratigraphic architecture of extensional basins is subject to factors such as sediment supply and the relative elevation of the base level.

Other models have also been proposed to explain how extensional fault systems accommodate stress. One such model is the fault block model where linear extensional faults separate rigid fault blocks that detach at their base, allowing them to rotate (Fig. 4.1.6). A problem with this model is that it does not conserve area and requires an incompetent substrate to fill in the 'empty space' created by the block tilting (Fig. 4.1.6). Antithetic faults are not common in the fault block model since they would impede sliding during rotation, but tilting of the fault blocks still produces growth stratal wedges over the hanging wall that thicken toward the fault plane (Fig. 4.1.6a). Model experiments by McClay and Ellis (1987) documents the coexistence of extensional block faults and listric faults during deformation. In these experiments, the problem of space

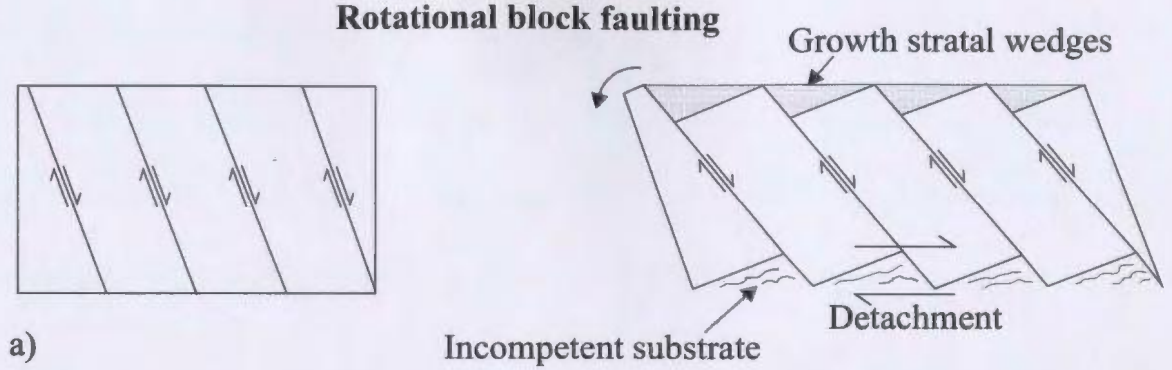

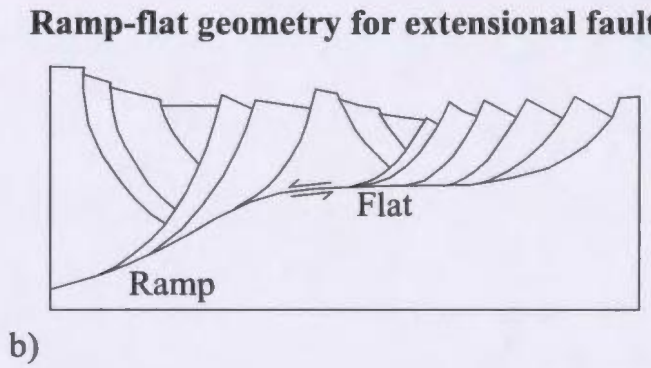

Figure 4.1.6: a) The rotationing block model for extension (Modified from McClay and Ellis, 1987). b) Listric faults sometimes link to form a ramp-flat master fault similar to those formed during thrust faulting (Modified from McClay and Ellis, 1987).

conservation associated with planar fault blocks is remedied by internal deformation of the fault blocks and their interaction with the surrounding listric fault fans. A variation on the listric fan is the ramp-flat listric fan where two listric faults are connected by a sub-horizontal detachment surface (Fig. 4.1.6b; Gibbs, 1984). The fault pattern generated from ramp-flat listric master faults is typically more complex with the likely development of dual roll-over anticlines separated by high angle reverse faulting (McClay and Ellis, 1987). There must be an appreciation of the geometric variations within extensional fault systems before the interpretation of such structures is attempted.

Strike slip Faults

Modelled experiments of lateral movement between fault blocks show that slip occurs along a deformation zone that trends at a low angle (25-35°) to the applied maximum principal compressive stress (Figs. 4.1.1 and 4.1.7a; Schreurs, 1994). A plan view of this deformation zone shows that it is delineated by a series of stepped Riedel shears connected by sigmoidal, cross-cutting faults (Fig. 4.1.7b; Schreurs, 1994; Fauteuil and Mart, 1998). These steeply-dipping faults are often arcuate at depth and separate relatively undeformed fault blocks that rotate in coherence with the sense of shear (e.g., counterclockwise rotation for sinistral shear), provided there is adequate detachment at depth (Schreurs, 1994). The high angle of fault trends relative to the regional shear zone orientation leads to restraining and releasing bends within the fault zone which generate both compressional and extensional features such as positive flowers, negative flowers,

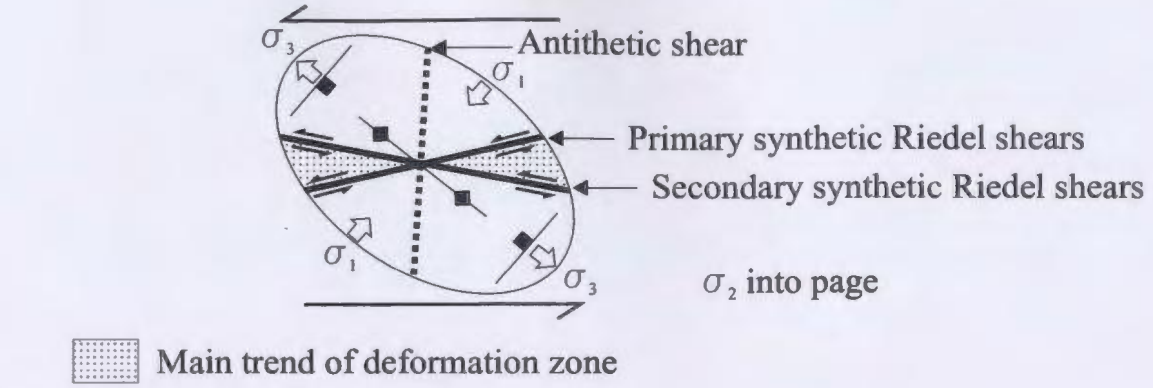

a)

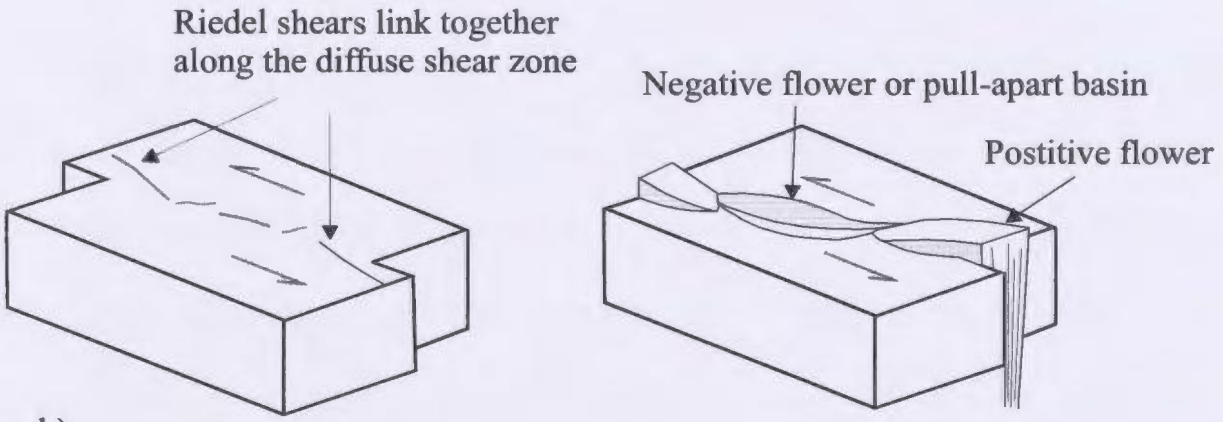

b)

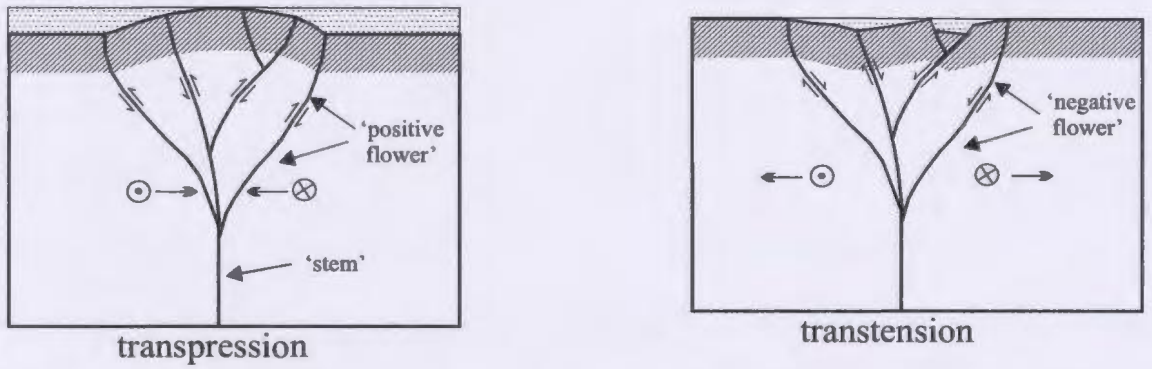

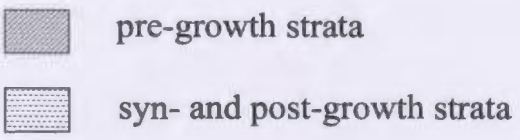

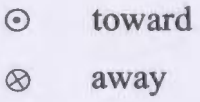

c)

Figure 4.1.7: a) A plan-view strain ellipse for sinistral shear illustrating the expected fault development. b) Deformation via strike slip deformation often occurs along a broad zone of Riedel shears linked by sigmoidal cross faults. Flower structures occur along the restraining (positive flower) and releasing (negative flower) bends of the often sigmoidal trajectory (Figure modified from Park (1997). c) Cross sections through positive and negative flower structures illustrating the bidirectional sense of faulting.

folds and extensional (sometimes *en échelon*) basins (Fig. 4.1.6). Although these second-order features of strike-slip faulting are consistently observed in strike-slip fault models, it is recognized that changing the rheology of the layers used in the modelling can have a significant impact on the specific structural geometries (Richard and Krantz, 1991, Fauteuil and Mart, 1998).

Harding (1985) examines several natural examples of strike-slip faulting from seismic data. Noting that the development of syn-sedimentary growth strata over flower structures is very similar to that of regular normal and reverse faults, Harding (1985) stresses the importance of imaging the pre-growth stratal architectures and upward diverging fault trajectories, high angle vertical offsets, fold geometries and rapidly changing sense of separation or regional uplift. Unfortunately, the highly deformed nature of most strike-slip systems do not often allow sufficiently clear imaging of the pre-growth strata to make such clear determinations. Plan views of strike slip faults often better illustrate the changing sense of vertical motion of strike slip faults along restraining and releasing bends as well as their *en échelon* geometry along trend.

A thickening wedge of strata could indicate either reverse or normal faulting: but the presence of secondary structures, such as minor antithetic faults or asymmetric, pre-growth folds, can assist in discriminating between the two causative mechanisms. Table 4.1.1 summarizes some of the most diagnostic properties of normal, reverse and strike slip faults that can be used to make such determinations.

Characteristic	Normal Fault	Reverse Fault	Strike Slip Fault
Fault plane dip	> 45°	< 45°	subvetical
pre-growth stratal architeture	▸ Stratal cut-offs showing hanging wall down relative to footwall up. ▸ Horizontal separation of strata ▸ If listric, presence of roll-over anticline.	▸Stratal cut-offs showing hanging wall up relative to footwall down. ▸Possible vertical repetition of strata. ▸ Ramp anticline illustrating short, steep forelimb and long, gently dipping backlimb.	▸In general, look for juxtaposition of dissimilar strata. ▸If transpressional, antiformal architectures bound by steeply inclined, upwardly diverging reverse faults. ▸If transtensional, synformal architectures bound by steeply inclined, oppositely-dipping normal faults.

Table 4.1.1: A summary of the diagnostic features of normal, reverse and strike slip faults.

4.2: Structural Domains

On the basis of geographic location and structural style, the Rhodes Basin is divided into three structural domains that broadly correspond with the bathymetric domains identified in Figure 3.1.6. These structural domains are (Fig. 4.2.1): the heavily sheared platform (Domain 1), the folded and faulted deep Rhodes Basin (Domain 2) and the Turkish continental slope (Domain 3). Stratigraphic and structural associations within and along the boundaries of each domain suggest that they may have shared a common origin prior to the middle Pliocene. Since then, Domains 1-3 have followed separate deformation paths dominated by transpression, southeast-vergent reverse faulting and extension respectively.

Timing of deformation over the study area is constrained by interpreting the stratigraphic relationships between seismic Units 1, 2a and $2b_{1\text{-}3}$. Structural fabrics within Unit 1 that illustrate sedimentary growth, internal onlap, or form an angular relationship with the overlying M reflector are interpreted to be of pre-Pliocene age. Progressive unconformities within syn-sedimentary growth strata of Unit 1 that merge with the M reflector near ridge crests indicate deformation during the Messinian erosive event. Sedimentary growth strata wedges, rotated downlap surfaces and progressive onlap unconformities within Unit 2 indicate deformation during the Pliocene-Quaternary (Figs. 4.1.4, 4.1.5). The subdivision of Unit 2 into the laterally extensive Subunits $2a\text{-}2b_{1\text{-}3}$ allows relative timing of periods of structural activity to be compared across the survey area.

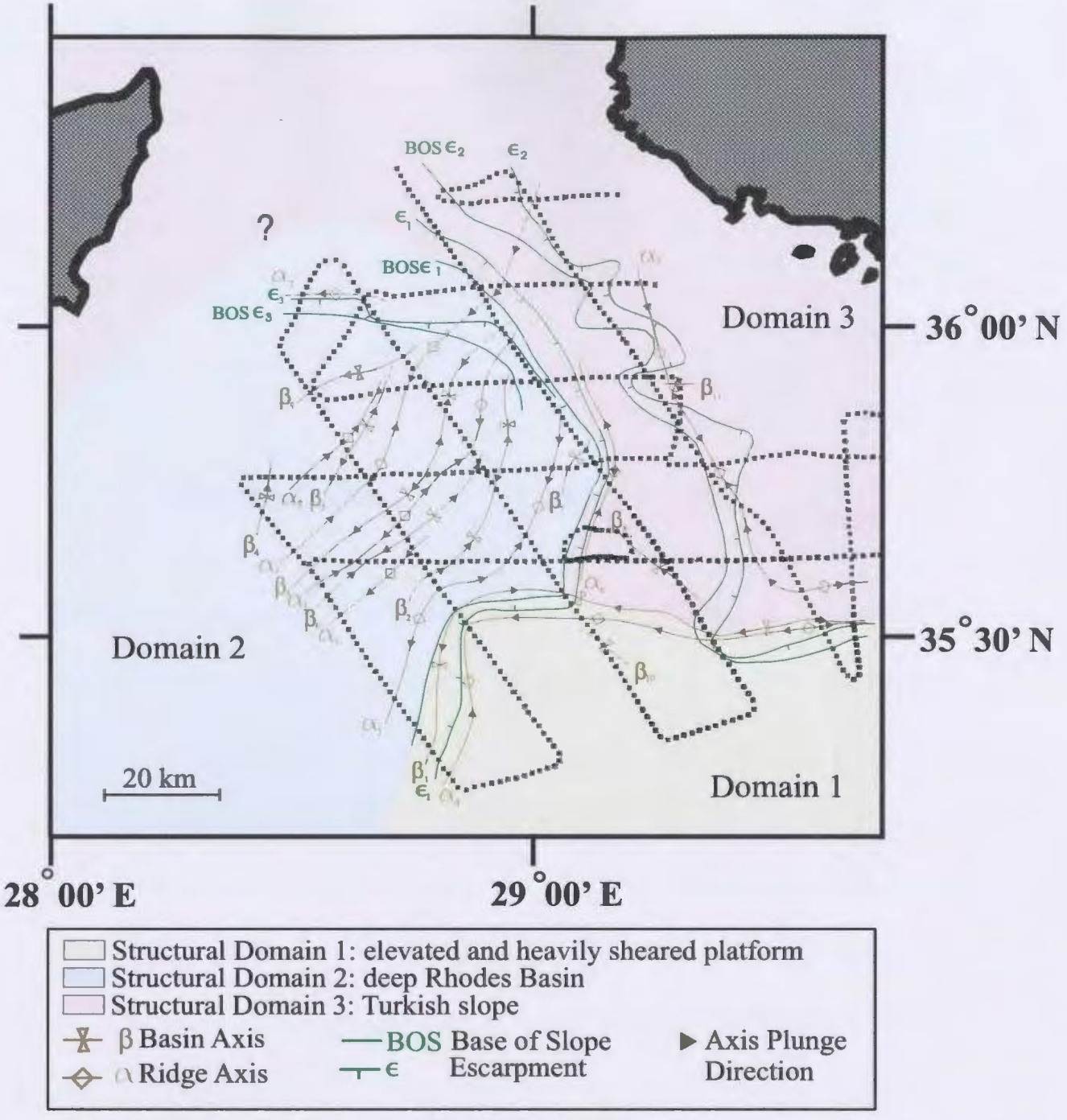

Figure 4.2.1: Map of the survey area showing the 3 structural domains and major structural features.

4.2.1: Structural Domain 1- the Heavily Sheared Platform

This platform lies immediately south of escarpment ϵ_1 at the southern margin of the Rhodes Basin (Fig. 4.2.1). Within the platform, the short wavelength (~3 km) of basins and ridges make correlations of individual structures across adjacent seismic profiles difficult (Figs. 4.2.2, 4.2.3). Poor imaging of reflectors below the M reflector makes the identification of coherent fabrics within Unit 1 difficult. However, the overlying subunits 2a and $2b_1$ typically exhibit continuous reflectivity within several narrow depocentres separated from one another by high-standing blocks of Unit 1that create as much as 800 ms of relief along the M reflector (Fig. 4.2.2).

Symmetric thickening of the Subunits 2a and $2b_1$ toward the axis of the narrow depocentres (e.g., Fig. 4.2.2, Fixes 2104-2105) suggests that sedimentary growth occurred during the early-middle Pliocene in response to relative subsidence. Although the contact between this basin fill and the adjacent, high-standing block of Unit 1 is not well imaged, the large vertical separation of the M reflector across the abrupt, high angle boundary between the ridge crest and the basin suggests the presence of a steeply dipping fault (X in Fig. 4.2.2). The thinning and upward bending of the Subunits 2a and $2b_1$ toward the basin margins does not agree with the typical architecture for normal faulting where the syn-sedimentary growth strata typically dip downward and thicken toward the fault plane on top of a 'roll-over antiform' architecture (Fig. 4.1.5). Rather, the upward drag of the basin fill toward the hangingwall and thickening away from the fault plane is typical of an evolving forelimb basin immediately in front of a reverse fault (Fig. 4.1.4a, b). The sense

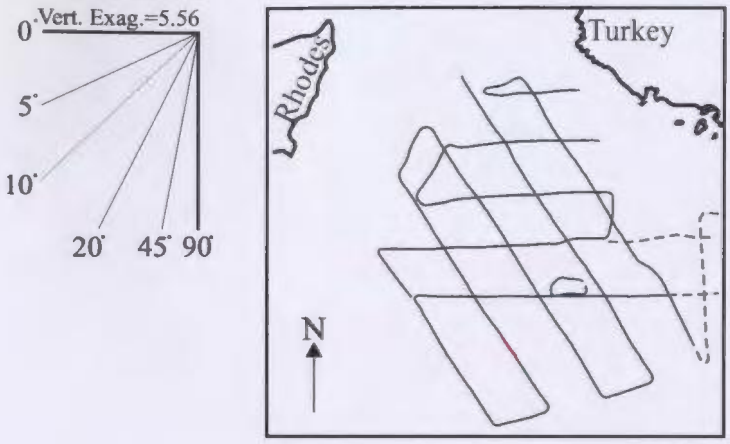

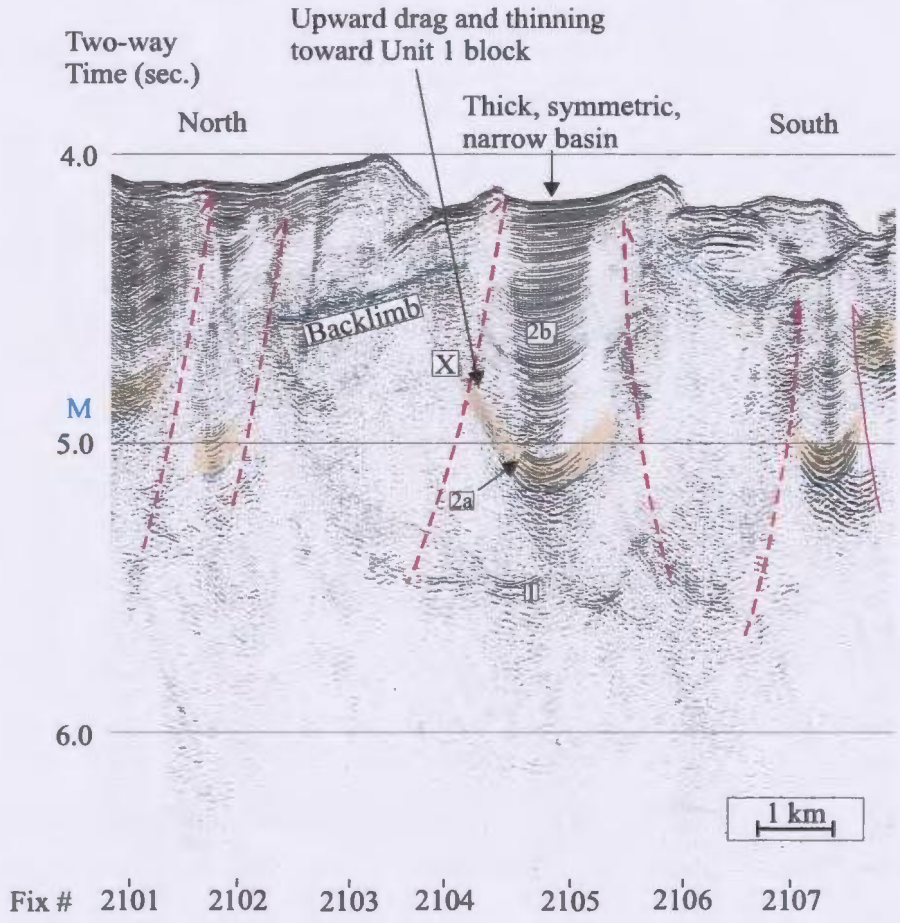

Figure 4.2.2: The elevated and sheared platform shows evidence of positive flower development.

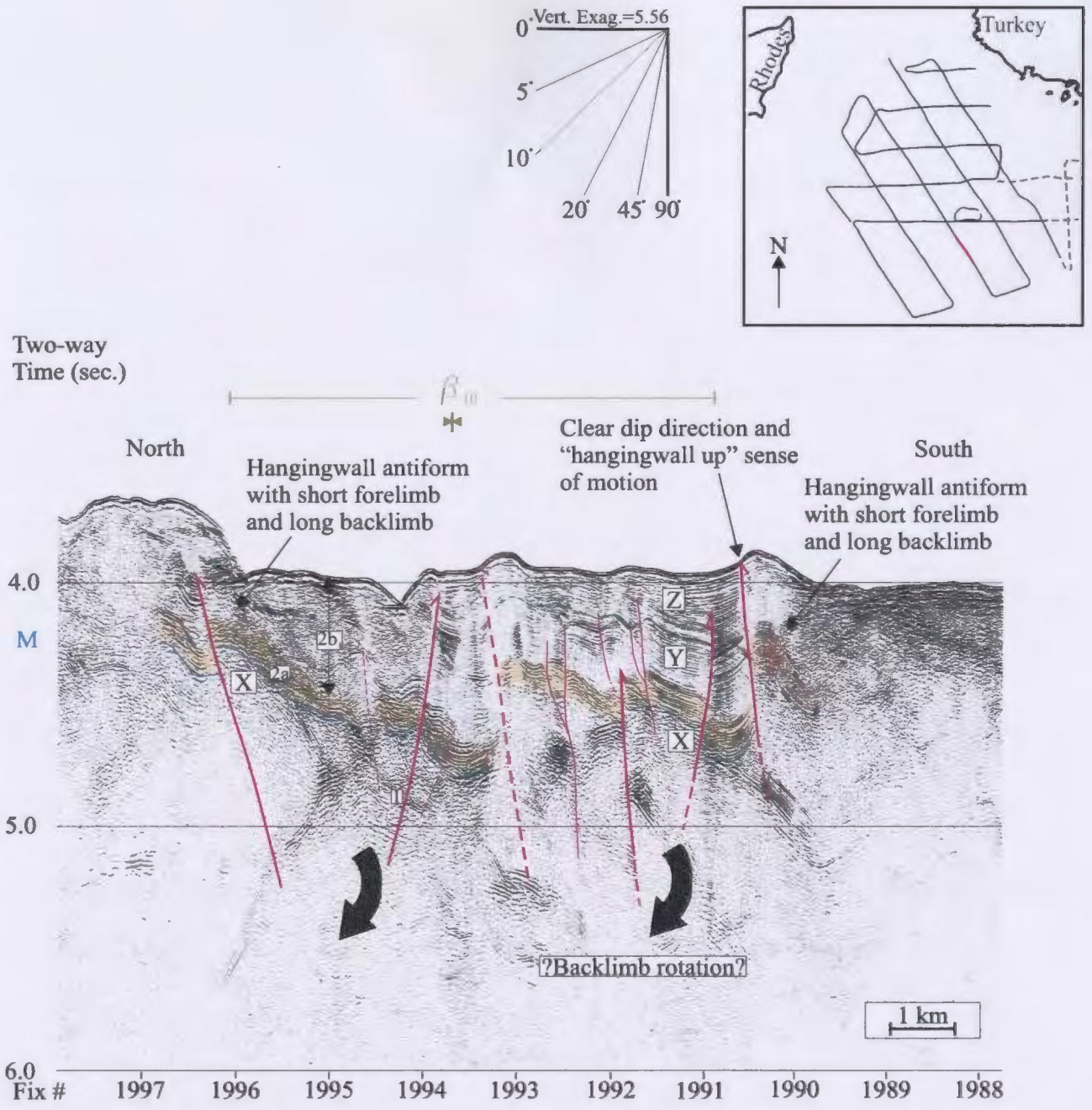

Figure 4.2.3: The elevated and sheared platform shows intense transpressional deformation with evidence of divergent reverse faulting and fault block rotation (from line 64).

of vertical separation, therefore, implies that this northern ridge is carried on a southeast-verging, high-angle reverse fault. Therefore, the gentle ~5°NW dip of the northward-facing crest of the Unit 1 high-standing block is interpreted to represent the backlimb of a ramp anticline, whereas the subvertical, discontinuous contact of the ridge with the narrow basin to its south is interpreted as a forelimb (Fig. 4.2.2). The symmetry of the deep, narrow basin suggests that it formed by relative subsidence in front of the forelimbs of two converging, high-angle reverse faults (Fig. 4.2.2); this is an architecture indicative of transpressional domains characterized by positive flower structure. The growth stratal wedges observed in the narrow basins between positive flower structures suggest that they developed during the early-middle Pliocene (Figs. 4.1.7, 4.2.2).

Basin β_{10} lies just south of the boundary between Domains 1 and 2 (Fig. 4.2.3). Subunit 2a maintains an approximately uniform thickness across the basin and allows clear identification of several sub-vertical faults that truncate/offset the entire basin fill and the underlying Unit 1 (Fig. 4.2.3). The steeply inclined (~45-80°) dips of these faults are determined in zones where Subunit 2a (and the conformably overlying Subunit $2b_1$) show well-defined truncations (Fig. 4.2.3). The relative offset of Subunit 2a and the M reflector across the faults suggest a dominant 'hanging wall up' sense of verging toward the north with throws of up to ~280 ms (~210 m) (Fig. 4.2.3). Subunit 2a and the underlying M reflector located on the hanging walls have an asymmetric antiformal architecture, whereas those portions located on the footwalls frequently have synformal architectures. The hanging wall antiforms demonstrate an abbreviated flank toward the

interpreted fault tips with longer, steeper flanks (10-12°) dipping oppositely (Fig. 4.2.3). Occasionally, the crest of the antiform is cut by several steeply inclined faults that provide small vertical separations that are near the limit of resolution of the data.

The asymmetrical architecture of Subunit 2a antiformal structures suggests that they are thrust anticlines displaying short forelimbs and long backlimbs consistent with a north-verging sense of emplacement (Fig. 4.2.3). The offset of an isochronous Subunit 2a across these reverse faults, lack of growth in lower Subunit $2b_1$ (Y in Fig. 4.2.3), and upward drag of Subunit $2b_1$ reflectors toward the hanging walls suggest that deformation has occurred since its early Pliocene deposition (Fig. 4.1.3). The upper portion of Subunit $2b_1$ in the south end of basin β_{10} shows gradual thickening toward the south (Z in Fig. 4.2.3), but is not sufficiently well imaged to delineate the internal architecture of the growth strata. This southward thickening demonstrates sedimentary growth during inferred movement along the back limbs of dominantly north-verging reverse faults during the middle Pliocene. The unexpected greater dip magnitude of the back limbs of these reverse faults than that of the forelimbs and the fine-scale faulting over their antiformal crests imply that the backlimbs of the folds have rotated. It is this backlimb rotation that likely facilitated the southward thickening of the upper Subunit $2b_1$ during the middle Pliocene (Fig. 4.2.3).

The observations of this study and those of Woodside et al. (2000) and Zitter et al. (2003), suggest that the Messinian evaporates are absent in the Rhodes Basin as well as the nearby Finike Basin and Anaximander Mountains. On the basis of a high correlation

between the location of gravity cores that contain mud, silt and marls with areas that exhibit a low acoustic reflectivity, Galinda-Zaldivar et al. (1996) have suggested the presence of mud volcanism along the Mediterranean Ridge, south of Crete. In addition, Woodside et al. (2002) have interpreted mud volcanism in areas characterized by high seismic backscatter, circular relief and dome architecture along the western extremity of the Florence Rise. In keeping with this previous work, several seismically discontinuous, upward-diverging protrusions with ill-defined boundaries within Domain 1 are similarly interpreted to be mud-related structures- perhaps mud-intruded positive flower structures (Fig. 4.2.4). These features are distinguishable from those uplifted blocks of Unit 1 cited earlier (e.g., Fig. 4.2.2) in that the M reflector is not imaged between their boundaries with the adjacent strata and they have a smoother, dome-shaped morphology. The small amount of thickening and upward drag of Subunits 2a and $2b_1$ in the well-stratified depocentres intervening between these interpreted mud intrusions suggests that their growth may have initiated as early as the early Pliocene. The uplifted seabed over these structures suggests that they may still be active today (Fig. 4.2.4)

The complementary pairs of high-angle reverse faults within Domain 1 outline positive flower structures that separate narrow, sometimes deep basins (Figs. 4.2.2, 4.2.3). Based on the thickening of Subunits 2a and $2b_1$ in these basins, it is determined that the development of these flower structures varied with time from the early Pliocene (Fig. 4.2.2) to the middle Pliocene (Fig. 4.2.3). The positive flower structures, high spatial frequency of deformation and inferred rotation of the Unit 1 fault blocks suggests

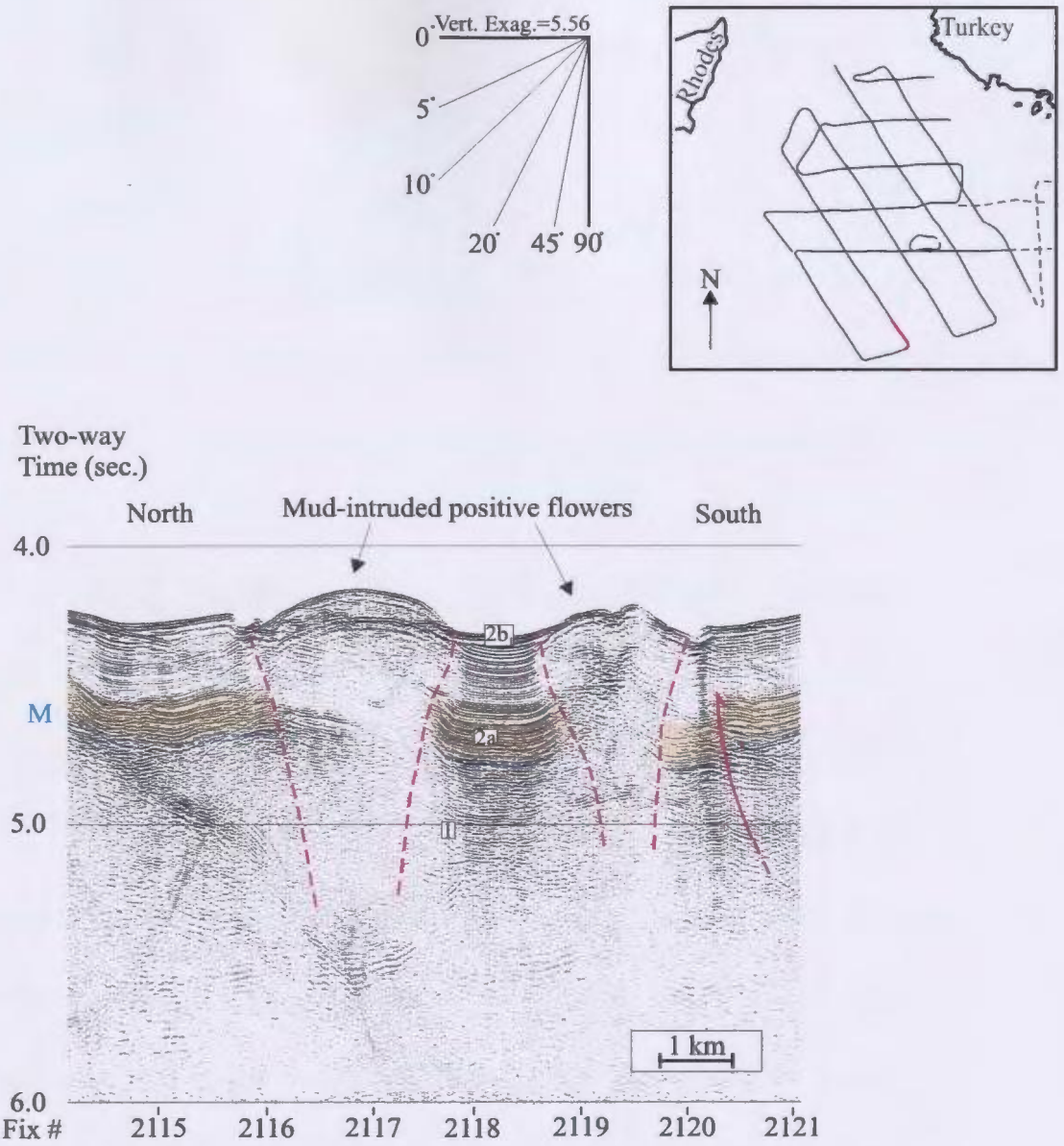

Figure 4.2.4: Interpreted mud-intruded positive flower structures (from line 68).

that Domain 1 is a heavily sheared plateau that has suffered from transpression throughout the early-middle Pliocene.

4.2.2: Structural Domain 2- the Folded and Faulted Deep Rhodes Basin

Domain 2 occupies half of the survey area, north and west of escarpment ϵ_1 (Fig. 4.2.1) where both the M reflector and the seabed within Domain 2 dip gently (~2°NW) toward the northwest (Figs.4.2.5, 4.2.6). The M reflector has a gently undulating morphology that is broadly matched in phase and amplitude by antiform/synform pairs delineated by reflectors in the Unit 1 fabric (Figs. 4.2.5, 4.2.6). These undulations delineate several doubly-plunging, northeast-southwest-trending basins and ridges with wavelengths from 7-17 km and reliefs reaching up to ~900 ms (675 m) from ridge crests to basin troughs (Figs. 4.2.1, 4.2.5, 4.2.6). Sediment fill within these basins generally wedges and thickens toward the northwest and dips 1-4°NW (Fig. 4.2.5, 4.2.6). These structures cannot be carried across domain boundaries toward either the Domain 1 or Domain 3 (Fig. 4.2.1).

A major thrust: TT

The boundary between Domains 1 and 2 marks a change from short wavelength, high angle structures to longer wavelength, more shallowly dipping structures with a definite dip and thickening toward the northwest (Figs. 4.2.5 and 4.2.6). This abrupt transition is also noticed further east where folded reflectors in Unit 1 delineate a clear

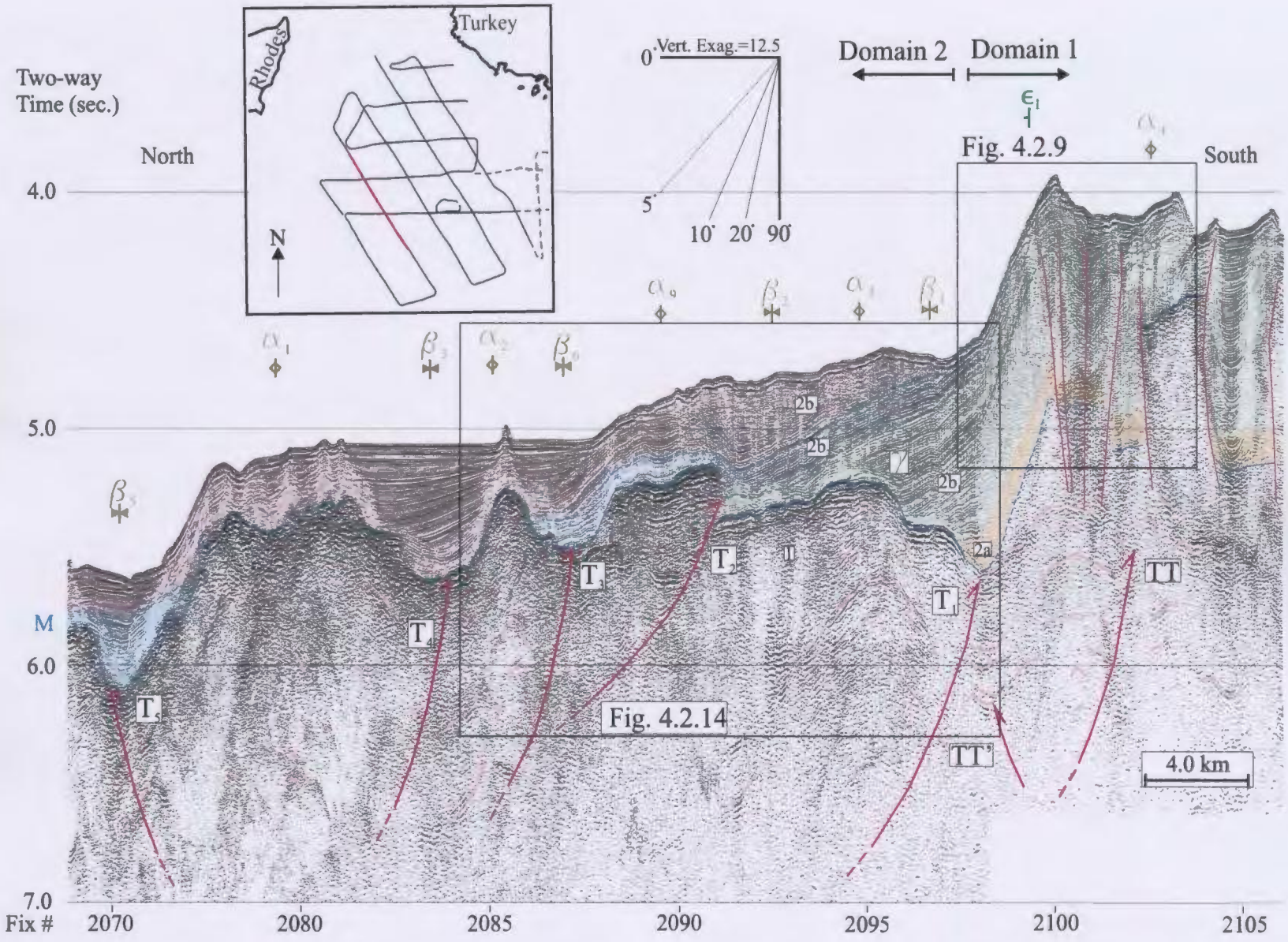

Figure 4.2.5: A section of line 68 illustrating the continuity of Subunit $2b_1$ across the Domain 1/Domain 2 boundary where thrust TT tips.

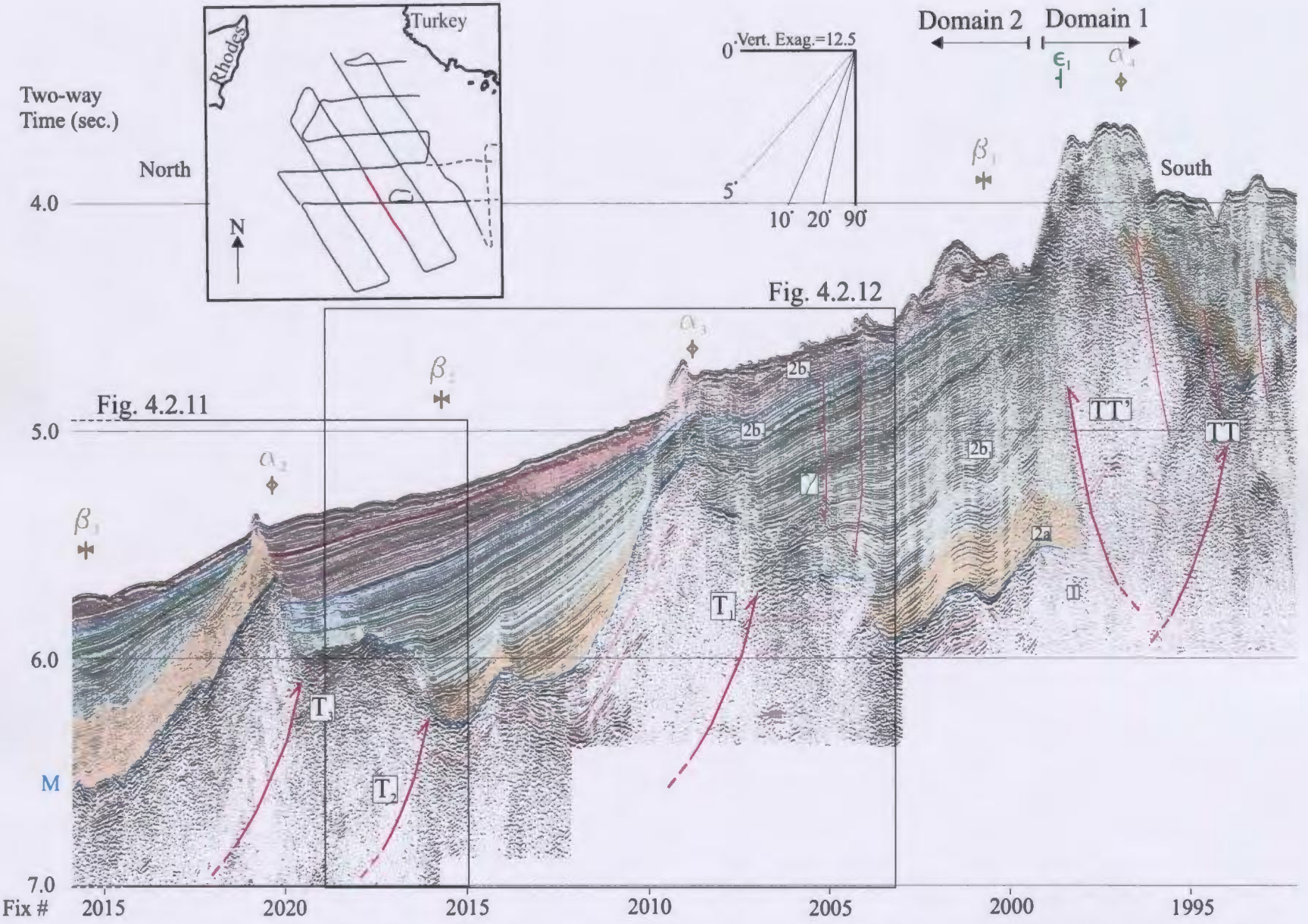

Figure 4.2.6: A section of line 64 illustrating the discontinuity of Subunit $2b_1$ across the Domain 1/Domain 2 boundary where thrust TT' tips.

antiform/synform pair truncated at the M reflector (Fig. 4.2.7). Hence, this folded fabric is interpreted to have developed, at least in part, prior to the late Messinian erosive event. The seismic imaging of this folded fabric is not often of high enough quality to confidently identify stratal relationships within Unit 1. However, where Unit 1 is imaged well, there is no indication of syn-sedimentary growth and therefore the folds are taken to be post-Unit 1 structures (Fig. 4.2.7). On the basis of the short, more steeply dipping southeastern flanks and longer more shallowly-dipping northwestern flanks of these antiforms, they are interpreted as ramp antiforms carried on an underlying south to southeast-verging thrust TT (Fig. 4.1.5, 4.2.7). The absence of progressive unconformities within Unit 1 that merge with the M reflector suggests that there was very little movement of thrust TT during the late Messinian erosive event. This determination is somewhat speculative, however, since the nature of erosive events is that they remove the rock record and remove the stratigraphic evidence of syn-erosion deformation. A thick, nearly isopachous cover of Subunit 2a and sub-γ reflectors of Subunit $2b_1$ over ridge α_4 and the backlimb of thrust TT indicate that structural inactivity continued through the early-middle Pliocene (Figs. 4.2.5 and 4.2.7). Above the γ reflector, growth stratal wedges within Subunits $2b_1$-$2b_3$ thicken down the backlimb of thrust TT, shifting the locus of Pliocene-Quaternary deposition toward the north (Fig. 4.2.7). These stratal wedges converge rapidly toward the south to form a package of stacked onlap unconformities (Fig. 4.2.7). This strong growth stratal architecture indicates a middle Pliocene-Quaternary reactivation of thrust TT during which time the pre-sedimentary

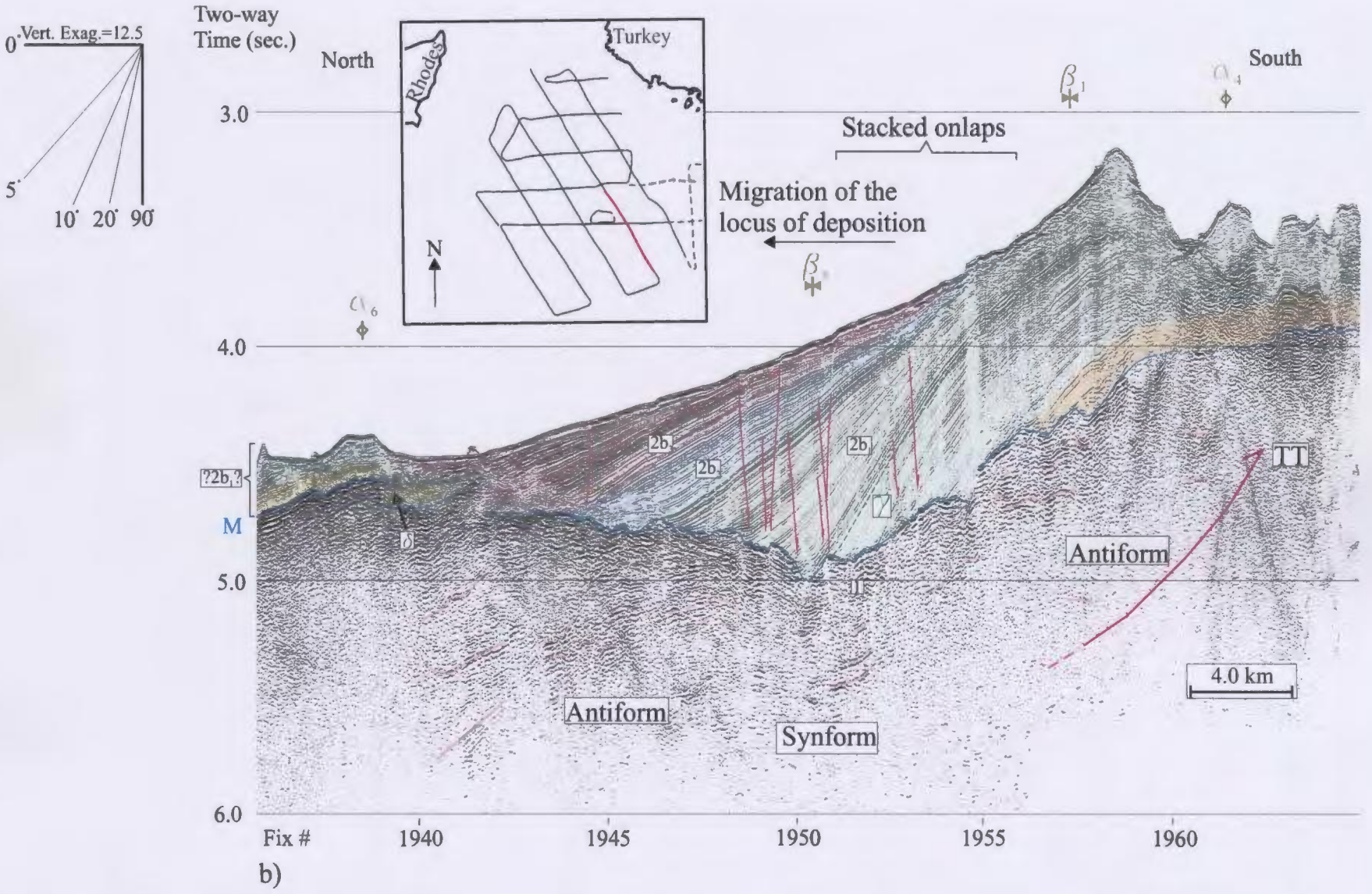

Figure 4.2.7: Line 64a shows clear folding of the Unit 1 reflectors as well as the effect of the middle Pliocene rotation of the backlimb of thrust TT on the pre- and syn- growth strata.

growth strata (sub-γ reflectors) were rotated from a presumed original onlap contact with the M reflector to their present-day downlap contact at the axis of basin β_8 (Fig. 4.2.7). Figure 4.2.8 also illustrates the long gently northwest dipping backlimb of thrust TT carrying early Pliocene pre-sedimentary growth strata and northwest-thickening middle Pliocene-Quaternary syn-sedimentary growth strata. Here, the locus of Pliocene-Quaternary deposition has migrated away from the thrust front, whereas onlap contacts within the upper succession migrate toward the thrust front (Fig. 4.2.8). This suggests that the rate of sediment supply slightly outpaced the rate of uplift along thrust TT (Fig. 4.2.8). The steeply dipping forelimb of thrust TT and clear up-to-the-southeast sense of vertical offset of the M reflector suggest that the thrust tip lies near the seabed (Fig. 4.2.8).

Thrust TT is correlated toward the west where it continues to create a gentle northwest tilt of the Pliocene-Quaternary succession along its inclined backlimb (Figs. 4.2.5 and 4.2.6). At its western extremity, sub-γ reflectors gently dip and thicken toward the northwest over the crest of ridge α_4 (Figs. 4.2.5, 4.2.9). Over escarpment ϵ_1, however, Subunits 2a and $2b_1$ form a more or less uniform drape into basin β_1. This modest amount of northward-thickening implies that the M reflector was gently tilting toward the northwest during the early Pliocene, and that the region where escarpment ϵ_1 is now present was the southern portion of basin β_1 during the earliest Pliocene. Supra-γ reflectors onlap onto the γ reflector toward the south, suggesting that ridge α_4 experienced an episode of accelerated uplift in the middle Pliocene (Fig. 4.2.9). The

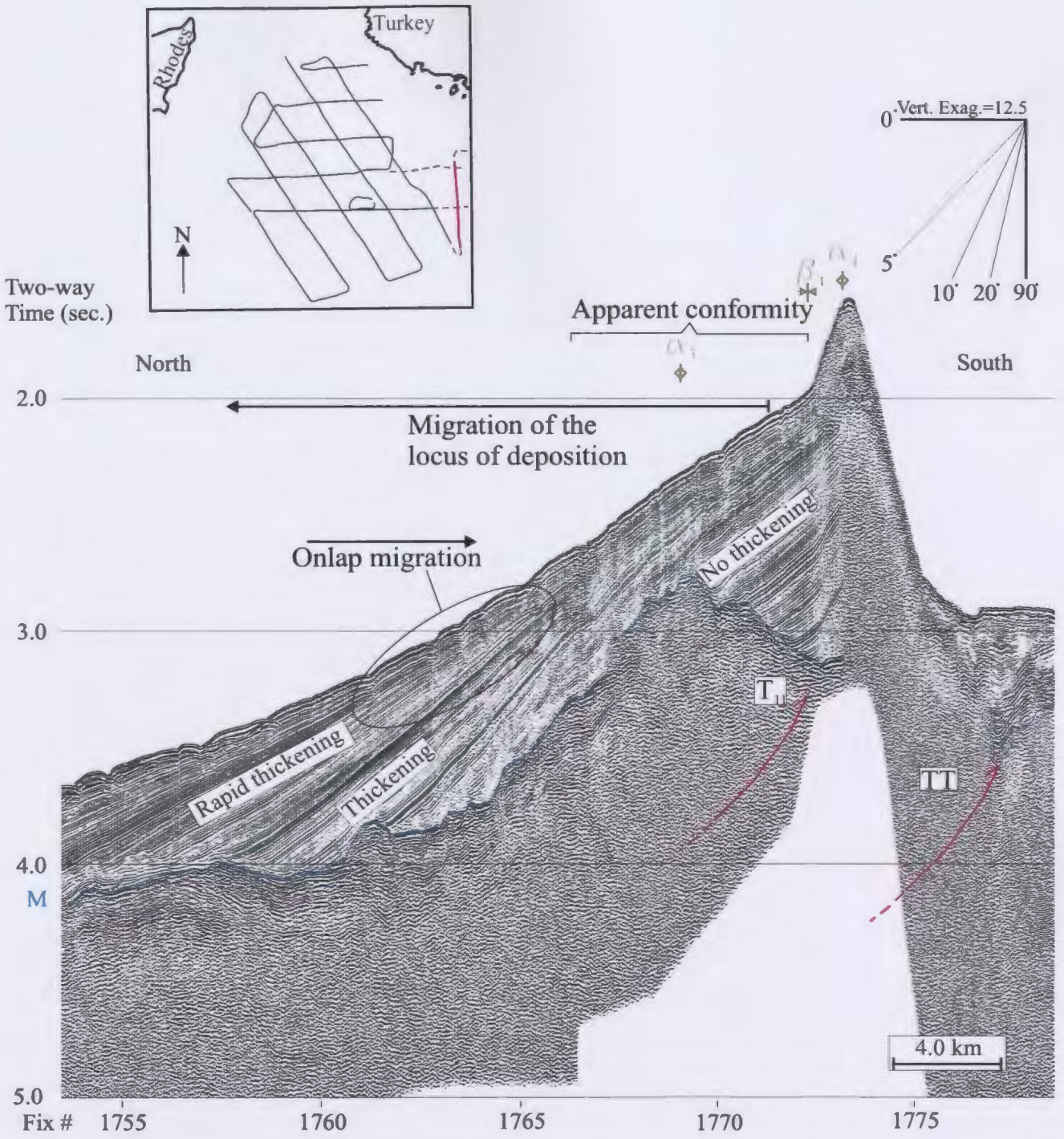

Figure 4.2.8: A supplement of data from line 58,(immediately east of the study area) showing the enormous impact of thrust TT on the morphology of the southern Rhodes Basin. Note the rotation and growth stratal architecture of sedimentary sequences above thrust TT

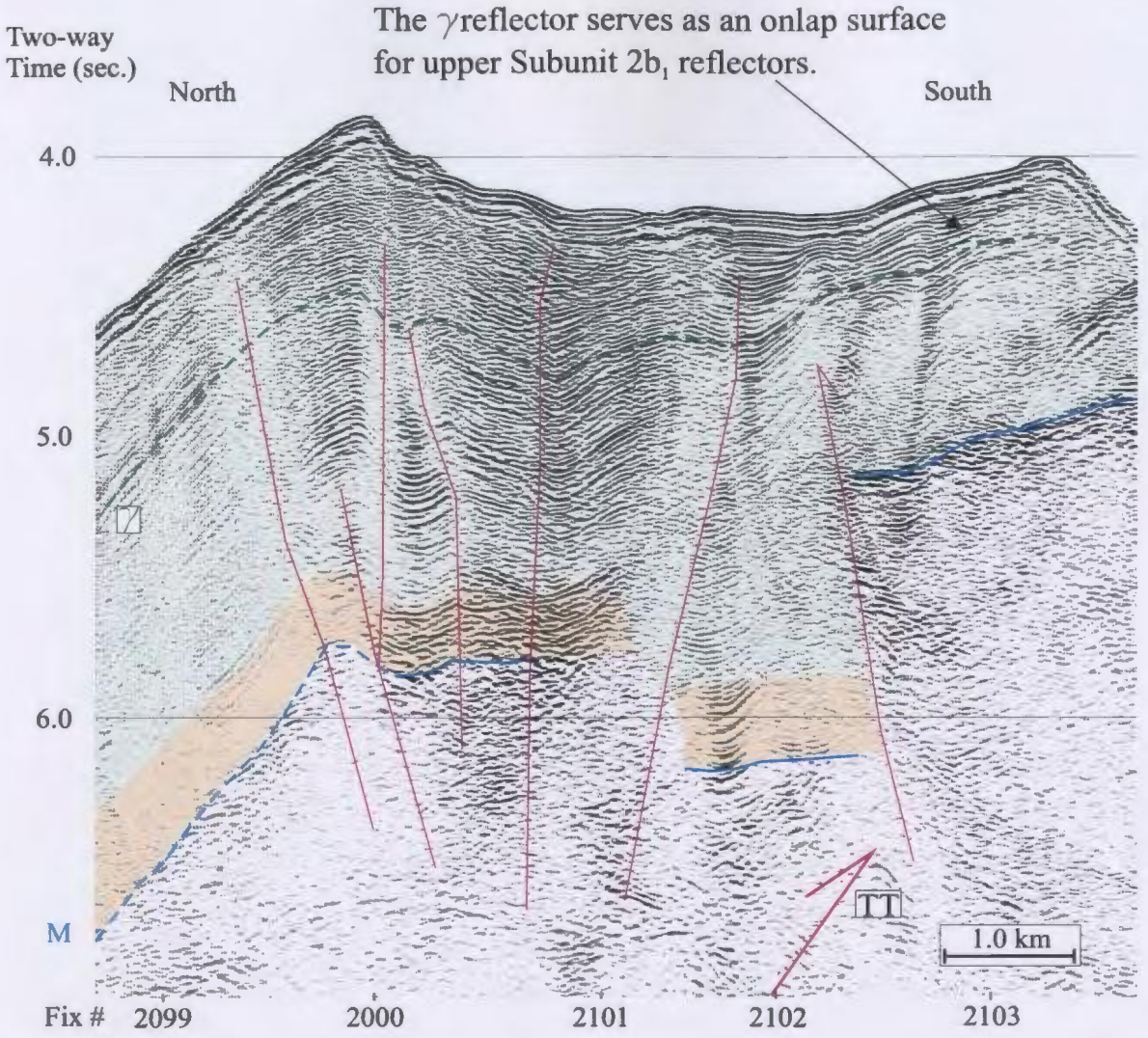

Figure 4.2.9: The crest of ridge α_4 has a heavily sheared appearance. The northwest-directed thickening and onlap of supra-γ reflectors onto the γ reflector suggest an episode of enhanced uplift of ridge α_4 during the middle Pliocene. The location of this figure relative to the survey grid is shown in Figure 4.2.5.

northwest-thickening growth wedges and southeast-directed progressive onlap unconformities within Subunits $2b_2$ and $2b_3$ suggest that, like to the east, southeast-verging uplift continued through the late Pliocene-Quaternary in the west (Figs. 4.2.5, 4.2.9). Short wavelength folds in Subunit 2a and $2b_1$ reflectors located over the crest of ridge α_4 and the proximity of the thrust TT tip point to Domain 1 lends to the possibility that middle Pliocene rapid uplift of ridge α_4 above thrust TT may have been partially facilitated by the middle Pliocene development of positive flower structures (Figs. 4.2.5, 4.2.6). As such, a northward-verging backthrust (backthrust TT') is interpreted to cut between basin β_1 and ridge α_4 in the western portion of the study area (Fig. 4.2.5 an 4.2.6). Figure 4.2.10 illustrates the mapped trajectory of thrusts TT and TT' as well as all other major structural features identified in the survey area.

Thrusts T_1-T_{10}

Structural mapping in the study area shows a series of southeast-verging fold/thrust belts (thrusts T_1-T_4, T_6-T_9) and with two, oppositely-verging thrusts (thrusts T_5 and T_{10}) within Domain 2 (Figs. 4.2.5, 4.2.6 and 4.2.10). Some of the better imaged of these thrusts are illustrated in Figures 4.2.11-4.2.13. Structural analysis and interpretation of these structures are provided below.

Figures 4.2.11 and 4.2.12 each illustrate a synform/antiform pair delineated by reflectors in Unit 1. These folds have a half-wavelength of ~10 km and an amplitude of ~450 ms. The long limbs connecting the culmination of the antiforms with the synforms

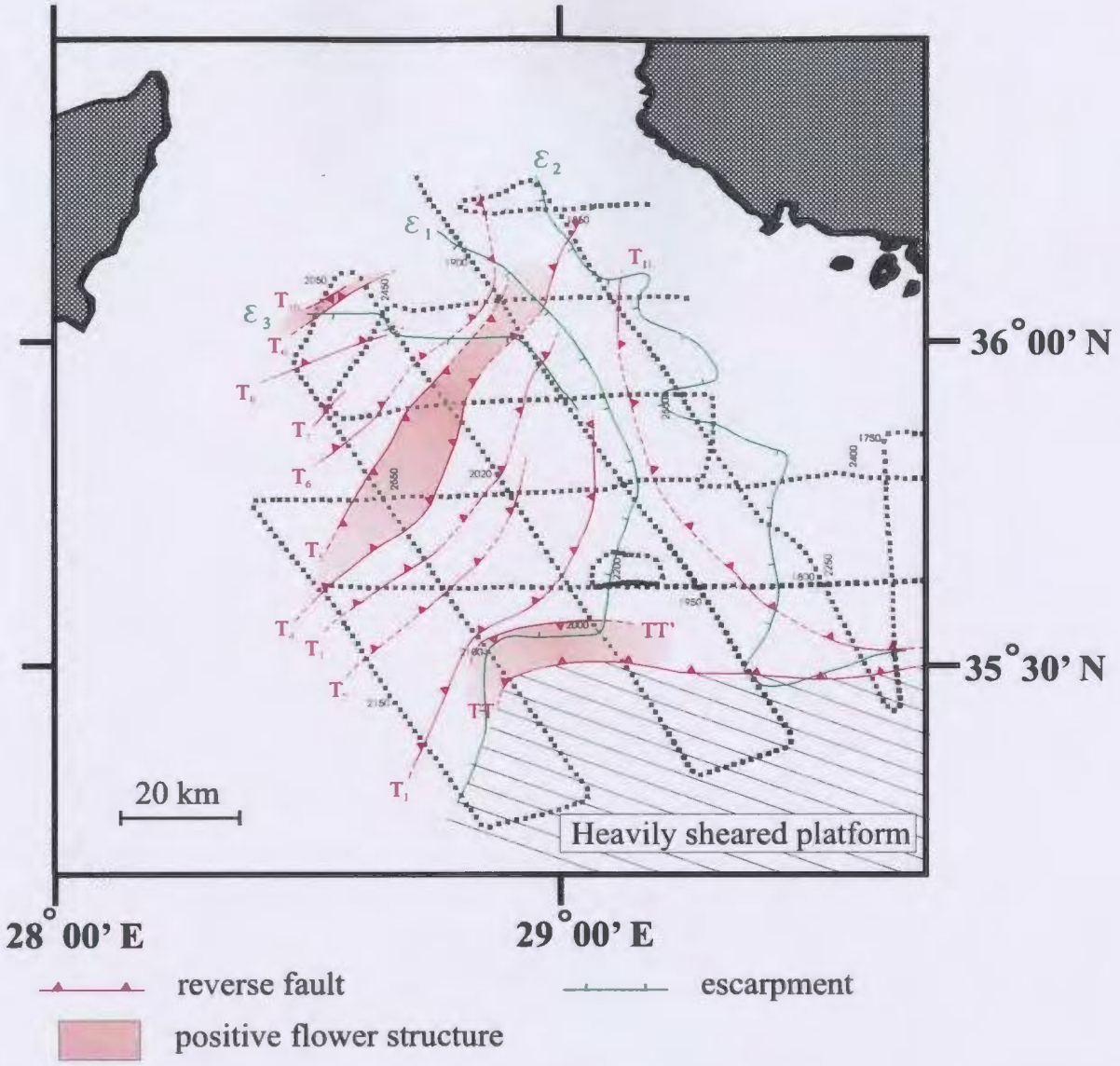

Figure 4.2.10: The uplifted and deformed platform is separated from the deep Rhodes Basin by a major, ~east-west-trending reverse fault that has transpressional attributes (thrusts TT and TT'). The deep Rhodes Basin is dominated by northeast-southwest-trending transpressional faults (thrusts T_1-T_{10}). The Turkish shelf illustrates a third, north northwest-south southeast trend (escarpments and thrust T_{11}).

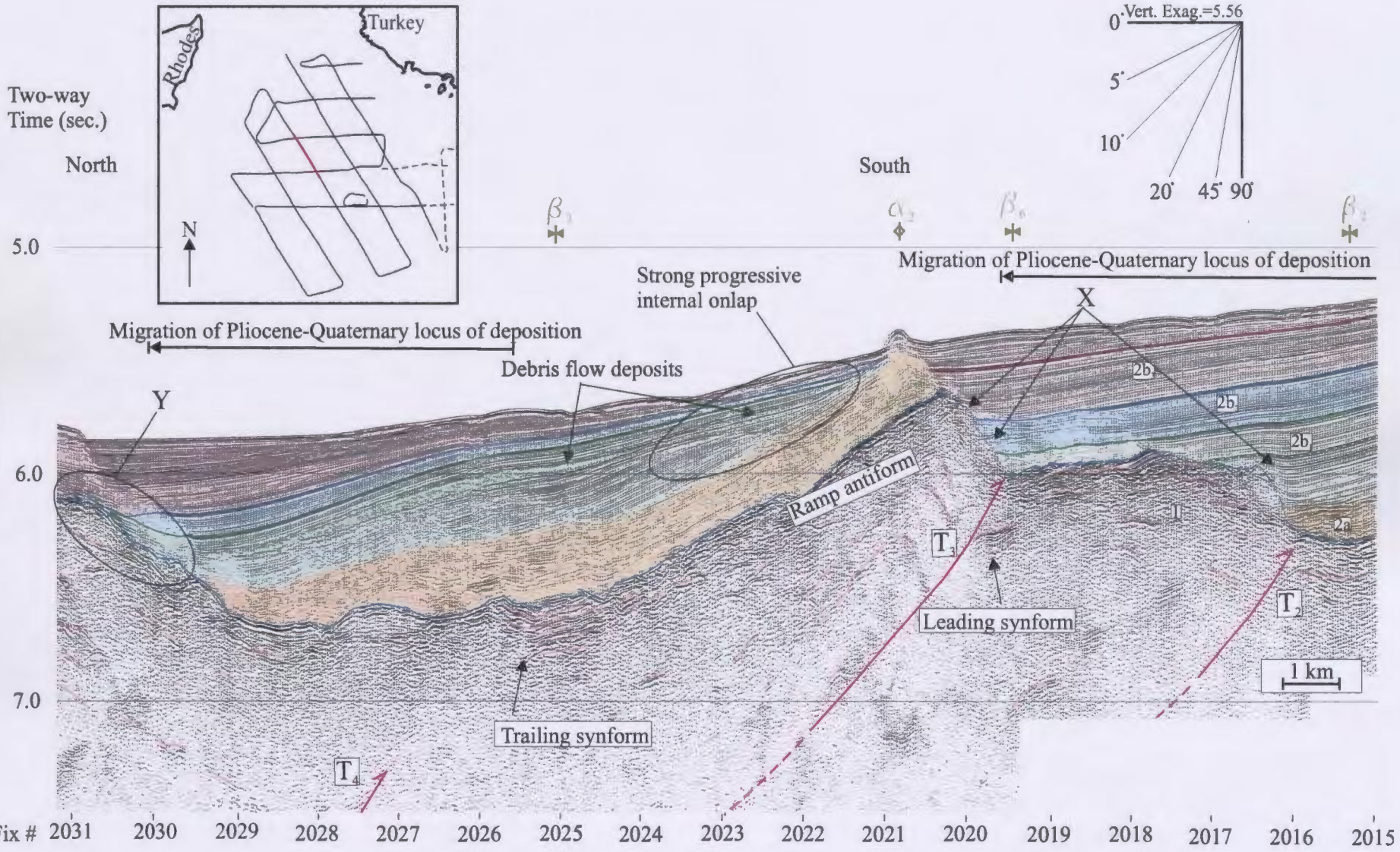

Figure 4.2.11: Thrusts T_2 and T_3 verge toward the southeast.

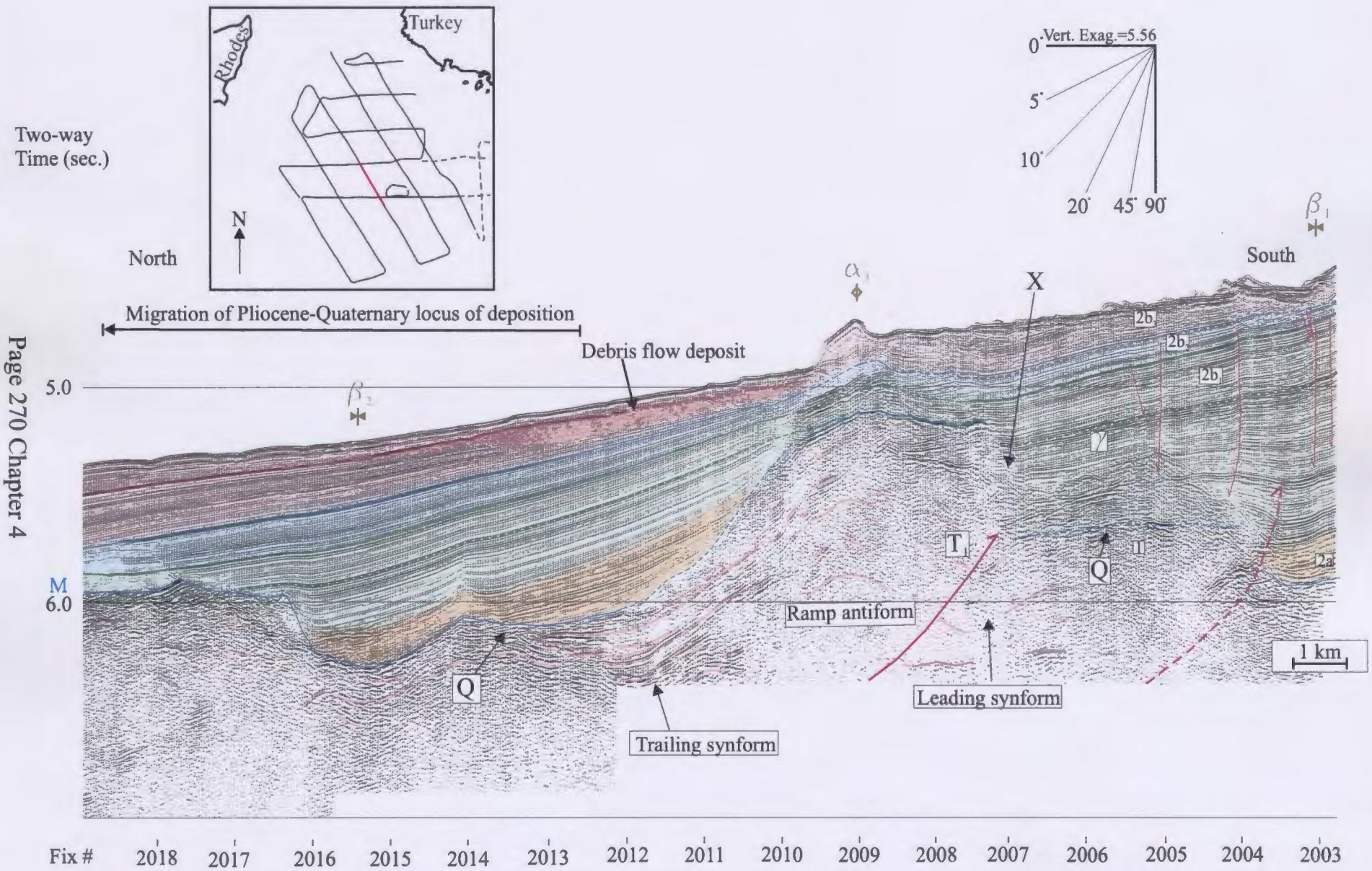

Figure 4.2.12: Thrust T_1 is part of the southeast-verging sequence of thrusts. Thickening along the backlimb is accomplished mostly by the divergence of growth strata wedges with only very week progressive onlap toward the thrust antiform crest.

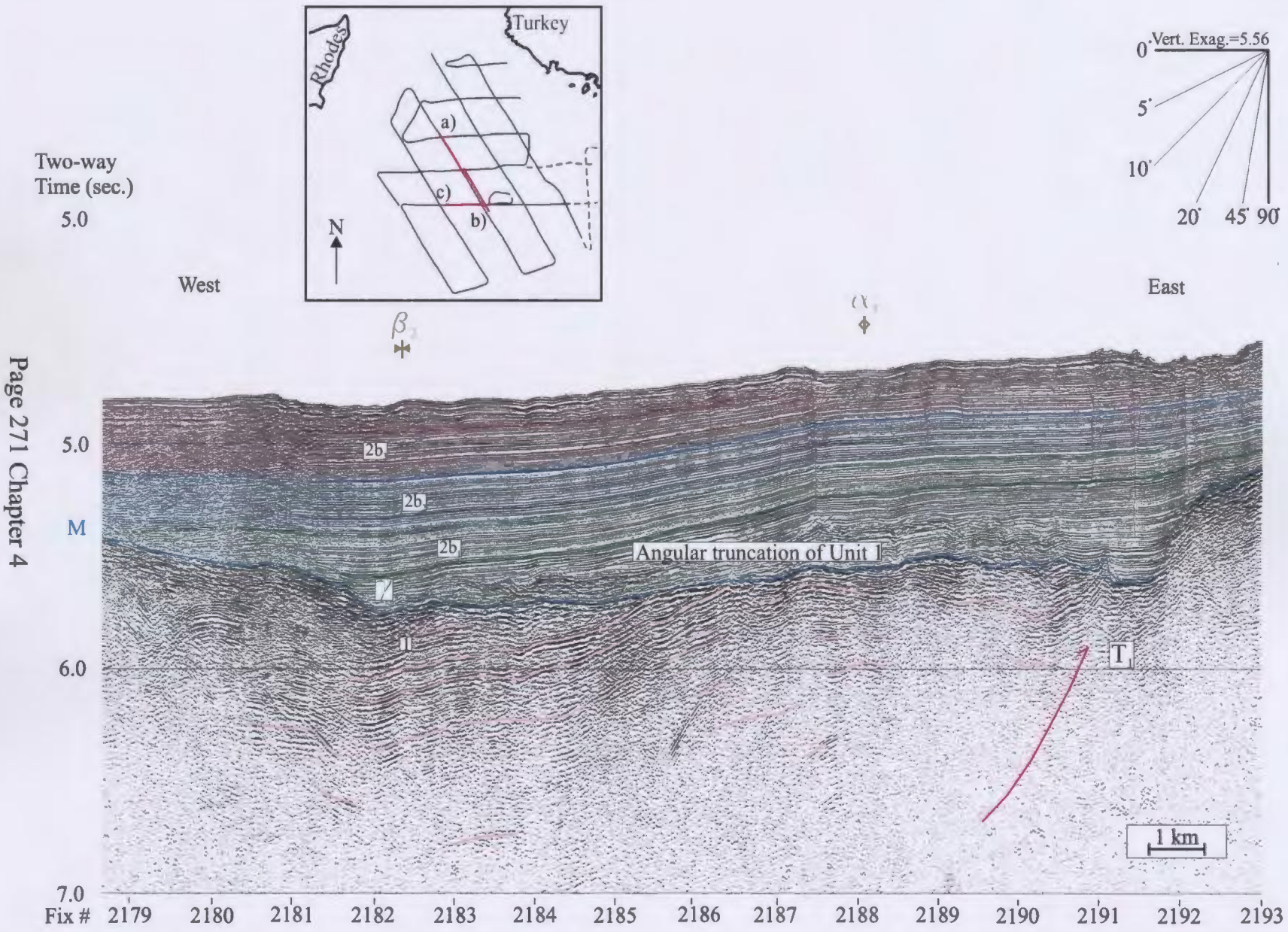

Figure 4.2.13: An east-west seismic section cutting thrust T_1 showing that the M reflector clearly truncates gently dipping Unit 1 reflectors.

to the north have a shallower dip (~5°NW) than the shorter, more steeply- dipping southern limbs (~15°SE). This asymmetry suggests that these folds outline the shallowly-dipping backlimb and steeply-dipping forelimb of a southeast-verging ramp antiform, as well as its leading and trailing synforms (Figs. 4.2.11, 4.2.12). A discontinuous transition from the inclined forelimbs to the leading synforms highlights the probable position of the thrust ramps for the underlying thrusts T_1 and T_3 (compare Figs. 4.2.11, 4.2.12 with Figs. 4.1.3b, 4.1.4b). These folded reflectors in Unit 1 are truncated by the M reflector (Fig. 4.2.12, at location Q) , indicating that at least some of the folding took place before the late Messinian erosive event (Figs. 4.2.11, 4.2.12). With the exception of poorly imaged, localized evidence of internal onlap and growth stratal wedges in the trailing synform behind thrust T_1 (Fig. 4.2.12), the folded strata in Unit 1 are generally isopachous, indicating that they are pre-sedimentary growth strata (Figs. 4.2.5, 4.2.6, 4.2.11). The absence of progressive unconformities within Unit 1 that merge with the M reflector toward thrust antiform crests suggests again that progressive uplift was not occurring during the late Messinian (Fig. 4.2.11d, 4.2.12). The correlation of thrust T_1 and associated Unit 1 strata toward the southwest further illustrates the isopachous nature of Unit 1 and its well-imaged, southeast verging, ramp antiform geometry (Figs. 4.2.13, 4.2.14). Reflectors within Unit 1 comprising the hanging wall of thrust T_2 do not clearly illustrate a thrust antiform geometry (Figs. 4.2.13, 4.2.14). However, their truncation against thrust T_2 and the vertical repetition M reflector toward the southeast provides the best example of a thrust duplex within the study area (Fig. 4.2.14).

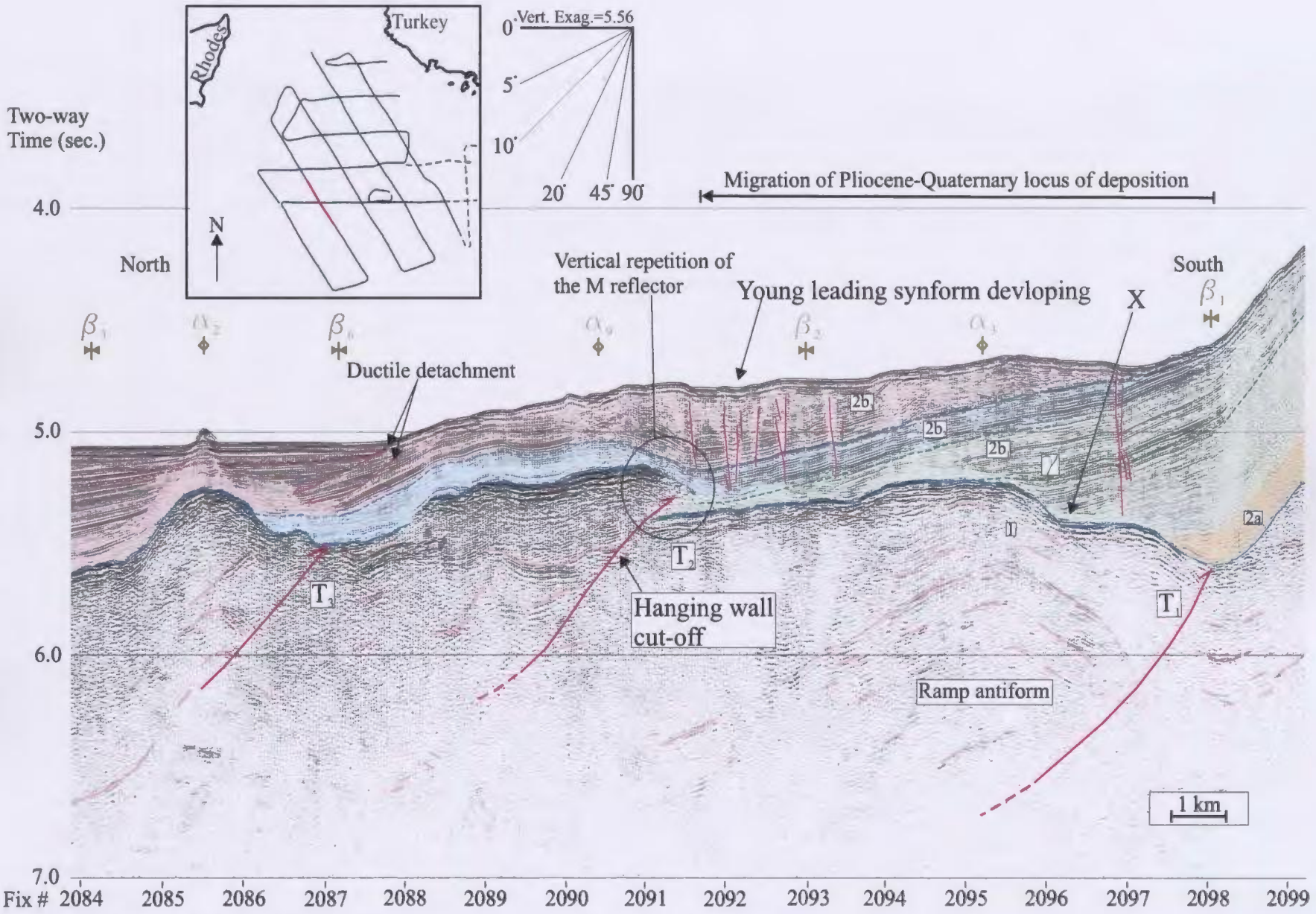

Figure 4.2.14: Thrusts T_1-T_3 share a common sense of southeast vergence.

Seismic imaging within Subunit 2a degrades toward the centre of basin β_3, but is sufficiently clear along the backlimb of thrust T_3 to delineate the isopachous nature and parallel relationship of Subunit 2a with the M reflector (Fig. 4.2.11). The absence of any significant growth stratal architectures or progressive onlap surfaces within Subunit 2a here, or at other localities throughout the Rhodes Basin, suggests that the time of inferred structural quiescence during the late Messinian continued into the early Pliocene (Figs. 4.2.11, 4.2.12, 4.2.14). The onlap of Subunit 2a onto ridge flanks and its laterally extensive, uniform distribution throughout a large portion of the Rhodes Basin (including Domains 1 and 3) suggests that only a weak undulation of the folded Unit 1 morphology survived the late Messinian erosive event (Figs. 3.1.9, 4.2.11, 4.2.12, 4.2.14). The uplift of the relatively isopachous Subunit 2a along the backlimb of T_3 and the southward-directed onlap of Subunit 2b onto it indicates a post-early Pliocene initiation of uplift along thrust T_3 (Fig. 4.2.11).

Northwest-thickening growth stratal wedges of Subunit 2b within the trailing basins of the thrust antiforms provides direct evidence of middle Pliocene-Quaternary structural activity (Figs. 4.2.11, 4.2.12, 4.2.14). The majority of this laterally extensive northward thickening is achieved by the coherent divergence of reflectors that demonstrate gentle, progressive onlap toward the thrust antiform crest. These periods of stratal growth are interrupted by intervals of strong internal onlap and/or debris flow deposits with erosive bases that mark punctuated reactivations of the underlying thrusts (Figs. 4.2.11, 4.2.12). A consistent migration of the locus of sediment deposition toward the northwest from the

early Pliocene through to the Quaternary indicates that southeast-verging uplift along these thrusts, and the associated backlimb rotation throughout the Pliocene-Quaternary (Figs. 4.2.11, 4.2.12, 4.2.14). At some locations, these wedging strata thin, curve upward and onlap onto the forelimb of the trailing thrust, whereas adjacent localities are characterized by continued strata wedging toward the trailing forelimb with only minor amounts of upward drag (compare X and Y in Fig. 4.2.11).

At some locations, the Pliocene-Quaternary succession near the underlying, blind thrusts are deformed in an upward convex sense. This upward bulging of the overlying sediments forces the development of young depocentres immediately in front of the thrust tips and indicates that the underlying thrusts have been recently active (e.g., thrust T_1 in Fig. 4.2.11 and thrust T_2 in Fig. 4.2.14). Minor, high-angle, extensional faults cut through the Pliocene-Quaternary succession in front and/or over the crest of these inverted successions and may indicate failure due to flexure (Figs. 4.2.12, 4.2.14). The backlimbs of these blind thrusts also show evidence of low-angle, gravity-driven, ductile detachments in the young Pliocene-Quaternary succession (Fig. 4.2.14) The spatial and temporal variations in these growth stratal architectures implies that there is a large degree of structural independence between structures, as well as along the strike of a single structure.

In the northwest corner of Domain 2, the gentle (~0.5-1.5) northwest dip of the seabed flattens to become horizontal (Fig. 4.2.15). Here, northeast-southwest-trending faults are clearly imaged as discrete discontinuities that cut the succession from the M

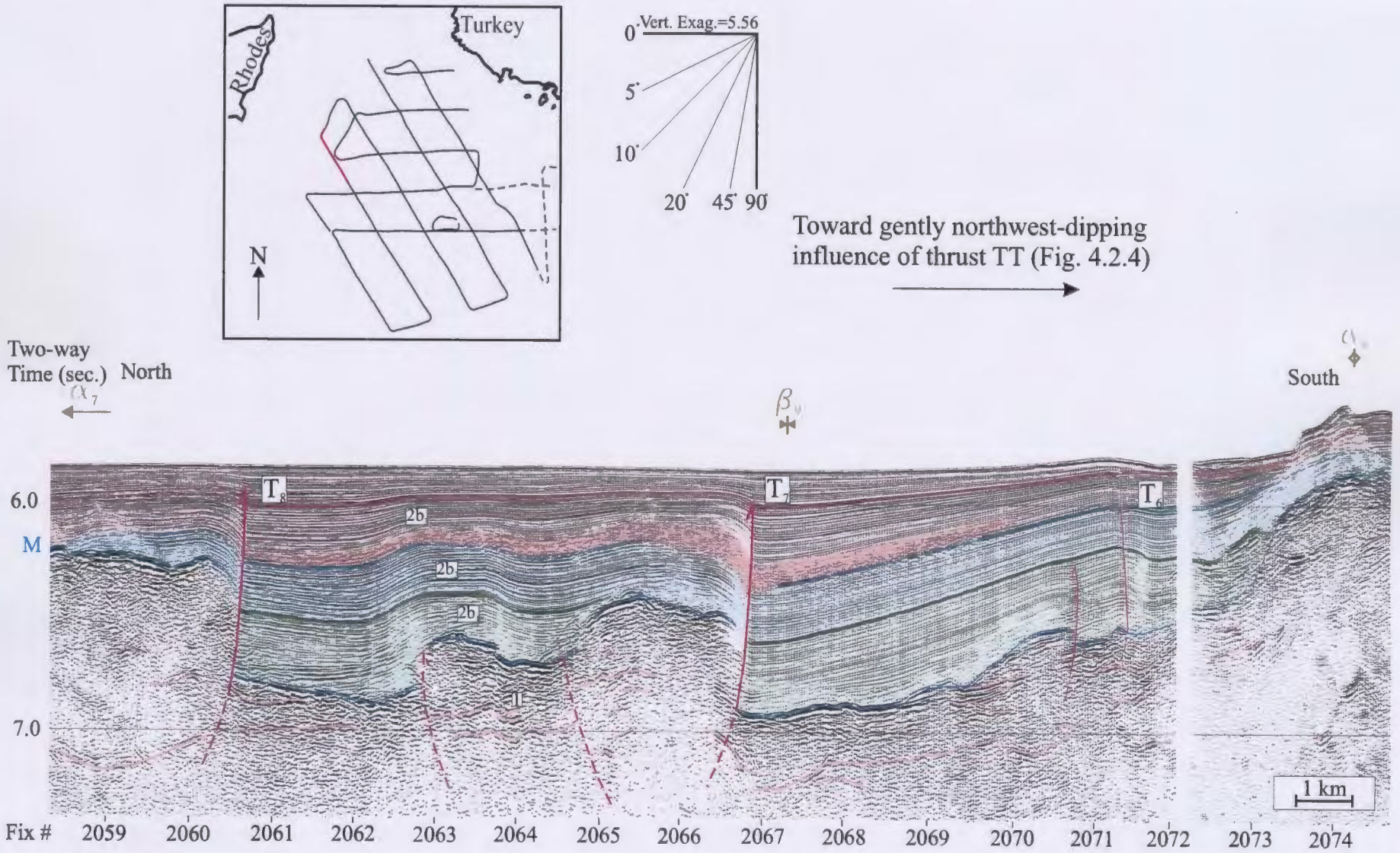

Figure 4.2.15: The northeast corner of Domain 3 displays high angle transpressional faulting. Flat portions of the deep plateau clearly illustrate high angle faults with reverse sense of motion.

reflector to the upper portion of Subunit $2b_3$ and are therefore interpreted to have been active since the late Pliocene-Quaternary. The dip direction of the fault planes, the relative offset of the basin fill across the faults and the drag of the Pliocene-Quaternary reflectors on their hangingwalls imply that most of the faults are southeastward-verging reverse faults with occasional evidence of thrust with the opposite sense of polarity (Fig. 4.2.15). The subvertical dip of the fault planes (~70-80°NW), abrupt subvertical juxtaposition of thick basin fill against Unit 1 and large discrepancies between the vertical offset of reflectors in the Pliocene-Quaternary basin fill versus that of the M reflector and divergent nature of the thrust faults collectively suggest that these faults have experienced strike slip movements. This interpretation is further supported by nearby evidence of positive flower structures; some of which produce inversions of the overlying subunit $2b_3$ (e.g., α_1 in Fig. 4.2.5 and α_7 in Fig. 4.2.16).

4.2.3: Structural Domain 3- the Turkish Continental Slope

The portion of the Turkish continental slope within the Rhodes Basin survey area includes ~3750 metres of bathymetric relief along an ~4-8°WSW gradient (Fig. 3.1.6). The orientation of the bathymetric contours and escarpments ϵ_1 and ϵ_2 suggests that the dominant trend of the Turkish slope is north northwest-south southeast (Figs. 3.1.6 and 4.2.1). It is generally characterized by a drape of Subunits 2a and $2b_1$ over its lower portion that extends a short distance into the deep Rhodes Basin (Fig 3.1.9). These Subunits are most often terminated or become discontinuous toward mainland Turkey

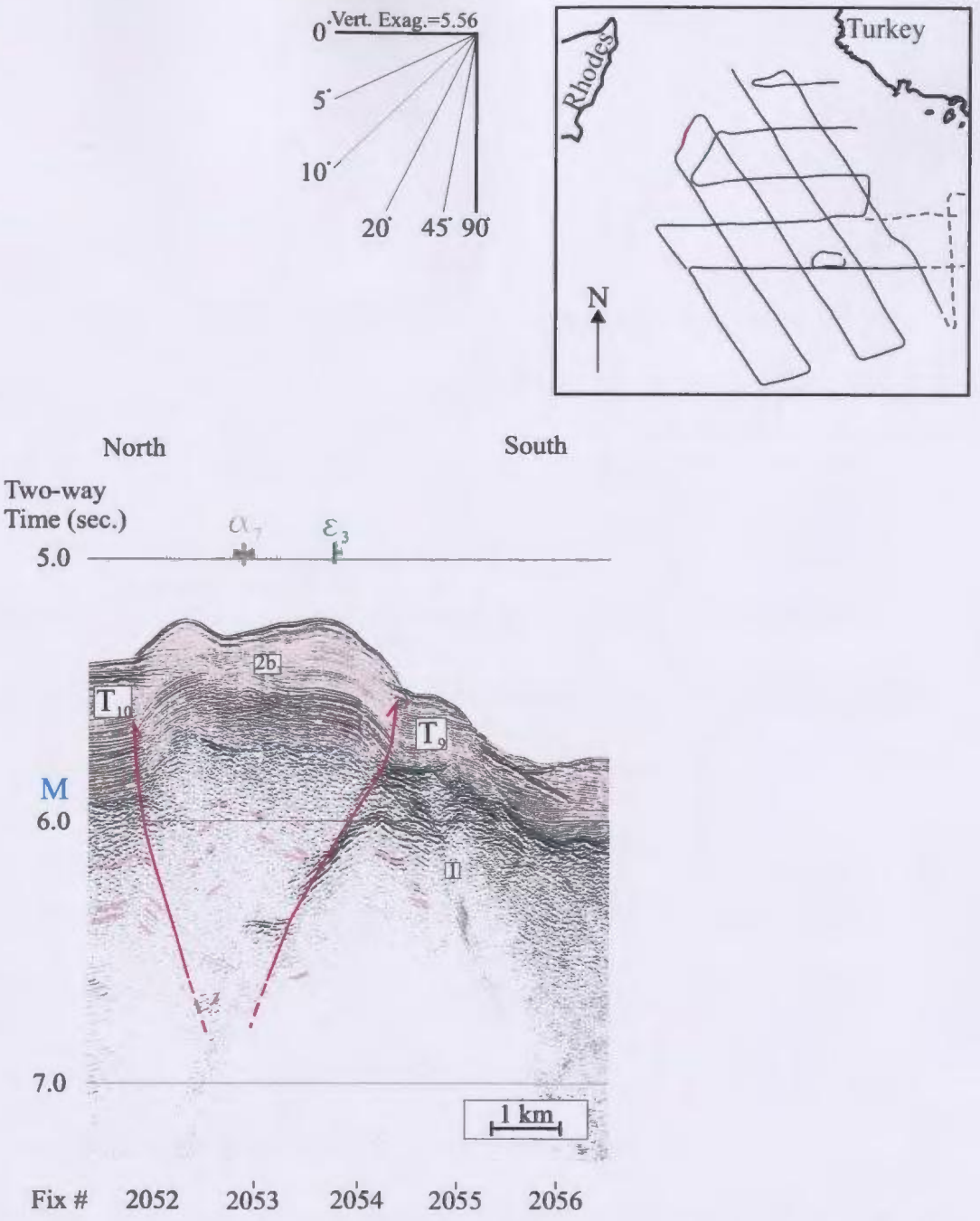

Figure 4.2.16: A Positive flower structure invertes Subunit $2b_3$ immediately northeast of Figure 4.2.15.

(Fig. 4.2.17). The upper Turkish slope often contains only a thin veneer of disturbed Subunit $2b_1$ (Fig. 4.2.18).

Evidence for rapid Pliocene subsidence

Subunit $2b_1$ contains a series of vertically stacked sequences separated by unconformities (Fig. 4.2.19). Each package is ~75 ms (56 m) thick and is characterized by oblique/sigmoid oblique prograded clinoforms that terminate updip by toplap and down dip by downlap at local unconformities. This architecture is characteristic of stacked delta successions developed at the continental shelf extending to the shelf edge (Aksu et al., 1992; Hiscott, 2001). The stacked, aggradational geometry and equal thicknesses of each package suggests that they were deposited during the glacial low stands of sea level when the shoreline was situated near the shelf edge (1, 2 and 3 in Fig. 4.2.19). The intervening shelf-crossing unconformities represent the ravinement surfaces developed during the interglacial periods (A, B and C in Fig. 4.2.19). The vertically stacked architecture and equal thickness of each sequence suggests that the magnitude of consecutive sealevel oscillations remained approximately the same during their deposition and the rate of subsidence was constant. This geometry suggests that each prograded clinoform package was initially deposited in water depths of < 200 m. Today, these packages have an apparent dip of ~1°W and are observed at a water depth of ~1900 ms (~1425 m). A similar succession is observed ~17 km to the ENE at a depth of 3300 ms (~2475 m) and has an apparent dip of ~4°SW (Fig. 4.2.20). These stacked delta

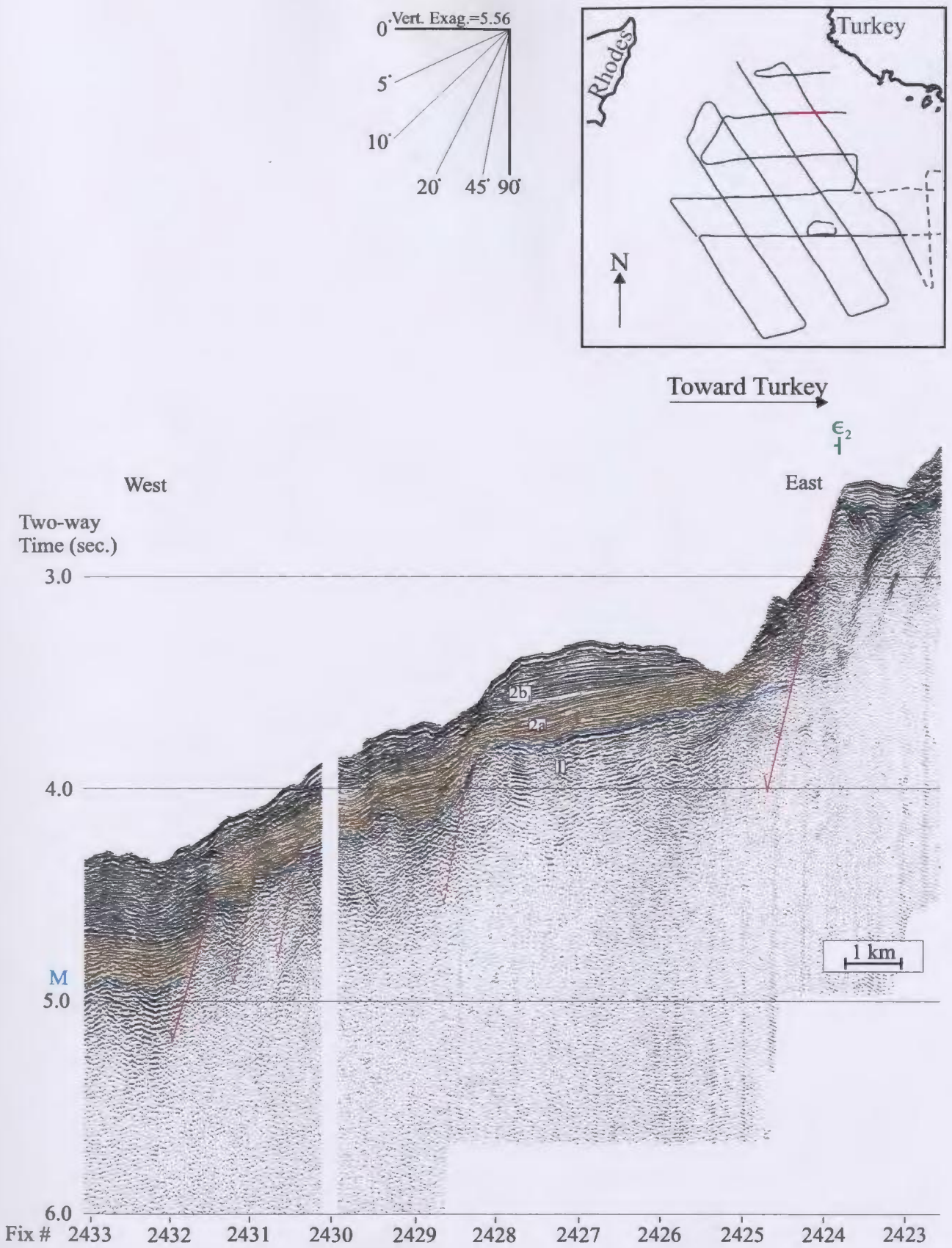

Figure 4.2.17: An example of Subunit 2a termination against escarpment ε_2 toward mainland Turkey and inferred extensional faulting down the Turkish slope.

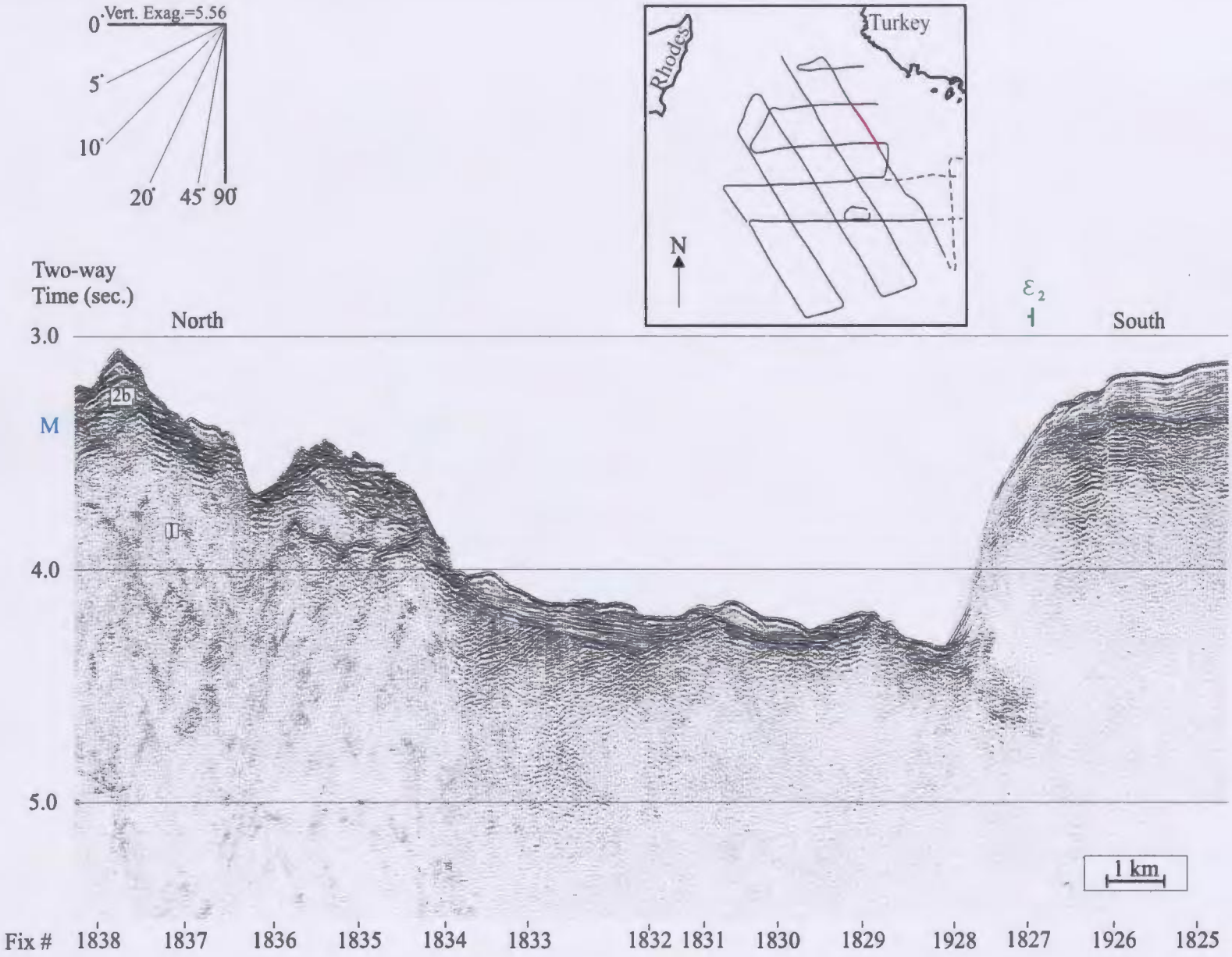

Figure 4.2.18: Deep channels trend toward the centre of the Rhodes basin from the Turkish shelf.

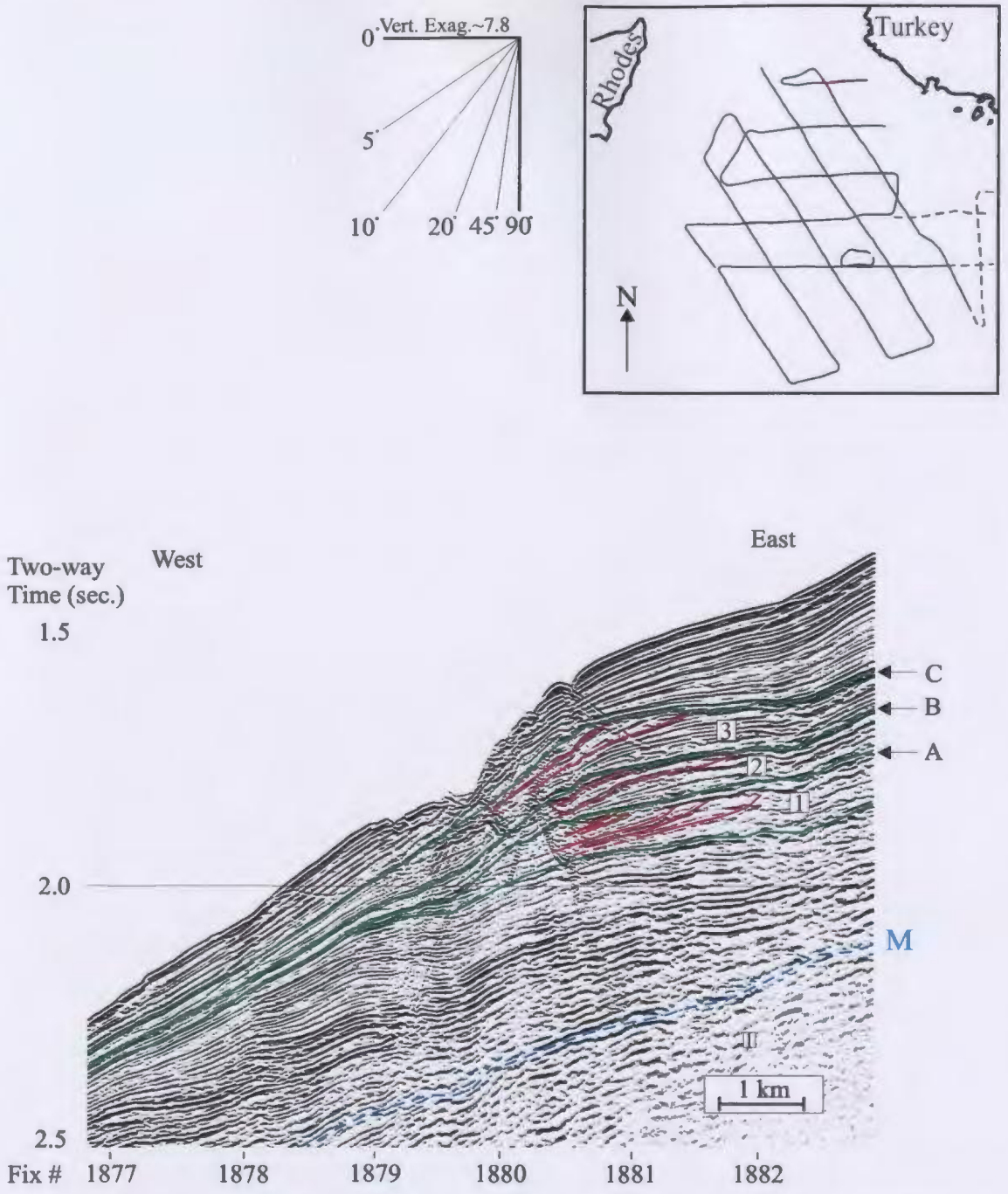

Figure 4.2.19: Aggraded clinoform packages provide evidence of rapid subsidence since <4Ma.

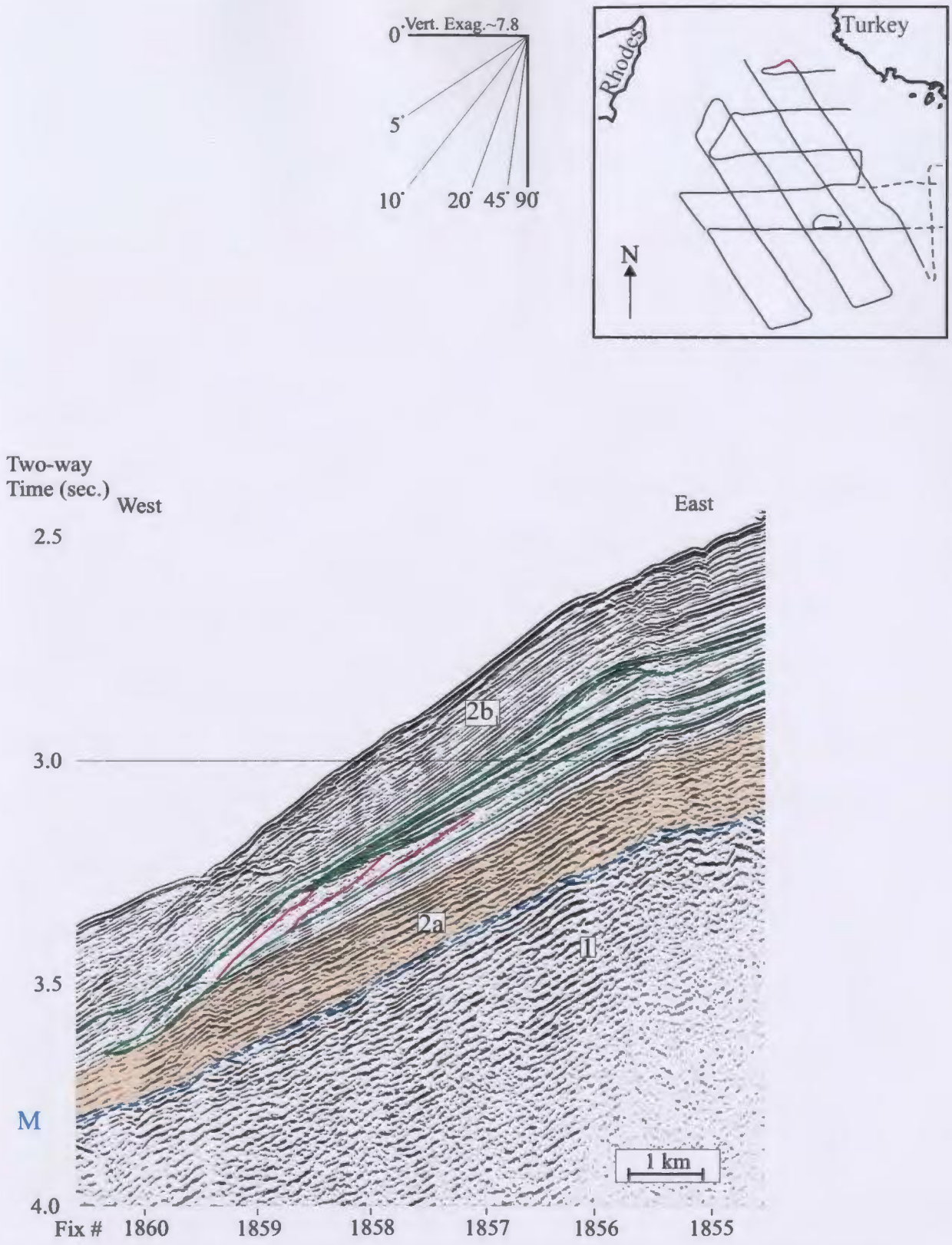

Figure 4.2.20: Aggraded clinoform packages provide evidence of rapid subsidence since <4Ma.

successions imply that up to ~2217 m of subsidence must have occurred in the Rhodes Basin since the early-middle Pliocene (~3-4Ma), suggesting a rate of subsidence of ~555-740 m/Ma. These ~8-9°W-dipping portions of the Turkish continental accommodate considerable (~1100 ms) of bathymetric relief without any observable evidence of faulting (Figs. 3.1.9a, 4.2.19, 4.2.20). Hence, these remarkably continuous slopes are interpreted as basin sag. Other areas demonstrate ~1000-1500 ms (750-1125 m) of relief via a series of down-stepping ~20°W-dipping discontinuities (Fig. 4.2.17). Based on this basinward dip orientation of these discontinuities and the down-to-the-west sense of offset of the M reflector and Subunits 2a and $2b_1$ across them, these discontinuities are interpreted as extensional faults (Fig. 4.2.17). Lack of stratal growth within Subunits 2a and $2b_1$ suggests that these faulted slopes subsided since the early Pliocene. This subsidence occurred at a sufficient rate to quickly incline the basin slopes enough to prevent further sediment accumulation since the early-middle Pliocene, leaving them relatively sediment-starved. At the base of the slope, the Subunit 2a and lower Subunit $2b_1$ are onlapped by flat-lying upper Subunit $2b_1$ (and younger) reflectors (Fig. 3.1.9a), suggesting that the vast majority of subsidence along the Turkish slope may already have been accomplished by the time the upper portion of Subunit $2b_1$ was deposited. This architecture implies an increased rate of early-middle Pliocene subsidence that initiated at ~3-4 Ma and was completed by ~2-3 Ma (Fig. 3.1.9a).

Across ridge α_6, west-dipping reflectors steepen from ~1.5°W to ~8°W toward escarpment ε_1 and are truncated by the overlying M reflector, forming an angular

unconformity (Fig. 4.1.21). The internally-disturbed δ package fills small irregularly-shaped troughs in the M reflector, pinches out up-slope and is truncated at an intra Unit 2 angular unconformity (Fig. 4.2.21). Both the δ package and the overlying Subunit $2b_1$ are offset across escarpment ε_1, below which they form a wedge-shaped, internally chaotic package at the base of the escarpment onlapped by Subunits $2b_2$ and $2b_3$ of basin β_7 (Fig. 4.2.21). Although there is a lack of strongly diagnostic structural features and stratigraphic relationships in this area, the westward-steepening and angular truncation of the reflectors in both Unit 1 and the δ package suggest the possibility of uplift of ridge α_6, both before the late Messinian erosive event and during the early Pliocene. There is no positive evidence to either support or refute deformation during the late Messinian erosive event. However, the lack of intervals of growth strata bound between successive progressive unconformities that merge with the M reflector suggest that uplift was not active during the Messinian. The steeper apparent dip of the reflectors in Unit 1 (~8°W) versus the dip of the reflectors in the δ package (~5°W) over the steeply-inclined forelimb of thrust T_{11}, implies that deformation was cumulative over at least two episodes of deformation: one before the Messinian erosive event and a second after the deposition of the early Pliocene δ package (Fig. 4.2.21). The slumped appearance of Subunit $2b_1$ reflectors at the base of escarpment ε_1 suggests a subsequent, rapid ~early-middle Pliocene, normal-sense failure of the forelimb of thrust T_{11} (Fig. 4.2.21).

The Pliocene succession near escarpment ϵ_2 and ridge α_5 also consists of only a

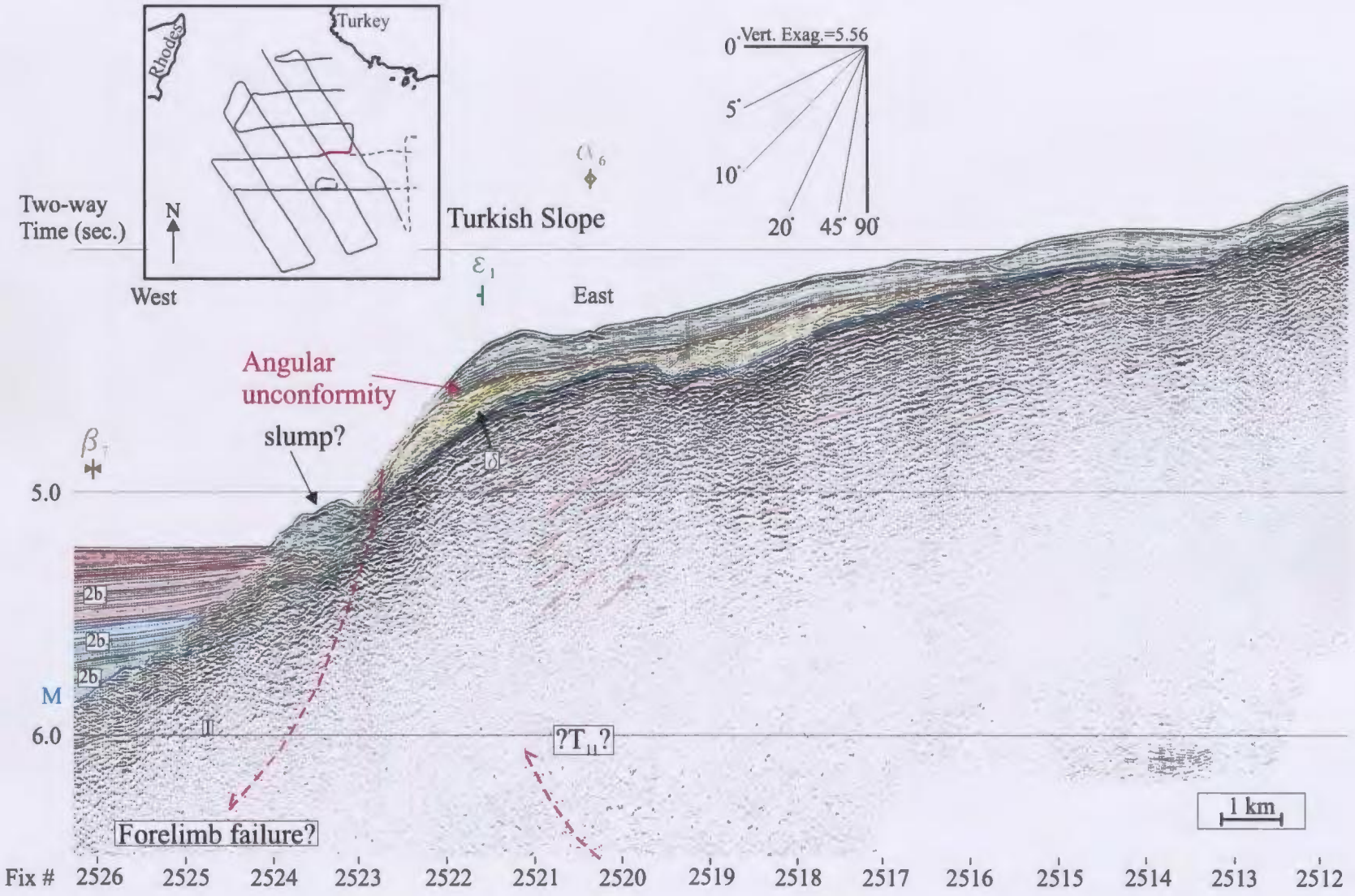

Figure 4.2.21: Early-middle Pliocene extensional failure/slumping may have reshaped an older, compressional fabrics imposed by thrust T_{11}.

thin cover of Subunit $2b_1$ (Fig. 4.2.22). A supplement of data from line 70a shows that the long, eastern limb of ridge α_5 dips ~1°E and is onlapped by sub-horizontal Subunit $2b_1$ reflectors (Fig. 4.2.22). Along this eastern flank, narrow dimples in Subunit $2b_1$ delineate several linear, sub-vertical (60-90°-dipping) thin-skinned faults, some of which produce minor offsets of the reflectors (X in Fig. 4.2.22). The thin cover over the crest of ridge α_5 is also cut by minor steeply-dipping faults. The short, western limb of ridge α_5 (escarpment ϵ_2) dips at ~15°W and is virtually bare of sediment. The eastern limb of a well-imaged, broad synform delineated by reflectors in Unit 1 forms an angular relationship with the M reflector immediately west of escarpment ϵ_2 (4.2.22). On the basis of these architectures, a west-verging thrust T_{11} is inferred to have uplifted ridge α_5 and generated the leading synform to its west prior to the late Messinian erosive event. The gentle eastward dip and wedging of Subunit $2b_1$ along the backlimb of thrust T_{11} suggests that it has continued to be active into the early Pliocene (Fig. 4.2.22). A minor amount of thinning over the crest of a slight bulge of the M reflector along the backlimb of thrust T_{11} collectively suggest that it too was rising during the early Pliocene. To the far east, a large, vertical fault terminates the eastward-thickening backlimb succession (Fig. 4.2.22). This abrupt, vertical contact suggests that this fault likely accommodates strike slip motion. Structures of this magnitude are unlikely to be isolated and it is expected that the high angle faulting noted throughout even the youngest Subunit $2b_1$ strata along the backlimb of thrust T_{11} are associated with this strike slip motion. The westward-thickening growth stratal wedges of subunits $2b_{1\text{-}3}$ and their gentle onlap

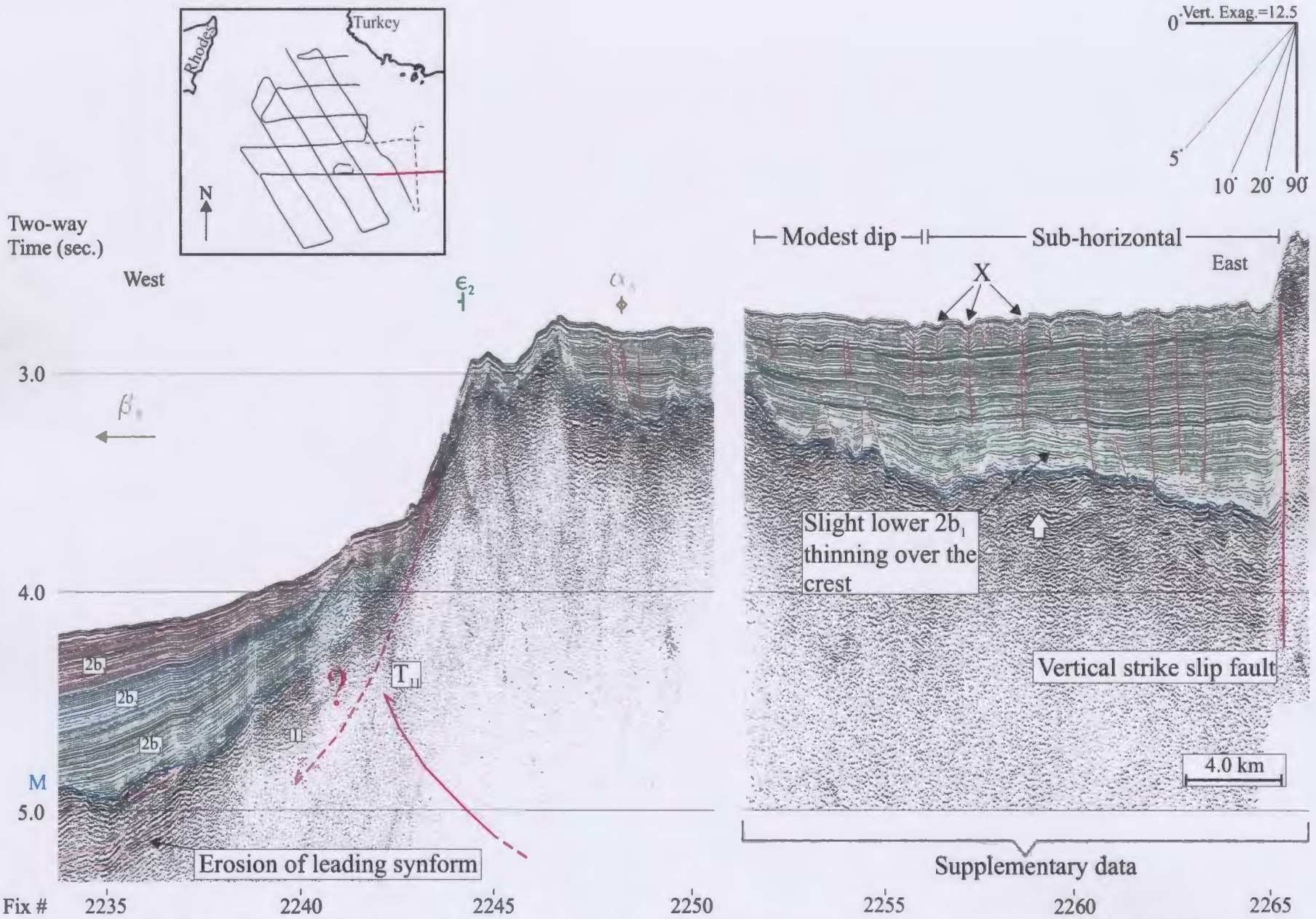

Figure 4.2.22: Thrust fault T_{11} carries a gently eastward-wedging and dipping package of sediment on its backlimb. This package is then truncated by a sub-vertical strike slip fault to the east.

toward the forelimb of thrust T_{11} suggests that they were deposited on the forelimb of the developing thrust T_{11}. The mechanism for the formation of escarpment ϵ_2 is unclear: it may represent the steep forelimb of thrust T_{11} directly in front of the leading synform. Another possibility is that extensional activity, like that interpreted further downslope (Fig. 4.2.21), may be related to strike slip motion east of thrust T_{11} and created extensional failure along the forelimb of T_{11}. The advantage in considering the early-middle Pliocene re-shaping of the southern Turkish slope by extensional activity, possibly derived from strike slip motion, is that it is in agreement with the early-middle rapid Pliocene rapid subsidence documented by the clinoform packages along the northern Turkish slope.

Bathymetric channels

Several bathymetric channels cut the Turkish continental slope (Fig. 3.1.6). Seismic data show that some of these broad sediment-starved channels (up to ~15 km wide) are coincident with ~1000 ms (750 m) offsets of the M reflector, presumably across faults that may have focussed more recent erosion via bottom currents (Fig. 4.2.18). Because there are Pliocene-Quaternary sediments preserved at the top of some of the channel-bounding escarpments (i.e., Subunit $2b_1$), it is suggested that the low-standing channel axes also initially contained Subunit $2b_1$ sediments. If this is the case, the M reflector may be a still-evolving submarine unconformity and, as such, it is not possible to get an indication of how much of the offset of the M reflector is due to structural control (bounding faults) or submarine erosion along the channel axes.

Chapter 5: Discussion

The structural interpretations of Chapter 4 are optimized by separating the major structural styles temporally and inferring the orientation of their causative stress fields. This leads an understanding of the Neogene kinematic development of the Rhodes Baisn and its integration into the geo-tectonic framework of the eastern Mediterranean, specifically the junction between the Hellenic and Cyprus Arcs.

5.1: Major episodes of deformation: P_1 and P_2

The structural interpretation of seismic reflection profiles within the Rhodes Basin (Chapter 4) provides evidence of two major deformation episodes: (1) pre-M reflector (late Messinian) compression and (2) middle Pliocene-Quaternary transpression. Because Messinian stratigraphy is absent in the Rhodes Basin, it is difficult to confirm whether the pre-late Messinian deformation episode was active during the Messinian. However, on the basis of what portion of the stratigraphic section is available, it is suggested that the Messinian may have been a period of relative structural quiescence.

5.1.1: Pre-late Messinian Thrusting: Deformation Episode P_1

Folded reflectors within Unit 1 delineate a series of asymmetrical thrust antiforms that highlight southeast-verging fold/thrust belts within Domain 2 (Figs. 4.2.5, 4.2.6, 5.1.1; thrust TT and thrusts T_1-T_4 and T_6-T_9). The angular truncation of these folded thrust

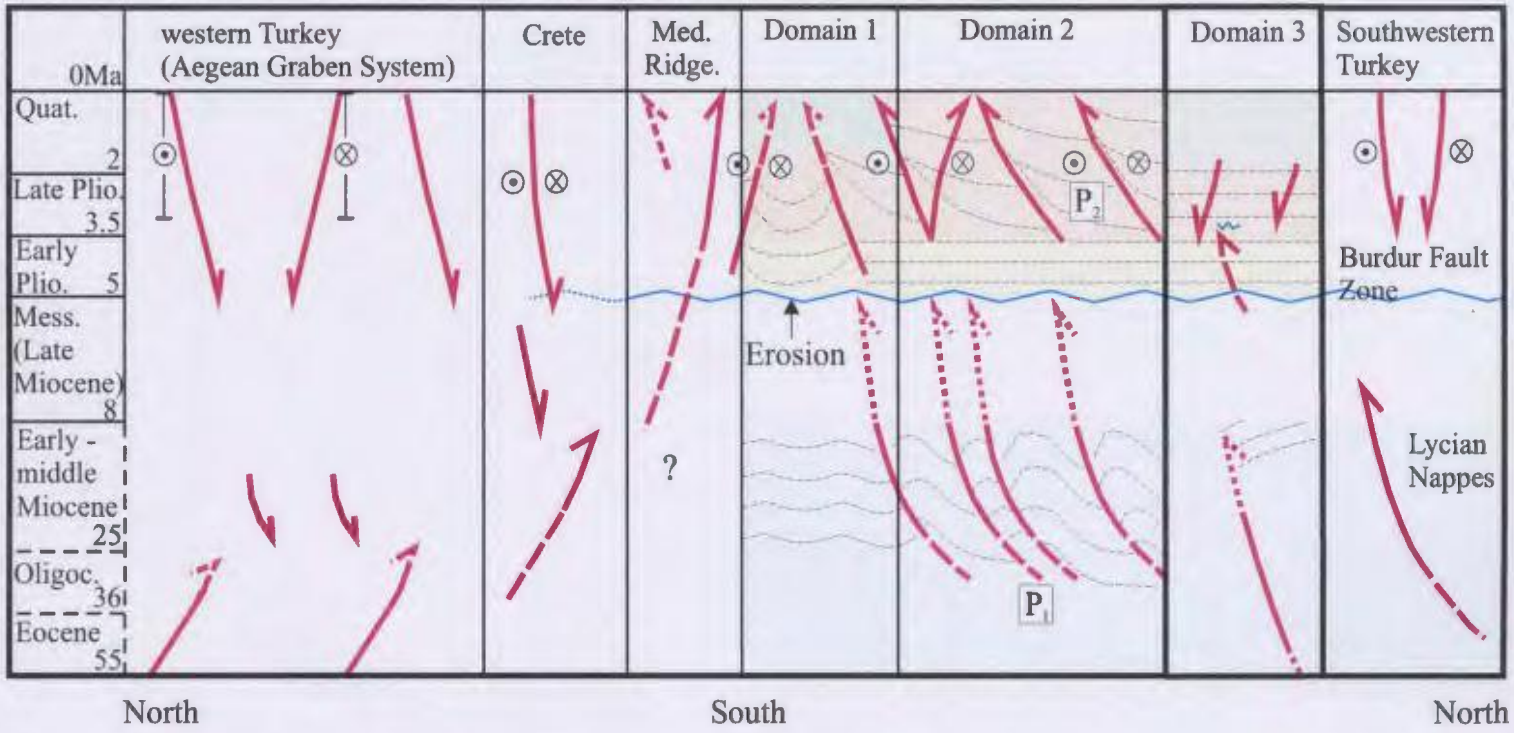

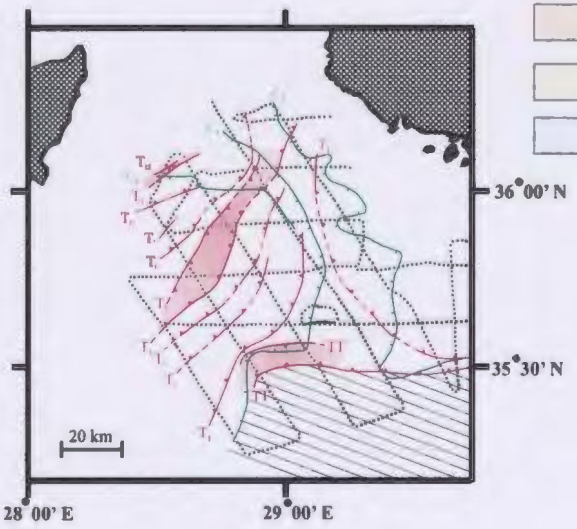

Subunit 2b

Subunit 2a

Unit 1

Non deposition

Note: Time scale is compressed for times greater than 8 Ma.

Figure 5.1.1: A simplified tectonic chart of the eastern Aegean region showing the major stratigraphic relationships within the Rhodes Basin. Generalized episodes of deformation for regions outside the study area are compiled from Jackson (1994), Price and Scott (1994), Barka et al. (1995), Galindo-Zaldivar et al. (1996), ten Veen and Meijer (1998), Glover and Robertson (1998), Woodside et al. (2000) and Bozkurt (2000).

antiforms in Unit 1 by the overlying M reflector demonstrates that the underlying thrusts were active prior to the late Messinian erosive event (Fig. 4.2.5, 4.2.6). This episode of pre-late Messinian northwest-southeast-oriented compression is referred to as P_1 (Fig. 5.1.1). There is no direct evidence to provide the absolute age or lithology of Unit 1. However, it is reasonable to suggest that Unit 1 can be correlated with the late Mesozoic limestones and/or Oligocene flysch noted on land in southern Turkey (e.g., Lycian Nappes and Bey Dağari Unit; Collins and Robertson, 1998), the Island of Rhodes (Hanken et al., 1996) and the Island of Cypus (Collins and Robertson, 1998). Unfortunately, Unit 1 is not imaged sufficiently well to discriminate whether it consists dominantly of the Mesozoic limestones or the Oligocene flysch. Assuming Unit 1 is of Mesozoic-Oligocene age and that the M reflector defines a late Messinian erosive unconformity, the isopachous nature of its folded strata and their angular truncation at the M reflector provide evidence that broadly constrain the age of P_1 fold/thrust deformation to the pre- late Messinian portion of the Miocene- a portion of the stratigraphic succession that is most likely to have been removed by the subsequent late Messinian erosive event. Hence, there is little preserved evidence of Unit 1 syn-sedimentary growth.

South of thrust TT (Domain 1), the seismic character of Unit 1 is less clearly stratified than that within Domain 2 and therefore does not permit as thorough an analysis of the Unit 1 stratigraphic architecture (compare Figs. 4.2.2 and 4.2.3 with Figs. 4.2.11 and 4.2.12). This relatively abrupt change in Unit 1 seismic character and the transition from long to short wavelength basin and ridge architectures from Domain 2 to Domain 1

may be due to a change in Unit 1 composition across the Domain boundary. It will be discussed later that such a transition can be understood if Domain 1 is more closely related to the Anaximander Mountains than to western Turkey.

The angular truncation of antiformal reflectors in Unit 1 at the overlying M reflector above thrust T_{11} suggests that uplift along thrust T_{11} was also active prior to late Messinian erosion (Fig. 4.2.21). However, the southwest-verging polarity of thrust T_{11} is highly oblique to that of thrust TT and thrusts T_1-T_4, T_6-T_9. As such, it likely developed separate from thrust TT and thrusts T_1-T_4 and T_6-T_9. A possible explanation of this second, pre-late Messinian structural trend is presented in the following section (section 5.2) where the structures within the Rhodes Basin are related to the broader, eastern Mediterranean geo-tectonic framework.

5.1.2: Late Messinian-early Pliocene Regional Subsidence

The above evidence of pre-late Messinian compression and uplift is supported by the subsequent development of the laterally extensive, erosive M reflector. The majority of the eastern Mediterranean basins contain a thick sequence of Messinian evaporites (e.g., Antalya, Cilicia, and Ionian basins) as a result of the Messinian salinity crisis related to the isolation of the Mediterranean from the rest of the world oceans. The absence of such evaporites within the Rhodes Basin suggests that its uplift during P_1 deformation exceeded that of the majority of the eastern Mediterranean basins. The lack of clearly imaged progressive unconformities that merge with the M reflector toward the ridge

crests and syn-tectonic growth strata within Unit 1 suggest that P_1 thrusts may have been relatively inactive during late Messinian erosion (Figs. 4.2.5, 4.2.6, 4.2.11, 5.1.1). Although it can be correctly argued that the syn-tectonic growth strata may have been removed by late Messinian erosion, progressive unconformities formed by continued uplift during erosion would be expected to be preserved. However, determining with certainty whether deformation was active during a major erosive event is often difficult.

The drape architecture of Subunit 2a over the M reflector throughout the majority of the Rhodes Basin, including the now-inclined Turkish continental slope (Fig. 3.1.9a) suggests that late Messinian erosion removed much of the relief imposed by P_1 deformation and that the Rhodes Basin experienced a rapid relative sea level rise during the earliest Pliocene. The parallel-bedded and isopachous nature of Subunit 2a implies that the inferred structural quiescence during the late Messinian continued into the earliest Pliocene. The onlap of Subunit 2a onto the M reflector within Domain 2, however, verifies that a slight undulation of the northeast-southwest-trending, P_1 fold/thrust morphology survived late Messinian erosion, permitting sediment accumulation in the low-standing troughs (Fig. 4.2.12). The most likely source of Subunit 2a sediments is the nearby Taurides to the north. This sediment source is comprised of Carboniferous-Tertiary ophiolite, volcaniclastic and carbonate rocks (Collins and Robertson 1998; Robertson, 2000).

5.1.3: Middle Pliocene-Quaternary Transpression: Deformation Episode P_2

Seismic imaging within Unit 2 is generally clear, permitting the confident identification of growth stratal architectures that record a middle Pliocene-Quaternary transpression episode (P_2). The most significant of the P_2 structures is the deeply-rooted thrust TT: a reactivated, crustal-scale thrust that provides the regional, northward tilt of the Pliocene-Quaternary sediments along its backlimb. Based on growth stratal architectures, thrust TT clearly shows accelerated growth during the middle Pliocene-Quaternary (e.g., supra-γ reflectors in Figs. 4.2.5, 4.2.6) with continued uplift slightly outpacing sedimentation rates (Figs. 4.2.7, 4.2.8). Thrusts behind thrust TT are characterized by middle-Pliocene-Quaternary, northwest-thickening growth stratal wedges and progressive onlap unconformities within a series of developing piggy-back basins carried on reactivated, southeast-verging P_1 thrusts (e.g., Fig. 4.2.6, 4.2.7). Evidence of oppositely-verging thrusts (e.g., thrusts T', T_5 and T_{10}; Figs., 4.2.5, 4.2.6, 4.2.16, 5.1.1) and northeast-southwest-oriented strike faults with compressional attributes (e.g., thrusts T_6-T_8; Fig. 4.2.15) with associated Pliocene-Quaternary growth stratal architectures provide convincing evidence of the P_2 middle Pliocene-Quaternary transpressional reactivation of the P_1 northeast-southwest-oriented fold/thrust belt (Fig. 5.1.1). The prevalence of transpression during the middle Pliocene is also implied by the intense shearing and development of positive flower structures within Domain 1 to the south (Figs. 4.2.2, 4.2.3).

East-dipping and thickening growth stratal wedges within Subunit $2b_1$ down the

backlimb of thrust T_{11} (Fig. 4.2.22) and the angular truncation of the δ package at an intra-Subunit $2b_1$ unconformity (Fig. 4.2.21) suggest early Pliocene, west-verging uplift along thrust T_{11} (Fig. 5.1.1). As with the P_1 deformation episode, the trend of thrust T_{11} during P_2 is not in agreement with the sense of deformation in the reminder of the Rhodes Basin (Fig. 5.1.1). This apparent conflict will be addressed later when the Rhodes Basin is discussed in its regional context (section 5.2). The forelimb of thrust T_{11} is clearly cut by escarpment ϵ_2 and shows evidence of post-Subunit $2b_1$ (middle Pliocene) extensional slumping and failure (Figs. 4.2.21, 5.1.1). Escarpment ϵ_2 trends north northwest-south southeast, as do escarpments ϵ_1 and ϵ_3 further down the Turkish continental slope. Although this trend is ~25° off of what the expected trend for extensional faults in a northeast-southwest-trending strike slip system (Fig. 5.1.1), it corresponds well with the middle Pliocene timing of transpressional P_2 deformation within Domains 1 and 2. As such, escarpments ϵ_1-ϵ_3 and the rapid, early-middle Pliocene subsidence along the Turkish continental slope (e.g., clinoforms in Fig. 4.2.19) are interpreted as a result of extension within a sinistral, transpressional system.

5.2: The Rhodes Basin within the Context of the eastern Mediterranean

The wide lateral extent of the Eocene-Oligocene limestone-rich deposits (correlated with Unit 1) suggest that the eastern Mediterranean was comprised of an extensive array of forarc basins spanning ~east-west along the African/Eurasin convergence zone during the Mesozoic-lower Tertiary (Robertson, 1998). It is important

to remember that the present-day orientation of structures along the Hellenic Arc (and Cyprus Arc) have been altered from their original orientations by Neogene rotations of western Turkey, Greece and Rhodes (Fig. 1.4.5; Kissel and Laj, 1988; Duermeijer et al., 2000). As a result, of these rotations, the curvature of the African/Eurasian plate boundary has been increasing since the middle Miocene (Fig. 5.2.1; Ten Veen and Kleinspehn, 2002). Figure 5.2.1 illustrates how P_1 (pre-Messinian) thrusting deformation thrusting may have been more strongly south-verging during the time of its ~Miocene emplacement. Assuming that the plate boundary during the Miocene was less curved and that the African and Eurasian Plates were undergoing nearly north-south convergence, it is expected that P_1 deformation would accommodate mostly thrusting; thus accounting for the well-developed P_1 fold/thrust belts. Because the Lycian Nappes share a similar trend to that of the P_1 fold/thrust belts, it is reasonable to infer that the timing of thrusting of deformation phase P_1 coincides with the middle-late Miocene emplacement of the Lycian Nappes on land in western Turkey (Figs. 5.1.1, 5.2.1; Robertson, 2000; Ten Veen and Kleinspehn, 2002).

Domain 1 is relatively uplifted, contains only a thin cover of sediment and its Unit 1 seismic character is very discontinuous. These characteristics and its southerly location suggest that it may have a genetic tie with the adjacent Anaximander Mountains (Fig. 5.2.2). Previous studies have proposed that the Anaximander Mountains may represent exotic pieces of lithosphere such as upthrusted blocks of Neotethyan sea floor (Ryan et al., 1970) or fragments of northward-accreting African lithosphere (Rotstein and

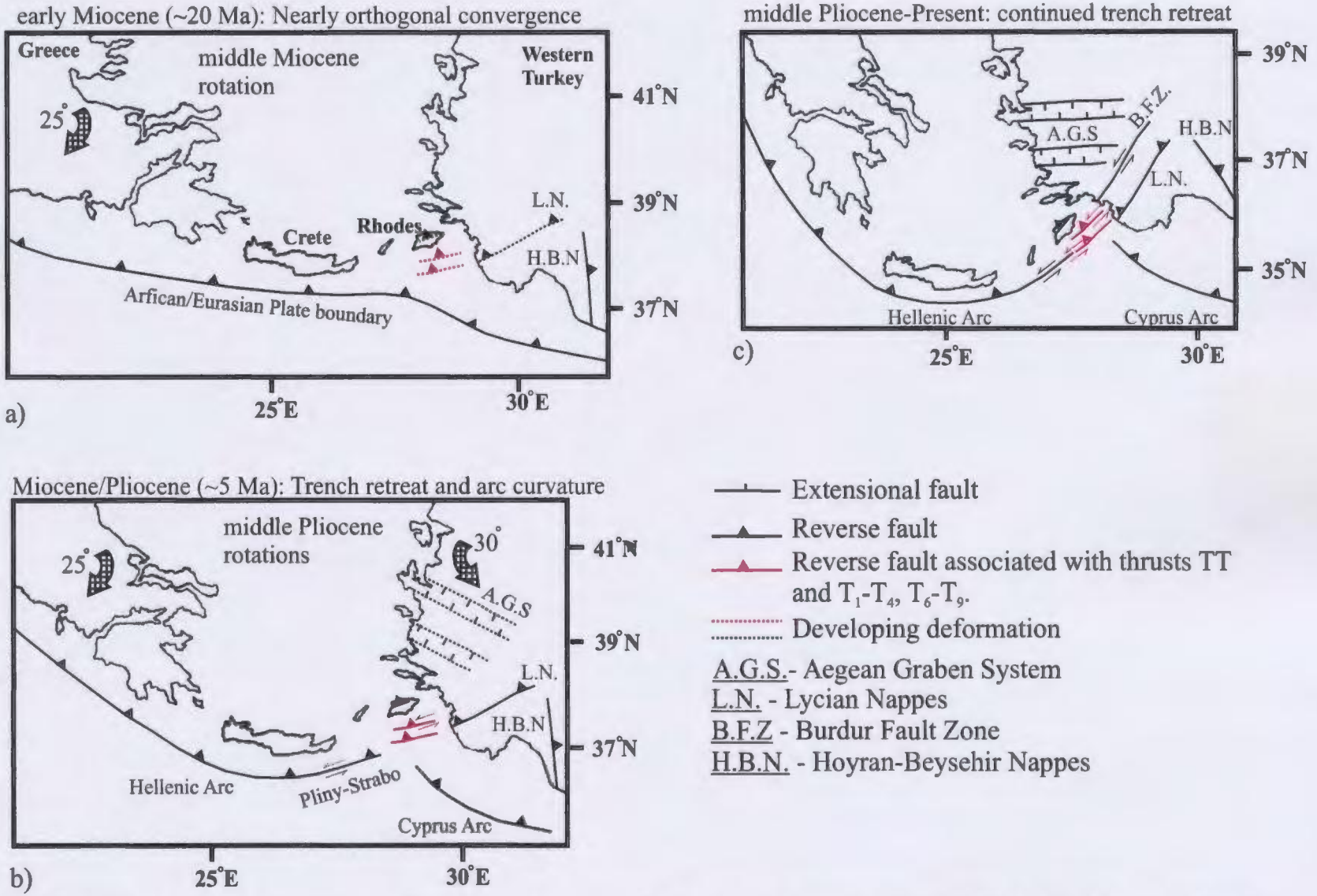

Figure 5.2.1: Schematic reconstruction of the early Pliocene and early Miocene architecture of the African/Eurasian convergence zone near the Rhodes Basin based on the Neogene rotations presented in Figure 1.4.5. Note the southward migration and increased curvature of the convergence zone since the Miocene. Rotations are assumed to occur around the centres Greece, Crete and western Turkey respectively. Structures are assumed to have roatated with the continental blocks.

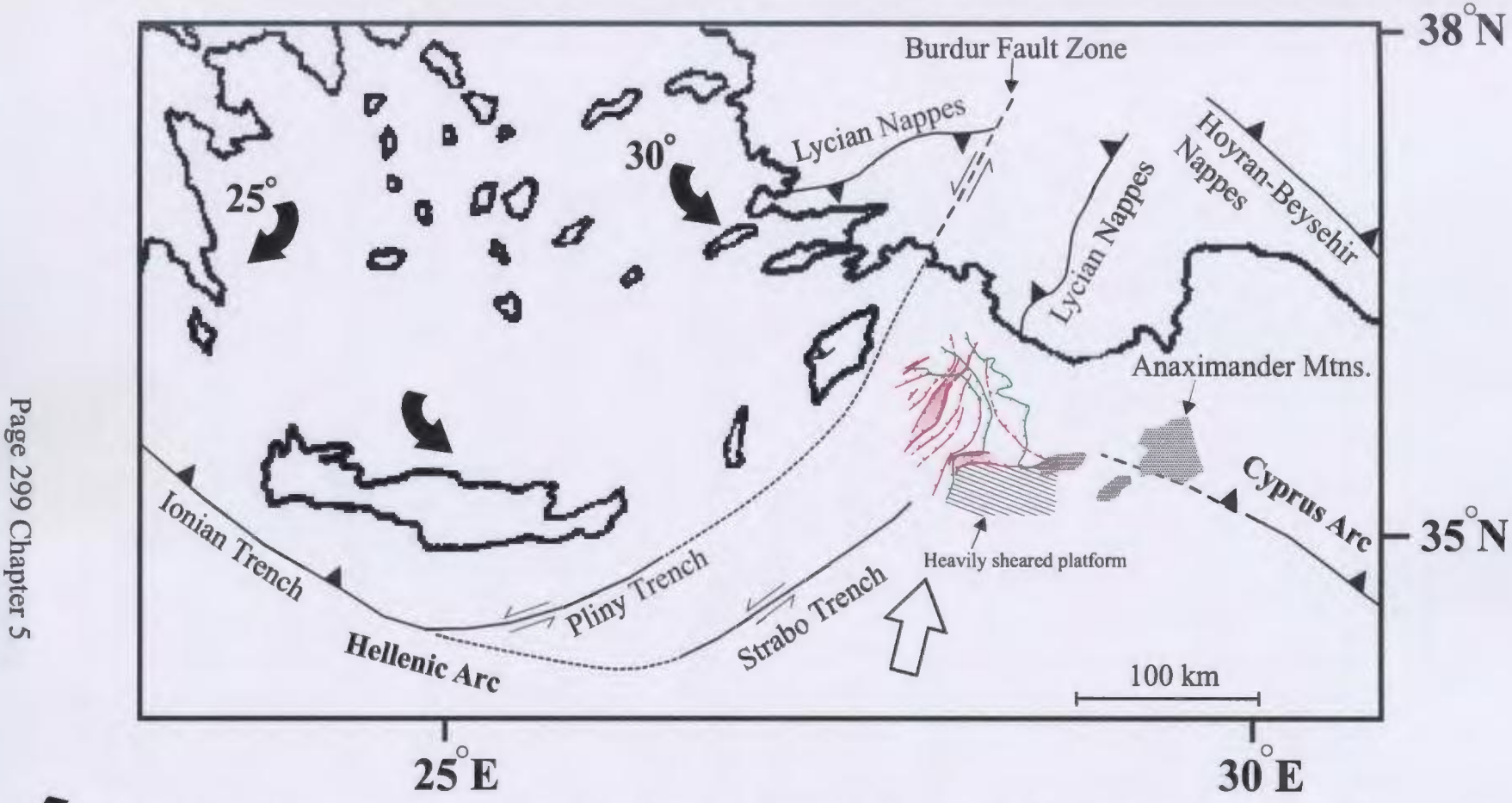

Sense of Plio-Quaternary rotation from Laj, Jamet et al. (1982), Duermeijer, Krijgsman et al. (1998) and Duermeijer, Nyst, et al. (2000)

Relative motion of the African Plate relative to a fixed Eurasian Plate.

Reverse Fault

Escarpment (?Extension?)

Positive flower structure

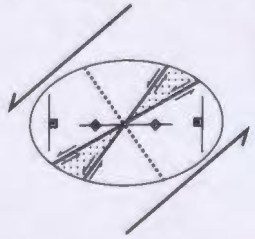

Main trend of deformation for sinistral shear (homogeneous substance).

Fig. 5.2.2: A map showing the major faults and escarpments mapped in the Rhodes Basin and their relationship to the intersection of the Hellenic and Cyprus Arcs along the African/Eurasian convergence zone. Base map modified from Kissel and Laj (1988).

Ben-Abraham, 1985). As such, the inferred Eurasian continental composition of Unit 1 within Domain 2 may contrast with that of Domain 1, accounting for their very different seismic character which may result from their different strain responses to the P_1 stress system. This proposed compositional contrast between Domain 1 (and the Anaximander Mountains) and the remainder of western Turkey and the Rhodes Basin conflicts with the interpretation presented by Zitter et al. (2003) who suggest that the Anaximander Mountains are blocks of Eurasian continental curst rifted from southern Turkey since the latest Miocene.

The north northwest-south southeast trend of thrust T_{11} contrasts sharply with the northeast-southwest trend of thrusts T_1-T_{10} and the Lycian Nappes (Fig. 5.2.2), indicating that the pre-late Messinian motion of thrust T_{11} was not likely activated by the middle-late Miocene P_1 compressive episode. Instead, its trend is more closely associated with that of the Hoyran-Beyşehir Nappes and may have been active during their emplacement during the Eocene-Oligocene (Fig. 5.2.2; Kissel et al., 1988).

A change from Messinian erosion to early-middle Pliocene sedimentation throughout the Rhodes Basin (and most of the eastern Mediterranean) may be associated with one, or both, of two major events: (1) regional subsidence due to the ~early Pliocene opening of the east-west-trending Aegean Graben System in western Turkey in response to the westward escape of the Anatolian/Aegean Microplate (Bozkurt, 2000). This period of north-south extension was likely assisted by a strong slab roll-back force from the steeply-subducting, oceanic crust beneath the southwardly-advancing Hellenic Arc (Fig.

5.2.1; Royden, 1993; McClusky and Balassanian, 2000) coupled with southward-directed gravitational body spreading of the thicker Aegean crust over the thin oceanic crust to its south (Martinod et al., 2000). (2) A rapid eustatic sea level rise around the time of the Miocene/Pliocene boundary (McKenzie et al., 1999) that may have introduced a large influx of seawater into the parched eastern Mediterranean. Because Subunit 2a is relatively isopachous and spans the vast majority of the Rhodes Basin (including the Turkish continental slope), it is argued that the Rhodes Basin subsided as a whole during the early Pliocene due to this regional subsidence, perhaps in combination with eustatic sea level rise and/or isotatic depression due to added seawater. The relatively isopachous lower portion of Subunit $2b_1$ may have also been deposited during this early-middle Pliocene episode of relative subsidence. McKenzie et al. (1999) interpret benthic oxygen isotope fluctuations acquired by the Schakleton et al. (1998) and Eberli et al. (1997) as eustatic glacial-interglacial oscillations with a dominant period of ~0.5Ma overprinted by shorter period, ~50,000 yr cycles. If the eastern Mediterrnean was indeed connected with the world oceans during the early to middle Pliocene, the clinoform packages sited in this study may be a sedimentological record of the shorter period cycles (Figs. 3.1.7, 4.2.19, 4.2.20).

During the early-middle Pliocene, the eastern limb of the curved Hellenic Arc was sufficiently oblique to the African/Eurasian convergence vector to prefer sinistral transpression rather than compression, resulting in the latest Miocene-early Pliocene development of the Pliny-Strabo trench system (Fig. 5.2.1; Peters and Huson, 1985; Ten

Veen and Kleinspehn, 2002). Although the Pliny Trench contains an array of *en échelon* basins that verify a sinistral sense of strike slip, the Strabo Trench is not as well-developed (younger, ?~middle Pliocene age?) and lies in bathymetric continuity with the southernmost portion of the Rhodes Basin (Peters and Huson, 1985). It is this link between the Rhodes Basin and Pliny-Strabo trench system that serves as the driving force for P_2 middle Pliocene-Present transpression within the Rhodes Basin. A strain ellipse shows that the rotated, middle Pliocene-Present P_1 fold/thrust trend is well-oriented to accommodate sinistral transpressional motion imposed by the Pliny-Strabo trench system (Fig. 5.2.2). Therefore, it is inferred that the P_1 fabric provides surfaces of weakness that are easily reactivated by northeast-southwest-oriented lateral motion. It is this middle Pliocene transpression that likely initiated the rapid, early-middle Pliocene subsidence of the Rhodes Basin as evidenced by the now-drowned clinoform packages along the Turkish continental slope (Figs. 4.2.19, 4.2.20, 5.1.1, strain ellipse 5.2.2).

On land, the Burdur Fault Zone is a young (late Pliocene) lateral fault system with a strong component of extension (Price and Scott, 1994). There is debate regarding whether this broad fault zone accommodates sinistral or dextral strike slip motion (e.g., Price and Scott, 1994; Barka et al., 1995). However, given its location northeast of the Pliny-Strabo trench system and Rhodes and late Pliocene time of activation, it is likely that the Burdur Fault Zone accommodates sinistral strike slip motion. Hence, the Pliny-Strabo trench system, Rhodes Basin and Burdur Fault Zone may represent the northeast propagation of sinistral strain during the early, middle and late Pliocene respectively.

The trend of thrust T_{11} is ~60° off from the trend of compressional faults expected to form by the P_2 transpressional stress field (Fig. 5.2.2). Therefore, its middle Pliocene motion is not likely associated with the northeast propagation of the Pliny-Strabo trench system. Hence, it is more likely that middle Pliocene uplift along the eastern margin of the Rhodes Basin is due to compression along the western limb of the Cyprus Arc (e.g., Florence Rise; Woodside et al., 2002).

Based on the above interpretation, the Rhodes Basin is a transpressional basin trapped between the vice-like convergence of the Hellenic and Cyprean Arcs. The acute geometry of the intersection between the Hellenic and Cyprus arcs near the Rhodes Basin is similar to that observed to the north where the Izmir-Ankara suture and Isparta Angle have accommodated ocean closures in the past (Fig. 5.2.3; Robertson, 2000; Barka, Reilinger et al., 1995). By comparison, then, it is probable that the African/Eurasian collision in the vicinity of the Hellenic and Cyprus Arcs is also near its terminal collision.

5.3: A Comparison with the Japanese Arc-Arc junction

From previous works (e.g., Kimura, 1986; Ida, 1991; Kamata and Kodama, 1994; and Mazzotti et al.,1999), the intensity and rate of strain at the intersection between the Suruga and Sagami troughs is greater than that of the southwest Kuril/northeastern Japan arc or Ryukyu/southwest Japan arc junctions (Fig 5.3.1) (Mazzotti et al. 1999; Kamata and Kodama, 1994). The most obvious difference between these arc junctions is the degree of curvature at their intersection point: the angle between the Kuril Arc and

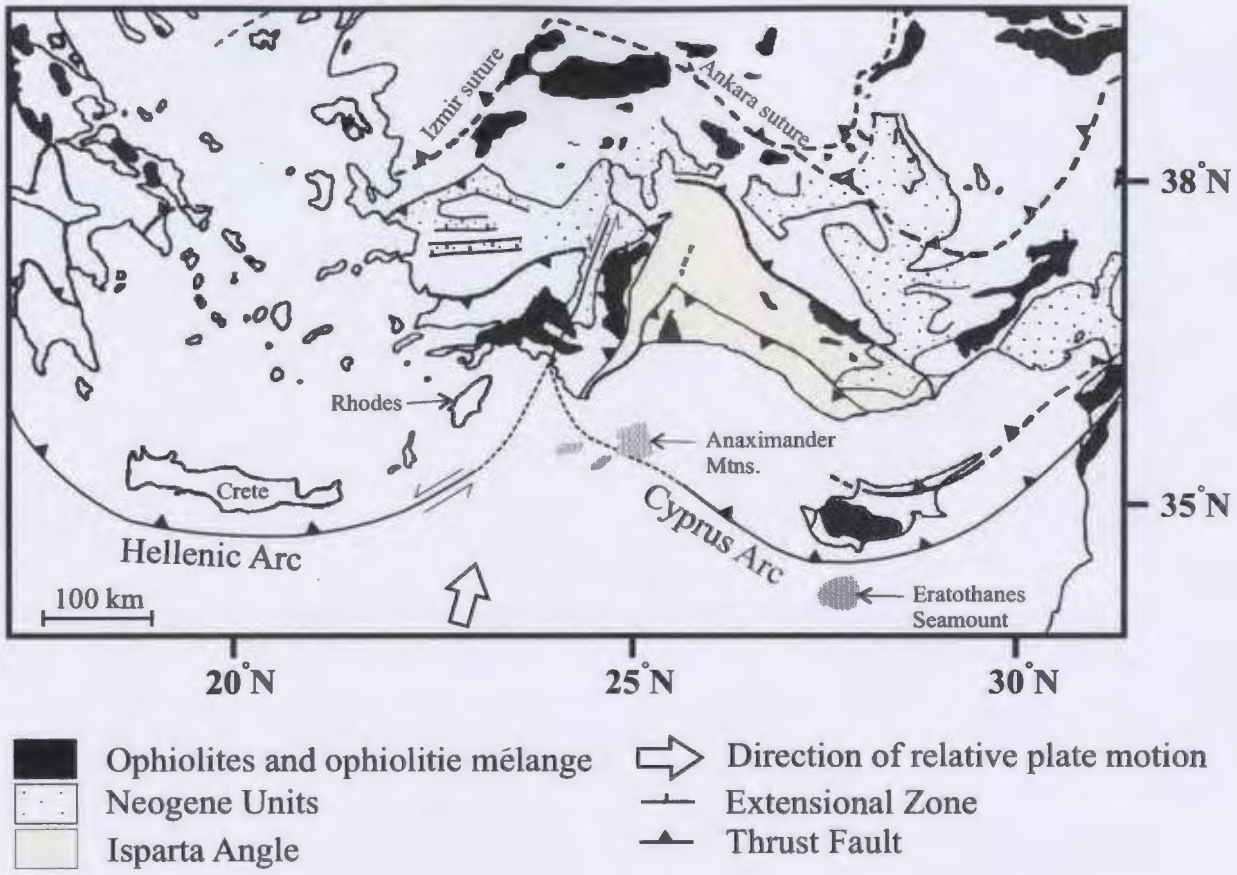

Figure 5.2.3: The Hellenic and Cyprus Arcs link in a tight corner similar to the geometry of the Isparta Angle and Izmir-Ankara suture. Hence, in this geographically small region there is preserved evidence of ancient terminal collisions as well as a still-active one. Figure modified from Robertson (2000).

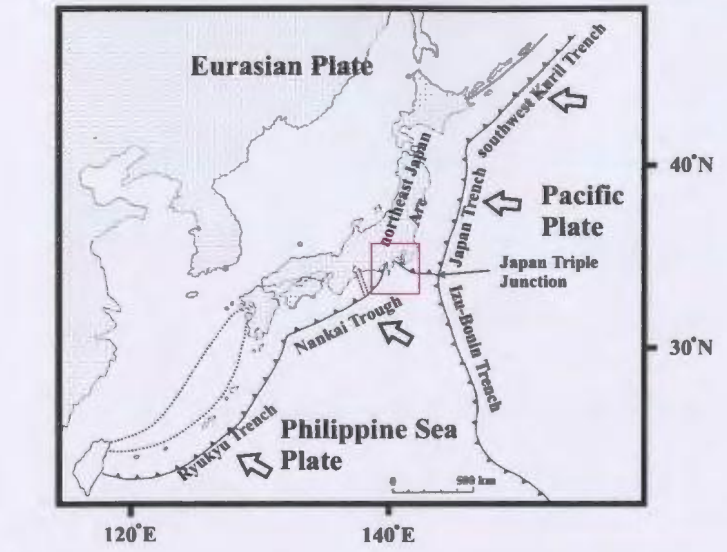

a)

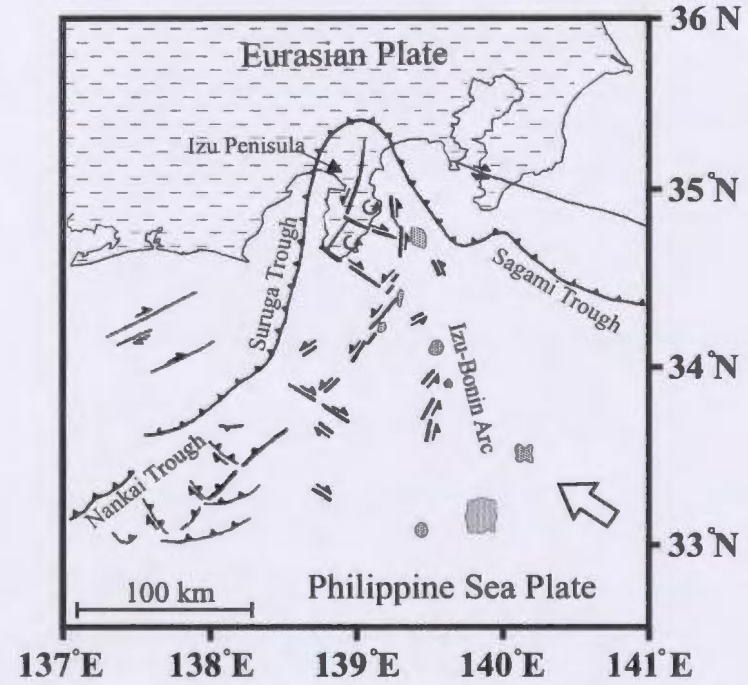

b)

Figure 5.3.1: a) The Japan triple junction illustrating the major troughs associated that form arc junctions. b) The highly curved junction between the Sagami and Suruga troughs. Note the presence of counterclockwise rotation and strike slip faulting as a result of divergent subdution along each trough. Figures modified from Mazzotti et al. (1999) and Kamata and Kodama (1994).

northeastern Japan Arc as well as that between the Ryukyu Arc and southwest Japan Arc being greater than 90° while the angle between the Suruga and Sagami troughs is significantly less than 90° (Figs. 5.2.3, 5.3.1). The intersection of the Hellenic and Cyprus arcs also forms an angle of approximately 90° (or less). Furthermore, the breadths of the Suruga/Sagami trough junction and the Hellenic/Cyprus Arc junction are similar (~350-400 km wide) (Figs. 5.2.3, 5.3.1). Hence, both junctions have been developing as tight corners during the Pliocene. These morphological similarities between the arc Suruga/Sagami and Hellenic/Cyprus arc junctions suggest that they may represent similar stages of arc evolution.

Due to the close proximity of differently oriented structures near strongly curved arc junctions, incompatible strain relationships both near the Izu Peninsula and the Hellenic/Cyprus arc junction has resulted in rapid Pliocene rotation and strike slip deformation (Ida, 1991; Mazzotti et al., 1999; Duermeijer et al., 2000; Huchon et al., 1982; Peters and Huson, 1985). There are, however, noteworthy differences between the Japanese and eastern Mediterranean examples of arc junctions. The Suruga trough accommodates nearly orthogonal subduction (Fig. 5.3.1). The Sagami trough also allows subduction, possibly assisted by slab pull forces and 'tearing' of the Philippine Sea Plate along the thermally-weakened Izu-Bonin Arc (Mazzotti et al. 1999). In contrast, the eastern Hellenic Arc accommodates sinistral transpression. Despite near orthogonal convergence between the western Cyprus Arc and the African Plate, the western Cyprus Arc appears locked in transpression associated with resistance to subduction by the

Eratothanes Seamount and Anaximander Mountains- possibly including the elevated, heavily sheared plateau identified in this study (Woodside, 2002). It seems reasonable to infer, then, that the sub-parallel orientation of zone of weakness (e.g., Izu-Bonin Arc) to subducting trenches has encouraged rapid subduction, whereas blocks of thick crust such as the Anaximander Mountains and Eratothanes Seamount that collide orthogonally with tectonic plate boundaries impede subduction processes and therefore introduce an asymmetrical component and different course of evolution.

5.4: Major Contributions of this Study

Work done by others in and near the Rhodes Basin (Woodside et al., 2000, Ten Veen and Kleinspehn, 2002; Zitter et al., 2003) has been based on structural trends extrapolated from the fringes of adjacent locations (e.g., Isparta Angle, Pliny-Strabo trench system and Anaximander Mountains) and sparse seismic data correlated with swath bathymetry. Hence, although a northeast-southwest structural trend and rapid Pliocene subsidence of the Rhodes Basin had been proposed previous to this study (e.g., Woodside et al., 2000), there has been little direct supporting evidence of these claims from data derived in the Rhodes Basin itself. For example, Woodside et al. (2000) rely on the non-existence of structures on adjacent seismic profiles to infer structural trends the absence of Messinian evaporates to argue rapid post-Messinian subsidence. On the basis of the amount of data collected, the area of the Rhodes Basin covered by the survey and the balanced representation of two, nearly orthogonal, survey line orientations, the multi-

channel source seismic coverage of the Rhodes Basin acquired for this thesis is superior to that acquired by Woodside et al. (2000) and Zitter et al. (2003). As a result, the structural and stratigraphic interpretations of the Rhodes Basin presented here are the most complete of any published to date- providing unprecedented, direct, structural and stratigraphic evidence of southeast-verging, pre-late Messinian thrusting, late Messinian erosion, laterally extensive Pliocene-Quaternary transpressional reactivation of pre-Messinian structures and rapid, post-Messinian (early-middle Pliocene) subsidence.

Other contributions of this study to the understanding of the Rhodes Basin and its relationship with the intersection between the Hellenic and Cyprus arcs includes the identification of three structural domains that each have very different structural and stratigraphic architectures. In the case of the Domain 1/Domain 2 boundary, the sharp contrast may be the result of a compositional contrast between their basements (?crust?) and subsequent resistance to the transmittance of thrust TT toward the south. Because the southern extremity of the Rhodes Basin, interpreted by Woodside et al. (2000) to be dominated by Pliocene northward-verging nappe development, was not sampled by the 2001 seismic survey it is not included in the structural domains of this thesis.

Major crustal-scale structures, such as thrust TT and its first-order influences on the morphology of the M reflector, stratigraphic architecture of Pliocene-Quaternary basin fill and present-day tilt of the sea floor within the Rhodes Basin have each been entirely undetected by previous studies of the Rhodes Basin- clearly demonstrating the inadequacy of earlier data coverage (e.g., Woodside et al., 2000). In addition, this thesis proposes that

there may be genetic link between the Turkish continental slope and the western limb of the Cyprus Arc, implying that the intersection between the Hellenic and Cyprus Arcs may occur within the Rhodes basin itself rather than inland Turkey as suggested by Zitter et al. (2003).

5.5: Recommendations for Further Study

The 2001 multi-channel seismic survey provides a broad coverage of the Rhodes Basin. This precursory study was sufficient to identify major structures, their trends and place broad time constraints on two major episodes of punctuated deformation that has permitted the Rhodes Basin to be interpreted in the context of its tectonic setting and relationship with adjacent structural trends (e.g., Pliny-Strabo Trench, Burdur Fault Zone and Island of Rhodes). However, the structural analysis provided in this study were limited by two factors: (1) the shallow penetration depth of the seismic source limits the confidence with which structural and stratigraphic architectures below the M reflector can be identified and interpreted, and (2) the coarseness of the survey grid makes structural and stratigraphic correlations away from survey cross-over points difficult, especially in areas where structure is complex and sediment cover is thin.

Many of the structures identified and interpreted in this study likely represent the superficial expression of more deeply-rooted, crustal scale features associated with strike-slip reactivation and rotation of pre-existing fold-thrust fabrics. As such, their morphology is complex and cannot be well understood in two dimensions. To adequately

sample these structures, survey line spacing must not exceed 5 km- requiring three additional seismic lines between those of the 2001 seismic survey. Although such an approach would increase correlation confidence and provide an improved sense of basin and ridge morphology, it may not contribute much toward understanding their deeply-rooted, causative, crustal-scale structures. For this reason, it would be preferable to acquire deep-crustal seismic lines between the 2001 survey lines, with large receiver offsets. Such an approach would improve the spatial sampling of the shallow Pliocene-Quaternary structures, provide new and valuable information regarding the architecture of the deeply-rooted structures that link them and increase the precision with which seismic velocities for units at shallow and intermediate depths could be determined. In addition, deep crustal imaging would help determine how regional subsidence along the steeply-inclined, Turkish continental slope has been accommodated and provide a means by which the northeast-southwest-tending structural fabric of the deep Rhodes Basin could more easily be traced across the Turkish continental slope to link with the Fethiye-Burdur Fault Zone. It may also be of benefit to collect wide angle seismic or refraction seismic over both the uplifted, heavily sheared platform (Domain 1) and faulted and folded deep Rhodes Basin (Domain 2) to get an indication of whether the seismic velocity (?composition?) of Unit 1 and the crustal basement changes across the Domain 1/Domain 2 boundary. The acquisition of both magnetic and gravity data during seismic data collection would be of benefit by providing additional constraint for any modelling procedures that would be of benefit to attempt.

Bibliography

Aksu, A. E., T. J. Calon, T. J., Piper, D. J. W., Turgut, S., Izdar, E. 1992. Architecture of late orogenic Quaternary basins in northeastern Mediterranean Sea. Tectonophysics, 210, 191-213.

Aksu, A. E., Uluğ, A., Piper, D. J. W., Konuk, Y. T., Turgut, S. 1992. Quaternary sedimentary history of Adana, Cilicia and Iskenderun Basins, northeastern Mediterranean Sea. Marine Geology, 104, 55-71.

Anastasakis, G., Kelling, G. 1991. Tectonic connection of the Hellenic and Cyprus arcs and related geotectonic elements. Marine Geology, 97, 261-277.

Barka, A. 1999. The 17 August 1999 Izmit earthquake. Science, 285, 5435, 1858-1859.

Barka, A., Reilinger, R., Şaroğlu, F., and Şengör, C. 1995. The Isparta Angle: Its importance in the neotectonics of the eastern Mediterranean region. In: Pişkin, O., Ergün, M., Savaşçin, M, Tarcan, G. (Eds.), International Earth Sciences Colloquium on the Aegean Region, p. 3-18, 9-14 October, 1995 Izmir-Golluk, Turkey.

Beach, A., Trainer P. 1991. The geometry of normal faults in a sector of the offshore Nile Delta, Egypt. In: Roberts, A.M., Yielding, B., Freeman, B. (Eds.), The Geometry of Normal Faults (p. 173-182). Geological Society Special Publication 56.

Ben-Avraham, Z., Ivanov, M., Leybov, M., Limonov, A., Tibor, G., Tokarev, Yu., M., Woodside, J. 1995. Structures and tectonics of the eastern Cyprean Arc. Marine and Petroleum Geology, 12, 3, 263-271.

Bernard, C., Phillipe, Y., Letouzey, J., Richert, J., P., Chermette, J., C., Specht, M. 1995. Experimental models of thrust belt fronts. AAPG Bulletin, 79, 8, 1204.

Bozkurt, E. 2000. Timing of extension on the Büyük Menderes Graben, western Turkey, and its tectonic implications. In Bozkurt, E., Winchester, J. A. and Piper, J. D. A.. Tectonic and Magmatism in Turkey and the Surrounding Area (p.385-403). London: Geological Society of London.

Bozkurt, E., Mittewede, S., 2001. Introduction to the geology of Turkey - A synthesis. International Geology Review, 43, 578-594.

Collins, A., Robertson, A. 1998. Processes of late Cretaceous to late Miocene episodic thrust - sheet translation in the Lycian Taurides, SW Turkey. Journal of the Geological Soceity, London, 155, 759-772.

Crittenden, M. D., Coney, P. J., Davis, G. H., (Eds.), 1980. Tectonic significance of metamorphic complexes of the North American Cordillera. Memoirs of the Geological Society of America, 153, 490.

Delibasis, N., Ziazia, M., Vulgaris, N., Papadopoulos, T., Stavrakais, G., Papanastassiou, D., Drakatos, G., 1999. Microseismic activity and seismotectonics of Heraklion Area (central Crete Island, Greece). Tectonophysics. 308, 237-248.

Doutsos, T., Kokkalas, S., October 2001a (Oct.). Stress and deformation patterns in the Aegean region. Journal of Structural Geology, 23, 455-472.

Doutsos, T., Kokkalas, S., 2001b (Feb.). Strain-dependent stress field and plate motions in the south-east Aegean region. Journal of Geodynamics, 32, 3, 311-332.

Duermeijer, C.E, Krijgsman, W., Langereis, C. G., Meulenkamp, J.E., Triantaphyllou, M. V., Zachariasse, W. J. 1999. A late Pleistocene clockwise rotation phase of Zakynthos (Greece) and implications for the evolution of the western Aegean Arc. Earth and Planetary Science Letters, 173, 315-331.

Duermeijer, C. E., Krijgsman, W., Langereis, C. G., Ten Veen, J. H. 1998. Post-early Messinian counterclockwise rotations on Crete: implications for Late Miocene to Recent kinematics of the southern Hellenic Arc. Tectonophysics, 298, 177-189.

Duermeijer, C. E., Nyst, M., Meijer, P. T., Langereis, C. G., Spakman, W. 2000. Neogene evolution of the Aegean arc: paleomagnetic and geodetic evidence for a rapid and young rotation phase. Earth and Planetary Science Letters, 176, 509-525.

Dziewonski, A. M., Chou, T. A., Woodhouse, J. H. 1981. Determination of earthquake source parameters from waveform data for studies of blobal and regional seismicity. Journal of Geophysical Research, 86, 2825-2852.

Eberli, G. P., Swart, P. K., Malone, M. J., et al. 1997. Proceedings of the ODP initial Reports, 166, College Station TX (Ocean Drilling Program).

Faill, R. T. 1973. Kink band folding, Valley and Ridge province, Pennsylvania. Geological Society of America Bulletin, 84, 1289-1314.

Fauteuil, O., Mart, Y. 1998. Analogue modelling of faulting pattern, ductile deformation and vertical motion on strike-slip fault zones. Tectonics, 17, 2, 303-310.

Fischer, M. P., Woodward, N. B., Mitchell, M. M. 1992. The kinematics of break-thrust folds. Journal of Structural Geology, 14, 451-460.

Galindo-Zaldivar, J., Nitto, L., Woodside, J. 1996. Structural features of mud volcanoes and the fold system of the Mediterranean Ridge, south of Crete. Marine Geology, 132, 95-112.

Gibbs, A. D., 1984. Structural evolution of extensional basin margins. Journal of the Geological Society, 141, 609-620.

Glover, C., Robertson, A. 1998. Neotectonic intersection of the Aegean and Cyprus tectonic arcs: extensional and strike-slip faulting in the Isparta Angle, SW Turkey. Tectonophysics, 298, 103-132.

Hanken, N., Bromley, R. G., Miller, J. 1996. Plio-Pleistocene sedimentation in coastal grabens, north-east Rhodes, Greece. Geological Journal, 31, 393-418.

Harding, T. P. 1985. Seismic characteristics and identification of negative flower structures, positive flower structures and positive structural inversion. AAPG Bulletin, 69, 4, 582-600.

Hiscott, R. N. 2001. Depositional sequences controlled by high rates of sediment supply, sea-level variations, and growth faulting: the Quaternary Baram Delta of northwestern Borneo, Marine Geology, 175, 67-102.

Huchon, P., Lybéris, N., Angelier, J., Le Pichon, X., Renard, V. 1982. Tectonics of the Hellenic Trench: A Synthesis of Sea-beam and submersible observations, 86, 69-112.

Huguen, C., Mascle, J., Chaumillon, E., Woodside, J., Benkhelil, J., Kopf, A., Volkonskaïa, A. 2001. Deformational styles of the eastern Mediterranean Ridge and surroundings from combined swath mapping and seismic reflection profiling. Tectonophysics, 343, 21-47.

Imber, J., Childs, C., Nell, P. A. R., Walsh, J. J., Hodgetts, D., Flint, S. 2003. Hanging wall fault kinematics and footwall collapse in listric growth fault systems. Journal of Structural Geology, 25, p. 197-208.

Ida, Y. 1991. Interpretation of Seismic and Volcanic Activities in the Izu Block in Relation to Collision Tectonics. Journal of Physics of the Earth, 39, 421-440.

Jackson, J. 1994. Active Tectonics of the Aegean Region. Annual Review of Earth and Planetary Sciences, 22, 239-271.

Jackson, J., McKenzie, D. 1988. The relationship between plate motions and seismic moment tensors, and the rates of active deformation in the Mediterranean and Middle East, Geophysical Journal of the Royal Astronomical Society, 93, 45-73.

Jamison, W. R. 1987. Geometric analysis of fold development in over thrust terranes. Journal of Structural Geology, 9, 207-219.

Kale, H., Coward, M., Peter, Y., Geiger, A., Reilinger, R., McClusky, S., King, R., Barka, A, Veis, G. 1999. The GPS strain rate field in the Aegean Sea and western Anatolia. Geophysical Reasearch Letters, 26, 16, 2513-2516.

Kamata, H., Kodama, K. 1994. Tectonics of and arc-arc junction: an example from Kyushu Island at the junction of the Southwest Japan Arc and Ryukyu Arc. Tectonophysics, 233, 69-81.

Kimura, G., 1986. Oblique subduction and collision: Forarc tectonics of the Kuril arc. Geology, 14, 404 - 407.

Kissel, C., Averbuch, O., Frizon de Lamotte, D., Monod, O, Alberton, S. 1993. First paleomagnetic evidence for a post-Eocene clockwise rotation of the Western Taurides thrust belt east of the Isparta rentrant (Southwestern Turkey). Earth and Planetary Science Letters, 117, 1-14.

Kissel, C., Laj, C. 1988. The Tertiary geodynamical evolution of the Aegean arc: a paleomagnetic reconstruction. Tectonophysics, 146, 183-201.

Laj, C., Jamet, M., Sorel, D., Valente, J. P. 1982. First Paleomagnetic results from Mio - Pliocene series of Hellenic sedimentary arc. Tectonophysics, 86, 45-67.

Lazear, G., 1993. Mixed wavelet estimation using fourth-order cumulants. Geophysics, 58, 7, 1042-1051.

Lister, G. S., Etheridge, M. A., Symonds, P.A., 1991. Detachment models for the formation of passive continental margins, Tectonics, 10, 5, 1038-1064.

Lopez, J. E., 1990. Structural styles of growth faults in the U.S. Gulf Coast Basin. In: Brooks, J. (Ed.), Classic Petroleum Provinces, (p. 203-219). Geological Society Special Publication 50.

Mantovani, E., Viti, M., Cenni, N., Albarello, D., Babbucci, D. 2001. Short and long term deformation patterns in the Aegean-Anatolian systems: insights from space geodetic data (GPS). Geophysical Reasearch Letters. 28, 12, 2325-2328.

Martinod, J., Hatzfeld, D., Brun, J., Davy, P., Gautier, P. 2000. Continental collision, gravity spreading, and kinematics of Aegea and Anatolia. Tectonics, 19, 2, 290-299.

Mascle, J., Le Cleach'h, A., Jongsma, D., 1986. The eastern Hellenic margin from Crete to Rhodes: Example of progressive collision. Marine Geology, 73, 145-168.

Mazzotti, S., Henry, P., Le Pichon, X., Sagina, T., 1999. Strain Partitioning in the zone of transition from Nankai subduction to Izu-Bonin collision (Central Japan): implications for an extensional tear within the subducting slab. Earth and Planetary Science Letters, 172, 1-10.

McClay, K. R., Ellis, P. G., 1987. Geometries of extensional fault systems developed in model experiments. Geology, 15, 4, 341-344.

McClusky, S., Balassanian, S., Barka, A., et al. 2000. Global positioning system constraints on plate kinematics and dynamics in the eastern Mediterranean and Caucasus. Journal of Geophysical Research, 105, 5695-5719.

McKenzie, J., Spezzaferri, S., Isern, A., 1999. The Miocene-Pliocene boundary in the Mediterranean Sea and Bahamas: Implications for a global flooding event in the earliest Pliocene. Memorie della Societa Geologica Italiana, 54, 93-108.

Mitchell, M. M., Woodward, N.B., 1988. Kink detachment fold in the southwest Montana fold and thrust belt. Geology, 16, 165-165.

Papazachos, C. B. 1999. Seismological and GPS evidence for the Aegean-Anatolia interaction. Geophysical Reasearch Letters. 26, 17, 2653-2656.

Papazachos, B., Karakostas, V., Papazachos, C., Scordilis, E. 2000. The geometry of the Wadati - Benioff zone and lithospheric kinematics in the Hellenic Arc. Tectonophysics, 319, 275-300.

Park, R.G. (1997). Foundations of structural geology. 3rd edition. London; New York: Chapman and Hall (1997).

Peters, J., Huson, W. 1985. The Pliny-Strabo trenches (eastern Mediterranean): Integration of seismic reflection data and seabeam bathymetric maps. Marine Geology. 64, 1-17.

Price, P., Scott, B. 1994. Fault block rotations at the edge of a zone of continental extension; southwest Turkey. Journal of Structural Geology, 16, 3, 381-392.

Robertson, A. H. F. 2000. Mesozoic-Tertiary tectonic-sedimentary evolution of a south Tethyan oceanic basin and its margins in southern Turkey. In Bozkurt, E., Winchester, J. A. and Piper, J. D. A.. Tectonic and Magmatism in Turkey and the Surrounding Area (p.97-139). London: Geological Society of London.

Richard, P. and Krantz, W., 1991. Experiments on fault reactivation in strike-slip mode. Tectonophysics, 188, 117-131.

Robertson, A., Woodcock, N. 1986. The role of the Kyrenia Range linement, Cyprus, in the geological evolution of the Eastern Mediterranean area. Philosophical Transactions of the Royal Society of London, Series A.317, 141-177.

Rotstein, Y., Ben-Avraham, Z. 1985. Accretionary processes at subduction zones in the eastern Mediterranean. Tectonophysics, 112, 551-561.

Royden, L., 1993. Evolution of the retreating subduction boundaries formed during continental collision. Tectonics, 12, 303-325.

Ryan, W. B. F., 1969. The floor of the Mediterranean Sea. Ph. D. Thesis, Columbia Univ., N.Y..

Ryan, W., Hsü, K., Cita, M., Dumitrica P., Lort, J., Maync, W., Nester off, W., Pautot, G., Strainer, H., Wezel, F. 1973. Initial Reports of the Deep Sea Drilling Project, 13. U.S. Government. Printing Office, Washington, D.C., 1-1455.

Ryan, W. B. F., Stanley, D. J., Hersey, J. B., Fahlquist, D. A., Allan, T. D., 1970. The tectonics and geology of the Mediterranean Sea. In: Maxwell A. E. (ed.), The Sea (p. 387-392). New York: John Wiley & Sons.

Schakleton, N. J., Hall, M. A., Pate, D., 1998. Pliocene stable isotope stratigraphy of Site 846. In: Pisias, N. G., Mayer, L., A., et al. (Eds.), Proceedings of the ODP, Scientific Results, 138, College Station, TX (Ocean Drilling Program), 337-356.

Schreurs, G., 1994. Experiments on strike-slip faulting and block rotation. Geology, 22, 567-570.

Seyitoğlu, G. and Scott, B. C.1991. Late Cenozoic extension and basin formation in west Turkey. Geological Magazine. 128, 155-166.

Seyitoğlu, G. and Scott, B. C.1992. The age of Büyük Menderes Graben (west Turkey) and its tectonic implications. Geological Magazine, 129, 239-242.

Shaw, J. H., Suppe, J., 1994. Active faulting and growth folding in the eastern Santa Barbara Channel, California. Geological Society of America Bulletin, 106, 607-626.

Shelton, J. W., 1984. Listric normal faults: an illustrated summary. The American Association of Petroleum Geologists Bulletin, 68, 7, 801-815.

Sorti, F., Pablet, J., 1997. Growth stratal architectures associated to decollement folds and fault-propagation folds. Inferences on fold kinematics. Tectonophysics, 282, 353-373.

Steininger, F. F. and Rögl, F. 1984. Palaeogeography and palinspastic reconstruction of the Neogene of the Mediterranean and Paratethys. In Dixon, J. E. and Robertson, A. H. F.. The Geological Evolution of the Eastern Mediterranean. (p. 659-668), Geological Society, London, Special Publications, 14.

Suppe, J. 1983. Geometry and kinematics of fault-bend folding. American Journal of Science. 283, 684-721.

Suppe, J., Chou, G. T., Hook, S. C., 1992. Rates of folding and faulting determined from growth strata. In: McClay, K.R. (Ed.), Thrust Tectonics. (p. 105-121), Chapman and Hall, London.

Suppe, J., Medwedeff, D. A., 1984. Geometry and kinematics of fault-propagation folding. Eclogae Geol. Helv. 83, 409-454.

Taviani, M., Rossi, S. 1989. Salt-related deformations in the deep Antalya Basin: Preliminary results of the Mac Gan Cruise, Marine Geology, 87, 1, 5-13.

Ten Veen, J. H. and Kleinspehn, K. L. 2002. Geodynamics along an increasingly curved convergent plate margin: Late Miocene-Pleistocene Rhodes, Greece. Tectonophysics. 21, 3, **8**-1 - **8**-21.

Ten Veen, J. H. and Postma, G. 1999. Roll-back controlled vertical movements of outer-arc basins of the Hellenic subductions Zone (Crete-Greece). Basin Research. 11, 243-266.

Walcott, C.R., White, S.H. 1998. Constraints on the kinematics of post-orogenic extension imposed by stretching lineations in the Aegean region. Tectonophysics, 298, 155-175.

Woodside, J., Mascle, J., Huguen, C., Volkonskaia, A. 2000. The Rhodes Basin, a post - Miocene tectonic trough. Marine Geology, 165, 1-12.

Woodside, J. Mascle, J., Zitter, T., Limonov, A., Ergün, M., Volkonskaia, A. 2002. The Florence Rise, the Western Bend of the Cyprus Arc. Marine Geology, 185, 175-194.

Zitter, T., Woodside, J., Mascle, J., 2003. The Anixmander Mountains: a clue to the tectonics of southwest Anatolia. Geological Journal, 38, 375-394.

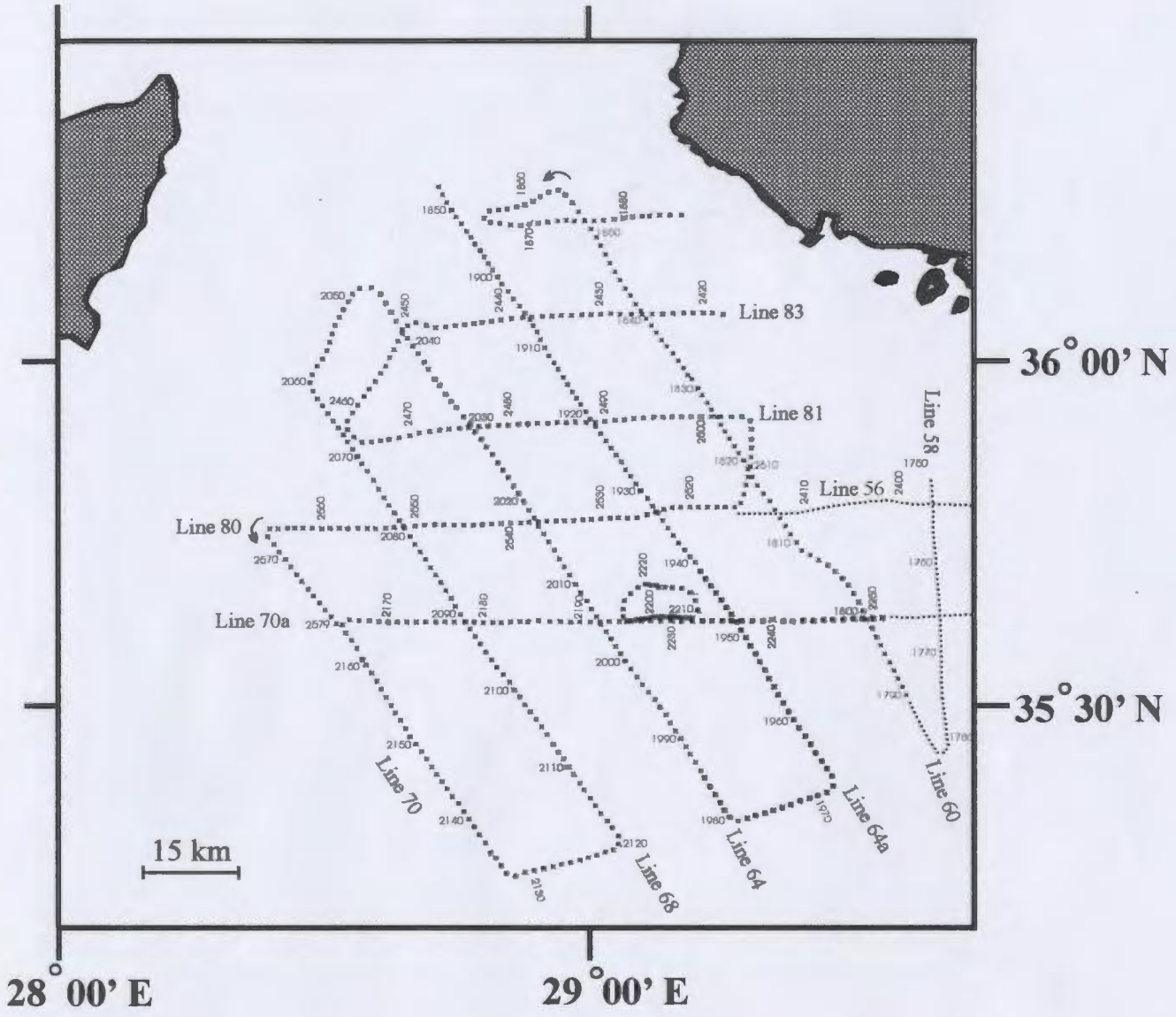

..... 2001 survey lines not processed by the author.

..... 2001 survey lines processed by the author.

A Map of the survey area showing the seismic lines acquired over the Rhodes Basin during the 2001 cruise. Line numbers and location (fix) numbers are shown.